THE UNIVERSITY *of* EDINBURGH

The Influence of Adhesive Curing Temperature upon the Performance of FRP Strengthened Steel Structures at Ambient and Elevated Temperatures

Daryan Jalal Othman

A thesis submitted to the institute of infrastructure and environment

in partial fulfilment of the requirements for the Degree of

Doctor of Philosophy

The University of Edinburgh

2016

Daryan Jalal Othman: *The Influence of Adhesive Curing Temperature upon the Performance of FRP Strengthened Steel Structures at Ambient and Elevated Temperatures*, Doctor of Philosophy, 2016

Declaration

I hereby declare that the thesis entitled

"*The Influence of Adhesive Curing Temperature upon The Performance of FRP Strengthened Steel Structures at Ambient and Elevated Temperatures*"

and the work reported in the thesis, with the exception sources of help, which have been acknowledged, were originated entirely by myself, under the supervision of Dr Tim Stratford in the School of Engineering at The University of Edinburgh.

I, also, confirm that except the following conference publications, which are made accessible to the researches via The University of Edinburgh Research Explorer online system, and presentations, the content of this document has previously not been submitted for any other degree or professional qualification

- Othman, D., Stratford, T. J., Bisby, L. A., "The Impact of Adhesive Conditioning upon Glass Transition Response", In: Advanced Composites in Construction 2013, Belfast (on CD), 10 – 12 September 2013.

- Othman, D., Stratford, T. J., Bisby, L. A., "A Comparison of On-Site and Elevated Temperature Cure of an FRP Strengthening Adhesive", In: *Proceedings of Fibre Reinforced Polymer Reinforced Concrete Structures FRPRCS 11th, Porto (on CD), 26-28 June 2013.*

- Othman, D. "Analysis of the Interfacial Stresses in an FRP to Metallic Subtract Adhesive Joint Subjected to Warm Temperatures", In: *Joining Technologies for Fibre-Reinforced Polymer Composite Materials, University of Warwick Thursday 8th May 2014.*

Glasgow, 2016

Abstract

The structural adhesives widely used in structural strengthening applications are thermoset ambient cure adhesive polymers. At ambient temperatures, these polymers are in a relatively hard and inflexible state. At higher temperatures, the material becomes soft and flexible. The region where the molecular mobility changes dramatically is known as the glass transition temperature T_g and often is presented as a single value. Epoxy polymers exhibit a significant reduction in mechanical properties near glass transition temperature T_g when they are exposed to elevated temperatures. Glass transition temperature T_g is used to characterise the change in epoxy adhesive properties with changing temperature. The mechanical properties of epoxies tend to improve with curing temperature. This is because the crosslink density between the adhesive molecular structures increases during the curing process consequently the T_g improves.

The aims of this work are first to demonstrate the importance of curing temperature. Second, to investigate the influence of glass transition temperature T_g improvement on the performance of EB-FRP strengthened steel structures in flexure at ambient and elevated temperatures. Third, to compare analytical results with experimental results from the flexure tests results. Finally, to compare the current design guideline recommendations with the flexure tests results.

The most commonly used methods to evaluate T_g Dynamic Mechanical Analysis (DMA) and Differential Scanning Calorimetry (DSC) were used to study T_g. Two off-shelf structural adhesives were investigated to understand their property variation with temperature. Epoxy coupons were cured at different elevated temperature and humidity environments up to 28 days. A combination of two extreme relative humidity of 0 and 100% and variable curing temperatures between 15 to 80°C were considered. From a test matrix of 300 DMA and over 250 DSC coupons these conclusions were drawn. First, ambient cured thermosets have a linear relationship between T_g and curing temperature, but T_g is reduced if a certain temperature is reached. Second, a fully cured adhesive requires heating treatment. Without a curing regime, designed T_g may never be achieved. Finally, curing time is crucial at the low curing temperatures while it is less significant at the higher curing temperature.

The results of T_g investigation were used to select appropriate curing temperature that the adhesives resistance to temperature can be maximised without

damaging the mechanical properties. The study helps designs to understand and assess the behaviour of these two adhesives when they are exposed to extreme temperatures. The study increases the awareness that a fully cured adhesive may never be achieved at ambient or low temperatures. It is important to find the mechanical properties and T_g when the coupons are exposed to the same curing temperature.

To investigate the influence of glass transition temperature T_g improvement on the performance of EB-FRP strengthened steel structures in flexure at ambient and elevated temperature, nine three metre length beams were designed to behave as a concrete-steel composite bridge deck. The beams were tested in four-point bending. Lap shear, DMA test, and pull-off adhesion samples were prepared and cured at the same conditions and tested at ambient temperature. Six beams were tested under only mechanically loading at ambient temperature, including the control specimen. Five beams were tested at ambient temperature to show the effects of adhesive curing on FRP strengthened sections. A significant increase of load capacity of the adhesive joints was achieved due to the curing of the joints at elevated temperature. The failure occurred was in the same manner. An increase in the load capacity was observed with increasing curing temperature. An increase of approximately 25% was noticed in the ultimate load capacity of the specimens cured at 50°C compared to the specimens cured at 30°C. The load capacity of lap-shear specimens cured at 50°C was 28% higher than the specimens cured at 30°C. Three specimens were tested under mechanical and thermal loading. A bespoke thermal chamber was designed and fabricated to apply a controlled thermal loading. The beams were loaded mechanically up to 350kN, first. The temperature of the specimens was then increased at a rate of 0.8°C/min. The sustained load 350kN remained constant during the heating phase. Digital Image Correlation (DIC) technique was used to detect the slippage of the tip of the FRP plates. The only specimen cured at 30°C showed relatively poor performance compared to the two specimens cured at 50°C. The plate ends started to slip when the adhesive storage modulus from the DMA runs reduced approximately by 15 and 18% for the beams cured at 30 and 50°C respectively. Pull-off adhesion tests confirmed that adequate surface preparation of over 25 MPa was achieved

The flexural model for the composite steel section represented to predicate load-deflection behaviour of the specimens using semi-experimental constitutive material law. The model successfully predicts the load-deflection behaviour of specimens, considering the strain hardening contribution. A bond stress analysis is also

presented, which counts for the effect of FRP plate moment effect. The experimental and theoretical FRP plate slippage assuming only adhesive degradation with temperature are compared. The analytical bond models cannot predict the experimental failure because the linear elastic material properties were assumed and the failure was adhesion.

Lay Summary

Across the globe roads and railways interlink countries. These motorways and tracks require to bridge across rivers and valleys. When these bridges originally designed it was never foreseen that in the future these structures would have to cope with the present-day volume of traffic. These structures and their location have become such a vital part of mass transportation that renewal is not an option; renewal would mean closure of a main artery of communication.

Engineers have therefore had to come up with solutions to ensure that these structures remain open and fit for purpose. This has presented particular challenges for the engineering community.

The first of these challenges is that these structures remain safe and operational during the lifetime. The second challenge is that the costs of these repairs are kept to a minimum. New materials such as Fibre Reinforced Polymer (FRP) with exceptional properties are capable of delivering this demand.

When strengthening of an existing steel or concrete structure is required, the crucial factor in the whole work is the effectiveness of the adhesive joint between the structure and these reinforcements.

This thesis is a study of widely available adhesives in strengthening technique to enhance steel structures. The structural adhesives that are widely used in the structural applications are thermoset ambient cure adhesives.

Adhesives are in a relatively hard and inflexible state, while at higher temperatures, the material becomes soft and flexible state. The region, which this transition occurs, is known as the glass transition temperature T_g. Adhesive mechanical properties near glass transition temperature reduce dramatically. The aim of this work is to study the relationship between the adhesive glass transition temperature and performance of a FRP strengthened steel structure at ambient (room) and elevated temperatures. The tests were also compared with design guidelines. The beams were tested in bending.

To achieve this aim over 550 samples from two types of adhesives were made and tested. The relationship between curing temperature and glass transition temperature was obtained. It was also noticed that a fully cured adhesive requires heating treatment, and curing time is crucial at the low curing temperatures while it is less significant at the higher curing temperature.

One adhesive was selected from the two adhesives to study in detail and to understand its behaviour in joints. Nine 3-metre length beams were designed to replicate bridge deck. Six of the nine beams were tested under only mechanical loading at ambient temperature. An increase in the load capacity was observed with increasing curing temperature. The other three beams were tested under mechanical and thermal loading. The only beams cured at 30°C showed relatively poor performance compare to the two beams cured at 50°C.

Acknowledgment

Endless thanks, with gratitude, to my parents (Lawlaw and Jalal) and siblings (Kalyan and Sana) for their constant support, and for funding this project.

I would like to express my deepest appreciation to the principal supervisor Dr Tim Stratford and second supervisor Prof Luke Bisby for their patient guidance, advice and encouragement throughout this work and my degree in Master of Science.

I would like to acknowledge my debt of thanks to Prof Albert Simeoni for this aid during difficult times.

For all of my colleagues at the University of Glasgow and University of Edinburgh, thanks for being there and for all motivations.

In addition, my thanks go to all the laboratory assistance from the University of Edinburgh technicians. I thank Derek Jardine, Jim Hutcheson, Michal Krajcovic, Christopher Sturgeon, Mark Partington, George Cairns, Ewan McLean, Bryan Mitchell, Steven Gourlay, William Leslie, Kevin Tierney, Kevin Anderson and Alex Kirkland also the administrators who worked hard to help the students achieve their goals and finish their study.

I would like to thank my friends Fiona Hart, Richard Mackinnon and Graham Shields to take the proof reading responsibilities.

Definitions and abbreviations

Latin upper-case letters

Symbol	***Description***
A_b	Area of the beam
A_{frp}	Area of Fibre Reinforced Polymer material
$C_{1,2,3,4,5}$	Constants - Coefficient
E'	Storage modulus
E''	Loss modulus
E_b	Young's modulus of the beam
E_{frp}	Young's modulus of Reinforced Polymer material
E_{sh}	Strain hardening modulus
F_{bf}	Force in the bottom flange
F_{frp}	Force in the FRP material
F_{sp}	Force in top flange strengthening plate
F_{tf}	Force in the top flange
F_{w1}	Force in the tension part of the web
F_{w2}	Force in the compression part of the web
I_b	Second moment of areas of the beam
I_{frp}	Second moment of areas of the FRP material
M_a	Total moment in the adhesive
M_b	Total moment in the beam
M_{cr}	Critical Lateral torsional buckling
M_{frp}	Total moment in the FRP material
M_p	Plastic moment
N_b	Total force in the beam acting at the centroid of the section
N_{frp}	Total force in the FRP material acting at the centroid
T_g	Glass transition temperature
V_a	Adhesive shear force
V_b	Steel beam shear force
V_{frp}	FRP shear force
X_{bf}	Bottom flange force distance from neutral axis
X_{frp}	FRP material force distance from neutral axis
X_{sp}	Top flange strengthening plate force distance from neutral axis
X_{tf}	Top flange force distance from neutral axis
X_{w1}	Tension part of the web force distance from neutral axis
X_{w2}	Compression part of the web force distance from neutral axis
DMA	Dynamic mechanical analysis/analyser
DSC	Differential scanning calorimetry/calorimeter
E	Young's modulus
FRP	Fibre Reinforced Polymer material
G	Shear modulus
J	Torsion constant
L	Beam length between points, which is the length from support to support
X	Horizontal direction x-direction
Y	Vertical direction y-direction
Z	Distance between the N_b and N_{frp}

Latin lower-case letters

Symbol	***Description***
f_u	Ultimate strength
f_y	Yielding strength
b_{bf}	Bottom flange width
b_{frp}	FRP width
b_{sp}	Top flange strengthening plate width
b_{tf}	Top flange width
$b_{w1\ and\ w2}$	Web width
C_p	Specific heat capacity
$f_{bf}(x)$	Strain function
h_o	Distance between centre of the tension and compression flanges
I_w	Warping constant
I_x	Second moment of area about the major axis
I_y	Second moment of area about the minor axis
I_{yc}	Section minor axis second moment of area of the compression flange
t_a	Adhesive thickness
t_{bf}	Bottom flange thickness
t_{frp}	FRP thickness
t_{sp}	Top flange strengthening plate thickness
t_{tf}	Top flange thickness
$t_{w1\ and\ w2}$	Web thickness
u_{b-a}	Horizontal displacement at the steel I-beam-adhesive interface
u_{frp-a}	Horizontal displacement at the FRP-adhesive interface
v_b	Vertical displacement at the centre of steel I-beam
v_{frp}	Vertical displacement at the centre of FRP material
y_b	Neutral axis depth from the bottom of the I-beam section
y_{frp}	Neutral axis depth from the bottom of FRP material
h	Steps length
i	Step number
n	Holmond-Ludwik's parameter; number of steps
$q(x)$	Applied load
x	Distance from the bottom of the section; distance along the beam
y	Neutral axis depth from the bottom of the section

Greek lower-case letters

Symbol	***Description***
α_b	Beam coefficient of thermal expansion
α_{frp}	FRP coefficient of thermal expansion
β_x	Mono-symmetry property of the section
γ_a	Adhesive shear strain
ε_a	Adhesive normal (peeling) strain
ε_b	Beam strain at the bottom fibres
ε_c	Compression strain
ε_{frp}	Strain in the FRP material
ε_{sh}	Strain hardening strain
ε_t	Tensile strain
ε_u	Ultimate strain
ε_x	Strain at distance x
ε_y	Yielding strain
$\mu_{1,2}$	Constants - Coefficient
σ_a	Adhesive normal (peeling) stress
τ_a	Adhesive shear stress
$\Phi_{1,2}$	Constants - Coefficient
ψ_b	Beam curvature
ψ_{frp}	FRP curvature
ΔT	Change in temperature
k	Constants - Coefficient
v	Constant; Poisson's ratio
ε	Strain
σ	Stress
ψ	Curvature
δ	Phase angle between stress and strain in DMA

Table of Content

Introduction 1

1.1 Introduction 1

1.2 Research objectives 2

1.3 Thesis organisation 3

Literature Review 7

2.1 Materials used in strengthening and rehabilitation of structural members using externally bonding method 8
- 2.1.1 Fibre reinforced polymer (FRP) materials 9
- 2.1.2 Polymeric matrices 11
- 2.1.3 Epoxy adhesives 12

2.2 Plastic analysis for steel structures 13
- 2.2.1 The basics of plastic design 14
- 2.2.2 Research into the plastic behaviour of steel 15
- 2.2.3 The plastic moment resistance of steel sections 16
- 2.2.4 Strain hardening effect 17

2.3 Externally Bonded FRP strengthening of steel structural elements 18
- 2.3.1 Flexural strengthening 19
- 2.3.2 Shear strengthening 29
- 2.3.3 Tensile strengthening 32
- 2.3.4 Finite element modelling studies 35

2.4 Analytical approaches for modelling externally bonded adhesives to strengthen elements in flexural 37
- 2.4.1 Compatibility approach 37
- 2.4.2 Fracture mechanics and cohesive zone approach 40

2.5 FRP strengthening design guidelines and recommendations 41

2.6 The effects of elevated temperature on FRP strengthening 43
- 2.6.1 Definition of the glass transition temperature Tg definition 43
- 2.6.2 The effect of cross-links upon adhesive properties 44
- 2.6.3 The effect of temperature upon adhesive cure and properties 45
- 2.6.4 The effect of moisture upon adhesive cure and properties 46
- 2.6.5 The effect of physical ageing upon adhesive cure and properties 46

2.7 The theory of linear viscoelasticity and thermal analysis techniques 47
- 2.7.1 Theory of linear viscoelasticity 48
- 2.7.2 Thermal analysis techniques 50

2.8 Dynamic Mechanical Analysis (DMA) 51
- 2.8.1 DMA specimen and clamping configuration 52
- 2.8.2 Storage and loss modulus calculation with DMA 55
- 2.8.3 Storage modulus and Young's modulus definition 55
- 2.8.4 Single cantilever vs. dual cantilever 57
- 2.8.5 Temperature scanning and storage modulus variation in DMA 59
- 2.8.6 Determining a characteristic glass transition temperature, Tg using DMA 61

2.9 Differential Scanning Calorimetry (DSC) 63
2.9.1 Determining a characteristic glass transition temperature, Tg using DSC 65
2.10 Thermal effects on bonded FRP performance 66
2.10.1 Service temperature of steel structures 66
2.10.2 Lap-shear joins at elevated temperature 68
2.10.3 Flexural strengthening at elevated temperature 76
2.10.4 Analytical approaches for modelling externally bonded adhesives at elevated temperature 81
2.10.5 FRP strengthening design guidelines and recommendations at elevated temperatures 84
2.11 Summary 84
Glass Transition Temperature Tg Characterisation of the Investigated Adhesives 86
3.1 Investigated adhesives 87
3.1.1 Sikadur-330 87
3.1.2 Tyfo-S 87
3.2 Experimental programme and specimen preparation 88
3.2.1 Experimental programme 88
3.2.2 Sikadur-330 coupon preparation 90
3.2.3 Tyfo-S coupon preparation 92
3.2.4 Specimen conditioning 92
3.2.5 Filler content testing (Burn-off test) 92
3.3 Dynamic Mechanical Analysis (DMA) testing equipment and pre-testing preparation 93
3.3.1 Testing equipment 93
3.3.2 Pre-test preparation 93
3.4 Parametric study 96
3.4.1 Heating rate dependence experiments 96
3.4.2 Frequency dependence experiments 98
3.4.3 Specimen free length dependence experiments 99
3.4.4 Finding of DMA parametric study 101
3.5 Experimental results and discussion of curing condition using DMA 103
3.5.1 Curing age effect on Tg using DMA 103
3.5.2 Curing temperature effect Tg using DMA 107
3.6 Differential Scanning Calorimetry (DSC) testing equipment and pre-testing preparation 113
3.6.1 Testing equipment 113
3.6.2 Pre-test Preparation 114
3.6.3 DSC scanning experiments and test settings 114
3.6.4 Determination of the DSC glass transition temperature 115
3.7 Experimental results and discussion of curing condition using DSC 115
3.7.1 Curing age effect on Tg using DSC 116
3.7.2 Curing temperature effect Tg using DSC 118
3.8 Summary 122
Steel Specimen and Thermal Chamber Design Methodology 124

4.1 Steel specimens 124
4.1.1 Beam design methodology 124
4.1.2 Steel beam fabrication 126
4.1.3 Geometrical properties 127
4.2 Design and fabrication of thermal chamber (O-105) 128
4.2.1 Chamber design methodology 128
4.2.2 Chamber fabrication 129
4.3 FRP strengthening and specimens conditioning 132
4.3.1 Steel surface preparation 132
4.3.2 Specimen preparation and FRP strengthening 133
4.3.3 Specimen curing and conditioning 137
4.4 Overview of the experimental programme 138
4.5 Strengthening material properties 140
4.5.1 Adhesive material properties 141
4.5.2 CFRP properties 142
4.5.3 Steel material properties 142
4.6 Summary 144
Performance and Behaviour of Cured Steel-FRP Joints 146
5.1 Lap-shear tests 147
5.1.1 Lap-shear specimen preparation 147
5.1.2 Lap-shear test procedure 149
5.1.3 Lap-shear test results 149
5.2 Dynamic Mechanical Analysis DMA tests 151
5.2.1 DMA specimen preparation 151
5.2.2 DMA specimen test procedure 151
5.2.3 DMA test results 152
5.3 Pull-off adhesion tests 155
5.4 Overview of the flexure test methodology 156
5.4.1 Testing configuration and set-up 156
5.4.2 Monitoring instrumentation 159
5.5 Ambient temperature beam tests 162
5.5.1 Load-deflection behaviour and failure modes 163
5.6 Transient temperature tests 172
5.6.1 Load-deflection behaviour 175
5.6.2 Testing temperature 176
5.6.3 CFRP plate movement relative to the beam 180
5.6.4 Failure mechanism 185
5.7 Summary 188
Analysis and Interpretation 190
6.1 Analytical model for flexure 191
6.1.1 Assumptions behind the flexure model 191
6.1.2 Development of the flexural model 192
6.1.3 Verification of the flexure model 196
6.2 Lateral-torsional buckling capacity 198
6.3 Strain hardening effect and predictions 200

6.4 Analytical model for bond 204
6.4.1 The bond model assumptions 206
6.4.2 Development of the bond model 206
6.4.3 Model comparison at ambient temperature 216
6.4.4 Experimental and prediction slippage 219
6.5 Summary 223
Conclusions, Recommendations and Future Work 225
7.1 Conclusions and findings 225
7.2 Design recommendations 228
7.3 Research limitations 228
7.4 Future work 228

List of Figures

Figure 1-1: The general organization of the thesis chart 4
Figure 2-1: Stress-strain curves of epoxy matrix resins of different modulus (FIB, 2006) 13
Figure 2-2: Stress and strain distribution in a beam section with increasing curvature (Baker *et al.*, 1980). 15
Figure 2-3: Loading is directly applied to the steel element with gap 33
Figure 2-4: Loading is directly applied to the steel element without any gap 34
Figure 2-5: Pull-off test specimen and set-up (Zhao and Zhang, 2007) 34
Figure 2-6: Indirectly loading the FRP and the steel plate set-up (Zhao and Zhang, 2007) 35
Figure 2-7: Soffit-plated beam and differential segment of a soffit-plated beam in the model by (Smith and Teng, 2001) 38
Figure 2-8: Comparison of interfacial shear and normal stresses for a RC beam with a bonded CFRP soffit plate subjected to a UDL by (Smith and Teng, 2001) 39
Figure 2-9: The schematic diagram of PerkinElmer DMA 8000, and the applied sinusoidal oscillation (Menard, 2008) 52
Figure 2-10: Schematic of various testing fixtures (Gabbott, 2008) 54
Figure 2-11: Strain and shear regions in flexure test configurations (Menard, 2008) 57
Figure 2-12: Single and dual cantilever configuration temperature scans with DMA 58
Figure 2-13: DMA test configurations for single and dual cantilever bending (Menard, 2008) 59
Figure 2-14: Storage modulus vs. temperature curve, states and transitions of a polymer (Menard, 2008) 60
Figure 2-15: Various methods of reporting Tg from the DMA runs (Othman *et al.*, 2013a, b). 62
Figure 2-16: Typical heat flow vs. temperature curve for polymers (Osswald *et al.*, 2006). 64
Figure 2-17: Illustration of the Tg determination from the heat flow vs. temperature (Gabbott, 2008). 66
Figure 2-18: Scheme of Anchorages. 1-Steel Ring; 2-Horizontal Sleeve; 3-Clamp; 4-Pin (Tadeu and Branco, 2000) 69
Figure 2-19: Summary of the lap-shear results (Tadeu and Branco, 2000) 69
Figure 2-20: Geometry of GFRP double-lap joint specimen (dimensions in [mm]), and thermo mechanical behaviour of epoxy adhesive and GFRP laminates (Zhang *et al.*, 2010) 70
Figure 2-21: Experimental results by (Zhang *et al.*, 2010) 70
Figure 2-22: Experimental results (Al-Shawaf *et al.*, 2009) 71
Figure 2-23: Experimental results for the tests by (Nguyen *et al.*, 2011) 72
Figure 2-24: The test specimens and the results by (Abed, 2012) 73
Figure 2-25: Double-lap shear test setup and failure load double-lap shear tests (Klamer *et al.*, 2006) 74

Figure 2-26: Glass transition temperature, Tg of the adhesives and average bond strength with increasing temperature (Wu *et al.*, 2005) 75

Figure 2-27: Single lap-shear transient test results (Al-Safy *et al.*, 2012) 75

Figure 2-28: Schematic experimental set up showing the loading, heating arrangements, cross-sectional dimensions, and material properties of the strengthened beams (Stratford and Bisby, 2012) 76

Figure 2-29: The observed variation in plate-end slip according to temperature and the failure temperatures for strengthened beams carrying different loads (Stratford and Bisby, 2012) 77

Figure 2-30: Schematic of heating system setup and three-point bending test setup (Abed, 2012) 78

Figure 2-31: Load vs. mid-span deflection for FRP reinforced beams (Abed, 2012) 79

Figure 2-32: Three point-bending test setup and failure load three point-bending tests (Klamer *et al.*, 2006) 80

Figure 2-33: Measured loss in elastic stiffness of the epoxy bonding adhesive through the glass transition and the elasto-plastic adhesive constitutive model used in the bond analysis (Stratford and Bisby, 2012) 82

Figure 2-34: Representative sketch of adhesive stress-strain behaviour and shear stress at the tip of CFRP plat (Abed, 2012) 83

Figure 3-1: (Left) Bi-component adhesive Sikedur-330; (Right) Epoxy matrix Tyfo-S 88

Figure 3-2: DMA coupons and the moulds 91

Figure 3-3: Triton Dynamic Mechanical Analysis machine model Tritec 2000 93

Figure 3-4: Schematic diagram of single cantilever fixture in typical DMA machine 95

Figure 3-5: Storage, loss modulus and tan δ variation with temperature for different heating rates 97

Figure 3-6: Storage, loss modulus and tan δ variation with temperature for different frequencies 99

Figure 3-7: Storage, loss modulus and tan δ variation with temperature for different free lengths. 101

Figure 3-8: Curing age effect on Tg at 24°C, Adhesive S and Adhesive T for dry and saturate conditions using DMA 105

Figure 3-9: Storage modulus and normalised storage modulus variation with temperature cured at 24°C for Adhesive S dry (left) saturated (right) condition using DMA 106

Figure 3-10: Normalised loss modulus and tan δ variation with temperature cured at 24°C for Adhesive S for dry and saturated conditions 107

Figure 3-11: Curing age and temperature effect on Tg according to peak loss modulus methods for Adhesive S and Adhesive T for dry and saturated conditions using DMA 108

Figure 3-12: Recorded $\boldsymbol{Tg}$ according to different methods at 7 days and different curing temperature, Adhesive S and Adhesive T for dry and saturated conditions using DMA 109

Figure 3-13: Storage and Normalised storage modulus variation with temperature cured at different temperatures for 7 days Adhesive S dry and saturated conditions 111

Figure 3-14: Normalised loss modulus and tan δ variation with temperature cured at different temperatures for 7 days Adhesive S dry and saturated conditions 112
Figure 3-15: Mettler Toledo (TGA/DSC1) Differential Scanning Calorimeter machine. 113
Figure 3-16: Illustration diagram of TGA/DSC1 chamber (Mettler Toledo, 2007). 114
Figure 3-17: Curing age effect on Tg of Adhesive S and Adhesive T for dry and saturated conditions using DSC at 24°C 117
Figure 3-18: Normalised heat flow versus temperature for Adhesive S and Adhesive T for dry and saturate conditions cured at 24°C 118
Figure 3-19: Curing age and temperature effect on Tg according to inflection point method for Adhesive S and Adhesive T for dry and saturated conditions using DSC 119
Figure 3-20: Recorded $\boldsymbol{Tg}$ according to different methods at 7 days and different curing temperature, Adhesive S and Adhesive T for dry and saturated conditions using DSC 120
Figure 3-21: Normalised heat flow versus temperature for Adhesive S and Adhesive T for dry and saturate conditions cured at different temperatures for 7 days. 121
Figure 4-1: Typical cross section of composite steel-concrete girders 125
Figure 4-2: The equivalent top flange strengthened universal beam with steel and composite steel-concrete girder 126
Figure 4-3: Cross-section nominal manufacture's dimensions and stiffener locations for the un-strengthened test specimens 127
Figure 4-4: Photograph of a steel beam specimen after adding the top flange plate and web stiffeners 127
Figure 4-5: Notations used in Table 4-1 128
Figure 4-6: Elevation and top view of the O-105 Chamber 130
Figure 4-7: Various stages of O-105 chamber fabrication and in operation 131
Figure 4-8: Various stages of the surface preparation 135
Figure 4-9: Various stages of the CFRP plates strengthening 136
Figure 4-10: Thermocouple locations on the beams 138
Figure 4-11: Curing temperature of the beams and small-scale samples 140
Figure 4-12: Cross section of a CFRP strengthened test specimens. 141
Figure 5-1: Front and side view of lap-shear specimens 148
Figure 5-2: Prepared and ready to test double lap-shear specimens 149
Figure 5-3: Lap-shear test results for the first and second series 150
Figure 5-4: DMA coupon results for different beam cure conditions in single cantilever fixture 153
Figure 5-5: Normalised storage and loss modulus and tan δ for the DMA results in Figure 5-4 154
Figure 5-6: Spread beam and extension loading shaft details 157
Figure 5-7: Schematic diagram of the test set up during ambient and transient tests 158
Figure 5-8: Location of the cameras and lighting during the test 160
Figure 5-9: The CFRP bonded length 160

Figure 5-10: The mechanical clamp details 160
Figure 5-11: Photo of the flexural test set up 161
Figure 5-12: Four-point bending test load versus deflection (at the loading points) for the specimens tested at ambient temperature 163
Figure 5-13: Control specimen after testing 165
Figure 5-14: Beam no.1_30 after testing and local damages to the specimen 167
Figure 5-15: Beam no.2_30 after testing 169
Figure 5-16: Beam no.3_50 after testing 170
Figure 5-17: Beam no.3_50 and 4 plate tips after testing 170
Figure 5-18: Beam no.5_25 after testing 171
Figure 5-19: The relationship between failure load of CFRP strengthened beams and curing temperature and DMA specimens for the same cure in single cantilever configuration 172
Figure 5-20: Mechanical loading and thermal loading during the test (top figure), and the point load deflection up to the ends of heating (bottom figure) for Beam no.6_30, Beam no.7_50, and Beam no.8_50 174
Figure 5-21: Four-point bending test load versus deflection (at the point loads) for the specimens Beam no.6_30, Beam no.7_50, and Beam no.8_50 and the control specimens. 176
Figure 5-22: O-105 chamber air temperature during transient temperature tests 178
Figure 5-23: Specimens temperature during transient temperature tests 179
Figure 5-24: Digital image analysis north camera of Beam no.6_30* 181
Figure 5-25: The CFRP plate movement during transient temperature Beam no.6_30* 182
Figure 5-26: The CFRP plate movement during transient temperature Beam no.7_50 183
Figure 5-27: The CFRP plate movement during transient temperature Beam no.8_50 184
Figure 5-28: Tip of the CFRP plate movement and temperature of the steel beams during transient temperature tests 186
Figure 5-29: Tip of the CFRP plate movement and point load deflection during transient temperature tests 187
Figure 5-30: Beam no.6, Beam no.7, and Beam no.8 after testing 188
Figure 6-1: The assumed linear strain profile for composite beam 193
Figure 6-2: Flowchart of the flexural model algorithm 195
Figure 6-3: Idealised stress-strain relations for the fabricated section 196
Figure 6-4: Moment-curvature relations for the fabricated section 197
Figure 6-5: Load-deflection and lateral-torsional buckling capacity predictions 198
Figure 6-6: Buckling capacity and load-deflection predictions 200
Figure 6-7: Stress-strain relations of the fabricated section from the models by Byfield and Dhanalakshmi (2002); (Byfield *et al.*, 2005) 201
Figure 6-8: Load-deflection response for different strain hardening model 202
Figure 6-9: Experimental and predicted load-deflection relationship 204
Figure 6-10: The bond analysis definitions, geometry, and differential segment of strengthened beam 207
Figure 6-11: Boundary conditions and finite difference variables 212

Figure 6-12: The global matrix formation of the differential equations 215
Figure 6-13: Flowchart of the computer programme 216
Figure 6-14: Details of the strengthened beam for the bond analysis 217
Figure 6-15: Convergence of numerical procedure 217
Figure 6-16: Comparing shear and normal stresses in the adhesive and internal plate force and moment calculated from different models 218
Figure 6-17: Shear and normal stresses in the adhesive and internal plate force and moment at different temperatures along the joint 220
Figure 6-18: Adhesive property changes, experimental and analytical slip displacement at the tip of the CFRP plate with temperature 221
Figure A-1: a) Tyfo-S resin before burning b) During burning-off on Bunsen burner c) residue of the resin. 244
Figure A-2:High-temperature thermal muffle furnace and crucible with the filler 245
Figure B-1: Recorded Tg according to inflection point method at different age and curing temperature for Sikadur-330, dry condition 247
Figure B-2: Recorded Tg according to peak loss modulus method at different age and curing temperature for Sikadur-330, dry condition 248
Figure B-3: Recorded Tg according to onset normal scale method at different age and curing temperature for Sikadur-330, dry condition 248
Figure B-4: Recorded Tg according to onset logarithmic scale method at different age and curing temperature for Sikadur-330, dry condition 249
Figure B-5: Recorded Tg according to tan δ method at different age and curing temperature for Sikadur-330, dry condition 249
Figure B-6: Recorded Tg according to different methods at 3 days and different curing temperature for Sikadur-330, dry condition 250
Figure B-7: Recorded Tg according to different methods at 7 days and different curing temperature for Sikadur-330, dry condition 250
Figure B-8: Recorded Tg according to different methods at 14 days and different curing temperature for Sikadur-330, dry condition 251
Figure B-9: Recorded Tg according to different methods at 28 days and different curing temperature for Sikadur-330, dry condition 251
Figure B-10: Storage and normalised modulus variation with temperature for specimens cured at different temperature for 3 days, Sikadur-330 dry condition 252
Figure B-11: Normalised loss modulus and tan δ variation with temperature for specimens cured at different temperature for 3 days, Sikadur-330 dry condition 253
Figure B-12: Storage and normalised modulus variation with temperature for specimens cured at different temperature for 7 days, Sikadur-330 dry condition 254
Figure B-13: Normalised loss modulus and tan δ variation with temperature for specimens cured at different temperature for 7 days, Sikadur-330 dry condition 255
Figure B-14: Storage and normalised modulus variation with temperature for specimens cured at different temperature for 14 days, Sikadur-330 dry condition 256

Figure B-15: Normalised loss modulus and tan δ variation with temperature for specimens cured at different temperature for 14 days, Sikadur-330 dry condition 257

Figure B-16: Storage and normalised modulus variation with temperature for specimens cured at different temperature for 28 days, Sikadur-330 dry condition 258

Figure B-17: Normalised loss modulus and tan δ variation with temperature for specimens cured at different temperature for 28 days, Sikadur-330 dry condition 259

Figure B-18: Recorded Tg according to inflection point method at different age and curing temperature for Sikadur-330, saturated condition 260

Figure B-19: Recorded Tg according to peak loss modulus method at different age and curing temperature for Sikadur-330, saturated condition 260

Figure B-20: Recorded Tg according to onset normal scale method at different age and curing temperature for Sikadur-330, saturated condition 261

Figure B-21: Recorded Tg according to onset logarithmic scale method at different age and curing temperature for Sikadur-330, saturated condition 261

Figure B-22: Recorded Tg according to tan δ method at different age and curing temperature for Sikadur-330, saturated condition 262

Figure B-23: Recorded Tg according to different methods at 3 days and different curing temperature for Sikadur-330, saturated condition 263

Figure B-24: Recorded Tg according to different methods at 7 days and different curing temperature for Sikadur-330, saturated condition 263

Figure B-25: Recorded Tg according to different methods at 14 days and different curing temperature for Sikadur-330, saturated condition 264

Figure B-26: Recorded Tg according to different methods at 28 days and different curing temperature for Sikadur-330, saturated condition 264

Figure B-27: Storage and normalised modulus variation with temperature for specimens cured at different temperature for 3 days, Sikadur-330 saturated condition 265

Figure B-28: Normalised loss modulus and tan δ variation with temperature for specimens cured at different temperature for 3 days, Sikadur-330 saturated condition 266

Figure B-29: Storage and normalised modulus variation with temperature for specimens cured at different temperature for 7 days, Sikadur-330 saturated condition 267

Figure B-30: Normalised loss modulus and tan δ variation with temperature for specimens cured at different temperature for 7 days, Sikadur-330 saturated condition 268

Figure B-31: Storage and normalised modulus variation with temperature for specimens cured at different temperature for 14 days, Sikadur-330 saturated condition 269

Figure B-32: Normalised loss modulus and tan δ variation with temperature for specimens cured at different temperature for 14 days, Sikadur-330 saturated condition 270

Figure B-33: Storage and normalised modulus variation with temperature for specimens cured at different temperature for 28 days, Sikadur-330 saturated condition 271

Figure B-34: Normalised loss modulus and tan δ variation with temperature for specimens cured at different temperature for 28 days, Sikadur-330 saturated condition 272

Figure B-35: Recorded *Tg* according to inflection point method at different age and curing temperature for Sikadur-330, dry condition 273

Figure B-36: Recorded *Tg* according to onset point method at different age and curing temperature for Sikadur-330, dry condition 273

Figure B-37: Recorded *Tg* according to different methods at 3 days and different curing temperature for Sikadur-330, dry condition 274

Figure B-38: Recorded *Tg* according to different methods at 7 days and different curing temperature for Sikadur-330, dry condition 274

Figure B-39: Recorded *Tg* according to different methods at 14 days and different curing temperature for Sikadur-330, dry condition 275

Figure B-40: Recorded *Tg* according to different methods at 28 days and different curing temperature for Sikadur-330, dry condition 275

Figure B-41: Normalised heat flow variation with temperature for specimens cured at different temperatures for 3, 7, 14, and 28 days, Sikadur-330 dry condition 276

Figure B-42: Recorded *Tg* according to inflection point method at different age and curing temperature for Sikadur-330, saturated condition 277

Figure B-43: Recorded *Tg* according to onset point method at different age and curing temperature for Sikadur-330, saturated condition 277

Figure B.B-44: Recorded *Tg* according to different methods at 3 days and different curing temperature for Sikadur-330, saturated condition 278

Figure B-45: Recorded *Tg* according to different methods at 7 days and different curing temperature for Sikadur-330, saturated condition 278

Figure B-46: Recorded *Tg* according to different methods at 14 days and different curing temperature for Sikadur-330, saturated condition 279

Figure B-47: Recorded *Tg* according to different methods at 28 days and different curing temperature for Sikadur-330, saturated condition 279

Figure B-48: Normalised heat flow variation with temperature for specimens cured at different temperatures for 3, 7, 14, and 28 days, Sikadur-330 saturated condition 280

Figure C-1: Recorded *Tg* according to inflection point method at different age and curing temperature for Tyfo-S, dry condition 288

Figure C-2: Recorded *Tg* according to peak loss modulus method at different age and curing temperature for Tyfo-S, dry condition 289

Figure C-3: Recorded *Tg* according to onset normal scale method at different age and curing temperature for Tyfo-S, dry condition 289

Figure C-4: Recorded *Tg* according to onset logarithmic scale method at different age and curing temperature for Tyfo-S, dry condition 290

Figure C-5: Recorded *Tg* according to tan δ method at different age and curing temperature for Tyfo-S, dry condition 290

Figure C-6: Recorded *Tg* according to different methods at 3 days and different curing temperature for Tyfo-S, dry condition 291

Figure C-7: Recorded Tg according to different methods at 7 days and different curing temperature for Tyfo-S, dry condition 291

Figure C-8: Recorded Tg according to different methods at 14 days and different curing temperature for Tyfo-S, dry condition 292

Figure C-9: Recorded Tg according to different methods at 28 days and different curing temperature for Tyfo-S, dry condition 292

Figure C-10: Storage and normalised modulus variation with temperature for specimens cured at different temperature for 3 days, Tyfo-S dry condition 293

Figure C-11: Normalised loss modulus and tan δ variation with temperature for specimens cured at different temperature for 3 days, Tyfo-S dry condition 294

Figure C-12: Storage and normalised modulus variation with temperature for specimens cured at different temperature for 7 days, Tyfo-S dry condition 295

Figure C-13: Normalised loss modulus and tan δ variation with temperature for specimens cured at different temperature for 7 days, Tyfo-S dry condition 296

Figure C-14: Storage and normalised modulus variation with temperature for specimens cured at different temperature for 14 days, Tyfo-S dry condition 297

Figure C-15: Normalised loss modulus and tan δ variation with temperature for specimens cured at different temperature for 14 days, Tyfo-S dry condition 298

Figure C-16: Storage and normalised modulus variation with temperature for specimens cured at different temperature for 28 days, Tyfo-S dry condition 299

Figure C-17: Normalised loss modulus and tan δ variation with temperature for specimens cured at different temperature for 28 days, Tyfo-S dry condition 300

Figure C-18: Recorded Tg according to inflection point method at different age and curing temperature for Tyfo-S, saturated condition 301

Figure C-19: Recorded Tg according to peak loss modulus method at different age and curing temperature for Tyfo-S, saturated condition 301

Figure C-20: Recorded Tg according to onset normal scale method at different age and curing temperature for Tyfo-S, saturated condition 302

Figure C-21: Recorded Tg according to onset logarithmic scale method at different age and curing temperature for Tyfo-S, saturated condition 302

Figure C-22: Recorded Tg according to tan δ method at different age and curing temperature for Tyfo-S, saturated condition 303

Figure C-23: Recorded Tg according to different methods at 3 days and different curing temperature for Tyfo-S, saturated condition 304

Figure C-24: Recorded Tg according to different methods at 7 days and different curing temperature for Tyfo-S, saturated condition 304

Figure C-25: Recorded Tg according to different methods at 14 days and different curing temperature for Tyfo-S, saturated condition 305

Figure C-26: Recorded Tg according to different methods at 28 days and different curing temperature for Tyfo-S, saturated condition 305

Figure C-27: Storage and normalised modulus variation with temperature for specimens cured at different temperature for 3 days, Tyfo-S saturated condition 306

Figure C-28: Normalised loss modulus and tan δ variation with temperature for specimens cured at different temperature for 3 days, Tyfo-S saturated condition 307

Figure C-29: Storage and normalised modulus variation with temperature for specimens cured at different temperature for 7 days, Tyfo-S saturated condition 308

Figure C-30: Normalised loss modulus and tan δ variation with temperature for specimens cured at different temperature for 7 days, Tyfo-S saturated condition 309

Figure C-31: Storage and normalised modulus variation with temperature for specimens cured at different temperature for 14 days, Tyfo-S saturated condition 310

Figure C-32: Normalised loss modulus and tan δ variation with temperature for specimens cured at different temperature for 14 days, Tyfo-S saturated condition 311

Figure C-33: Storage and normalised modulus variation with temperature for specimens cured at different temperature for 28 days, Tyfo-S saturated condition 312

Figure C-34: Normalised loss modulus and tan δ variation with temperature for specimens cured at different temperature for 28 days, Tyfo-S saturated condition 313

Figure C-35: Recorded Tg according to inflection point method at different age and curing temperature for Tyfo-S, dry condition 314

Figure C-36: Recorded Tg according to onset point method at different age and curing temperature for Tyfo-S, dry condition 314

Figure C-37: Recorded Tg according to different methods at 3 days and different curing temperature for Tyfo-S, dry condition 315

Figure C-38: Recorded Tg according to different methods at 7 days and different curing temperature for Tyfo-S, dry condition 315

Figure C-39: Recorded Tg according to different methods at 14 days and different curing temperature for Tyfo-S, dry condition 316

Figure C-40: Recorded Tg according to different methods at 28 days and different curing temperature for Tyfo-S, dry condition 316

Figure C-41: Normalised heat flow variation with temperature for specimens cured at different temperatures for 3, 7, 14, and 28 days, Tyfo-S dry condition 317

Figure C-42: Recorded Tg according to inflection point method at different age and curing temperature for Tyfo-S, saturated condition 318

Figure C-43: Recorded Tg according to onset point method at different age and curing temperature for Tyfo-S, saturated condition 318

Figure B.C-44: Recorded Tg according to different methods at 3 days and different curing temperature for Tyfo-S, saturated condition 319

Figure C-45: Recorded Tg according to different methods at 7 days and different curing temperature for Tyfo-S, saturated condition 319

Figure C-46: Recorded Tg according to different methods at 14 days and different curing temperature for Tyfo-S, saturated condition 320

Figure C-47: Recorded Tg according to different methods at 28 days and different curing temperature for Tyfo-S, saturated condition 320

Figure C-48: Normalised heat flow variation with temperature for specimens cured at different temperatures for 3, 7, 14, and 28 days, Tyfo-S saturated condition 321
Figure D-1: Dimensions of steel dog-bone specimen 330
Figure D-2: Prepared and ready to test steel dog-bone specimens 331
Figure D-3: Tensile test set up 332
Figure D-4: Approximate location of the DIC patches in the analysis 332
Figure D-5: Measured stress-strain curve of the top flange dog-bone tension specimens 334
Figure D-6: Measured stress-strain curve of the web dog-bone tension specimens 335
Figure D-7: Measured stress-strain curve of the top flange dog-bone tension specimens 336
Figure D-8: Measured stress-strain curve of the top flange strengthening plate dog-bone tension specimens 337
Figure D-9: Measured stress-strain curve of the 2 mm plate dog-bone tension specimens 338

Chapter 1

Introduction

1.1 Introduction

Strengthening and repairing existing structures has become increasingly important in the construction industry. Factors such as traffic load increase, and stricter safety requirements have to be considered. Deterioration of structures by weathering is another important factor. The unprotected steel sections are, in particular, the tension flange, vulnerable to corrosion in an average rate of 0.1mm/year in a damp clean atmosphere (Bussell, 1997).

Many present-day bridge infrastructures are in need of upgrading. In most cases, strengthening is less expensive compared to rebuilding. From an environmental and economical point of view, strengthening is preferred to demolition and subsequent rebuilding. According to NBI (2013) in 2010 68.5% of the national bridges were 26 years old or older, the share of total bridges in the U.S. classified, as structurally deficient was 11.5%, and 12.8% of bridges were functionally obsolete. Bridge repairs can be carried out and traffic can still operate where renewal of a bridge will cause major traffic disruption.

There are available composite materials with properties suitable for repair of civil infrastructure. FRP materials have superior properties such as excellent strength-to-weight ratio, durability, creep and fatigue resistance, and easy handling in construction. Carbon fibre reinforced polymers (CFRP) have strength up to ten times the strength of mild steel. FRP materials mechanical properties and general background of their application in structural and construction engineering can be found in Bank (2006); ACI 440R-07 (2007); Hollaway and Teng (2008); Hollaway (2010).

Externally bonded fibre reinforced polymers (EB-FRP) have been widely used for rehabilitation of concrete structures, for over 50 years. Much research on FRP has been carried out over this period. Study of bond performance, creep effect, the ductility of the repair, fatigue performance, force transfer, peel stresses, resistance to fire, and ultimate strength is available. Guidelines for the design and application of

these materials for flexural retrofit of concrete elements are available (FIB, 2001; Mufti *et al.*, 2007; ACI 440.2R-08, 2008; Concrete Society, 2012). Researchers investigated the use of CFRP materials for strengthening and repair of steel structures. Although, the conventional repairing methods such as rivets and bolts, and welding steel plates to the defective elements was effective, there were drawbacks. Local stresses concentration around the drilled holes and the continuity of galvanic corrosion, have limited their use. These conventional solutions tend to be expensive and difficult to implement.

This thesis considers the properties of the materials available to civil engineers. In particular the thesis measures the performance of the adhesives that are required to bond FRP materials to in-situ steel structures. The adhesives are tested in a range of varying temperature and humidity conditions.

1.2 Research objectives

The aim of this work is to investigate glass transition temperature, T_g improvement on the performance of EB-FRP strengthened steel structures in flexure at ambient and elevated temperatures.

Glass transition temperature, T_g is a crucial property of thermoset polymers. The mechanical properties of polymers improve with increasing T_g. Ambient cure structural adhesives are dependent on the curing temperature. Therefore, it is important to ensure that the manufacturers minimum reported mechanical properties and T_g are achieved on-site. Some adhesive manufacturers use a curing regime period to the adhesive coupons testing, and such a curing condition may not be achieved on-site. This research studies the effect of curing temperature on two structural adhesives for up to 28 days at dry and saturated conditions. The experimental results show the importance of curing and conditioning on the glass transition temperature T_g. The relationship between glass transition temperature T_g and curing temperature of the two adhesives are illustrated.

Other research has studied the bond behaviour of metallic structures at ambient temperature when the structure is subjected to various loading such as, monotonic and cyclic load. Little work has been carried out to investigate the joint performance at ambient and elevated temperatures (thermal loading).

Research into T_g is easy to find. The manufacturer's mechanical properties and T_g are used in flexural strengthening design. The relationship between T_g and flexural behaviour has not been researched in depth. It is the intention of this thesis to address the lack of existing research into the performance of cured adhesive joints in flexure.

Steel-concrete composite sections are commonly used in construction. Extreme heat and moisture during summer season can damage adhesives. Researchers have shown that the temperature of parts of a bridge below the tarmac can rise by up to 53°C (Hülder *et al.*, 2008). At ambient temperature, it is important to measure T_g and to ensure that the corresponding mechanical properties are achieved. When FRP strengthened structures are exposed to elevated temperatures, T_g is a crucial factor to consider. The guidelines recommendation (Cadei *et al.*, 2004; ACI 440.2R-08, 2008; Concrete Society, 2012) is that the maximum operating temperature of an adhesive joint should be 15°C lower than the T_g $(T_g - 15)$. This T_g is the corresponding temperature of the peak of $\tan\delta$. The curve $\tan\delta$ is obtained from DMA test. This peak of $\tan\delta$ is measured according to British Standard ISO 6721 (2011). The study also considers whether the current guideline recommendation is safe or some adjustment is required. It should be noted that the recommendations in the guidelines have never been subjected to laboratory testing. The findings of this study lead to the conclusion that some adjustment to the current design guidelines is required.

Other research has examined the performance of adhesive joints analytically. Simplified analytical solutions (linear-elastic) and adhesive property degradation (tensile strength and Young's modulus) with temperature were used in these analyses. This research addresses the limitation of these simplified approaches.

1.3 Thesis organisation

This thesis consists of seven chapters. Figure 1-1 shows the over view of the thesis. Following the introduction (chapter 1), chapter 2 reviews externally bonded CFRP and related research. Chapters 3 to 6 details the laboratory tests and analysis associated with the objectives of this thesis. Finally, the conclusions, the limitations of this research, and the discussion regarding future work are presented in chapter 7.

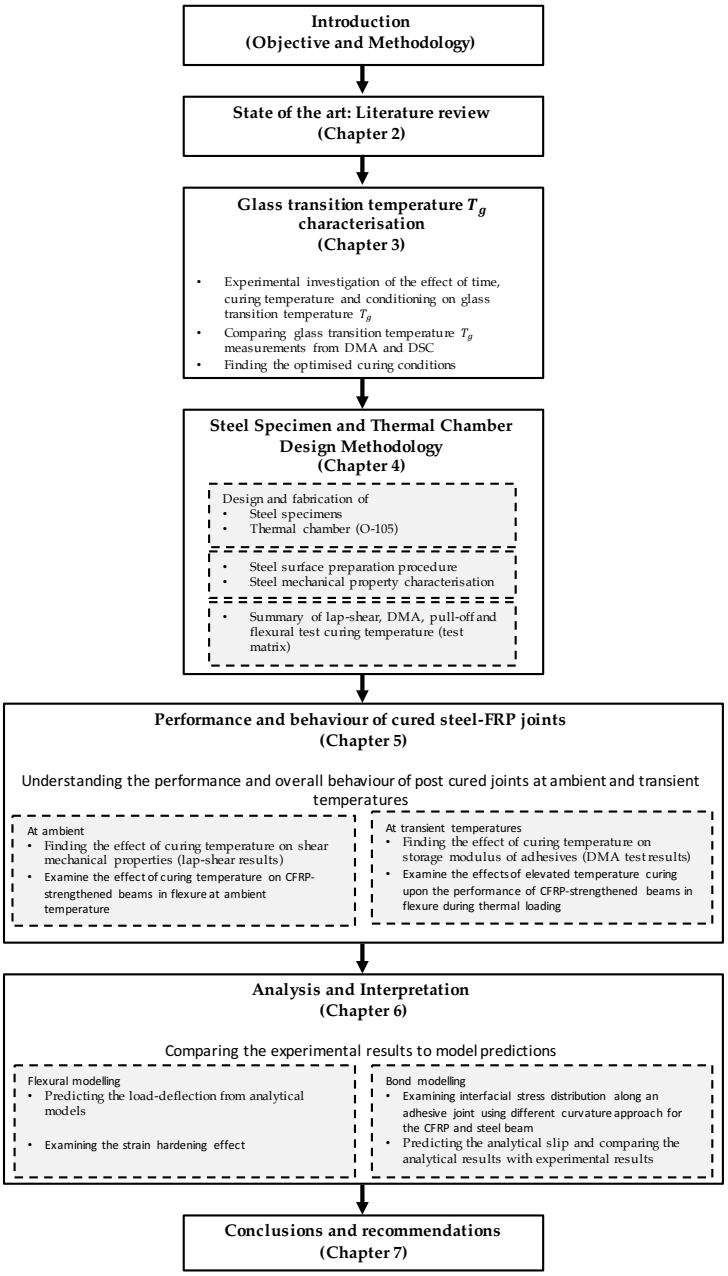

Figure 1-1: The general organization of the thesis chart

Chapter 1: an introduction, which explains the need of bridge infrastructure to strengthening using CFRP, is given. The objectives of the project are presented.

Chapter 2: presents a state-of-art review of the previous work conducted on externally bonded CFRP, methods of characterising T_g of adhesives, and the influence of temperature on the adhesives and CFRP joints. It also reviews the current analytical solutions to examine the interfacial stresses.

Chapter 3: effect of curing and conditioning on glass transition temperature T_g of two widely used structural epoxy adhesives is studied. The T_g of structural adhesives for up to 28 days is studied after exposure to the combination of elevated temperature up to 80°C in dry and water. The two commonly used methods Dynamic Mechanical Analysis (DMA) and Differential Scanning Calorimetry (DSC) are used in the T_g charectrising of the adhesives. The results of the study and data interpretation are presented in this chapter. The optimised curing temperature of adhesive Sikadur-330 was identified.

Chapter 4: contains the description and the methodology of the steel I-sections specimens that are designed to represent steel-concrete bridge deck. The steel specimens are used to study the influence of curing temperature. Details of the specimen fabrication are given. Thermal chamber (O-105) design to cure and test the flexural specimens is shown in detail. Test matrix and curing temperatures to study the performance of adhesive joints are summarised. The steel surface preparation and FRP strengthening procedure is presented. Finally, the mechanical properties of steel used in the fabrication of the specimens are tabulated.

Chapter 5: contains the results of the lap-shear, DMA, pull-off adhesion test and flexural tests. Lap-shear tests under monotonic static load were studied to demonstrate the importance of curing temperature. DMA coupons were prepared to measure glass transition temperature T_g and examine the adhesive storage modulus variation with temperature. The surface preparation adhesion pull-off tests were carried out. Due to the complexity and interaction of the stresses within the adhesive joints in bending, FRP strengthened steel beams under four-point bending were tested. Monotonic static load was carried out on five beams to show the impact

of curing. Three specimens were tested under sustained loading with transient temperature to study the impact of curing on the performance of FRP strengthened steel section subjected to elevated temperature. Finally, test results and interpretation of the results are summarised.

Chapter 6: contains the analyses that were carried out in this research. The model used to study the effect of strain hardening of steel and to examine the load-deflection behaviour of steel beams with and without the FRP materials. A bond analytical model is also developed base on the compatibility approach. The latter model is similar to the previous bond model, but the coupled effect of shear and normal stress was not decoupled. The influence of transient thermal loading is examined using the Young's modulus reduction assuming the DMA adhesive property variation with temperature.

Chapter 7: summarises the conclusions and findings of the research. Design recommendations and possible future research in the field of steel/FRP joint at elevated temperature are given.

Chapter 2

Literature Review

This chapter focuses upon prior research on strengthening structures using bonded FRP plates. It gives a brief description of the properties of commonly used materials, the FRP and the adhesive. A review of existing knowledge of externally bonded Fibre Reinforced Polymer (EB FRP) strengthening techniques is given. Although the current thesis is focused on FRP-strengthened steel structures at warm temperature, relevant information upon steel-to-steel, FRP-to-concrete and steel-to-concrete bonded joints, is also reviewed.

This chapter is divided into two main parts; the first part considers the ambient temperature of EB FRP strengthening of metallic structures, and the second part reviews the effects of temperature on EB FRP strengthening of metallic structures.

Section 2.1 gives a description of the different properties of the materials used in this study, including the adhesive and FRP that are used for structural strengthening applications. The focus is on externally bonded FRP as it is the common way of strengthening steel structures. Plastic analysis method for steel beams is described in section 2.2, as these are relevant to the design and interpretation of the test results and it is intensively used in practice. Previous studies on EB FRP strengthening of metallic structures in different applications are reviewed in section 2.3. Flexural strengthening of metallic structure is considered in detail and the recommendations are followed in the design of the flexure specimens in this research. Section 2.4 reviews some of the analytical approaches for the bond behaviour of FRP materials used to strengthen structures in flexure; in particular the methods that are used in the development of the current design guidelines to strengthen metallic structures in section 2.5.

Epoxy adhesives are the most significant element of EB FRP strengthening of metallic structures. Their behaviour is heavily dependent on temperature, during curing and service. The possible service temperature of steel structures and factors that affect their mechanical properties are discussed in section 2.6. Particular

attention is given to the glass transition response and glass transition temperature, T_g of polymers and the methods used to characterise this property in section 2.7.

The thermal effects on adhesive joint and previous work on the exposure of EB-FRP structures (including metal to concrete, FRP to concrete, and CFRP to steel bonded joints) to elevated temperatures are reviewed in section 2.10 because the behaviour of the adhesive bonds is similar at elevated temperatures. The limited work that looks at the behaviour of flexural strengthening performance and the analytical approaches to predict their behaviour at elevated temperature are also reviewed.

2.1 Materials used in strengthening and rehabilitation of structural members using externally bonding method

Fibre Reinforced Polymers (FRPs) are widely used in a variety of industries, such as the Aeronautical engineering, automotive and marine engineering, and construction industry. Important applications in the construction industry include the strengthening of existing concrete and steel structures with externally bonded FRP reinforcement and the reinforcement of concrete structures with internal FRP bars FIB (2001). FRP composites are defined as a polymer matrix, sometimes known as binder, either thermoset or thermoplastic. Fibres or other reinforcing materials with a sufficient aspect ratio (length-to-thickness), are embedded to provide a discernible reinforcing function in one or more directions (ACI 440R-07, 2007). Often some fillers and additives of various natures are added to the binder.

The main function of the matrix material is to spread the load between the individual fibres, hold the fibres in place, influence the physical properties of the end product and protect the fibres against environmental influences, such as moisture, alkaline in concrete, corrosion and wear. The matrix material is generally a polymer such as unsaturated polyesters, epoxies, vinyl esters, and phenolics. The reinforcement provides the mechanical strength; the continuous fibres will usually be stiffer and stronger than the matrix. The fillers and additives are used as process or performance aids to impart special properties to the end product (ACI 440R-07, 2007).

2.1.1 Fibre reinforced polymer (FRP) materials

Various fibres are commercially available, with a wide range of material properties that directly affect the composite's mechanical properties. Carbon fibre (CFRP), glass fibre (GFRP), and basalt fibre are the types of fibres commonly used in the construction industry. Some of the mechanical properties are covered in this section. The main function of fibre reinforcement is to carry load along the length of the composite. FRP composite properties are directional; the fibres can be oriented to reinforce the composite in various directions, which results in a maximum strength and modulus in the direction of the fibre axis (ACI 440R-07, 2007). Not only are they different in mechanical properties, in particular stiffness and tensile strength, but also their environment resistance. Therefore, the physical and mechanical properties of the composites vary considerably, as does the cost.

The suitability of the fibres mainly depends on the composite properties. These fibres have a tensile strength that is greater than that of steel. Unlike steel, fibres have linear elastic behaviour up to failure, while steel has yield plateau. Reinforcing fibres can be both natural and synthetic, but the most commercial reinforcements are manufactured. The most common form of FRPs used in structural applications is called laminate. Laminates are made by stacking a number of thin layers of fibres and matrices, and consolidating them into the desired thickness (ACI 440R-07, 2007).

Carbon fibres

Carbon fibres (CFRP) are commonly used in polymer matrix composite material. The fibres could be either continuous or discontinuous, usually unidirectional, or woven into a cloth. Carbon fibres are produced from polyacrylonitrile (PAN), pitch, or rayon. Pitch fibres with an approximate diameter of 9-18 μm and PAN-based fibres with an approximate diameter of 5-8 μm are made from carbonizing polyacrylonitrile through burning (FIB, 2001). The properties of carbon fibre depend on fibre microstructure, derived from the precursor type and the processing temperature between 1000 and 3000°C. There are two basic types of carbon fibre: high modulus and high strength. These fibres behave elastically to failure and fail in a brittle manner. The tensile modulus and strength of carbon fibres are stable as temperature rises, and are highly resistant to aggressive environmental factors. Some carbon fibres, particularly higher-modulus, fibres are not easily wet by resins, and surface treatments are necessary before embedding them in a matrix. Due to

markedly low interfacial bond strength, failure in higher-modulus PAN-based fibres occurs on its surface. To overcome this issue and increase the interfacial bond strength, surface treatments have been developed for some resin matrix materials. However, matrix-fibre interfacial bond strength reaches the strength of the resin matrix for lower-modulus carbon fibres. Carbon fibres are used for reinforcing the polymer matrix since carbon fibres are very durable and resistant against creep, fatigue, moisture, chemicals, UV light, and have excellent mechanical properties. However, they can give galvanic corrosion in contact with metals and are expensive. Carbon fibres generally range in diameter from 6 to 10 μm (ACI 440R-07, 2007).

Typical mechanical properties of various types of carbon fibre materials are provided in Table 2-1. The values can be typical mean values obtained from regular testing but the design values of the FRP composite systems should account for both the presence of resin and loading rate.

Table 2-1: Typical properties of carbon fibre (FIB, 2001)

Carbon Fibre	***Mechanical Properties***		
	Young's modulus [GPa]	***Tensile strength [MPa]***	***Ultimate tensile strain [%]***
High strength	215-235	3500-4800	1.4-2.0
Ultra-high strength	215-235	3500-6000	1.5-2.3
High modulus	350-500	2500-3100	0.5-0.9
Ultra-high modulus	500-700	2100-2400	0.2-0.4

Carbon fibres are 10 to 30 times more expensive than E-glass because of the high price of raw materials and the long process of carbonization and graphitization, they possess the highest specific mechanical properties per weight, such as modulus of elasticity and ultimate strength (FIB, 2006).

Glass fibres

Glass fibres are made of silicon oxide with the addition of small amounts of other oxides. Glass fibres are the predominant fibre for many civil engineering applications because of an economical balance of cost and specific strength properties. Glass fibres are very surface active. Hydrophilic and a sizing agent generally coats individual fibres immediately after fibre forming. The sizing also acts to minimize abrasion damage and to aid coupling with polymer matrices. Continues glass fibres reinforcements are classified into three types: E-glass, S-glass,

and alkali resistant ER-glass fibres. Although E-glass fibres are commercially available in E-glass formulations a disadvantage of E-glass is low alkali resistance. A considerable amount of zircon is added to produce alkali resistance glass fibres. Glass fibres generally range in diameter from 9 to 23 μm. Glass fibres are generally a good impact-resistant fibre, but are denser than carbon or aramid. GFRP composites exhibit very good electrical and thermal insulation properties. Table 2-2 contains some of the mechanical properties of these fibres, the values can be typical mean values obtained from regular testing, but the design values of the FRP composite systems should account for both the presence of resin and loading rate.

Disadvantages of glass fibre are sensitivity to stress corrosion at high stress levels, and sensitivity to moisture.

Tensile strength of glass fibres reduces at elevated temperatures, but it can be considered constant for the range of temperatures to which polymer matrices are exposed. Tensile strength also reduces with chemical corrosion and with time under sustained loads (FIB, 2006).

Table 2-2: Typical properties of glass fibre (FIB, 2001)

Aramid Fibre	***Mechanical Properties***		
	Young's modulus [GPa]	***Tensile strength [MPa]***	***Ultimate tensile strain [%]***
E Glass	70	1900-3000	3.0-4.5
S Glass	85-90	3500-4800	4.5-5.5

2.1.2 Polymeric matrices

The matrix accounts for 30-60% by volume of a polymeric composite. The matrices will affect both the mechanical and physical properties of the final product. There are two basic classes of polymeric matrices used in FRP composites: thermosetting and thermoplastic resins (FIB, 2006). Thermoplastic resins become soft when heated, and may be reshaped or moulded while in this state. They can be repeatedly softened and hardened by subjecting them to temperature cycles reaching values above their forming temperature. These polymers do not develop a network structure (cross-links). Thermosets, on the other hand, develop cross-links that set them in shape, and they cannot be reshaped as discussed in section 2.6.2. Thermosets do not melt and flow but will soften when heated, and on further heating they thermally decompose at high temperatures. The region, in which the

polymers lose hardness, is called the glass transition region. The most common thermosetting polymeric matrix materials used in the composites industry with high-performance reinforcing fibres are polyesters, epoxies, and vinylesters. The mechanical properties of typical thermoset resins are shown in Table 2-3.

Table 2-3: Typical properties of thermosetting matrices (FIB, 2001)

Property	***Matrix***		
	Epoxy	***Polyester***	***Vinylesters***
Density (kg/m^3)	1200-1400	1200-1400	1150-1350
Tensile strength (MPa)	55-130	34.5-104	73-81
Longitudinal modulus (GPa)	2.75-4.10	2.10-3.45	3.0-3.5
Poisson's coefficient	0.38-0.40	0.35-0.39	0.36-0.39
Thermal expansion coefficient (10^{-6}/°C)	45-65	55-100	50-75
Moisture content (%)	0.08-0.15	0.15-0.60	0.14-0.30

2.1.3 Epoxy adhesives

Epoxies are classified in the plastics industry as thermosetting resins. Epoxy resin can be engineered to achieve varying levels of performance. High-performance epoxies have been prepared with a variety of phenolic and aromatic amines. Small amounts of reactive curing agents (an anhydride or an amine hardener) are added to liquid resin to initiate polymerization. Generally, epoxies are a two-part system. Different hardeners, or different quantities of hardener, produce different cure profiles and give different properties to the finished composite (ACI 440R-07, 2007). The curing agent used will determine whether the epoxy cures at ambient or elevated temperatures. Low viscosity, low molecular weight Bisphenol Epoxies, are the ones most widely used in the composites industry. Cross-links are formed and epoxy liquid resin changes to a solid material. The density of cross-links depends on the chemical structure of the starting resin, curing agent and reaction conditions, which plays a major role in establishing the final properties of the solid epoxy (FIB, 2006), and by adding additives the mechanical properties can be improved. The main advantages of epoxy resins are high mechanical properties, easy processing, low shrinkage around 4% during cure (FIB, 2006), good adhesion to a wide variety of fibres and excellent adhesion to a substrate. Figure 2-1 shows the stress strain response of typical high-, intermediate-, and low-modulus. Epoxies have high corrosion resistance and are less affected by humidity and elevated temperature than other polymeric matrices. Curing of such resins can be achieved at temperatures ranging between 5°C and 150°C (FIB, 2006). Epoxies, however, are

relatively high cost, (more expensive than polyesters and vinyl esters), and they need more careful processing to maintain moisture resistance (Zoghi, 2013). They also require a long curing period unless a post-curing at elevated heat used to obtain ultimate mechanical properties. The same post-curing conditions, as tested coupons, which are provided by the manufacturer, should be followed to achieve ultimate mechanical properties.

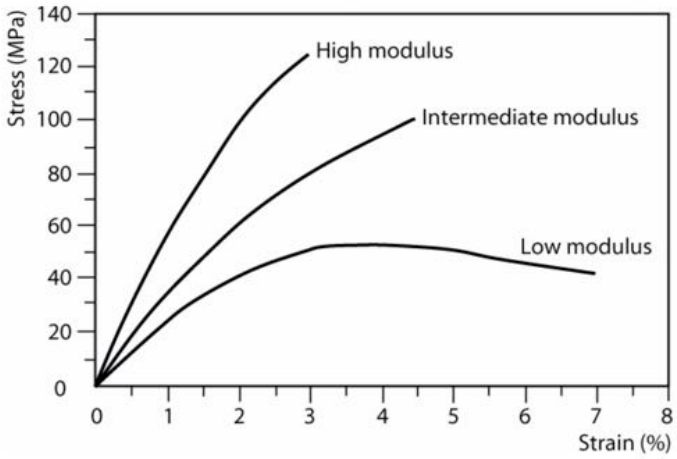

Figure 2-1: Stress-strain curves of epoxy matrix resins of different modulus (FIB, 2006)

Currently, epoxy is the predominant resin used in external repair of concrete using FRP sheet and fabric products (ACI 440R-07, 2007). The epoxies provide a load path during the service life of the strengthened structure, carrying shear and normal stresses and exposed to various environmental conditions such as variable temperatures. Therefore, the structural adhesives need to be strong and provide a good bond over a long period. In this research, two types of epoxy investigated under different curing temperatures varying from ambient up to 80°C at 0% and 100% relative humidity. The details are provided in section 3.

2.2 Plastic analysis for steel structures

This section covers some of the assumption of the plastic design, the background of the theory and history of research. In practise, the moment capacity of a steel section is found using this method, which does not count for the

contribution of strain hardening. The plastic moment capacity M_p finding that is based on these assumptions, which can underestimate the actual moment capacity of the section. The plastic moment capacity M_p finding procedure is allowed by codes of practice. A briefed background of plastic analysis, the material property requirements for plastic design are discussed in more detail and the assumptions that are used in the estimation of the ultimate plastic moment of steel section are discussed in section 2.2.1 and 2.2.2. The steel I-section that was used in this research satisfy the requirements of Eurocode 3 to be used for plastic design. Due to the simplifications that are accepted by the design standards and the elimination of the effect of strain hardening, the ultimate plastic moment capacity is underestimated. The ultimate plastic moment capacity finding for standard section is detailed in section 2.2.3. It is important to consider the contribution of the strain hardening when the slender section may buckle before yielding occurs. The strain hardening effect and its contribution is addressed in section 2.2.4.

The experiments carried out in section 5 are analysed in section 6 and compared to the analytical predictions that use some of the assumptions in this section.

2.2.1 The basics of plastic design

Plastic collapse analysis of structures is increasingly used to assess the true strength of the structure. In contrast, elastic analysis is widely used to find a conservative estimate of the Ultimate Limit State for the structure. The two methods assume that there is corresponding deformation including curvature within the beam when a transverse load is applied to a steel element. Due to the deformation, internal forces and bending moments occur. Similar to the simple elastic theory of bending of beams, in the elastic-plastic and fully plastic analysis, it is assumed that strain varies linearly across the cross-section (plane sections remain plane), that adjacent fibres do not affect each other, and that the effect of shearing stress on bending can be ignored.

In plastic design, the behaviour is idealised as "rigid plastic", in which no deformation occurs until the plastic moment is reached. The assumption of rigid plastic material behaviour is satisfactory if the material can sustain stresses at increasing deformation "ductile". The yield stress in tension is equal to the yield stress in compression. Full plastic moment occurs in the section. It is also assumed

that there is no other mechanism of failure, such as buckling, before the plastic collapse mechanism has fully developed.

2.2.2 Research into the plastic behaviour of steel

The initial methods of analysis and design of steel structures in the nineteenth century were based on the theory of elasticity. Baker *et al.* (1956) established plastic design theory of steel structures application. However, Ewing (1899) suggested that the stress distribution across the section would be of the form shown in Figure 2-2. It is not known whether Ewing confirmed his hypothesis by any tests on steel beams.

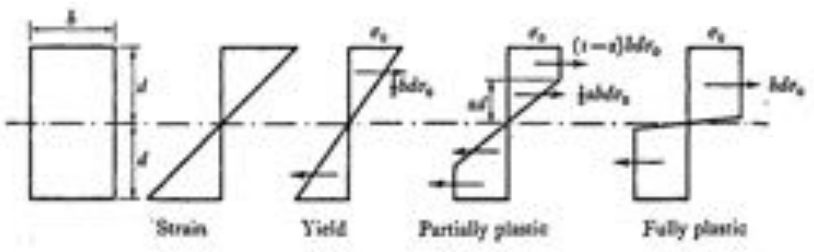

Figure 2-2: Stress and strain distribution in a beam section with increasing curvature (Baker *et al.*, 1980).

"The distribution of stress will then be modified. The outer layers of the beam are taking permanent set while the inner layers are still following Hooke's law. As a simple instance it will be sufficient to consider in a general way a material which is strictly elastic up to a certain limit of stress and then so plastic that any small addition to the stress produces a relatively very large amount of strain…

... if the material tested is in the form of a rectangular bar...the distribution of stress may approach an ultimate condition in which the upper half of the section is in uniform tension f_1*, and the lower half is in uniform compression of the same intensity"* see Figure 2-2.

Early research of plastic behaviour of beams was undertaken by Maier-Leibnitz (1936). Tests on simple and continuous beams were performed, observing the ductile behaviour of steel beams. Some beams eventually failed by lateral buckling.

The major experimental programs took place at Lehigh University in the USA and at Cambridge University in the UK. The history of these developments since the War is well documented, and there is a large number of published papers, which are listed. In recent years, the focus has been on the use of cold-formed sections in portal frames (Wilkinson and Hancock, 1999), since plastic design of cold-formed (rectangular hollow section) portal frames is not yet permitted by Eurocode 3 (European Committee for Standardisation 1992). This is because most cold-formed RHS do not satisfy the requirements of clause 3.2.2.2, which includes the properties that are assumed in the development of plastic design for slenderness limits and material ductility requirements.

2.2.3 The plastic moment resistance of steel sections

Consider the I-section in bending, according to simple engineering bending theory (strain compatibility), the distribution of strain across the section is linear regardless of the stress state, and the value of the strain at the extreme fibres is proportional to the curvature. Generally, an idealized stress-strain curve is used, which is a linear-elastic perfect plastic (elastic – plastic) response. In the elastic range, the stress distribution is linear in relation to the strain, and yielding stress occurs when a certain level of strain is reached.

Consequently, the stress distribution within the section changes with increasing levels of curvature within the section. The stress which yielding is occurred is known as yielding strength f_y. The extreme fibres reach the yield stress at the yield moment M_y, where $M_y = f_y\, Z$ and Z is the elastic section modulus. With increasing curvature, yielding spreads toward the neutral axis. For the elastic – plastic response and at high values of curvature, the section yields almost completely and it is called fully plastic. The plastic moment M_p, is calculated $M_p = f_p\, S$ and S is the plastic section modulus. Once the cross-section is fully plastic, increases in curvature can occur without a corresponding moment increase.

For most of the standard section, the values of Z and S are given in tables of section properties (Davison and Owens, 2012), that the full plastic moment of the section is quickly calculated without having to do the full evaluation. The ratio of plastic section modulus to elastic section modulus is known as "shape factor". A low shape factor is an indication of a section that uses the material efficiently; it

implies that the moment where yield begins is close to the fully plastic state; the I-sections shape factor is very close to unity, and it is round 1.15 (Baker *et al.*, 1980). The section with one axis of symmetry such as steel concrete composite section, the elastic and plastic section modulus requires calculation.

According to the design methodology, the requirement design data is the grade of the used steel. The grade is the yielding strength f_y of the material; simple coupon test is the measure of f_y. There are two standards to specify the yielding strength f_y; British Standard (British Standard ISO 4360, 1990; British Standard EN 10025, 2004) and ASTM standard (ASTM A0370-03a, 2003; ASTM E8/E8M-09, 2009). Although there are minor differences in the geometry of the coupons, the major difference is the position within the cross section from which the test coupons are taken. The former specifications recommend that the coupons to be taken from the flanges since they contribute most of the strength when the section is bending. While according to ASTM standards the coupons shall be cut from the web of the section this can lead to higher recorded values for strength. This is because firstly, strength tends to increase with decreasing thickness, and webs are thinner than flanges; secondly, the webs tend to contain higher carbon due to the manufacturing process (Byfield and Nethercot, 1997; Byfield *et al.*, 2002). The variation in the results for a section rarely exceeds 10-15% (Byfield *et al.*, 2002).

2.2.4 Strain hardening effect

The contribution of strain hardening is significant, and the plastic theory does not consider this contribution. In an experimental study carried out Byfield (1996); Byfield and Nethercot (1998); Byfield *et al.* (2002), 12 fully restrained against lateral movement standard I-sections were tested and it was concluded that M_p according to the pre-mentioned procedure underestimated flexural strength by an average of 18%. In another work by Hasan and Hancock (1988) on cold-formed rectangular hollow sections it was demonstrate that sections were capable of exceeding the predicted plastic moment capacity by an average of 23%. The experimental work on steel sections by Wilkinson *et al.* (1997); Wilkinson and Hancock (1999) showed that the theoretical M_p significantly underestimates the ultimate strength of the section, in some cases it reached 27%. Regardless of the member method of manufacturing and producing, plastic theory remarkably

underestimated the capacity of the section. The increase is due to the complex nature of the three-dimensional stress system, which is different from the stresses when the coupons are tested in pure tension (Byfield and Nethercot, 1998). Strain hardening branch from the coupon tests starts after yielding plateau; the onset of the strain hardening is in the range of 6−10 ε_y, where ε_y is the yielding strain.

The scaled specimens in section 5 have one axis of symmetry, and two different grades of steel used in the fabrication. The coupon tests have shown significant amount of strain hardening as shown in Appendix D. The theoretical plastic moment capacity M_p of the section according to this method underestimates the capacity of the section, therefore, the contribution of strain hardening is considered. The details of this calculation are provided in section 6.4; different strain hardening proposals are studied and presented in section 6 of this research.

2.3 Externally Bonded FRP strengthening of steel structural elements

Adhesives were used in construction industry for decorating such as the attachment of ceramic tiles and mosaics to floors and walls, ceiling tiles, and thermal insulation materials, and several civil engineering applications such as asphalt or flexible road and runway pavements (Mays and Hutchinson, 2005). The use of adhesives in civil engineering follows the successful use of them in other branches of engineering, such as aerospace where adhesives were used in bonded composite air frames to achieve weight savings and improve the strength-to-weight ratio when compared with metal construction (Dunn, 2010).

Nowadays, adhesives are used to bond structural and semi-structural elements; composite steel/concrete bridge decks, structural steelwork connections, sleeved steel bar and rebar connectors, as a substitute for or in combination with conventional joining methods (Mays and Hutchinson, 2005). Advances have been made in bridge construction, the most mature application of FRP/steel composite construction is the use of glass FRP (GFRP) bridge decks acting in a composite manner with steel girders (O'Connor and Hooks, 2003). FRP composite bridges and the most up-to-date applications are discussed in section 11 (Examples and Case Studies). In the past few decades, FRP reinforcement and epoxy systems have been widely used in repair and refurbishment applications to enhance the service life of

existing structures, such as steel–concrete composite bridges. Externally bonding FRP laminates to the steel structure is the common method of strengthening.

In particular Externally Bonded FRPs method, which are used to retrofit structural members such as columns, slabs, beams, and girders in structures such as bridges, parking decks, smoke stacks, and buildings (Steckel *et al.*, 1999). Externally bonded FRP for strengthening concrete structures has been investigated intensively; extensive research on FRP exists on bond performance, creep effects, ductility of the repairs, fatigue performance, force transfer, peel stresses, resistance to fire, and ultimate strength. Guidelines for the design and application of these materials for flexural retrofit of concrete elements are available from the manufacturers (du Béton, 2001; Mufti *et al.*, 2007; ACI 440.2R-08, 2008; Concrete Society, 2012). Therefore, this review does not cover any concrete strengthening of concrete section.

A comprehensive state-of-the-art review of research work on FRP strengthening steel structures was conducted by Shaat *et al.* (2004); Ragab *et al.* (2007); Zhao and Zhang (2007) on retrofitting steel structures using FRP. The review on strengthening steel structures is summarised in this chapter including the most recent work related to strengthening steel and steel-concrete composite sections.

The focus of this review is on the steel sections and steel-concrete composite section only; these sections are mostly used in short and medium span bridges. More than 40% of the bridges in North America built in the fifties and sixties are in serious and urgent need of repair and rehabilitation or replacement (Ragab *et al.*, 2007). According to NBI (2013) in 2010 the share of total bridges in the USA classified, as structurally deficient was 11.5%, and 12.8% of bridges were functionally obsolete. Flexural and shear rehabilitation of steel girder are reviewed in detail.

2.3.1 Flexural strengthening

In the earlier study, Mertz and Gillespie (1996) report on six small scale specimens 1500-2000 mm long W200x15 members retrofit with the five different adhesively bonded schemes and 6 mm thick CFRP plates bonded to the tension flanges. The beams were tested in a four-point loading. All specimens demonstrated an increase in flexural stiffness and strength compared to the un-strengthened control specimen; there was approximately 20% increase in the flexural stiffness and

more than 50% increase in strength before the test of these beams was stopped due to the buckling of the top cover plate. Based on the results of the small-scale program, full scale tests were carried out on two girders 610 mm deep, 6400 mm long I-beams taken from a demolished bridge that had a severely corroded bottom flange. The test results showed a significant increase in the ultimate strength and flexural stiffness of the repaired beams due to the present of CFRP strips applied to both the top and bottom of the tension flanges. The first girder had an original condition resulting in about 62% of its un-corroded stiffness. In this case the strengthening significantly improved the behaviour but was unable to restore the un-corroded stiffness or strength. The second girder had a stiffness and strength, prior to strengthening, of approximately 87% of that expected for a new, un-corroded girder. In this case, the stiffness was increased to that of the un-corroded girder and the strength was found to exceed that of the un-corroded girder. Buckling of the compression flange controlled the ultimate capacity of both specimens; this failure was not addressed in the strengthening scheme.

Sen *et al.* (2001) tested six steel-concrete composite specimens; wide flange steel W200×36 of 6100 mm long and a 114 mm thick by 710 mm wide reinforced concrete slab. Three of the beams had yield strength of 310 MPa, while the remaining had higher yielding strength of 370 MPa. The beams were first loaded to cause yielding of the tension flanges to simulate severe service case. Then three beams were strengthened using 2 mm CFRP plate, while the remaining three beams were strengthened using 5 mm thick CFRP plate. Two out of the three beams strengthened using 2 mm CFRP plate were tested without end anchorage, while the third beam was tested using a bolted clamp assembly anchorage consisting of a pair of bolts at 89 mm from the ends of the plates damaged beams. For the beams strengthened with 2 mm CFRP plate, the test was terminated because the load cell reached its capacity. The behaviour of the beam having anchorage did not differ from that with epoxy adhesive only because no debonding was observed in either cases. For beams strengthened with 5 mm CFRP plate, one beam was tested without end anchorage that had a premature sudden failure by the delaminating of the CFRP plate. This beam was then re-tested to determine the ultimate capacity of the steel section that was used to fine- tune the finite element model used to determine the flexural behaviour of all specimens. The rest of the beams strengthened using 5 mm CFRP plate, had a bolted clamp assembly consisting of two lines of three 19 mm diameter bolts at each end. The failure mode was by the CFRP rupture along

the bolts. The results showed a significant increase in the ultimate capacity of steel composite bridge sections containing 310 MPa wide flange shape. The increase in ultimate capacity was 21% and 52% for the 2 mm and 5 mm CFRP plates, respectively. Corresponding increase in ultimate load capacity for the bridge sections containing 370 MPa wide flange shapes were 9% and 32% for the 2 mm and 5 mm CFRP plates, respectively. The results indicated modest increases in the elastic stiffness, particularly when the thinner 2 mm CFRP plates were used. For all beams, the results indicated that failure was ductile because of the noticeable deflection before failure.

Mertz *et al.* (2002) extended their initial work investigating the transfer length of bonded CFRP and the fatigue performance of FRP strengthened girders. Simple steel tensile specimens having CFRP strips bonded to both faces were used to investigate the force transfer between steel and CFRP. In all specimens, regardless of load level considered, approximately 99% of the total force transfer occurs within the first 75 to 100 mm of the bonded reinforcement. This result is consistent with standard calculations of "effective bond length". Mertz *et al.,* recognize the importance of a thin adhesive bond line in allowing stress transfer between the steel substrate and CFRP. Debonding was only reported in one tension specimen at strains corresponding to yield of the steel specimen. Although the adhesive properties were not provided in the report, the lack of debonding in the other specimens was attributed to the use of adhesive with a low shear modulus and high elongation properties.

A field installation report by Miller *et al.* (2001) on a single girder of a bridge. A single W610x125 girder spanning 7.5 m feet was retrofit with CFRP on the bottom of the tension flange. Load tests indicated a reduction in tension flange strains of 11.4% under a vehicle equivalent to approximately H32 loading.

In 2003, Tavakkolizadeh and Saadatmanesh (2003a, 2003b) studied strengthening steel-concrete composites beam with different number of CFRP sheets. Three beams were fabricated using W335×13.6 A36 steel beams and a concrete slab of 75 mm thick and 910 mm wide. The beam had a span of 4780 mm and four-point bending tests were performed with a 500 mm constant moment region. A wooden block was placed to fit tightly between the steel flanges at the location of the point load to play a stiffness role and prevent web crippling. A unidirectional CFRP sheet of width 76 mm and thickness of 1.27 mm was bonded to the bottom flange of the steel beam

using one, three, and five layers for the three strengthened beams, respectively. The strengthening technique used increased the ultimate capacity by 44%, 51%, and 76% for one, three, and five-layer retrofitting systems, respectively. The effect of strengthening on the stress level at the elastic range and the elastic stiffness was insignificant due to the low Young's modulus of the CFRP sheets (144 GP). A simple analytical model was used in the analysis of the behaviour of the beam and then compared to the AASHTO ultimate strength design method. The analytical model showed good correlation with the experimental results.

In 2004, Chajes *et al.* (2005) report is a related demonstration project involving the strengthening of two concrete slab-on-steel bridge girders in Ashland Bridge in Delaware. The bridge is steel through girder bridge with a 30.5 m simple span has a concrete deck supported on 19 floor beams (W610×149) that are spaced 1.83 m on centre and span 8.23 m between through girders. The pultruded CFRP plates composed of unidirectional carbon fibres and a vinyl ester resin matrix were applied to the bottom face of two floor beams. The pultruded plates were 37 mm wide and 5.3 mm thick and several plates were used to make up the full width of the flange. In this application, a decrease in tension flange strain of 5.5% was observed under service load conditions. The projects are used to investigate the long-term performance and durability of CFRP strengthening techniques for steel bridge girders.

Patnaik and Bauer (2004) report on an experimental program of CFRP strengthened steel beams. This study also addresses flexural strengthening by adhering CFRP strips to the tension flange by using built-up steel I-beams in their investigation in the first series of testing program. Three beams designed to fail in flexure, with the web consisted of a 305×9.5 mm plate and a 153×9.5 mm plate for the flanges. The beams had a total length of 3550 mm. One beam tested as control specimen. The two left beams were strengthened using CFRP plates attached to the tension flange to cover the whole width. As the plates used had only 51 mm width, they were assembled first to the required width before being bonded. The CFRP plate had a tensile strength and tensile modulus of 2790 MPa and 155.1 GPa, respectively. The moment capacity of the beam was increased by 14.1% and 14.5%. Both strengthened beams are reported to have failed due to lateral torsional buckling, however the authors report a final failure involving rupture of the CFRP. This latter observation demonstrates that in this application, bond of the CFRP to the steel substrate was adequate.

The work by Al-Saidy *et al.* (2004) investigated the behaviour of steel-concrete composite beams. The investigation focused on the behaviour of beams damaged intentionally at their tension flange to simulate corrosion and then repaired with carbon fibre reinforced polymer plates attached to the tension area. Six steel-concrete composite beams were tested in this study. The steel beams were W200×22 grade A572 structural steel acting compositely with a 76 mm thick by 812 mm wide reinforced concrete slab. The experimental program consisted of two undamaged girders and four damaged girders. The damage to the beams was induced by removing part of the bottom flange; varying between no damage and a loss of 75% of the bottom flange. In this study, longitudinal strains as well as shear stresses along the CFRP plate of all tested beams were measured by utilizing extensive instrumentation along CFRP plate. The experimental results showed that the damage to the bottom flange affected both the flexural stiffness and the strength of the beam. The results indicated that the elastic flexural stiffness of damaged beams up to 50% can be restored with the use of CFRP plates for the system investigated.

Schnerch *et al.* (2003); Schnerch *et al.* (2004); Schnerch and Rizkalla (2006) investigated resin and adhesive selection for wet lay-up of carbon fibre sheets and bonding of pre-cured laminate plates and their effect on the flexural behaviour of a steel monopole. Ten different types of adhesives were investigated using double lap-shear test. The results of the first series of testing used in the second series of testing to determine the development length. A Super-Light Beam (SLB 100 x 5.4) with an additional steel plate welded along the length of the compression flange was used as the strengthening technique. The tests were carried out in four-point loading scheme loading points 101.6 mm apart. It is reported that the addition of the steel plate in the compression region simulates the presence of a concrete slab by decreasing the neutral axis depth such that the strain profile of the cross-section would be similar to that in bridge girder acting compositely with a concrete deck. Test results of the first scaled monopole tower showed a 25% increase in stiffness in the elastic range over the same monopole before strengthening. In further work by the same team strengthened 6400 mm long steel-concrete composite girders consisting of W12×30 A36 I-steel beams with an 840×100 mm concrete slab. The four-point loading scheme used in the experiment with the constant moment region was 1,000 mm, with two equal shear spans of 2,700 mm. Strengthening was performed using Intermediate Modulus CFRP plates with elasticity modulus of 440 GPa and High Modulus CFRP plates with elasticity modulus of 660 GPa. The

reinforcing ratios were 4.5% for intermediate strengthened beam and 7.6% for the high modulus beam, where the reinforcing ratio is the ratio of CFRP reinforcement to steel beam area. The girders were loaded up to 60% of the specified yield stresses at the bottom flange and then unloaded before strengthening; this was to compare the increase of stiffness of the section after reinforcing with the CFRP plates. To reduce the risk of premature debonding failure at the plate ends the plates were wrapped around the flange using 330 mm CFRP sheets at the splice locations and the ends. Also, the plate's ends were detailed using a 20° reverse bevel. The ultimate flexural capacity was increased by 16% and 45%, respectively, for each strengthening type specimen while the flexural stiffness increased only by 10% and 36%.

Nozaka *et al.* (2005) proposed an alternative technique to single and double lap specimen testing, which can be used to determine minimum bond length required to achieve the maximum strength of the rehabilitation scheme. Loading is indirectly applied to the FRP via the steel plates, which are bolted to a beam at the mid-span. A large hole and a slit, 13 mm in width, were made at mid-span of the girder. The slit was intended to represent a severe crack in the tension flange of a girder in the field, although the width of the crack was larger than those found in the field. The new test setup, which accounts for flexure together with tension, would be more accurate for obtaining the effective bond length for polymers in civil engineering applications. The work also discusses the weaknesses and strengths of standard single-lap and double-lap specimens.

Lenwari *et al.* (2005, 2006) reported on the flexural behaviour of steel beams that were strengthened with partial-length adhesively bonded CFRP plates; strengthened seven W100×17.2 beams using three different lengths of CFRP plates (500, 650 and 1200 mm). Steel plates of 200×12.2 mm were welded at the compression flange of the steel beam in order to ensure no compressive yielding. A four-point loading scheme was used to test the beams having a span of 1800 mm and the constant moment region of 150 mm. The CFRP plates were bonded to the bottom flange with lengths of 500 mm for two beams, 650 mm for three beams, and 1200 mm for two beams. The failure mode was by debonding for the beams with CFRP plate length of 500 and 650 mm while for the beams strengthened with CFRP plate with length 1200 mm, the failure was by rupture of the CFRP plate. The two beams tested with 500 mm CFRP plate were reused in the 650 mm and 1200 mm CFRP plate. The last two samples experienced an increase in the strength of 61%

and 75%, respectively. In the second series of the experimental program, the authors tested similar samples to investigate fatigue in the bonded area. Variables studied in the static and fatigue tests were CFRP plate thickness and modulus, adhesive bond line thickness, adhesive modulus, and adhesive spew-fillet angle. The authors concluded that the stress intensity at the end of CFRP plates governs the debonding strength and that this region was critical for the initiation of debonding.

Colombi and Poggi (2006a) used CFRP plates to strengthen traditional hot rolled HEA 140 shaped beams. Four identical 2500 mm long steel beams were strengthened in tension using two different epoxy adhesives. The testing carried out under three-point bending. Force transfer mechanisms, strength, and stiffness of the beams were the main interest of the study. The CFRP plates were strengthened with one layer a pair of parallel plates each of 2000 mm in length. While the specimen reinforced using 2 layers, two pairs of CFRP plates of length 2000 mm and 1800 mm, respectively. The beams were tested under three-point loading. Two pairs of lateral bracing were provided to the remaining specimens to prevent the torsional buckling that took place while testing the first beam. This investigation focused on the evaluation of the local stresses at the laminate ends and the effect of using different adhesives and number of layers on both the stiffness and load carrying capacity. The elastic stiffness of the strengthened beams was increased by 13.8% for beams strengthened using two layers. The yield load increased by approximately 11% for beams strengthened using one layer and just over 23% for two layers. The use of two different epoxy adhesives had no significance on the beam behaviour. An analytical model using ABAQUS was developed to predict the behaviour of the strengthened beams. The proposed model showed good agreement with the experimental results.

Photiou *et al.* (2006) investigated the effectiveness of an ultra-high modulus, and a high modulus, CFRP prepreg in strengthening artificially degraded rectangular hollow sections (RHS 145×82) steel beam with 1700 mm clear span under four-point loading with 400 mm constant moment region. The damage was introduced by removing 50% of only one narrow side. The upgrading material system used was made from a hybrid of unidirectional CFRP (either high or ultra-high modulus) and ±45° GFRP composite for all the specimens had the same hybrid lay-up. Two different strengthening schemes were used in the study; two beams were upgraded with U shaped prepreg units, which extended up the vertical sides of the beam to the neutral axis height, and another two beams were strengthened using prepreg

strips attached only to their soffit. The authors reported that the failure load for all specimens exceeded the plastic collapse load of the undamaged beam and by using the U-shaped configuration for the fibres, composite action was provided between the steel member and fibre layer leading to better performance even at failure levels. Debonding was observed for the specimens with composite material only at the soffit.

Shaat and Fam (2006) studied the behaviour of artificially damaged steel-concrete composite beam strengthened using two types of CFRP sheets. Four beams of 1950 mm were tested under four-point bending with constant moment region of 400 mm. The beam consists of W150×22 hot rolled steel section with 465×75mm concrete deck. The tension flange of three beams was notched at mid-span to simulate the fatigue cracks or section loss. One beam was strengthened using Type1 CFRP sheets with tensile strength 510 MPa and Young's modulus of 230 GPa. While two beams were strengthened with Type 2 CFRP sheets with tensile strength 1130 MPa, Young's modulus of, and 107 GPa. Using 14 layers of Type 1 sheets recovered all the loss in strength and stiffness and an increase of 10% in the strength and 25% was observed in comparison with the undamaged control beam. They reported rupture of the high modulus CFRP sheets. However, using 5 layers of Type 2 CFRP sheets recovered only 87% and 85% of the original strength and stiffness for one beam and 50% and 91% in the other beam due to the premature debonding failure mode. The low recovery level of original strength and stiffness in the last beam could also be due to the long-time interval between the sand blasting and application of the CFRP sheets.

El-Hacha and Ragab (2006); Ragab and El-Hacha (2006a, 2006b) tested six steel-concrete composite beams having a 6000 mm span. The girder's steel cross section was a standard W200x19.3 hot rolled I-beam with a 435×56 mm concrete flange. One beam was an un-strengthened control, and the remaining five beams were strengthened using different strengthening materials including Steel Reinforced Polymer (SRP) sheets, Intermediate Modulus Carbon Fibre Reinforced Polymer (IM CFRP) pultruded plate, unidirectional pre-impregnated Carbon Fibre Reinforced Polymer (CFRP) sheets, High Modulus Carbon Fibre Reinforced Polymer (HM CFRP) pultruded plate, and Ultra High Modulus Carbon Fibre Reinforced Polymer (UHM CFRP) pultruded plate. The FRP reinforcement ratio was 8.1%, 3.87%, 21.4%, 5.64%, and 6.45%, for the SRP sheet, IM CFRP plate, CFRP sheet, HM CFRP plate, and UHM CFRP plate, respectively. The FRP reinforcement ratio was calculated as

the ratio between the applied FRP area and the area of the steel section. The increase in the yield load for the strengthened beams with respect to the un-strengthened control beam was 22.5%, 29.0%, 21.3%, 52.4%, and 70.8%, respectively. While the increase in the ultimate load for the strengthened beams with respect to the un-strengthened control beam was 31.0%, 37.4%, 24.3%, 48.7%, and 42.9%, for the SRP sheet, IM CFRP plate, CFRP sheet, HM CFRP plate, and UHM CFRP plate, respectively.

Sallam *et al.* (2010) investigated flexural behaviour of strengthened steel–concrete composite beams by either adhesively bonded carbon fibre reinforced polymers (CFRP) sheet or welded/bonded steel plate was studied. Eight steel–concrete composite beams of 1800 mm in length were fabricated; standard steel I-beam with a reinforced concrete deck slab 500×100 mm. The testing was conducted under four-point bending with a constant moment region of 500 mm. One specimen was tested as a control. Three specimens were strengthened with steel plates. Three different attachment patterns of steel plate to the soffit of the beams were used; discontinuously welded, end welded, and bonded/welded steel plates. Four specimens were strengthened with CFRP sheet wrapped around the flange of the I-beam and a part of the web. Two of these beams were strengthened by fully bonded CFRP sheet. Similarly, the last two specimens were strengthened but have pre-intermediate debonding area of 50 mm length flange width at the bottom surface of the lower flange. The results showed that there is no growth of the intermediate debonding before the yield of the lower flange occurred for all strengthened beams by CFRP sheet. After yielding, the beams with pre-debonding area showed lower flexural capacity than those with fully bonding due to the rapid growth of the intermediate debonding. There is a difference in the yield load between the three different patterns of the welded steel plates with a marginal difference in the elastic stiffness. Timber blocks were used to delay lateral torsional buckling of the specimens.

Galal *et al.* (2011) studied the effectiveness of using carbon fibre-reinforced (CFRP) composite systems in retrofitting deteriorated steel beams. A total of 13 medium-scale steel I-beams with a span of 1600 mm was tested in a four-point bending. The tested beams were divided into four groups according to their studied parameter. Group 1 consists of four un-strengthened beams with different percentages of intentional damage to simulate corrosion in the bottom flange with the aim of investigating their behaviour and to determine the residual flexural

capacity. The damage was introduced by drilling holes in the bottom flange to reduce 33% of the flange in the mid span, and forming notches to present 33% and 50% of the flange loss in the middle one-third of the beam's span. The other three groups have deteriorated steel beams that were retrofitted with different CFRP systems with the aim of evaluating the effectiveness of the proposed retrofit schemes. Four damaged beams were retrofitted with CFRP sheets bonded to the tension flange, and were tested in Group 2. Two were damaged by drilling eight holes and another two by forming two notches each side of the bottom flange. Group 3 consists of two deteriorated steel beams that were retrofitted with CFRP plates externally bonded to the bottom flange of the tested beams. Group 4 consists of three beams retrofitted using an un-bonded CFRP sheet attached to two ductile anchorage systems at the ends. Group 3 and 4 damaged using eight 6.35 mm diameter holes. The study shows that steel beams retrofitted with external bonded CFRP systems experienced limited ductility upon the failure of the CFRP either by de-bonding or rupture at higher load capacities than that of the un-strengthened beams. The proposed anchorage system could increase the strength of the deteriorated beam, behave in a ductile manner, and eliminate the early CFRP sheet peel off.

Narmashiri *et al.* (2012) reports the experimental and numerical investigations on the Carbon Fibre Reinforced Polymer failure analysis and structural behaviour of the CFRP flexural strengthened steel I-beams. Thirteen beams 2000 mm in length were tested in four-point bending with constant moment region of 600 mm. Various bond length of 600, 1000, 1500, 1700, and 1800 mm were used in the study. The results show the CFRP failure modes used in flexural strengthening of steel I-beams include below point load splitting (BS), below point load debonding (BD), end delamination (EDL), and end debonding (ED). The occurrences and sequences of CFRP failure modes depended on the strengthening schedule. The structural performance of the CFRP strengthened steel beams also varied according to the strengthening specifications investigated in this research. To simulate the specimens, ANSYS software in full three-dimensional (3D) modelling case and non-linear analysis method was utilized.

Afefy *et al.* (2016) studied experimentally and analytically the flexural behaviour of CFRP strengthened steel-concrete I-girders. Four identical composite steel-concrete girders were fabricated; the steel-concrete composite beams having a 6000 mm span. The overall length of the specimen was 4200 mm. The steel cross section

was a standard W150 × 22 hot rolled I-beam with a with 75×600 mm concrete flange. One girder was un-strengthened to act as a reference girder, while the remaining three girders were strengthened with 2, 3 and 4 layers of CFRP sheets mounted on the bottom side of the steel girder's tension flange considering complete anchorages of the CFRP sheets at both ends. To obtain a comprehensive overview of the flexural behaviour of both un-strengthened and the CFRP-strengthened girders, the composite girders were tested under a four-point loading system with constant moment region of 300 mm. The comparison showed good agreement between the proposed analytical results and the experimental findings with a maximum variation less than 10%.

Abed (2012) investigated the influence of CFRP plate length on the flexural behaviour of standard steel sections. Four 1.1-metre length beams were strengthened and tested in three-point bending at ambient temperature; one un-strengthened and three strengthened with 450, 600 and 700 mm CFRP. An increase of 4%, 34%, and 35% was noted in the ultimate capacity, respectively.

2.3.2 Shear strengthening

In comparison to flexural strengthening as previously discussed, there has been relatively little work investigating the use of bonded FRP materials for shear strengthening of steel members.

Patnaik and Bauer (2004) tested second series of deep beams. Three beams, among six, were designed to fail in shear at the web. The aim of the study was to investigate the shear strengthening of beams with CFRP. The beams were 350 mm deep beams with 3 mm web thickness and overall depth of 325 mm. As expected, the un-strengthened beam failed due to elastic web buckling prior to flexural yielding. Two of these beams were strengthened with vertically oriented, unidirectional CFRP to both sides of the web. The application CFRP to the web is reported to have allowed the section to yield prior to the onset of inelastic web buckling. Furthermore, although significant debonding of the short CFRP strips was evident, the failure is reported to have been ductile and "it was possible to sustain the load for a short time even after the initiation of web shear buckling". The shear strength increase was 26% for one specimen and was negligible in the other one

because of the failure at the butt joint. However, the strengthening scheme is not cost effective, for only 26% increase in shear strength.

In 2009, a more efficient strengthening technique was presented by Okeil *et al.* (2009); the technique introducing additional stiffness to buckling prone regions in thin-walled steel sections. The out-of-plane stiffness of web panels was studied by bonding pultruded GFRP sections. The tested girder was designed to fail in shear buckling mode and test results showed that the failure load for the strengthened girder was 56% higher than the un-strengthened specimens. However, the proposed strengthening technique reduced the ductility.

Narmashiri *et al.* (2010) experimentally and numerically studied shear strengthening of I-beams. The web was strengthened with CFRP on one or both sides, using different values of CFRP area on the web. Five specimens 1000 mm in length were tested in four-point bending with constant moment region of 600 mm. The first specimen was a control specimen. The second and third beams were upgraded on both sides of web with the CFRP ratios of 0.72 and 0.48, respectively. The fourth and fifth specimens were strengthened on one side of web with the CFRP ratios of 0.72 and 0.48, respectively. The results show that the use of CFRP strips on web could increase the load bearing capacity up to appropriately 51%. Also, the CFRP ratios of 0.72 and 0.48 for both sides of web have produced the same load capacity. Using less CFRP in the shear zone with the same load capacity of the steel I-beams was one of the significant achievements of this research.

Okuyama *et al.* (2012) investigated the reinforcement effect and debonding behaviours of CFRP strengthened steel plate girders. They performed shear-buckling tests on seven plate girders having two different aspect ratios of web, namely, 1.0 and 1.5. Test results of the experimental work, for all specimens, shows that displacements progressed linearly until the maximum load. After reaching the maximum load, load decreased gradually due to the breaking of CFRP sheets for the reinforced specimens. The tension field action was observed in test panels for each specimen regardless of the reinforcement. Breaking of CFRP sheets progressed along the fibre orientation angles. Test results confirmed that the CFRP sheet improves shear strength by 6-29%.

In another study by Wakabayashi *et al.* (2012) made an attempt to simulate the web corrosion attack of steel plate girders by reducing the thickness of the web mechanically at the junction with the bottom tension flange. Four plate girders were

tested for shear buckling, two of which had 50% web material loss and the other two were simulating a through-hole (severe corrosion condition). From each group, one was strengthened with CFRP sheet and the other kept as a control specimen. The results show that shear load-carrying capacity was recovered by appropriately bonding CFRP sheets to the corroded webs, even when severe corrosion occurs. The required CFRP is determined by converting the CFRP thickness to steel via Young's moduli. CFRP sheets should be bonded to the corroded section in the direction of ±45 degrees.

An extended version of Okuyama *et al.* (2012) was carried out by Bhutto (2014). Eight specimens were tested including one specimen as a control specimen. In four specimens strengthened with GFRP pultruded section, the maximum increase in the ultimate load carrying capacity was 48%; this is for the specimen with the diagonal strengthening alignment. In the second series three specimens were tested, the maximum increase of the load carrying capacity was 54% for the specimens strengthened with 8 layers of GFRP fabric sheets. The comparison is made with a control specimen, which failed due to the end support stiffener crippling.

A large experimental study by Assoodani (2014) on shear behaviour, strength of steel plate girders and steel-concrete composite plate girders retrofitted with adhesively bonded CFRP composites to the web plate and loaded primarily in shear. The programme included two main series. In the first small-scale plate girders were used to optimize the best strengthening technique. The second series used large-scale steel and steel-concrete composite plate girders. The aim of the work was to quantify the effectiveness of strengthening the web with the optimized technique. A combination of pultruded CFRP plates and fabric CFRP sheets were used to strengthen the plate girders. Each series is divided into two groups, web slenderness ratios of 245 and 163 corresponding to steel plate's thicknesses of 2 and 3mm, respectively. In the experimental results for the small-scale plate girders tests, the maximum increase in the capacity of the strengthened specimens was 132%; this specimen was strengthened with mechanically anchored pultruded CFRP plates in both tension and compression diagonals of the web. For the experimental results for the full-scale steel-concrete composite plate girders, the maximum increase in the capacity of the strengthened specimens was 63%; for the specimen strengthened with both pultruded CFRP plates and fabric CFRP sheets in both compression and tension diagonals of the web, respectively.

More recently, Al-Azzawi (2016) performed an experimental programme investigating a novel technique to strengthen web plates of steel plate girders. Thin-walled steel girders were strengthened against web shear buckling using a corrugated CFRP or GFRP panel bonded externally along the compression diagonal of the web plate. Two series of tests were carried out; the initial series involved tests on 13 steel plates strengthened with the proposed preformed corrugated FRP panel and subjected to in-plane shear loading frame, specially designed and manufactured to induce the appropriate boundary conditions and stresses in the web plates of realistic plate girders. This initial test series investigated the performance of different forms of strengthening under static load, in preparation for a subsequent series of cyclic tests to investigate their fatigue performance. The test variables included FRP type (CFRP or GFRP), form of FRP (closed or open section), number of FRP layers, and orientation of GFRP fibres used to build the FRP panel. In the second series, six specimens were manufactured to simulate the end panel of a 15-metre plate girder. These were strengthened with the optimized FRP panel from the first series and tested for shear buckling under repeated cyclic loading having an amplitude of 80% of the static ultimate capacity. For the GFRP and CFRP strengthened specimens, the maximum surface principal stress was reduced by 81% and 51% respectively, and the maximum surface principal shear stress was reduced by 89% and 77%. A considerable increase in the stiffness of the strengthened specimens was evident in the observed reductions of the maximum out-of-plane displacement, which was reduced by approximately 90% for both GFRP and CFRP strengthened specimens. Fatigue analyses indicated that the proposed strengthening technique should be able to considerably reduce the secondary bending stresses at the web plate welded boundaries, and therefore elongate the life expectancy of some plate girders by a factor of 7 to 1. In addition, the proposed strengthening technique did not show any debonding or delamination under both static and cyclic loading which makes it a good candidate for strengthening thin-walled structural members, especially, when ductility is a concern.

2.3.3 Tensile strengthening

Tests in tension are summarised in this section under lap-shear joints. A review on FRP strengthened steel structures in tension and strengthening of steel hollow section members in Zhao and Zhang (2007). Research took a different

approach to the tensile test using two steel plates with a gap in between. This comes in two forms either one side strengthened single lap-shear (Hart-Smith, 1973b; Fernando *et al.*, 2013) or two sides strengthened double lap-shear (Hart-Smith, 1973a; Schnerch *et al.*, 2004; Fawzia *et al.*, 2005a, b; Colombi and Poggi, 2006b; Fawzia *et al.*, 2010). The conventional single lap-shear joint is not suitable for the determination of the real adhesive properties due to the complicated stress state within the adhesive joint, but can be used for comparison and quality control of adhesives purposes (da Silva *et al.*, 2011). Al-Zubaidy *et al.* (2012) carried out a study to investigate bond characteristics between CFRP fabrics and steel plate joints experimentally under impact tensile loads, double strap steel joints loaded at different loading rates of 2 mm/min, 3.35, 4.43 and 5 m/s.

In the current work only double lap-shear specimens were prepared and tested, further details and results are in section 5. The tests were used to examine the effect of curing on adhesives, and estimate the amount of improvement that can be obtained in the scaled beam tests. The design guidelines use this approach in the FRP strengthening design procedure.

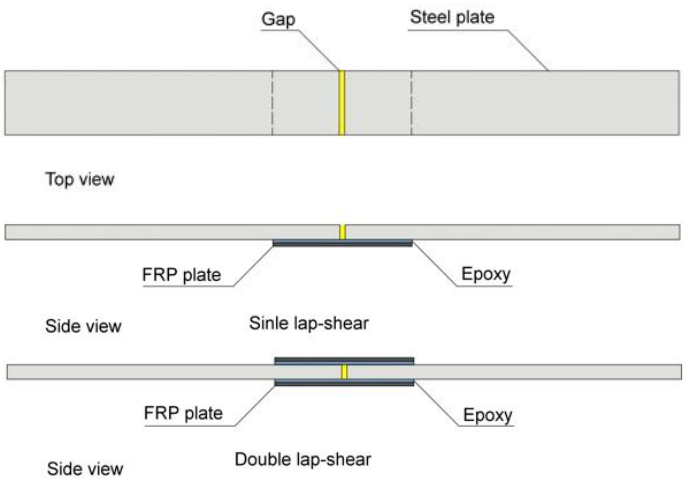

Figure 2-3: Loading is directly applied to the steel element with gap

Steel plates without a gap are investigated in different shapes; the load is directly applied to the steel plates. The work by Miller *et al.* (2001) used uniform width steel plate as shown in Figure 2-4, Colombi and Poggi (2006b); Ishikawa *et al.* (2006) used

coupon shaped steel plate, and Al-Emrani *et al.* (2005) used dog-bone shape steel plate.

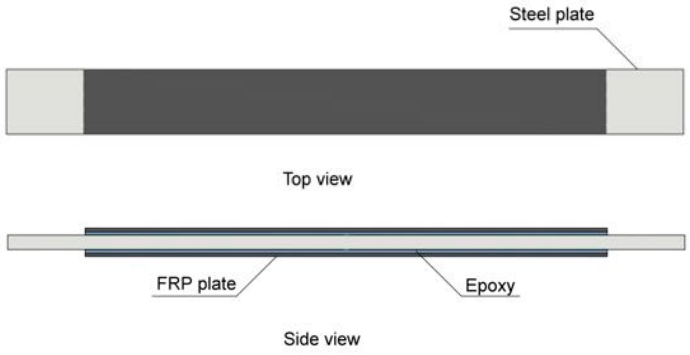

Figure 2-4: Loading is directly applied to the steel element without any gap

Other types of lap joint where the load applied directly to the FRP plates in the form of pull-off test (Xia and Teng, 2005), as shown in Figure 2-5.

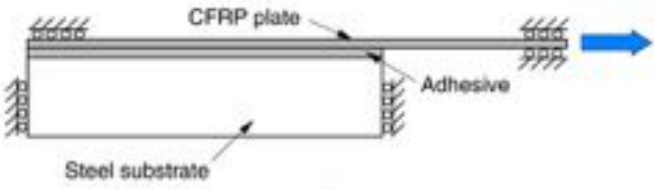

Figure 2-5: Pull-off test specimen and set-up (Zhao and Zhang, 2007)

Jiao and Zhao (2004) tested 21 butt-welded very high strength steel tubes strengthened with CFRP in axial tension. Lap-shear strength between CFRP and very high strength (VHS) tubes was obtained as a preliminary study before testing the welded connections. Three types of failure were reported: adhesive failure, fibre tear, and mixed failure. Butt joints were also used to investigate surface preparation of steel.

Yu *et al.* (2011a) developed a new bond failure model to predict the bond failure load of fibre reinforced polymer (FRP) strengthened steel surface. The authors experimentally studied the effects of different strengthening parameters including

laminate thickness, bond length, and adhesive thickness on the bond strength using double-lap joint, single-lap joint and T-peel joint. They found that the most important factors that influence the final bond failure is the stress concentration at the end of the bond line.

In the above-mentioned tests, the FRP material is in direct tension and the effect of curvature is not considered. Nozaka et al. (2005) developed a new testing method that considers the effect of curvature; the test set up method involves a steel plate bolted to the tensile flange of a beam. The loading is indirectly applied to the FRP. The test setup is shown in Figure 2-6. This type of testing replicates the adhesive interfacial stresses that are induced by the curvature. A similar testing approach was adopted by other researchers to investigate bond strength of Near Surface Mounted (NSM) Basalt Fibre Reinforced Polymer (BFRP) bars in normal strength concrete slabs (Martin *et al.*, 2012, 2013); the vertical load was applied to the specimens so that the effect of tensile pull out forces combined with bending could be investigated.

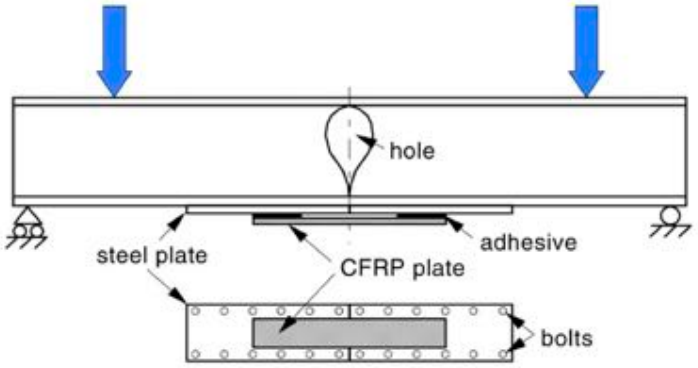

Figure 2-6: Indirectly loading the FRP and the steel plate set-up (Zhao and Zhang, 2007)

2.3.4 Finite element modelling studies

Sayed-Ahmed (2004, 2006) investigated strengthening the web of the steel I-beam against web buckling. In-thin walled I-beams, the risk of web buckling is high, and for strengthening the tension flange, premature failure can occur due to web buckling. A nonlinear finite element analysis was conducted to predict the performance of strengthening the web of composite I-beams. Strengthening was performed through bonding 100 mm width by 1.4 mm thickness CFRP strips to the

mid-height of the web from both sides. The web buckling load capacity increased up to 61%, and the flexural capacity increased by 9%.

Yu *et al.* (2011a) developed a new bond failure model to predict the bond failure load of fibre reinforced polymer (FRP) strengthened steel surface. The same authors (Yu *et al.*, 2011b) experimentally studied FRP strengthened steel beams under four-point bending, and investigated the effects of different strengthening parameters including laminate thickness, bond length, and adhesive thickness on the bond strength. As a part of the investigation, numerical analyses on the strengthened steel beams were carried out. By calculating the equivalent strain energy density in the bond-line, the bond strengths of the specimens were predicted. The advantage of this equivalent strain energy density based bond failure model was demonstrated by comparing the results predicted by the proposed model and those predicted by using the traditional maximum value based model. They concluded that the application of the proposed bond failure model is no longer limited to the hypothesis of elastic material or geometry linearity, and unlike the misleading results predicted by using maximum value based models, the relationship between adhesive thickness and the bond strength of FRP strengthened beams can be predicted correctly. Finally, a parametric study was conducted to investigate the effects of the thickness of FRP laminate, the tensile modulus of FRP laminate, the thickness of epoxy adhesive and the bond length on bond strength.

Abed (2012) used FE analyses using ABAQUS to study the effect of elevated temperature on the externally bonded FRP to steel materials and validate the modified Deng et al., (Deng *et al.*, 2004). Good FE analyses validated well the analytical model for a reinforced beam subjected to thermal loads only. However, the shear stress distribution and the length of the plastic zone obtained from the FE analyses were slightly larger from those obtained from the analytical model for a reinforced beam subjected to mechanical and thermal load due to different assumptions made in the two models. In the analytical model, linear elasticity is assumed for the adhesive along the entire bonded plate, but the FE model bilinear elastic plastic is considered. The details of the lap shear tests and flexural tests at elevated temperatures are in sections 2.10.2 and 2.10.3 respectively. The analytical approach and FE model at elevated temperatures are discussed in Section 2.10.4.

Sargazi and Narmashiri (2015) studied the structural behaviour of steel I-beams strengthened by anchored carbon composite under bending. Testing 2-metre length

beams in four-point bending the I-sections were strengthened with 1000 mm Fibre Reinforced Polymer (CFRP). The ends of the CFRP plates were anchored horizontally with different length of 20, 40, 82, 123, and 164 mm at the tensile flange, and the anchor height extended to some parts of the steel beam web of 80 mm. Finite element analyses (FEA) ABAQUS software, three-dimensional, and non-linear static analysis was used in the modelling. Seven models were studied in that steel beams' dimensions and CFRP length for flexural strengthening were fixed although length of CFRP anchors was varying. Results obtained by this research show that using CFRP wraps as end-anchoring system can effectively increase load-bearing capacity and flexural strength and reduce stresses and strains at the tips of CFRP strips. Modelling results indicate 4% reduction of Von-Mises stresses, 60% reduction of major maximum stress, and 50% reduction of shear stress and 60% shear strain at the end of CFRP strip.

2.4 Analytical approaches for modelling externally bonded adhesives to strengthen elements in flexural

da Silva *et al.* (2009) reviewed the models and proposals for small single and double lap-shear. These are not reviewed in this section. The models used to predict the failure of steel and concrete structures strengthened using FRP plates are reviewed in this section. Failure modes in concrete structures can be remarkably different and dominated by concrete failure in tensile strength. This topic is beyond the scope of this research, however, the FRP strengthening of concrete elements is reviewed since failure is likely to occur within the adhesive or the interfaces of the adhesive.

The models are used to predict plate-end debonding. The concentration of the interfacial stresses (shear and normal stresses at the plate ending) is normally the reason for the premature failure. This failure occurs at loads that are much lower than required to cause rupture of the FRP material. Various approaches have been considered; several simple approximate close-form and high-order complicated solutions of these interfacial stresses have been developed.

2.4.1 Compatibility approach

From late the 1980s, researchers modelled adhesively bonded steel plates to the soffit of a beam using relatively simple closed-form solutions. Vilnay (1988); Täljsten (1997); Malek *et al.* (1998) considered deformation compatibility conditions directly, and Roberts and Hajikazemi (1989) took a staged approach. Smith and Teng (2001) reviewed the assumptions and limitations of these approaches for interfacial stresses. Although the same authors presented a general solution based on a deformation compatibility approach to estimate the shear and the normal stresses in the adhesive layer, their work from a literature point of view is considered as an original solution.

The solution by Smith and Teng (2001) can be used to estimate the stresses within an adhesive layer of any beam with uniform section strengthened with a thin plate assuming linear-elastic material behaviour for the beam, FRP material and adhesive. Although this solution was restricted to a uniformly distributed load (UDL), the model was adapted for different loading cases. The solution is considered as a classic first-order analytical solution because the stresses within the adhesive thickness are assumed uniform, which leads to the violation of the zero-shear stress condition at the end of the plate. Moreover, the bending moment in the adhesive layer is ignored in the determination of the shear stresses, which is a conservative assumption for design purposes. This model also assumes that the curvature of the CFRP plate and the beam is the same. This assumption is considered to separate the effect of coupled action between the shear and normal (peeling) stresses. The assumption simplifies the problem and, therefore, mathematical closed form formulas are driven. Figure 2-7 shows the differential segment of a soffit-plated beam in the model presented by Smith and Teng (2001), and Figure 2-8 shows the interfacial stresses produced from the model with a comparison to the previous model.

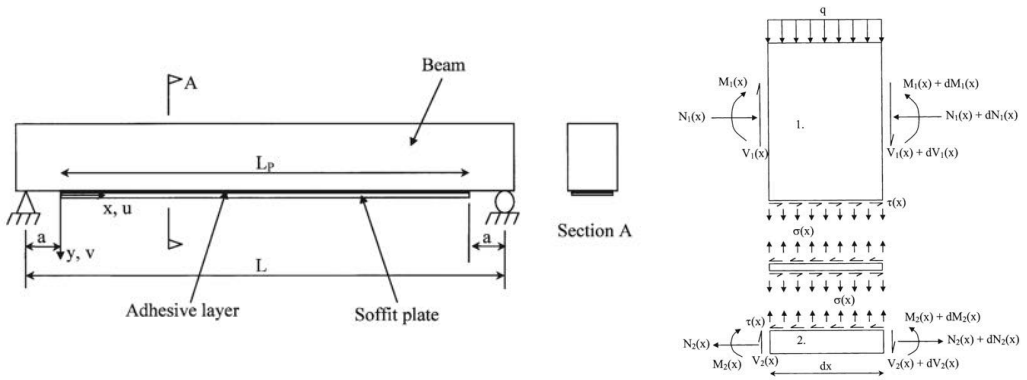

Figure 2-7: Soffit-plated beam and differential segment of a soffit-plated beam in the model by (Smith and Teng, 2001)

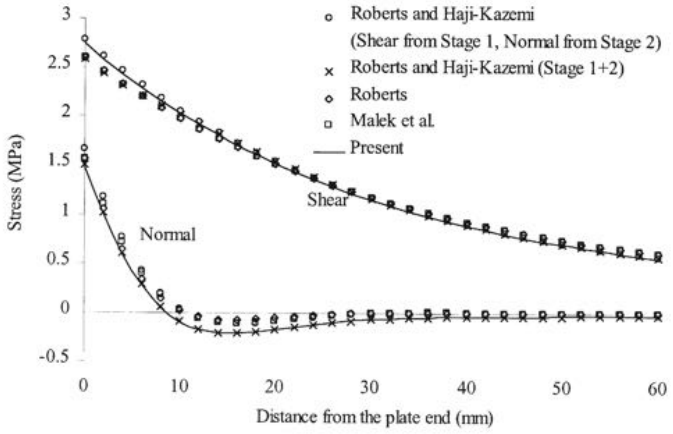

Figure 2-8: Comparison of interfacial shear and normal stresses for a RC beam with a bonded CFRP soffit plate subjected to a UDL by (Smith and Teng, 2001)

Several researchers have adopted the model by Smith and Teng and extended its application to investigate the influence of temperature in metallic beams. Denton (2001), studied the interfacial stresses only due to the differential expansion of a metallic beam and FRP material. Deng *et al.* (2004) and Stratford and Cadei (2006), adopted the same model to study the combination of thermal and mechanical loading of metallic elements. The authors in Deng *et al.* (2004) used finite deference to study the influence of a tapered end plate. The work Stratford and Cadei (2006) also investigated FRP plate pre-stress loading and clamping force impact at the

plate ends. De Lorenzis *et al.* (2006) extended to the case of curved beams; the analysis does not cover the thermal loading.

Yang and Wu (2007) introduced and solved the governing differential equations for the Smith and Teng (2001) model to account for the effect of the shear deformation. The Fourier series method was used to expand the shear deformation and obtain uncoupled equations. The unknown constants are determined from the governing equations and boundary conditions by means of the Galerkin procedure. Zhang and Teng (2010) presented a very general solution to plated beams of all geometric (e.g., curved beams), sectional (e.g., tapered beams), loading (e.g., a linearly varying distributed load), and boundary conditions.

Several high-order analytical solutions exist to determine the interfacial shear and normal stresses (Rabinovich and Frostig, 2000; Shen *et al.*, 2001; Yang *et al.*, 2009). These solutions take into consideration the non-uniform stress distribution in the adhesive layer and the stress-free boundary condition at the ends of the plate. Rabinovich and Frostig (2000) solution does not provide explicit expressions for the interfacial stresses, and the constants of integration are not provided, but the boundary conditions are listed. Shen *et al.* (2001) introduced a high-order analysis and they obtained some other explicit expressions but only uniformly distributed load in combination with a uniform bending moment are considered. The new analytical approach in Yang *et al.* (2009) is for the interfacial stresses in plated beams subjected to arbitrary mechanical and thermal loads which are symmetrically positioned about the mid-span. The solution is represented by a Fourier series and is based on the minimisation of complementary energy. Due to the complexity of the models, it seems impossible to obtain a simple design rule.

In this research, a simple first order solution that considers different curvature between the beam and the CFRP plate. The derivation of the model is presented in section 6. The model is compared with two previous models by Deng *et al.* (2004); Stratford and Cadei (2006)

2.4.2 Fracture mechanics and cohesive zone approach

A different approach uses fracture mechanics concepts to predict the failure load of the strengthened beam. This approach is used in aerospace and mechanical engineering. The model assumes a given crack length and estimates the elastic

energy release rate. To evaluate the stability of the interfacial crack, the released energy is compared to the fracture energy of the relevant material or interface. However, this method was used in the analysis and design of RC structures (Shah et al., 1995; Xie and Karbhari 1998). Generally, the used of this method is limited. Linear elastic fracture mechanics (LEFM) simulations of the crack growth process have been used, which include a stress analysis phase and a fracture analysis phase. Rabinovitch and Frostig Rabinovitch and Frostig (2001) proposed an approach in the stress phase, the stress and deformation fields of the strengthened member are determined using the higher-order theory. The fracture mechanics phase, where an energetic failure criterion is derived and evaluated, the J-integral formulation is adopted for the evaluation of the energy release rate. In other works, by Rabinovitch (2004, 2008); De Lorenzis *et al.* (2010), different approaches were adopted for the stress analysis and the fracture analysis phases.

Another approach in the debonding mechanism is the cohesive zone (CZ) approach. This method is considered as a bridge between the stress based approaches and energy based approaches. The approach is extensively used for the study of bond between FRP and concrete. In the cohesive zone, as the cohesive interface gradually separates, the magnitude of the interfacial stress at first increases, and then decreases with increasing separation, finally approaching zero. The cohesive interface experiences the entire spectrum of behaviour ranging from perfect bonding to complete separation. The main advantage of this approach is the implementation of the crack nucleation and growth mechanisms in a stress analysis procedure. However, the main disadvantage of this approach is due to the considerable computational efforts required for the numerical solution of the nonlinear model. The recent work published De Lorenzis and Zavarise (2009); De Lorenzis *et al.* (2013) proposed closed-form expression for the debonding load and discussed the comparison between cohesive zone modelling and linear-elastic fracture mechanics predictions, while Rabinovitch (2008) discussed the main advantages and disadvantages of the two approaches of the LEFM and CZ.

The above-mentioned works require considerable amount of computational efforts for the numerical solution, and entail a large number of parameters. Therefore, it seems this approach is not an appropriate for this investigation.

2.5 FRP strengthening design guidelines and recommendations

Guidelines for the design and application of FRP materials for flexural retrofit of concrete elements are available from the manufacturers (FIB, 2001; Mufti *et al.*, 2007; ACI 440.2R-08, 2008; Concrete Society, 2012; National Research Council Advisory Committee, 2013). This section gives a brief summary of recent design guidelines published in relation to the steel structure strengthening using FRP materials.

ICE published the design and practice guidance on the use of fibre reinforced polymer composites in Moy (2001). This very first publication demonstrates that fibre reinforced polymer composites can be used with complete confidence in structural applications. The recommendations give advice on the selection of laminate materials, design of strengthening, and guidance is given on short and long-term behaviour. It contains case studies of projects on the London Underground network with contributions from industry research groups.

CIRIA report C595 (Cadei *et al.*, 2004) describing current best practice for strengthening metallic structures using FRP materials was published in the UK. C595 is a comprehensive design guide; the complete life cycle of an FRP strengthening scheme for a metallic structure, from conception, through design, procurement, installation and maintenance, to decommissioning is addressed. Sectional design that includes the effects of locked-in permanent stress is applied to estimate the FRP material. Elastic design limitations are introduced when a brittle metallic structure such as cast-iron elements are strengthened. To prevent debonding failure of the externally bonded FRP materials, the maximum principle stress in the adhesive joint does not exceed the strength of the adhesive obtained from direct tension lap-shear tests. Similar to other design guidelines, it suggests load and material safety factors should be included in the design, and practical issues such as temperature effects, a high-quality installation, and the post-installation inspection regime are covered.

Significant attention has been given to strengthening steel structure with HM CFRP since 2005 in the University of North Carolina. Various aspects such as bond behaviour, flexural strengthening, fatigue, and over loading behaviour were studied, and Schnerch *et al.* (2007a); Schnerch *et al.* (2007b) proposed design guidelines for strengthening steel concrete composite beams with HM-CFRP composites. The guideline addresses surface preparation of the materials, the application of the

adhesive and the detailing of the strengthening in detail. The design guidelines include the structural design criteria for the use of high modulus CFRP materials. The flexural design procedure is based on a moment–curvature analysis and a specified increase of the live load carried by the structure to satisfy specific serviceability requirements.

- The total service load of the strengthened beam, including the dead load and the increased live load, should not exceed 60% of the estimated increased yield moment capacity of the strengthened beam.
- The total factored (dead and live) load should not exceed the ultimate capacity of the strengthened beam after applying an appropriate strength reduction factor.
- To ensure that the structure remains safe in the case of a possible loss of the strengthening system, the combined effect of the dead load and increased live load should not exceed the capacity of the un-strengthened beam.

Italian National Research Council provided guidelines on design and construction of externally bonded FRP system for metallic structures National Research Council Advisory Committee (2007). Considering durability of the system, the guidelines proposed conversion factors for various types of FRP and exposure conditions. These factors introduced as the same as ACI guidelines, but included an extra parameter. Similar approach to the CIRIA report C595 (Cadei *et al.*, 2004) are proposed in the analysis.

2.6 The effects of elevated temperature on FRP strengthening

The previous works were carried out at ambient temperature and they showed that the FRP strengthening was used successfully in strengthening structures. Ultimate load capacity and fatigue life of steel structure was significantly improved using this technique. Few researchers have studied the behaviour of the FRP strengthened structure at elevated temperature and it is known that the adhesive material properties are heavily affected by elevated temperature exposure. This section covers the terms that are important to understand the curing of adhesives and are used to characterise adhesives. The glass transition temperature, T_g is main focus if this research. The terms that are related to this research and

referred to in section 3 are illustrated, and the effect of temperature, moisture and physical ageing of thermosets are reviewed.

2.6.1 Definition of the glass transition temperature T_g definition

The glass transition of a polymer is commonly referred to by its glass transition temperature T_g but in reality, the glass transition occurs gradually over a range of temperatures. Tammann, in the late 1920s, was the first to introduce the term T_g for the glass transition temperature, and were summarised subsequently in his monograph (Tammann, 1933). According to Tammann, the glass transition temperature, T_g is the temperature at which the brittleness disappears (Mazurin, 2007).

The adhesive changes in state from a glassy material to a rubbery state as the mobility of molecules in the polymer network increases (Petrie, 2006). The glass transition temperature, T_g is defined as a measure of the mobility of the molecular chains in the polymer network as a function of temperature. The T_g is dependent on the chain flexibility and the free volume associated with the chemical structure as well as the overall cross-link density (Pizzi and Mittal, 2003) see section 2.6.2.

There are, however, several different methods to characterise the glass transition temperature, T_g, the values of which can differ widely. Dynamic Mechanical Analysis (DMA, see section 2.8) and Differential Scanning Calorimetry (DSC, see section 2.9) are most commonly used in engineering applications. DMA is far more sensitive to the glass transition than DSC (Mulligan *et al.*, 2003).

2.6.2 The effect of cross-links upon adhesive properties

Epoxies generally comprise two components (a resin and a hardener), which are mixed either at room temperature or on heating depending on the type of the hardener. In some applications post curing is used to achieve an adequate level of cross-link between the chains of the polymer. The resulting polymer is usually heavily cross-linked, so thermosets are sometimes described as network polymers. The bonds in polymers are divided into two major groups: the primary bonds (strong covalent bonds) and the secondary bonds (Van der Waals and hydrogen

bonds) (Ashby and Jones, 2013). The covalent bond is the backbone of the polymer chains. Thermosets undergo a curing process or conversion, where the polymer chains link together. The cross-links form during the polymerization of the liquid resin and hardener; the structure is usually amorphous. The cross links between the chains can be in a weak bond form or through covalent bonds, such as a disulfide bond.

Crosslink density is the definition of the number of effective crosslinks per unit volume. The crosslink density is a key parameter in determining the properties of an epoxy resin after cure (Petrie, 2006). This depends on the type of the polymer and crosslinking agent. The properties of thermosetting materials depend greatly on their chemical formulation or composition and the curing conditions (temperature and time). Any changes in the formulation or processing conditions affects the curing of the resins, and consequently it can have a significant influence on the properties of the end product (Turi, 1981; Ellis, 1993).

2.6.3 The effect of temperature upon adhesive cure and properties

Epoxies are commonly used in FRP composite applications, and are classified according to the curing temperatures as hot and cold cured epoxies. Hot-cured epoxies are used as the resin matrix material. They are used in the production of the FRP laminates and FRP rebars are post-cured to give a glass transition temperature, T_g that is as high as 200°C (Hollaway, 2010). The cold (ambient temperature) cured epoxies that are typically used for structural strengthening have a T_g that can be as low as 40°C (ACI 440.2R-08, 2008; Stratford and Bisby, 2012).

The hot-cured and cold-cured adhesives have different mechanical properties, because the degree of crosslink is much higher in hot-cured than cold-cured adhesives. This is mainly due to differences in the epoxy resin and curing agent molecular structures. In hot-cured adhesives the molecules are mobile and reaction (between the hydroxyls group and the epoxy group) is more likely to happen (Petrie, 2006). Previous work on adhesives have found that there is a linear relationship between T_g and curing temperature, and this is true up to the point when the density of the crosslinking reaches the maximum limit, and no further improvements in T_g can be achieved (Chang *et al.*, 1982; Enns and Gillham, 1983;

Stevens and Richardson, 1983; Wu, 1992). Post-curing of ambient cured thermoset adhesives is widely used in engineering applications to increase their T_g, which is dependent on the type of the adhesive formula. Measurements of the mechanical properties of two-component room temperature curing adhesive paste (Araldite 2014) were studied. The test results showed that 28 days are needed at room temperature to complete the curing process (only 4 hours at 64 °C) and that the properties of the adhesive during that period of time changed dramatically.

Some adhesive manufacturers recommend a post-curing regime, e.g. 72 hours post cure at 60°C, and the T_g (and the accompanying mechanical properties) that are reported on the manufacturer's data sheets are obtained after the post-curing regime has been applied (Tyfo-S, 2011).

Researchers have found that the interfacial bond in the CFRP/concrete system also improves due to post-curing, as well as the mechanical properties of the adhesive (Al-Safy *et al.*, 2013). The authors reported that post-curing at a lower temperature 60°C and longer period is preferable to post-curing at high temperatures (2 hours at 100°C followed by 2 hours at 140°C) for a concrete substrate (Al-Safy *et al.*, 2012).

The current work investigates the significance of post-curing at various temperatures from room temperature up to 80°C (above T_g), for two ambient cure epoxies, and the significance of this upon plate-bonded FRP strengthening systems (see section 3).

2.6.4 The effect of moisture upon adhesive cure and properties

Moisture can affect an adhesive and degrade the properties of the bulk adhesive, due to absorption of water molecules into the polymer structure. All polymers absorb water to some extent, a process is known as hydrolysis, in which the adhesive material properties change by reducing its glass transition temperature, inducing cracks, or by chemically reacting with the polymer (Petrie, 2000). The presence of water in polymers generally reduces the forces between the molecules which leads to a reduction in the glass transition temperature, of the polymer. It has been demonstrated in Lapique and Redford (2002) that the absorbed water works as a plasticizer, leading to softening of the adhesive. Consequently, mechanical properties such as tensile strength and modulus of elasticity are reduced, and hence

the rupture strain increases (Comyn, 1997; Lapique and Redford, 2002). These parameters largely recover upon drying unless irreversible hydrolysis has taken place (Comyn, 1997). Adhesive joints can resist low relative humidity (e.g. 50% or less) for a long period of time (Comyn, 1997). However, there is a critical humidity for weakening, because humidity leads to water migration in the adhesive.

Nguyen *et al.* (2012) investigated the impact of seawater and temperature upon adhesively bonded CFRP/steel joints. This research investigates the effect of water on the glass transition temperature, T_g of two different types of adhesives in section 3.

2.6.5 The effect of physical ageing upon adhesive cure and properties

Physical ageing involves two significant changes in the structure of an epoxy: reduction in the free volume, and volume-independent configuration changes in the molecular network (Odegard and Bandyopadhyay, 2011). Free volume is the free space in the locked-in amorphous molecular structure of the epoxy, and is a direct consequence of the non-equilibrated amorphous state. As a result, it has significant impact on density and mechanical properties (Odegard and Bandyopadhyay, 2011). Free volume is still not possible to define uniquely or unambiguously, and effects can only be explained qualitatively in terms of a change in free volume (Ellis, 1993). They concluded that physical ageing involves the simultaneous reduction of free volume and conformational changes of the cross linked molecular structure when exposed to sub-T_g temperatures for extended periods of time, and it significantly changes the overall response of these materials since the mechanical, thermodynamic, and physical properties of epoxies are influenced. During the ageing process, mechanical properties such as stiffness and strength change.

Physical ageing is a gradual process towards an equilibrium state. It is not evident over short time periods, but it continues indefinitely over the service life of the polymer (Martin, 2008). Above its glass transition temperature, T_g, a polymer can reach thermodynamic equilibrium instantaneously. However, below T_g the polymer requires a very long time to achieve thermodynamic equilibrium (Martin, 2008). Jaipuriar *et al.* (2012) demonstrated the T_g evolution by ageing at three different temperatures below T_g. In the study, they used an isoconversion map to

conclude that no progress in chemical cure occurred in the resin cured and aged at 22°C beyond the first 7 days of curing. The projected T_g values at infinite time at ageing temperatures of 22°C, 30°C, and 35°C are 52°C, 56°C, and 60°C, respectively.

In section 3 of the work, the development of T_g with physical ageing is studied for two commercially used adhesives for structural strengthening applications.

2.7 The theory of linear viscoelasticity and thermal analysis techniques

Temperatures affects all polymers as discussed in section 2.6. All polymers exhibit viscoelastic behaviour, and when the temperature is involved this behaviour is more significant. Valuable information can be obtained through the study viscoelastic properties of polymers. This section provides basic background to viscoelasticity and the equations that are used in some of the modern thermal analysis devices are listed. Dynamic Mechanical Analysis (DMA) is the implementation of this theory.

2.7.1 Theory of linear viscoelasticity

Viscoelasticity combines the properties of elasticity and viscosity. Material responses can be considered as the result of two extreme contributing behaviours, elastic and viscous. Viscoelastic behaviour means that a material exhibits liquid-like and solid-like characteristics. Elastic (solid) behaviour is described by Hooke's law, for which the stress is directly proportional to the strain in small deformations, but is independent of the strain rate. While viscous (liquid-like) is described from classical hydrodynamics in accordance with Newton's law which states that the stress is directly proportional to the strain rate but independent of the strain itself. Deviation from ideal behaviour occurs when; first finite strains are imposed on a solid and the stress-strain relations become non-Hookean, or similarly in steady flow under finite strain rates many fluids exhibit non-Newtonian flow; or second even if strain or strain rates are infinitesimala system may exhibit solid-like and liquid-like behaviour simultaneously.

Considering only materials, which do not belong to such subsets, solid and liquid-like behaviour can be treated using models combining Newton's and Hooke's

laws. A dashpot can be used to represent Newtonian law, and a spring to represent Hookean law. The elements can be combined in series is known as a Maxwell element. The combination of the elastic and viscous elements in parallel is known as a Voigt element (some times as a Kelvin or Kelvin-Voigt element). Considering viscoelastic material, which have a linear relationship between the stimulus and the response. A single element alone (whether Maxwell or Voigt) does not approach the behaviour of a real system. Therefore, it is necessary to combine several elements in parallel from which one obtains a distribution of relaxation (Maxwell elements in parallel) or retardation times (Voigt elements in series). The viscoelastic functions of the system are obtained by summation of the functions over all elements. The theoretical background can be found in a classic work of the theory of viscoelasticity by Christensen (1982). The full details of development the pure mathematical terms and the basic treatment of the derivation of DMA equations are in Ferry (1980); Fabrizio and Morro (1992); Cho (2016). A summary of the equations is listed in this section.

Considering an isotropic viscoelastic material under small isothermal and deformation conditions, both strain $\varepsilon\ (t)$ and stress $\sigma\ (t)$ can be used as stimulation for a rheological system; both quantities are considered as functions of time t. When strain is given as a stimulus, stress is measured as the response and vice versa. The constitutive relationship between stress and strain for a one-dimensional system can be expressed as a convolution integral.

$$\sigma(t) = \int_{-\infty}^{t} E(t - t')\, \varepsilon(t).\, dt' \qquad \text{Equation 2-1}$$

Equation 2-1 is the *Boltzmann superposition principle*. The principle states that the effects of mechanical history are linearly additive when stress is described as a function of history of strain or strain rates, or conversely when the strain is expressed as a function of the historical rate of change of stress. The mechanical history is only additive given that the material is linearly viscoelastic. This may be manifested in an experiment where the ratio of stress to strain is a function of time alone, and not of the stress magnitude. The function $E(t)$ in Equation 2-1 is called relaxation modulus. It represents the response of the rheological system, which can be determined by the measurement of the response driven by the stimulation of the unit step function. Since strain is used as the stimulation, the dimension of the

response function $E(t)$ is that of modulus. However, it must be noted that Equation 2-1 is valid for any strain although relaxation modulus that is determined by the strain of the unit step function.

A convenient way of representing the viscoelastic behaviour in the frequency domain is through the complex modulus approximation. Such an experiment is referred to as dynamic. It is experimentally straightforward to generate dynamic experiments and implement sinusoidal stimulation. If sinusoidal stimulation is generated without any limitation of frequency, then the response function from dynamic testing is more accurate than from a static experiment.

Consider harmonic strain such as $\varepsilon^*(t) = \varepsilon_0 e^{i\omega t}$ and $\sigma^*(t) = \sigma_0 e^{i(\omega t+\delta)}$ where ε_0 and σ_0 are the strain and stress amplitude respectively. ω is the angular frequency. δ is phase delay between the stress and strain. Then, the Boltzmann superposition principle gives

$$\sigma^*(t) = \varepsilon_0 i\omega \int_{-\infty}^{t} E(t-t')\, e^{i\omega t}.dt' = E^*(t)\, \varepsilon^*(t) \qquad \text{Equation 2-2}$$

Where the complex modulus $E^*(\omega)$

$$E^*(\omega) = i\omega \int_0^{\infty} E(t)\, e^{-i\omega t}.dt' \qquad \text{Equation 2-3}$$

Applying Euler's formula such as $e^{i\theta} = cos\,\theta + i\,sin\theta$ Equation 2-2 can be rewritten as

$$E^*(\omega) = E'(\omega) + iE''(\omega) = E'(\omega)[1 + i\eta(\omega)] \qquad \text{Equation 2-4}$$

Where $E'(\omega)$: storage modulus; $E'(\omega)$: loss factor. The storage and loss moduli, as well as the loss factor, are related to the phase and amplitude differences between stress and strain:

The loss factor $\eta(\omega) = E''(\omega)/E'(\omega)$ is a measure of the energy dissipated in the material, expressed in terms of recoverable energy.

$$E'(\omega) = \frac{\sigma_0(\omega)}{\varepsilon_0(\omega)} cos[\delta(\omega)] \qquad \text{Equation 2-5}$$

$$E''(\omega) = \frac{\sigma_0(\omega)}{\varepsilon_0(\omega)} sin[\delta(\omega)] \qquad \text{Equation 2-6}$$

$$\eta(\omega) = tan[\delta(\omega)] \qquad \text{Equation 2-7}$$

In summary, storage modulus represents elastic characteristics of viscoelastic material, while loss modulus represents viscous characteristics (Cho, 2016).

2.7.2 Thermal analysis techniques

There are various types of thermal analysis technique used to study material property variation and measure the glass transition response. The most widely used methods are:

- Dynamic Mechanical Analysis (DMA), Heat Distortion Temperature, or Deflection Temperature Under Load (DTUL), which are stiffness based.
- Differential Scanning Calorimetry (DSC), which is reaction energy based.
- Thermo Mechanical Analysis (TMA), which is thermal expansion based.

Dynamic Mechanical Analysis (DMA) is a direct measure of the mechanical performance of an adhesive, and hence is the most relevant test method to determine the maximum allowable service temperature for FRP strengthening (Hülder *et al.*, 2008). Differential Scanning Calorimetry (DSC), however, measures the heat required to raise the temperature of the adhesive so that the glass transition appears as a change in enthalpy. DSC is useful to assess the degree of chemical cure of the adhesive; the proportion of the possible crosslinks that have been formed between polymer chains (Mulligan *et al.*, 2003).

Methods such as The Heat Distortion Temperature (HDT) currently Deflection Temperature Under Load (DTUL) can also be used to characterise the thermal response of an adhesive. This determines the temperature that 2% strain is reached in a small adhesive beam under a specific load and heating rate. Whilst HDT is a pragmatic quality assurance test method, it does not directly characterise the glass transition (Mulligan *et al.*, 2003) and it is not clear how the HDT can be used for the detailed design of an adhesive joint.

In section 3 of this research, both Dynamic Mechanical Analysis (DMA) and Differential Scanning Calorimetry (DSC) are used to investigate the glass transition response and the effects of curing and conditioning of adhesives. These two techniques are discussed in this section; a brief introduction on the techniques; the methods of reporting glass transition temperature, T_g; and the responses that are obtained from each technique.

2.8 Dynamic Mechanical Analysis (DMA)

Dynamic Mechanical Analysis (DMA) also called Dynamic Mechanical Thermal Analysis (DMTA) (Turi, 1981; Mulligan *et al.*, 2003), is a stiffness based technique. Since all polymers exhibit viscoelastic behaviour, valuable information can be obtained through an investigation of the polymers' viscoelastic properties. Dynamic mechanical analysis (DMA) is a technique used to investigate the viscoelastic properties of a polymer. It applies a small sinusoidal oscillating force to a sample that is continually deformed; oscillating sinusoidal stress and measuring the resulting oscillating sinusoidal strain or applying an oscillating sinusoidal strain and measuring the resulting oscillating sinusoidal stress (Craver and Carraher, 2000). Traditional mechanical testing applies a force to a sample which is gradually increased and ultimately deforms the sample sometimes irreversibly. In DMA, the deformations introduced are very small and do not fatigue the sample. This means that the sample will respond to each sinusoidal oscillation in the same way. The sinusoidal oscillatory at a set frequency is applied to a sample of known geometry and reports changes in stiffness and damping to obtain modulus information and transitions sensitively, as shown in Figure 2-9.

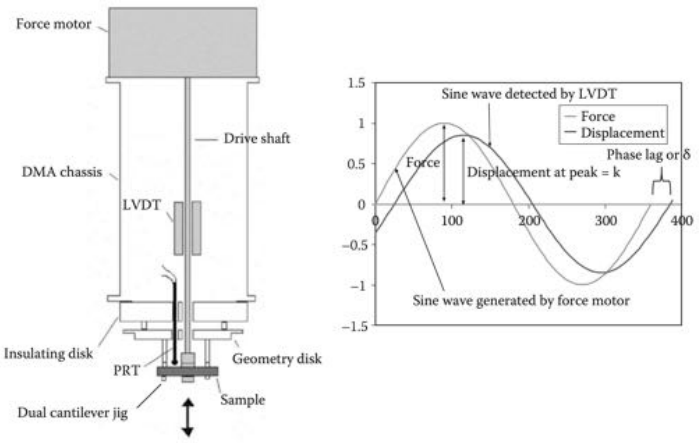

Figure 2-9: The schematic diagram of PerkinElmer DMA 8000, and the applied sinusoidal oscillation (Menard, 2008)

A force motor is used to generate the sinusoidal wave and this is transmitted to the sample via a drive shaft. The sample is subjected to an applied stress, and the material responses with strain by a phase angle δ. For a known stress, the sample

will then deform to a certain degree in relation to its stiffness. Various clamping arrangements are available to accommodate different samples into a frame. Material properties such as storage modulus, elasticity and viscosity, are calculated from the two sine wave curves. There are a number of variables that can be investigated in a DMA. These properties can be measured as a function of another variable, such as temperature or frequency, in a short time (Lampman, 2003). The modulus variation with temperature allows the user to determine the characteristic glass transition temperature, T_g.

2.8.1 DMA specimen and clamping configuration

There are a number of variables that can be investigated in a DMA as mentioned above. Samples of various shapes and sizes can also be analysed. There is a mathematical expression for each testing configuration that considers the size of the sample known as geometry factor; they are used in the calculation of the storage modulus. A schematic of the most commonly used configurations is shown in Figure 2-10. The list of geometry factors is given in Table 2-4.

The distance between the static sample clamp and the drive shaft clamp is the free length l in a clamped bending configuration. This applies to both single and dual cantilever bending. In a three-point bending the distance l refers to the span between the static clamp and the drive shaft contact point. This will be half the distance between the two static clamps. The t and w refer to the samples thickness and samples width, respectively.

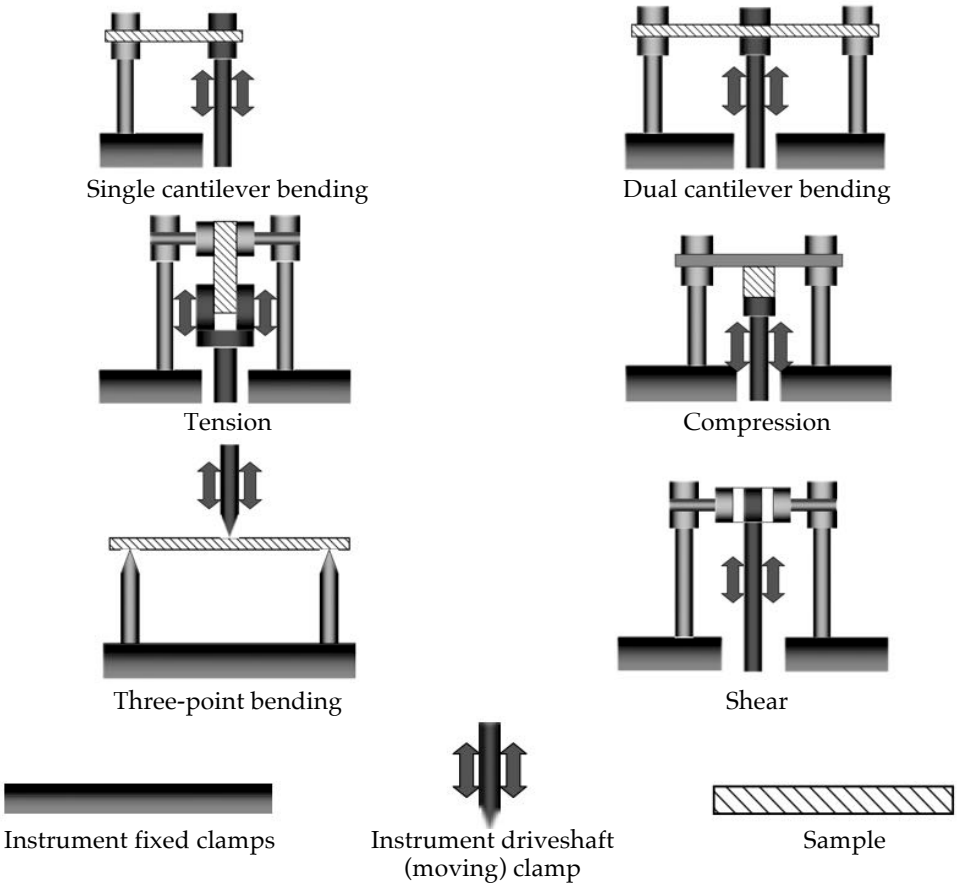

Figure 2-10: Schematic of various testing fixtures (Gabbott, 2008)

Table 2-4: Testing geometry factors (Gabbott, 2008)

Geometry	***Geometry factor***
Three-point bending	$k = w\frac{(t/l)^3}{2}$
Single cantilever bending	$k = w(t/l)^3$
Dual cantilever bending	$k = 2w(t/l)^3$
Shear	$k = 2\,A\,/\,t$
Tension and compression	$k = A\,/\,l$

A: Area, w: Width, l: Free length, t: Thickness

2.8.2 Storage and loss modulus calculation with DMA

By measuring the time response of a sample of material to an imposed strain, DMA testing allows the measurement of the complex modulus defined in Equation 2-4. The equations in section 2.7.1 are based on deformation and phase lag. Most commercial DMA equipment is limited to the low-frequency domain. Storage and loss modulus can be found from

$$E^*(\omega) = E'(\omega) + iE''(\omega) = \left|{}^{F}/_{y}\right| {}^{1}/_{k} \qquad \text{Equation 2-8}$$

Where F is the max force (N) at the peak of the sine wave, y is the maximum displacement of the sample at peak, k is the geometry constant m^{-3}, δ is the phase angle, and k is the sample geometry term from Table 2-4. Therefore, the Equation 2-5 and Equation 2-6 can be re-written as follow:

$$E'(\omega) = \frac{\sigma_0(\omega)}{\varepsilon_0(\omega)} cos[\delta(\omega)] = \left|{}^{F}/_{y}\right| {}^{1}/_{k}\, cos[\delta(\omega)] \qquad \text{Equation 2-9}$$

$$E''(\omega) = \frac{\sigma_0(\omega)}{\varepsilon_0(\omega)} sin[\delta(\omega)] = \left|{}^{F}/_{y}\right| {}^{1}/_{k}\, sin[\delta(\omega)] \qquad \text{Equation 2-10}$$

The storage component may be calculated from Equation 2-9, and the loss component may be calculated from Equation 2-10. The damping factor, which is independent of geometry factor, is the ratio of the loss to the storage modulus. The damping factor $tan\,\delta$ is an indicator of how efficiently the material loses energy to molecular rearrangements and internal friction (Menard, 2008). It can be found from Equation 2-11.

$$tan[\delta(\omega)] = {}^{E''(\omega)}\Big/_{E'(\omega)} \qquad \text{Equation 2-11}$$

2.8.3 Storage modulus and Young's modulus definition

The (dynamic) storage modulus is the response of a material to oscillating sinusoidal strain (stress) in specific geometry. The equations in section 2.8.2 are used in the determination. Young's modulus is calculated from the slope of the initial part of a stress-strain curve from direct tensile test. Young's modulus will not have the same value as the storage modulus, but they may be similar since the initial modulus is measured from geometry. In DMA, the complex modulus E^*, has an in-

phase component E' and an out of phase component E'' that are calculated from the material response to the sine wave (Menard, 2008). The ability of the material to return energy E', to lose energy E'', and the ratio of these effects (tan δ=E'/E'') damping allows better characterization of the material (Menard, 2008).

However, three-point bending and tension geometry can be used to accurately measure the modulus; three-point bending (simply supported refer to Figure 2-11) is free of such clamping errors. Hence, the error in the dual- and single- cantilever configuration is due to movement of the sample within the clamps, which is not factored in the geometry constant. The clamp error is important when a stiff sample is tested; it is better to avoid using thick and short (very stiff) specimens in bending configuration. The measured E' and E'' values have the similar amount of error (this is true where the phase angle is small), therefore the (tan δ) damping value will be accurate (Gabbott, 2008).

There are recommendations to choose appropriate configurations; three-point bending is typically used to measure glass transition temperature, T_g, and it is only performed in the vertical position. Three-point bending configuration is more appropriate for the material with reinforcement, which will have higher stiffness, and the clamp error would be minimised.

Moduli from dual cantilever configuration tend to run 10–30% different than the same material measured in three-point bending at the best. This is due to the clamping effect at the centre and the end of the specimen, which makes the sample deformation difficult (Menard, 2008). The error is likely to be less in single cantilever fixture since the effect of shear is less. Figure 2-11 shows the strain and shear regions in the dual and three-point bending fixtures. In advanced DMA equipment shear correction is considered, but often work for either hard or soft materials, but not both (Menard, 2008). A small shear correction is normally applied, which is $k/(1 + 2.9\left(t/l\right)^2)$ for clamped bending and $k/(1 + 2.9\left(t/2l\right)^2)$ for three-point bending. This correction is based on an average Poisson ratio of 0.33 for glassy polymers and 0.5 for rubbers, namely 0.45 (Gabbott, 2008).

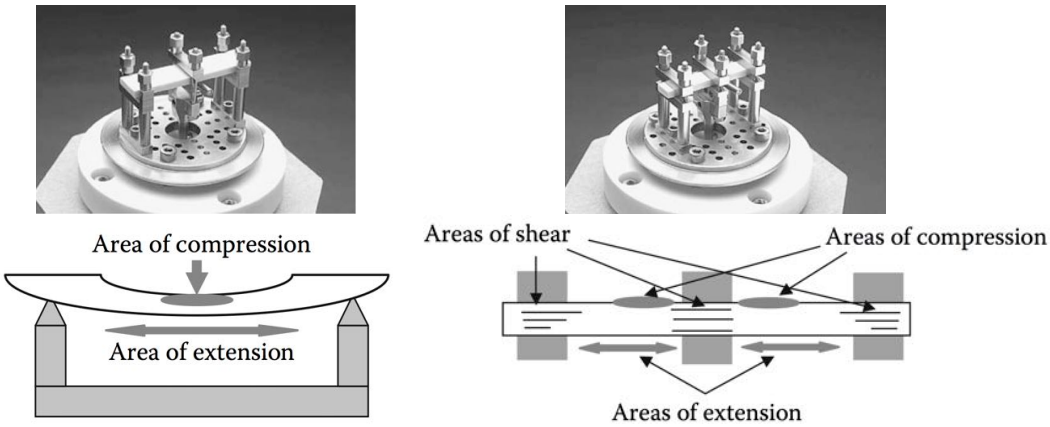

Strain in three-point bending specimen

Strain and shear region in a dual cantilever specimen

Figure 2-11: Strain and shear regions in flexure test configurations (Menard, 2008)

Young's modulus from direct tensile test and the modulus from DMA using three-point bending configuration for thin metallic specimens agrees very well because the shear effect is close to zero and metallic specimens have the same stiffness in tension and compression. Young's modulus of metals can be determined using three-point bending within 5% of the values that are obtained from direct tensile test, however, values from single cantilever fixture can vary between 50-100% (Menard, 2008). It is possible to use the same method to study modulus of polymers but in plastic materials tension and compression properties are not the same; the neutral axis tends to move from the centroid of the section. Therefore, Young's modulus and the modulus from three-point bending can vary. In three-pint bending, it is important to ensure that the sample is completely flat as a twisting force could otherwise result (Menard, 2008). There can also be a frictional force between the sample and the clamp and this would lead to an increase in the tan δ (which is a ratio of the viscous and elastic material responses) as a frictional force would be measured as a viscous response.

2.8.4 Single cantilever vs. dual cantilever

The single cantilever configurations performed better than dual cantilever configurations (Gabbott, 2008). Since dual cantilever support configuration restrains the sample during the test, expansion due to thermal strain causes buckling of the

specimen. This phenomenon was observed in an unpublished parametric study at the University of Edinburgh; two samples of the same polymer material, age, and cure were tested in single and dual cantilever configuration test runs as shown in the Figure 2-12. At temperatures, around 90°C, the DMA drive shaft is not being able to measure true response of the specimen, and it caused a crash in the software, which automatically terminated the test.

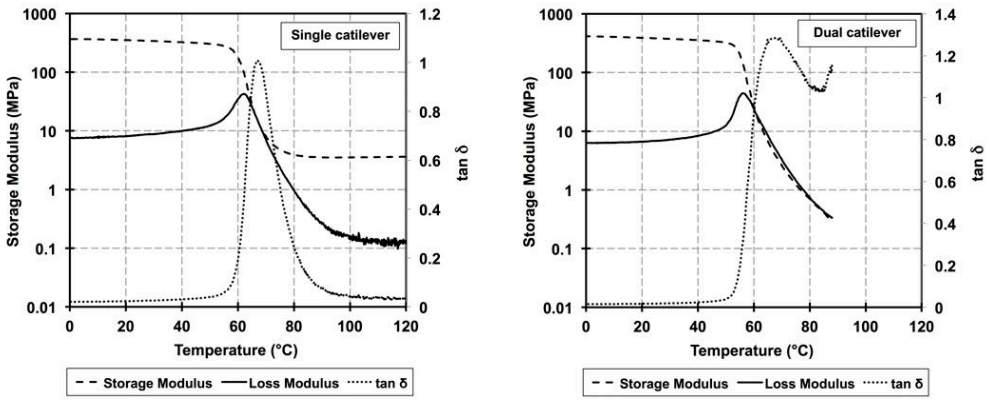

Figure 2-12: Single and dual cantilever configuration temperature scans with DMA

In this research, a single cantilever configuration was used to study the effects of curing and conditioning. The specimen length between inside edges of the clamp is 15mm (refer to Figure 2-13. Details of the testing and diagrams for single cantilever bending are provided in section 3.

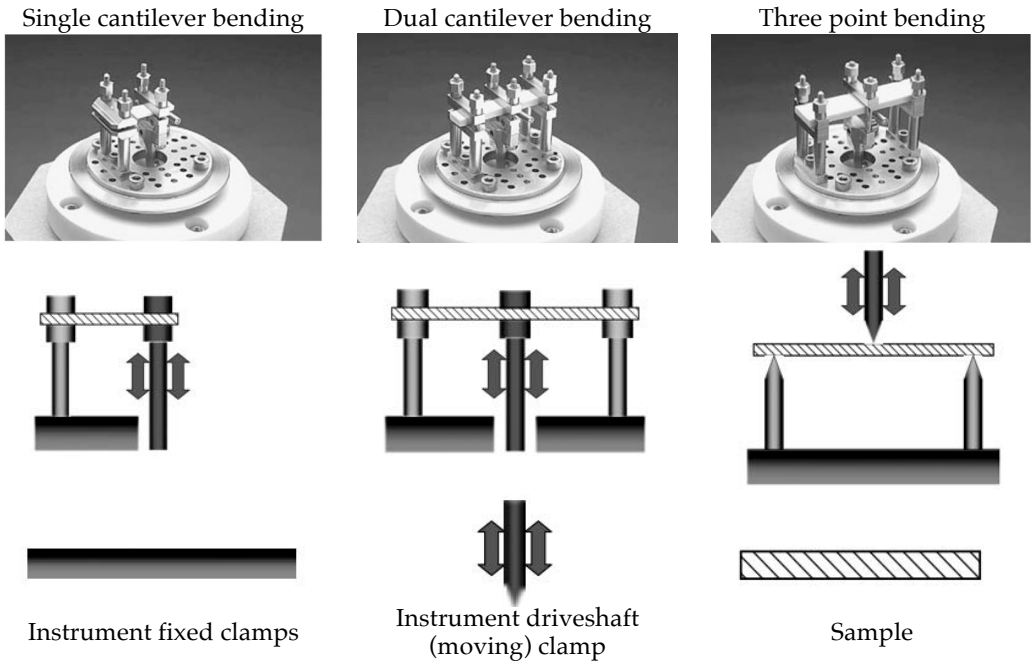

Figure 2-13: DMA test configurations for single and dual cantilever bending (Menard, 2008)

2.8.5 Temperature scanning and storage modulus variation in DMA

Generally, a specimen is excited with a low frequency stress input which is recorded along with the strain response. The shapes of the test specimen and the testing procedure vary from one test to another. The various tests and their corresponding specimen shapes factor are described in section 2.8.1. Further description of DMA concept and the equations that relate to each variable can be found (Menard, 2008).

In DMA stiffness and damping are reported as dynamic complex modulus and tan δ. The motor applies stress to relate dynamic complex modulus E^*; an in-phase component E', the dynamic storage modulus, and an out of phase component E'', the dynamic loss modulus can be expressed (Thomas *et al.*, 2014). DMA does not plot dynamic complex modulus E^*, instead the in-phase component E', and the out of phase component E'' are plotted. Section 2.8.2 describes the determination of these values in DMA. The ratio of the loss to the storage is the damping, which is a measure of the energy dissipation in a material under cyclic load. The storage modulus–temperature response for a typical amorphous polymer is given, the

stages are shown in Figure 2-14. It should be noticed the regions in Figure 2-14 are only for demonstration since the transition regions are dependent on the type of the material tested.

- The glassy region where the modulus of most amorphous polymers is in the order of 3 GPa. At the glassy state where the temperatures are low, primary and secondary bonds characterize the material; therefore, the response is almost constant.
- The transition region, where the modulus changes rapidly with temperature from 3 GPa to around 3 MPa. Due to the broken secondary bonds, the E-modulus in the leathery state is much lower than in the glassy state, while the viscosity is much higher.
- The rubbery plateau region, which is apparent only when polymers form a loose network by cross-linking
- The rubbery flow region (viscous regime).
- The liquid flow region. The modulus in these various regions of viscoelastic behaviour is affected differently when the molecular weight of the polymer is changed.

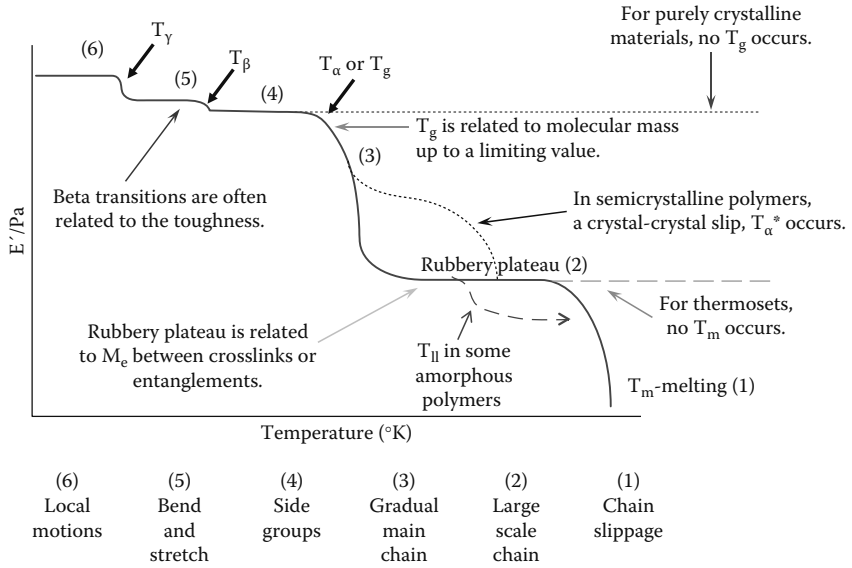

Figure 2-14: Storage modulus vs. temperature curve, states and transitions of a polymer (Menard, 2008)

The most common application of DMA is to determine of the glass transition temperature, T_g. The transitions from glassy or rubbery state can be seen as the temperature increases; modulus values E', E'' and tan δ are functions of temperature.

Although the glass transition temperature, T_g is quoted as a single value section 2.8.6, it is usually a narrow temperature range rather than a sharp point, as is the freezing or boiling point (Petrie, 2006). According to the DMA storage modulus vs. temperature curve, the glass transition temperature, T_g refers to the drop in storage modulus. The change in storage response of cured adhesive is a function of temperature; it decreases with rising temperatures. The softening takes place over a range of temperatures sometimes several degrees (°C) depending on the thermal history and age.

2.8.6 Determining a characteristic glass transition temperature, T_g using DMA

Although the glass transition takes place over a range of temperatures, it is usually quoted as a single value of T_g. There are, however, numerous definitions for T_g, according to different codes and standards. Five different methods are used to report T_g from a DMA test as shown in Figure 2-15. They are summarised as:

1. The intercept method or T_g onset: is the corresponding temperature to the intersection of the tangents to the glassy state and the second tangent leathery region of the storage modulus curve (ASTM E1640-99, 1999; British Standard ISO 6721-11, 2012).
2. The intercept method or T_g 2% onset: is similar to the previous method, the temperature at which the storage modulus has dropped by 2% compared to a tangent to the storage modulus below transition (Hülder et al., 2008)
3. The point of inflection (mid-point) method: is the corresponding temperature to the inflection in the storage modulus curve (British Standard ISO 6721-11, 2012).
4. The peak of tan δ: is the corresponding temperature to the maximum tan δ (ASTM E1640-99, 1999; British Standard ISO 6721-11, 2012).

5. The peak of loss modulus: is the corresponding temperature to the peak of loss modulus curve (ASTM E1640-99, 1999; ASTM D4065-01, 2001).

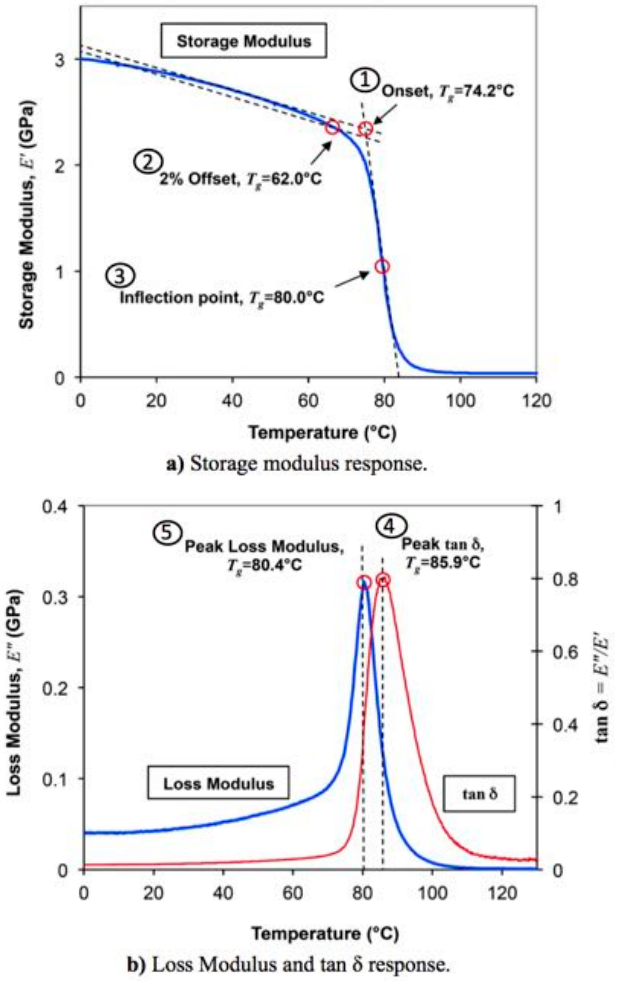

Figure 2-15: Various methods of reporting T_g from the DMA runs (Othman *et al.*, 2013a, b).

According to ASTM E1640-99 (1999); British Standard ISO 6721-11 (2012) the glass transition temperature, T_g is defined as the intersection between tangent extended from initial storage modulus and tangent to the transition part of storage modulus. Due to the fact that the tangent intersection lies outside the crescent of the change from glassy state to rubbery state; this point is called extrapolated onset glass transition temperature, ($Onset\ T_g$) as shown in Figure 2-15. However, they are sensitive to how the tangent lines are drawn (Mulligan *et al.*, 2003), and different

values are obtained if a logarithmic or normal scale is used to plot the storage modulus.

The method presented which is used in aircraft construction, is similar to the described method (ASTM E1640-99, 1999; British Standard ISO 6721-11, 2012). The intersection between 2% drop of the initial storage modulus tangent and storage modulus response is suggested as 2% onset glass transition temperature, 2% $offset\ T_g$ in Figure 2-15.

The peak of the tan δ and loss modulus curve is more easily identified and more consistent between tests, while to identify the inflection point of storage modulus accurately in the transition region the first derivative of the modulus is required, and the data acquisition of the DMA should be set high. The scale (logarithmic or normal) of the plots does not affect the T_g value obtained from peak and inflection method. The values achieved from the peak of loss modulus are close to the values of the inflection point of the storage modulus. It must be noted that the inflection and peak method give high values of T_g (Mulligan *et al.*, 2003).

In this research, T_g reported from the DAM tests in section 3 and 5 are reported in five methods; peak tan δ and loss modulus curve, onset of the storage modulus with logarithmic and normal scale, and finally the point of inflection of storage modulus response.

2.9 Differential Scanning Calorimetry (DSC)

Differential Scanning Calorimetry (DSC) measures the energy changes that occur as a sample is heated, cooled, or held isothermally, together with the temperature at which these changes occur. It is thermal analysis technique heat flow based, in which the difference between the heat flux into a test specimen and an empty reference crucible is measured as a function of temperature or time. There are two types of DSC, "heat flux" and "power compensation". DSC devices are equipped with a sensitive heating chamber to maintain the temperature of the sample and the reference crucible while the sample undergoes a physical transformation.

The flow of energy into or out of the sample as a function of temperature or time on the x-axis is measured; usually flow of energy is measured in mW on the y-axis.

The DSC sensor measures the difference between the sample and reference crucible heat flows, and consists of a series of thermocouples underneath the crucible positions (Wagner, 2009). Depending on the type of system, endotherm reaction can be in the downward or upward direction (Gabbott, 2008; Menczel and Prime, 2009). Figure 2-16 shows various stages of typical polymer heating using DSC.

- Heat flux systems endotherms are shown as going down, since endothermic transitions result in a negative temperature differential.
- Power compensation systems they are shown as going up, since with this principle endothermic transitions result in an increase in power supplied to the sample.

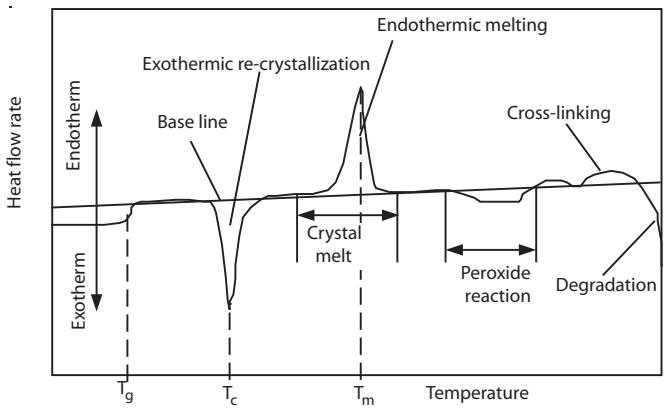

Figure 2-16: Typical heat flow vs. temperature curve for polymers (Osswald *et al.*, 2006).

One of the main advantages of DSC is that samples are easily encapsulated, relative to DMA, and no proportion is required. A great deal of information can be obtained from the DSC runs such as the glass transition temperature, T_g, melting temperature T_m, heat of fusion, and entropy of fusion. The melting behaviour in DSC permits a determination of the extent of crystallinity. In the measurement of reaction, heat for the types of polymerization in DSC is the more frequently used technique because it gives a quantitative measure of the heat and the rate of the curing reaction (Pizzi and Mittal, 2003; Gabbott, 2008). DSC is the most widely used for thermal analysis, and researchers have successfully used to study curing behaviour of adhesives (Atarsia and Boukhili, 2000; Moussa, 2001; Cai *et al.*, 2008; Hidalgo-medina, 2015)

2.9.1 Determining a characteristic glass transition temperature, T_g using DSC

Similar to the DMA, various methods are used to determine the glass transition temperature, T_g. The glass transition temperature, is usually reported from the DSC heat flow output. The DSC signal (heat flow response with temperature) two transitions (the melting and glass transition) can be identified. At the glass transition temperature, exhibits a generally abrupt the specific-heat capacity change which in most cases large enthalpy relaxation occurs. The enthalpy of a material is energy required to heat the material to a given temperature and is obtained by integrating the heat capacity curve (Gabbott, 2008). The enthalpy change is calculated from the temperature difference between the sample and the reference crucible. In amorphous and crystalline polymer materials, the measurement of enthalpy can allow an estimate of crystallinity (Della Gatta *et al.*, 2006). If the sample exhibited an enthalpy relaxation peak, the T_g can be reported as the temperature corresponding to the peak. The degree of enthalpy relaxation depends on the mechanical and thermal conditioning during manufacturing and storing process (Wagner, 2009).

In the absence of the enthalpy relaxation peak, the DSC heat flow output is proportional to the sample heat capacity, and the T_g may be determined from the characteristic discontinuity in heat capacity. There are different methods to identify the T_g from the ΔC_p. They are summarised as:

- Onset: is the corresponding temperature to the intersection of tangents from the baseline and initial slope of the step.
- Endpoint: is the corresponding temperature to the intersection of tangents from the step and final baseline.
- Midpoint: is the corresponding temperature to the middle of the step measured as half the step height (ASTM D3418-99, 1999), which is the mean of the Onset and Endpoint.
- Inflection point: is the corresponding temperature to the inflection point of the ΔC_p step.
- Richardson method: is the corresponding temperature to the temperature that corresponds to the point of intersection of the extrapolated enthalpy

curves of the glass and liquid in the enthalpy or heat capacity versus temperature (Wagner, 2009).

Figure 2-17 shows the methods that are widely used. The modern DSC packages come with software, which allows the operator to automatically perform T_g calculations. The T_g values in section 3 of this research are reported according to the onset and the point of inflection. The T_g of a cross-linked polymer in general shows an increase with increasing degree of cross-linking, and therefore the degree of cure can be measured (Pizzi and Mittal, 2003).

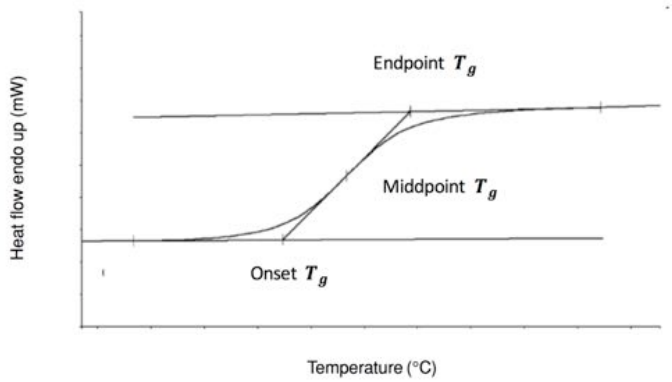

Figure 2-17: Illustration of the T_g determination from the heat flow vs. temperature (Gabbott, 2008).

In section 3, Glass transition temperature, T_g is evaluated using the onset and mid-point methods to study the effect of curing using DSC and the results are compared with the ones obtained from DMA.

2.10 Thermal effects on bonded FRP performance

2.10.1 Service temperature of steel structures

Due to changes in the surrounding environment, steel bridge structures change continually. Tong *et al.* (2002) and Au *et al.* (2002) conducted a comprehensive investigation into the thermal behaviour of bridges in Hong Kong with special emphasis on steel concrete composite bridges. The outcome of the

study demonstrated that the temperature distribution in bridge structures depends primarily on the solar radiation, ambient air temperature and wind speed in the vicinity. In some parts of the bridge girders, temperatures over 54°C were recorded. The combination of weather conditions which will result in an extreme temperature distribution in bridge structures would be clear days with high solar radiation and very low wind speeds (Potgieter and Gamble, 1989). During the daytime bridges undergo significant heating cycles. As the sun rises, the bridge typically experiences a net gain of heat, which leads to an increase in temperature throughout the structure. The temperature changes in the bridge can come from two primary sources; changes in the ambient air temperature, and direct exposure to solar radiation. Heating resulting from changes in the ambient air temperature leads to uniform changes in the bridge temperature and is generally not significant during a given day when compared to the heating from direct solar radiation that tends to heat the bridge very quickly. Whilst a large change in air temperature will increases the differential temperature in the bridge to a lesser degree, (Potgieter and Gamble, 1989), the significant thermal gradient throughout the bridge is due to the solar radiation. The parts of the bridge that are exposed to direct sunlight experience much quicker temperature changes than those that are shaded. However, the amount of absorbed energy from solar radiation depends upon the nature, colour of the receiving surface and the time of day as well as the time of year as the intensity of solar radiation varies. Researchers have shown that the temperature of parts of a bridge below the tarmac can rise up to 53°C (Hülder *et al.*, 2008). In a composite steel girder bridge, significant temperature gradients exist due to the relatively high thermal conductivity of steel, which is approximately 50 times greater than that of concrete material. Liu *et al.* (2013) used the temperature numerical simulation method to study temperature distribution and thermal behaviour of a typical steel structure, the lattice shell structures. The study showed that the solar radiation had a significant effect on the temperature distribution of steel structures. Considering the solar radiation, the temperature of steel structures is about 20°C higher than the corresponding ambient air temperature, and the temperature change during the day and night is similar to sine curve. From the previous studies it is clear that temperature changes during the day and from one season and to another are important, and there are places that experience extreme air temperatures up to 65°C in middle eastern areas.

2.10.2 Lap-shear joins at elevated temperature

The focus in this section is on the work carried out using structural adhesives. In other engineering branches such as, aeronautical and mechanical engineering, the impact of temperature (low and elevated) has been studied, but they are not covered in this section since the adhesives and the temperature are significantly different from the ones that are widely used in structural applications in civil engineering. The strengthening plates used in structural strengthening tend to be thicker than the ones used in aeronautical and mechanical engineering, consequently the stresses are different within the adhesive layer and the pealing stresses are significant.

Studies were carried out to understand the behaviour of adhesive joints at elevated temperature on small scales. Different adherents were used to effectively study the joints. Although different adhesives were used, a significant reduction in the joint strength and stiffness was observed. This is because the adhesive properties were reduced. The effects of differential thermal expansion in some studies was reduced to minimum by using the same material to fabricate the double lap-shear sample or material that have relatively the same thermal expansion.

Tadeu and Branco (2000) carried out a study to investigate the effect of temperature on concrete specimens strengthened with externally bonded steel strips. Epoxy resin SIKA ICOSIT K101-AC was used as a bonding material between steel reinforcement and concrete elements. Joint exhibited very poor behaviour when they were subjected to increased temperature. The bond strength reduced by 50% at 60°C compared to the specimens tested without exposure to heat. At 90°C, strength was reduced to values of between 24 and 29%. At 120°C, a film of water was observed on the surface of the concrete, in addition to the deterioration of the resin. The failure modes changed from concrete rupture for specimens in the absence of heating to failure at the bond for exposure to temperatures above 60°C. Although thermal stresses do not develop between the steel strips and the concrete due to very close coefficient of thermal expansion, a reduction of the failure load with an increase in temperature was noticed. The authors believe it is due to the mechanical property changes in the adhesive at elevated temperatures. The testing configuration and the summary of the results are shown in Figure 2-18 and Figure 2-19.

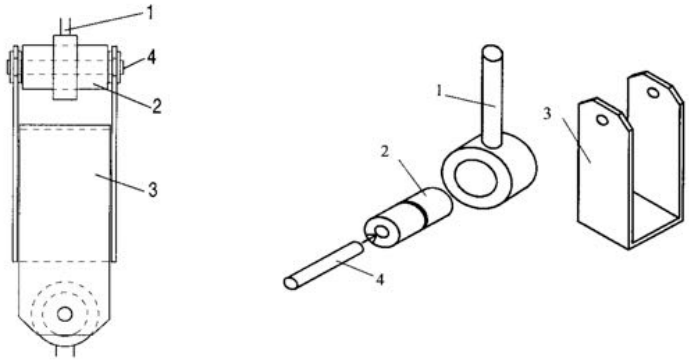

Figure 2-18: Scheme of Anchorages. 1-Steel Ring; 2-Horizontal Sleeve; 3-Clamp; 4-Pin (Tadeu and Branco, 2000)

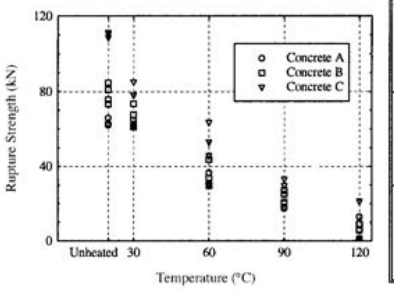

	Temp. (°C)	F_m (kN)	τ_m (MPa)	$F_m/F_{m\,20°C}$
A	unheated	63.4	3.9	100.0
	30	62.8	3.9	99.1
	60	32.6	2.0	51.4
	90	17.6	1.1	27.8
	120	4.8	0.3	7.5
B	unheated	79.7	4.9	100.0
	30	67.4	4.2	84.5
	60	35.6	2.2	44.7
	90	23.2	1.5	29.1
	120	7.1	0.4	8.9
C	unheated	110.2	6.9	100.0
	30	75.3	4.7	68.2
	60	54.1	3.4	49.0
	90	26.8	1.7	24.3
	120	8.0	0.5	7.3

Figure 2-19: Summary of the lap-shear results (Tadeu and Branco, 2000)

Zhang *et al.* (2010) studied the behaviour 6 and 12 mm adhesively bonded pultruded GFRP plates in double lap shear configuration and the dimensions of the double lap-shear specimens are shown in Figure 2-20. A two-component epoxy system was used SikaDur-330 from Sika AG. Coupons were prepared to measure the thermo mechanical properties of the GFRP and the adhesive; the test results are also shown in Figure 2-20. The glass transition temperature, was estimated as being in the range between 40°C and 50°C after ten days of curing under ambient laboratory conditions. The double lap-shear specimens were manufactured under ambient laboratory conditions and cured under ambient laboratory conditions for ten days. The tests were carried out at temperatures ranging between -35°C and 60°C. The testing results are shown in Figure 2-21.

The authors reported that the strength and stiffness of the joint were not affected by temperatures below the glass transition temperature, of the adhesive -35°C to

40°C. The highest strength was obtained at 40°C due to a statistical size effect caused by the smoothing of the normal tensile and shear stress peaks. At temperatures above glass transition, strength and stiffness decreased following the trend of the thermo mechanical behaviour of the adhesive. Different failure modes were observed and the failure mechanism changed with increasing temperature at glass transition from fibre-tear to adhesive failure.

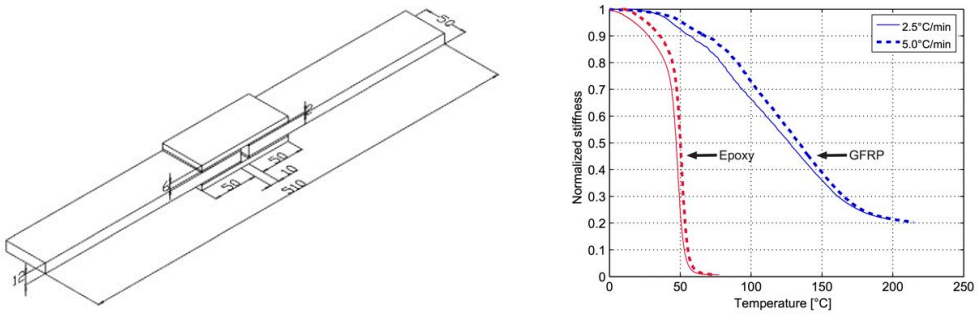

Figure 2-20: Geometry of GFRP double-lap joint specimen (dimensions in [mm]), and thermo mechanical behaviour of epoxy adhesive and GFRP laminates (Zhang *et al.*, 2010)

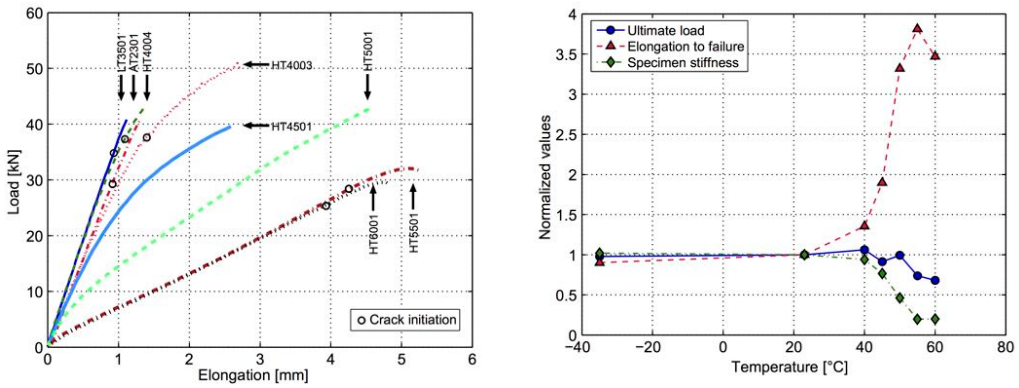

Load vs. elongation response of specimens at different temperatures

Normalized ultimate load, elongation and specimen stiffness vs. temperature

Figure 2-21: Experimental results by (Zhang *et al.*, 2010)

Al-Shawaf *et al.* (2009) carried out a series of tests on wet lay-up CFRP laminates double-lap shear joints subjected to temperatures between 20 and 60°C. The specimens were made of 5 mm steel plates, high modulus (640 GPa) unidirectional carbon fibre plies. Three different epoxy resins were used for the fabrication of the CFRP/steel specimens; Araldite 420 (HA) with T_g of 42.7°C, Mbrace Saturant (HMS)

with T_g of 55.5°C, and Sikadur-30 (HSD) with T_g of 62°C. The sample was cured for 14 days at room temperature after fabrication. The test results are shown in Figure 2-22.

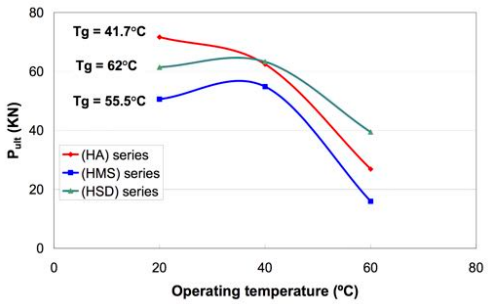

Variations in ultimate joint load with current elevated environmental temperature exposures

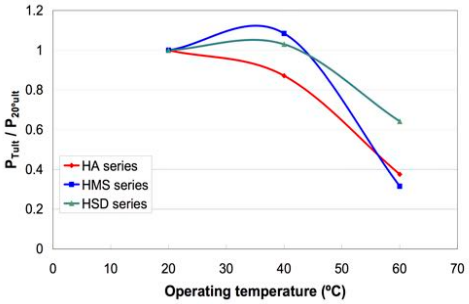

Normalized ultimte joint load vs. exposure temperature

Figure 2-22: Experimental results (Al-Shawaf *et al.*, 2009)

The authors concluded that there is an inverse proportionality between operating temperatures and joint capacity, and a significant deterioration in the joint capacity was observed above the adhesive's T_g. It is reported that different adhesives have different strain profiles at operating temperatures above ambient and below their T_g values. This is mainly due to adhesive individual responses with temperature. Ductility and shear deformations tend to increase with temperature. Above the T_g of the adhesive, and as a result of increased adhesive's softening and deterioration in its shear modulus, the strain level almost totally declines except for a narrow part at the joint to cope with the remaining joint capacity.

Nguyen *et al.* (2011) experimentally investigated the change of the mechanical properties of steel/CFRP double-strap joints at elevated temperatures. The adhesive was two-part epoxy Araldite 420 with T_g 42°C. The specimens were cured for 10 days at room temperature. A series of joints with different bond lengths were tested to failure at temperatures between 20°C and 60°C. It was concluded that the effective bond length of adhesively bonded steel/CFRP double strap joints was found experimentally to increase with temperature. Similar to the joint stiffness degradation, the strength dropped about 15%, 50% and 80% when temperatures reached T_g, 10°C above T_g, and 20°C above T_g, respectively. The joint failure mode

changed from adherend failure to debonding failure as the temperature approached T_g. It was found that effective bond length depended on temperature and the ultimate load capacity reduced significantly, when temperature reached to T_g.

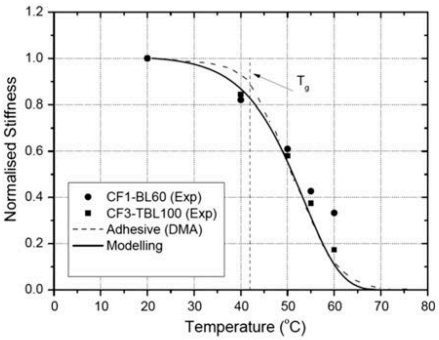

Fig. 7. Experimental (see Section 3.2) and modelling (see Section 4.2) results of temperature-dependent normalized stiffness for joint types CF1-BL60 and CF3-BL100 and the adhesive.

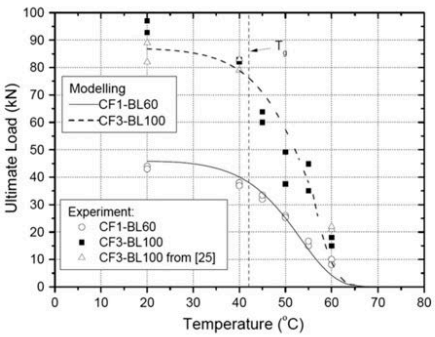

Fig. 8. Experimental (see Section 3.3) and modelling (see Section 4.4) results of strength degradation for CF1 and CF3 joints from 20 °C to 60 °C.

Figure 2-23: Experimental results for the tests by (Nguyen *et al.*, 2011)

Abed (2012) conducted an experimental study on double-lap shear specimens at temperature ranges from 20 to 60°C. The specimens were bonded using Sikadue-30, and they were cured for at least three days at room temperature before testing. Test results showed that the joint capacity of the double-lap shear specimens decreased with temperature increase. The average failure load decreased by 55% when the temperature increased from 24 to 60°C. Figure 2-24 shows the schematic of the double lap shear specimen and failure load variation with temperature. In addition, the failure mode was changed from combined failures between steel/adhesive and CFRP/adhesive interfaces at 24°C to CFRP/adhesive interfaces failure at 60°C.

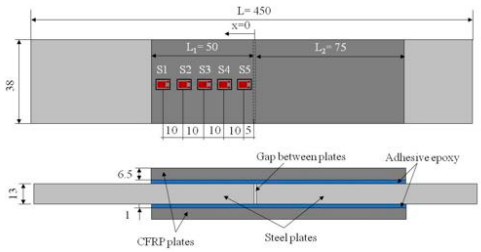

Schematic of the double lap shear specimen

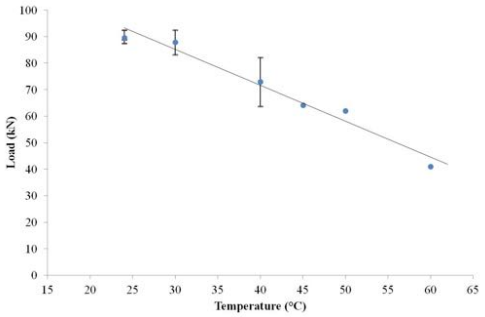

Variation in the failure load of double-lap shear joint with temperature

Figure 2-24: The test specimens and the results by (Abed, 2012)

Liu *et al.* (2014) investigated the bond characteristics between high modulus CFRP sheet and steel plates under elevated temperature exposures. Double lap shears sample were prepared to examine the joint behaviour. Two part adhesive Araldite 420 (HA) with T_g of 42.7°C was used in this research, and the double lap-shear specimens were cured for minimum ten days at room temperature similar to the work by Al-Shawaf *et al.* (2009). Double lap shears tests were tested at temperatures of 20°C, 40°C and 50°C. The lap-shear specimens were made of 5 mm steel plates with high modulus CFRP (640 GPa) using wet lay-up fabrication method (one and three layers). The strain distribution along the bond length, ultimate strength, failure patterns, and effective bond length under those thermal exposures were investigated. The study showed that the ultimate load decreased significantly when the test temperature was above the glass transition temperature, of the adhesive. Larger effective bond lengths were found for the joints tested at glass transition temperature. Evidently short-term thermal exposure has little effect on their failure patterns. All the specimens failed by fibre breakage at the joint and cohesive failure accompanied some joints with very short bond length.

Klamer *et al.* (2006) carried out double-lap shear tests with externally bonded CFRP laminates as shown in Figure 2-25. Two- component epoxy adhesive SikaDur-30 was used in this research but the curing temperature and specimen ages are not given. The specimens which were tested at temperatures from -20°C to 50°C failed in an explosive way by failure of the concrete at the interface with the adhesive, leaving a small layer of concrete (1–3 mm) attached to the adhesive. An increase in failure load with increasing temperatures was found up to circa the glass transition temperature of the adhesive refer to Figure 2-25. Further increasing the temperature

resulted in a decrease of the failure load and a changed type of failure. The authors concluded that three factors had affected the capacity; the difference in coefficient of thermal expansion, the reduced adhesive stiffness, and the reduced bond strength of the concrete-adhesive interface. The difference in coefficient of thermal expansion between concrete and CFRP was expected to be the main cause for the increase of the failure load up to the glass transition temperature, as thermal stresses after heating acted in the opposite direction as the interfacial shear stresses due to loading. The results of the double-lap shear are in agreement with the testes carried out by Blontrock (2003).

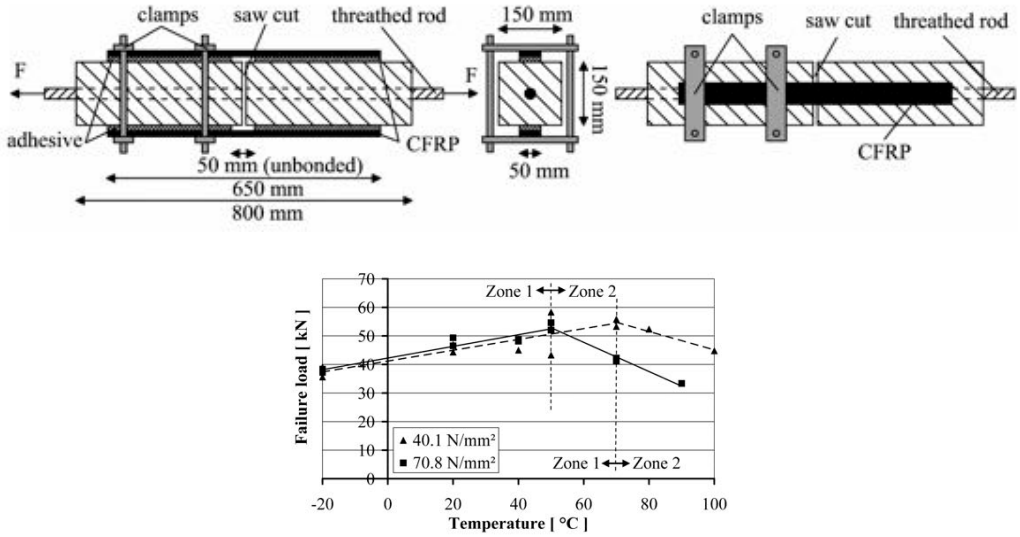

Figure 2-25: Double-lap shear test setup and failure load double-lap shear tests (Klamer *et al.*, 2006)

Wu *et al.* (2005) investigated two different types of resin and various temperature and plate lengths. A similar test set up to Klamer *et al.* (2006) was applied. The glass transition temperature, T_g of the adhesives was measured using HDT methods and are shown in Figure 2-26. For the specimens with the same FRP length, reduction in bond strength with increasing temperature was found. Further, with increasing plate length, debonding failure occurs at higher temperature, and with increasing temperature the type of failure varies from debonding with concrete fracture to debonding along the interface between epoxy and primer. In this research, the ordinary epoxy is referred to non-thermal-resistance.

Table Ⅱ. T_g and HDT for Different Types of Epoxy Resin.

Type of Epoxy	Curing Condition	T_g	HDT
Ordinary Epoxy	80℃ 3hour	38℃	48℃
	60℃ 3hour	34℃	43℃
Ordinary Primer	80℃ 3hour	42℃	*
	60℃ 3hour	34℃	*
Thermo-resistant Epoxy	80℃ 3hour	38℃	55℃
	60℃ 3hour	40℃	57℃
Thermo-resistant Primer	80℃ 3hour	46℃	68℃
	60℃ 3hour	55℃	76℃

* HDT of ordinary primer is not measured.

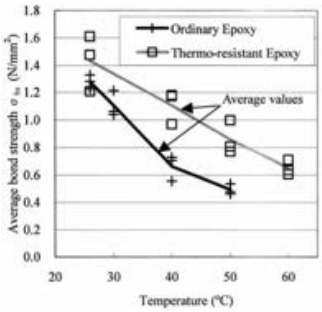

Figure 2-26: Glass transition temperature, T_g of the adhesives and average bond strength with increasing temperature (Wu *et al.*, 2005)

Al-Safy *et al.* (2012) studied the effects of post-curing temperature on adhesive properties in CF fabrics/concrete systems. Single lap-shear specimens were tested under 40% sustained load and gradual increase in the temperature at a constant rate of 2°C/min until failure. MBrace Saturant epoxy with glass transition temperature, T_g of 70°C according to peak tan δ at ambient curing conditions was used in this research. Post curing was carried out at 60°C for more than 7 days resulting in an increase in the glass transition temperature, T_g by 13°C. The bond between CF fabric and concrete substrate for the post-cured samples (AB PC) was observed to be lost at a temperature 10°C higher than the ambient temperature (AB) as shown in Figure 2-27. Single-lap shear tests of CF fabrics/concrete samples also were also tested at constant elevated temperatures was concluded that temperature less than the T_g of the adhesive (tests at 40°C) without post-curing an 8% reduction in the ultimate failure load when compared with the same samples tested at ambient temperatures.

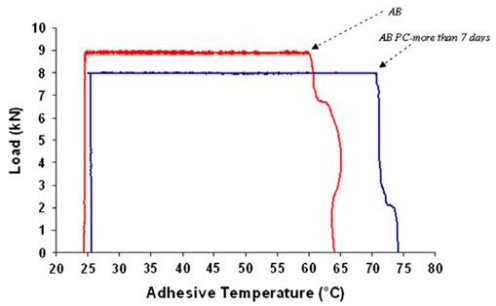

Figure 2-27: Single lap-shear transient test results (Al-Safy *et al.*, 2012)

The same authors Al-Safy *et al.* (2013) studied the influence of post-curing of adhesively bonded CF fabrics /concrete systems at moderately elevated temperatures. Adhesive MBrace Saturant samples and single lap-shear CF fabrics concrete specimens were subjected to a post-curing regime at 60°C after different periods of ambient temperature curing of 3 hours, 6 hours and 72 hours. The samples post-cured at moderately elevated temperatures (60°C) for 4 hours. The CF fabrics /concrete lap-shear specimens have seen improvement with post-curing; samples cured at ambient temperature for 72 hours then post cured, the ultimate failure load increased by 41%, while the samples cured at ambient temperature for more than 7 days the failure load increased only by 9%.

2.10.3 Flexural strengthening at elevated temperature

Stratford and Bisby (2012) investigated the effect of elevated temperatures on the behaviour of steel beams strengthened with CFRP plates. Nine 2-metre length beams including a control beam (un-strengthened) were tested in four-point bending. Two of the beams were strengthened and tested at ambient temperature. Six beams were tested at constant sustained load and transient temperature; only 450 mm from one plate end was heated while the rest of the beam was kept at room temperature as shown in Figure 2-28. The beams were first loaded to above their un-strengthened ambient capacity at a rate of 10 kN/min. This load was held constant while the temperature in the adhesive at T_2 was increased at a rate of 5.5° C/min until failure occurred.

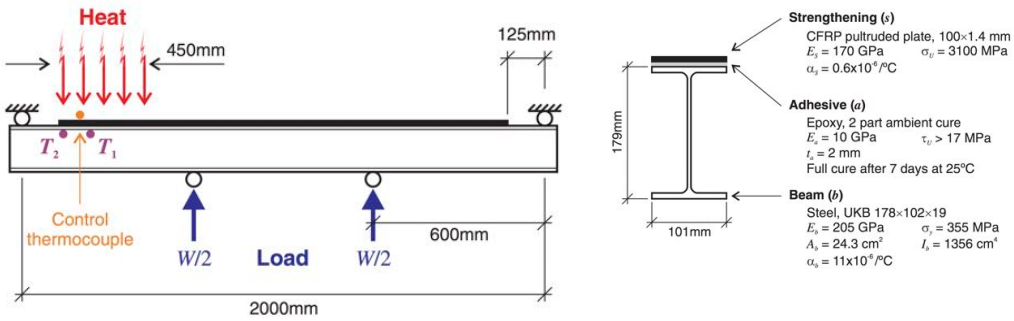

Figure 2-28: Schematic experimental set up showing the loading, heating arrangements, cross-sectional dimensions, and material properties of the strengthened beams (Stratford and Bisby, 2012)

The heated tests showed that considerable joint slip appeared before T_g of the adhesive and reduced the strength of the system. The joint slip began at around 40°C and reached the maximum amount at T_g around 65°C according to tan δ, refer to Figure 2-29. The curing condition and duration of the beams is not clearly stated neither the type of adhesive used in this research. However, the manufacturers minimum properties are stated. The failure load was reduced at elevated temperatures due to the increased deformation capacity of the adhesive and the reduced stiffness; the heated beams all failed by debonding in the adhesive joint. The authors concluded that for the beam geometry, properties, and heating rate considered, both the tests and analysis suggest that the failure temperature is insensitive to the applied load, if the load is greater than the capacity of the un-strengthened beam.

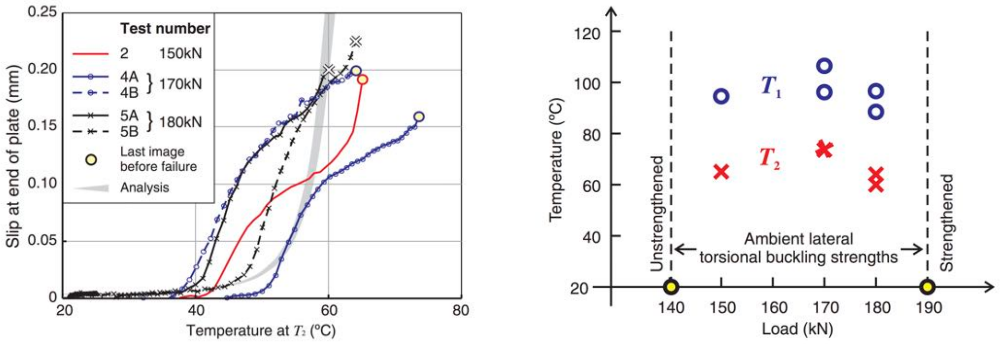

Figure 2-29: The observed variation in plate-end slip according to temperature and the failure temperatures for strengthened beams carrying different loads (Stratford and Bisby, 2012)

Abed (2012) investigated the influence of temperature on the flexural behaviour of standard steel sections. Five 1.1 metre length beams were strengthened with 700 mm CFRP and tested in three-point bending and one un-strengthened. Sikadur-30 epoxy adhesive was used. The FRP strengthened beams were cured for at least three days at room temperature before testing. The beams were tested after a certain temperature was achieved; the test set up is shown in Figure 2-30.

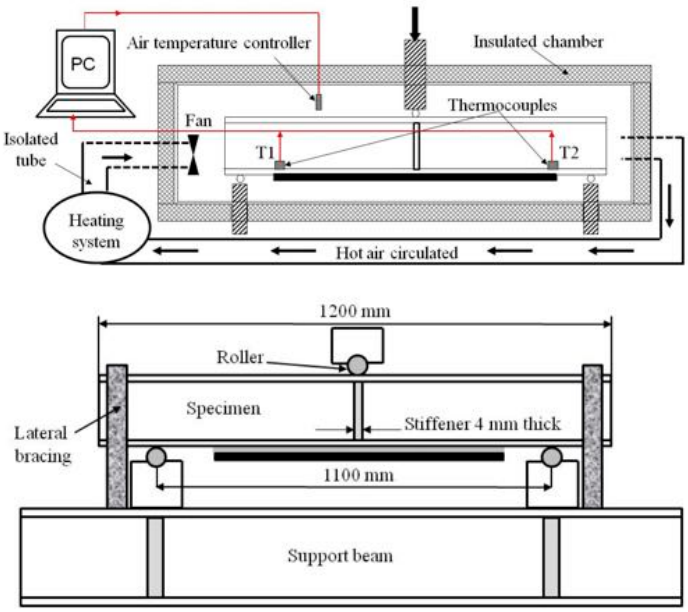

Figure 2-30: Schematic of heating system setup and three-point bending test setup (Abed, 2012)

It was concluded that although the capacity of the beam was increased by 35% at 20°C, the capacity of the reinforced beam decreased with temperature increases; at around the T_g the ultimate capacity reduced by about 50%. The beam totally lost the benefit of CFRP plate reinforcement at 60°C and the load-deflection curve became similar to that of the un-strengthened beam as shown in Figure 2-31. The glass transition temperature, T_g of the adhesive was not measured using thermo mechanical methods. It is recommended that the CFRP plate reinforcement length of steel beams exposed to high temperatures should be extended by 30% compared to those exposed to 20°C. It is also suggested that structure service temperature should remain at least 15°C The glass transition temperature, T_g.

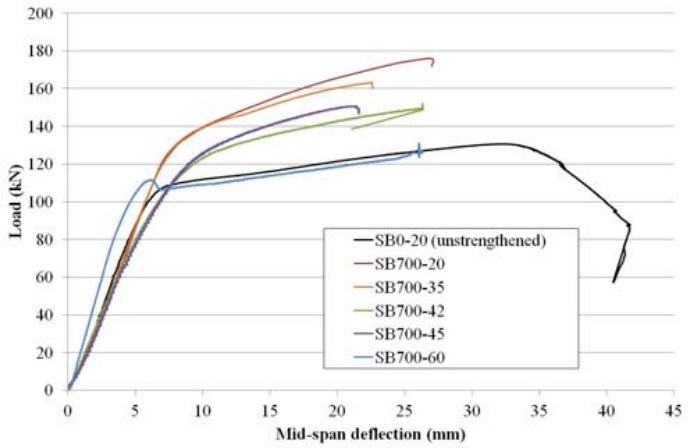

Figure 2-31: Load vs. mid-span deflection for FRP reinforced beams (Abed, 2012)

Research was also carried out to study the behaviour of FRP/concrete joint in bending. Di Tommaso *et al.* (2001) investigated the influence of temperature using three-point bending tests at temperatures ranging from -100°C up to 40°C. The tests on small-scale concrete specimens that did not contain internal reinforcement, but were strengthened with normal or high modulus CFRP laminates. Sikadur-30 CFK Kleber was used to bond the FRP plates to concrete. The specimens strengthened at room temperature (20°C). The specimens were tested to failure at –100, –30, and +40°C after an approximately homogeneous temperature distribution within the concrete specimen had been reached. The results were compared to the specimens tested at room temperature. Decreases in failure loads were found for both increasing and decreasing temperatures. Different types of failure were found depending on the applied temperature. For high temperatures (40°C), cohesive failure of the adhesive was found. For moderate temperature, failure of the concrete was found near the interface with the adhesive, while for very low temperatures (-100°C) delamination within the CFRP was found. The same authors presented a theoretical equation based on a kinematic model to calculate the shear stresses between the laminate and the concrete. The glass transition temperature, T_g of the adhesive was not mentioned.

Klamer *et al.* (2006) performed tests on small-scale three-point bending tests to investigate the influence of temperature. The test set up and the results are shown in Figure 2-32. In these tests, an increase in failure load was found with increasing temperatures, until circa the glass transition temperature, of the adhesive Sikadur-

30. The glass transition temperature, T_g from the manufacturer of 62°C is reported. The method by which the value of glass transition temperature, T_g 62°C is determined is not given. A decreasing failure load was found due to the changed type of failure, at higher temperatures. At above the glass transition temperature, the debonding failure changed from concrete interface failure with concrete residues in the adhesive layer to failure exactly in the interface in between the concrete and the adhesive.

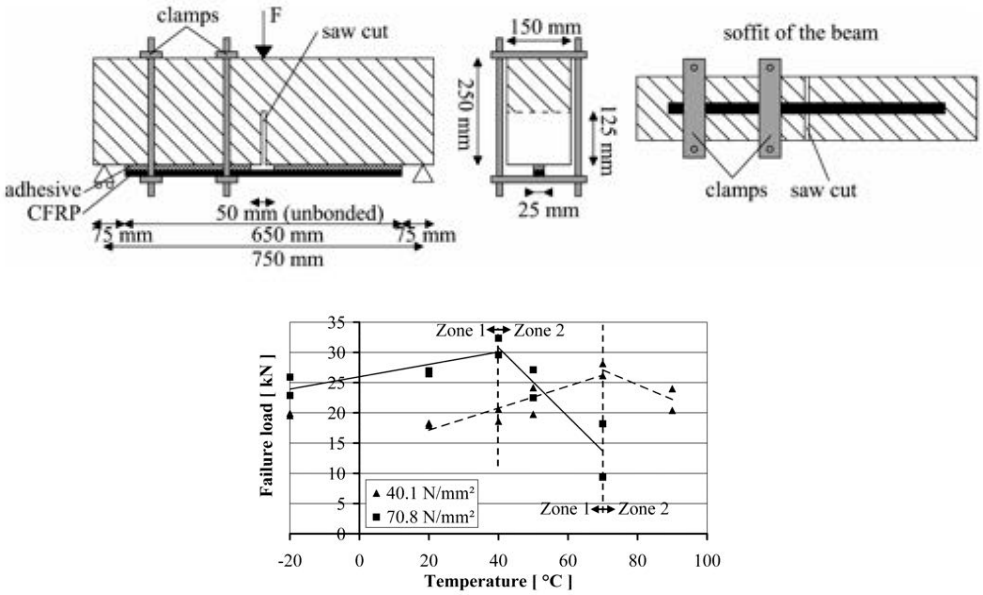

Figure 2-32: Three point-bending test setup and failure load three point-bending tests (Klamer *et al.*, 2006)

The same authors Klamer *et al.* (2008) tested twelve 4-metre long beams in a four-point bending configuration using the same adhesive (Sikadur-30). The curing conditions and period were not given. However, prior to testing the beams were heated, which took approximately 6 hours for the beams tested at 50°C and 30 hours for the beams tested at 70°C. The glass transition temperature, T_g of the adhesive was not measured after the long period of exposure which potentially increased the value of T_g. Four different CFRP-strengthened reinforced concrete beams that were designed to fail by four different debonding mechanisms were investigated at 20°C, 50°C and 70°C. For all the beams tested at 50°C, no change in the type of debonding was observed compared to the beams tested at 20°C. Nor was failure load

(significantly) affected at 50°C in comparison with the beams tested at 20°C. beams tested at 70°C, different debonding was recorded. Debonding failure changed from bond failure in the concrete to failure where significantly less concrete remained attached to the adhesive and concrete cover rip-off. One specimen with shorter CFRP and exposed to 70°C failed at significantly lower in comparison with the beams tested at 20°C, the authors clime that the beam, which had a shorter laminate length, failed by debonding at the end anchorage zone.

2.10.4 Analytical approaches for modelling externally bonded adhesives at elevated temperature

To study the effects of thermal loading on externally bonded metallic structure with FRP, several researchers adopted the model by Smith and Teng and extended its application to investigate the influence of temperature. Denton (2001), studied the interfacial stresses due to the differential expansion of a metallic beam and FRP material. Deng *et al.* (2004) and Stratford and Cadei (2006), adopted the same model to study the combination of thermal and mechanical loading. The degradation of adhesives was not considered in these investigations, and linear elastic material properties were assumed.

The same model is adapted to consider adhesive degradation by Dawood and El-Tahan (2011). They used the equations that were developed in Stratford and Cadei (2006) to study the influence of elevated temperature of concrete composite section under service loading. They also introduced the adhesive degradation with temperature. The adhesive Young's modulus degradation was taken into account; this approach is covered in section 6.5.4. There are a few sections of the work by Dawood and El-Tahan that need to be looked at again; perhaps the original work by Stratford and Cadei should be referred to.

Recently, Stratford and Bisby (2012) presented a new approach to study FRP bond at elevated temperature. The flexural tests were carried out under localised heating; the bond area near the plate ends (only the bonded flange) heated. Therefore, the analytical model assumed linear-elastic the adhesive properties at the mid-span, while the heated area treated as elasto-plastic. The authors used DMA storage modulus variation with temperature in the analysis. Figure 2-33 shows modulus variation of the adhesive with temperature and the constitutive material

low that was assumed in the analysis. The model not only assumes stiffness reduction but also considers the strength reduction. This approach creates a plastic zone at the end of CFRP plate and the analysis suggests that failure is due to a rapid increase in slip as the plastic adhesive zone spreads along the whole length of the beam, and consequently the failure temperature is not sensitive to the strain capacity of the adhesive joint. The results of the model and the experiments are shown in Figure 2-29.

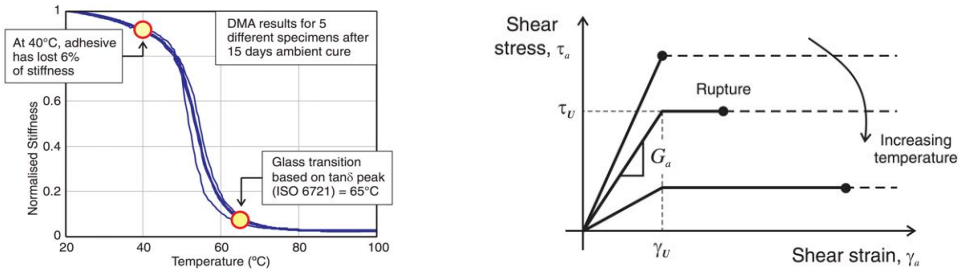

Figure 2-33: Measured loss in elastic stiffness of the epoxy bonding adhesive through the glass transition and the elasto-plastic adhesive constitutive model used in the bond analysis (Stratford and Bisby, 2012)

The work presented by Abed (2012) is the modified the model by Deng *et al.* (2004), linear elastic and perfectly plastic behaviour of the adhesive material is assumed similar to the work by Stratford and Bisby (2012). The adhesive plastic strength was obtained from FE analyses on double-lap shear joint, and the analytical solution was validated with FE model. However, it is important to note the two different constitutive laws used in the two models; elasto-plastic in the analytical model and linear elasticity in the FE analysis. The representative sketch of adhesive stress-strain behaviour and shear stress is shown in Figure 2-34.

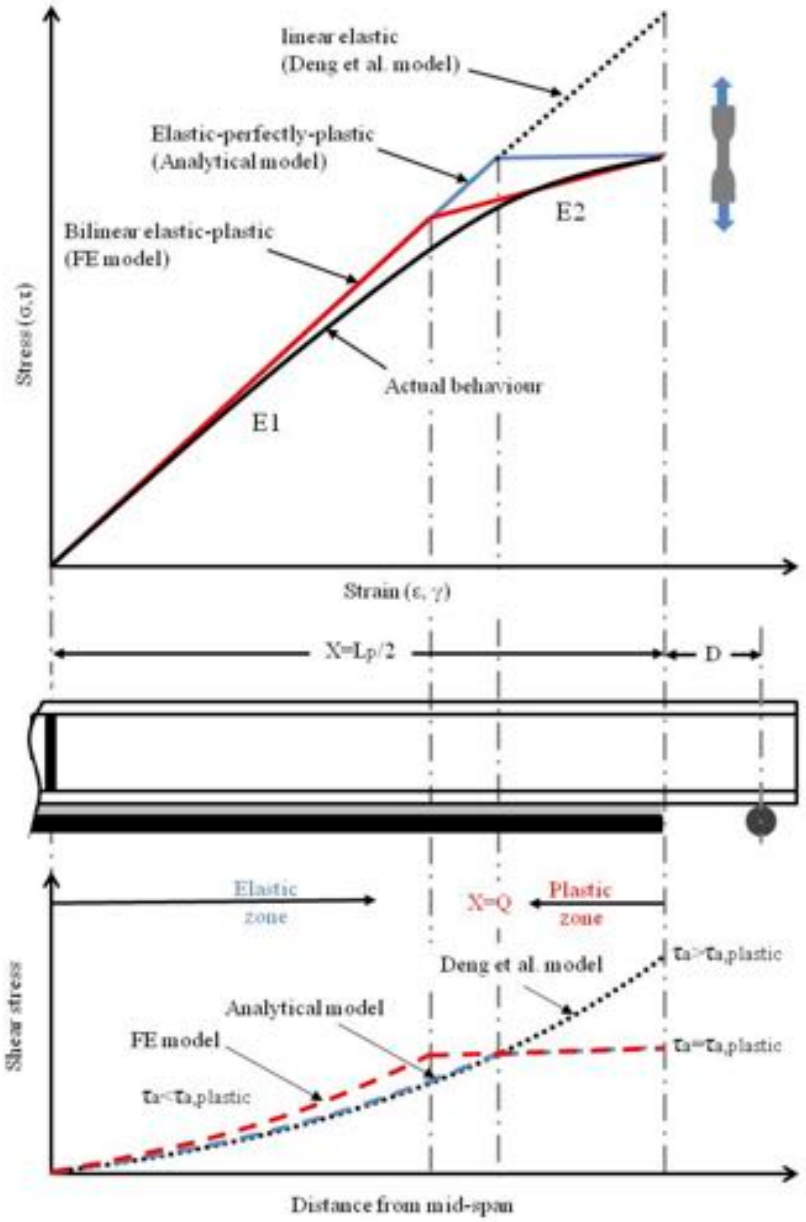

Figure 2-34: Representative sketch of adhesive stress-strain behaviour and shear stress at the tip of CFRP plat (Abed, 2012)

2.10.5 FRP strengthening design guidelines and recommendations at elevated temperatures

According to the current strengthening design guidelines recommendations mentioned in section 2.5, since the adhesive loses considerable strength at temperatures approaching its glass transition temperature, T_g, care must be taken. Depending on the application the operating temperature remains a margin of 10–20°C below T_g (Cadei *et al.*, 2004), where T_g is the peak of $\tan\delta$ of the DMA according to British Standard ISO 6721 (2011). Similar recommendations (T_g–15°C) are adopted for externally bonded FRP systems. Abed (2012) also suggested using an adhesive with a glass transition temperature that exceeded the maximum expected structural temperature by at least 15°C.

The adhesives' properties including glass transition temperature, T_g significantly vary with temperature, and they are heavily dependent on curing temperature. Although the guidelines recommend preparing DMA coupons for each strengthening project, designers mostly rely on the glass transition temperature, T_g reported by the manufactures. The on-site curing conditions are likely to be very different to the laboratory conditions, and consequently the targeted glass transition temperature, T_g may not be achieved.

The methods of characterisation of glass transition temperature, T_g that are described in sections 2.8.6 and 2.9.1 to some extent yield different values of glass transition temperature, T_g. It is possible the highest value of glass transition temperature, T_g to be used.

2.11 Summary

From the literature, it is concluded that very limited work in relation to elevated temperature influence on strengthening steel structures have been carried out. It is assumed that the ambient cure epoxies will gain ultimate mechanical properties and the manufacturers' data is reported as the adhesive mechanical properties. The available adhesives at the market have different mechanical properties and T_g varies significantly. The manufacturers tend to use a variety of methods to define glass transition temperature, T_g, which makes it difficult task to

make direct comparisons between the products. In the limited work at elevated temperature, the T_g from the product data sheet is reported or the details of the finding T_g are not stated clearly or not mentioned despite the fact the tests were carried out at elevated temperatures. Tests on small-scale specimens completed after the samples were subjected to a curing regime and good results were achieved because the adhesive reached the ultimate cure. Flexural behaviour of fully cured joints is not investigated.

Some manufacturers prescribe a curing regime for the product to achieve the targeted T_g. This approach may not be practical or the prescribed curing may be ignored. Therefore, the reported T_g may never be achieved; consequently, the mechanical properties will not be achieved. This aspect has not been covered by research and requires investigation.

Although various modes of failure are reported in literature, the dominant theme is premature failure due to stress concentration within the adhesive at the FRP plate end; failure occurs when the stresses reach the critical adhesive strength. The FRP joint is susceptible to this failure when the joint is subjected to elevated temperature. Thin and high conductive steel members are likely to be affected by temperature changes after the FRP installation and the adhesive properties to be reduced due to the temperature changes. The current guidelines recommend that the service temperature of the structure does not exceed 10–20°C below T_g, but this recommendation has not been investigated, and because there are different methods to report T_g this may be miss interpreted.

This research bridges the gaps in literature by looking at the effects of curing on glass transition temperature, T_g. Two adhesives, widely used in structural engineering were investigated. The relationship between glass transition temperature, T_g and curing temperature and curing conditions are demonstrated. Based on the knowledge gathered from this chapter flexural specimens were designed to demonstrate the impact of curing temperature on the behaviour of scaled FRP strengthened steel members. The work is expanded to examine the behaviour of partially and fully cured scaled beams under sustained load and subjected to a constant transient temperature increase. Analytically the effects of temperature are examined and recommendations on the use of EB-FRP in structures when they are subjected to temperature are given.

Chapter 3

Glass Transition Temperature T_g Characterisation of the Investigated Adhesives

This chapter addresses an investigation of the two commonly used adhesives in structural strengthening applications. The adhesives Sikadure-330 and Tyfo-S used in CFRP plate bonding and impregnating carbon-strengthening fabrics. Although some current design guidelines do not specify the curing duration at ambient temperature, the manufactures report the mechanical properties at different ages and curing circumstances. Sikadur-330 is an ambient cure adhesive. Tyfo-s manufacturer recommends a curing regime prior to the application. It is known that adhesives are highly sensitive to temperatures not only during the service, but also during the curing period.

Glass transition temperature, T_g is the property that is used to characterise polymers with temperature variation because it measures the cross-linking of the polymer chains. The mechanical properties and the performance of adhesives improve with increasing glass transition temperature, T_g. The increase in the glass transition temperature, T_g with increasing curing temperature is limited to the structure of the adhesive, which is different from one adhesive to another.

In this chapter, the influence of curing temperature and humidity is studied. Coupons were tested using Dynamic Mechanical Analysis DMA and Differential Scanning Calorimeter DSC to study the influence of curing and conditioning. The importance of curing conditions is illustrated. The relationship between the curing temperature and glass transition temperature, T_g of the two adhesives is shown.

The temperature and curing period to fully cured Sikadur-330 is identified, and the results are used in chapter 5 to strengthen I-section steel beams.

3.1 Investigated adhesives

The effect of curing and conditioning on Sikadur-330 was studied and the findings were used in strengthening I-section steel beam in chapter 5. The Tyfo-S was used to study the effect of curing and conditioning only in this chapter.

The characteristics of each adhesive provided by the manufacturers are given below.

3.1.1 Sikadur-330

Sikadur-330 is a thixotropic bi-component resin / adhesive, which is shown in Figure 3-1. The base resin (Part A) is a bisphenol-A-based epoxy, and the hardener (Part B) is of aliphatic amines. The mixing ratio Part A: Part B is 4:1 according to manufacturer's data sheet Sikadur-330 (2012). This epoxy is hereafter referred to as Adhesive S. Burn off tests results are in (Appendix A1). The adhesive cured resin contains < 20% by weight of silica-based fillers, according to ASTM D2584-02 (2002). According to the manufacturer's data sheet Adhesive S, Heat Distortion Temperature (HDT) method was used to measure thermal stability (ASTM D648-01, 2001). The reported value is 47°C for samples cured at 23°C for 7 days. This adhesive is used to bond FRP strips and to impregnate FRP fabrics applied to enhance existing concrete or/and steel structures. The mechanical properties of this epoxy are given in section 4.5.1.

3.1.2 Tyfo-S

Tyfo® S is a two-component epoxy matrix material by Fyfe Co. LLC, which is shown in Figure 3-1. The mixing ratio Part A: Part B is 100: 42 by volume (100: 34.5 by weight) given in Tyfo-S (2011). Burn off test results are shown in appendix A1 ASTM D2584-02 (2002); British Standard ISO 14127 (2008). The adhesive contains 0% filler. Due to its low viscosity the adhesive is used in wet-layup composite applications for strengthening structures. Fumed silica (such as Cab-O-Sil TS-720) is recommended to thicken mixed epoxy to the desirable consistency to be used as a prime or finish coat depending on the application requirements. The manufacturer's data sheet reports mechanical properties after curing for 72 hours at +60°C according to ASTM D0638-03 (2003), which specifies the loading rate as 5±25%

mm/min. The flexural properties are found according to ASTM D0790-03 (2002), and the speed of the test should not be greater than 2 mm/min. Table 3-1 contains some of the mechanical properties. According to the manufacturer's data sheet T_g is 82°C after 72 hours of curing at 60°C. Glass transition temperature, T_g is measured according to ASTM D4065-01 (2001). This adhesive is hereafter referred to as Adhesive T.

Table 3-1: Tyfo-S mechanical properties from the manufacturers datasheet Tyfo-S (2011)

Properties	***Test Method***	***Performance of Tyfo-S***
Tensile Strength, (MPa)	**ASTM D638**	72.4
Young's Modulus, *E* (GPa)	**ASTM D638**	3.18
Elongation at break %	**ASTM D638**	5.0
Flexural Strength, (MPa)	**ASTM D790**	123.4
Flexural Modulus, (GPa)	**ASTM D790**	3.12

Adhesive S Adhesive T

Figure 3-1: (Left) Bi-component adhesive Sikedur-330; (Right) Epoxy matrix Tyfo-S

3.2 Experimental programme and specimen preparation

3.2.1 Experimental programme

Post-cured epoxy samples were studied to assess the effect of curing and conditioning on two structural adhesives after being cast and treated at laboratory conditions (24±1°C and 45±5%RH) for 24 hours. The specimens were then moved to various conditioning environments. Different age, temperature and humidity were considered. The samples were conditioned over short-term exposure for 3, 7, 14, and

28 days. Various curing temperatures (15, 24, 35, 50, 65, and 80°C) and two extreme humidity conditions (0% RH and the saturated condition) were selected.

These temperatures were studied because FRP strengthened structures are likely to experience these temperatures in different seasons during the service and glass transition temperature, T_g of the epoxy adhesives that are used in construction is in the range of approximately 40–82°C (ACI 440.2R-08, 2008; Stratford and Bisby, 2012). The two extremes of humidity were examined in case the FRP strengthened structure is exposed to water for a short period of time, which may happen in offshore structures. Table 3-2 shows the test matrix for the two investigated adhesives in this research.

Table 3-2: Adhesive T and Adhesive S test matrix

Specimen Name	***Curing Temperature (°C)***	***Curing Age***			
		3 Days	***7 Days***	***14 Days***	***28 Days***
0% RH	**15**	3 sample were tested for each curing temperature at a different age			
	24				
	35				
	50				
	65				
	80				
Saturated	**15**	3 sample were tested for each curing temperature at a different age			
	24				
	35				
	50				
	65				
	80				

There are different methods to examine T_g as described in section 2.7.2. From the structural point of view Dynamic Mechanical Analysis (DMA) is more beneficial to study T_g and the modulus variation with temperature. However, Differential Scanning Calorimetry (DSC) is the most widely used method in thermal analysis and defining T_g by the industry. Although the design guidelines of FRP strengthening recommend DMA to characterise T_g, it is likely to obtain similar results from the two techniques.

In this research, Dynamic Mechanical Analysis (DMA) and Differential Scanning Calorimetry (DSC) were used to study the effect of the curing environment on the

glass transition temperature, T_g. The tests were performed on epoxy specimens after curing.

- **Dynamic Mechanical Analysis (DMA):** is widely used to characterise a material's properties as a function of temperature, time, frequency, stress, atmosphere or a combination of these parameters. DMA is also called DMTA for Dynamic Mechanical Thermal Analysis

- **Differential Scanning Calorimetry (DSC):** is a thermal analysis technique that records a material's heat capacity, C_p. The tests are mostly conducted at atmospheric pressure. This allows the detection of transitions such as melts, glass transitions, phase changes, and degree of curing to be investigated.

Dynamic Mechanical Analysis (DMA) tests were performed up to 120°C. A parametric study was carried out to select the length of the coupons and test settings. The details are addressed in section 3.4.

Differential Scanning Calorimetry (DSC) tests were performed from 25 to 120°C at constant heating rate of 10°C/min (Mulligan *et al.*, 2003). The details are addressed in section 3.6.

3.2.2 Sikadur-330 coupon preparation

Epoxy adhesive coupons were made specifically to perform dynamic mechanical analysis (DMA). Bespoke moulds were constructed from plywood, PVC strips, and ethylene vinyl acetate films, as shown in the Figure 3-2.

Figure 3-2: DMA coupons and the moulds

The moulds were prepared in stages. First, the plywood panels were cut approximately (300×75 mm). They were then covered with ethylene vinyl acetate films. In the next part of the process, pre-punched (100×1.5 mm) PVC strips were attached to the plywood using pins approximately 12 mm apart. The edges of the PVC strips were coated with bees wax to ease coupon removal after casting. Prior to injecting the epoxy, another acetate film and transparent 10 mm PVC sheet was placed on the top of pre-punched PVC strips. G-clamps were used to secure the top and bottom part of the mould. This method was adopted based on the recommendations from Broughton and Gower (2003).

The weight of each epoxy part was measured according to the manufacturer's ratio instructions using sensitive weight scales. The epoxy adhesive was mixed 1:4 with a mixing paddle attached to a cordless drill in a well-ventilated area. A slow speed drill setting was used for the mixing process to minimise entrapped air. The adhesive was mixed for at least 5 minutes until smooth in consistency and uniform colour mixture was achieved. The mixture was then placed in a vacuum vessel for 20 minutes to extract any entrapped air at room temperature. Finally, the adhesive was injected into the moulds using a syringe, taking care to avoid air bubbles.

As part of the curing process the samples were left on a level surface at laboratory conditions (24±1°C and 45±5% RH), for 24 hours before being removed from the moulds.

3.2.3 Tyfo-S coupon preparation

A different sample preparation method was used for Tyfo-S, as it is a less viscose adhesive. The moulds were made from ethylene vinyl acetate films and 2 mm bees wax sheets treated with an adhesive coat on one side. Straight edge strips were cut from the wax sheets then stuck to the acetate film to form 10×100×2 mm strips. The moulds were left on a smooth and flat surface to avoid any distortion in the coupons. Similar mixing procedure in section 3.2.2 was followed. The air free mixture then poured instead of injecting into the pre-assembled moulds carefully to prevent over filling of the moulds.

3.2.4 Specimen conditioning

After curing for 24 hours at laboratory conditions, the specimens were removed from the moulds, and transferred to a sealed Pyrex container to be cured at controlled temperature and relative humidity. An oven was used to achieve the required curing temperatures. Half of the specimens were cured in a dry environment (close to 0%RH), with desiccant (Moisture Gone®) used to absorb moisture within the containers. The second half were cured under distilled water representing a saturated environment. A special metallic rack covered with acetate film was made to keep the dry cured samples level and separate from the desiccant in order to eliminate any possible effect on the curing process. The submerged samples were placed on a PVC sheet to maintain their shape and to avoid distortion. This was important for the samples treated at high temperature. The containers were then moved to an oven with precise temperature control to cure the samples. They were left to cur for different periods before testing, refer to Table 3-2.

3.2.5 Filler content testing (Burn-off test)

Burn off tests were carried out to find the weight fraction of filler in the two epoxy-resins. Three samples cut from the larger DMA coupons. The test was carried out according to ASTM D2584-02 (2002). To avoid releasing a large amount of smoke during ignition and burning of the resin, moderate sample sizes were selected, weighing approximately 7g each. A sensitive weight scale was used to record the weight at each stage of measurement to limit possible measuring error.

The test results show that Sikadur-330 contains just over 18.6±0.13%, and Tyfo-S contains 0% filler. The results of the burn-off test are presented in Table Ai-1 (Appendix A).

3.3 Dynamic Mechanical Analysis (DMA) testing equipment and pre-testing preparation

3.3.1 Testing equipment

A Triton Tritec 2000 DMA machine with 1-litre liquid nitrogen cryogenic tank, as shown in Figure 3-3, was used to determine the storage modulus, loss modulus, and tan δ variation with temperature of the cured epoxy coupons. The machine is attached to a computer to log in the test results.

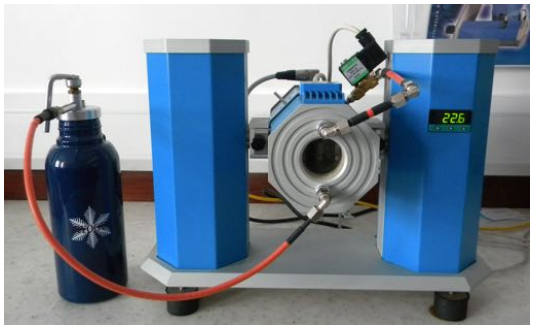

Figure 3-3: Triton Dynamic Mechanical Analysis machine model Tritec 2000

3.3.2 Pre-test preparation

Each strip was visually inspected for air pockets that may have been trapped during adhesive injection. They were then cut into 3×25mm long specimens. According to the Triton Tritec 2000 DMA the distance between the inside edges of the clamps is considered as a specimen length, for instance the specimen that is shown in Figure 3-4 is 15mm. Before testing, the DMA samples were inspected again and rough edges were carefully treated with a file or knife to remove excess cured adhesive. In some cases a file was used level the edges and ensure that vernier calliper external jaws are in contact with the sample edges. Sensitive digital callipers, specified by ASTM E1640-99 (1999); ASTM D4065-01 (2001); British

Standard ISO 6721-1 (2011), were used measure the thickness and width dimensions. The dimensions are mostly squared or cubed in the geometry factor equations. Therefore, it is important to measure them accurately. The equations for widely used geometries are provided in section 2.8.1.

The nitrogen cryogenic tank was connected to the DMA machine to cool the specimens below 0°C. A temperature of approximately -5°C was selected to chill the sample. This temperature was found to be sufficient to commence the experiment at 0°C. The samples were then tested at a constant heating rate of 2°C/min up to 120°C.

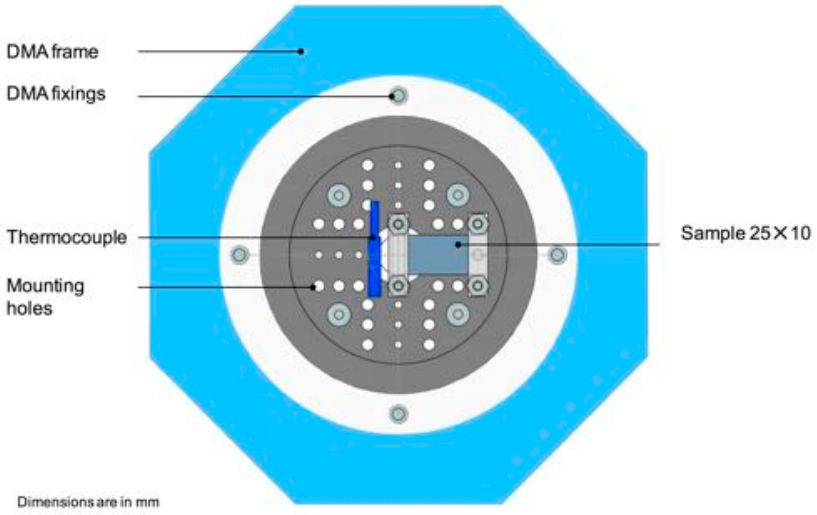

Top view

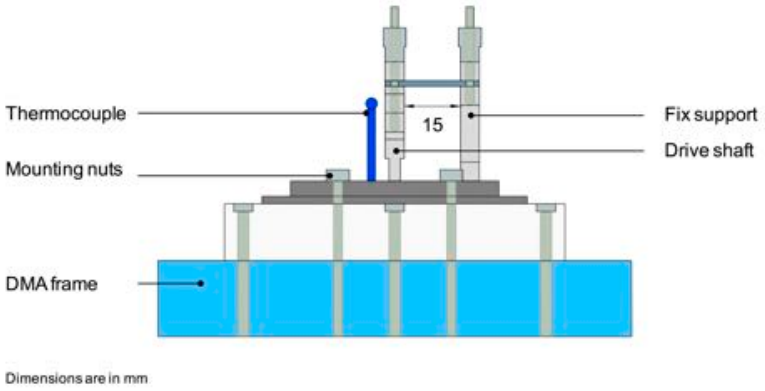

Front view

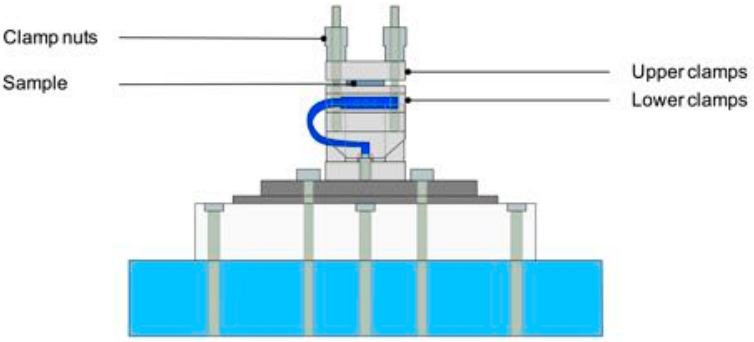

Side view

Figure 3-4: Schematic diagram of single cantilever fixture in typical DMA machine

3.4 Parametric study

A dependency study was carried out to investigate the effect of heating rate, loading rate (frequency), and length of the coupons (stress). These parameters are known to play an important role on the T_g. Sims and Gnaniah (2009) highlighted the significance of thermal lag. Therefore, it is important to assess the effect of each parameter on the coupon geometry used in this research. The influence of each parameter on the modulus response with temperature were studied while the other parameters were set constant. Maximum displacement was set to 0.05 mm in a single cantilever configuration. Displacement of 0.05 mm is understood to produce a deformation within the linear viscoelastic region and the strains remain below 0.2% for the tested material and geometry. However, a strain scan can be performed on the glassy material between 0.01 and 5% (or the maximum possible strain) to ensure that the applied strain is within the elastic range (Gabbott, 2008). The parametric study was carried out on Adhesive S.

3.4.1 Heating rate dependence experiments

Testing heating rate can have an influence on results from DMA. Typically scanning rate of 2, 3 or 5 °C/min is recommended (Mulligan *et al.*, 2003). The sample geometry and material type are also important. Relatively thick samples require slower heating rates to avoid temperature variation with in the sample. A temperature lag of 6°C was recorded for a composite sample tested by DMA at a heating rate 3 °C/min (Sims and Gnaniah, 2009). Although the thickness of the specimen is not reported in their work, the insertion of a sensor in to the sample to measure internal temperature suggests that the sample thickness was over 5 mm. Slow heating rate is also not recommended for materials such as epoxy because they may be cured during the test. Heating rates of 1 or 2 °C/min will produce reasonably accurate transition temperatures (Gabbott, 2008).

In this research to find a reasonable heating rate four tests were carried out. Four 2 mm thick epoxy samples were scanned at different heating rates. Scanning frequency of 1 Hz, sample length of 15 mm (between the inside edges of the clamp refer to Figure 3-4), and single cantilever configuration in all four tests were used.

Storage modulus, loss modulus, and tan δ responses for the runs are shown in Figure 3-5. The recorded T_g values according to five different methods (see in section 2.8.6) are listed in Table 3-3. Although higher heating rate of 5–10 °C/min will provide rapid results for comparative testing, Gabbott (2008) suggests that there will be error associated with the heating rate of 5–10 °C/min. The results confirm that T_g is not heavily influenced by the heating rate. This is due to the relatively small sample thickness. The slight increase in the T_g value with increasing heating rate is related to the use of the single cantilever configuration and the sample length 12 to18 mm (Mulligan *et al.*, 2003).

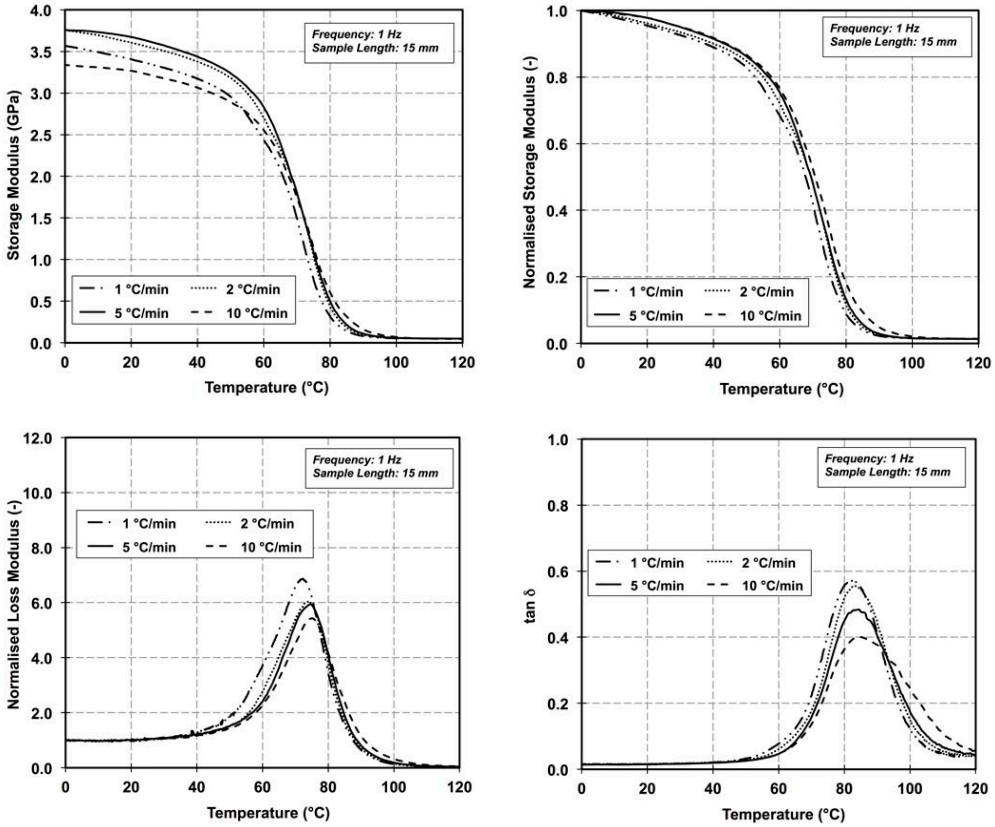

Figure 3-5: Storage, loss modulus and tan δ variation with temperature for different heating rates

Table 3-3: Glass transition temperature, T_g results for different heating rates

Sample No.	*Heating Rate (°C/min)*	*Recorded T_g in °C with different methods*				
		Peak Loss Modulus	*Inflection Point*	*Peak tan δ*	*Onset Logarithmic Scale*	*Onset Normal Scale*
Sample 1	1	72.1	73.2	82.2	68.1	60.2
Sample 2	2	73.5	74.1	83.3	68.7	61.3
Sample 3	5	73.6	75.2	83.7	69.0	59.3
Sample 4	10	73.9	75.3	85.9	67.5	58.6

3.4.2 Frequency dependence experiments

Test frequency (loading rate) is one of the test parameters that can be controlled. Test frequency is directly related to the storage modulus response E' of the specimen (Christensen, 1982; Osswald *et al.*, 2006; Gabbott, 2008). This is related to the molecular of the material. Similar to the heating rate dependence experiments, four 2 mm thick epoxy specimens were tested at constant heating rate of 2 °C/min and sample length 15 mm in single cantilever mode. Four different frequencies 1, 2, 5, and 10 Hz were studied.

The test results are shown in Figure 3-6. The recorded T_g values according to five different methods (see in section 2.8.6) are listed in Table 3-4. The measured glass transition temperature, T_g in Table 3-4 showed an increase with frequency, but the values reported according to the inflection of storage modulus were among the least affected.

The number of cycles were not measured, but with increasing frequency the number of cycles increases, which may cause the sample to fatigue. This topic is not covered in this research.

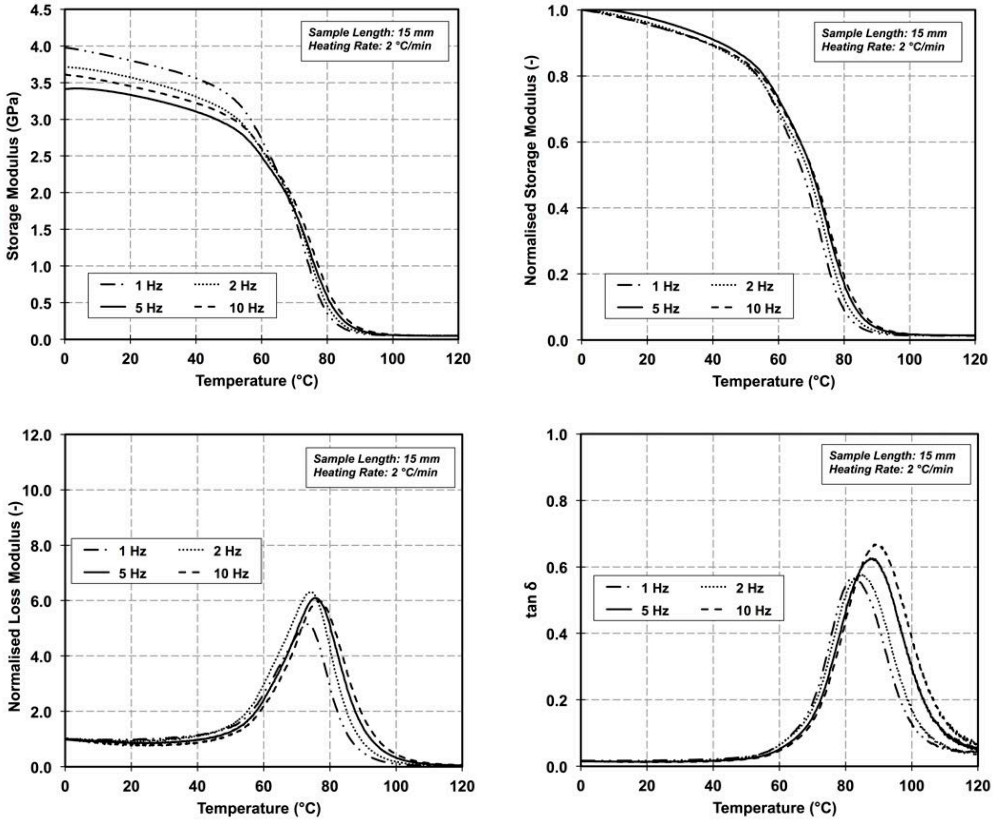

Figure 3-6: Storage, loss modulus and tan δ variation with temperature for different frequencies

Table 3-4: Glass transition temperature, T_g results for different frequencies

Sample No.	*Frequency (Hz)*	*Recorded T_g in °C with different methods*				
		Peak Loss Modulus	*Inflection Point*	*Peak tan δ*	*Onset Logarithmic Scale*	*Onset Normal Scale*
Sample 1	1	73.0	75.1	82.6	68.6	56.7
Sample 2	2	74.3	75.0	84.7	69.4	58.3
Sample 3	5	75.6	74.7	87.7	70.4	59.5
Sample 4	10	76.8	74.2	89.3	70.9	60.0

3.4.3 Specimen free length dependence experiments

The specimen length was studied to find an appropriate free length (distance between the inside edges of the clamps, see Figure 3-4) of the test samples. For a single cantilever mode, Gabbott (2008) recommends to use 5-10 mm free

length. In the preliminary investigation with 5 mm length specimen at constant applied displacement of 0.05 mm it was noted that the dynamic applied force was high and reached approximately the maximum limit of the Triton Tritec 2000, which is 10 N. This is because flexural stiffness of shorter specimens is higher than longer specimens, and larger force is required to achieve the same amount of displacement. For shorter specimens the displacement should be reduced because it may produce strains in the nonlinear viscoelastic region. Since the samples were also chilled before testing, the risk of damage to 10 mm free length samples increased. This is due to the fact that adhesives tend to be brittle at low temperature and the specimen may fail before any measurements can be taken due to temperature.

The clamp error associated with the single cantilever fixture increases with the reduction in the free length because of the relative stiffness of the sample. This amount of clamp error is not counted for in DMA (Gabbott, 2008). Therefore, 15 mm of free sample length is used in this research in order to avoid any possible source of error.

Figure 3-7 shows the storage modulus variation with temperature. The curves in Figure 3-7 shifted to the right because higher temperatures are required to achieve movement of the molecules in the shorter (relatively stiffer) sample.

Table 3-5 contains the summary of reported glass transition temperature, T_g according to the different methods. The results reveal that there is decreasing monotonic trend in the T_g with free length, except the peak $\tan\delta$ values because the measured $E'$and E'' values will be in error by a similar amount ($\tan\delta = {E'}/{E''}$). This is can be observed in Figure 3-7.

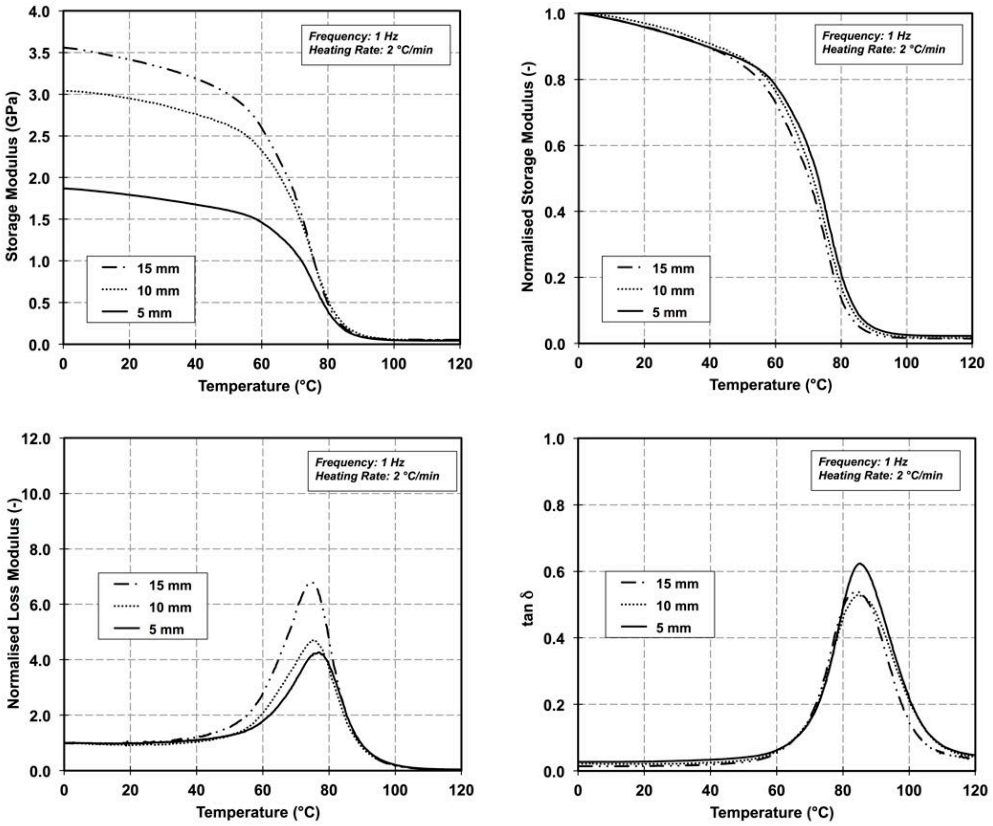

Figure 3-7: Storage, loss modulus and tan δ variation with temperature for different free lengths.

Table 3-5: Glass transition temperature, T_g results for different free length.

Sample No.	*Length (mm)*	*Recorded T_g in °C with different methods*				
		Peak Loss Modulus	*Inflection Point*	*Peak tan δ*	*Onset Logarithmic Scale*	*Onset Normal Scale*
Sample 1	5	76.8	78.1	85.4	72.1	65.4
Sample 2	10	75.1	75.1	84.9	70.4	62.6
Sample 3	15	74.6	73.1	84.1	69.6	60.8

3.4.4 Finding of DMA parametric study

The three testing aspects in the parametric study show that glass transition temperature, T_g is to some extent dependant on the test settings in the DMA. It is clear that a single value of T_g could be manipulated for the reporting purposes by

changing the testing variables. Variations in sample free length, heating rate, and frequency on epoxy coupon geometry were studied. Although there are recommendations to select appropriate set of parameters, an extreme combination of these parameters can affect the glass transition temperature, T_g. This can lead to a different value of the glass transition temperature, T_g.

The parametric study shows that it is crucial to report the test settings when T_g is reported as a single value, and these parameters have less impact on some methods of reporting T_g. The methods of reporting T_g were discussed in section 2.6.8.

The initial value of the storage modulus differs significantly even though it is the same material. A large variation in the initial storage modulus occurred using single cantilever configuration despite the fact that efforts were made to ensure that the samples clamped in the same manner and manufacturers torque wrench was used to fasten the nuts. Although the difference is not significant, it is known that dynamic mechanical thermal analysis is poor at reproducibility of modulus (Broughton and Gower, 2003).

Therefore, the storage modulus E', loss modulus E'', and $\tan\delta$ variation with temperature were obtained for the DMA runs. The corresponding glass transition temperature, T_g is only reported. In the dependency experiments, the maximum displacement is set to 0.05 mm. To avoid confusion and misreporting T_g, the setting of the DMA runs reported in this research are kept constant as follow:

- Configuration: Single Cantilever
- Heating Rate: 2 °C/min
- Frequency: 1 Hz
- Coupon Length: 15 mm

From the recorded results of glass transition temperature, T_g in Table 3-3, Table 3-4, and Table 3-5 (peak loss modulus, inflection point, peak $\tan\delta$, and onset methods) it is clear that peak loss modulus method is the least affected method with changing heating rate, frequency, and free length. The method of reporting glass transition temperature, T_g according to peak loss modulus method is preferred by ASTM D4065-01 (2001). The conclusions in chapter 7 are drawn in relation to the T_g found according to the peak loss modulus.

Moreover, it shows that using single cantilever fixture, the direct mechanical properties cannot be measured due to the impact of the geometry constant on the calculation of the storage modulus. Storage modulus is dependant on the geometry constant, which is cubic dependent on the free length. This is evidence that Storage modulus E' and Young's modulus E are not in exact agreement (Menard, 2008). This difference between the two is often misunderstood.

To determine the flexural modulus of the epoxy coupons, three-point bending can be used. This is not discussed in this work.

3.5 Experimental results and discussion of curing condition using DMA

This section examines the effects of curing conditions temperature and relative humidity on the Adhesives S and T. The experimental matrix and temperatures are listed in section 3.2.1. The coupons preparation procedure fro the two adhesives are listed in section 3.2.2 and 3.2.3. The conditioning details are listed in section 3.2.4. The coupons were tested using Dynamic Mechanical analysis (DMA) with the settings summarised in section 3.4.4. The test results are presented in this section. The glass transition temperature, T_g values are reported according to the inflection point of the storage modulus, peak of loss modulus, peak of tan δ, onset of storage modulus (based on normal and logarithmic scale methods). The effects of dry and saturated conditions on glass transition temperature, T_g with age and curing temperature are discussed.

The glass transition temperature, T_g values in section 3.5.1 and 3.5.2 are the average of three samples. Glass transition temperature, T_g and standard divisions are listed in Appendices B and C, for the Adhesive S and T respectively.

3.5.1 Curing age effect on T_g using DMA

The development of the glass transition temperature, T_g versus curing time (age) for dry and saturated curing conditions at 24°C are shown in the Figure 3-8. The data points are the average for the group of three samples cured and tested under the same conditions.

When reporting glass transition temperature, T_g for different curing temperatures in both dry and saturated conditions similar trends are observed. In this section only glass transition temperature, T_g according to peak loss modulus are discussed. The methods of reporting glass transition temperature, T_g were discussed in section 2.8.6. The glass transition temperature, T_g are average of three coupons. Due to the small amount of variation in the results, the variation is not shown.

The glass transition temperature, T_g of Adhesive S coupons under dry conditions and after 3 days of curing at 24°C is 48.6°C. The standard deviation is ±0.7°C. The results are in agreement with manufacturer's data Sikadur-330 (2012) see section 3.1.1. The manufacturer used a different technique to measure glass transition temperature, T_g.

The glass transition temperature, T_g of Adhesive T coupons under dry conditions and after 3 days of curing at 24°C is 52.7°C. The standard deviation is ±0.6°C. Although the same technique and method is used to report the glass transition temperature, T_g, the results differ significantly from the manufacturer's data Tyfo-S (2011) see section 3.1.2. This is due to the fact that the manufacturer's used a different curing regime to treat the coupons prior to testing.

The glass transition temperature, T_g improvement in Figure 3-8 tends to slow down as it approaches plateau after 7 days. This is because at this temperature no further reaction occurs to increase the cross-link between the polymer chains. Ageing for an extra 21 days increases the value of glass transition temperature, T_g by approximately 10 to 15% in comparison with glass transition temperature, T_g after 7 days.

Under saturated conditions glass transition temperature, T_g is approximately 48°C. There was no significant increase in glass transition temperature, T_g after 7 days and plateaus at 50°C. The glass transition temperature, T_g values are lower than the dry values at all conditioning ages. This is due to the fact that water acts as a retarder to the chemical cure of the epoxy by weakening the bonds between the polymer chains.

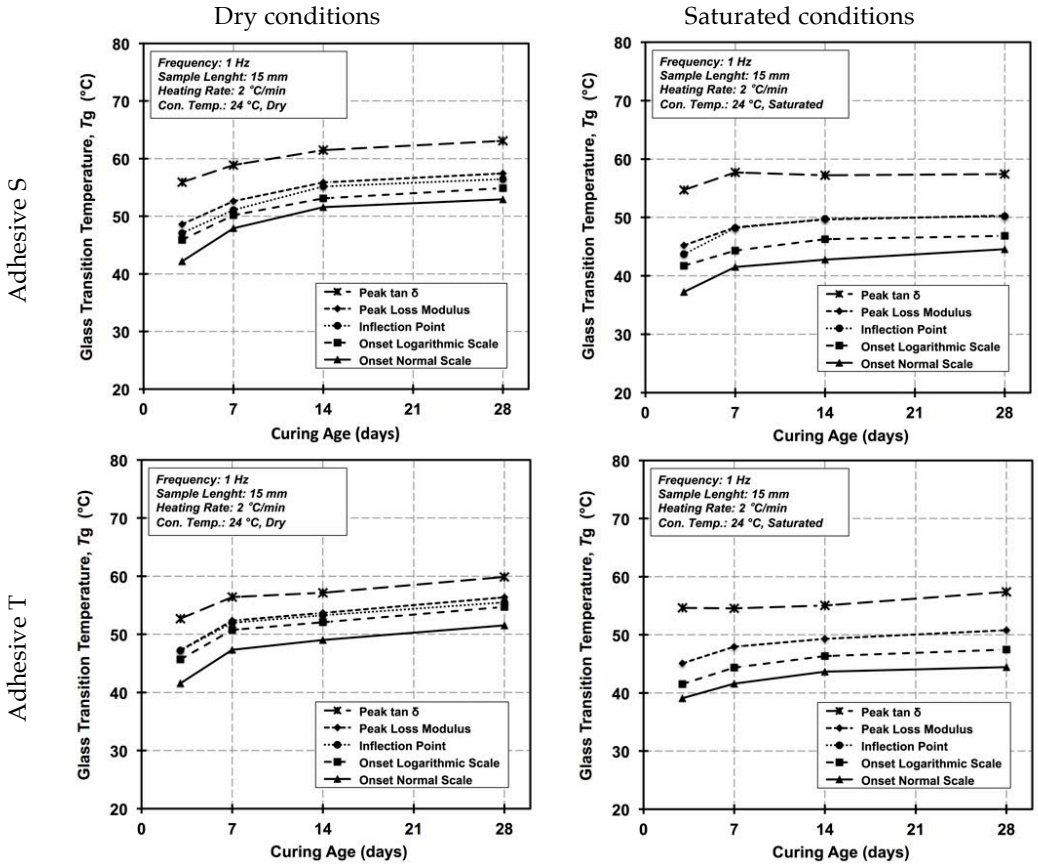

Figure 3-8: Curing age effect on T_g at 24°C, Adhesive S and Adhesive T for dry and saturate conditions using DMA

The data points in Figure 3-8 are the glass transition temperature, T_g values obtained from Figure 3-9 and Figure 3-10. The storage modulus, loss modulus responses in Figure 3-9 and Figure 3-10 are normalised at 0°C for comparison purposes.

The storage modulus, loss modulus and tan δ plots for dry cur in Figure 3-9 and Figure 3-10 (left plots) shift right. This means that cross-link between the polymer chains increased with age. A higher temperature is required to cause movement in the polymer structure. The shift in Figure 3-9 and Figure 3-10 (right plots) for saturated cure is less in comparison to the dry cure. This is evidence of the impact of saturated cure. It confirms the substantial effect of moisture upon the adhesive's performance. The degradation in storage modulus at low temperatures is more pronounced in Figure 3-9 (right plots), and the loss modulus response records lower

peak than for the dry samples. Consequently, there is a less distinct transition (appeared as a double peak in tan δ) due to the effect of the water upon the cure kinetics of the adhesive.

The plots in Figure 3-9 and Figure 3-10 are only for 24°C, and other temperatures (15, 35, 50, 65, and 80°C) can be found in Appendix B and C for Adhesive S and T, respectively. It appears that with increasing curing temperature curing age is less significant.

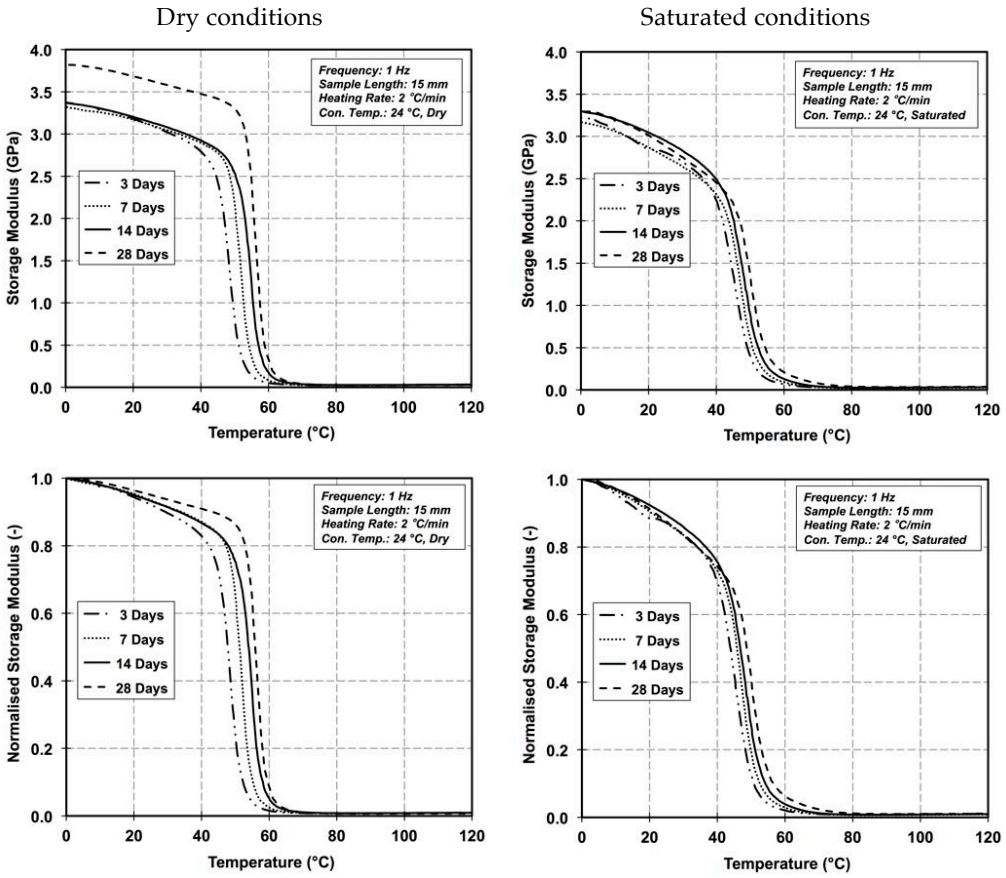

Figure 3-9: Storage modulus and normalised storage modulus variation with temperature cured at 24°C for Adhesive S dry (left) saturated (right) condition using DMA

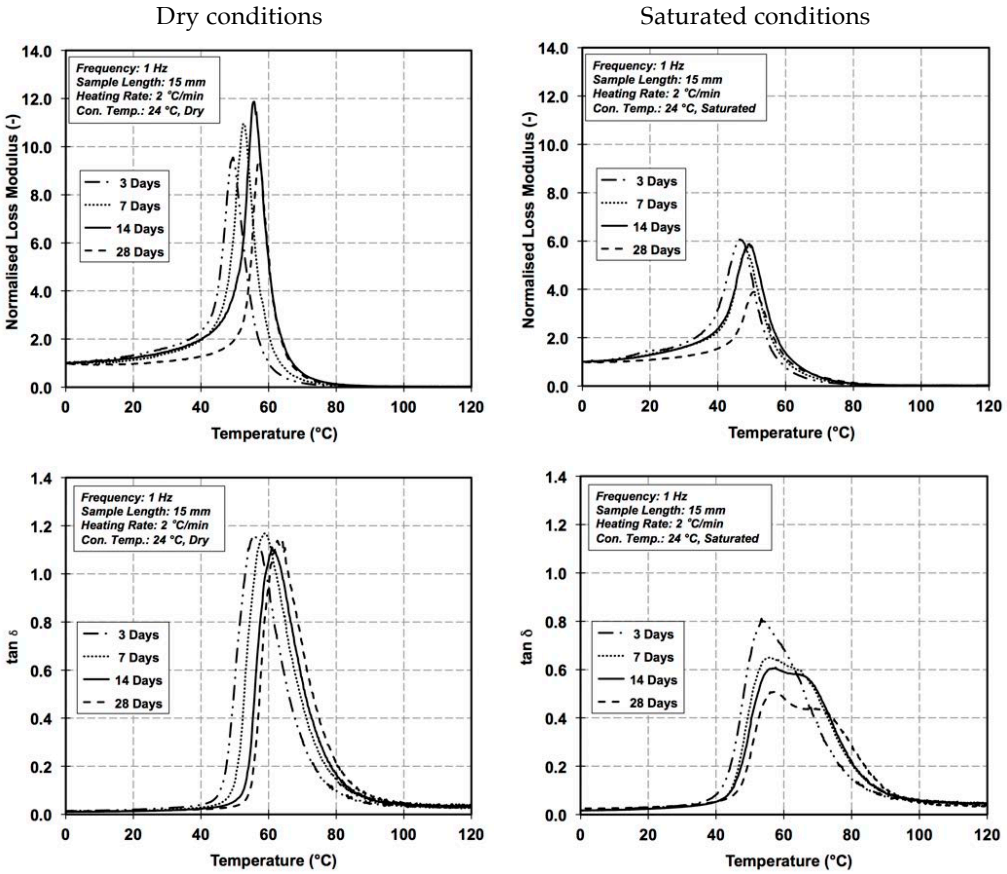

Figure 3-10: Normalised loss modulus and tan δ variation with temperature cured at 24°C for Adhesive S for dry and saturated conditions

3.5.2 Curing temperature effect T_g using DMA

The effect of curing temperatures and conditions on Adhesive S and T at different ages is shown in Figure 3-11. The adhesives cured at dry condition showed similar behaviour as shown in Figure 3-11 (left side). The T_g improved significantly with curing temperature. The glass transition temperature, T_g increases linearly with the curing temperature. For Adhesive S, the rate of T_g improvement after 50°C is slower in comparison with the sample cured at temperatures below 50°C. The coupons cured at 80°C do not show further improvement. While, for the Adhesive T the rate of T_g improvement is not affected up to 65°C, this is due to a different polymer structure. The results are in good agreement with studies on other epoxy systems (Wu, 1992) using DSC. The glass transition temperature, T_g values for 14

and 28 days are close at all curing temperatures (see section 3.5.1). However, 7-day samples cured at higher temperature tend to reach the same values. This shows that the elevated temperature curing affects the structure of the polymers and glass transition temperature, T_g improves. This means that the adhesive mechanical properties are improved.

Figure 3-11 also shows that Adhesive S coupons cured at 80°C, exhibit a slight reduction in the glass transition temperature, T_g value at all curing ages. Adhesive T shows reduction only for coupons cured at 80°C for a longer period (14 and 28 days).

Similarly, the samples cured at saturated conditions have shown improvement, but on a much slower scale, and the impact of water contact with the adhesives is significant. The Adhesive T samples cured beyond 50°C exhibit no further improvement, while Adhesive S coupons exhibit negative impact.

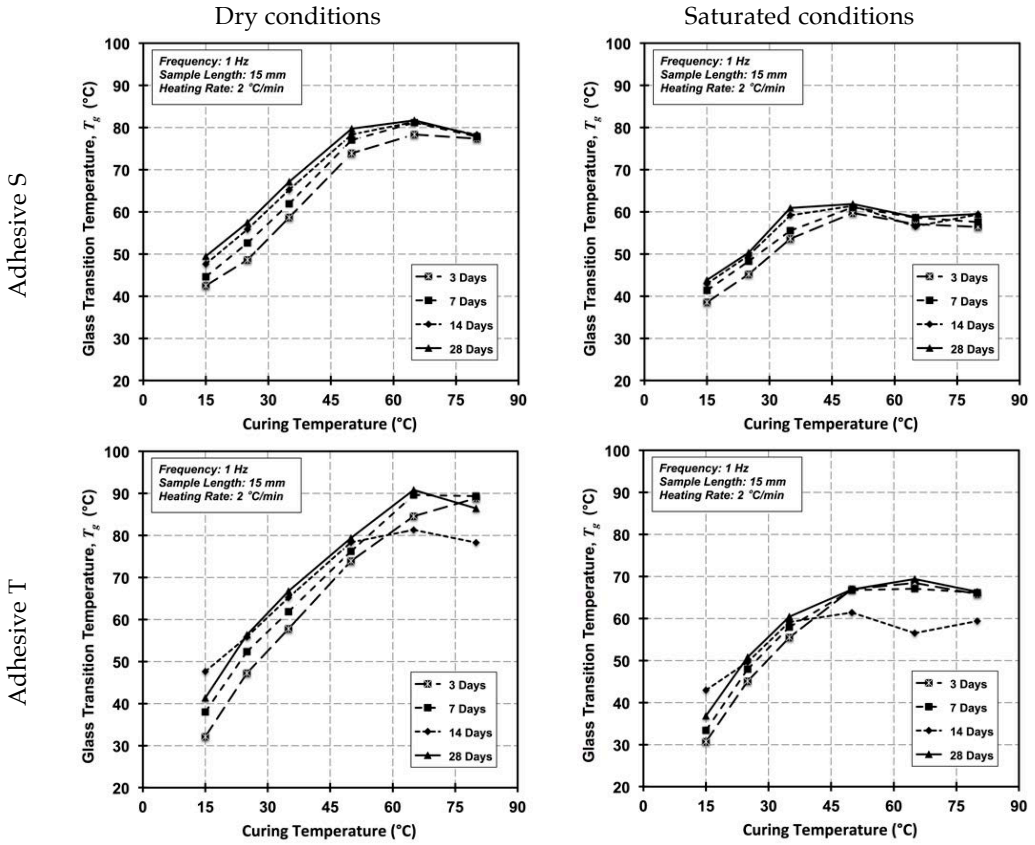

Figure 3-11: Curing age and temperature effect on T_g according to peak loss modulus methods for Adhesive S and Adhesive T for dry and saturated conditions using DMA

A similar trend can be seen in Figure 3-12 for different methods of defining glass transition temperature, T_g. The T_g values for Adhesive S cured at saturated conditions using onset normal scale method could not be found precisely. This is due to the impact of water and presence of the filler, which absorbs water. This affects the performance of the adhesive structure by weakening the polymer chains.

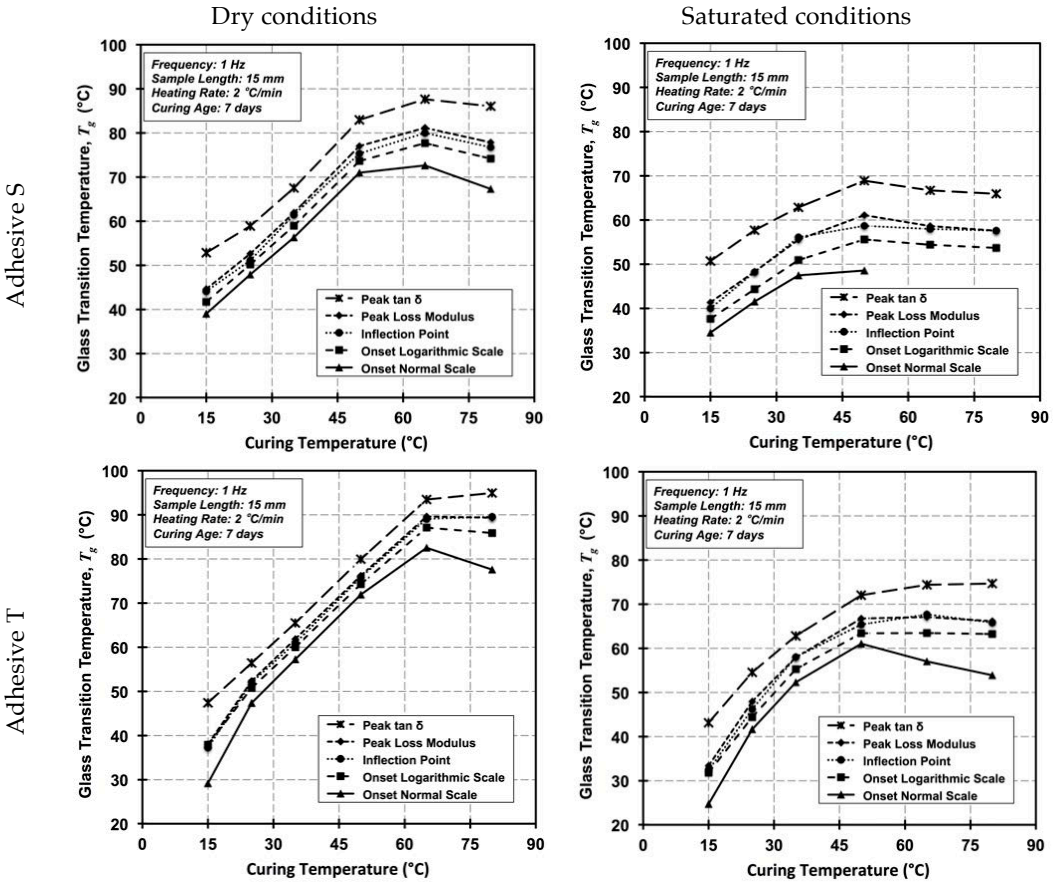

Figure 3-12: Recorded T_g according to different methods at 7 days and different curing temperature, Adhesive S and Adhesive T for dry and saturated conditions using DMA

This section discusses only the Adhesive S. The DMA results in Figure 3-13 are the average of three coupons. The average of three DMA coupons with the amount of variation for some DMA runs is shown in section 5.4.3. Dry and saturated conditions at various temperatures for 7 days are shown in Figure 3-13 (for other curing ages refer to Appendix B and C for Adhesive S and Adhesive T, respectively). The effect of age was discussed in section 3.5.1.

In Figure 3-13 dry conditioned storage modulus responses shift towards the right side because increasing the curing temperature required more energy to soften the adhesive and the molecules start moving. The plots in Figure 3-14 also shifted to right by the same amount. The shifts are significantly higher than the shifts that occurred due to curing age in Figure 3-9 and Figure 3-10. The shifts after 7 days cured are larger than 3 day cured coupons, but slightly smaller than 14 and 28 days.

However, at higher curing temperatures 7, 14 and 28 days T_g values tend to be very close, see Figure 3-11.

In addition, the slope of transition for the samples cured at 65°C and 80°C is broader, which means the transition spread is over a wider temperature range. The reasons for this are not clear. It could be due to an increase in the stiffness of the samples, and consequently the clamp error becomes an issue. Alternatively, it could be that the high cure has negative influence on the polymer's microstructure.

The influence of the water on the storage modulus variation with temperature is shown in Figure 3-13 for saturated conditioned coupons. It appears that from the very early stages of the test, storage modulus drops significantly.

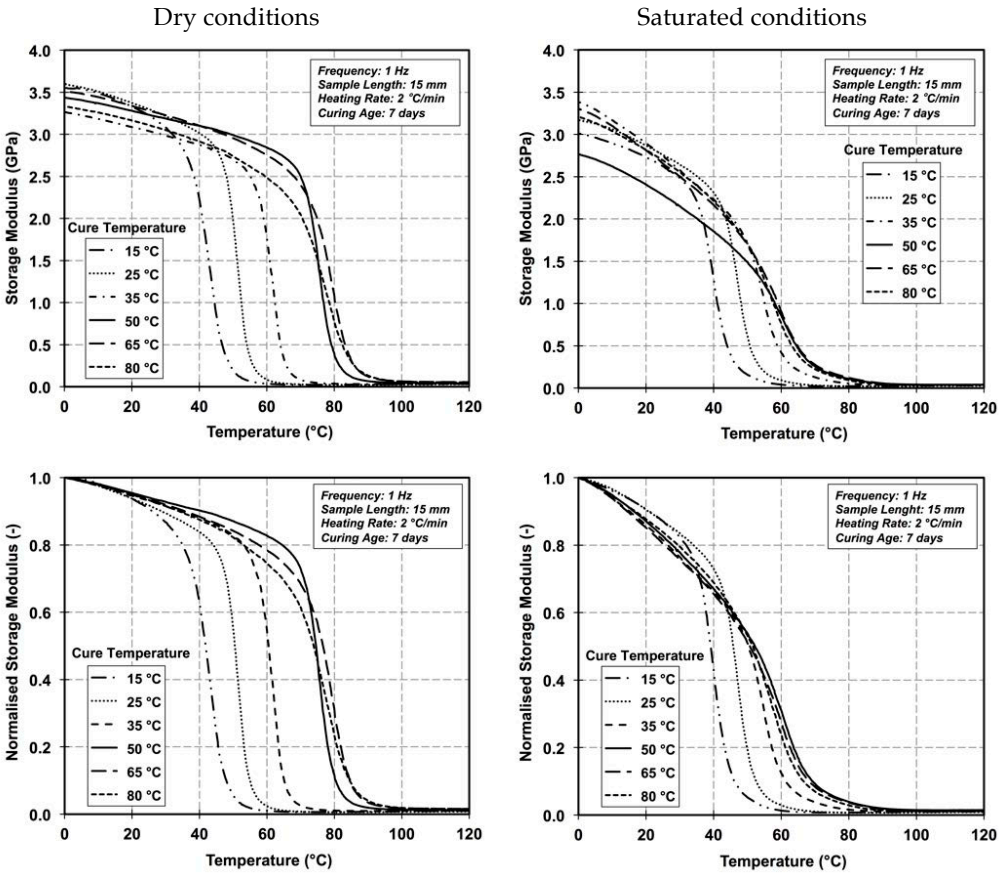

Figure 3-13: Storage and Normalised storage modulus variation with temperature cured at different temperatures for 7 days Adhesive S dry and saturated conditions

Figure 3-14 shows the impact of water on tan δ response. Wide peaks in some cases and double peaks in some other cases were seen. These double peaks in the tan δ response (refer to Figure 3-14) can be related to the double transition phenomena of adhesives. This phenomenon is not the scope of this work.

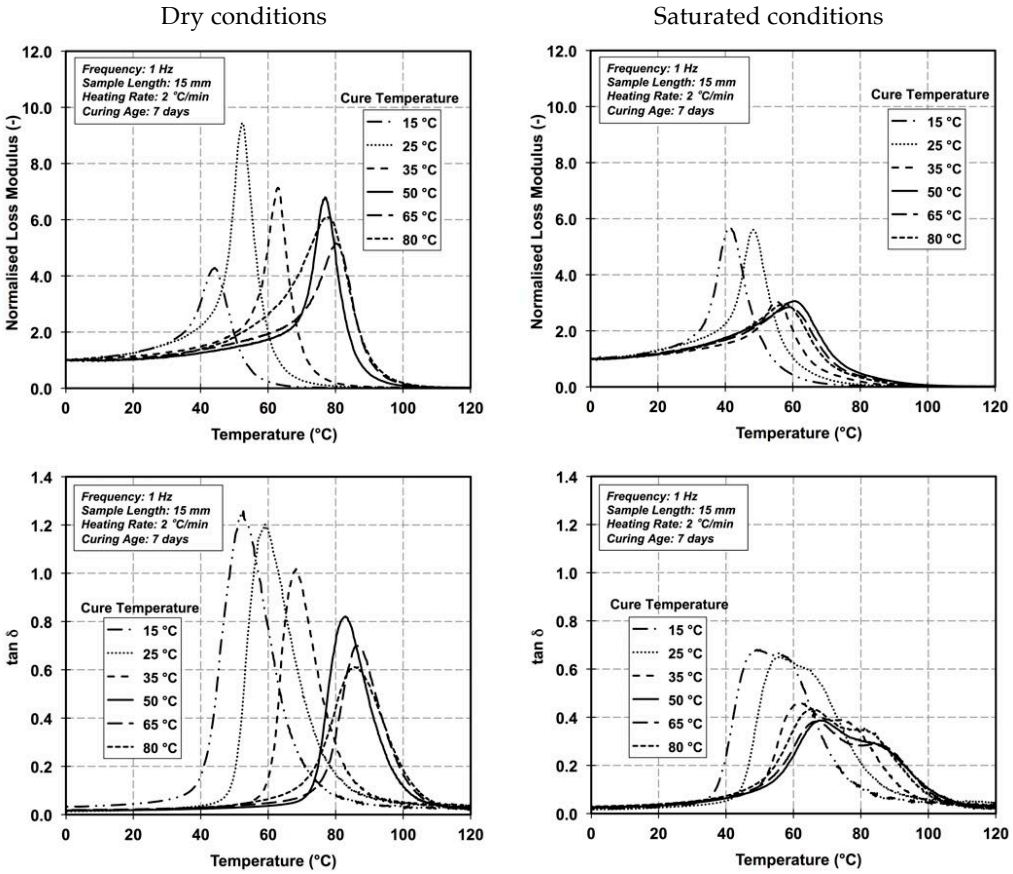

Figure 3-14: Normalised loss modulus and tan δ variation with temperature cured at different temperatures for 7 days Adhesive S dry and saturated conditions

In this investigation using DMA to study glass transition temperature, T_g at different curing conditions and ages, it is found that the curing environment has an important effect on the glass transition temperature, T_g. Among the methods of reporting glass transition temperature, T_g, peak loss modulus was found to be the preferred method. This method is recommended in ASTM D4065-01 (2001).

3.6 Differential Scanning Calorimetry (DSC) testing equipment and pre-testing preparation

3.6.1 Testing equipment

Differential Scanning Calorimeter DSC is widely used in thermal analysis by industry to measure glass transition temperature, T_g. In this research, this technique was used to study the influence of curing and ageing on glass transition temperature, T_g of the two adhesives in section 3.1.1 and 3.1.2. Thermo Gravimetric Analyser and Differential Scanning Calorimeter (TGA/DSC1) by Mettler Toledo was used in this study as shown in Figure 3-15.

Figure 3-15: Mettler Toledo (TGA/DSC1) Differential Scanning Calorimeter machine.

The principles of DSC and the methods of finding glass transition temperature, T_g from the heat flow profile versus temperature were discussed in chapter 2.

The equipment is capable of measuring heat flow and weight change during the test in a horizontal furnace. The TGA is an ultra-micro balance cell. The DSC sensor consists of six thermocouples, which measure the sample and reference temperatures. They are located directly below a protective ceramic support. The sample and reference crucibles are housed on the top of the DSC sensor during the test refer to Figure 3-16.

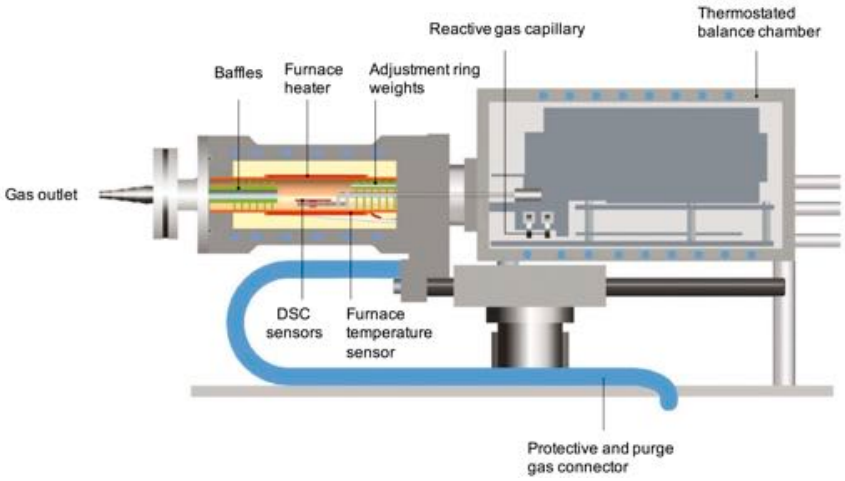

Figure 3-16: Illustration diagram of TGA/DSC1 chamber (Mettler Toledo, 2007).

3.6.2 Pre-test Preparation

The samples to carry out the DSC runs were taken from the large DMA coupons that were cured and aged as mentioned in section 3.2.1. It is important to state that the samples were not tested in the DMA. Hand tools such as diagonal cutters were used to cut relatively large samples from the DMA coupons. The samples' weight was approximately 10 and 20 mg to increase measurement sensitivity. This was important for the Adhesive S samples as the epoxy contains over 18% filler. The samples were placed in 100 µl aluminium crucibles and then automatically scanned with a reference crucible.

3.6.3 DSC scanning experiments and test settings

The samples were placed in clean and undamaged crucibles. It is vital to ensure a good contact between the sample and the crucible (Mulligan *et al.*, 2003). An empty crucible of the same type and size was used as a reference crucible during each scanning series. Data acquisition was carried out using the accompanying software (STARe). The scans were conducted at constant heating rate 10°C/min between temperatures ranging 25 and 120°C. The maximum temperature was set to 120°C as T_g of the most structural adhesives is less than 120°C and the DMA runs showed that. The samples were heated once to avoid post-curing effect. One run

may contain some error due to the release of strain during sample fabrication. The weight and heat flow changes with temperature were analysed. Glass transition temperature, T_g is reported as the onset and inflection point of the step in heat flux vs. temperature.

3.6.4 Determination of the DSC glass transition temperature

Various methods can be used to characterise T_g using DSC. In general, the T_g values are reported from heat flow profile. The height of the specific heat capacity C_p step is used to report T_g. According to ASTM D3418-99 (1999) T_g represents the sigmoidal part of the curve preceding the exothermic. The method consists of extending tangents at some specific points (see section 2.9.1). The tangent construction is crucial (Wagner, 2009). Glass transition temperature, T_g can be reported as the inflection point of the heat capacity curve. Another method to find T_g is from the enthalpy curves, which is obtained by integrating the heat capacity variation curve. According to this method glass transition temperature, T_g is reported as the corresponding temperature to the enthalpy relaxation peak. The extrapolated onset temperature and point of inflection of the C_p curve methods were used to report glass transition temperature, T_g throughout this study.

3.7 Experimental results and discussion of curing condition using DSC

Differential scanning calorimeter test results for Adhesive S and T are presented in this section. The effect of dry and saturated conditions on T_g with time and curing temperature is discussed. The glass transition temperature, T_g values are reported according to extrapolated onset temperature and point of inflection of the C_p curve methods. Differential scanning calorimeter runs for Adhesive S and T for 7 day curing period at both conditions are presented. 3, 14, and 28-day period are in Appendix B and C for Adhesive S and T.

3.7.1 Curing age effect on T_g using DSC

Similar plots to the ones in section 3.5.1 are produced in Figure 3-17. The T_g values are obtained from the heat capacity C_p plots from DSC. In this section, a trend similar to that observed in section 3.5.1 was noted. With increasing age a little improvement is seen in the T_g. At curing age of 7 days and the same curing temperature, approximately 90% of T_g value at 28 days is achieved.

Since the mass of the samples was slightly different, to compare the heat capacity variation with temperature, the heat flow curves are normalised to the sample mass. Wagner (2009) states that there is a correlation between the heat flow and sample mass. A larger mass requires more heat. The samples are normalised at 30°C in Figure 3-18. For the samples cured at 24°C and at different curing ages, there is a shift in the heat capacity C_p step. This indicates that cross-linking is in progress. The shift also tends to slow down with curing age.

Saturated samples showed poor response during the testing. At 24°C curing, very little progress was noticed for the two adhesives.

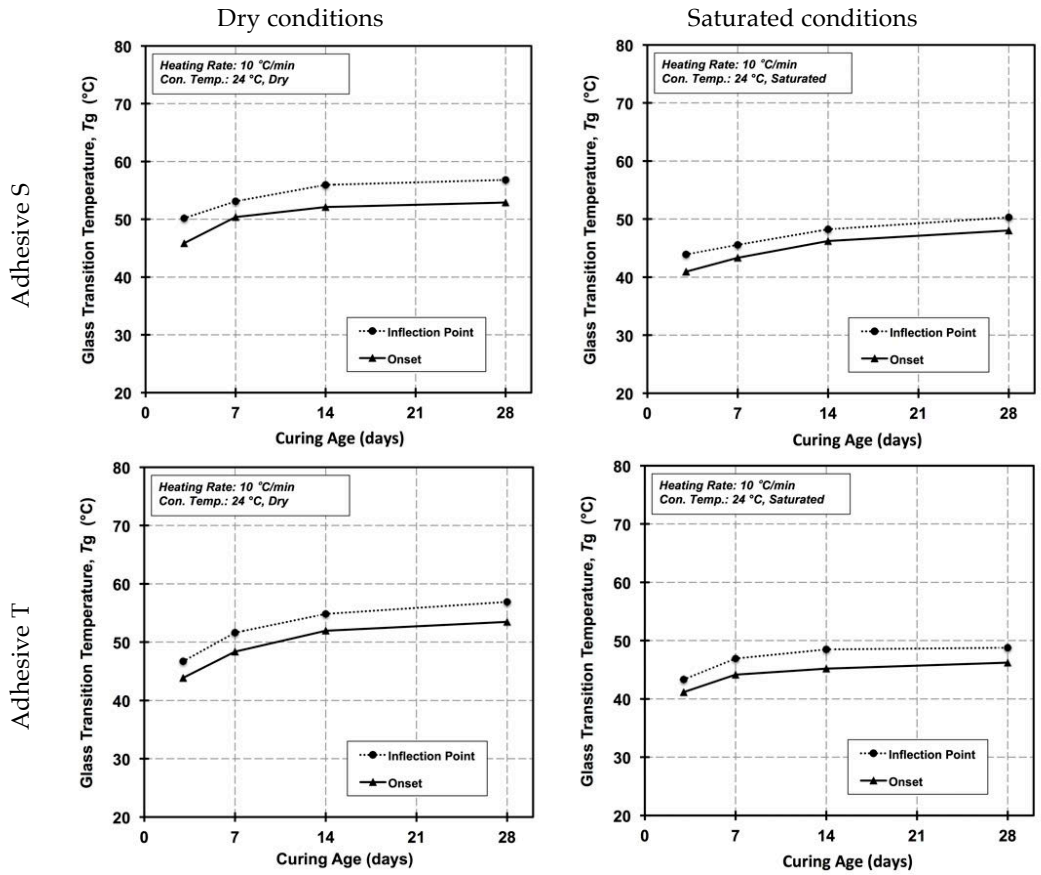

Figure 3-17: Curing age effect on T_g of Adhesive S and Adhesive T for dry and saturated conditions using DSC at 24°C

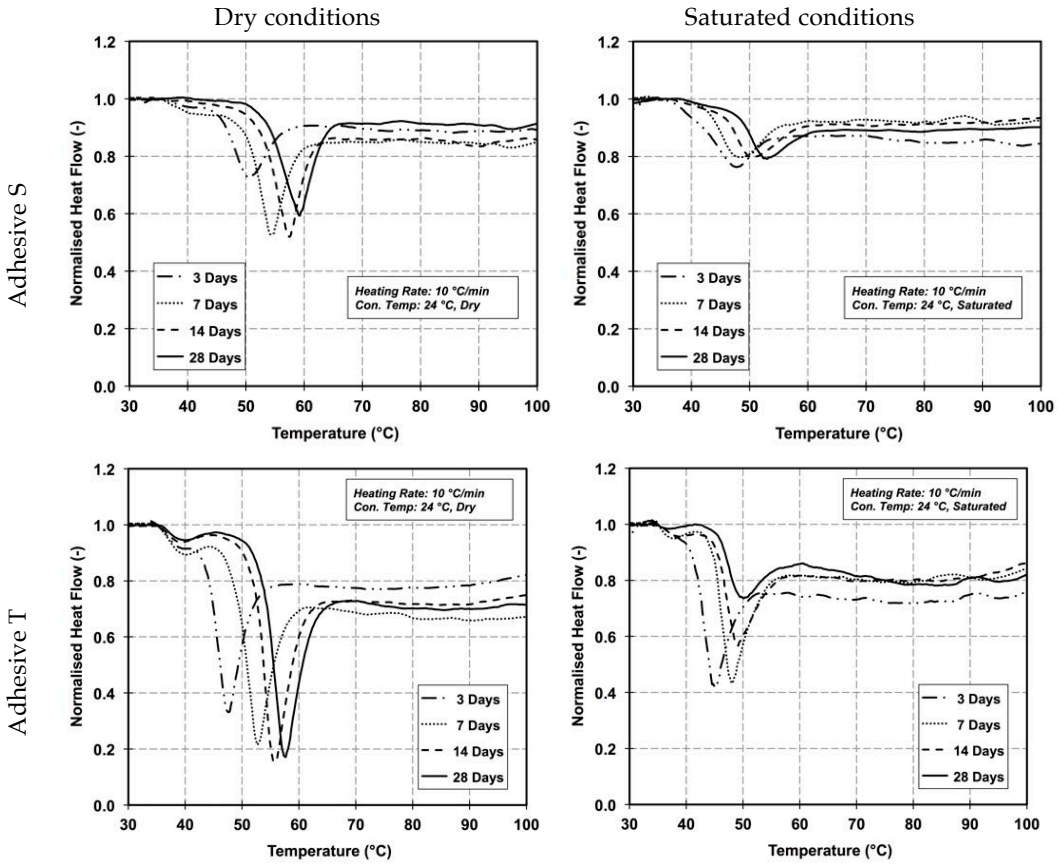

Figure 3-18: Normalised heat flow versus temperature for Adhesive S and Adhesive T for dry and saturate conditions cured at 24°C

3.7.2 Curing temperature effect T_g using DSC

In this section, similar to section 3.5.2 plots of T_g versus curing temperatures are presented for the two adhesives. For the dry samples at low cure temperatures (up to 50°C and 65°C for Adhesive S and T respectively) the T_g increases linearly with the curing temperature as shown in Figure 3-19. However, glass transition temperature, for the saturated samples in Figure 3-19 was not easy to determine. This is due to the influence of water and the amount of water that is present in the samples.

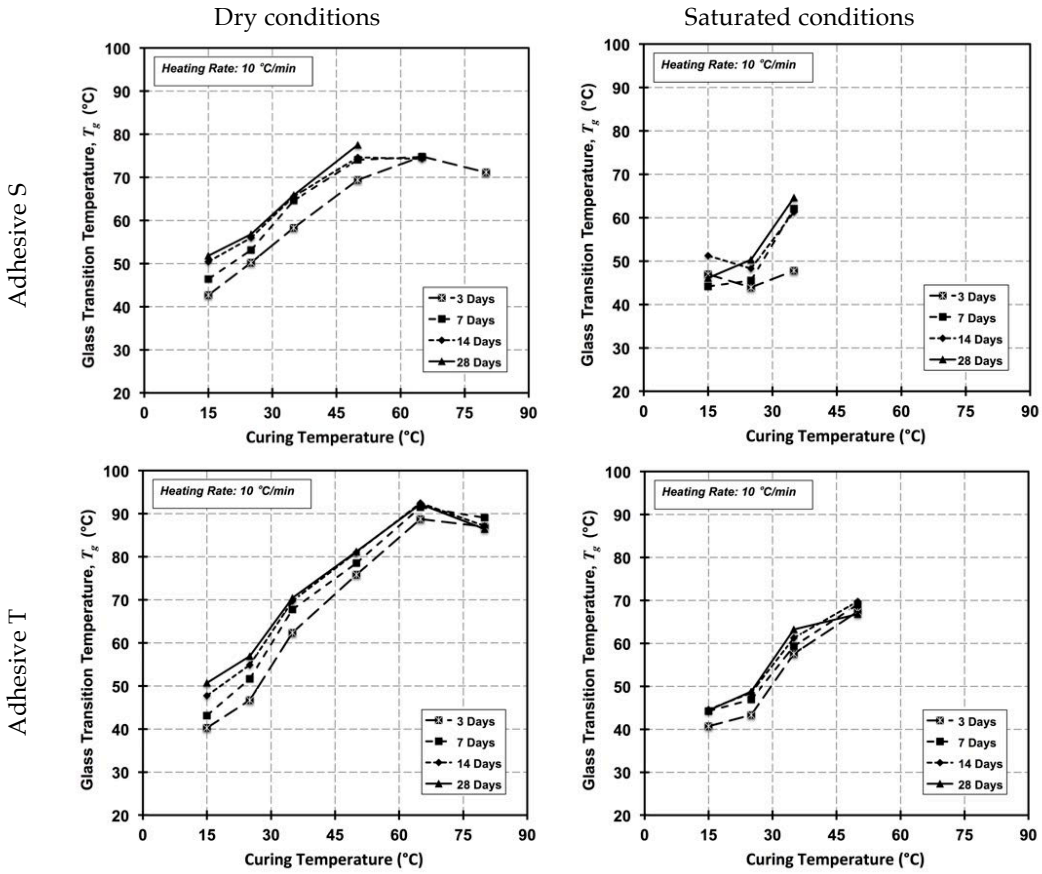

Figure 3-19: Curing age and temperature effect on T_g according to inflection point method for Adhesive S and Adhesive T for dry and saturated conditions using DSC

The same trend was noticed in both (inflection point and onset) methods refer to Figure 3-20. Glass transition temperature, T_g value for Adhesive T samples cured at 15°C and dry conditioned were not found precisely, this is likely to be due to the fact that even up to 7 days cross-linking is under development and requires longer curing period. It is important to mention that the manufacturer of the Adhesive T recommends a post-curing regime for its application.

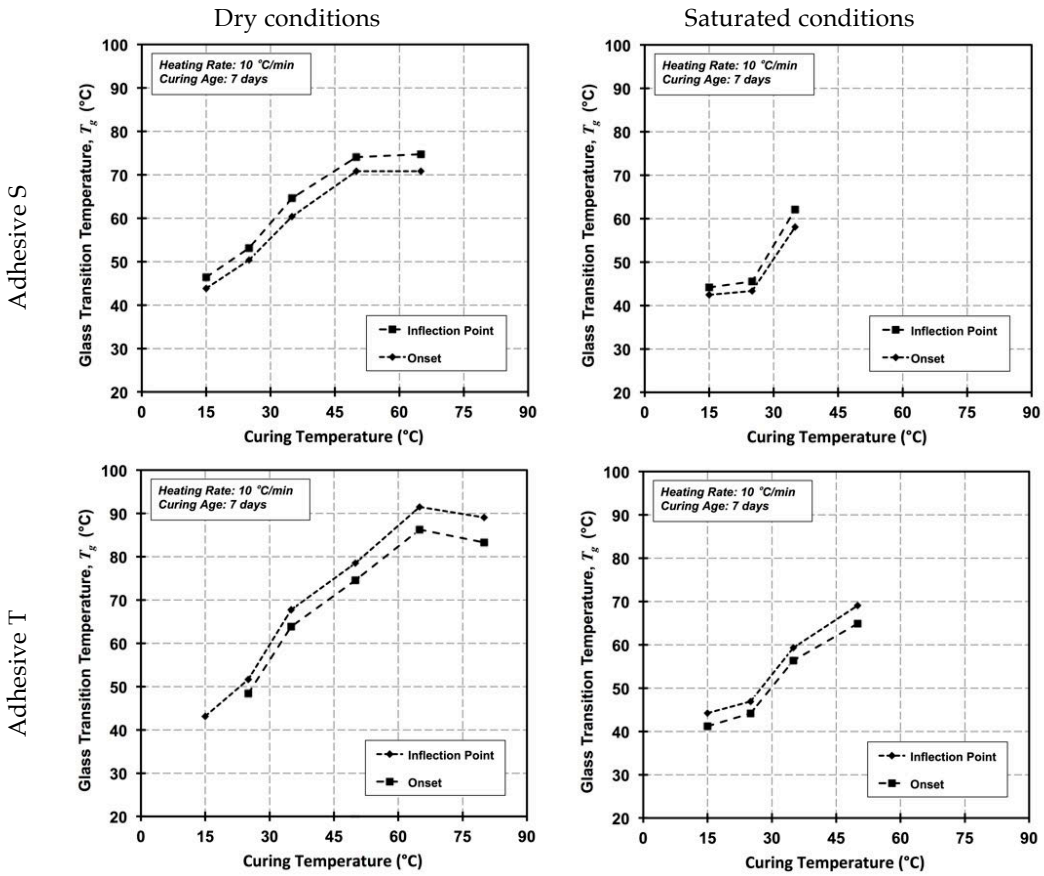

Figure 3-20: Recorded T_g according to different methods at 7 days and different curing temperature, Adhesive S and Adhesive T for dry and saturated conditions using DSC

Heat flow of the samples are presented in Figure 3-21, the slope of sigmoidal base line reduces with increasing curing temperature. This is caused by the increase of the network cross-link in the temperature range of the glass transition (Wu, 1992). The glass transition temperature, T_g values for the saturated samples cured above 65°C and 50°C for Adhesive S and T respectively was difficult to observe.

With regard to the samples cured at saturated conditions, it was noticed that Adhesive S heat capacity response was impaired. This may be due to the presence of voids and the filler, which increased the water absorption during the curing process. This has not been considered in the analysis, however the saturated cure also affected Adhesive T, but it is on a smaller scale. The values obtained from inflection point of the heat capacity response are in a good agreement to the values obtained from the peak loss modulus of the DMA runs.

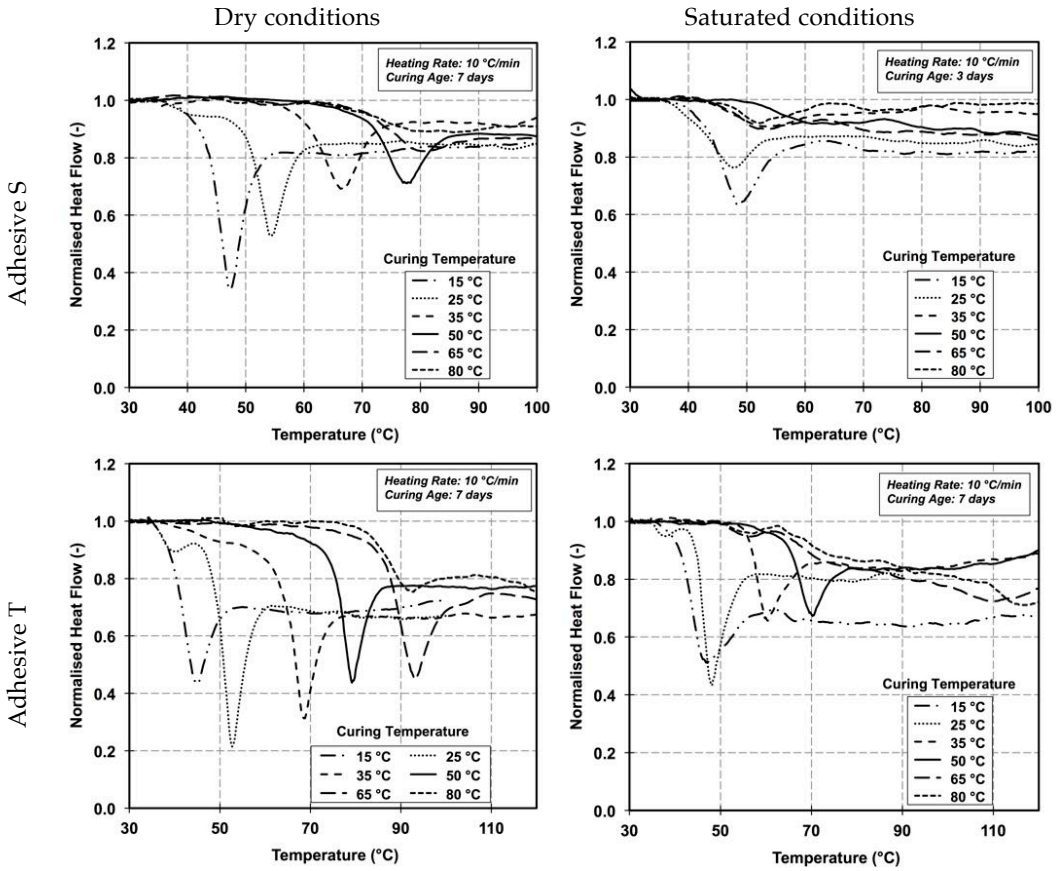

Figure 3-21: Normalised heat flow versus temperature for Adhesive S and Adhesive T for dry and saturate conditions cured at different temperatures for 7 days.

3.8 Summary

Glass transition temperature, T_g, is a property of the adhesives. It is the measure of the polymer chain cross-link density. Glass transition temperature, T_g, is dependent on the curing environment. The tests were carried out to study glass transition temperature, T_g and the influence of curing conditions on Sikadur-330 and Tyfo-S. Although similar work is carried out on different adhesives, little information is provided in published literature on the studied adhesives in this research. Glass transition temperature, T_g was assessed using Dynamic Mechanical Analysis (DMA) and Differential Scanning Calorimetry (DSC).

The investigation shows that curing temperature is significantly important, and certain glass transition temperature, T_g, can only be achieved from elevated temperature curing. A curing regime in some cases is adopted by manufacturers to yield high T_g and consequently improved the mechanical properties. It is important to measure the mechanical properties including the glass transition temperature, T_g at the same conditioning and clearly state the method and the testing parameters when the glass transition temperature, T_g is reported as a single value. The influence of curing temperature, with water impact, and ageing up 28 days on glass transition temperature, T_g days was investigated. The data provides designers and the industry the linear relationship of the curing temperature and the glass transition temperature, T_g of the adhesives. The study using DMA and DSC confirmed, that the required glass transition temperature, T_g may never be achieved at low temperatures even if it is left for as long as 28 days.

It is found that each glass transition temperature, T_g evaluating method yields a somewhat different result depending on the test parameters. It is recommended that the details of the test parameters should be stated. However, glass transition temperature, T_g values according to the peak loss modulus are very close to glass transition temperature, T_g the inflection point obtained from DMA. They are lest affected by the testing parameters. The single glass transition temperature, T_g values from the two methods using DMA are in a good agreement with glass transition temperature, T_g of the inflection point using DSC. The optimised glass transition temperature, T_g for Sikadur-330 and Tyfo-S is dry cure at 50°C and 65°C respectively for 7 days. Beyond these temperatures no improvement was noticed.

The study has shown that the specimens cured under combined of saturated conditions and high temperatures cure, exhibit poor T_g improvement in general. This combination showed negative impact beyond 35°C and 50°C respectively.

The single value of glass transition temperature, T_g after adhesive exposure to high temperature up to 28 day may not be affected significantly but the storage modulus variation with temperature is affected. Therefore, it is important to study storage, loss modulus and tan δ variation with temperature as they provide more information on the adhesives. It is possible that high temperatures and long exposure causes reverse reaction in the structure of the adhesives, and this is likely to affect the mechanical properties.

Chapter 4

Steel Specimen and Thermal Chamber Design Methodology

This chapter describes the approach, which was taken to design flexural specimens, and the details of the fabricated beams are presented. The actual dimensions of the specimens are compared with nominal manufacturers dimensions, and the tolerances are compared with the British Standard. This chapter also contains the details of the bespoke thermal heating chamber to function as a curing and testing chamber; the martials and off shelf electrical and mechanical components that were used in the fabrication.

The steel surface preparation procedure is reviewed and the adopted procedure of the surface preparation of the beam FRP strengthening, lap-shear preparation is summarised. The steps of the CFRP strengthening procedure and the details maintaining the CFRP alignment and controlling the adhesive thickness are addressed.

Lay out of the thermocouple location, the method of attachment, and the instrumentation to record the temperature during the post curing process and testing are listed. The post curing temperatures and the duration of the CFRP strengthened specimens are demonstrated in this chapter.

Finally, the coupon test results of the steel used in the fabrication of the beam specimens are presented.

4.1 Steel specimens

4.1.1 Beam design methodology

Several researchers investigated the use of bonded FRP materials for the retrofit of steel members. The main focus was on the use of FRP for flexural retrofit; applying FRP materials to the tensile flange of a section to increase its capacity, cast-iron section (Moy and Lillistone, 2006), mild-steel section (Patnaik and Bauer, 2004;

Schnerch *et al.*, 2004; Colombi and Poggi, 2006; Moy and Bloodworth, 2006; Narmashiri *et al.*, 2011), and steel-concrete composite girders (Sen *et al.*, 2001; Tavakkolizadeh and Saadatmanesh, 2003b, a; Al-Saidy *et al.*, 2004; Schnerch and Rizkalla, 2006; Sallam *et al.*, 2010). Research on mild-steel section and steel-concrete composite girders at ambient temperature, and little experimental work at elevated temperature (Abed, 2012; Stratford and Bisby, 2012) were reviewed in chapter 2.

The published literature concluded that the bottom flange of bridge girders typically needs strengthening. To study the behaviour of such structure, an alternative approach was taken in the design of the specimens. Instead of casting large amounts of concrete, the concrete deck was replaced by a steel plate welded to the top flange of a standard hot rolled I-section. The size and weight of the specimens was reduced. More importantly, the effect of thermal gradient in the section can be minimised. Schnerch and Rizkalla (2006) reported that the addition of the steel plate in the compression region simulates the presence of a concrete slab by locating the neutral axis depth closer to the compression flange such that the strain profile of the cross-section would be similar to steel-concrete bridge girders. Typical cross section of composite steel-concrete bridge girders is shown in Figure 4-1.

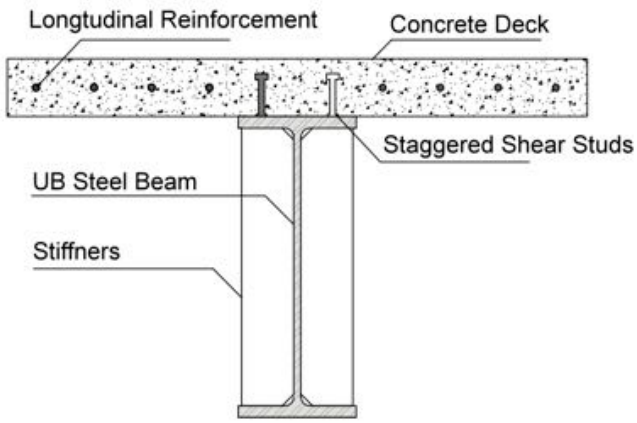

Figure 4-1: Typical cross section of composite steel-concrete girders

Stability of thin-wall structures is an important aspect to consider. Lateral torsional buckling is a critical failure in flexural strengthening steel structures (Patnaik and Bauer, 2004), and local yielding due to load concentration under the loading points and supports was observed (Abed, 2012). Therefore, vertical

stiffeners were welded to the web to increase stability of the specimens. This research focuses only on the flexural strengthening steel beams, and the beams designed to fail due to yielding of the bottom flange. A 12.5×100mm steel plate used to replace a concrete deck of 50×176mm as shown in Figure 4-2; both sections have the same second moment of area. It is assumed that the concrete was moderate strength and Young's modulus of concrete was assumed to be ten times less than steel (200GPa). The contributions of longitudinal reinforcement and shear studs were eliminated.

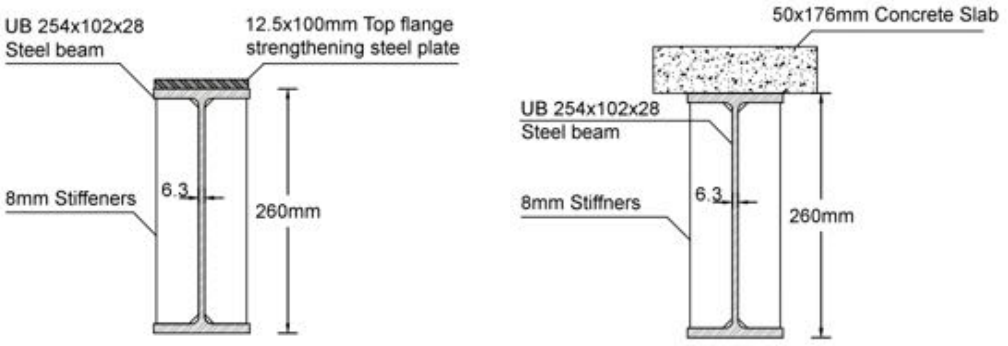

Figure 4-2: The equivalent top flange strengthened universal beam with steel and composite steel-concrete girder

4.1.2 Steel beam fabrication

The nine test specimens used in this research were 3-metre long hot rolled I-section steel beams UB 254×102×28. The compression flange of each specimen was strengthened with an additional 100 mm wide and 12.5 mm thick steel plate; continuous weld on the two sides along the flange and both ends attached the top flange and the steel plates. The mechanical properties of the hot rolled I-section beam and top flange strengthening steel plate are listed section 4.5.3. In addition to the compression flange strengthening, the web of the I-section was stiffened at five points. The 8 mm thick steel plates were welded to the beam web and the flanges at the concentrated loading points (the supports and point loads) and at mid-span to prevent elastic buckling at the early stages of loading and local yielding at high load. Figure 4-3 shows the cross-section dimensions of the specimens and details of the stiffener locations. A stiffened and top flange strengthened beam is shown in Figure 4-4.

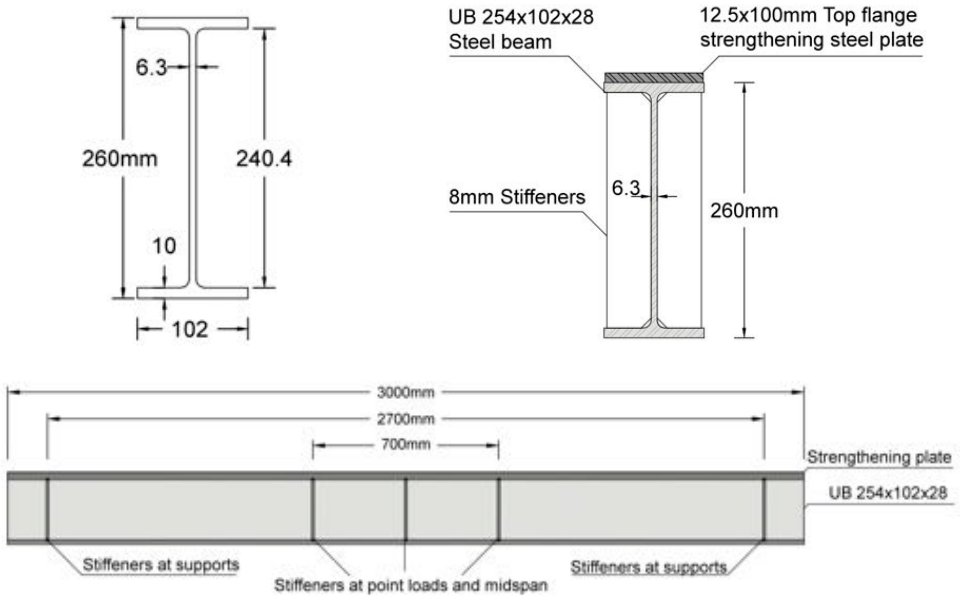

Figure 4-3: Cross-section nominal manufacture's dimensions and stiffener locations for the un-strengthened test specimens

Figure 4-4: Photograph of a steel beam specimen after adding the top flange plate and web stiffeners

4.1.3 Geometrical properties

The geometric properties of each test specimen were measured using external micrometre and recorded. The dimensions were taken for comparison purposes with the nominal manufacturer's dimensions; the dimensions were within the tolerance given in British Standard EN 10034 (1993). The measurements are

listed in Table 4-1. Figure 4-5 is the explanation of the notations that are used in the Table 4-1.

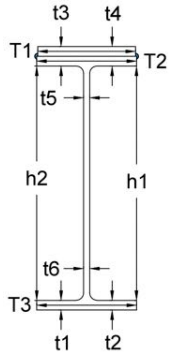

Figure 4-5: Notations used in Table 4-1

Table 4-1: Geometric properties of the tested specimens (all in mm)

Beam No.	T_1	T_2	T_3	h_1	h_2	t_1	t_2	t_3	t_4	t_5	t_6
Control beam	99.32	104.10	103.70	237.80	238.90	10.18	10.38	22.25	22.35	5.89	5.91
Beam no.1_30	99.61	104.74	103.17	237.80	238.10	10.38	10.24	22.28	22.48	5.58	5.57
Beam no.2_30	99.83	104.54	104.30	238.90	238.50	10.41	10.27	22.58	22.97	5.96	5.86
Beam no.3_50	99.73	104.48	104.52	238.67	238.78	10.33	10.39	22.27	22.47	5.91	5.87
Beam no.4_50	99.88	104.79	104.30	238.75	238.43	10.20	10.45	22.22	22.39	5.88	5.91
Beam no.5_25	100.42	104.17	104.75	238.41	238.25	10.30	10.32	22.45	22.35	5.82	5.83
Beam no.6_30	100.01	104.55	104.44	238.46	238.08	10.44	10.34	22.23	22.43	5.83	5.84
Beam no.7_50	100.51	105.05	103.33	238.36	238.50	10.46	10.31	22.38	22.44	5.88	5.78
Beam no.8_50	100.16	104.12	104.92	238.73	238.4	10.42	10.29	22.27	22.53	5.89	5.91

4.2 Design and fabrication of thermal chamber (O-105)

4.2.1 Chamber design methodology

For the purposes of this project a multi-function bespoke convection thermal chamber was designed to be as robust and safe curing cabinet, and a reliable method of heating during loaded tests. The chamber consists of heat source and appropriate air circulation similar to a domestic oven. Although researchers used conduction method such as heating pads (Stratford and Bisby, 2012), radiation method (halogen lights) as a source of heat (Webb *et al.*, 2013) only for testing.in these approaches non-uniform heating within the specimens was the main concern. However, convection heating method of the specimen was successfully used by

Abed (2012). The thermal gradient in the specimens was minimised during curing and testing; the curing temperature of the specimens at various location were measured during curing and testing, and the results are presented in chapter 5. Efforts were made to make the chamber efficient, reduce the heat losses and be able to achieve the required temperature with the available resources. Therefore, detailed heat transfer analysis and wattage estimation carried out to meet the curing and testing requirement was achieved.

4.2.2 Chamber fabrication

Plywood and sawn timber were used to construct the shell of the chamber. Polyisocyanurate (PIR) insulation panels produced by Recticel Insulation Products (2011) and plasterboard were used as the insulation material. The two layers were glued using a heat resistance silicon sealant. The chamber was located on the top reaction beam of the universal Avery 7104 testing machine as shown in Figure 4-6 and Figure 4-7.

Two powerful (2 kW) electrical heaters, which connected to a proportional-integral-derivative (PID) controller Omega CSi8D Series (User's Guide), were used to maintain the temperature of the chamber. The heaters were mounted at both ends of the chamber. To minimize the heat losses and make the chamber efficient, air-circulation method used; a (0.75 kW) centrifugal fan placed at one end to circulate hot air via tubes running inside the chamber from one end to the other. Double glazed windows were placed on the sides of the chamber, at the end furthest from the centrifugal fan, for observation and Digital Image Correlation (DIC) purposes. To ensure that the chamber was safe to run for a long period, up to 7 days during the curing process and in case of the lack of air circulation the chamber was safely switched off, a flow switch (Series V4-2-U) produced by Flotect® was installed to cut the power supply to the PID controller and heaters.

The specimen test configuration, instrumentation and results are in chapter 5.

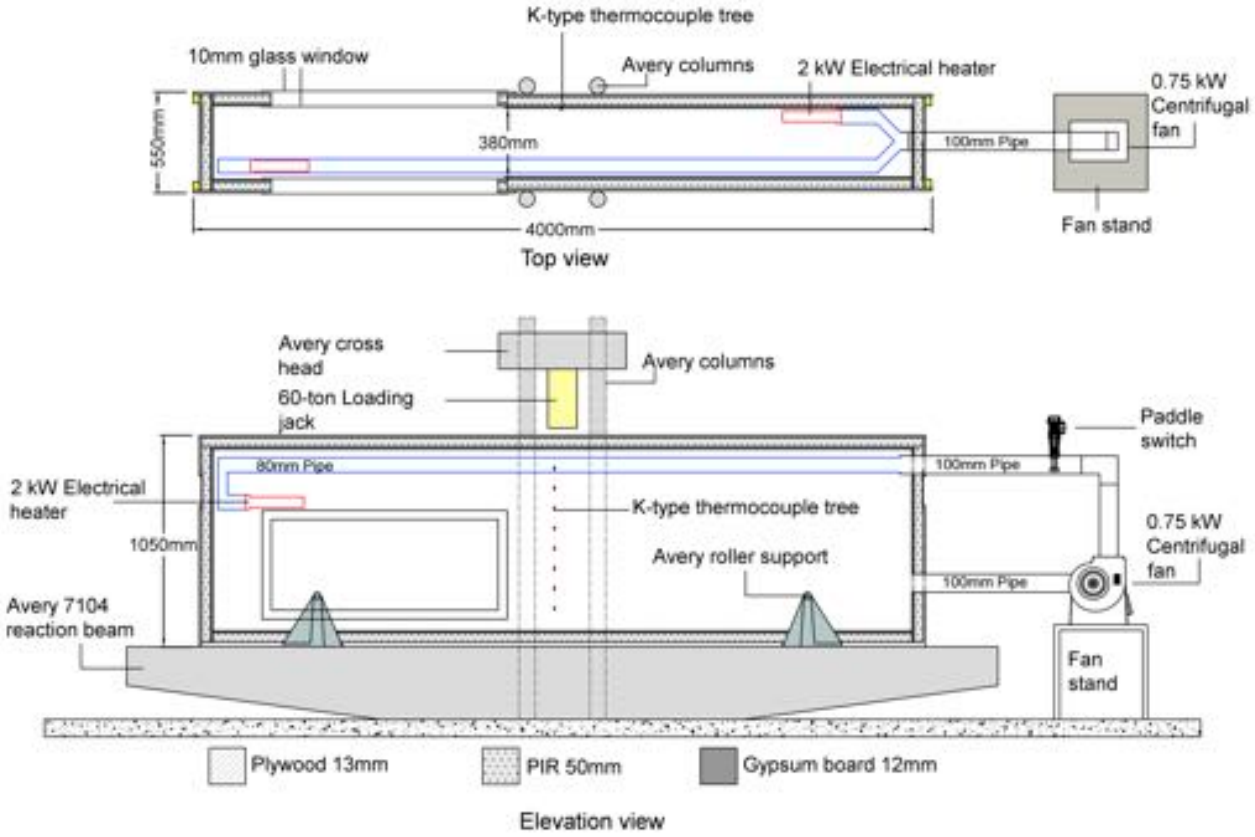

Figure 4-6: Elevation and top view of the O-105 Chamber

a) O-105 chamber fabrication

b) O-105 chamber in operation

c) O-105 chamber and Avery frame

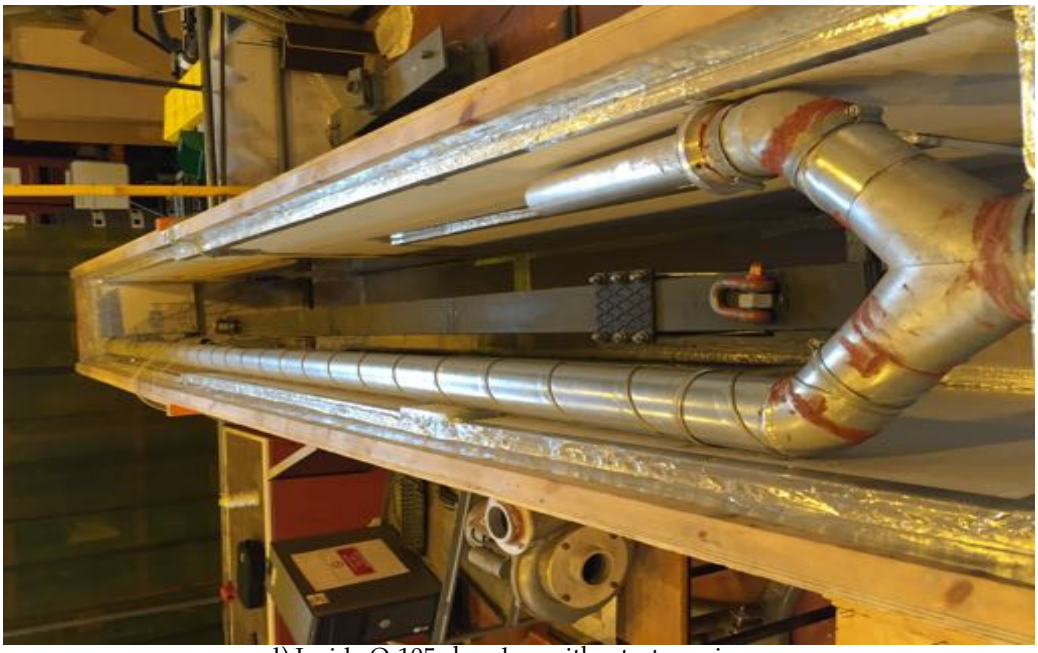

d) Inside O-105 chamber with a test specimen

Figure 4-7: Various stages of O-105 chamber fabrication and in operation

4.3 FRP strengthening and specimens conditioning

4.3.1 Steel surface preparation

In EB-FRP strengthening it is important to take into account different types of failure. Debonding in FRP strengthened metallic structures can occur in various modes, mainly:

- Cohesion failure, which occurs within the adhesive material.
- Adhesion failure that occurs at the adhesive/adherend interface.
- Debonding is likely to occur as a combination of cohesion and adhesion failure.

Since the adhesives that are used in construction have high mechanical properties, cohesive failure is less likely to occur. However, adhesion failure depends mainly on the surface preparation of the adherend; an active and clean surface was required to prevent this failure. Surface preparation of metallic structure was significantly important, and different methods were studied, such as (a) physical, (b) mechanical, (c) chemical, (d) photochemical, (e) thermal, or (e) plasma methods (Baldan, 2004). Solvent cleaning, mechanical abrasion, and grit blasting of the surface were among the most widely used methods. Although solvent cleaning removes contaminant materials, the mechanical properties of the surface remain the same (Hollaway and Cadei, 2002). Grit blasting was found to be the most effective methods to control the desired level of surface roughness and joint strength (Harris and Beevers, 1999; Hollaway and Cadei, 2002; Baldan, 2004). The grit-blasting process introduces chemical changes on the surface of the substrate, and it affects the surface energy (Harris and Beevers, 1999). The properties that significantly affect the adhesion strength and the adhesion mechanism were beyond the scope of this research and were not covered in this research. Further information on the topics can be found in published literature (Adams *et al.*, 1997; Baldan, 2004; Mays and Hutchinson, 2005).

The steel surface preparation in this research took place in accordance with ASTM D2651-01 (2001) and the steel surface preparation guidelines are described in Cadei *et al.* (2004); Schnerch *et al.* (2007); Hollaway and Teng (2008). The surface treatment of the steel dog-bone coupons in this chapter and bottom flange of the

beam specimens and the inner plates for double lap specimens in chapter 5 was carried out as follow:

- The surface was wiped with acetone to remove any contaminants. Solvent wash cleaning was not used. This was to avoid contaminating the grit in the blasting chamber.

- The surfaces were grit-blasted with aluminium oxide powder size 60 grit under 6 bar air pressure to remove mill scale, any rust and introduce rough surfaces to achieve required bond strength. Researchers have found that there was no difference in the joint strength between fine and coarse grits (Harris and Beevers, 1999), new grit had to be added to the system due to reduction in the grit from the filtration process within the system.

- The surfaces were vacuum cleaned with dusting brush to remove any dust and sanding debris from the sandblasting process. Following the grit blasting no further cleaning, such as wiping, dry blasting, and solvent cleaning after abrasion of the surface, was carried out. This decision was made to reduce spreading contamination; Hollaway and Cadei (2002) recommends the use of solvent cleaning after abrasion should not be undertaken as this only partially removes the debris and spreads it over the surface, oil and water traps in the dry blasting can cause contamination. However, El Damatty and Abushagur (2003); El Damatty *et al.* (2003) following grit blasting used alcohol methanol acid in order to remove any dirt. Due to the health and safety regulations at the University of Edinburgh, using a large amount of solvent, such as acetone or alcohol methanol acid was not allowed in an enclosed area.

4.3.2 Specimen preparation and FRP strengthening

This section covers the procedure of FRP strengthening of the fabricated beam specimens in section 4.1.2 with FRP. In addition to the surface preparation method in section 4.3.1, the mill scale on the beams surface was removed using a cordless angle grinder before degreasing the surface. In this research alumina oxide grit size 60 (Clark, 2016) , which has particle diameter of approximately 0.25mm, was used based on the recommendations in Fernando *et al.* (2013). Grit blasting of

the beams was carried out using five bar air pressure. Figure 4-8 shows the grit blasting chamber and various stages of the steel surface preparation.

The CFRP plate (MBRACE® LAMINATE, 2008) had a peel-ply layer on both surfaces to keep the surfaces clean and protect it during transportation. The peel-ply provides a rough surface to the CFRP plates; therefore, no further treatment was required to provide good adhesion.

The necessary quantity of two-part Sikadur-330 (2012) adhesive was mixed using a mixing paddle attached to a slowly revolving cordless drill until a consistent mixture was achieved. One side of the CFRP peel-ply was then removed to apply the epoxy on the CFRP plate and the flange of the beam. The eight FRP strengthened specimens were reinforced with pre-cut 2200mm FRP laminated plate, positioned with its ends 250mm from the support position.

a) Grit blasting chamber

b) A specimen placed in the blasting chamber

c) Specimen grit blasting

d) Specimen vacuum cleaning

Figure 4-8: Various stages of the surface preparation

To reduce trapped air and maintain the adhesive thickness of the adhesive layer, the applied adhesive on the two surfaces had a crown in the middle (thicker adhesive in the centre than the edges). Spherical silver coated glass beads 1-1.3 mm diameter were sprinkled on the adhesive that had already been applied to the beam surface. The mixing ratio of 1% by mass was the typical percentage and this ration is recommended by Broughton and Gower (2003), the same ratio was also used by other researches (Fernando, 2010; Abed, 2012). The 1% by mass was equivalent to approximately 0.5% by volume for the adhesive and glass beads used in this research. The glass beads were not added to the adhesive during the mixing process

to avoid clotting. The relatively small amount of glass beads used to maintain the constant thickness is believed to be sufficient to keep bond-line thickness constant without affecting the discontinuity in the adhesive bond. To avoid any movement of the FRP plate and to maintain the 1-1.3mm adhesive thickness during the first 24 hours curing, lead weights were used. The lead weights were placed over pre-cut 2200mm plywood, which was separated from the FRP plate with a cling film. Figure 4-9 shows various stages of the CFRP strengthening process. The specimens were cured for 24 hours at approximately 18°C at laboratory temperature before being moved into O-105, and the curing temperatures were measured.

a) Mixing adhesive

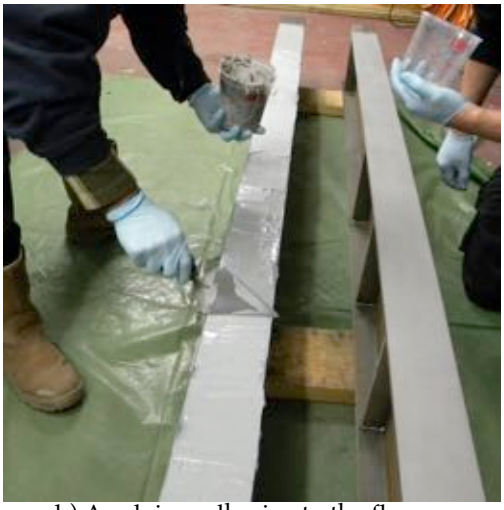

b) Applying adhesive to the flange

c) Spreading adhesive to the CFRP plate

d) Applying lead weights

Figure 4-9: Various stages of the CFRP plates strengthening

4.3.3 Specimen curing and conditioning

The samples were placed in an inverted orientation over the supports in the O-105 chamber and were cured for six days, except Beam no.6_30, which was cured for an extra 3 days. The beam temperature was controlled using an accurate high-temperature magnetic RTD (class B: pt-100) sensor, which was connected to the PID controller to efficiently and accurately manage the heaters. T-type fibreglass insulated thermocouples were used to measure the beam temperature. Eight T-type fibreglass insulated thermocouples were distributed on the beam specimens; six thermocouples on the bottom flange, one thermocouple on the web and one thermocouple top flange as shown in Figure 4-10. The tip of T-type thermocouples, which has an accuracy of 1°C, were spot welded to each beam at pre-marked locations, and they were secured to the beams using ready mixed high-temperature resistance cement to avoid detaching during curing, handling, and testing. The thermocouple wires were 3-metre in length, and they were designed to come out from the side of O-105 chamber and connect to a data logger using TC-08 USB data logger (Picotech, 2016). The targeted curing regime was 25°C for four FRP strengthened specimens and 50°C for four FRP strengthened specimens. The recorded experimental curing temperatures were ±1.5°C (in some cases) from the targeted curing temperature. The real curing temperature was recorded, and it is presented in Figure 5-1.

K-type thermocouples were used in the chamber to monitor air temperatures through the depth of the chamber during the curing period to measure the air temperature during testing. The K-type thermocouple tree of eight thermocouple was fixed to the inside of the O-105 chamber, and they were connected to a 12-channel temperature recorder (Omega RDXL12SD Series, User's Guide). The location of the K-type thermocouple tree is shown in Figure 4-6. The thermocouples were marked as TC1 to TC8, and were located 100 mm from the top of the chamber to the bottom at 100mm intervals. The recorded temperatures during the testing are presented in chapter 6.

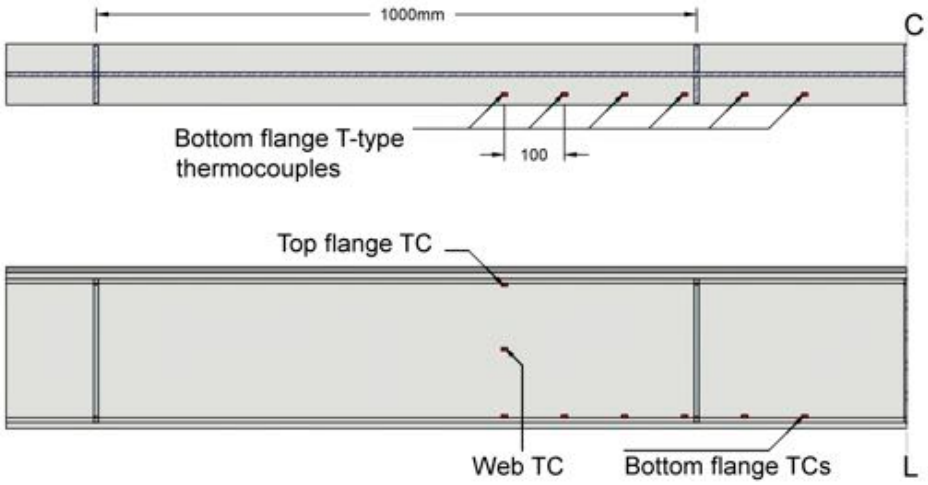

Figure 4-10: Thermocouple locations on the beams

4.4 Overview of the experimental programme

The beam tests' purpose is to examine the effect of elevated temperate curing on the structural behaviour of FRP strengthened beams. The second purpose is to measure the influence of thermal loading on the beams cured at low and high temperatures.

The fabricated I-section beams in section 4.1.2 were designed for CFRP strengthening in flexure using FRP laminated plates section 4.5.2. After strengthening, the specimens were first initially cured in laboratory conditions for 24 hours, and then cured in the O-105 chamber for a minimum period of six days at a controlled temperature.

A total of nine beams were tested in four-point bending, and Table 4-2 shows the test matrix. The control specimen was the only specimen that was tested without FRP strengthening. Five beams were mechanically loaded to determine their strength at ambient temperature. While only three beams were loaded to 350kN, which was the design plastic moment of the section, and then thermal loading was applied until failure occurred. Lap-shear and DMA sets of three specimens were prepared for each beam curing temperature; the results are demonstrated in section 5.1 and Suction 5.2. Pull-off tests specimens were prepared and cured with each FRP strengthened beam specimens. They were tested at ambient temperature, and the results are shown in section 5.3. Table 4-3 contains the lap-shear, DMA, and pull-off

test matrix. The beam specimens, lap-shear, DMA samples, and pull-off adhesion dollies were conditioned as described in section 4.3.3.

Table 4-2: Beam test programme

Beam no.	***Curing Temperature***	***Strengthening method***	***Four-point bending testing loads***	
			Mechanical	***Thermal***
Control Beam	------	------	Monotonic loading	Steady state (Ambient)
Beam no.1_30	30°C	CFRP	Monotonic loading up to failure	Steady state (Ambient)
Beam no.2_30	30°C	CFRP		
Beam no.3_50	50°C	CFRP		
Beam no.4_50	50°C	CFRP		
Beam no.5_25*	25°C	CFRP		
Beam no.6_30*	30°C	CFRP	Monotonic loading, sustained at 350kN	Transient (Ambient until failure)
Beam no.7_50	50°C	CFRP		
Beam no.8_50	50°C	CFRP		

* Beam no.5, and Beam no.6 were cured at 25°C for 7 days, Beam no. 6 was cured at 30°C 3 extra days.

Table 4-3: Lap-shear, DMA, and Pull-off test programme

Beam no.	***Curing Temperature***	***Pull-off specimens***	***DMA specimens***	***Lap-shear specimens***
Beam no.1_30	30°C	3 specimens	3 specimens	Series 1
Beam no.2_30	30°C	3 specimens		
Beam no.3_50	50°C	3 specimens	3 specimens	Series 1
Beam no.4_50	50°C	3 specimens		
Beam no.5_25*	25°C	3 specimens	3 specimens*	Series 2*
Beam no.6_30*	30°C	3 specimens		
Beam no.7_50	50°C	3 specimens	3 specimens	Series 2
Beam no.8_50	50°C	3 specimens		

* The DMA specimens and Series 2 lap-shear specimens were cured at 25°C for only 7 days.

It is assumed that the temperature within the chamber reaches equilibrium. Therefore, only the temperature of the steel beams was recorded, and the temperature profile for the curing period is shown in Figure 4-11, which is the average of the eight T-type thermocouples and the minimum and maximum reading is shown Table 4-4. Beam no.1 and Beam no.2 were cured at the chamber for the first time, and the PID controller was set on self-learning mode to maintain the temperature at 30°C. This method of controlling the temperature of the chamber led to a substantial amount of fluctuation of ±0.7°C during the curing of the specimens. Due to these fluctuations, the temperature controlling method changed. Switching the heaters on and off automatically was used instead of self-learning mode of the PID controller.

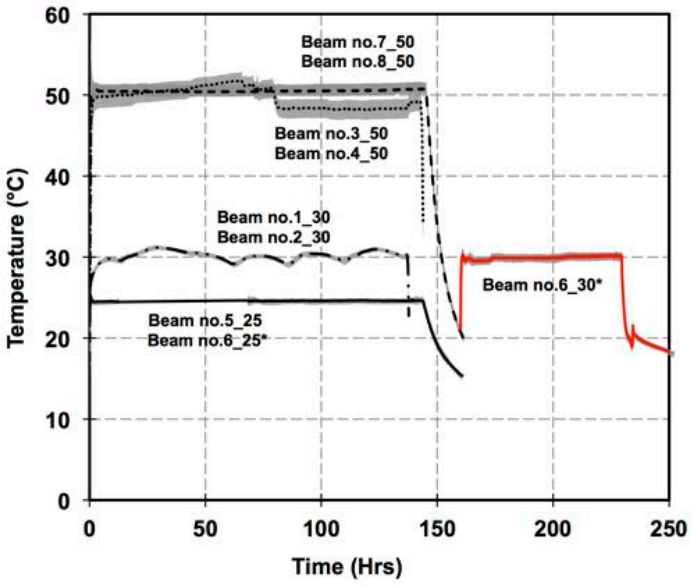

Figure 4-11: Curing temperature of the beams and small-scale samples

Table 4-4: The average curing temperature and standard deviation of the curing period

Beam no.	*Average temperature*	*Standard deviation*	*Maximum negative*	*Maximum positive*
Beam no.1_30 Beam no.2_30	30.1°C	0.2°C	0.35°C	0.26°C
Beam no.3_50 Beam no.4_50	49.7°C	0.7°C	1.23°C	1.10°C
Beam no.5_25* Beam no.6_25*	24.5°C	0.2°C	0.26°C	0.30°C
Beam no.6_30*	29.9°C	0.3°C	0.53°C	0.49°C
Beam no.7_50 Beam no.8_50	50.5°C	0.5°C	0.63°C	0.85°C
* Beam no. 5, and 6 were cured at 25°C for 7 days, Beam no. 6 was cured at 30°C 3 extra days.				

4.5 Strengthening material properties

The material properties in the fabrication of the specimens are presented in this section. Figure 4-12 shows the cross section of the FRP strengthened beam with the used material dimensions. The adhesive epoxy used in the strengthening scheme was Sikadur-330, which was referred to Adhesive S in chapter 3. The mechanical properties of the CFRP material were taken from the manufacturers' data sheet since the focus of this research was on the bond behaviour, and the specimens were not designed to fail in FRP rupture. The mechanical properties of

the steel were reported from testing that was carried out at the University of Edinburgh.

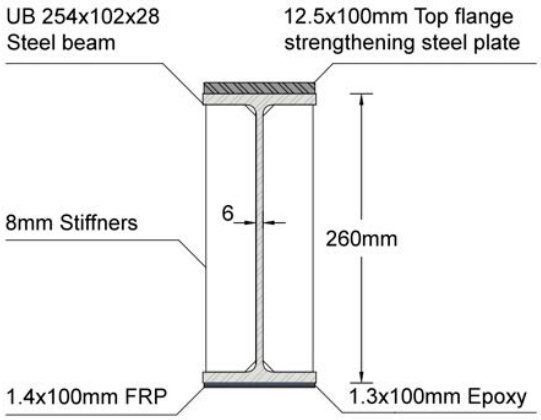

Figure 4-12: Cross section of a CFRP strengthened test specimens.

4.5.1 Adhesive material properties

Two-part Sikadur-330 adhesive was used in this research to strengthen the beams in flexure. The mechanical properties of the adhesive at room temperature are shown in Table 4-5, according to the manufacturers datasheet Sikadur-330 (2012). The mixed two-part adhesive density from the data sheet is 1.3 kg/l. The reported data were from coupons cured for 7 days at +23°C. These were found compliant with DIN 53455 and DIN 53452. These standards are superseded by EN ISO 527-2 (1996); EN ISO 178 (2003). The testing speed of the test shall be 1 mm/min (EN ISO 527-2, 1996). The storage modulus variation with temperature and the effects of curing on Sikadur-330 (Adhesive S) was intensively studied in chapter 3. Three-point bending tests using DMA and single cantilever tests on Sikadure-330 were carried out and they are presented in section 5.3.2. The shear properties of the adhesive were found using double-lap shear tests; the results are presented in section 5.1.

Table 4-5: Sikadur-330 mechanical properties from the manufacturers datasheet Sikadur-330 (2012)

Properties	***Test Method***	***Performance of Sikadur-330***
Tensile Strength, (MPa)	**DIN 53455**	30
Young's Modulus, *E* (GPa)	**DIN 53455**	4.5
Elongation at break %	**DIN 53455**	0.9
Flexural Modulus, (GPa)	**DIN 53452**	3.8

4.5.2 CFRP properties

The CFRP plate used to strengthen the tension side of the beam was a product of BASF Construction Chemicals (UK) Ltd. Medium modulus (MM) CFR plate was used MBRACE® LAMINATE (2008), with a peel-ply layer on both surfaces to keep the surfaces clean and protected prior to application. The peel-ply provides a rough surface to the CFRP plates; therefore, further surface treatment was not required to provide better adhesion. The mechanical properties of the adhesive at room temperature according to the manufacturer's datasheet are shown in Table 4-6. Loading rate of the CFRP tensile tests were not given in the manufacturer's data sheet.

Table 4-6: CFRP mechanical properties from manufacturers datasheet MBRACE® LAMINATE (2008)

Properties	***Performance of MBRACE® FRP LAMINATES***
Tensile strength, (MPa)	3100
Young's Modulus, E (GPa)	170
Width, w (mm)	100
Thickness, t (mm)	1.4
Elongation at break %	1.9
Fibre content %	70
Density g/cm^3	1.61
Inter laminate shear strength, (MPa)	70
Thermal expansion m/mm/°C	0.6×10^{-6}

4.5.3 Steel material properties

The mechanical properties of the steel and plates were measured for later use in the analysis. The details of the analysis are discussed in chapter 6. Direct tensile tests were used to measure the steel's mechanical properties, such as tensile strength and Young's modulus. Digital Image Correlation DIC analysis was used to measure the strain hardening stage after yielding. This was used to complete the stress strain curve. The test procedure and set up are addressed in Appendix D. The coupon test results in Table 4-7 are from the hot rolled universal steel beams (UB 254×102×28) and are labelled as follows; W_n for the coupons from the beam web, TF_n and BF_n for top and bottom flange respectively. The coupons from the top flange strengthening steel plate in Table 4-8 are labelled as SP_n. The test results in Table 4-9

are from a 2 mm thick plate, which was used in the fabrication of double lap shear specimens; the specimens are labelled as TP_n. The double lap shear specimens are covered in section 5.1.

Table 4-7: Beam section mechanical properties

Specimen Location	***Properties***	***Specimen no.***			
		TF_1	***TF_2***	***TF_3***	***Avg ± SD***
Top Flange	**Width, w (mm)**	12.39	12.48	12.34	12.4 ± 0.06
	Thickness, t (mm)	10.33	10.24	10.3	10.29 ± 0.04
	Young's Modulus, E (GPa)	197	197	202	199 ± 3
	0.2% Offset Strength, f_y (MPa)	393	400	405	399 ± 5
	Yield Strain, ε_y	0.0019	0.002	0.00203	0.0019± 0.6×10^{-4}
	Ult. Strength, f_u (MPa)	510	506	516	510 ± 4
	Ult. Strain, ε_u	0.181	0.190	0.176	0.182 ± 0.006
	Testing speed, mm/min	1	1	1	
		W_1	***W_2***	***W_3***	***Avg ± SD***
Web	**Width, w (mm)**	12.42	12.39	12.46	12.42 ± 0.03
	Thickness, t (mm)	5.83	5.76	5.9	5.83 ± 0.06
	Young's Modulus, E (GPa)	204	204	201	203 ± 1.5
	0.2% Offset Strength, f_y (MPa)	420	407	409	412 ± 6
	Yield Strain, ε_y	0.0022	0.0019	0.00199	0.002 ± 1.2×10^{-4}
	Ult. Strength, f_u (MPa)	515	501	512	509 ± 6
	Ult. Strain, ε_u	0.189	0.196	0.177	0.187 ± 0.008
	Testing speed, mm/min	2	1	1	
		BF_1	***BF_2***	***BF_3***	***Avg ± SD***
Bottom Flange	**Width, w (mm)**	12.41	12.41	12.46	12.43 ± 0.02
	Thickness, t (mm)	10.16	10.33	9.99	10.16 ± 0.14
	Young's Modulus, E (GPa)	200	193	210	201 ± 7
	0.2% Offset Strength, f_y (MPa)	385	393	407	395 ± 9
	Yield Strain, ε_y	0.0019	0.002	0.0019	0.0019 ± 0.5×10^{-4}
	Ult. Strength, f_u (MPa)	497	503	518	506 ± 9
	Ult. Strain, ε_u	0.176	0.206	0.171	0.184 ± 0.015
	Testing speed, mm/min	1	1	1	

Table 4-8: Top flange strengthening plate mechanical properties

Specimen Name	***Properties***	***Specimen no.***			
		SP_1	***SP_2***	***SP_3***	***Avg ± SD***
Beam Strengthen Steel Plate	**Width, w (mm)**	12.49	12.51	12.48	12.5 ± 0.012
	Thickness, t (mm)	11.76	12.04	11.77	11.85 ± 0.13
	Young's Modulus, E (GPa)	200	201	195	198 ± 3
	0.2% Offset Strength, f_y (MPa)	273	290	275	279 ± 8
	Yield Strain, ε_y	0.00136	0.00144	0.00141	0.0014 ± 0.3×10^{-4}
	Ult. Strength, f_u (MPa)	469	469	465	468 ± 2
	Ult. Strain, ε_u	0.231	0.211	0.213	0.218 ± 0.009
	Testing speed, mm/min	1	1	1	

Table 4-9: 2 mm thick steel plate mechanical properties

Specimen Name	***Properties***	***Specimen no.***			
		TP_1	TP_2	TP_3	***Avg ± SD***
2mm Plate	**Width, w (mm)**	12.40	12.41	12.40	12.4 ± 0.005
	Thickness, t (mm)	1.93	1.93	1.94	1.93 ± 0.005
	Young's Modulus, E (GPa)	199.5	201.2	200.5	200 ± 1
	0.2% Offset Strength, f_y (MPa)	233	232	231	232 ± 1
	Yield Strain, ε_y	0.00117	0.00115	0.0015	$0.00116 \pm 0.7\times10^{-5}$
	Ult. Strength, f_u (MPa)	320	317	321	319 ± 2
	Ult. Strain, ε_u	0.207	0.206	0.209	0.207 ± 0.001
	Testing speed, mm/min	1	1	1	

4.6 Summary

The hot rolled steel beam dimensions were within the tolerance given in British Standard EN 10034 (1993). The nominal manufacturer's dimensions were used in the analysis that is carried out in chapter 6 of this research. Dog-bone coupon tests were carried out to measure the mechanical properties of the fabricated steel specimens. Strain gauges were used to measure Young's modulus of the coupons and the average values were 200 GPa for the top flange strengthening steel plate and for the hot rolled section at different locations. The yielding strength of the used steel was different, approximately 280 MPa and 400 MPa for the top flange strengthening steel plate and the I-section beam respectively. These values were used in the analysis that is carried out in chapter 6. Digital Image Correlation DIC was successfully used to measure non-linearity (strain hardening) of the stress-strain curve after yielding. The material properties of the CFRP plate and Sikadur-330 adhesive were taken from the manufacturer's data sheet.

To avoid contamination of the active steel surface, the FRP strengthening procedure was carried out immediately after grit blasting and on the same day. The pull-off tests were conducted to ensure that adequate surface preparation was achieved. The details are provided in section 5.3.

A bespoke thermal chamber O-105 was fabricated from off shelf materials. The chamber was used to test the specimens. The curing temperatures of the specimens are tabulated in section 4.2.

A total of eight beams were cured. Five beams were cured at different temperatures to investigate the effects of adhesive curing on their overall performance. These beams were loaded mechanically up to failure. Two of these

five beams were cured at 30°C. Two of the five beams were cured at 50°C. One of the five beams were cured at 25°C. All five beams were cured for a duration of 7 days.

The other three remaining beams were cured to study the behaviour of their adhesive joints under sustained mechanical loading, but were also subjected to transient thermal loading. Two of these three beams were cured at 50°C for a duration 7 days. The remaining beam was cured at 25°C for 7 days, and further three days at 30°C.

A ninth beam was a control beam. This was not FRP strengthened, and mechanically loaded. Lap-shear, DMA, and puff-off specimens were prepared with these beams for each curing temperature.

The results of these tests are addressed in chapter 5.

Chapter 5

Performance and Behaviour of Cured Steel-FRP Joints

This chapter contains the experimental programme that was carried out to study the influence of curing on adhesive joints at ambient and elevated temperatures. The test results of the lap-shear, DMA, pull-off tests and four point bending flexural beam tests are addressed in this chapter.

Firstly, the lap-shear, DMA, pull-off tests specimens were prepared together with each of the beam specimens tested. The lap-shear samples provide information on the shear strength of the adhesive, and these results were used to estimate the failure load of the four-point bending flexural beam tests. The adhesion pull-off tests were used to ensure that the required adhesion was achieved, and the surface preparation was adequate. The lap-shear and adhesion pull-off tests were undertaken at ambient temperature. Dynamic Mechanical Analysis (DMA) specimens were prepared to compare the variations in the material properties of the adhesive under temperature. The results of the lap-shear, DMA, pull-off tests are presented. This chapter also describes the four-point bending flexural beam set-up, the test parameters, the test monitoring instrumentation, and the results of these tests.

A total of nine beams were tested, including one control specimen. Five beams were tested at ambient temperature to investigate the effects of adhesive curing on the overall performance of the FRP strengthened sections. Three specimens were tested at transient temperature to study the behaviour of adhesive joints at elevated temperature. Load-deflection responses were measured during the tests.

Three specimens were tested at transient temperature after post curing at 30°C, and 50°C. Load-deflection response was recorded, and CFRP relative slip was measured using Digital Image Correlation (DIC).

The results of the tests are used in chapter 6 to compare the experimental results with the analytical results of the un-strengthened and strengthened specimens.

5.1 Lap-shear tests

Lap-shear tests are the most commonly for determining the shear strength of an adhesive joint. This is because it is an uncomplicated test to carry out (Zhao and Zhang, 2007; da Silva *et al.*, 2011). The conventional single lap-shear joint was not suitable for determining the real adhesive properties due to the complicated stress state within the adhesive joint, but it can be used for the purposes of comparison of adhesives and quality control of adhesives properties (da Silva *et al.*, 2011). Double lap-shear sample are recommended as the peeling stresses are reduced due to the load alignment (Hart-Smith, 1973a, b). Therefore, double lap-shear specimens were used in this research. However, in the single- and double-lap shear specimens the adhesive shear stress is still not uniform due to the differential straining effect according to Volkersen (1938); Hart-Smith (1973a); da Silva *et al.* (2011).

In this research two series of lap-shear samples similar to the ones were prepared with the beams in Schnerch (2005). From the first series, the failure was due to yielding of the steel inner layer and the influence of adhesive curing could not be seen. Therefore, in the second series of the double lap-shear specimens, thicker plates were used to investigate the curing of the adhesive using lap-shear test set up. The first test series was prepared for beams 1-4 (which were tested to find the load capacity at ambient temperature), and the second series was prepared for beams 5-8 (which were tested to find the response at elevated temperature and a sustained load). Three lap-shear specimens were prepared with each pair of beams. Although Beam no.5_25 and Beam no.6 were cured at 25°C for 7 days, Beam no.6_30 was cured at 30°C for 3 extra days, but the lap-shear specimens and the DMA specimens were cured at 25°C for only 7 days.

They were prepared at the same time as the beams, and were cured and conditioned in the O-105 chamber with the beams. The test specimens in the first series were fabricated from a 2mm steel plate for the inner plate with the mechanical properties shown in Table 4-4. The test samples for the second series were thicker and were made from 5mm plate taken from the web of the steel beams which had the material properties given in Table 4-2.

5.1.1 Lap-shear specimen preparation

The same surface preparation procedure in section 4.3.1 was used to prepare the steel plates. The steel plates were joined together on a level surface

approximately 1 mm apart, with a small pre-cut CFRP plate (25×55 mm), applied to each side. Figure 5-1 shows the dimensions of the lap-shear specimen used for the first and second test series.

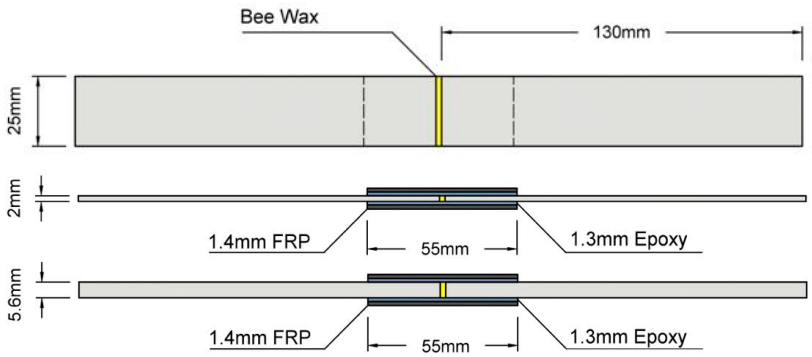

Figure 5-1: Front and side view of lap-shear specimens

First, the steel plates were positioned on the level surface using tape. To avoid filling the 1mm gap between the plates with adhesive (and to avoid direct end-to-end load transfer between the plates), one-sided sticky wax sheet was used. The adhesive that was used to bond the lap-shear specimens was taken from the same mix as used to strengthen the beams. The adhesive was spread over the steel plates and the CFRP plates, and the adhesive thickness was maintained by spreading a few glass beads of 1.3mm in diameter over the joint area. The pre-cut FRP plates were marked at the centre, and they were aligned with the gap. At this stage, the two steel plates were joined on one side, to avoid any FRP plate movements and ensure the bond thickness the sample was covered with cling film and light metal weights placed over the joint. The strengthening of the reverse side was carried out a few hours after curing the first side at laboratory temperature. Due to the limited pot life of Sikadue-330, the same mixed adhesive could not be used for the opposite side therefore freshly mixed adhesive was used. To ensure the quality of the mixture the same scale was used and mixing procedure was followed. Then the lap specimens left to cure for a few hours before finally placed in the O-105 heating chamber for the same period to cure with the beams.

5.1.2 Lap-shear test procedure

Before the testing, the excess adhesive was removed from the edges and the CFRP plate ends using a file to achieve a uniform plate ending in all the samples. The same universal hydraulic tension machine Instron 600LX was used to load the specimens as in section 4.6.3. The samples were carefully aligned between the grips and tested under displacement control with a loading rate of 1mm/min at ambient temperature, and the load and extension data were recorded.

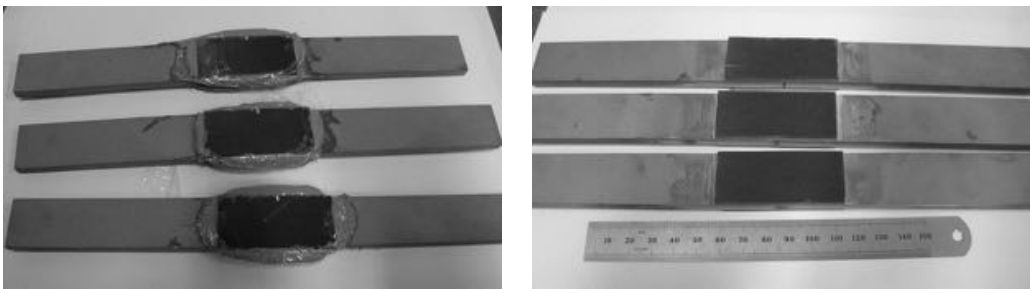

Figure 5-2: Prepared and ready to test double lap-shear specimens

5.1.3 Lap-shear test results

The results from the two series of double lap-shear test are shown in Figure 5-3. The extension of the Instron 600LX was normalised for the comparison purposes. The normalised extension was the relative movement of the crosshead of the Instron 600LX; this extension includes both strain in the steel plates and the shear strain of the adhesive joint if there was any.

The first series of lap-shear samples failed due to yielding of the inner steel plates. This was not intended, and consequently the influence of curing could not be examined using these 2mm thick steel plates. The load-extension response Figure 5-3 confirms that there was a plastic deformation in the lap-shear samples, which was related to the steel yielding, and there was no adhesive failure. Calculating the yield strength using the material properties from chapter 2 confirms that this was the yield capacity of the plates in the lap-shear specimens.

The thickness of the plates in the second series of lap-shear tests was consequently increased to 5mm. These showed better performance, and the influence of curing could be examined. The load-extension response is presented in

Figure 5-3, and a summary of the test results is shown in Table 5-2. The samples cured at 50°C showed an increase of approximately 29% of the total load capacity compared to those cured at 30°C. The failure for this second series of lap-shear tests was at the interfaces between the adhesive and adherend (adhesion failure), and it was a brittle failure. Although digital image correlation DIC was set up to measure the slip displacement, due to the nature of the failure, no slip was measured. This may be related to the very small amount of shear strain within the adhesive layer due to the brittle behaviour of the adhesive used, and the limited deformation cannot be measured using DIC.

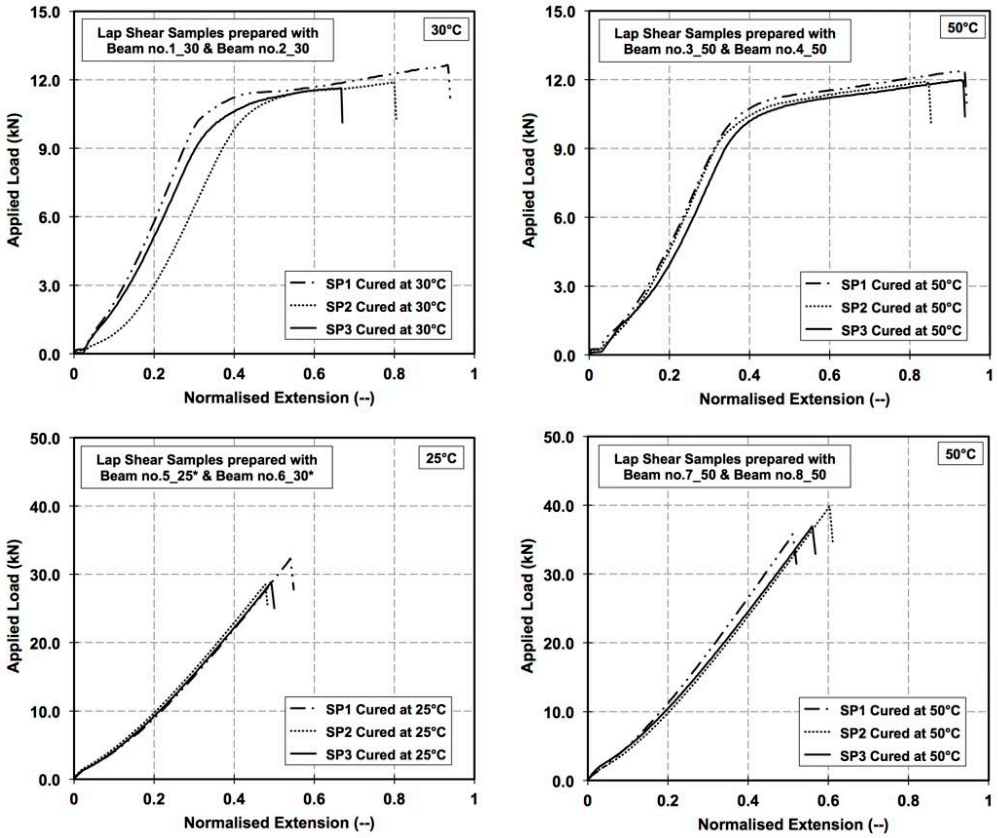

Figure 5-3: Lap-shear test results for the first and second series

Table 5-1: The first series lap test results

		The first lap-shear test series				
Beam no.	***Sample No.***	***Width, w***	***Length, L***	***Area***	***Max. Load***	***Average Strength***
		mm	***mm***	***mm²***	***N***	***MPa***
Beam no.1_30	**SP1**	25.1	27.1	680	12648	9.3
Beam no.2_30	**SP2**	24.4	27.3	666	11756	8.8
	SP1	24.7	25.9	640	11629	9.1
					Avg ± SD	***9.1 ± 0.2***
Beam no.3_50	**SP1**	24.4	26.7	651.48	12365.59	9.49
Beam no.4_50	**SP2**	24.0	27.0	648.00	11934.35	9.21
	SP1	23.9	26.1	623.79	11980.79	9.60
					Avg ± SD	***9.4 ± 0.2***

Table 5-2: The second series lap test results

		The second lap-shear test series				
Beam no.	***Sample No.***	***Width, w***	***Length, L***	***Area***	***Max. Load***	***Average Strength***
		mm	***mm***	***mm²***	***N***	***MPa***
Beam no.5_25	**SP1**	25.1	27.2	683	32266	23.6
Beam no.6_30	**SP2**	24.8	25.6	634	28418	22.4
	SP1	25.5	25.2	643	28873	22.5
					Avg ± SD	***22.8 ± 0.6***
Beam no.7_50	**SP1**	24.7	24.6	608	35648	29.3
Beam no.8_50	**SP2**	24.9	26.6	662	39858	30.1
	SP1	24.7	25.9	640	36889	28.8
					Avg ± SD	***29.4 ± 0.5***

5.2 Dynamic Mechanical Analysis DMA tests

DMA specimens were made to characterise the glass transition response of the adhesive in the strengthened beams. Sets of three samples were tested in single cantilever configuration for each pair of beam specimens.

5.2.1 DMA specimen preparation

The DMA specimens were prepared following the same procedure in section 3.3.2. The sample pre-test preparation was as detailed in section 3.4.1.

5.2.2 DMA specimen test procedure

The DMA testing equipment in section 3.4 was used, with the settings described in section 3.4.6. DMA was used to study the storage modulus variation with variation of temperature variation, and it can be used to determine mechanical

properties such as flexural modulus of thin plates at ambient temperature. However, this procedure requires attention and adjustments to the testing equipment such as, complete detachment of the heating chamber. Although attempts were made to carry out at 23±2°C (room temperature) according to ASTM D4065-01 (2001); ASTM D0293-02 (2002), the temperature could not be controlled easily.

5.2.3 DMA test results

The glass transition response is shown in terms of storage modulus variation with temperature for each set in Figure 5-4. Figure 5-5 shows normalised and averaged storage modulus, loss modulus, and tan δ for three of the tested samples in single cantilever fixture. The shaded area in Figure 5-5 is the test variation in the sample sets and shows that the difference was not significant. The glass transition temperatures, T_g recorded according to different characterisation methods are summarised in Table 5-3. The average glass transition temperatures, T_g of three samples according to peak loss modulus for the Beam no.1_30 and no.2_30 (cured at 30°C for 7 days) was 57.9°C, and the glass transition temperatures, T_g of Beam no.3_50, Beam no.4_50, Beam no.7_50, and Beam no.8_50 (cured at 50°C for 7 days) was 75°C. The glass transition temperatures, T_g of Beam no.5_25 and Beam no6_30 (cured at 25°C for 7 days) was 53°C. To achieve the same value of glass transition temperatures, T_g Beam 6 was cured extra 3 days at 30°C, assuming that Beam 6 reaches the same cure as Beam 1 and 2. The values in this section were in agreement with the ones given in chapter 2. This shows that adhesive at the joint cured in chamber O-105 reached the same cure as in the specimens cured in a small oven for the same temperature. The normalised storage modulus variation with temperature from the single cantilever mode tests in Figure 5-5 are in agreement.

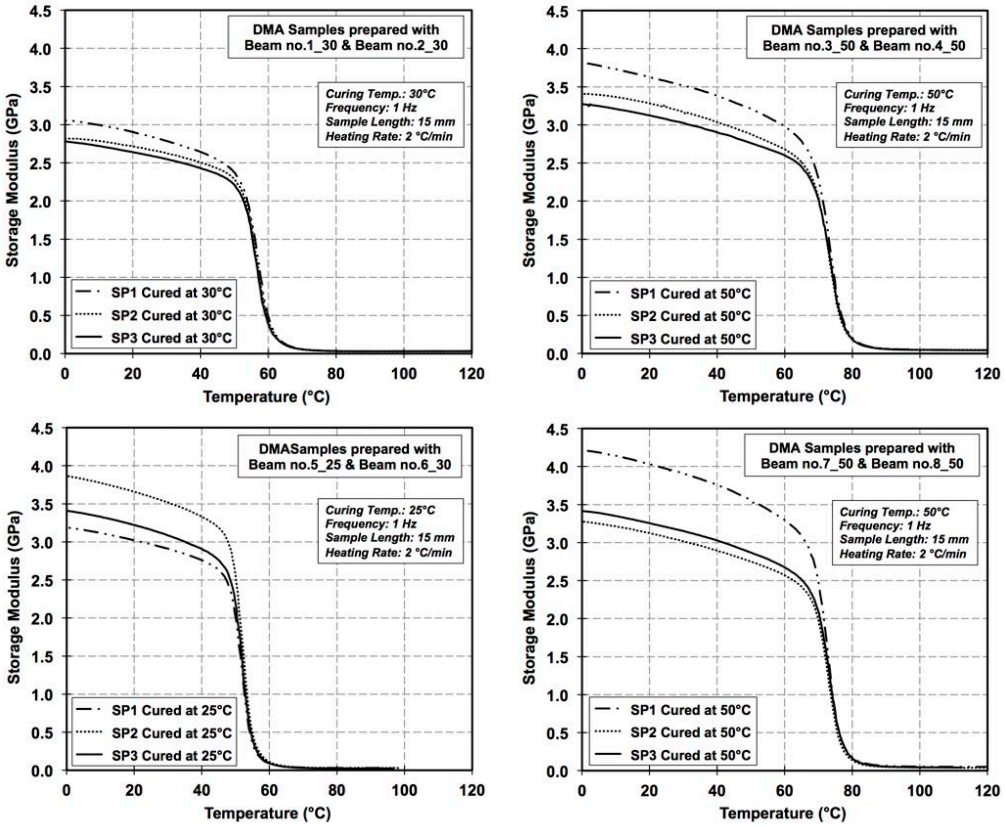

Figure 5-4: DMA coupon results for different beam cure conditions in single cantilever fixture

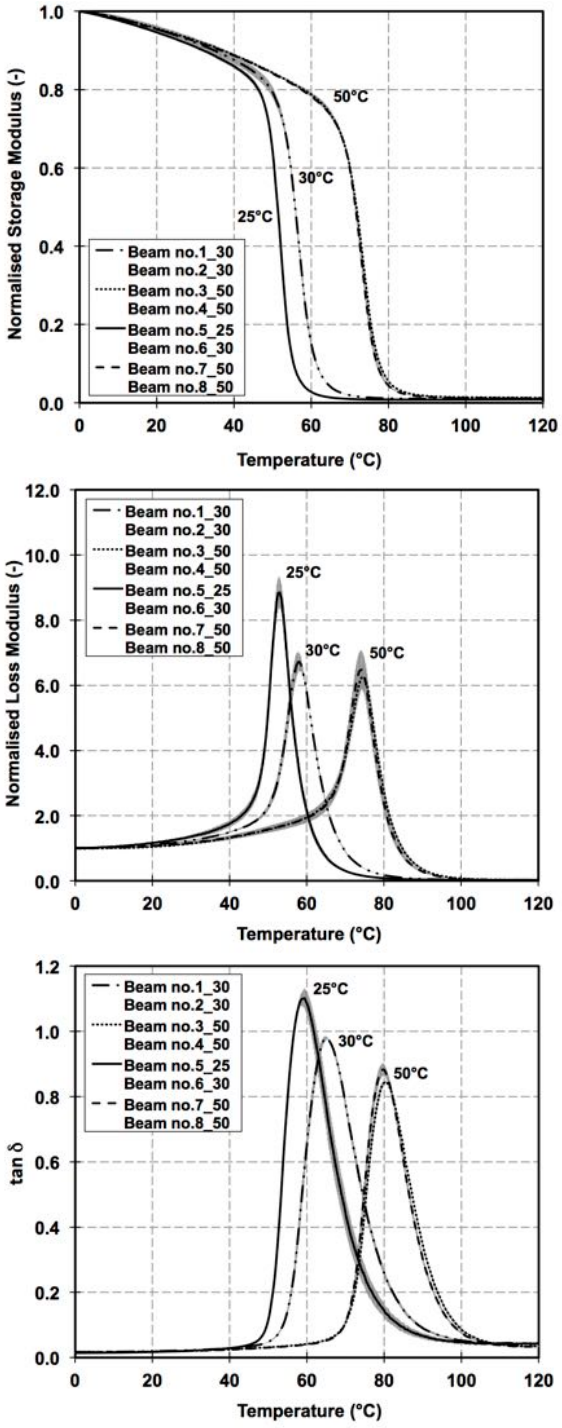

Figure 5-5: Normalised storage and loss modulus and tan δ for the DMA results in Figure 5-4

Table 5-3: Recorded T_g for the DMA coupons prepared with the beams.

Beam no.	*Sample No.*	*Recorded T_g in °C with different methods*				
		Peak Loss Modulus	*Inflection Point*	*Peak tan δ*	*Onset Logarithmic Scale*	*Onset Normal Scale*
Beam no.1_30 Beam no.2_30	**SP1**	58.3	57.5	65.2	54.6	52.2
	SP2	57.8	57.6	65.2	54.2	51.6
	SP3	57.6	56.8	64.8	54.3	52.1
	Avg ± SD	***57.9 ± 0.29***	***57.3 ± 0.36***	***65.1 ± 0.19***	***54.4 ± 0.17***	***52.0 ± 0.26***
Beam no.3_50 Beam no.4_50	**SP1**	74.7	74.8	80.6	70.7	67.4
	SP2	74.4	73	80	70.9	67.3
	SP3	74.5	75	80.5	71	66.7
	Avg ± SD	***74.5 ± 0.12***	***74.3 ± 0.9***	***80.4 ± 0.26***	***70.9 ± 0.12***	***67.1 ± 0.31***
Beam no.5_25 Beam no.7_25	**SP1**	52.8	52.3	58.4	50.3	47.7
	SP2	53.1	50.8	59.4	50	48.1
	SP3	52.9	52.2	59.5	50.3	48.2
	Avg ± SD	***52.9 ± 0.12***	***51.8 ± 0.68***	***59.1 ± 0.5***	***50.2 ± 0.14***	***48.0 ± 0.22***
Beam no.7_50 Beam no.8_50	**SP1**	73.9	73.6	79.4	70.6	66.9
	SP2	73.8	73.1	79.6	70.7	67.3
	SP3	74.2	73.4	80.2	70.8	67.5
	Avg ± SD	***74.0 ± 0.17***	***73.4 ± 0.21***	***79.7 ± 0.34***	***70.7 ± 0.08***	***67.2 ± 0.25***

It should be noticed that presented values in the manufacturers data sheet for each of the flexural modulus and Young's modulus were 3.8 and 4.5 GPa. Young's modulus is obtained from the direct tensile test, and it is the slope of the stress-strain curve in the elastic region under direct tensile test. The presented values in the manufacturers data sheet for each of the flexural modulus and Young's modulus were 3.8 and 4.5 GPa (cured for 7 days at +23°C refer to Table 4-2), and were found according to the DIN 53452, which is equivalent to ASTM D0293-02 (2002); EN ISO 178 (2003).

5.3 Pull-off adhesion tests

Pull-off adhesion tests were used to check the quality of the surface preparation of the steel beams, according to the recommendations given in Cadei *et al.* (2004). A series of three pull-off samples were prepared for each beam after the grit blast and after applying the FRP plates to the soffit of the steel I sections. A pull-off adhesion tester, Elcometer-506 (2015), as used. The test method was according to ASTM standard (ASTM D4541-02, 2002; ASTM D7234-12, 2012), using 25mm diameter aluminium pull-off stubs provided by the manufacturer, which were intended for the moderate operating range of 2-25 MPa.

The pull-off stubs were placed close to the tip of the FRP plates, as the critical area. A few glass beads of 1.3 mm in diameter were added to the adhesive layer to ensure a uniform thickness of the adhesive and the pull-off stubs were levelled. The testing was carried out after the beams and the pull-off stub specimens were cured. Before testing, the excess adhesive around the pull-off stubs was cleaned using the cutter tool provided by the manufacturer. The experiments were carried out at room temperature.

Precise values could not be measured for the test because none of the pull-off stubs separated from the beam; in fact, the pull-off stubs were being damaged at the grips with the tester. Nevertheless, the test results indicated that sufficient surface preparation was achieved and the bond strength was > 25 MPa.

While it has not been possible to provide definite answers to the pull-off tests using 25mm diameter pull-off stubs, a separate set of pull-off tests were carried out using a 200 mm length section of the tested beam and undertaking the same surface preparation procedure as before, but 14.2 mm diameter pull-off stubs introduced to increase the applies stress by a factor of two (up to 50 MPa). These samples were prepared and cured at different temperatures for seven days then tested using the same instrument and procedure. A significant amount of discrepancy was recorded in the results. This is understood to be due to brittle nature of the studied adhesive as it was noticed in section 5.1, and de Castro and Keller (2008) also the impact glass beads that possibly caused failure at different loading levels.

5.4 Overview of the flexure test methodology

This section describes testing configuration and test set-up section 5.4.1. The test monitoring instruments are summarised in section 5.4.2. Chamber O-105 that was used to cure the beams and the small specimens were used in testing the specimens at ambient temperature and elevated temperatures.

5.4.1 Testing configuration and set-up

Mechanical loading in four-point bending was applied using 60-tonne hollow jack RCH-606 (Enerpac, 2014), which was attached to the crosshead of the Avery 7104 universal testing machine in inverted position as shown in the testing

test set-up diagram Figure 5-7. The load was applied to a specially designed and manufactured load extension shaft and to the spreader beam via an opening in the top O-105 thermal chamber. The spreader beam was a 1.2 m (UC 203 ×203×60) stiffened at the point loads and the extension shaft was a 60 mm solid high strength rod. A pin support was located between the extension shaft and the spreader beam, while at the bottom of the spreader beam two rollers (700 mm apart) were welded on to load the test beam via a 200×65 mm grooved high strength steel block acting as a pin support under each roller. The spreader beam configuration allowed the beams to behave in simply supported manner. The details of the spreader beam and the test beam loading point are illustrated in the Figure 5-6.

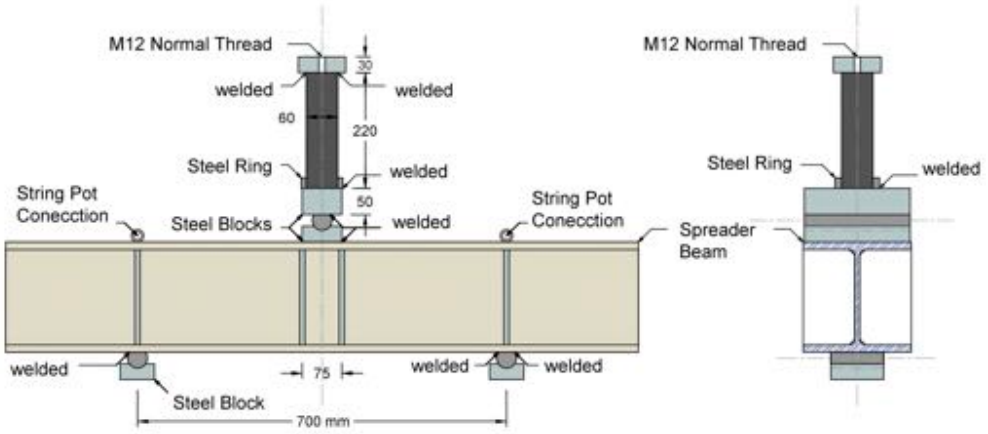

Figure 5-6: Spread beam and extension loading shaft details

An Enerpac hydraulic system was assembled for this project. The 60-tonne cylinder RCH-606 (Enerpac, 2014) was connected to a 25-tonne cylinder RC-2510 (Enerpac, 2014) using high-pressure hydraulic hoses 700-Series (Enerpac, 2014). Hydraulic pressure was introduced to the system by loading the 25-tonne cylinder using an Instron 8800 250kN actuator. The benefit of the system was that the load and displacement could be precisely controlled using the Instron actuator during the testing period. The actuator was kept away from the heated test area. A pressure transducer (PX3O9-1OKG) with operation range 0-69 MPa (Omega-dyne Inc, 2012) was also included in the hydraulic pipeline at the 60-ton hollow jack end to measure the net pressure at that end.

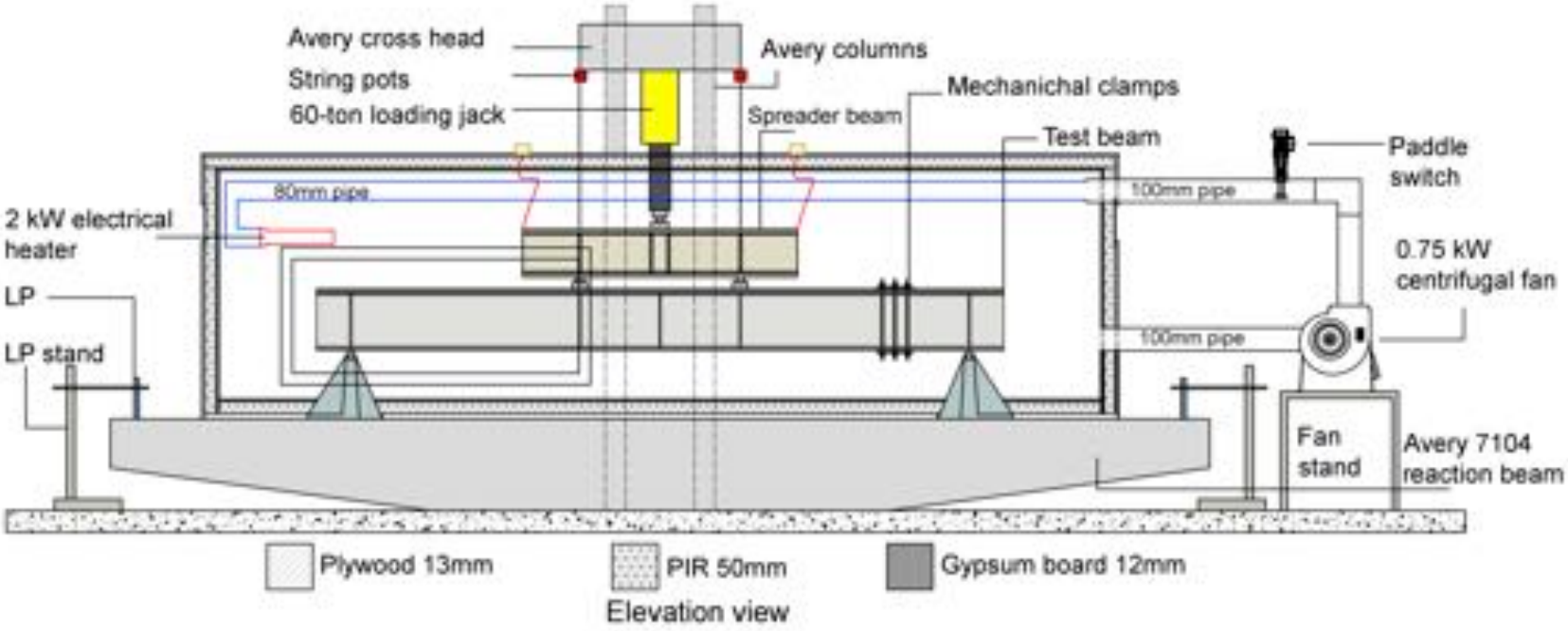

Figure 5-7: Schematic diagram of the test set up during ambient and transient tests

5.4.2 Monitoring instrumentation

The temperatures on the test beam were recorded using the same thermocouples and instrumentation that were used during curing (section 5.6.2). The deflection of the test beam at the loading points was measured using cable-extension potentiometer transducers PT1A, 500 to 10K ohm (Celesco Transducer Products, 2005), which were attached to the top flange of the spreader beam see Figure 5-6. A third cable-extension transducer was used to measure the settlement of the Avery 7104 reaction beam, and two further linear potentiometer (LP) displacement transducers were used to measure the Avery reaction beam settlement at the both ends, to check for any differential settlement of the reaction system refer to Figure 5-7.

The Instron actuator load, the hydraulic pressure (close to the 60-tonne cylinder), the deflections, and settlements were recorded using a Vishay 7000 data logging system at 10 Hz.

Digital Image Correlation (DIC) was used to measure the slip of the FRP plate at the ends where the windows in the thermal chamber were located. Figure 5-8 shows the location of the digital SLR cameras and the halogen lights during the test.

All the beams were reinforced using constant 1100 mm CFRP from the right half (far end), where the mechanical clamps were used to prevent any slippage. While the CFRP length were varied at the left half of the beam (monitored end). These lengths were 1100 mm for Beam no.1_30, 810 mm for Beam no.2_30-1, and 675 for the rest of the beams (Beam no.2_30-2, Beam no.3_50, Beam no.4_50, Beam no.5_25, Beam no.6_30, Beam no.7_50 and Beam no.8_50); refer to Figure 5-9 for more details. Failure of the adhesive joint at the remote end of the plate was prevented using mechanical clamps at 250mm from the right support, as illustrated in Figure 5-9. The same mechanical clamps were used in all the tests, and the details are shown in Figure 5-10. The test set-up and the instrumentation during the tests are shown in Figure 5-11.

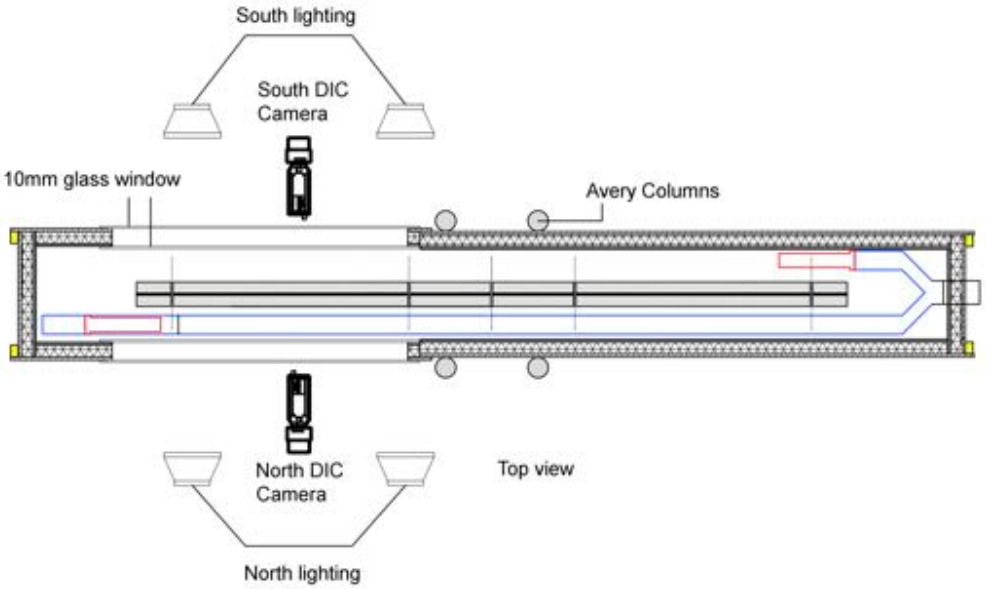

Figure 5-8: Location of the cameras and lighting during the test

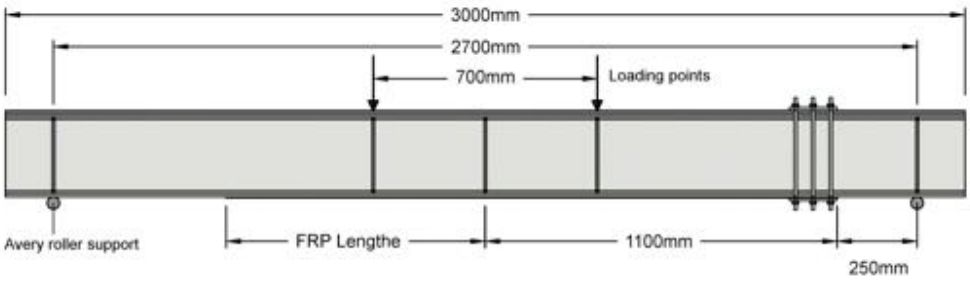

Figure 5-9: The CFRP bonded length

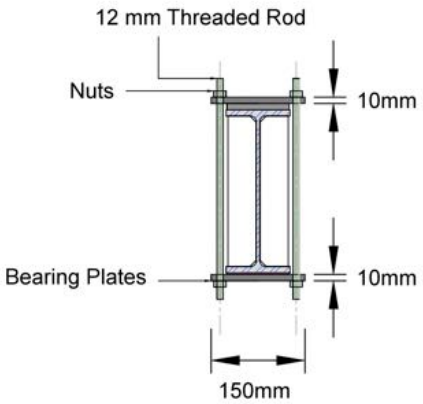

Figure 5-10: The mechanical clamp details

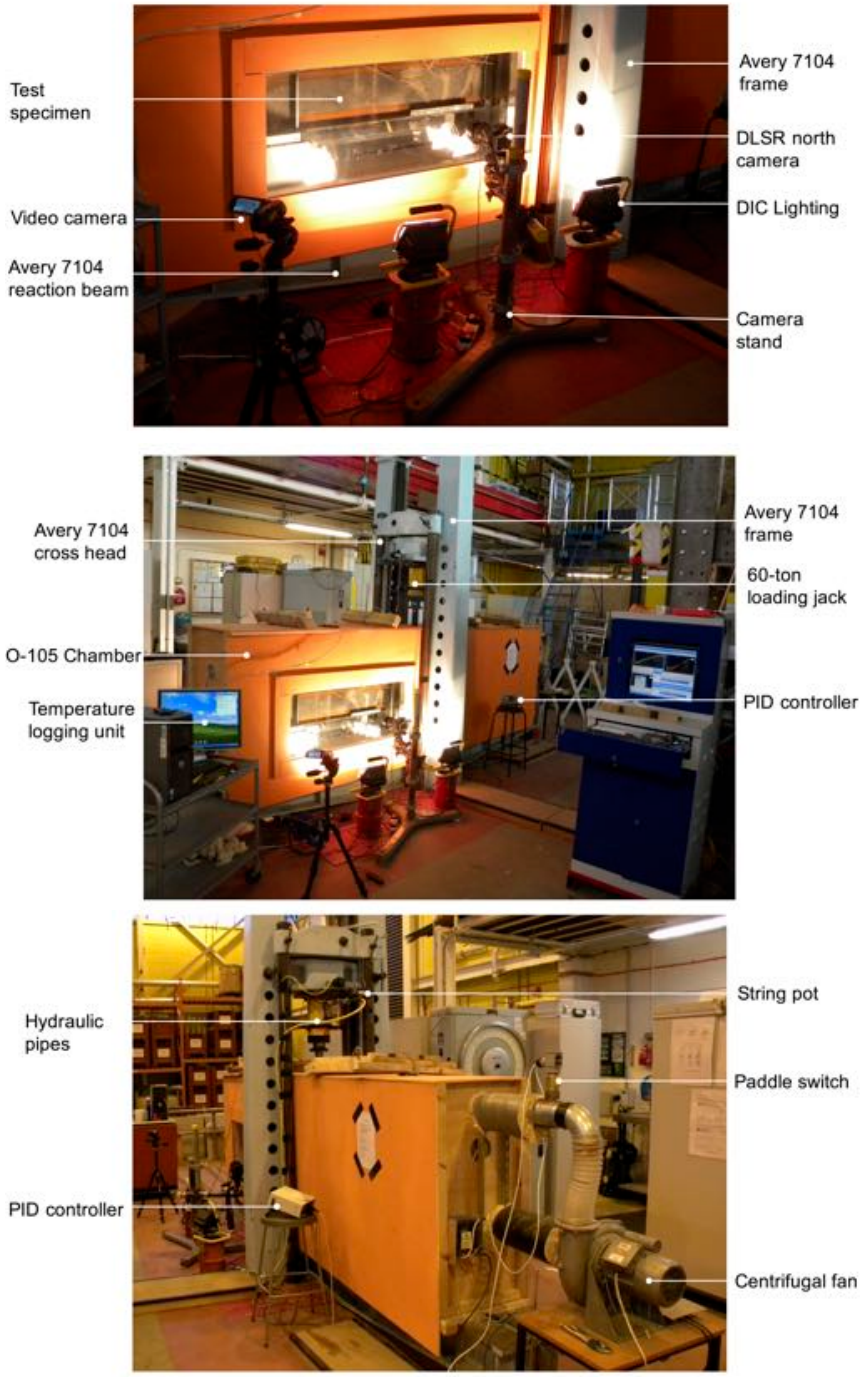

Figure 5-11: Photo of the flexural test set up

5.5 Ambient temperature beam tests

The aim of the ambient tests was to determine the effect of curing on the four-point bending flexural beam CFRP strengthened specimens and these tests were used to develop an ambient load test that failed due to debonding failure, which could then be used in the elevated temperature tests.

Six beams were tested to determine their ambient temperature capacity and behaviour, including an un-strengthened control specimen. The beams were cured at different elevated temperatures. Table 5-4 contains the curing temperature, CFRP bonded lengths, maximum load, and the corresponding deflection. The clear span of the beams was 2700 mm a with constant moment region of 700 mm.

Table 5-4: Four-point bending maximum load and corresponding deflection at the loading point at ambient temperature

Beam no.	*Curing Temp.*	*CFRP length/ span ratio*	*CFRP length* (mm)*	*Max. Load (kN)*	*Deflection at Max. Load (mm)*
Control beam	-----	-----	-----	408	57.63
Beam no.1_30	30°C	81.5%	1100	470	35.97
Beam no.2_30-1**	30°C	60%	810	406	18.66
Beam no.2_30-2	30°C	50%	675	402	20.08
Beam no.3_50	50°C	50%	675	447	24.44
Beam no.4_50	50°C	50%	675	474	31.04
Beam no.5_25*	25°C	50%	675	353	12.77
* FRP length is shown in Figure 5-9, which is only the left side (monitored end).					
** Beam no.2 was tested twice after reducing the FRP length by further 10%.					

The actual curing temperatures were recorded using eight T-type thermocouples (which have an accuracy of 1°C), for each specimen, and are shown in Figure 4-11. The recorded experimental curing temperatures were ±1.5°C from the targeted ones in Table 5-4.

The CFRP length/span ratio Table 5-4 is calculated only for the left side of the FRP strengthened beam (CFRP length/1350mm), and the right side FRP length remained 1100mm in all the tests refer to Figure 5-9.

The control beam and Beam no.1_30 were loaded in a constant displacement control at a rate of 0.46 mm/min, which resulted in an elastic loading rate of 12.51kN/min with the bespoke loading system. The relatively slow loading

required long testing period, therefore the rest of the specimens were tested in a higher rate at 0.8 mm/min, which resulted in an elastic loading rate of 25kN/min.

5.5.1 Load-deflection behaviour and failure modes

The flexural four-point ambient test results are presented in Figure 5-12. The maximum loads and corresponding deflections at the loading points are summarised in Table 5-4. All of the beams were tested to failure, except for Beam no.2_30, which was tested twice. Beam no.2_30 was the second beam cured at 30°C, and it was used to determine the effective length of CFRP plate experimentally. Figure 5-12 shows the load-deflection behaviour of the six beams that were tested at ambient temperature. A variety of failure modes were observed, Table 5-5 shows the mode of the failure for each specimen with the load capacity relative to the un-strengthened specimen. The details of the failure modes are addressed later in this section.

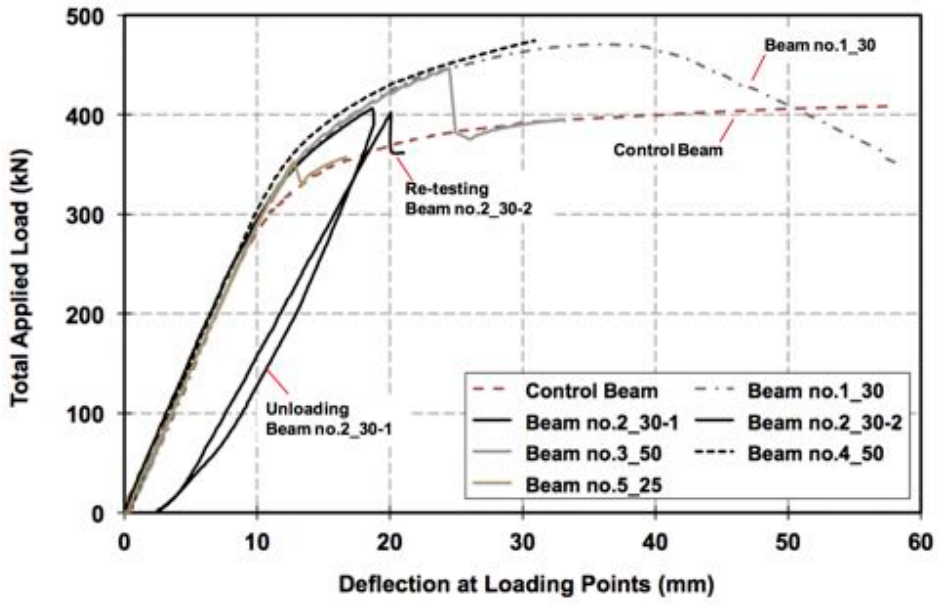

Figure 5-12: Four-point bending test load versus deflection (at the loading points) for the specimens tested at ambient temperature

Table 5-5: Four-point bending test failure mode at ambient temperature

Beam no.	***Normalised failure load (%)***	***Normalised ultimate displacement (%)***	***Failure mode***
Control beam	100.0	100.0	Yielding bottom flange
Beam no.1_30	115.2	62.4	Inelastic Buckling following top flange yielding
Beam no.2_30-1	99.5	32.4	Test manually terminated to test the specimens for the second time
Beam no.2_30-2	98.5	34.8	Debonding at the steel-adhesive interface
Beam no.3_50	109.6	42.4	Debonding at the steel-adhesive interface
Beam no.4_50	116.2	53.9	Test manually terminated, the specimens reached its buckling capacity
Beam no.5_25*	86.5	22.2	Debonding at the steel-adhesive interface

The general observation from Figure 5-12 is that the responses were linear up to 300kN, where the beams started to yield. The initial load-deflection responses for all the beams were similar to the un-strengthened beam; there was no significant increase in the initial stiffness of the samples because of the relatively small contribution of the CFRP to the section stiffness (due to the relatively low Young's modulus of the CFRP and small CFRP to steel area ratio). However, a substantial increase in stiffness can be noticed beyond 300kN, once the steel section starts to become plastic, up to failure, compared to the control beam. The post-elastic stiffness and ultimate load carrying capacity increase of the strengthened beams was due to the applied CFRP plates. The load-deflection and the failure mode results are discussed for each specimen.

The control beam

To determine the performance of the un-strengthened section only one beam was tested without CFRP. The control beam test, the response was linear up to 300kN, when yielding of the bottom flange occurred, and the stiffness gradually reduced. The test terminated at a maximum deflection of 57 mm recorded and a load of 408kN, which was 18% higher than the theoretical ultimate load capacity (350kN) of the section. This was due to the contribution of the strain hardening that was not counted for in the theoretical calculation. The results of this test were in agreement with the tests that were carried out Byfield and Dhanalakshmi (2002); Byfield *et al.* (2002).

Figure 5-13 shows the control beam after testing; the permanent lateral distortion of the top flange after the beam had experienced a large vertical deflection. The

sideways distortion was in the constant moment region. It was noticed that under one of the loading plates the top flange distorted locally, and it is believed that this caused the side way movement. A close inspection of the beam was carried out; there was no other damage to the beam. It is crucial to mention that the presence of the stiffeners at the concentrated points was the main reason for the stable behaviour and led the beam to fail without global buckling.

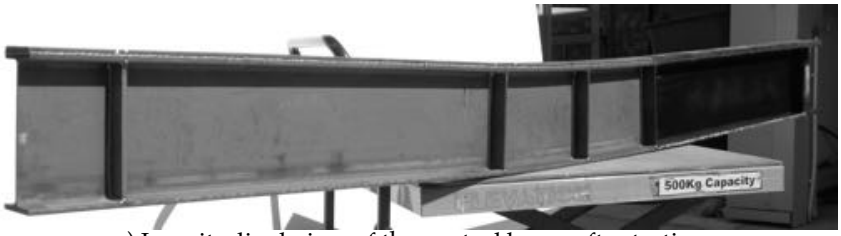

a) Longitudinal view of the control beam after testing

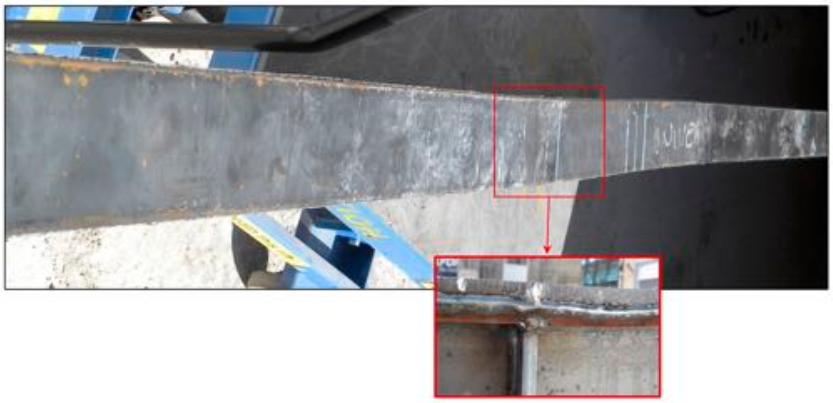

b) Top view of the of the control beam after testing with the distorted top flange

Figure 5-13: Control specimen after testing

Beam no.1_30

It was reinforced with a 2200mm CFRP plate, which was 81.5% of the clear span of the beam, as shown in Figure 5-9. The linear load-deflection response (refer to Figure 5-12) is similar to the control. The stiffness reduction after 300kN is much less than the control beam. The deflection recorded at 408kN was approximately 18mm, whereas the control beam exhibited over 57mm for the same load. The maximum load was 474kN, which is much higher than the predicted elastic buckling load 412kN without the stiffeners. Details of the load prediction calculation are given in chapter 6.

The CFRP strengthening resulted in a 17.5% increase in the failure load compared to the un-strengthened beam. The beam failed due to inelastic lateral-torsional buckling after local yielding of the top flange under one of the loading plates. The two welded stiffeners at the same loading point were significantly damaged and failed differently. On one side the stiffener detached from the flange. On the other side the stiffener was buckled. The tested beam and the localised damage are shown in Figure 5-14.

Further inspection of the specimen was carried out, and in several areas, where the stiffeners were attached to the web, cracks were found. It is believed that there was a lack of welding penetration and pre-welding surface preparation.

Due to the intensive distortion of the steel section and non-uniform stress in the CFRP plate, only one edge of the plate was ruptured locally in as shown in Figure 5-14.

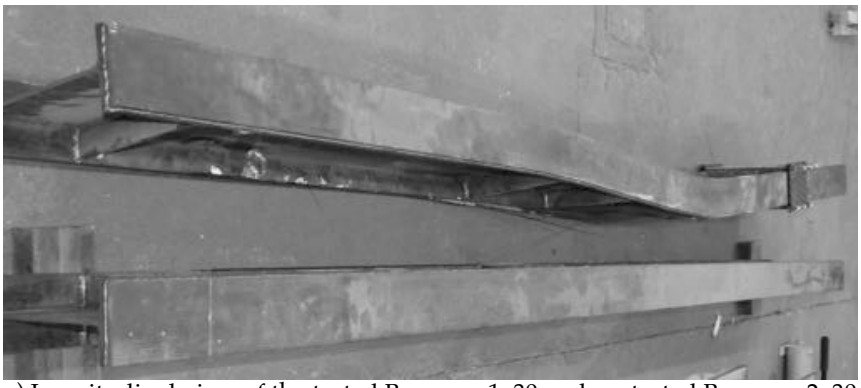

a) Longitudinal view of the tested Beam no.1_30 and un-tested Beam no.2_30

b) Top view of the of the control beam after testing with the distorted top flange

c) CFRP locally damaged on one edge

Figure 5-14: Beam no.1_30 after testing and local damages to the specimen

The design procedure Cadei *et al.* (2004) followed to estimate the maximum failure load. The experimental data of the lap-shear tests were used to extrapolate the failure load. Since the design equations are theoretically driven using simplified approaches, and the failure of the lap-shear was yielding of the steel inner plate, the maximum debonding failure load prediction was under estimated. To achieve debonding failure, the CFRP length was to be determined experimentally. Therefore,

Beam no.2_30, which was identical to Beam no.1_30, was used to determine the effective FRP plate length, and it required the plate length to be adjusted.

Beam no.2_30

This specimen was the only specimen that was loaded twice. In the first loading cycle (Beam no.2_30-1), the CFRP length was reduced to 60% (810 mm) of the original beam 1 length at the monitored end. The specimen was loaded up to the failure load of the control specimen (406kN). Debonding did not occur and the test was terminated because at this loading stage the specimen did not exhibit a large permanent deflection. However, Figure 5-12 shows permanent deflection of 2.6mm approximately. The specimen was examined after the test and some weld cracks at the stiffener-web connections were noticed. To reduce the risks of any local failure (at the point of stiffener detachment), the cracks were re-welded. Care was taken to carry out the essential repair without heat damage to the epoxy layer.

The length of the monitored end of the CFRP was reduced by a further 10%, so that the monitored end of the plate terminated 675mm from the centre of the beam, and the remote end terminated 1100 mm from the centre of the beam. The specimen was loaded for a second time to failure (Beam no.2_30-1). The load-deflection response for both cycles is presented in Figure 5-12 and the maximum load and corresponding deflection are given in Table 5-4. It can be noticed from the load-deflection that in the second cycle the beam behaves linearly up to the previous loading level (first cycle). The failure of Beam no.2_30-2 was due to debonding at the adhesive-steel interface. There was no residue of adhesive on the steel surface, as shown in Figure 5-15. It can be noticed that there was a limited residue of a thin layer of adhesive at the tip of the plate end. Beam no.2 in Figure 5-15 is from here on referred to as Beam no.2_30-2.

The second test on Beam no.2_30 (Beam no.2_30-2) was a successful test because it failed by debonding and the effective FRP material was determined experimentally. This plate length was used in all subsequent tests (Beam no.3_50 to Beam no.8_50). The specimens Beam no.3_50 to Beam no.8_50 were CFRP strengthened in the same way that Beam no.1_30 was CFRP strengthened. All of the beams were strengthened with 2200 mm CFRP plate and cured, prior to testing. On the left-hand side, the CFRP plate was reduced to 675 mm, which was 50% of the

half-length of the beam. A hacksaw was used to cut through the CFRP plate and adhesive and avoid introducing plate end effect.

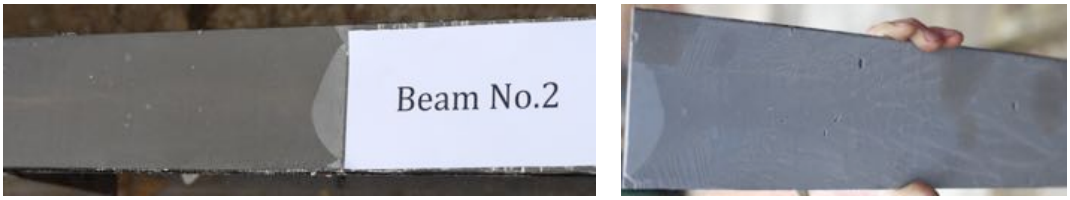

Figure 5-15: Beam no.2_30 after testing

Beam no.3_50 and Beam no.4_50

Beam no.3_50 and Beam no.4_50 were prepared and cured at 50°C (compared to 30°C for Beam no.1_30 and Beam no.2_30). Beam no.3_50 failed by debonding in a similar mode to Beam no.2_30-2, but in a more violent manner. Figure 5-16 shows the steel and adhesive surfaces after failure. The CFRP plate and adhesive separated violently. The adhesive surface was severely damaged and shattered. Since the CFRP plate hit the base of the O-105 chamber, cracks appeared though out the adhesive surface and at the edges the adhesive separated from the FRP plate see Figure 5-16. The shattered adhesive was collected at the base of the chamber. The maximum-recorded load was approximately 10% higher than the control beam, but the deflection at failure was 57.6% less. Loading was continued after debonding, and the load-deflection response after failure was in a good agreement with the control beam as shown in Figure 5-12. Beam no.4_50 was loaded to 474kN, which was slightly above the buckling load of Beam no.1_30. Debonding did not occur, and the beam did not fail at this load. The test was terminated manually due to safety reasons. There was risk of similar buckling as with Beam no.1_30, which could have damaged the O-105 chamber once again. Figure 5-17 shows CFRP plate ends for each of the deboned CFRP plate of Beam no.3 (Beam no.3_50) and un-deboned Beam no.4 (Beam no.4_50).

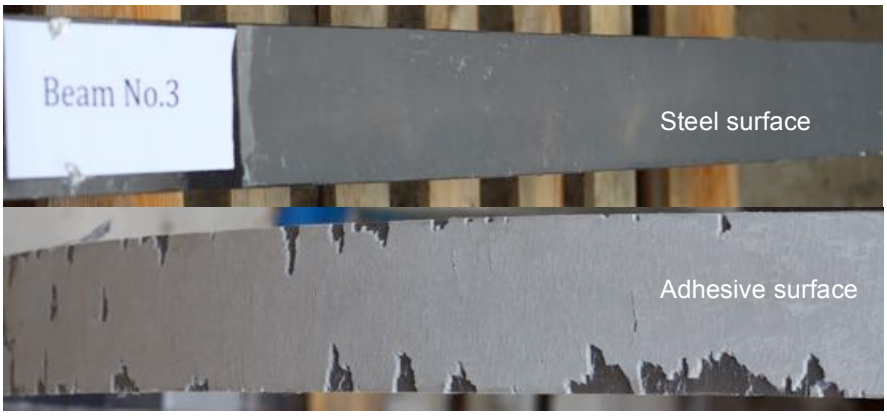

Figure 5-16: Beam no.3_50 after testing

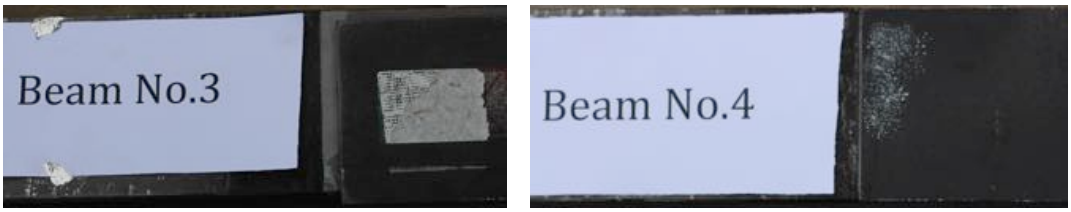

Figure 5-17: Beam no.3_50 and 4 plate tips after testing

Beam no.5_25

This specimen was cured at 25°C for 7 days. The aim was to cure Beam no.5_25 at 30°C similar to the Beam no.1_30 and Beam no.2_30. This is a clear example that even in a controlled environment accurate curing may not be achieved. It is possible to cure epoxy joints on-site at temperatures lower than the recommended curing temperature or not following the prescribed curing regime. 5°C less curing temperature may not be significant, but it affects the glass transition temperatures, T_g and the mechanical properties, which consequently affects the overall performance of the joints. The DMA results in Figure 5-4 showed relatively low performance with temperature variation, which lead to low glass transition temperatures, T_g.

Beam no.5_25 showed poor performance due to the low curing temperature, and debonding occurred at 353kN. The specimen was examined in detail, close to the central stiffener some voids were noticed in the adhesive layer, which may have triggered debonding failure from the centre. The steel surface remained clean after debonding, but at the void area near the centre of the specimens, as shown in Figure

5-18, some adhesive that was not attached to the CFRP plate during the FRP strengthening procedure remained on the steel surface.

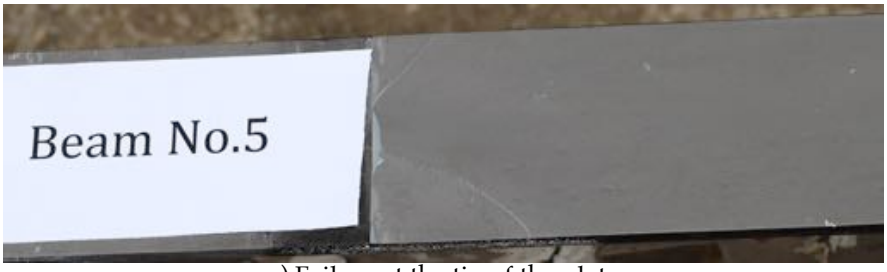

a) Failure at the tip of the plate

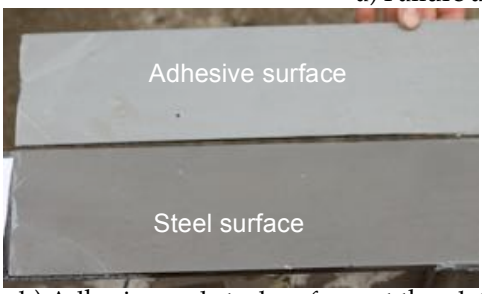

b) Adhesive and steel surfaces at the plate end

c) Adhesive layer void near the centre of the joint

Figure 5-18: Beam no.5_25 after testing

The ambient temperature loading tests showed that increasing the curing temperature enhances the performance of the strengthening elements. Figure 5-19 plots the increase in ultimate capacity with curing temperature. Using shorter CFRP plate (over 20%) and curing temperature of 50°C for Beam no.4_50, the same ultimate load capacity of Beam no.1_30 was achieved. This was with 81.5% CFRP plate and cured at 50°C.

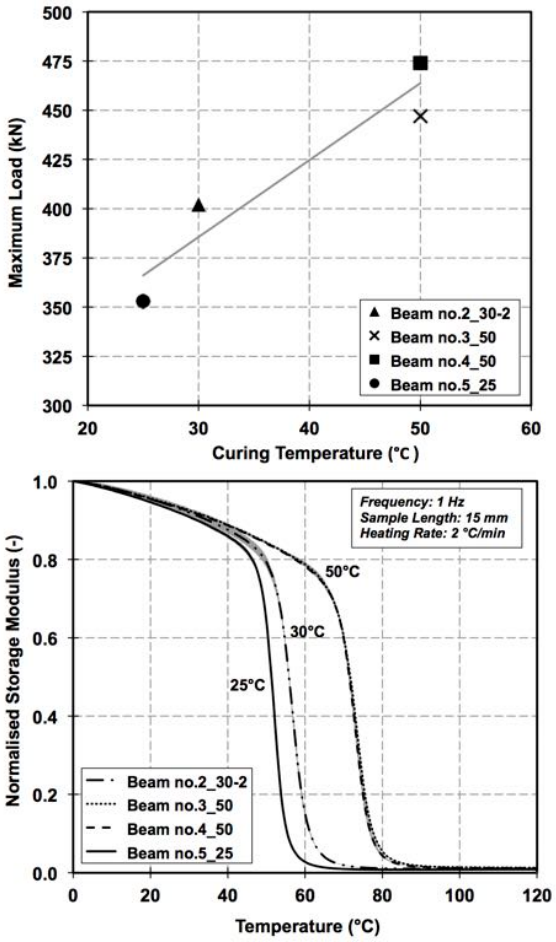

Figure 5-19: The relationship between failure load of CFRP strengthened beams and curing temperature and DMA specimens for the same cure in single cantilever configuration

5.6 Transient temperature tests

Three beams were tested under a combination of sustained load and transient increasing temperature. The tests examine the effects of curing temperature upon the elevated temperature performance of CFRP-strengthened beams. One of the beams was cured at 30°C, and the other two beams were cured at 50°C, and as shown in Table 5-6 all of the beams had the same lengths of CFRP plate (determined during the ambient temperature tests). The test configuration and the mechanical loading parameters remained the same as the ambient temperature tests.

The mechanical loading, thermal loading, and the deflection at the point loads of Beam no.6_30, Beam no.7_50, and Beam no.8_50 are shown in Figure 5-20. They were first loaded at a displacement rate of 0.8mm/min, before changing the loading method to load control. A sustained constant load of approximately 350 kN was applied. The temperature was increased at a rate of 0.8°C/min. When the CFRP plate was separated from the specimen, once again the beam was loaded under load control method. The same procedure was repeated for the three transient temperature tests. Beam no.6_30 was reloaded mechanically after approximately 75 minutes from the beginning of the test. Beam no.7_50 and Beam no.8_50 were reloaded mechanically after approximately 93 minutes from the beginning of the test. This is shown in Figure 5-20.

The aim was to increase the temperature at 1°C/min rate, but due to losses only rate of 0.8°C/min was achieved. Figure 5-20 are the average of eight thermocouples mounted on the beams in the locations shown in Figure 4-10. The recorded temperatures at the eight-thermocouple locations for each specimen are presented in detail in section 5.6.2. The sustained load was set to 350kN, which was the theoretical plastic moment of the section according to the steel coupon test results presented in section 4.5.3. From the ambient tests, it was found that at this load the FRP material is effective. The stiffness reduction due to the effects of temperature on the FRP strengthened specimens could be studied. The ambient tests Beam no.5_25 failed at 353kN. Generally, a real strengthening project would not be designed to carry service loads greater than the un-strengthened capacity of the beam.

The deflection of the control specimen at 350kN is reported in Table 5-6, the sustained loads and corresponding deflections of Beam no.6_30, Beam no.7_50, and Beam no.8_50 are also presented. The sustained load for Beam no.6_30, Beam no.7_50, and Beam no.8_50 were reached after approximately 14 minutes from the beginning of the test. The heaters were switched on when the targeted sustained load 350kN was achieved.

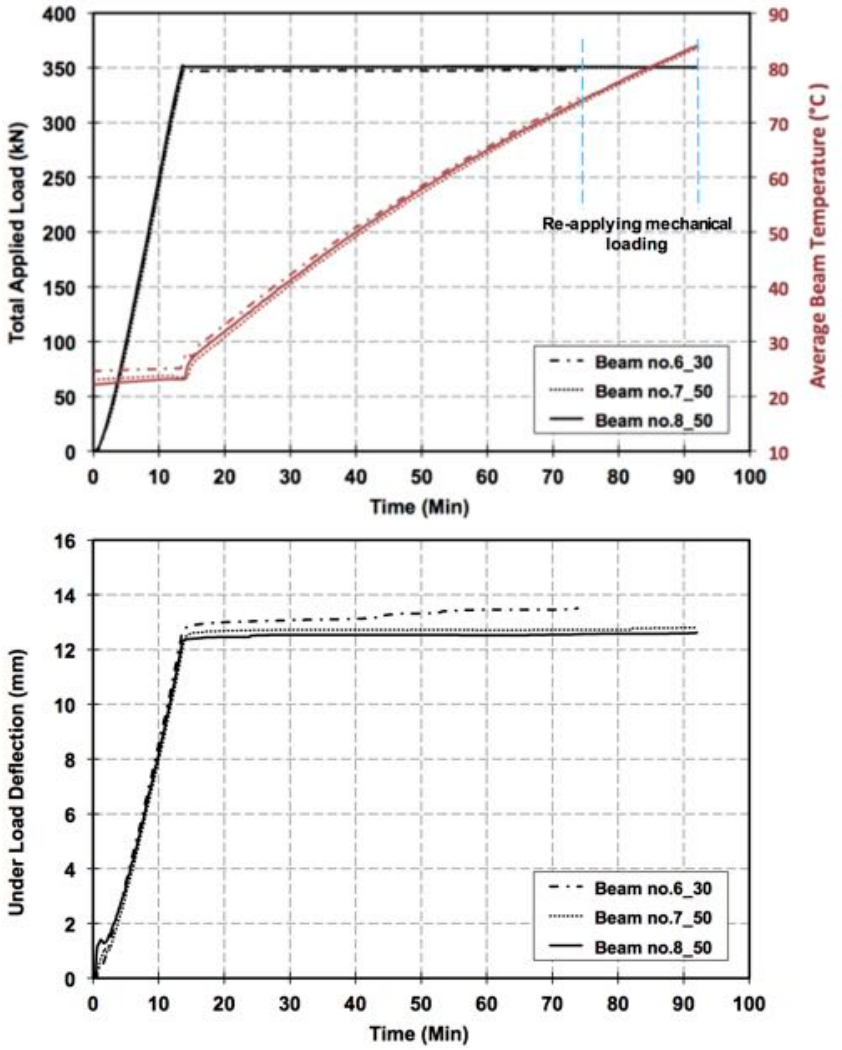

Figure 5-20: Mechanical loading and thermal loading during the test (top figure), and the point load deflection up to the ends of heating (bottom figure) for Beam no.6_30, Beam no.7_50, and Beam no.8_50

Beam no.6_30 was the first transient temperature test, and the sustained load was slightly (0.9%) below the targeted load. This was because the load dropped when the Instron settings were changed from displacement control to load control. Beam no.7_50 and Beam no.8_50 were loaded 2kN higher to allow for the reduction that occurred during the setting change over.

Table 5-6: Four-point bending sustained load and corresponding deflection at the loading point for tests conducted under transient increasing temperature

Beam no.	***Curing Temp.***	***CFRP length/ span ratio***	***CFRP length* (mm)***	***Sustained Load (kN)***	***Deflection at Sustained Load (mm)***
Control Beam	-----	-----	-----	350	16.05
Beam no.6_30**	30°C	50%	675	347	12.78
Beam no.7_50	50°C	50%	675	351	12.44
Beam no.8_50	50°C	50%	675	351	12.35
* FRP length is shown in Figure 5-9.					
** Beam no.6 was prepared with Beam no.5_25 and cured at 30°C for extra 3 days (see Figure 4-11)					

5.6.1 Load-deflection behaviour

The load-deflection behaviour of the three tested beams (Beam no.6_30, Beam no.7_50, and Beam no.8_50) under transient temperature and sustained load are shown in Figure 5-21. The load-deflection behaviour of the control specimen at ambient temperature is also shown in Figure 5-21 as a comparison. It can be seen that the responses were linear up to 300kN, where the beam starts to yield.

The maximum loads and corresponding point load deflections after 14 minutes are summarised in Table 5-6. The failure mode of the transient tests is discussed in section 5.6.4.

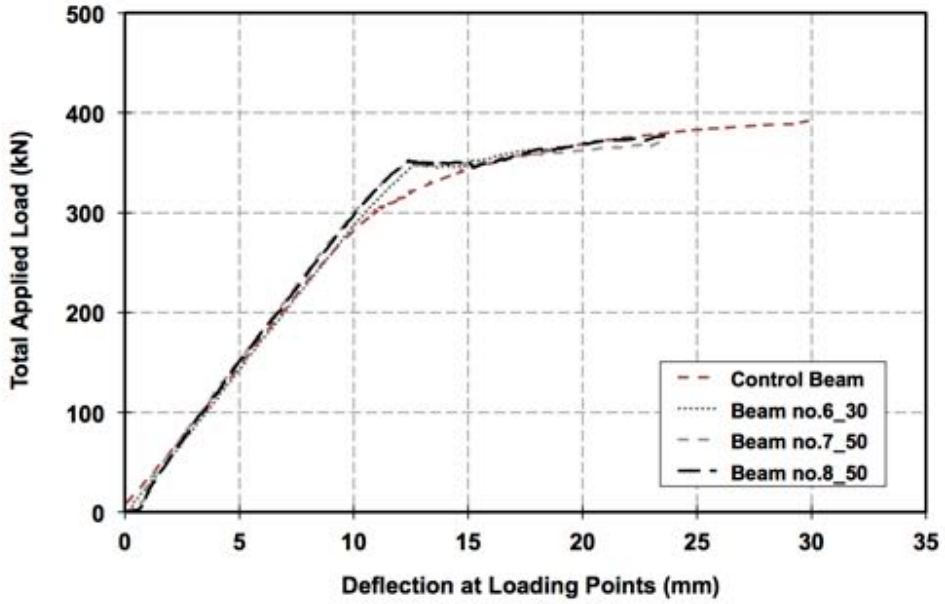

Figure 5-21: Four-point bending test load versus deflection (at the point loads) for the specimens Beam no.6_30, Beam no.7_50, and Beam no.8_50 and the control specimens.

Thermal loading continued until the deflection of the specimens reached approximately 16 mm and remained constant, where the FRP material was not effective any longer. During the heating phase the specimens exhibited deflection of approximately 3.5 mm, compared to the deflection values prior to the thermal loading in Table 5-6. The increase of beam deflection during the thermal loading was due to the reduction in the adhesive stiffness, which leads to slippage of the CFRP plate as the composite action was reduced. The specimens were then loaded mechanically as mentioned in section 5.6. It can be noticed that the tested beams follow the control beam after the complete separation of the CFRP plates. The deflection of the beams under the point loads during the thermal loading is discussed in section 5.6.4.

5.6.2 Testing temperature

As for the specimen temperature, the thermocouples marked, as TF, W, and BF were located at the top flange, web, and bottom flange respectively. Thermocouple BF1 was located at the tip of the plate, while the thermocouples BF1 to BF6 were attached along the bottom flange at 100mm intervals from each other

towards the centre of the specimen. The temperatures of the specimens during the test were recorded using the same thermocouples (T-type) and instrumentation (Picotech, 2016) used in the curing process. The variation in beam temperatures was relatively small because of the high thermal conductivity of steel. It was noticed the temperatures recorded from thermocouples (top flange) TF and (web) W were slightly higher than the (bottom flange) BF1 to BF6. This was because there was some radiation influence from the halogen lights used for DIC. Due to some technical issues the air temperature for Beam no.8_50 could not be recorded from the beginning of the test. The beam temperature during the test increased at an average of 0.8 °C/min. The right-hand side of the Figure 5-22 and Figure 5-23 is the average of the eight thermocouples and standard deviation.

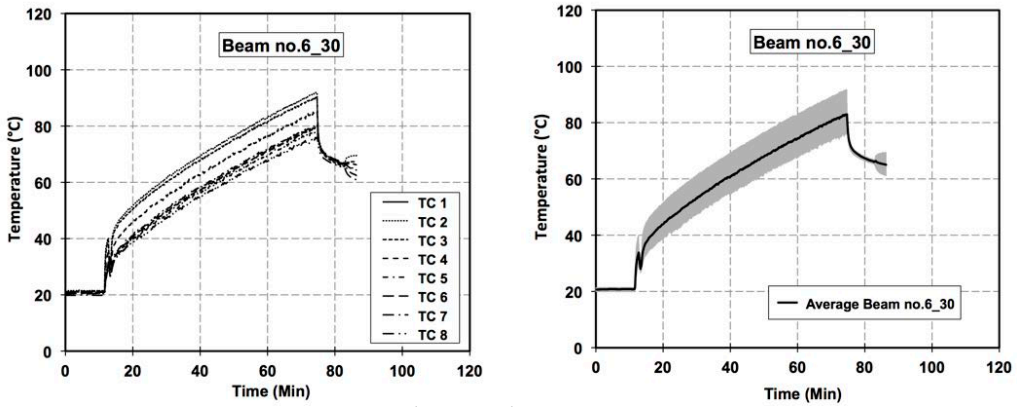

a) Air temperature of O-105 thermal chamber during testing Beam no.6_30

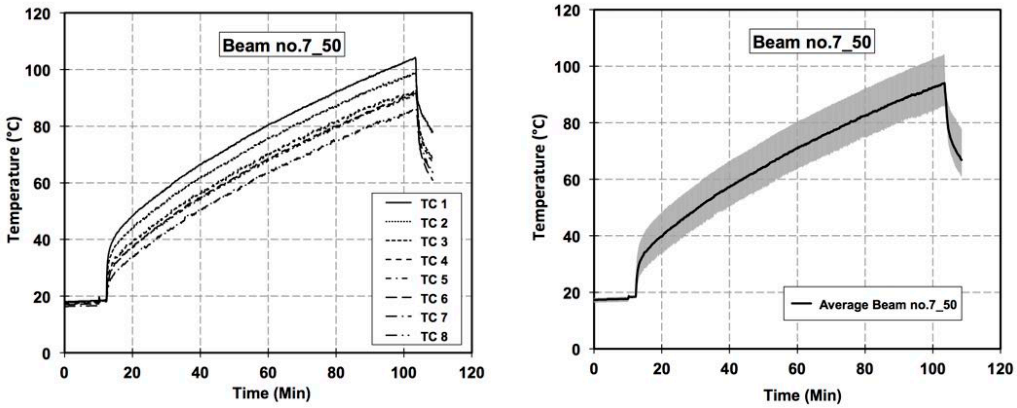

b) Air temperature of O-105 thermal chamber during testing Beam no.7_50

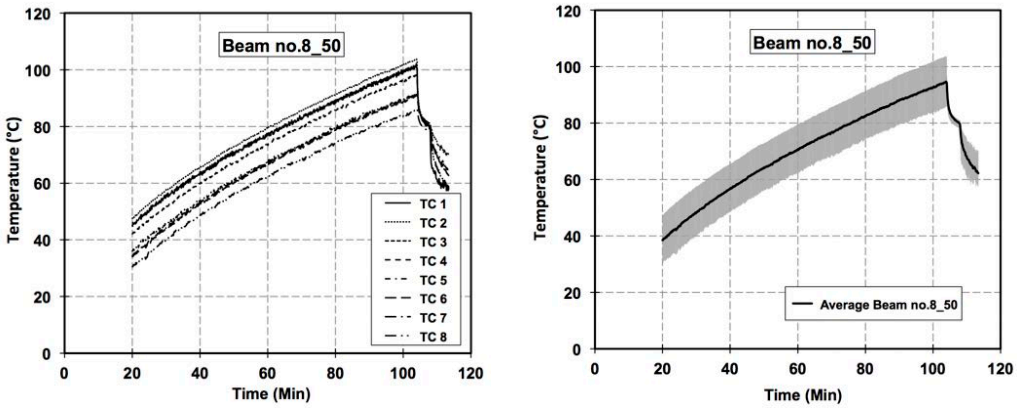

c) Air temperature of O-105 thermal chamber during testing Beam no.8_50

Figure 5-22: O-105 chamber air temperature during transient temperature tests

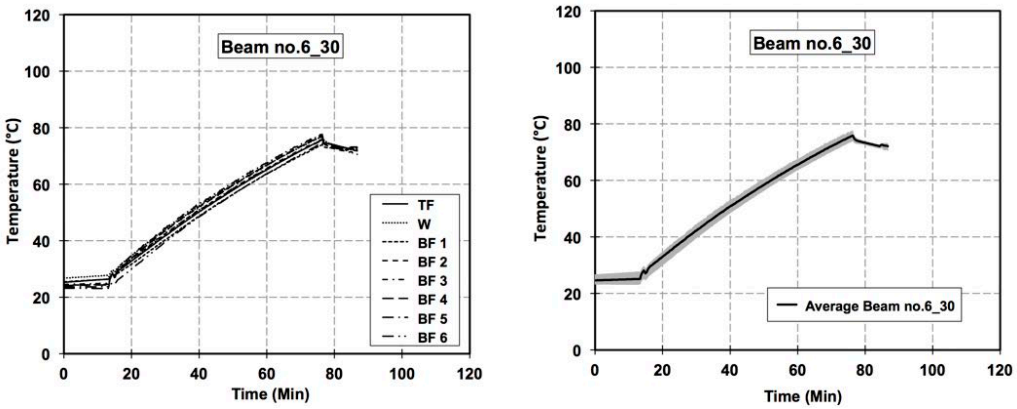

a) Beam no.6_30 temperature during testing

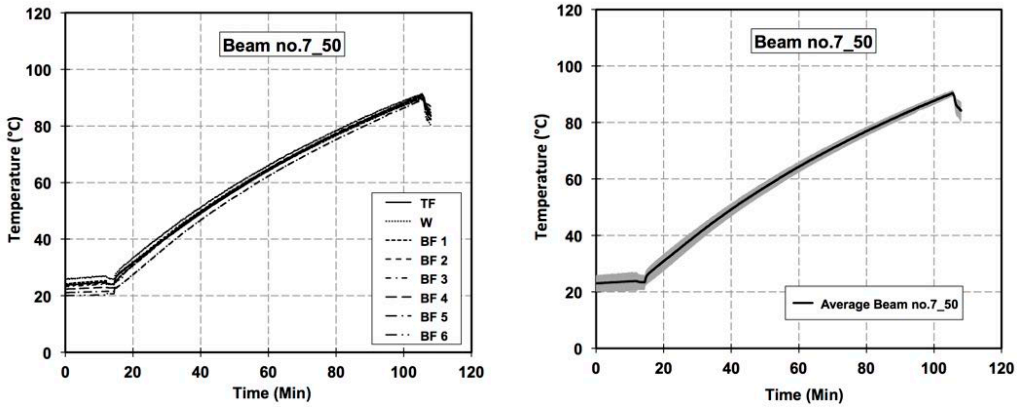

b) Beam no.7_50 temperature during testing

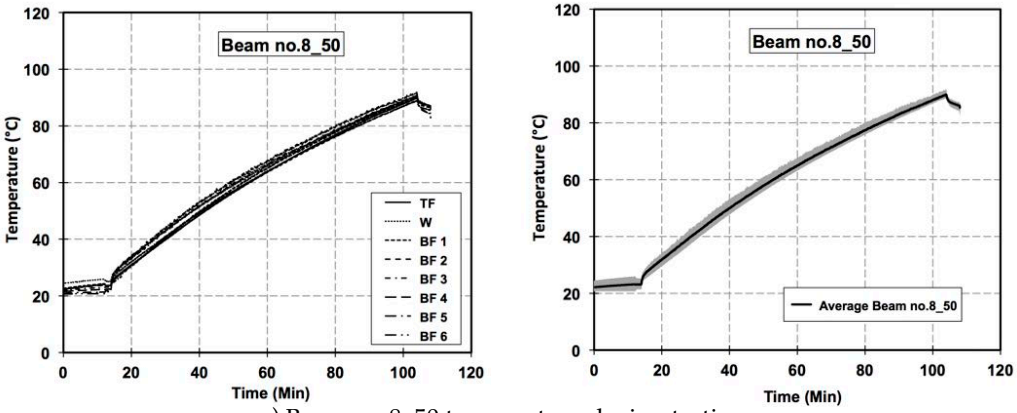

c) Beam no.8_50 temperature during testing

Figure 5-23: Specimens temperature during transient temperature tests

5.6.3 CFRP plate movement relative to the beam

Digital image correlation (DIC) was used to measure the slip between the plate and the flange of the beam, and the separation of the plate from the beam at its tip. Bisby *et al.* (2007) used DIC for taking strain measurements in Fibre-Reinforced Polymer (FRP) in confined concrete columns. A validation of the DIC technique applied to structures was given by Bisby and Take (2009). This technique was used to measure plate movement at the end of externally bonded CFRP by Stratford and Bisby (2012). The same off the shelf Digital Single-Lens Reflex (DSLR) that were used in the section 4.5.3 were also used in these experiments. The high-resolution photos of the CFRP plate ends were taken at regular intervals of five seconds throughout testing.

The DIC measurement technique is sensitive to errors for structural testing applications. Stable camera mounting and positioning of the opposite lighting are essential. Lighting should be in-front of the camera lens, to reduce the risk of the cameras from overheating and causing image distortion. The lighting should be balanced to limit projected shadows. Autofocus and image stabilisation should be turned off to minimise post-processing errors.

Figure 5-24 shows a sequence of images taken at different temperatures corresponding to temperatures for Beam no.6_30 using the north camera. The same behaviour was seen for the south camera from Beam no.6_30, therefore images are not included in Figure 5-24. Due to the high-sustained mechanical loading, in the post-processing of the images out-of-plane movement was not observed in the transient tests.

The plate slip and separation was recorded using the DIC analysis and are presented in Figure 5-25 (Beam no.6_30), Figure 5-26 (Beam no.7_50), and Figure 5-27 (Beam no.8_50). Each figure shows a plot of the plate-end slip (left hand vertical axis) and plate-end separation (right hand vertical axis). These measurements are taken from the adhesive joint at an 80 mm length from the end of the CFRP and during transient temperatures.

Images were only recorded using the north camera for Beam no.7_50, due to some technical issues. However, the two (north and south) cameras for Beam no.6_30 and Beam no.8_50 were in good agreement.

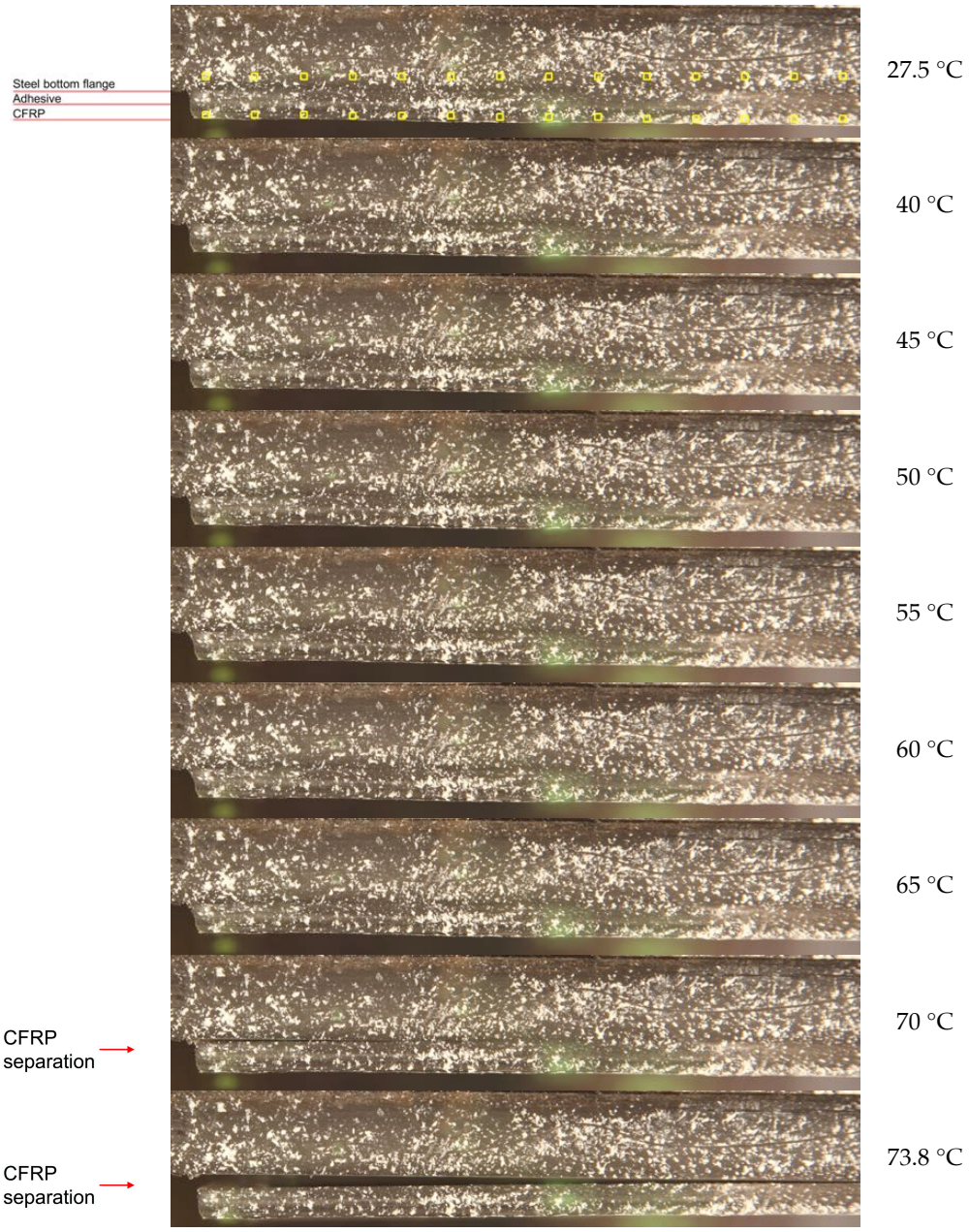

Figure 5-24: Digital image analysis north camera of Beam no.6_30*

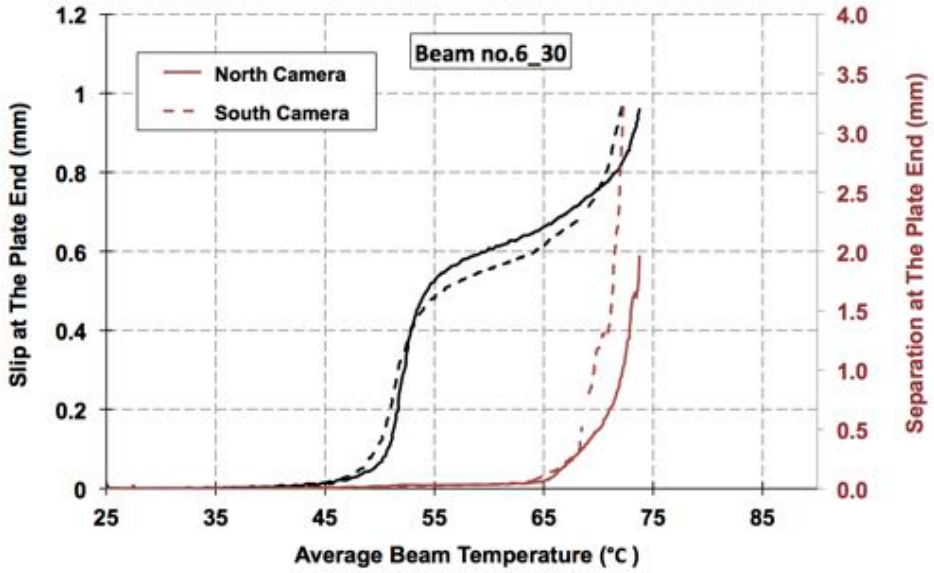

a) Beam no.6_30 tip of the CFRP plate movement

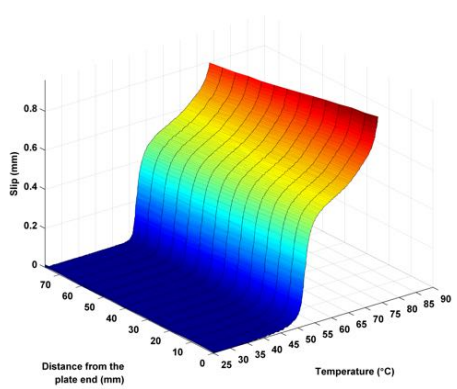

a) North camera slip

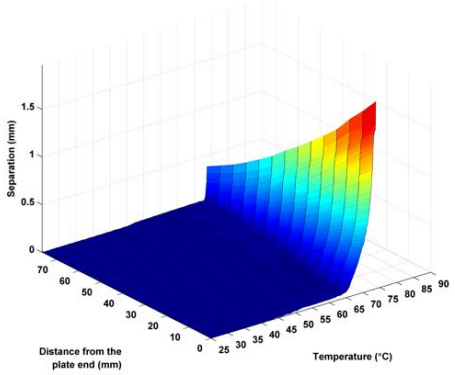

b) North camera separation

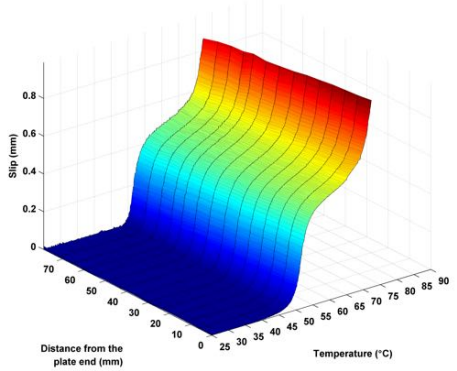

c) South camera slip

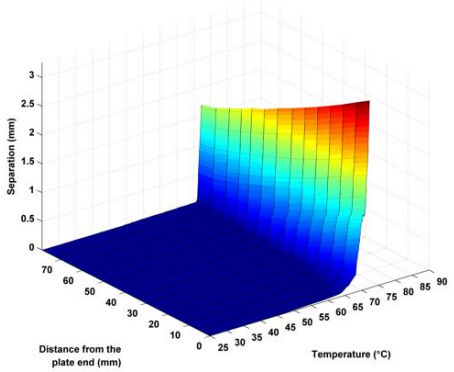

d) South camera separation

Figure 5-25: The CFRP plate movement during transient temperature Beam no.6_30*

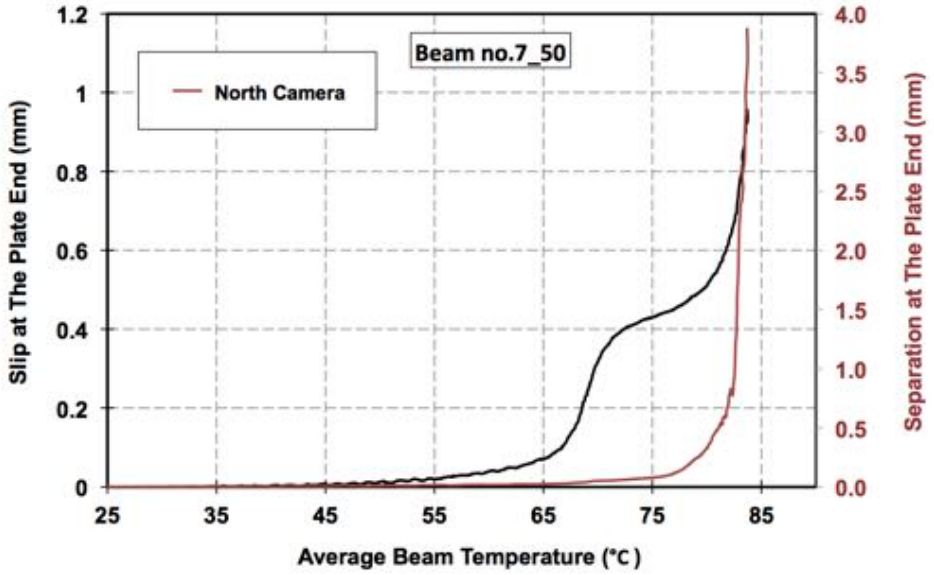

a) Beam no.7_50 tip of the CFRP plate movement

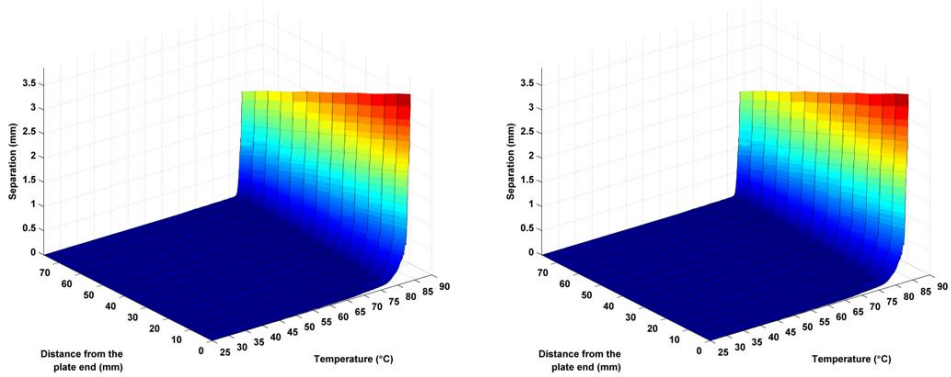

a) North camera slip b) North camera separation

Figure 5-26: The CFRP plate movement during transient temperature Beam no.7_50

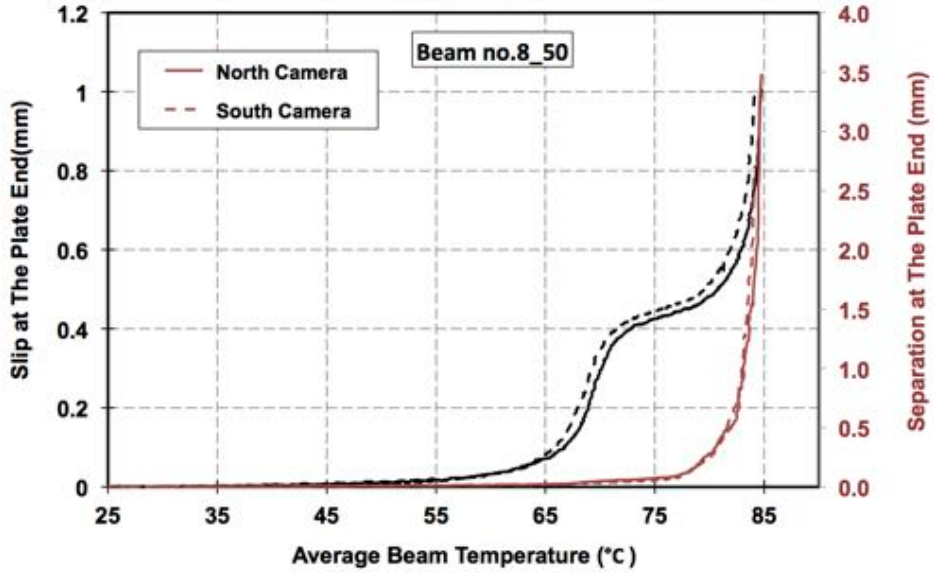

b) Beam no.8_50 tip of the CFRP plate movement

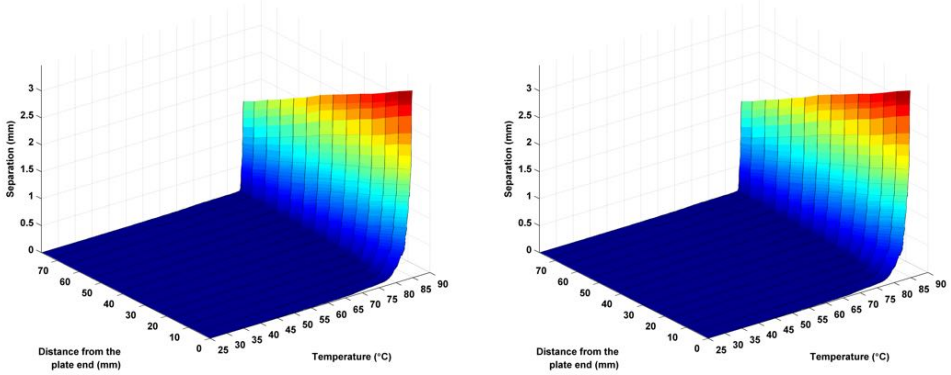

a) North camera slip

b) North camera separation

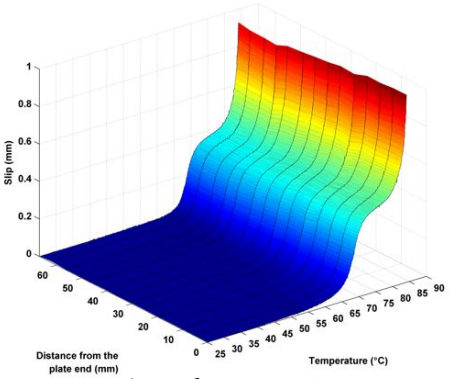

c) South camera slip

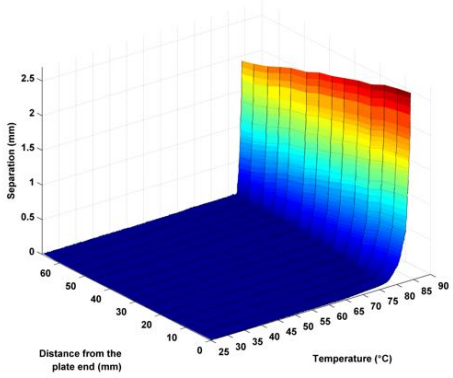

d) South camera separation

Figure 5-27: The CFRP plate movement during transient temperature Beam no.8_50

5.6.4 Failure mechanism

The three specimens failed in the same manner. During the early stages of the tests no slip was visible. From Figure 5-28 it can be seen that significant slip started shortly after the steel temperature reached 45°C for Beam no.6_30, and at 55°C for Beam no.7_50 and Beam no.8_50. The slip at this stage was due to the degradation of the adhesive. The DIC analysis shows that there was no separation between the adhesive and the steel surface. The DMA results confirm that there was a relative reduction in the storage modulus, refer to Figure 5-28.

As the temperature increased further, the slip increased dramatically at approximately 65°C (for Beam no.6_30) and 80°C (for Beam no.7_50 and Beam no.8_50). This occurred when over 0.6 mm of slip displacement was recorded. With further heating the separation displacement increased, resulting in a separation crack forming between the adhesive and the bottom steel flange. At this stage, the CFRP and adhesive were attached acting as a composite section, but separated from the steel beam section, see Figure 5-24. The CFRP material was not affected by the thermal loading, and it remained elastic. At the point of separation, the CFRP and adhesive inclined to a straight orientation. The separation from the edges reduces the effective contact area between the beam soffit and the adhesive. This leads to an increase in the stresses at the tip of the contact area and the adhesive exhibited further degradation, consequently, a runaway failure occurred and the separation displacement increased rapidly. Table 5-7 shows the temperature, at which point the tip of the FRP plate starts to move. The slip started at approximately 46°C and 60°C for the beams cured at 30°C and 50°C, respectively.

The guideline recommendations Cadei *et al.* (2004) suggest using $T_g - 15$. The single value of T_g is measured from DMA response of peak tan δ. Following this instruction, the temperature of the structure should not exceed 44.1°C and 64.7°C for the beams cured at 30°C and 50°C, respectively.

At 46°C and 60°C the storage modulus from the DMA tests was compared. It was found that storage modulus reduced by approximately 15% and 18%, for the specimens cured at 30°C and 50°C, respectively. The 15% drop in the storage modulus is shown in Figure 5-28. The comparison between the experiment findings and the theoretical analysis are discussed in section 6.4.4.

Table 5-7: Four-point bending temperature of start of slippage for tests at transient temperature

Beam no.	*Curing Temp.*	*CFRP length*/span ratio*	*Beginning of slippage at the plate end*
Beam no.6_30**	30°C	50%	46°C
Beam no.7_50	50°C	50 %	60°C
Beam no.8_50	50°C	50 %	59°C
* FRP length is shown in Figure 5-9.			
** Beam no.6 was prepared with Beam no.5_25 and cured at 30°C for extra 3 days, see Figure 4-11			

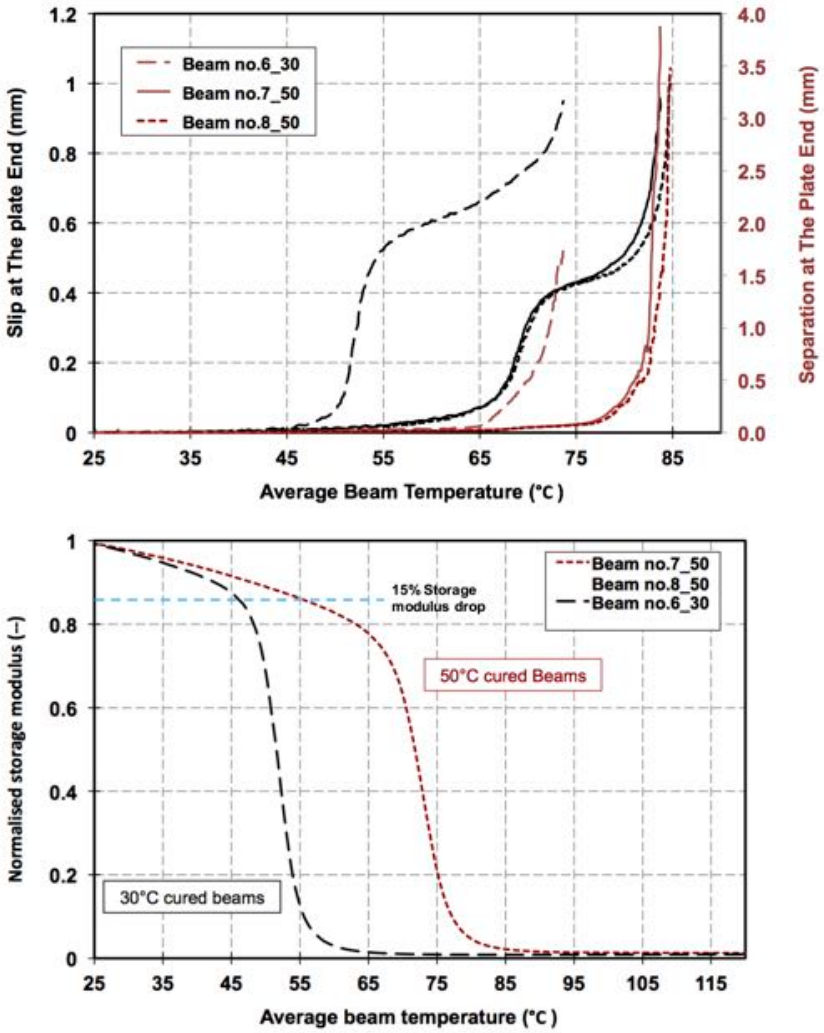

Figure 5-28: Tip of the CFRP plate movement and temperature of the steel beams during transient temperature tests

Figure 5-29 plots the same slip and separation for Beam no.6_30, Beam no.7_50, and Beam no.8_50 against the beam deflection (instead of the temperature). Deflection of Beam no.6_30 gradually increases when the specimens was heated, while Beam no.7_50 and 8 deflection remains constant for the most of the exposure time, then the deflection increases suddenly when the separation starts. Figure 5-29 also shows that the curvature of the beam has an influence on the CFRP bond.

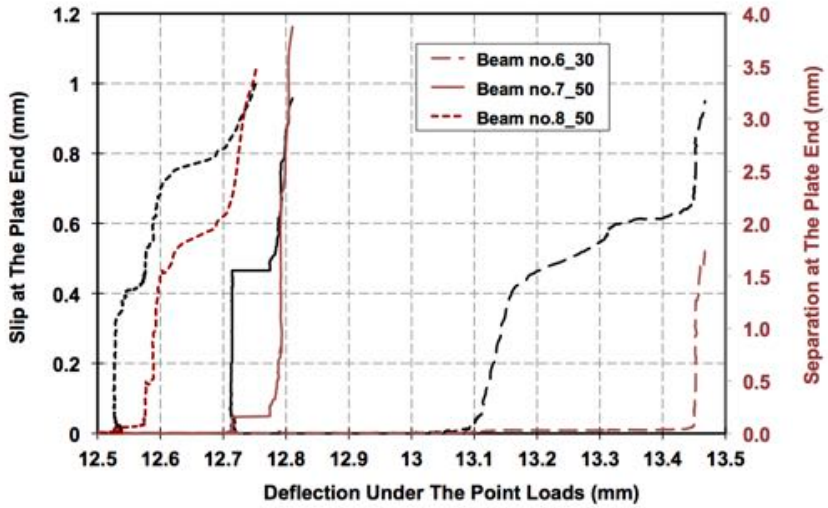

Figure 5-29: Tip of the CFRP plate movement and point load deflection during transient temperature tests

Figure 5-30 show the steel surface near the ends of the adhesive joints after the tests, unlike the ambient temperature tests, the steel surface was clear, and there was no evidence that indicates adhesive failure. Traces of adhesive residue similar to the ambient tests could not be found along the joint, however, due to some voids within the adhesive closes to the edges (Beam no.6 and Beam no.8), some adhesive remained on the steel surface, which was not attached to the FRP plate. The limited adhesive remained on the top edge of Beam no.6_30 and 8 are shown in Figure 5-30.

Figure 5-30: Beam no.6, Beam no.7, and Beam no.8 after testing

5.7 Summary

Two series of double lap-shear specimens were tested. From the first series, conclusive results on the effect of curing on adhesive shear strength were not obtained. This was due to the fact that the inner steel layer of the shear lap specimens yielded. The specimens cured at 30°C and 50°C had similar ultimate capacity. The second series of the lap-shear specimens were tested with thicker inner steel pallets. The specimens cured at 25°C and 50°C. Shear strength tests results showed an increase of approximately 29% of the adhesive shear strength with curing temperature.

The storage modulus variation from the DMA runs on adhesive coupons was carried out. Glass transition temperatures, T_g were reported according to different methods. The specimens cured in chamber O-105 reached the same curing level as the specimens cured in a small laboratory oven. The results in this chapter are in correlation with the results obtained from chapter 3 of this research.

The steel surface preparation was found to be adequate. The adopted surface preparation in chapter 4 found to be effective. Although the results from the adhesion pull-off tests were not conclusive, the bond strength was > 25 MPa.

Epoxy joints regardless of the size can be fully cured. Five beams were tested at ambient temperature to show the effects of adhesive curing on the overall performance of the FRP strengthened sections. In addition to these tests, three

specimens were tested at a transient temperature to study the behaviour of adhesive joints at an elevated temperature after post curing.

The beam tests showed that a significant increase of load capacity of adhesive joints was achieved using post curing the joints. This is because the mechanical properties of the adhesive exhibit a significant improvement with curing temperature. Only one specimen, which was FRP strengthened 81.5% of the span, had inelastic lateral-torsional failure, despite the fact the specimen was stiffened at the point loads and supports. One specimen did not fail and the FRP plate remained intact to the specimens. In the other three ambient tests, debonding failure occurred regardless the curing temperature. The failure was in the same manner. At the end of the CFRP plate at steel-adhesive interface traces of adhesive were found. An increase of approximately 25% was noticed in the ultimate load capacity of the specimens cured at 50°C compare to specimens cured at 30°C.

The three specimens that were tested at transient temperature showed that the specimens cured at high temperature showed a better performance. With increasing temperature, a failure mechanism occurred. The plate started to slip due to degradation of the adhesive, which eventually led to complete debonding of the adhesive-FRP reinforcement from the steel section. It should be noted that hardly any adhesive remained on the steel surface. The only specimen that was cured at 30°C, slip at FRP plate started when the beam temperature reached approximately 46°C. The two specimens that were cured at 50°C, slip at FRP plate started when the beam temperature reached approximately 60°C.

Comparing the results from the transient temperature and the DMA runs. It was found that at the temperatures where the slip started storage modulus was reduced by approximately 15% and 18%, for the specimens cured at 30°C and 50°C. The results suggest that guideline recommendations $T_g - 15$ requires some adjustments.

Chapter 6

Analysis and Interpretation

The main objective of this chapter is to compare the experimental results to the analytical prediction from the models that were developed. The discussion in this chapter is limited to the flexural analysis of steel beams strengthened with CFRP materials, elastic lateral-torsional buckling, and a theoretical investigation of the thermo-mechanics of the tested beams at elevated temperatures. However, there were other possible modes of failure to be considered such as, local buckling, web shear and web crippling. These failure modes have not been covered in this research because they were prevented during the experimental programme.

A classical bending model is redeveloped in section 6.1 to study flexural behaviour of steel sections considering equilibrium and compatibility, and the non-linearity of the material properties. The model used to analyse the flexural beam testing from chapter 4. The contribution of the strain hardening is addressed and various proposals to consider the effect of strain hardening were investigated. The model is computer programmed that it can be used to predict the moment-curvature and load-deflection behaviour of the CFRP reinforced beams. The state of strains and stresses of the section can be examined, and the allowable increase in live load can be determined.

A separate bond model is developed in section 6.4 to investigate the shear and normal stress in the adhesive layer, which cause slippage and / or debonding failure. The model is similar to the previous models, but it counts for the effect of moment that is carried by FRP strengthening plate. The coupled effect of shear and normal stresses can be studied. The bond model justifies the perfect bond between the CFRP and steel assumption in the flexural model. Finite deference method is used to solve the deferential equation of the model. The DMA results in chapter 5 were combined with the bond model to investigate the influence of thermal loading.

6.1 Analytical model for flexure

To develop the load-deflection relationship for the section, the moment curvature response of the steel-FRP composite section must be established. In this research, to predict the behaviour of the steel section, the same approach described by Culver (1960) is adopted, and the analytical procedure that is similar to the work carried out by Al-Saidy *et al.* (2004) is used. It is based on dividing the section into layers and segments throughout the section. The model is strain compatibility based; strain is calculated at various nodes, which were pre-defied with the material property and geometry, along the depth of the section. The moment curvature relationship for the section then can be established which allows and load deflection relationships to be established at any location along the beam.

The work Skogman *et al.* (1988); Schnerch (2005) have adopted Mattock procedure for calculating the flexural strength of pre-stressed concrete sections (Mattock, 1979). The procedure is originally developed for steel-concrete composite sections. Therefore, the same procedure can be evaluated for the section in chapter 4, by replacing the concrete section with a steel section on the top and adding the CFRP plates at the bottom. The new section is a composite of three materials. The only inputs to the scrip were the cross-section dimensions and the stress-strain relationship of the three sections.

6.1.1 Assumptions behind the flexure model

In the development of the moment-curvature relations, it is assumed that the Bernoulli-Navier hypothesis (bending strain is proportional to the distance from the neutral axis) holds. This assumes perfect bond between the layers, which means the slip or relative displacement at the inner face of the sections, is prevented. Therefore, premature deboning of the CFRP plate is neglected. The influence of vertical shear stress (shear deformation) is also neglected. The analysis satisfies force equilibrium and strain compatibility with in the section when the beam is subjected to transverse loads only. It is also assumed that the loads lie in the plane of symmetry of the cross-section.

6.1.2 Development of the flexural model

This section describes the development of the flexural model, which is a theoretical nonlinear analysis of members loaded in bending; the model can be used as a tool for design and analysis. A widely available commercial package is used to develop a script. The geometry of the section first is broken into different sections, for instance, tested section in this research is brake down in to the steel strengthening plate at the top, two flanged and the web of the steel I-sections beam, and finally the CFRP plate at the bottom of the section.

The full moment-curvature relationship of a composite section is established by increasing the strain at the bottom fibres of the bottom flange incrementally. The first step in the analysis is to give a value of strain at the bottom of the section, ε_t, and assume a neutral axis depth from the bottom, y. In this analysis, the strain ε_t and y were set at the bottom of the CFRP plate refer to Figure 6-1. Since for the current section finding the neutral axis in the elastic region is trivial, the assumed y is set to the depth of the neutral axis. When the steel section reaches the yielding strength, the new location of neutral axis has to be found, and the equilibrium in the section must be satisfied. The distribution of strain across the section is linear regardless of the stress state, and the value of the strain at the extreme fibres is proportional to the curvature. The corresponding curvature, ψ, of the section is defined as:

$$\psi = \frac{\varepsilon_t}{y} \qquad \text{Equation 6-1}$$

From the bottom surface strain ε_t, curvature ψ, and depth of neutral axis y the strain ε_x at any level from the bottom of the CFRP plate, x, in the section may be calculated as shown in Figure 6-1.

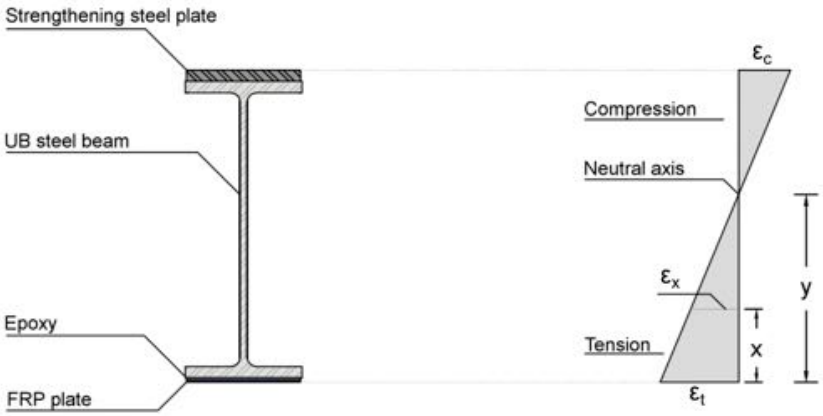

Figure 6-1: The assumed linear strain profile for composite beam

The depth of the section is split into several nodes, and the strain distribution through the depth of the beam is defined at these nodes. The stress distribution, $f\ (x)$, is determined from the strain distribution, pre-defined geometry and constitutive relationships for the different materials. The net axial force can then be determined by integrating the stress profile.

$$F_{bf} = b_{bf} \int_0^{t_{bf}} f_{bf}(x)\,.\,dx$$

Equation 6-2

Where, b_{bf} is the width of the section at level x, which is generally constant within a segment defined by the node spacing; t_{bf} is the thickness of the bottom flange. The strain ε_x can be related to the distance from bottom of the composite section, x, and the $f_{bf}(x)$ is stress at the same location.

$$\varepsilon_{bf} = \psi x$$

Equation 6-3

The contribution of the web is determined by assuming two rectangles; W_1 is the tension part of the web and, W_2 is the compression part of the web. Similar to the bottom flange, the top flange, strengthening plates, and FRP plate were separately added. For the purposes of future studies, the script is written in a way that the five sections may have independent non-linear material properties. The area of the fillets, weld, and adhesive layer contribution were neglected.

$$F_{sp} = b_{sp} \int_0^{t_{sp}} f_{sp}(x) \, . \, dx$$ Equation 6-4

$$F_{tf} = b_{tf} \int_0^{t_{tf}} f_{tf}(x) \, . \, dx$$ Equation 6-5

$$F_{W2} = b_W \int_0^{t_{W2}} f_{W2}(x) \, . \, dx$$ Equation 6-6

$$F_{W1} = b_W \int_0^{t_{W1}} f_{W1}(x) \, . \, dx$$ Equation 6-7

$$F_{frp} = b_{frp} \int_0^{t_{frp}} f_{frp}(x) \, . \, dx$$ Equation 6-8

$b_{sp}, b_{tf}, b_W, b_{frp}$ were the width of strengthening plate, top flange, web, and FRP plate respectively. $t_{sp}, t_{tf}, t_W, t_{frp}$ were the thickness of strengthening plate, top flange, web, and CFRP plate respectively. Trapezoidal numerical integration is used to solve the equations, because the nodes were closely spaced. The force contribution of the individual components of the cross-section is evaluated. The net axial force can be found by summing the contributions of each component of the section. Equilibrium requires that the total axial force is zero, and consequently the neutral axis depth y is iterated until this is satisfied.

$$F_{frp} + F_{bf} + F_{w1} + F_{w2} + F_{tf} + F_{sp} = 0$$ Equation 6-9

Once force equilibrium is satisfied, the cross-section moment may be determined using Equation 6-10. The distance from the neutral axis, X, multiplied the force in the nodes.

$$M = F_{frp}X_{frp} + F_{bf}X_{bf} + F_{w1}X_{w1} + F_{w2}X_{w2} + F_{tf}X_{tf} + F_{sp}X_{sp}$$ Equation 6-10

Once the moment and curvature for a given bottom flange strain is calculated, this procedure is automatically repeated for the next strain increment. The strain is incremented until the ultimate prescribed strain value is reached; typically, this value is set to the maximum strain of the CFRP. The complete moment-curvature relationship of the section can then be plotted. The moment-area method can then be employed to determine the load-deflection at any point along a beam length for a specified loading condition. Trapezoidal numerical integration technique is used to develop the load-deflection curve from the moment-curvature response. Flowchart of the algorithm is shown in Figure 6-2, and the computed programme script is provided in the Appendix E.

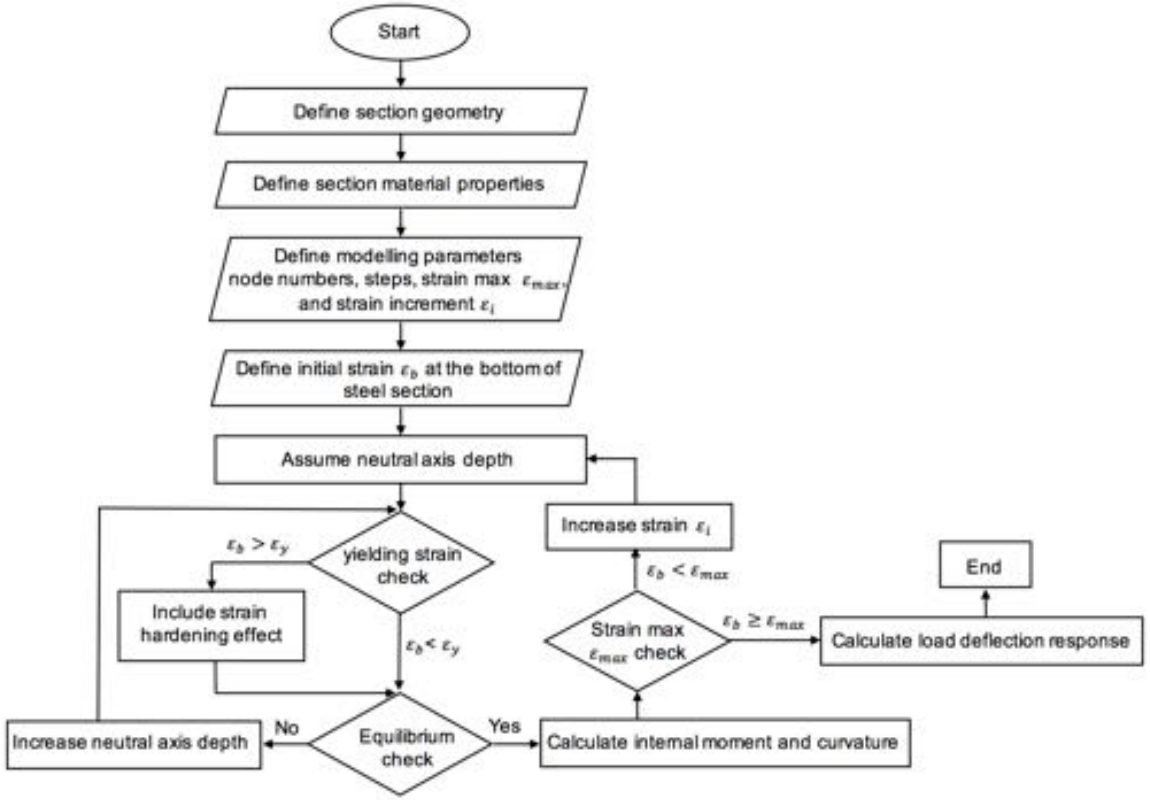

Figure 6-2: Flowchart of the flexural model algorithm

6.1.3 Verification of the flexure model

To verify the flexural model, the conventional plastic moment capacity of the section is found based on the elastic, perfectly plastic assumption using simple hand calculation. The coupon tests data that were presented in chapter 4 (Table 4-4 and Table 4-5) were the steel material properties used in this verification; in the theoretical moment capacity calculation, only yielding strength is required. However, the coupons exhibited significant strain hardening, refer to Appendix A. Figure 6-3 shows the general idealised elastic-plastic stress strain constructive material law (left side), and the stress-strain response that is used in the validation of the model. It is important to notice that Figure 6-3 (right side) is the idealised material properties of the fabricated section. The effects of strain hardening are discussed in section 6.3.

According to the idealised elastic-plastic stress distribution by Ewing (1899), the plastic moment capacity of the cross section M_p is defined as the product of the material (yield) strength and the plastic section modulus. It is estimated to be 174 kN.m, which is in a good agreement with the predicted moment by the script in Figure 6-4. Further details of finding the theoretical moment capacity can be found in Neal (1977). The geometrical values of the section were given in Table 6-1.

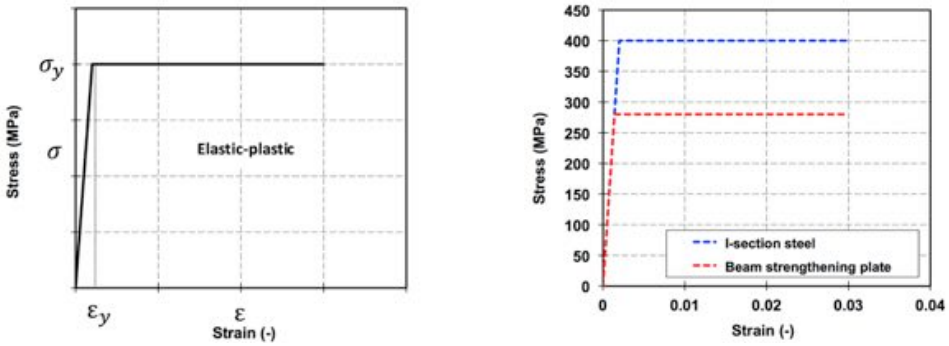

Figure 6-3: Idealised stress-strain relations for the fabricated section

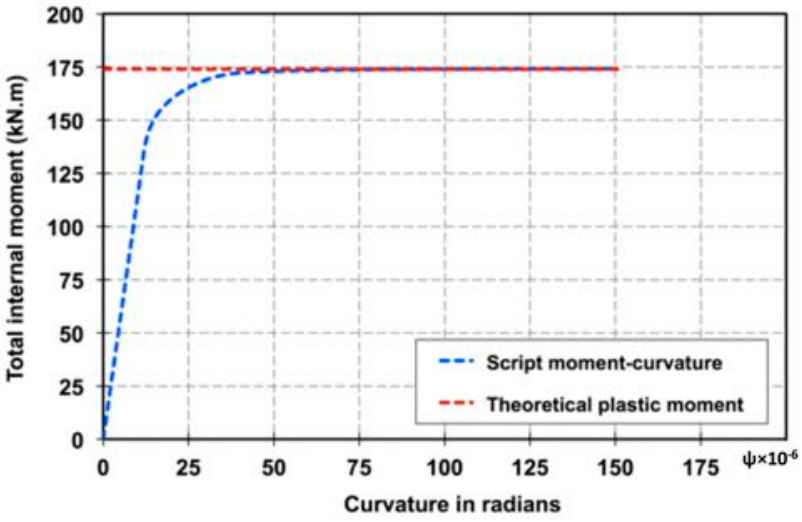

Figure 6-4: Moment-curvature relations for the fabricated section

Table 6-1: Symbol and values used to represent the geometry of the section

Symbol	***Value***	***Description***
b_{sp}	**100 mm**	Top flange strengthening plate width
t_{sp}	**12.5 mm**	Top flange strengthening plate thickness
b_{tf}	**102.2 mm**	Top flange width
t_{tf}	**10 mm**	Top flange thickness
$b_{w1\ and\ w2}$	**240.4 mm**	Web width
$t_{w1\ and\ w2}$	**6.3 mm**	Web thickness
b_{bf}	**102.2 mm**	Bottom flange width
t_{bf}	**10 mm**	Bottom flange thickness
b_{frp}	**100 mm**	FRP width
t_{frp}	**1.4 mm**	FRP thickness

The assumption that structural steel follows a simple bi-linear elastic-perfectly plastic, stress–strain law, is made at the time when plastic theory is being developed, and the same concept is used to calculate M_p of steel sections in practice.

The geometry of the section in Table 6-1 and four-point bending configuration moment distribution, the moment-curvature relationship of the cross-section is shown in Figure 6-4 were used to plot load-deflection response of the control specimen from the script as shown in Figure 6-5. For the idealised case, the curve includes a linear range followed by a transition from the yield moment to the plastic moment. Once the cross-section is fully plastic, increases in curvature can occur without a corresponding moment. The total load, which the section is fully plastic,

is much lower than the total applied load to the control specimen due to strain hardening that is ignored in idealised case. Strain hardening contributes to the ultimate capacity of the section as shown in Figure 6-5 over 13% at deflection 30mm, and it tends to increase as the deflection increases.

Elastic lateral-torsional buckling capacity of the section is also shown in Figure 6-5 and the calculation procedure is shown addressed in section 6.2. The contribution of strain hardening and various models were studied in section 6.3.

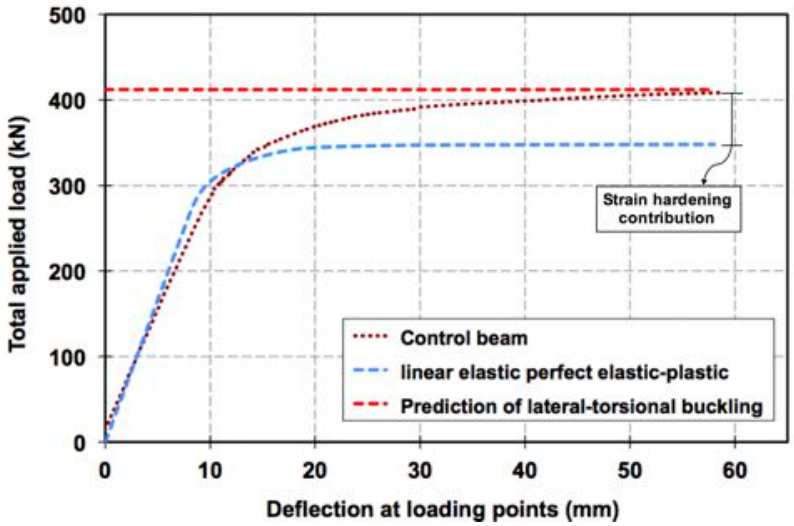

Figure 6-5: Load-deflection and lateral-torsional buckling capacity predictions

6.2 Lateral-torsional buckling capacity

The elastic lateral-torsional buckling capacity of the section without the FRP plate is calculated from Equation 6-11. The estimated elastic buckling capacity is based on the mono-symmetric section, and it is 412 kN for the loading configuration. The elastic buckling capacity equations can be found in Trahair (1993); Galambos (1998); Trahair *et al.* (2007); Ziemian (2010).

$$M_{cr} = \sqrt{\frac{\pi^2 E I_y}{L^2}} \left\{ \sqrt{\left[GJ + \frac{\pi^2 E I_w}{L^2} + \left\{ \frac{\beta_x}{2} \sqrt{\frac{\pi^2 E I_y}{L^2}} \right\}^2 \right]} + \frac{\beta_x}{2} \left(\sqrt{\frac{\pi^2 E I_y}{L^2}} \right) \right\}$$

Equation 6-11

$M_{cr}$is the critical buckling moment, β_x is the mono-symmetry property of the section, the evaluation of β_x is not straightforward (Trahair *et al.*, 2007), but according to Kitipornchai and Trahair (1979) β_x may be approximated using Equation 6-12 (84.5 mm).

$$\beta_x = 0.9\, h_o \left[2\left(\frac{I_{yc}}{I_y}\right) - 1\right]\left[1 - (\frac{I_y}{I_x})^2\right]$$

Equation 6-12

I_{yc} is the section minor axis second moment of area of the compression flange, h_o is the distance between centre of the tension and compression flanges. It is crucial to highlight the fact that the welded top steel plate treated as an extra part to the I-section. The torsion constant J and β_x were calculated based on this assumption, which leads to a conservative estimation. The values in Table 6-1 were used to calculate the geometric properties shown in Table 6-2. The estimation of lateral-torsional buckling moment according to Equation 6-11 seems to overestimate the buckling capacity of the section in elastic region and the critical buckling moment M_{cr} value is greater than the idealised M_p, however, the equation does not count for any out of straightness of the section and loading eccentricity. When a section approaches yielding, buckling predictions were more complicated. Buckling in post yielding is not the scope of this work, but further information can be found in Trahair (1993); Galambos (1998); Ziemian (2010). In most cases, a combination of yielding and buckling including local buckling can happen simultaneously. Therefore, the use of stiffeners believed to be a feasible solution to delay buckling.

Table 6-2: Symbol and values in Equation 6-11

Symbol	***Value***	***Description***
E	**200 GPa**	Young's modulus
G	**76.9 GPa**	Shear modulus
I_x	**5.659×10^7 mm^4**	Second moment of area about the major axis
I_y	**2.82×10^6 mm^4**	Second moment of area about the minor axis
I_{yc}	**1.93×10^6 mm^4**	Minor axis second moment of area of the compression flange
I_w	**4.65×10^{10} mm^6**	Warping constant
J	**1.44×10^5 mm^4**	Torsion constant
h_o	**256.6 mm**	Distance between centre of the tension and compression flanges
L	**2700 mm**	Distance between the supports

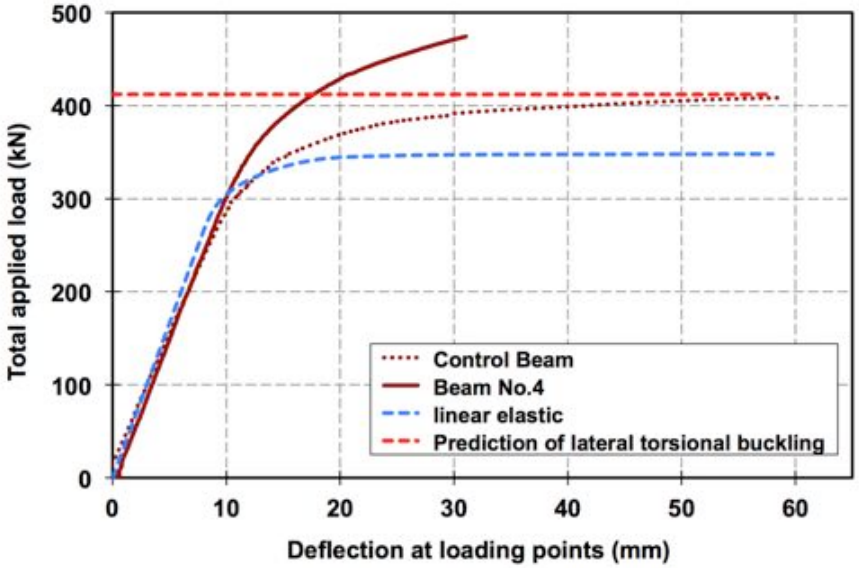

Figure 6-6: Buckling capacity and load-deflection predictions

6.3 Strain hardening effect and predictions

There is a substantial amount of research in to strain hardening. Based on the uni-axial coupon tests, various stress-strain response models have been suggested. Most of the models suggest a tri-linear stress-strain law. The first, linear region of the stress-strain is defined by the Young's modulus E, followed by a plateau to represent the plastic range of the coupon test, and the final region has a strain hardening modulus of E_{sh}. In the original proposal for strain hardening by Horne and Morris (1981), E_{sh} is 0.05 E and it commences at a strain ε_{sh} as shown in Figure 6-7. Table 6-3 contains the corresponding values of ε_{sh} for strain hardening models. The model proposed by Byfield and Dhanalakshmi (2002); Byfield *et al.* (2005) is similar to the values proposed by Lay and Smith (1965). Recently, Gardner *et al.* (2017) proposed a new strain hardening model for hot-rolled carbon steel and the proposed model is a quad-linear material model. The latter model is not studied in this research. The models in Table 6-3 and the bi-linear proposal from EC2 for reinforced steel were used to produce the load deflection response. These results are shown in Figure 6-8. The experimental results were discussed in section 5.5.1, and both sets of results are compared in Figure 6-8.

Table 6-3: Tri-linear strain hardening models from *Byfield and Dhanalakshmi (2002); Byfield et al. (2005)*

Models	E_{sh} ***(MPa)***	ε_{sh}
Horne (1981)	≅ 0.05 E	$6\text{-}10\ \varepsilon_y$
Lay and Smith (1965)	2550	$11\ \varepsilon_y$
Byfield and Dhanalakshmi (2002)	2700	$6\ \varepsilon_y$

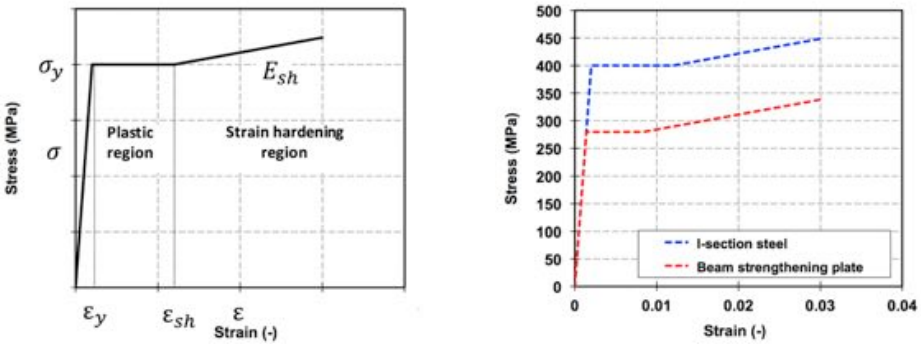

Figure 6-7: Stress-strain relations of the fabricated section from the models by Byfield and Dhanalakshmi (2002); (Byfield *et al.*, 2005)

The theoretical load-deflection results underestimate actual load-deflection found in these experiments. The tri-linear model by Horne and the experimental results approach similar deflection at a load of 400 kN. At this load, the theoretical strain level at the bottom of the steel section is 0.3%. This is sufficient to produce a stress that is more than yielding stress in most of the material. This means that there is sufficient curvature to produce a theoretical plastic hinge.

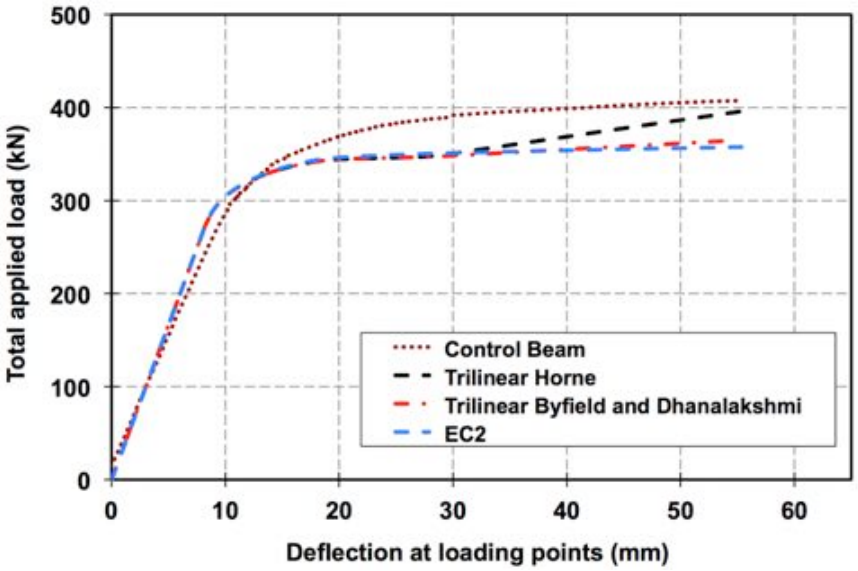

Figure 6-8: Load-deflection response for different strain hardening model

It is demonstrated that the idealised stress strain law and the proposed models do not represent the actual behaviour of the un-strengthened steel sections. From the shape of the load-deflection in Figure 6-8, it appears that there is no plastic plateau as strain hardening occurs immediately after yielding. The stress-strain response of present day structural steel behaves similar to aluminium and stainless steel. The strain hardening is observed immediately after elastic behaviour ends (Byfield and Nethercot, 1998; Byfield *et al.*, 2002).

Because there was a divergence between the theoretical results and the actual test results at approximately yielding point another model was studied. Semi empirical stress strain constitutive law (linear elastic followed by continually curved constitutive relationship) was compared.

The linear branch of this model was taken for the coupon tensile tests (summarised in Table 4-7 and 4-8, refer to chapter 4), while the strain hardening is calculated using Holmond-Ludwik's formula.

It should be noted that Ludwik's formula was derived from the original proposal by Ramberg and Osgood. Ludwik's work deviated from Ramberg and Osgood by neglecting the effect of the elastic strain region. In this case the linear part is separately included. As a model, the Ramberg-Osgood describes tensile curves for many materials. Equation 6-13 is a power law function of stress and strain and is a

simplified version of the work-hardening exponent proposed by Ludwik (1909). Equation 6-13 is frequently used in applications where an explicit expression for stress as a function of strain is required (Besseling and Van Der Giessen, 1994).

$$\sigma = \sigma_y \left(\frac{E\varepsilon}{\sigma_y}\right)^n$$

Equation 6-13

The values of σ_y and E for the steel properties are listed in Table 4-7 and Table 4-8, and the values are summarised in Table 6-4. It should also be pointed out that the parameter n lacks a physical meaning, and it can be found using ASTM E0646-00 (2000). The n value is strain dependent, and it often approximates to the strain value where necking commences in the coupon tests. Different n values were used in the analysis. 0.1 for the I-beam section and 0.14 for the top flange strengthening steel plate. The coupon tests confirm higher strain hardening for the strengthening plate than the coupons from the I-section beam, refer to Appendix D. The dimensions of FRP reinforcement and steel section are given in Table 6-1.

Other expressions can be used to model strain hardening such as The Modified Ramberg-Osgood formula, which is recommended by Mattock (1979). He used the formula to model pre-stress concrete. Schnerch (2005) used the same formula to model composite concrete girders.

Table 6-4: Parameters used in Equation 6-13 to estimate strain-hardening effect

Fabricated beam sections	***Parameters and the values***		
	σ_y	***E***	***n-value***
I-beam section	400 MPa	200 GPa	0.10
Top flange strengthening plate	280 MPa	200 GPa	0.14

Figure 6-9 compares the load-deflection behaviour of the un-strengthened FRP specimen (control beam) and CFRP reinforced beam No.4 obtained from the experiments with the output from the model.

The prediction for the un-strengthened control beam is in good agreement during the linear part of the response. At loads over 200 kN the prediction overestimates the response, most likely because the model ignores the shear deformation and the residual stresses in the steel. The prediction and the test results

agree at loads close to 350 kN, while the model over estimates the load when the loads reach over 400 kN. The explanation for this is that second order loading is not counted for in the model. In the test, the beam showed some signs of lateral deformation. This was caused by a combination of excessive deflection and the lack of lateral restraint.

The predictions and the test results of the FRP strengthened specimen are also shown in Figure 6-9. Between 200 and 400 kN, the predicted load for the same amount of deflection is higher than the test results. Similar to the control beam this is likely because the model ignores the shear deformation and the residual stresses in the steel. Over 400 kN, the predictions and the test results are in correlation.

In the load-deflection the FRP plate did not enhance the initial stiffness of the section. This is due to the fact that the relatively low Young's modulus of the FRP reinforcement in comparison to mild steel.

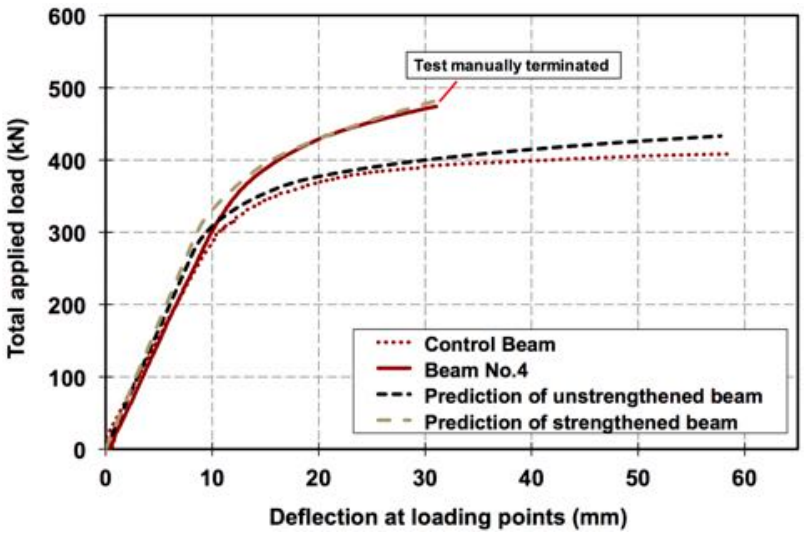

Figure 6-9: Experimental and predicted load-deflection relationship

6.4 Analytical model for bond

The flexural model used in the previous section to predict the load-deflection behaviour of the beam is based on the assumption of perfect bond between the steel and the FRP material. However, the aim of the present work is to examine the consequences of elevated temperature upon the adhesive joint, as seen during the

experimental work described in chapter 5. It is important to examine failure of the adhesive joint, to predict when debonding occurs of the FRP strengthening from the steel beam.

The analysis presented in this section is a bond analysis that allows temperature effects to be examined. A first-order, elastic, compatibility approach bond analysis is considered see section 2.5.1. The model is based on compatibility approach as discussed in section 2.8.1. It is similar to the previous works (Smith and Teng, 2001; Deng *et al.*, 2004; Stratford and Cadei, 2006).

The key differences are first that the curvature of the FRP plate is not set equal to the curvature of the beam, unlike previous analyses. Second, the effects of CFRP plate moment and the shear deformation of the adhesive are included in the analysis.

Assuming equal FRP plate and beam curvature is made to decouple the (shear and normal) differential equations, and solve the equations separately in mathematical closed form. The equal curvature may be partially true when a shallow section is strengthened and a thin FRP plate is used.

Due to the complexity of the problem, a finite difference approximation method is used to solve the coupled differential equation. This approach effectively studies the stresses within the adhesive layer in particular when the joint is subjected to elevated temperature. This approach may be used to investigate strengthened section with various geometries and local heating of the bonded joint.

The analysis assumes that the shear strain is constant through the thickness of the adhesive joint, and therefore the equations are easier to derive than a higher-order analysis (the expressions for which were not practical for design purposes). The constant stress assumption through the thickness, especially at the interface stresses, is important when a failure occurs close to the interface. The peak shear stress occurs at the FRP plate ends, which violates the stress-free condition. Analyses that ignore the stress-free condition overestimate the stress at the ends of the FRP plate and tend to give conservative failure load predictions (da Silva *et al.*, 2009). The predictions of stresses from high-order analyses and the first-order analysis are near the FRP plate tips. However, the high-order predictions indicate that the peak normal and shear interfacial stresses do not occur at the same location (Yang *et al.*, 2004).

A first-order, elastic, bond analysis is considered since the behaviour of adhesives is not perfectly elastic, and this is more so the case when it is subjected to elevated temperature. Due to the small adhesive thickness of the joints compounded by the effects of temperature, the stresses within the adhesive are likely to be the same and the stress variation is less significant.

6.4.1 The bond model assumptions

Uniform shear and normal stresses through the thickness of the adhesive layer is assumed. A thick adhesive is used in the tests, and hence adhesive shear deformation is taken into account. The bending deformations in the adhesive are neglected. The axial force in the adhesive layer is neglected. Shear deformation of the steel and CFRP material were neglected because both were shallow sections. Uniform adhesive stress and strain were assumed across the width of the joint. The constitutive material law for the sections (steel, adhesive, and CFRP) is assumed to be linear-elastic. The material properties are listed in section 4.5.

6.4.2 Development of the bond model

This section describes the development of the bond analysis used to study the influence of temperature on the FRP strengthened steel section. The bond model is separate from the flexural model. However, there were similar notations in the models.

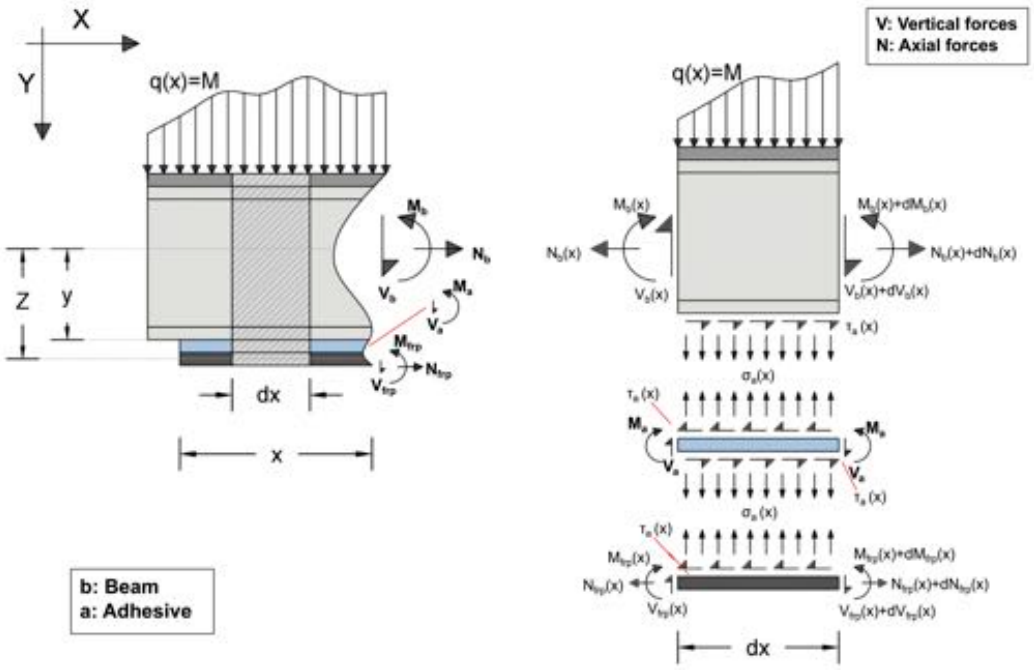

Figure 6-10: The bond analysis definitions, geometry, and differential segment of strengthened beam

From global equilibrium in Figure 6-10, the longitudinal (x-direction) direction and moment equilibrium may be written as in Equation 6-14 and Equation 6-15 respectively.

$$N_b = -N_{frp}$$ Equation 6-14

$$M = M_b + M_a + M_{frp} + N_{frp}Z$$ Equation 6-15

M is the moment due to applied load $q\ (x)$, M_b is the beam moment, M_a is adhesive moment, M_{frp} is the CFRP material moment. M_{frp} is considered in this model as discussed in section 6.4.

$$Z = y_{frp} + y_b + t_a$$ Equation 6-16

y_{frp} is distance from the adhesive-FRP interface to the centre of the FRP plate, t_a is the adhesive thickness, and y_b is the distance from the centroid of the beam to the adhesive-steel interface. The term $V_a dxdt$ (shear variation thorough the adhesive) is eliminated for the simplicity of the analysis.

$$M_a = -\int_0^x \tau_a(t) \, . \, t_a . dt = -t_a N_{frp}$$ Equation 6-17

Therefore, substituting M_a from Equation 6-17 in Equation 6-15, Equation 6-15 may be written as:

$$M = M_b + M_{frp} + N_{frp}(y_{frp} + y_b)$$ Equation 6-18

- Longitudinal (x-direction) equilibrium of the FRP element, of length dx and width b, gives.

$$\tau_a = \frac{1}{b_a}\frac{dN_{frp}}{dx}$$ Equation 6-19

- Traverse (y-direction) equilibrium of the FRP element, of length dx and width b, gives.

$$\sigma_a = \frac{1}{b_a}\frac{dV_{frp}}{dx}$$ Equation 6-20

b_a is the width of adhesive bonded CFRP plate,

- Rotational equilibrium of the FRP element (eliminating term $\frac{dV_{frp}dx}{2}$ because the value of dx is small) gives:

$$V_{frp} = \frac{dM_{frp}}{dx} + y_{frp}\frac{dN_{frp}}{dx}$$ Equation 6-21

Interfacial shear stress compatibility at adhesive layer:

Assuming that the displacement field varies linearly through the thickness of the adhesive segment, the average shear strain in the adhesive layer is given by considering horizontal and vertical displacement u_{xy} and v_{xy}, respectively.

$$\gamma_{xy} = \frac{du_{xy}}{dy} + \frac{dv_{xy}}{dx}$$ Equation 6-22

For a segment of adhesive with thickness t_a and length dx, horizontal shear strain at the adhesive segment can be presented as relative linear displacement within the adhesive thickness, and the vertical shear strain is the average of the beam and FRP plate vertical displacement. Equation 6-22 can be written as:

$$\gamma_a = \frac{u_{frp-a} - u_{b-a}}{t_a} + \frac{1}{2}\left(\frac{dv_{frp}}{dx} + \frac{dv_b}{dx}\right)$$ Equation 6-23

Where u_{frp-a} and u_{b-a} were longitudinal horizontal displacements at the FRP-adhesive and steel- adhesive interfaces, and $\frac{dv_{frp}}{dx}$ and $\frac{dv_b}{dx}$ were slops at the same locations, respectively.

To find the shear strain variation along the adhesive layer, the first derivative of shear strain Equation 6-22 with respect to *x* is needed:

$$\frac{d\gamma_a}{dx} = \frac{d^2u_{xy}}{dxdy} + \frac{d^2v_{xy}}{dx^2}$$ Equation 6-24

Therefore, Equation 6-23 becomes:

$$t_a\frac{d\gamma_a}{dx} = \frac{u_{frp-a}}{dx} - \frac{u_{b-a}}{dx} + \frac{t_a}{2}\left(\frac{d^2v_{frp}}{dx^2} + \frac{d^2v_b}{dx^2}\right)$$ Equation 6-25

Curvature of the FRP reinforcement and the steel can be written as:

$$\frac{d^2v_{frp}}{dx^2} = \psi_{frp} = \frac{M_{frp}}{E_{frp}I_{frp}}$$ Equation 6-26

$$\frac{d^2v_b}{dx^2} = \psi_b = \frac{M_b}{E_bI_b} = \frac{M - M_{frp} - N_{frp}(y_{frp} + y_b)}{E_bI_b}$$ Equation 6-27

Where E is the Young's modulus and I is the second moment of area. Equation 6-27 is written in terms of the FRP internal moment and force by substituting Equation 6-15. The strain at the top of the FRP material is given as:

$$\frac{u_{frp-a}}{dx} = \varepsilon_{frp-a}(x) = \varepsilon_{frp} - \psi_{frp}y_{frp} + \alpha_{frp}\Delta T$$ Equation 6-28

Where

$$\varepsilon_{frp} = \frac{N_{frp}}{E_{frp}A_{frp}}$$ Equation 6-29

Similarly, the strain at the bottom of the steel beam is given as:

$$\frac{u_{b-a}}{dx} = \varepsilon_{b-a}(x) = \varepsilon_b + \psi_b y_b + \alpha_b\Delta T$$ Equation 6-30

Where

$$\varepsilon_b = \frac{-N_s}{E_bA_b}$$ Equation 6-31

Where E is the Young's modulus, A is the area, ε is the strain, ψ is the curvature, α the thermal expansion coefficient, and ΔT the temperature change. Substituting Equation 6-26, Equation 6-27, Equation 6-28, Equation 6-29, Equation 6-30, and Equation 6-31 into Equation 6-25 gives the governing equation for shear strain along the adhesive joint.

$$t_a \frac{d\gamma_a}{dx} = C_1 N_{frp} + C_2 M_{frp} + \Delta\varepsilon(x)$$

Where C_1 and C_2 are coefficient.

$$C_1 = \left[\frac{1}{E_{frp}A_{frp}} + \frac{1}{E_b A_b} + \frac{(2y_b - t_a)(y_{frp} + y_b)}{2E_b I_b}\right]$$

$$C_2 = \left[\frac{y_b}{E_b I_b} - \frac{y_{frp}}{E_{frp}I_{frp}} + \frac{t_a}{2}\left(\frac{1}{E_{frp}I_{frp}} - \frac{1}{E_b I_b}\right)\right]$$

$$\Delta\varepsilon(x) = \Delta T(\alpha_{frp} - \alpha_b) - \left[y_b - \frac{t_a}{2}\right]\frac{M}{E_b I_b}$$

Equation 6-32

Interfacial normal stress compatibility at adhesive layer:

As the normal strain is assumed to be uniform through the thickness of the adhesive layer, the interfacial normal strain is given as:

$$\varepsilon_a(x) = \frac{dv}{dy} = \frac{v_s(x) - v_{frp}(x)}{t_a}$$

Equation 6-33

Where v_{frp} and v_b were the traverse displacements at the bottom of the steel beam and the top of the FRP plate, respectively (refer to Equation 6-23) and to find normal strain variation along the adhesive layer, the first derivative of shear strain Equation 6-33 with respect to x is needed:

$$t_a \frac{d^2\varepsilon_a}{dx^2} = \frac{d^2 v_{frp}}{dx^2} - \frac{d^2 v_b}{dx^2}$$

Equation 6-34

Substituting Equation 6-26 and Equation 6-27 into Equation 6-34, the governing equation for normal strain in the adhesive becomes:

$$t_a \frac{d^2\varepsilon_a}{dx^2} = C_4 N_{frp} + C_5 M_{frp} - \Delta\psi(x)$$

Where

$$C_4 = \frac{(y_{frp} + y_b)}{E_b I_b} \qquad C_5 = \left[\frac{1}{E_{frp} I_{frp}} + \frac{1}{E_b I_b}\right] \qquad \Delta\psi(x) = \frac{M}{E_b I_b}$$

Equation 6-35

Adhesive constitutive law

Assuming the linear-elastic response of the adhesive in Equation 6-19 and Equation 6-20, the shear and normal strain may be written as:

$$\gamma_a = \frac{\tau_a}{G_a} = \frac{1}{b_a G_a}\frac{dN_{frp}}{dx}$$

Equation 6-36

$$\varepsilon_a = \frac{\sigma_a}{E_a} = \frac{1}{b_a E_a}\frac{dV_{frp}}{dx}$$

Equation 6-37

Taking the first derivative of Equation 6-21, the relationship in Equation 6-38 can be produced.

$$\frac{dV_{frp}}{dx} = -\left[\frac{d^2 M_{frp}}{dx^2} + y_{frp}\frac{d^2 N_{frp}}{dx^2}\right] = \sigma_a$$

Equation 6-38

Substituting Equation 6-36, Equation 6-37, and Equation 6-38 into Equation 6-32, the governing equations for shear stresses may be written in terms of the FRP plate force and moment.

$$\frac{d^2 N_{frp}}{dx^2} - \left[\Phi_1 - \Phi_2 y_{frp}\right] N_{frp} - \Phi_2 M_{frp} = k\Delta\varepsilon(x)$$

Where C_1 and C_2 are coefficient from Equation 6-32.

$$C_1 = \left[\frac{1}{E_{frp} A_{frp}} + \frac{1}{E_b A_b} + \frac{(2y_b - t_a)(y_{frp} + y_b)}{2E_b I_b}\right] \qquad C_3 = \frac{t_a}{G_a b_a} \qquad \Phi_1 = \frac{C_1}{C_3}$$

$$C_2 = \left[\frac{y_b}{E_b I_b} - \frac{y_{frp}}{E_{frp} I_{frp}} + \frac{t_a}{2}\left(\frac{1}{E_{frp} I_{frp}} - \frac{1}{E_b I_b}\right)\right] \qquad \Phi_2 = \frac{C_2}{C_3} \qquad k = \frac{1}{C_3}$$

$$\Delta\varepsilon(x) = \Delta T(\alpha_{frp} - \alpha_b) - \left[y_b - \frac{t_a}{2}\right]\frac{M}{E_b I_b}$$

Equation 6-39

Substituting Equation 6-36, Equation 6-37, and Equation 6-38 into Equation 6-35, the governing equations for normal stresses may be written in terms of the FRP plate force and moment.

$$y_{frp}\frac{d^4N_{frp}}{dx^4}+\frac{d^4M_{frp}}{dx^4}+\mu_1 N_{frp}+\mu_2 M_{frp}=v\Delta\psi(x)$$

Where

$$C_4=\frac{(y_{frp}+y_b)}{E_bI_b} \qquad C_5=\left[\frac{1}{E_{frp}I_{frp}}+\frac{1}{E_bI_b}\right] \qquad \Delta\psi(x)=\frac{M}{E_bI_b}$$

$$C_6=\frac{t_a}{E_ab_a} \qquad \mu_1=\frac{C_4}{C_6} \qquad \mu_2=\frac{C_5}{C_6} \qquad v=\frac{1}{C_6}$$

Equation 6-40

Finite difference solution

The model is a boundary value problem, and the boundary values are known. The governing equations for shear and normal stresses along the adhesive joint in bending are coupled, and can be solved numerically using explicit finite difference approximation. The differential Equation 6-39 and Equation 6-40 were changed into a finite difference equation. The second and fourth order finite difference formulas were used to find the shear and normal stress distribution. The equations can be found the numerical text books such as Mathews and Fink (1999); (Chapra, 2012); Esfandiari (2017).

Boundary conditions:

- At the discontinuity (the end of the FRP plate $x=0$), the plate force, moment, and shear force were zero $V_{frp}^1=N_{frp}^1=M_{frp}^1=0$
- At the centre of the beam ($x=0.5L_{frp}$), $V_{frp}^n=\tau_a^n=0$

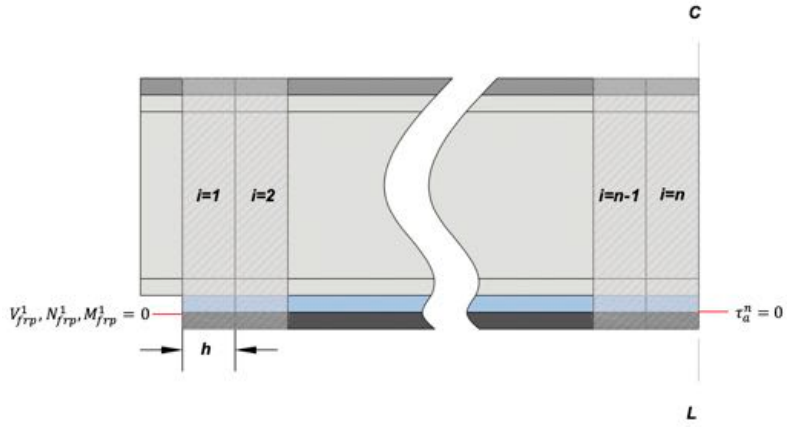

Figure 6-11: Boundary conditions and finite difference variables

The shear stress governing

Equation 6-39 may be written in second order finite difference form (three-point central difference formula):

$$\frac{N^{i-1}_{frp} - 2N^{i}_{frp} + N^{i+1}_{frp}}{h^2} - \left(\Phi^i_1 - \Phi^i_2 y_{frp}\right)N^i_{frp} - \Phi^i_2 M^i_{frp} = k^i \Delta\varepsilon^i_x$$

Equation 6-41

Where n, h and i were number of steps, step length and step number respectively as shown in Figure 6-11. Φ_2, Φ_2 and κ are co from Equation 6-39.

At the tip of the FRP plate (the first boundary condition), when $i = 1$, Equation 6-41 becomes:

$$-\left(2 + \Phi^i_1 h^2 - y_{frp}\Phi^i_2 h^2\right)N^i_{frp} + N^{i+1}_{frp} = k^i h^2 \Delta\varepsilon^i_x \qquad i = 1$$

Equation 6-42

When $1 \le i \le n$ Equation 6-41 can be rearranged to give:

$$N^{i-1}_{frp} - \left(2 + \Phi^i_1 h^2 - y_{frp}\Phi^i_2 h^2\right)N^i_{frp} + N^{i+1}_{frp} - \Phi^i_2 h^2 M^i_{frp} = k^i h^2 \Delta\varepsilon^i_x \qquad 1 \le i \le n$$

Equation 6-43

At the centre of the beam (the second boundary condition), the shear stress is zero $\tau_a = 0$ and Equation 6-19 in finite difference form gives:

$$\frac{1}{b_a}\frac{dN_{frp}}{dx} = \frac{N^{i-1}_{frp} - N^{i+1}_{frp}}{2h} = 0$$

Equation 6-44

When $i = n$ substituting Equation 6-45 in Equation 6-41 gives:

$$N_{frp}^{i-1} - 0.5 * \left(2 + \Phi_1^i h^2 - y_{frp}\Phi_2^i h^2\right)N_{frp}^i - \Phi_2^i h^2 M_{frp}^i = 0.5 * k^i h^2 \Delta\varepsilon_x^i \qquad i = n$$

Equation 6-45

The normal stress governing

Equation 6-40 may be written forth order finite difference form (three-point central difference formula):

$$\left(\begin{array}{c} y_{frp}\dfrac{N_{frp}^{i-2} - 4N_{frp}^{i-1} + 6N_{frp}^i - 4N_{frp}^{i+1} + N_{frp}^{i+2}}{h^4} \\ + \\ \dfrac{M_{frp}^{i-2} - 4M_{frp}^{i-1} + 6M_{frp}^i - 4M_{frp}^{i+1} + M_{frp}^{i+2}}{h^4} \end{array}\right) + \mu_1^i N_{frp}^i + \mu_2^i M_{frp}^i = v^i \Delta\psi_x^i$$

Equation 6-46

Where n, h and i were number of steps, step length and step number respectively. μ_2, μ_2 and v are coefficient from Equation 6-40.

At the tip of the FRP plate (the first boundary condition), $V_{frp} = 0$ and Equation 6-21:

$$V_{frp} = \frac{dM_{frp}}{dx} + y_{frp}\frac{dN_{frp}}{dx} = 0$$

Equation 6-47

Writing Equation 6-47 in second order finite difference form (two-point central difference formula):

$$M_{frp}^{i-1} = M_{frp}^{i+1} - y_{frp}\left(N_{frp}^{i-1} - N_{frp}^{i+1}\right)$$

Equation 6-48

When $i = 1$ substitute Equation 6-48 and $N_{frp} = M_{frp} = 0$ (from the first boundary condition) in Equation 6-46:

$$y_{frp}\left(\left(6 + \frac{1}{y_{frp}}\mu_1^i h^4\right)N_{frp}^i + N_{frp}^{i+2}\right) + (6 + \mu_2^i h^4)M_{frp}^i + M_{frp}^{i+2} = v^i h^4 \Delta\psi_x^i \qquad i = 1$$

Equation 6-49

When $i = 2$ substitute $N_{frp} = M_{frp} = 0$ due to discontinuity of the adhesive joint (the first boundary condition) in Equation 6-46:

$$\begin{pmatrix} y_{frp}(-4N_{frp}^{i-1} + (6 + \frac{1}{y_{frp}}\mu_1^i h^4)N_{frp}^i - 4N_{frp}^{i+1} + N_{frp}^{i+2}) \\ + \\ -4M_{frp}^{i-1} + (6 + \mu_2^i h^4)M_{frp}^i - 4M_{frp}^{i+1} + M_{frp}^{i+2} \end{pmatrix} = v^i h^4 \Delta\psi_x^i \qquad i = 2$$

Equation 6-50

When $1 \leq i \leq n$ Equation 6-46 can be rearranging as:

$$\begin{pmatrix} y_{frp}(N_{frp}^{i-2} - 4N_{frp}^{i-1} + (6 + \frac{1}{y_{frp}}\mu_1^i h^4)N_{frp}^i - 4N_{frp}^{i+1} + N_{frp}^{i+2}) \\ + \\ M_{frp}^{i-2} - 4M_{frp}^{i-1} + (6 + \mu_2^i h^4)M_{frp}^i - 4M_{frp}^{i+1} + M_{frp}^{i+2} \end{pmatrix} = v^i h^4 \Delta\psi_x^i \qquad 1 \leq i \leq n$$

Equation 6-51

At the centre of the beam (the second boundary condition), $V_{frp} = 0$ and Equation 6-21 in finite difference form:

$$V_{frp} = \frac{dM_{frp}}{dx} + y_{frp}\frac{dN_{frp}}{dx} = 0$$

Equation 6-52

Writing Equation 6-52 in second order finite difference form using the three-point forward formula (Lagrange interpolation approach):

$$M_{frp}^{i+2} = -3M_{frp}^i + 4M_{frp}^{i+1} + y_{frp}(-3N_{frp}^i + 4N_{frp}^{i+1} - N_{frp}^{i+2})$$

Equation 6-53

When $i = n$ substitute Equation 6-53 in Equation 6-46.

$$\begin{pmatrix} y_{frp}\left(N_{frp}^{i-2} - 4N_{frp}^{i-1} + \left(3 + \frac{1}{y_{frp}}\mu_1^i h^4\right)N_{frp}^i\right) \\ + \\ M_{frp}^{i-2} - 4M_{frp}^{i-1} + (3 + \mu_2^i h^4)M_{frp}^i \end{pmatrix} = v^i h^4 \Delta\psi_x^i \qquad \begin{matrix} i = n \\ i = n-1 \end{matrix}$$

Equation 6-54

The same Equation 6-54 applies to $i = n - 1$ because the N_{frp}^{i+1} and M_{frp}^{i+1} have already cancelled from the equation.

Equation 6-42, Equation 6-43, Equation 6-45, Equation 6-49, Equation 6-50, Equation 6-51 and Equation 6-54 together give a set of 2*n* simultaneous equations, involving 2*n* unknowns. These equations were compiled into matrix form for linear solution. The global matrix for the problem set up is shown in Figure 6-12. Further information on the global matrix formation of similar problems are discussed in Fox and Mayers (1987); Lapidus and Pinder (1999); LeVeque (2007). The computer

programme development flowchart is shown in Figure 6-13, and the computed programme script is provided in the Appendix E.

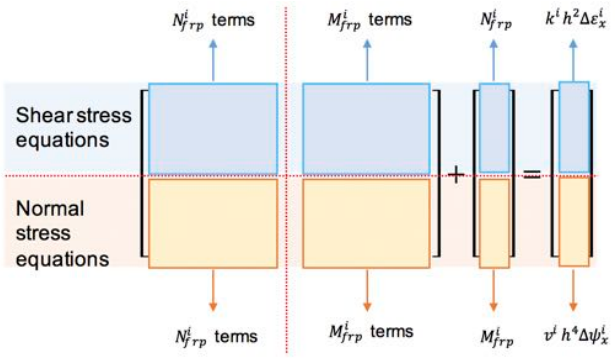

Figure 6-12: The global matrix formation of the differential equations

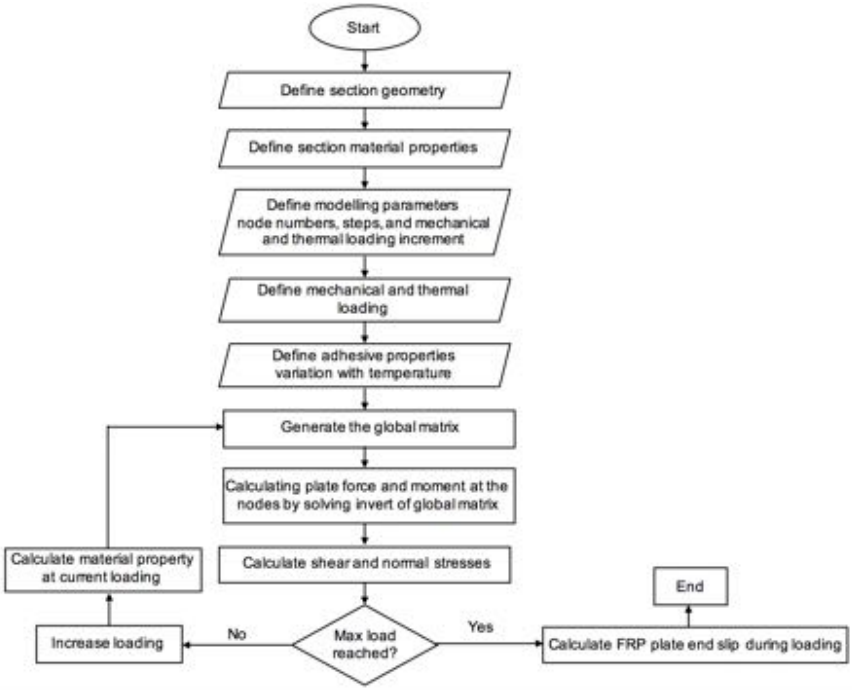

Figure 6-13: Flowchart of the computer programme

6.4.3 Model comparison at ambient temperature

In this section the current approached is compared with the original modes (Deng *et al.*, 2004; Stratford and Cadei, 2006). For comparison purposes, only mechanical loading of 350kN is applied to the beam using the properties given in

Figure 6-14. The convergence of the numerical procedure was examined, maximum shear and normal stresses for only mechanical loading versus different number of steps were plotted in Figure 6-15.

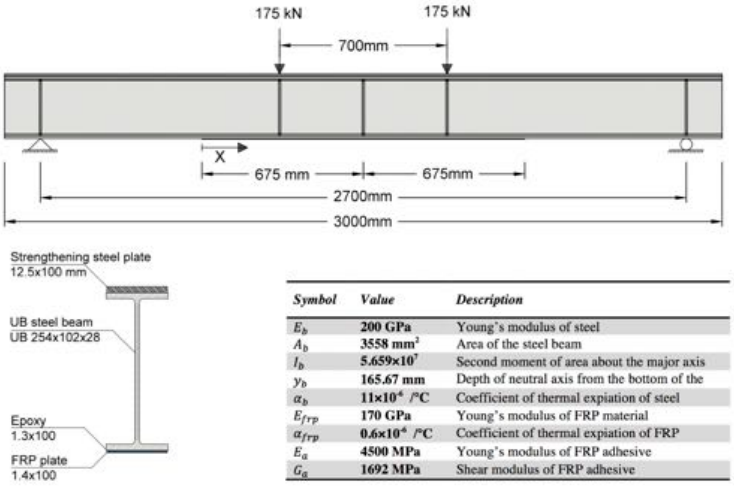

Symbol	*Value*	*Description*
E_b	**200 GPa**	Young's modulus of steel
A_b	**3558 mm^2**	Area of the steel beam
I_b	**5.659×10^7**	Second moment of area about the major axis
y_b	**165.67 mm**	Depth of neutral axis from the bottom of the
α_b	**11×10^{-6} /°C**	Coefficient of thermal expiation of steel
E_{frp}	**170 GPa**	Young's modulus of FRP material
α_{frp}	**0.6×10^{-6} /°C**	Coefficient of thermal expiation of FRP
E_a	**4500 MPa**	Young's modulus of FRP adhesive
G_a	**1692 MPa**	Shear modulus of FRP adhesive

Figure 6-14: Details of the strengthened beam for the bond analysis

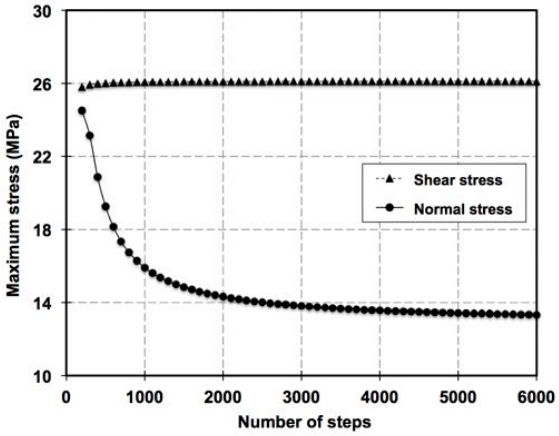

Figure 6-15: Convergence of numerical procedure

The shear stress converges with relatively small number of steps because shear-governing equation is the second order deferential equations while the normal stress equations were the fourth order. To compare the current model with the original models (Deng *et al.*, 2004; Stratford and Cadei, 2006), relatively high number of steps used, and the results were shown in Figure 6-16. Experimental

results and the predictions form the model for transient tests are presented in section 6.4.4.

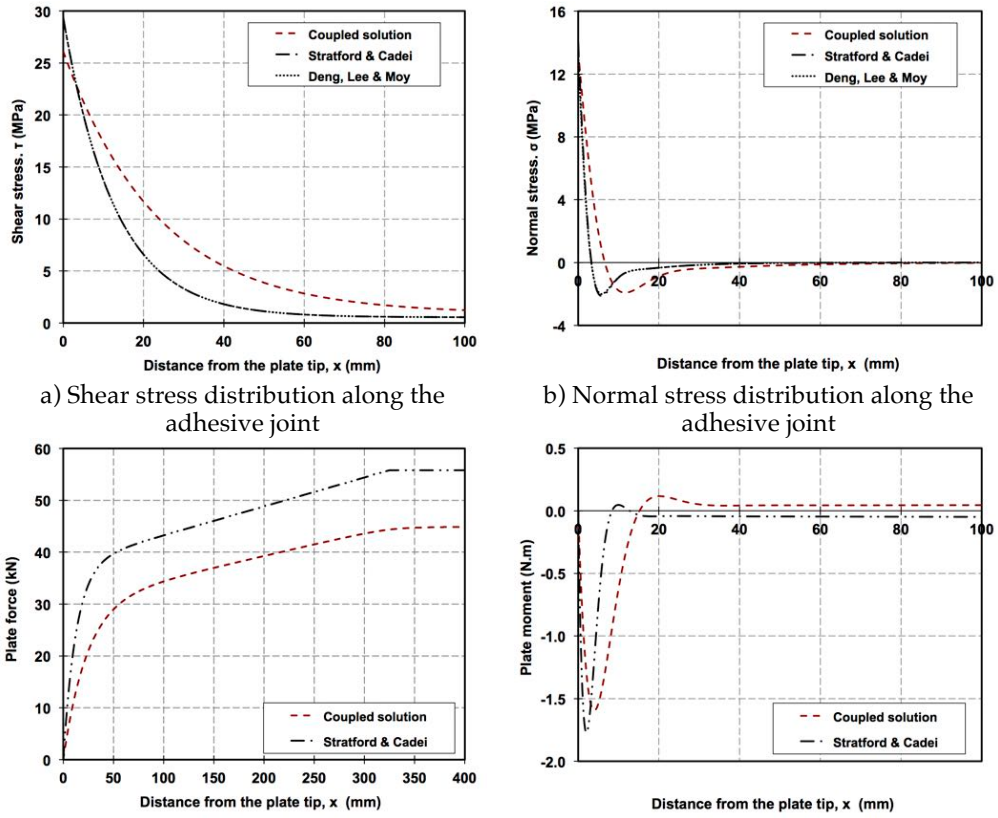

a) Shear stress distribution along the adhesive joint

b) Normal stress distribution along the adhesive joint

c) FRP plate force distribution

d) FRP plate moment distribution

Figure 6-16: Comparing shear and normal stresses in the adhesive and internal plate force and moment calculated from different models

The two well-presented modes (Deng *et al.*, 2004; Stratford and Cadei, 2006) assume the plate and beam curvature were the same to decouple the shear and normal stresses therefore the results seem to be identical. The maximum calculated shear stress from the two models is 29.3 MPa, while the current model estimates 26.1 MPa. The maximum calculated normal stress from the three models is approximately 14 MPa. The peaks shear and normal stresses were not very different, but the stress distributions at the critical areas were different. The difference is more likely to increase when thicker FRP plate is used. The distribution of the stresses is important when the effect of temperature is considered; in the previous models, the peaks were more affected and the values will change dramatically because the

stresses were concentrated in a short region. The current model shows that although the stresses peaks were at the tips, they were not intensively concentrated near that region. Therefore, when the temperature is increased the stresses redistribute before the peaks change dramatically.

6.4.4 Experimental and prediction slippage

The current model used to predict the slip displacement of the CFRP plate, using the same approach (Dawood and El-Tahan, 2011); due to some error in the equations, the original documents should be used. The work assumes linear reduction in the adhesive properties (tensile strength, Young's modulus) from room temperature to 40°C. The number steps for this analysis were kept at 1000 steps since it appears (refer to Figure 6-15) that it is sufficient to achieve accurate results. The thermal coefficient of the steel and CFRP martial is taken in to account (refer to Figure 6-14), and only the adhesive stiffness (Young's modulus) reduction assumed to follow the DMA storage modulus variation with temperature. The storage modulus is normalised at 23°C. The adhesive stiffness reduction results in the distribution of the same shear force to be carried through the adhesive joint over a greater length, as shown in Figure 6-17 a. The stiffness reduction approach also affects the distribution of the normal stress, FRP plate force and moment as shown in in Figure 6-17.

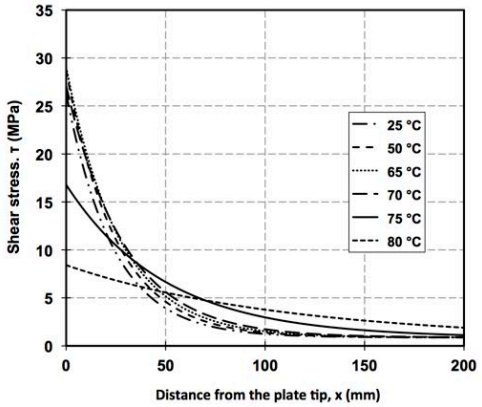

a) Shear stress distribution along the adhesive joint

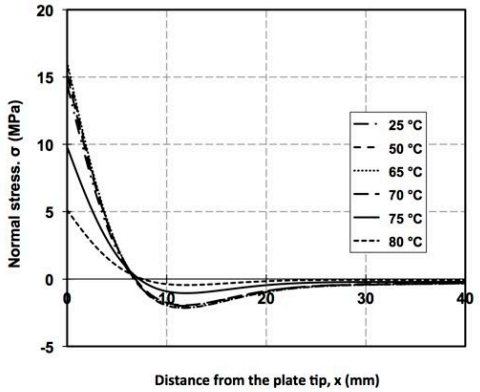

b) Normal stress distribution along the adhesive joint

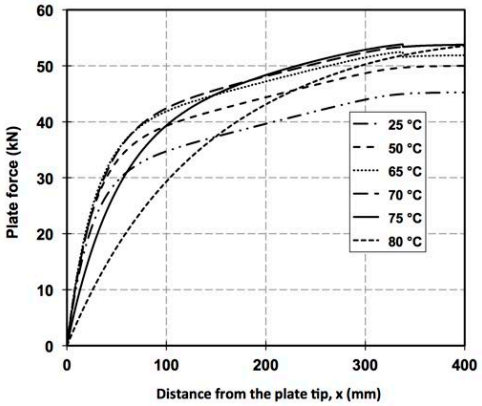

c) FRP plate force distribution

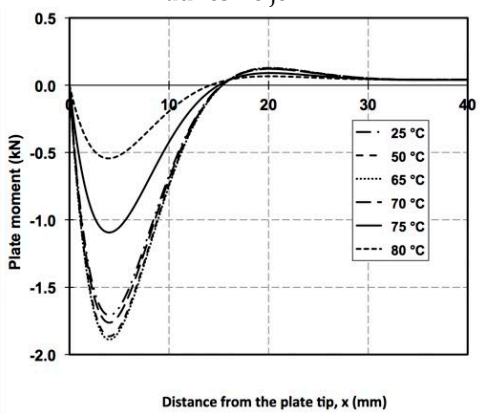

d) FRP plate moment distribution

Figure 6-17: Shear and normal stresses in the adhesive and internal plate force and moment at different temperatures along the joint

A comprehensive analysis is carried out to examine the behaviour of beams using the same approach. The shear strain can be interpreted as a slip deformation as shown in Equation 6-55.

$$s = t_a \gamma_a$$

Equation 6-55

The experimental results and bond analysis predictions were very different as shown in Figure 6-18. Not only at high temperature, but also at temperatures close to room temperature, the experiments show no slip at the start of the test while the predictions show as small amount of slip. This is due to the fact that the peak shear stress occurs at the FRP plate ends, which violates the stress-free condition. This slip would be more if the original models (Smith and Teng, 2001; Deng *et al.*, 2004;

Stratford and Cadei, 2006) were used as discussed in section 6.4.3. The original models predict higher shear stresses that the current presented model.

At high temperatures, the plate slip according to the model starts at higher temperatures than the experiments. This is because the model assumes material failure and the assumption of modulus reduction is not the true behaviour of the joint when it is subjected to elevated temperature. The experimental results that were discussed in section 5.8.4 showed that the failure is not in the material, and it is interface failure.

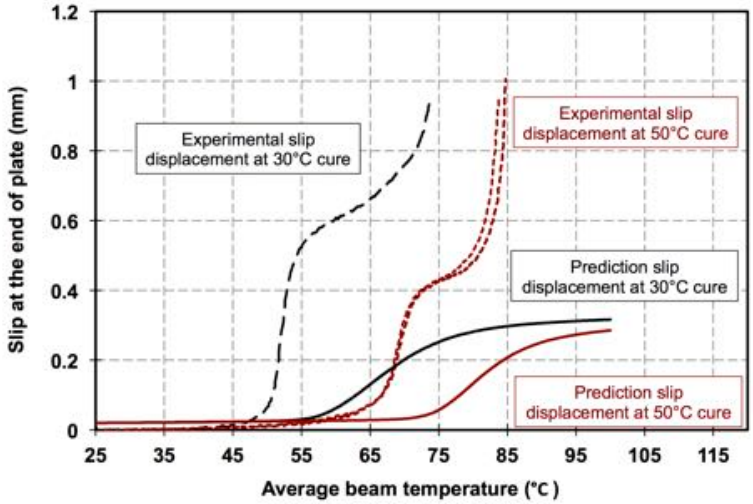

b) Experimental and analytical slip displacement at the tip of the CFRP plate

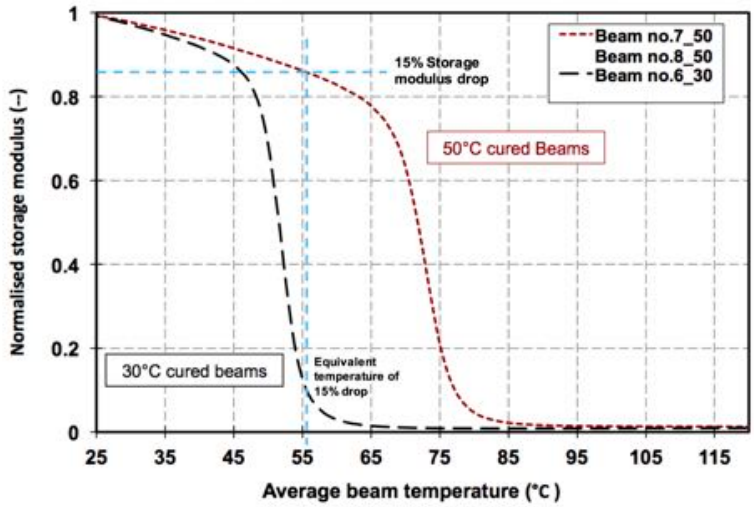

a) Adhesive storage modulus variation with temperature

Figure 6-18: Adhesive property changes, experimental and analytical slip displacement at the tip of the CFRP plate with temperature

Tests that were carried out by Abed (2012); Stratford and Bisby (2012) on specimens in bending. The numbers of tests were limited. The elevated temperature experimental results in this research were different from the tests that were reported in literature.

The tests by Stratford and Bisby (2012) were carried out under sustained load and transient temperature, it should be noticed that only 450mm of the FRP plate end is heated. The authors stated that failure occurred within the adhesive material, and they presented analytical model assuming linear-elastic perfectly plastic (elastoplastic) constitutive law and the combined effects of strength and stiffness reduction for the adhesive. They also compared experiments with a model. The analytical response follows the same trend as the experiments; slip starts to increase when the temperature approached glass transition temperature T_g.

The tests completed by Abed (2012) for specimens fully heated and then tested when a targeted temperature is reached. The author modified the analytical model by Deng *et al.* (2004) to accommodate linear-elastic perfectly plastic adhesive material law. The stress distribution along the FRP length from the analytical model is compared with stress distribution form FE model that assumed bilinear elastic-plastic stress strain for the adhesive that is different from the analytical assumption. The analytical mode is validated using the FE despite the fact that different material laws were used.

Adjustments can be made to the current model to accommodate a non-linearity of the adhesive and the combined effect of strength and stiffness reduction to examine the degradation of the adhesive prior to the separation of the FRP plate from the steel section. However, it is believed that adhesive interface failure caused the remarkable difference between the predictions and experiments.

Despite the disagreement between the theoretical and experimental results, the experiments revealed important information. The slip displacement of the CFRP plates starts at temperatures below T_g as shown in Figure 6-18. The current guidelines recommendation (Cadei *et al.*, 2004; ACI 440.2R-08, 2008; Concrete Society, 2012) is that the adhesive should remain at least 15°C below its maximum operating temperature; $(T_g - 15)$ where glass transition temperature T_g is the peak of $\tan\delta$ of the DMA accoutring to British Standard ISO 6721 (2011). The values of glass transition temperature T_g according to different methods were listed in Table

5-4. The maximum operating temperature for the tested beams cured at 30°C and 50°C were 44°C and 64°C respectively. However, the temperatures that the CFRP plates started to slip from the tests carried out in this research were 46°C and 60 °C, refer to Table 5-10. It seems these temperatures were critical and extra precautions should be considered.

Comparing the adhesive storage modulus variation with temperature and the slip of the CFRP plate in Figure 6-18, the slip started when adhesive storage modulus reduced by 15% for the applied sustained load. If the sustained load is greater than the applied load, slippage is expected to occur at lower temperatures. Therefore, based on this work the service temperature should not exceed the equivalent to the 15% drop in the storage modulus of the DMA specimen. Alternatively, the values of glass transition temperature T_g restricted to the peak of loss modulus according to ASTM D4065-01 (2001).

6.5 Summary

A flexural model was developed to study the behaviour of steel section in flexure based on strain compatibility and the constitutive material law. The model was shown to predict reasonably the behaviour of the section considering non-linearity of the materials and the effects of strain hardening. The effect of strain hardening was examined, and different models were considered. The models significantly under estimated the load-deflection response of the tested steel section. The Holmond-Ludwik's formula was used to estimate the effects of strain hardening, and good predictions were obtained. Different constitutive law of material used for the standard I-section and the top flange strengthening plate because of the different rates of strain hardening from the steel coupons.

Existing analytical models were modified to calculate the interfacial stresses within the adhesive layer. However, the model assumed that adhesive mechanical properties were linear elastic. The stresses at the plate ends increased continuously with loading, which may exceed the maximum adhesive strengths. Unlike the original model, the current model considers the coupled effects of shear and normal stress variation in the interfaces. Due to the complicity of the coupled effect, finite difference method was used to solve the differential equations. The bond model was

compared to the original modes, and the shapes of the stress distribution were different, which can be significant when thick CFRP plates were used.

The effects of elevated temperatures were studied using the model. It was assumed that only the adhesive stiffness (Young's modulus) was reduced with increasing temperature, but remained linear. The stiffness reduction was assumed to be the same as storage modulus variation response of the adhesive with temperature that was achieved from the DMA coupons tests. The stresses and the plate force and moment were examined; the shear stresses along the adhesive joint tended to spread along the length of the joint and eventually reduced the stress concentration at the CFRP plates. Although using only Young's modulus reduction may not be sufficient to predict the behaviour of the joints when they were subjected to elevated temperatures, the failure that occurred in the specimens regardless of the curing temperature was interface failure not material failure. Therefore, further investigations were required to understand adhesive joint when they were subjected to elevated temperature.

The test results recommend that the service temperature should not exceed the equivalent of the 15% drop in the storage modulus. The variation of storage modulus should be obtained from DMA tests using single cantilever configuration. Alternatively, if the recommendation of the design guidelines (Cadei *et al.*, 2004; Concrete Society, 2012) were used, the values of glass transition temperature T_g restricted to the peak of loss modulus according to ASTM D4065-01 (2001).

Chapter 7

Conclusions, Recommendations and Future Work

The aim of this work was to investigate the effect of curing temperature upon glass transition temperature T_g. Glass transition temperature T_g is an important property of epoxy adhesives, and it is dependent on the curing temperature. Two widely used epoxies in construction were studied. The T_g of structural adhesives was studied for up to 28 days after exposure to the combination of elevated temperature up to 80°C dry and in water.

The performance of EB-FRP strengthened steel beams in flexure was studied. Nine 3-metre beams were strengthened with CFRP plates and cured at elevated temperatures. Four point bending tests were carried out on the I-section specimens at ambient and elevated temperatures. The ambient tests under monotonic static load, and sustained load with transient temperature were tested to understand the complex interaction between the FRP and the steel sections. Double lap-shear, adhesion pull-off, and DMA specimens were prepared with the steel sections to provide information on the adhesive properties and surface preparation.

This study compares the current design guidelines and the tests as described in this research. It should be noted that the recommendations in the guidelines have never been subjected to laboratory testing. The findings of this study leads to the conclusion that some adjustment to the current design guidelines is required.

7.1 Conclusions and findings

Tests were carried out to study glass transition temperature T_g and the influence of curing conditions on Sikadur-330 and Tyfo-S adhesives. Glass transition temperature T_g was assessed using Dynamic Mechanical Analysis (DMA) and Differential Scanning Calorimetry (DSC). It was found that the curing temperature and the glass transition temperature T_g of the studied adhesives was in a linear relationship. The required glass transition temperature T_g may never be achieved at

low temperatures even if the system is left for as long as 28 days. The study shows that certain glass transition temperature T_g can only be achieved with elevated temperature curing.

The optimised glass transition temperature T_g for Sikadur-330 and Tyfo-S was at dry cure at 50°C and 65°C respectively for 7 days. Beyond these temperatures no further improvement was noticed. The specimens cured under combined saturated and high temperature conditions exhibited only slight T_g improvement. Beyond 35°C and 50°C the adhesive Sikadur-330 and Tyfo-S showed a decline in performance.

Glass transition temperature T_g values according to the peak loss modulus and the inflection point of storage response from DMA were very close, and they were least affected by the testing parameters.

A comparison of the results of the two methods (the peak loss modulus and the inflection point of storage response) was in correlation. In comparison DSC results were also in correlation with the values that are found at the inflection point.

Lap shear, DMA and pull-off tests results indicate that the flexural performance of the beams will improve with curing. The lap shear specimens show an increase of approximately 29% in the shear strength of the adhesive when the curing temperature as increased from 25°C to 50°C. The storage modulus variation with temperature was obtained from the DMA runs and the glass transition temperature T_g values were found from the DMA responses. The steel surface preparation was found to be adequate from adhesion pull-off tests.

To understand the performance and overall behaviour of post cured joints at ambient and transient temperatures flexural tests were carried out. Five beams were tested at ambient temperature to show the effects of adhesive curing on FRP strengthened sections. A significant increase of load capacity of the adhesive joints was achieved due to the curing of the joints at elevated temperature. Two different failure modes (inelastic lateral-torsional buckling and FRP debonding failure) were observed. Only one specimen failed in inelastic lateral-torsional buckling. This was due to the use of long FRP plate. In the three ambient tests, debonding failure occurred regardless of the curing temperature. The debonding failure was in the same manner. At the tip of the plate at steel-adhesive interface traces of adhesive were found on the steel surface. An increase of approximately 25% was noticed in

the ultimate load capacity of the specimens cured at 50°C compared to the specimens cured at 30°C.

The three specimens that were tested at transient temperature showed that the specimens cured at high temperature showed a better performance. With increasing temperature, a failure mechanism occurred. The plate started to slip due to degradation of the adhesive, which eventually led to complete debonding of the adhesive-FRP reinforcement from the steel section. It should be noted that hardly any adhesive remained on the steel surface. The only specimen that was cured at 30°C, slip at FRP plate started when the beam temperature reached approximately 46°C. The two specimens that were cured at 50°C, slip at FRP plate started when the beam temperature reached approximately 60°C.

The slip of the FRP plate from the transient temperature tests and the adhesive degradation from the DMA showed that the FRP plate slip started when the adhesive storage modulus was reduced by approximately 15% and 18%, for the specimens cured at 30°C and 50°C, respectively.

The guideline recommendations by Cadei *et al.* (2004) suggest using $T_g - 15$. The single value of T_g is measured from DMA response of peak tan δ. Following this instruction the temperature of the structure should not exceed 44.1°C and 64.7°C for the beams cured at 30°C and 50°C, respectively.

The flexural model, which was developed based on strain compatibility and constitutive material properties, was used to examine the effect of strain hardening. The model reasonably predicted the behaviour of the un-strengthened and FRP strengthened beams only when the effect of strain hardening was included. Holmond-Ludwik's formula was used to estimate the strain hardening effect for the standard I-section and the top flange steel strengthening plate.

An analytical bond model, which was based on compatibility approach and similar to the previous work in Smith and Teng (2001); Deng *et al.* (2004); Stratford and Cadei (2006), was presented. The model was modified to incorporate the coupled interfacial shear and normal stresses simultaneously, using finite difference approximation method. The effects of elevated temperatures were studied using the model. Young's modulus of the adhesive was assumed to change in the same manner as the storage modulus variation with temperature. The storage modulus variation was obtained from the DMA. The predictions from the model and experimental results were remarkably different. It is understood that this was due to

the simplification of the adhesive degradation and the adhesion failure in the adhesive steel interface.

7.2 Design recommendations

The findings according to the study suggest that the service temperature of an externally bonded (EB) FRP strengthened structure should remain below the temperature, which corresponds to a 15% drop in the storage modulus of the adhesive specimens. The DMA samples should be prepared and conditioned in the same environment, and tested in single cantilever configuration, 1Hz frequency and heating rate of 2 °C/min.

The parameters proposed by the guidelines (Cadei *et al.*, 2004; ACI 440.2R-08, 2008; Concrete Society, 2012) regarding the glass transition temperature T_g of the adhesive state that these temperatures should be at least 15°C above the structures' maximum operating temperature. Where the single value of T_g is measured from DMA response according to peak tan δ, this differs from the results found in the tests of this research. The glass transition temperature T_g should be measured according to the peak of loss modulus (ASTM D4065-01, 2001), and obtained from DMA.

7.3 Research limitations

The experimental work was carried out on a limited number of four point flexure tests and only one type of epoxy. Further tests are recommended using different types of adhesive that are cured to yield at the same glass transition temperature T_g.

The four-point tests represented flexural behaviour of a FRP strengthened steel-concrete bridge deck. A thicker top plate however is appropriate to represent the actual performance of such a structure.

The analytical bond model in this research assumes liner elastic material properties for adhesives and steel modifications are required to accommodate non-linear constitutive material properties for each section.

7.4 Future work

Sustained load and cyclic temperature for CFRP reinforced beams should be experimentally investigated to understand the properties of the structures exposed to load and daily temperature changes. In addition to this, time and the temperature dependency investigation is required to avoid creep failures.

The current analytical bond model may be used to investigate strengthened sections with various geometries along the bonded joint including the FRP material thickness, the local defect of adhesive, and local heating of the bonded joint. It also can be modified to accommodate non-linear constitutive material properties for each section.

The O-105 chamber performed well during the curing process. The temperatures were controlled accurately during testing. Considering the significant amount of steel the temperature increased approximately linearly at a rate of 0.8 °C/min. This was repeated during all the tests. The current work shows that a similar approach may be adopted for future research. However, to increase the performance of the chamber the installation of the third heater would improve the control of heating rate.

References

Abed G. M. H. (2012). *Effects of temperature on the adhesive bonding in steel beams reinforced with CFRP composites*, Faculty of Engineering and The Environment, School of Civil Engineering, University of Southampton, Doctorate in Philosophy (PhD) Thesis.

ACI 440.2R-08. (2008). Guide for the design and construction of externally bonded FRP systems for strengthening concrete structures, Farmington Hills, Michigan.

ACI 440R-07. (2007). Report on Fiber Reinforced Polymer (FRP) Reinforcement for Concrete Structures, Farmington Hills, Michigan.

Adams R. D., J. Comyn and W. C. Wake. (1997). *Structural adhesive joints in engineering*, Springer Science & Business Media.

Afefy H. M., K. Sennah and H. Akhlagh-Nejat. (2016). Experimental and analytical investigations on the flexural behavior of CFRP-strengthened composite girders, *Journal of Constructional Steel Research*, 120(2016):94-105.

Al-Azzawi Z. M. K. (2016). *Capacity of FRP strengthened steel plate girders against shear buckling under static and cyclic loading*, Institute of infrastructure and Environmental, The University of Edinburgh, Doctorate in Philosophy (PhD) Thesis.

Al-Emrani M., D. Linghoff and R. Kliger. (2005). Bonding strength and fracture mechanisms in composite steel-CFRP elements, *in*: International Symposium on Bond Behaviour of FRP in Structures (BBFS 2005), International Institute for FRP in Construction, Hong Kong, China, 7-9, December 2005.

Al-Safy R., R. Al-Mahaidi and G. P. Simon. (2012). Investigation of thermo-mechanical properties of adhesive used for bonding CF fabrics to concrete members using post-curing techniques, *Composites Part B: Engineering*, 43(2012):2950–2959.

Al-Safy R., R. Al-Mahaidi and G. P. Simon. (2013). A study of the practicality and performance of CFRP applications using post-curing at moderately elevated temperatures, *Composites Part B: Engineering*, 48(2013):140-157.

Al-Saidy A. H., F. W. Klaiber and T. J. Wipf. (2004). Repair of steel composite beams with carbon fiber-reinforced polymer plates, *Journal of Composites for Construction*, 8(2):163-172.

Al-Shawaf A., R. Al-Mahaidi and X.-L. Zhao. (2009). Effect of elevated temperature on bond behaviour of high modulus CFRP/steel double-strap joints, *Australian Journal of Structural Engineering*, 10(1):1-16.

Al-Zubaidy H., R. Al-Mahaidi and X.-L. Zhao. (2012). Experimental investigation of bond characteristics between CFRP fabrics and steel plate joints under impact tensile loads, *Composite Structures*, 94(2):510-518.

Ashby M. F. and D. R. H. Jones. (2013). *Engineering materials 2: an introduction to microstructures, processing and design*, Butterworth-Heinemann.

Assoodani F. A. (2014). *Shear behaviour and strength of CFRP retrofitted steel plate girders and steel-concrete composite plate girders*, University of Technology, Iraq, Doctorate in Philosophy (PhD) Thesis.

ASTM A0370-03a. (2003). Standard methods and definitions for Mechanical testing of steel products, American Society for Testing and Materials (ASTM) International, West Conshohocken, PA, United States.

ASTM A0370-77. (1977). Standard methods and definitions for Mechanical testing of steel products, American Society for Testing and Materials (ASTM) International, West Conshohocken, PA, United States.

ASTM D0293-02. (2002). Standard test method for flexural strength of concrete (using simple beam with center-point loading), American Society for Testing and Materials (ASTM) International, West Conshohocken, PA, United States.

ASTM D0638-03. (2003). Standard test method for tensile properties of plastics, American Society for Testing and Materials (ASTM) International, West Conshohocken, PA, United States.

ASTM D648-01. (2001). Standard test method for deflection temperature of plastics under flexural load in the Edgewise position, American Society for Testing and Materials (ASTM) International, West Conshohocken, PA, United States.

ASTM D0790-03. (2002). Standard test methods for flexural properties of unreinforced and reinforced plastics and electrical insulating materials, American Society for Testing and Materials (ASTM) International, West Conshohocken, PA, United States.

ASTM D2584-02. (2002). Standard test method for ignition loss of cured reinforced resins, American Society for Testing and Materials (ASTM) International, West Conshohocken, PA, United States.

ASTM D2651-01. (2001). Standard Guide for preparation of metal surfaces for adhesive bonding, American Society for Testing and Materials (ASTM) International, West Conshohocken, PA, United States.

ASTM D3418-99. (1999). Standard test method for transition temperatures of polymers by Differential Scanning Calorimetry, American Society for Testing and Materials (ASTM) International, West Conshohocken, PA, United States.

ASTM D4065-01. (2001). Standard Practice for Plastics: Dynamic Mechanical Properties: Determination and Report of Procedures, American Society for Testing and Materials (ASTM) International, West Conshohocken, PA, United States.

ASTM D4541-02. (2002). Standard test method for pull-off Strength of coatings using portable adhesion testers, American Society for Testing and Materials (ASTM) International, West Conshohocken, PA, United States.

ASTM D7234-12. (2012). Standard test method for pull-off adhesion strength of coatings on concrete using portable pull-off Adhesion testers, American Society for Testing and Materials (ASTM) International, West Conshohocken, PA, United States.

ASTM E8/E8M-09. (2009). Standard methods and definitions for tension testing of metallic materials, American Society for Testing and Materials (ASTM) International, West Conshohocken, PA, United States.

ASTM E0646-00. (2000). standard test method for tensile strain-hardening exponents (n - Values) of metallic sheet materials, American Society for Testing and Materials (ASTM) International, West Conshohocken, PA, United States.

ASTM E1640-99. (1999). Standard test method for assignment of the glass transition temperature by dynamic mechanical analysis, American Society for Testing and Materials (ASTM) International, West Conshohocken, PA, United States.

Atarsia A. and R. Boukhili. (2000). Relationship between isothermal and dynamic cure of thermosets via the isoconversion representation, *Polymer Engineering & Science*, 40(3):607-620.

Au F. T. K., S. K. Cheung and L. G. Tham. (2002). Design thermal loading for composite bridges in tropical region, *Steel and Composite Structures*, 2(6):441-460.

Baker J., L. Baker and J. Heyman. (1980). *Plastic Design of Frames 1. Fundamentals*, CUP Archive.

Baker J. F., M. R. Horne and J. Heyman. (1956). *The Steel Skeleton, Volume II, Plastic Behaviour and design*, The Cambridge University Press.

Baldan A. (2004). Adhesively-bonded joints and repairs in metallic alloys, polymers and composite materials: adhesives, adhesion theories and surface pretreatment, *Journal of materials science*, 39(1):1-49.

Bank L. C. (2006). *Composites for construction: structural design with FRP materials*, John Wiley & Sons.

Besseling J. F. and E. Van Der Giessen. (1994). *Mathematical modeling of inelastic deformation*, CRC Press.

Bhutto M. A. (2014). *FRP-strengthening of webs of steel plate-girders* Heriot-Watt University Doctorate in Philosophy (PhD) Edinburgh, Scotland, Thesis.

Bisby L., W. A. Take and A. Caspary. (2007). Quantifying strain variation in FRP confined concrete using digital image correlation: proof-of-concept and initial results, *in*: In Asia-Pacific Conference on FRP in Structures (APFIS 2007), Hong Kong, China,

Bisby L. A. and W. A. Take. (2009). Strain localisations in FRP-confined concrete: new insights, *Proceedings of the Institution of Civil Engineers - Structures and Buildings*, 162(5):301-309.

Blontrock H. (2003). *Analyse en modellering van de brandweerstand van betonelementen uitwendig versterkt met opgelijmde composietlaminaten (In Dutch)*, Ghent University, Doctorate in Philosophy (PhD) Ghent, Belguim, Thesis.

British Standard EN 10025. (2004). Hot rolled products of structural steels, British Standards Institution (BSI), London, UK.

British Standard EN 10034. (1993). Structural steel I and H sections-Tolerances on shape and dimensions British Standards Institution (BSI), London, UK.

British Standard ISO 4360. (1990). Specification for weldable structural steels, British Standards Institution (BSI), London, UK.

British Standard ISO 6721. (2011). Plastics determination of dynamic mechanical properties., British Standards Institution (BSI), London, UK.

British Standard ISO 6721-1. (2011). Plastics determination of dynamic mechanical properties. Part 1 - general principles, British Standards Institution (BSI), London, UK.

British Standard ISO 6721-11. (2012). Plastics determination of dynamic mechanical properties. Part 11 - glass transition temperature, British Standards Institution (BSI), London, UK.

British Standard ISO 14127. (2008). Carbon-Fibre-Reinforced Composites - Determination of the resin, fibre and void contents, British Standards Institution (BSI), London, UK.

Broughton B. and M. Gower. (2003). Preparation and testing of adhesive joints, Measurement Good Practice Guide No. 47, National Physical Laboratory (NPL) Materials Centre, Teddington, Middlesex, United Kingdom, ISSN 1368-6550, September 2001.

Bussell M. N. (1997). *Appraisal of existing iron and steel structures*, Steel Construction Institute Ascot/London, UK.

Byfield M. P. (1996). *Steel design and reliability using Eurocode 3*, Department of civil engineering The University of Nottingham, Doctorate in Philosophy (PhD) Thesis.

Byfield M. P., J. M. Davies and M. Dhanalakshmi. (2005). Calculation of the strain hardening behaviour of steel structures based on mill tests, *Journal of Constructional Steel Research*, 61(2):133-150.

Byfield M. P. and M. Dhanalakshmi. (2002). Analysis of strain hardening in steel beams using mill tests, *in*: Advances in Steel Structures., Hong Kong, China, 9–11 December 2002.

Byfield M. P., A. R. Kemp and D. A. Nethercot. (2002). Effect of strain hardening on flexural properties of steel beams, *The Structural Engineer*, 80(8):29-34.

Byfield M. P. and D. A. Nethercot. (1997). Material and geometric properties of structural steel for use in design, *Structural Engineer*, 75(21):1-5.

Byfield M. P. and D. A. Nethercot. (1998). An analysis of the true bending strength of steel beams, *Proceedings of the ICE-Structures and Buildings*, 128(2):188-197.

Cadei J. M. C., T. J. Stratford, W. G. Duckett and L. C. Hollaway. (2004). *Strengthening metallic structures using externally bonded fibre-reinforced polymers*, CIRIA C595.

Cai H., P. Li, G. Sui, Y. Yu, G. Li, X. Yang and S. Ryu. (2008). Curing kinetics study of epoxy resin/flexible amine toughness systems by dynamic and isothermal DSC, *Thermochimica Acta*, 473(1-2):101-105.

Celesco Transducer Products. (2005). Cable extension position transducer data sheet.

Chajes M. J., A. P. Chacon, M. W. Swinehart, D. R. Richardson, G. C. Wenczel and W. Liu. (2005). Applications of advanced composites to steel bridges: a case study on the Ashland Bridge (Delaware-USA), Department of Civil and Environmental Engineering College Of Engineering. University Of Delaware. File: Rpt, Mar, 2005.

Chang T. D., S. H. Carr and J. O. Brittain. (1982). Studies of epoxy resin systems: Part B: Effect of crosslinking on the physical properties of an epoxy resin, *Polymer Engineering & Science*, 22(18):1213-1220.

Chapra S. C. (2012). *Applied Numerical Methods With MATLAB for Engineers and Scientists.*, McGraw-Hill.

Cho K. S. (2016). Theory of linear viscoelasticity, in: Viscoelasticity of polymers : theory and numerical algorithms, SpringerNature.

Christensen R. M. (1982). *Theory of viscoelasticity: an introduction*, Academic Press.

Clark. (2016). Aluminium Oxide Abrasive - 60 Grit safty data sheet.

Colombi P. and C. Poggi. (2006a). An experimental, analytical and numerical study of the static behavior of steel beams reinforced by pultruded CFRP strips, *Composites Part B: Engineering*, 37(1):64-73.

Colombi P. and C. Poggi. (2006b). Strengthening of tensile steel members and bolted joints using adhesively bonded CFRP plates, *Construction and Building Materials*, 20(1):22-33.

Comyn J. (1997). *Adhesion science*, Royal Society of Chemistry.

Concrete Society. (2012). Design Guidance for Strengthening Concrete Structures Using Fibre Composite Materials, Technical Rep. 55, Third Edition Camberley, UK, May 2012.

Craver C. and C. Carraher. (2000). Dynamic mechanical properties of polymers, in: Applied Polymer Science: 21st Century, Elsevier.

Culver C. (1960). The moment curvature relations for composite beams, Lehigh University, December, 1960.

da Silva L. F. M., P. J. C. das Neves, R. D. Adams and J. K. Spelt. (2009). Analytical models of adhesively bonded joints—Part I: Literature survey, *International Journal of Adhesion and Adhesives*, 29(3):319-330.

da Silva L. F. M., A. Öchsner and R. D. Adams. (2011). *Handbook of Adhesion Technology*.

Davison B. and G. W. Owens. (2012). *Steel designers' manual*, John Wiley & Sons.

Dawood M. and M. El-Tahan. (2011). Effect of Extreme Temperatures on the Bond Behavior of Steel Beams Strengthened with CFRP Plates, *in*: Advanced Composites in Construction (ACIC), Warwick, UK, 6–8 September 2011.

de Castro J. and T. Keller. (2008). Ductile double-lap joints from brittle GFRP laminates and ductile adhesives, Part I: Experimental investigation, *Composites Part B: Engineering*, 39(2):271-281.

De Lorenzis L., D. Fernando and J. G. Teng. (2013). Coupled mixed-mode cohesive zone modeling of interfacial debonding in simply supported plated beams, 50(14):2477-2494.

De Lorenzis L., M. Paggi, A. Carpinteri and G. Zavarise. (2010). Linear elastic fracture mechanics approach to plate end debonding in rectilinear and curved plated beams, *Advances in Structural Engineering*, 13(5):875-889.

De Lorenzis L., J. G. Teng and L. Zhang. (2006). Interfacial stresses in curved members bonded with a thin plate, *International Journal of Solids and Structures*, 43(25):7501-7517.

De Lorenzis L. and G. Zavarise. (2009). Cohesive zone modeling of interfacial stresses in plated beams, *International Journal of Solids and Structures*, 46(24):4181-4191.

Della Gatta G., M. J. Richardson, S. M. Sarge and S. Stølen. (2006). Standards, calibration, and guidelines in microcalorimetry. Part 2. Calibration standards for differential scanning calorimetry (IUPAC Technical Report), *Pure and applied chemistry*, 78(7):1455-1476.

Deng J., M. M. K. Lee and S. S. J. Moy. (2004). Stress analysis of steel beams reinforced with a bonded CFRP plate, *Composite Structures*, 65(2):205-215.

Denton S. R. (2001). Analysis of stresses developed in FRP plated beams due to thermal effects, *in*: Proceedings of the International Conference on FRP composites in Civil Engineering, Hong Kong, China, 12-15, December 2001.

Di Tommaso A., U. Neubauer, A. Pantuso and F. S. Rostasy. (2001). Behavior of adhesively bonded concrete-CFRP joints at low and high temperatures, *Mechanics of Composite Materials*, 37(4):327-338.

du Béton F. I. (2001). Design and use of externally bonded fiber reinforced polymer reinforcement (FRP EBR) for reinforced concrete structures, FIB Bulletin 14: Externally bonded FRP reinforcement for RC structures, Fédération internationale du béton, Lausanne, July 2001.

Dunn D. J. (2010). *Update on engineering and structural adhesives*, ISmithers.

El Damatty A. A. and M. Abushagur. (2003). Testing and modeling of shear and peel behavior for bonded steel/FRP connections, *Thin-Walled Structures*, 41(11):987-1003.

El Damatty A. A., M. Abushagur and M. A. Youssef. (2003). Experimental and analytical investigation of steel beams rehabilitated using GFRP sheets, *Steel and Composite Structures*, 3(6):421-438.

El-Hacha R. and N. Ragab. (2006). Flexural strengthening of composite steel-concrete girders using advanced composite materials, *in*: the 3rd International Conference on FRP composites in Civil Engineering (CICE 2006), Miami, Florida, USA, 13-15 December, 2006.

Elcometer-506. (2015). Elcometer 506 push off adhesion tester data sheet.

Ellis B. (1993). *Chemistry and Technology of Epoxy Resins*, Chapman & Hall.

EN ISO 178. (2003). Plastics-determination of flexural properties, european committee for standardization, B-1000 Brussels.

EN ISO 527-2. (1996). Plastics–determination of tensile properties–Part 2, European committee for standardization, B-1000 Brussels.

Enerpac. (2014). High pressure hydraulic tools & equipment.

Enns J. B. and J. K. Gillham. (1983). Effect of the extent of cure on the modulus, glass transition, water absorptio, and density of an amine - cured epoxy, *Journal of applied polymer science*, 28(9):2831-2846.

Esfandiari R. S. (2017). *Numerical Methods for Engineers and Scientists using MATLAB®*, CRC Press.

Ewing J. A. (1899). *The strength of materials*.

Fabrizio M. and A. Morro. (1992). Linear viscoelasticity, in: Mathematical Problems in Linear Viscoelasticity.

Fawzia S., X.-L. Zhao and R. Al-Mahaidi. (2010). Bond–slip models for double strap joints strengthened by CFRP, *Composite Structures*, 92(9):2137-2145.

Fawzia S., X.-L. Zhao, R. Al-Mahaidi and S. Rizkalla. (2005a). Bond characteristics between CFRP and steel plates in double strap joints, *The International Journal of Advanced Steel Construction*, 1(2):17-27.

Fawzia S., X.-L. Zhao, R. Al-Mahaidi and S. Rizkalla. (2005b). Double strap joint tests to determine the bond characteristics between CFRP and steel plates, *in*: Proceedings of the the Fourth International Conference on Advances in Steel Structures, Shanghai, China, 13-15, June 2005.

Fernando D., J.-G. Teng, T. Yu and X.-L. Zhao. (2013). Preparation and characterization of steel surfaces for adhesive bonding, *Journal of Composites for Construction*, 17(6):040130121-12.

Fernando N. D. (2010). *Bond behaviour and debonding failures in CFRP-strengthened steel members* The Hong Kong Polytechnic University, Doctor of Philosophy (PhD) Thesis.

Ferry J. D. (1980). *Viscoelastic properties of polymers*, John Wiley & Sons.

FIB. (2001). Design and use of externally bonded fiber reinforced polymer reinforcement (FRP EBR) for reinforced concrete structures, FIB Bulletin 14: Externally bonded FRP reinforcement for RC structures, Fédération internationale du béton, Lausanne, July 2001.

FIB. (2006). Design and use of fibre reinforced polymer reinforcement (FRP) for reinforced concrete structures, FRP reinforcement for RC structures, Fédération internationale du béton, Lausanne, June 2006.

Fox L. and D. F. Mayers. (1987). *Numerical solution of ordinary differential equations*, Chapman and Hall.

Gabbott P. (2008). *Principles and applications of thermal analysis*, Blackwell publishing.

Galal K., H. M. Seif ElDin and L. Tirca. (2011). Flexural performance of steel girders retrofitted using CFRP materials, *Journal of Composites for Construction*, 16(3):265-276.

Galambos T. V. (1998). *Guide to stability design criteria for metal structures*, John Wiley & Sons.

Gardner L., X. Yun, L. Macorini and M. Kucukler. (2017). Hot-rolled steel and steel-concrete composite design incorporating strain hardening, 9(2017):21-28.

Harris A. F. and A. Beevers. (1999). The effects of grit-blasting on surface properties for adhesion, *International Journal of Adhesion and Adhesives*, 19(6):445-452.

Hart-Smith L. J. (1973a). Adhesive-bonded double-lap joints, Langley Research Center, Hampton, Virginia 23366, NASA CR 112235, January 1973.

Hart-Smith L. J. (1973b). Adhesive-bonded single-lap joints, Langley Research Center, Hampton, Virginia 23366, NASA CR 112236, January 1973.

Hasan S. W. and G. J. Hancock. (1988). Plastic Bending tests of Cold-formed Rectangular Hollow Sections, The University of Sydney, Sydney, Australia,

Hidalgo-medina J. (2015). *Performance-based methodology for the fire safe design of Insulation materials in energy efficient buildings* Institute of infrastructure and Environmental, The University of Edinburgh, Doctorate in Philosophy (PhD) Thesis.

Hollaway L. C. (2010). A review of the present and future utilisation of FRP composites in the civil infrastructure with reference to their important in-service properties, *Construction and Building Materials*, 24(12):2419-2445.

Hollaway L. C. and J. Cadei. (2002). Progress in the technique of upgrading metallic structures with advanced polymer composites, *Progress in Structural Engineering and Materials*, 4(2):131-148.

Hollaway L. C. and J.-G. Teng. (2008). *Strengthening and rehabilitation of civil infrastructures using fibre-reinforced polymer (FRP) composites*, Elsevier.

Horne M. R. and L. J. Morris. (1981). *Plastic design of low-rise frames*, The MIT Press.

Hülder G., R. Feulner and E. Schmachtenberg. (2008). Curing behaviour of epoxy-adhesives for bonded CFRP-reinforcements, *in*: Proceedings of the 4th International Conference on FRP Composite in Civil Engineering 2008 (CICE), Zürich, Switzerland, 22-24 July 2008.

Ishikawa T., I. Okura and N. Kita. (2006). Debonding shear stress in steel plates with a fiber sheet inserted under a CFRP plate, *JSCE. Journal of Structural Engineering*, 1317–26.

Jaipuriar A., C. E. Bakis and M. M. Lopez. (2012). Cure kinetics and physical aging of an ambient-curing epoxy resin, *in*: Proceedings of the 6th International Conference on Composite FRP in Civil Engineering (CICE 2012), Rome, Italy, 13-15, June 2012.

Jiao H. and X. L. Zhao. (2004). CFRP strengthened butt-welded very high strength (VHS) circular steel tubes, *Thin-Walled Structures*, 42(7):963-978.

Kitipornchai S. and N. S. Trahair. (1979). Buckling properties of monosymmetric I-beams, University of Queensland, Research report No.4, May, 1975.

Klamer E. L., D. A. Hordijk and M. C. J. Hermes. (2008). The influence of temperature on RC beams strengthened with externally bonded CFRP reinforcement, *Heron*, 53(3):157-185.

Klamer E. L., D. A. Hordijk and C. S. Kleinman. (2006). Debonding of CFRP laminates externally bonded to concrete specimens at low and high temperatures, *in*: Proceedings of Third International Conference on Composites in Civil Engineering (CICE 2006), Miami, Florida, USA, 13-15, December 2006.

Lampman S. (2003). *Characterization and failure analysis of plastics*, ASM International.

Lapidus L. and G. F. Pinder. (1999). *Numerical solution of partial differential equations in science and engineering*, John Wiley & Sons.

Lapique F. and K. Redford. (2002). Curing effects on viscosity and mechanical properties of a commercial epoxy resin adhesive, *International journal of adhesion and adhesives*, 22(4):337-346.

Lay M. G. and P. D. Smith. (1965). Role of strain hardening in plastic design, *Journal of the Structural Division*, 91(3):25-44.

Lenwari A., T. Thepchatri and P. Albrecht. (2005). Flexural response of steel beams strengthened with partial-length CFRP plates, *Journal of Composites for Construction*, 9(4):296-303.

Lenwari A., T. Thepchatri and P. Albrecht. (2006). Debonding strength of steel beams strengthened with CFRP plates, *Journal of Composites for Construction*, 10(1):69-78.

LeVeque R. J. (2007). *Finite difference methods for ordinary and partial differential equations: steady-state and time-dependent problems*, Siam.

Liu H., Z. Chen and T. Zhou. (2013). Investigation on temperature distribution and thermal behavior of large span steel structures considering solar radiation, *International Journal of Advanced Steel Construction*, 9(1):41-58.

Liu H. B., X. L. Zhao, Y. Bai, R. K. Singh, S. Rizkalla and S. Bandyopadhyay. (2014). The effect of elevated temperature on the bond between high modulus carbon fibre-reinforced polymer sheet and steel, *Australian Journal of Structural Engineering*, 15(4):355-366.

Ludwik P. (1909). *Elemente der technologischen mechanik*, J. Springer.

Maier-Leibnitz H. (1936). Test results, their interpretation and application, Preliminary Publication, International Association for Bridge and Structural Engineering, 2nd Congress, Berlin, Germany, 1936.

Malek A. M., H. Saadatmanesh and M. R. Ehsani. (1998). Prediction of failure load of R/C beams strengthened with FRP plate due to stress concentration at the plate end, *ACI structural Journal*, 95(1):142-152.

Martin A., S. Taylor, D. Robinson and D. Cleland. (2012). Basalt fibre reinforced polymer bar strengthening compared to arching actions within slabs *in*: Proceedings of the 6th International Conference on Composite FRP in Civil Engineering (CICE 2012)

6th International Conference on FRP Composites in Civil Engineering Rome, Italy, 13-15 June 2012, Rome, Italy, 13-15, June 2012.

Martin A., S. Taylor, D. Robinson and D. Cleland. (2013). Basalt fibre reinforced polymer strengthening of normal strength reinforced concrete floor slabs subject to arching effects, *in*, 2013/9/1.

Martin R. (2008). *Ageing of composites*, Woodhead Publishing Limited (Elsevier).

Mathews J. H. and K. D. Fink. (1999). *Numerical Methods Using MATLAB*, Prentice Hall.

Mattock A. H. (1979). Flexural strength of prestressed concrete sections by programmable calculator, *PCI journal*, 24(1):32-54.

Mays G. C. and A. R. Hutchinson. (2005). *Adhesives in civil engineering*, Cambridge University Press.

Mazurin O. V. (2007). Problems of compatibility of the values of glass transition temperatures published in the world literature, *Glass Physics and Chemistry*, 33(1):22-36.

MBRACE® LAMINATE. (2008). Ready to use carbon laminates (Fibre Reinforced Polymer) for the reinforcement of concrete, metal and wood members with Mbrace® FRP 'Laminate' system, Product Data Sheet, UK Version 6 – August 2008.

Menard K. P. (2008). *Dynamic mechanical analysis: a practical introduction*, CRC press.

Menczel J. D. and R. B. Prime. (2009). *Thermal analysis of polymers: fundamentals and applications*, John Wiley & Sons.

Mertz D. R. and J. W. Gillespie. (1996). Rehabilitation of steel bridge girders through the application of advanced composite materials, Transportation Research Board, Washington, D.C., USA, June 1996.

Mertz D. R., J. W. Gillespie, M. J. Chajes and S. A. Sabol. (2002). The rehabilitation of steel bridge girders using advanced composite materials, Transportation Research Board, Washington, D.C., USA, July, 2001.

Mettler Toledo. (2007). Mettler Toledo (TGA/DSC1) brochure.

Miller T. C., M. J. Chajes, D. R. Mertz and J. N. Hastings. (2001). Strengthening of a steel bridge girder using CFRP plates, *Journal of Bridge Engineering*, 6(6):514-522.

Moisture Gone®. http://www.hdltd.com

Moussa O. (2001). *Thermophysical and thermomechanical behavior of cold- curing ctructural adhesives in bridge construction*, Doctorate in Philosophy (PhD) Thesis.

Moy S. S. J. (2001). *FRP composites: life extension and strengthening of metallic structures*, Thomas Telford.

Moy S. S. J. and A. G. Bloodworth. (2006). Strengthening a steel bridge with CFRP composites, *Proceedings of the Institution of Civil Engineers (ICE)*, Structures & Buildings 160(SB2):81.

Moy S. S. J. and D. Lillistone. (2006). Strengthening cast iron using FRP composites, *Proceedings of the Institution of Civil Engineers (ICE)*, Structures & Buildings 159(SB6):10.

Mufti A. A., B. Bakht, N. Banthia, B. Benmokrane, G. Desgagne, R. Eden, M. A. Erki, V. Karbhari, J. Kroman and D. Lai. (2007). New Canadian Highway Bridge Design Code design provisions for fibre-reinforced structures, *Canadian Journal of Civil Engineering*, 34(3):267-283.

Mulligan D., S. Gnaniah and G. Sims. (2003). Thermal analysis techniques for composites and adhesives, Measurement Good Practice Guide No. 62, National Physical Laboratory (NPL) Materials Centre, Teddington, Middlesex, United Kingdom, 1368-6550,

Narmashiri K., M. Z. Jumaat and N. H. R. Sulong. (2010). Shear strengthening of steel I-beams by using CFRP strips, *Scientific Research and Essays*, 5(16):2155-2168.

Narmashiri K., N. H. Ramli Sulong and M. Z. Jumaat. (2011). Flexural strengthening of steel I-beams by using CFRP strips, *International Journal of Physical Sciences*, 6(7):1620-1627.

Narmashiri K., N. H. Ramli Sulong and M. Z. Jumaat. (2012). Failure analysis and structural behaviour of CFRP strengthened steel I-beams, *Construction and Building Materials*, 30(2012):1-9.

National Research Council Advisory Committee. (2007). Guidelines for design and construction of externally bonded FRP systems for strengthening existing structures – metallic structures, Rome, Italy.

National Research Council Advisory Committee. (2013). Guide for the design and construction of externally bonded FRP systems for strengthening existing structures materials, RC and PC structures, masonry structures, National Research Council, Rome, Italy,

NBI. (2013). 2013 Status of the Nation's Highways, Bridges, and Transit: Conditions and Performance, Report to Congress, Federal Highway Administration, Washington, DC, January 22.

Neal B. G. (1977). *The Plastic Methods of Structural Analysis*, Chapman and Hall.

Nguyen T., Y. Bai, X.-l. Zhao and R. Al-Mahaidi. (2012). Sea-water effects on adhesively bonded CFRP and steel double strap joints, *in*: Proceedings of CICE 2012 6th International Conference on FRP Composites in Civil Engineering © International Institute for FRP in Construction (IIFC) Rome, Italy, 13-16, Jun 2012.

Nguyen T.-C., Y. Bai, X.-L. Zhao and R. Al-Mahaidi. (2011). Mechanical characterization of steel/CFRP double strap joints at elevated temperatures, *Composite Structures*, 93(6):1604-1612.

Nozaka K., C. K. Shield and J. F. Hajjar. (2005). Effective bond length of carbon-fiber-reinforced polymer strips bonded to fatigued steel bridge I-girders, *Journal of Bridge Engineering ASCE*, 10(2):195-205.

O'Connor J. S. and J. M. Hooks. (2003). USA's experience using fiber reinforced polymer (FRP) composite bridge decks to extend bridge service life, Technical Momorandum of Public Works Research Institute, 2003.

Odegard G. M. and A. Bandyopadhyay. (2011). Physical aging of epoxy polymers and their composites, *Journal of Polymer Science Part B: Polymer Physics*, 49(24):46.

Okeil A. M., Y. Bingol and M. R. Ferdous. (2009). A novel technique for stiffening steel structures, Department of Civil and Environmental Engineering, Louisiana State University, Baton Rouge, LA, USA, Mar, 2009.

Okuyama Y., T. Miyashita, D. Wakabayashi, N. Koide, Y. Hidekuma, A. Kobayashi, W. Horimoto and M. Nagai. (2012). Shear Buckling Test for Steel Girder Bonded CFRP on Its Web, *in*: Proceedings of Conference of International Institute for FRP in Construction (IIFC), Rome, Italy, 13-15 June 2012.

Omega CSi8D Series. (User's Guide). Temperature & process controller manual CSi8D by OMEGA®.

Omega RDXL12SD Series. (User's Guide). 12-channel temperature recorder with excel-formatted data logging SD card by OMEGA®.

Omega-dyne Inc. (2012). Omega PX309 Pressure Transducer data sheet.

Osswald T., E. Baur and S. Brinkmann. (2006). *International Plastics Handbook-The Resource for plastics engineers*, Hanser.

Othman D., T. J. Stratford and L. A. Bisby. (2013a). A Comparison of On-Site and Elevated Temperature Cure of an FRP Strengthening Adhesive, *in*: 11th international symposium on Fiber Reinforced Polymers for Reinforced Concrete Structures (FRPRCS11). Guimaraes, Portugal, 26-28, June.

Othman D., T. J. Stratford and L. A. Bisby. (2013b). The impact of adhesive conditioning upon glass transition response, presented at the Advanced Composites in Construction 2013, Belfast (on CD), Belfast, UK.

Patnaik A. K. and C. L. Bauer. (2004). Strengthening of steel beams with carbon FRP laminates, *in*: 4th international conference on advanced composite materials in bridges and structures, Calgary, Canada., 20-23, July 2004.

Petrie E. M. (2000). *Handbook of adhesives and sealants*, McGraw-Hill.

Petrie E. M. (2006). *Epoxy Adhesive Formulations*, McGraw-Hill Companies.

Photiou N. K., L. C. Hollaway and M. K. Chryssanthopoulos. (2006). Strengthening of an artificially degraded steel beam utilising a carbon/glass composite system, *Construction and Building Materials*, 20(1-2):11-21.

Picotech. (2016). TC-08 thermocouple data logger data sheeet.

Pizzi A. and K. L. Mittal. (2003). *Handbook of adhesive technology, revised and expanded*, CRC Press.

Potgieter I. C. and W. L. Gamble. (1989). Nonlinear temperature distributions in bridges at different locations in the United States, *PCI JOURNAL*, 34(4):80-103.

Rabinovich O. and Y. Frostig. (2000). Closed-form high-order analysis of RC beams strengthened with FRP strips, *Journal of Composites for Construction*, 4(2):65-74.

Rabinovitch O. (2004). Fracture-mechanics failure criteria for RC beams strengthened with FRP strips—a simplified approach, *Composite Structures*, 64(3-4):479-492.

Rabinovitch O. (2008). Debonding analysis of fiber-reinforced-polymer strengthened beams: Cohesive zone modeling versus a linear elastic fracture mechanics approach, *Engineering Fracture Mechanics*, 75(10):2842-2859.

Rabinovitch O. and Y. Frostig. (2001). Delamination failure of RC beams strengthened with FRP strips-a closed-form high-order and fracture mechanics approach, *Journal of Engineering Mechanics*, 127(8):852-861.

Ragab N. and R. El-Hacha. (2006a). Effectiveness of various repair systems for flexural strengthening of steel-concrete composite girders, *in*: the 7th International Conference on Short and Medium Span Bridges (SMSB-VII), Montreal, Quebec, Canada, 23-25, August 2006.

Ragab N. and R. El-Hacha. (2006b). Flexural strengthening of steel-concrete composite girders, *in*: 1st International Structural Specialty Conference (ISSC-1), Calgary, Alberta, Canada, 23-26, May 2006.

Ragab N., R. El-Hacha and M. Aly. (2007). Strengthening steel-concrete composite girders using FRPs: state-of-the art, *in*: the 1st Asia-Pacific Conference on FRP in Structures (APFIS 2007), Hong Kong, China, 12-14 December, 2007.

Recticel Insulation Products. (2011). PIR Insulation Product Guide by Eurothane® EuroDeck TM,Product Data Sheet, Edition V4.1/09/11.

Roberts T. M. and H. Hajikazemi. (1989). Theoretical study of the behaviour of reinforced concrete beams strengthened by externally bonded steel plates, *Proceedings of the Institution of Civil Engineers*, 87(Part 2):39-55.

Sallam H. E. M., A. A. M. Badawy, A. M. Saba and F. A. Mikhail. (2010). Flexural behavior of strengthened steel–concrete composite beams by various plating methods, *Journal of Constructional Steel Research*, 66(8-9):1081-1087.

Sargazi S. and K. Narmashiri. (2015). Flexural strengthening of steel beams using end-anchored CFRP strips, *Indian Journal of Fundamental and Applied Life Sciences*, 5(S1):3857-3864.

Sayed-Ahmed E. Y. (2004). Strengthening of thin-walled steel I-section beams using CFRP strips, *in*: 4th international conference on advanced composite materials in bridges and structures, Calgary, Canada., 20-23, July 2004.

Sayed-Ahmed E. Y. (2006). Numerical investigation into strengthening steel I-section beams using CFRP strips, *in*: Structures Congress 2006 Structural Engineering and Public Safety, (ASCE), St. Louis, Missouri, United States, 18-21, May 2006.

Schnerch D., M. Dawood and S. Rizkalla. (2007a). Design guidelines for the use of HM strips: Strengthening of steel-concrete composite bridges with high modulus carbon fiber reinforced polymer (CFRP) strips, Technical Report No. IS-06-02, North Carolina State University, June 2007.

Schnerch D., M. Dawood, S. Rizkalla and E. Sumner. (2007b). Proposed design guidelines for strengthening of steel bridges with FRP materials, *Construction and Building Materials*, 21(5):1001-1010.

Schnerch D. and S. Rizkalla. (2006). Strengthening of scaled steel-concrete composite girders and steel monopole towers with CFRP, *in*: Proceedings of the 2nd International Conference on FRP Composites in Civil Engineering (CICE), Adelaide, Australia, 8-10 December 2004.

Schnerch D., K. Stanford, B. Lanier and S. Rizkalla. (2003). Use of high modulus carbon fiber reinforced polymers (CFRP) for strengthening steel structures, in:The second international workshop on structural composites for infrastructure applications,Cairo, Egypt,Dec. 2003.

Schnerch D., K. Stanford, E. Sumner and S. Rizkalla. (2004). Strengthening Steel Structures and Bridges with High-Modulus Carbon Fiber-Reinforced Polymers Resin Selection and Scaled Monopole Behavior, in:Transportation Research Record.

Schnerch D. A. (2005). *Strengthening of steel structures with High Modulus Carbon Fibre Reinforced Polymer (CFRP) materials*, Department of Civil, Construction and Environmental Engineering, North Carolina state university, Doctorate in Philosophy (PhD) Thesis.

Sen R., L. Liby and G. Mullins. (2001). Strengthening steel bridge sections using CFRP laminates, *Composites Part B: Engineering*, 32(4):309-322.

Shaat A. and A. Fam. (2006). Effectiveness of different composite materials for repair of steel bridge girders, *in*: the 3rd International Conference on FRP composites in Civil Engineering (CICE 2006), Miami, Florida, USA, 13-15 December, 2006.

Shaat A., D. Schnerch, A. Fam and S. Rizkalla. (2004). Retrofit of steel structures using fiber-reinforced polymers (FRP): State-of-the-art, in:Transportation research board (TRB) annual meeting.

Shen H.-S., J. G. Teng and J. Yang. (2001). Interfacial Stresses in Beams and Slabs Bondedwith Thin Plate, *Journal of engineering mechanics*, 127(4):399-406.

Sikadur-330. (2012). 2-Part Epoxy Impregnation Resin by Sikadur®, Product Data Sheet, Edition 2012-05_1, 2012.

Sims G. D. and S. J. P. Gnaniah. (2009). Improved procedures for the determination of Tg by dynamic mechanical analysis, in:Proceedings of 17th International Conference on Composite Materials (2009), 27 Jul 2009 - 31 Jul 2009.

Skogman B. C., M. K. Tadros and R. Grasmick. (1988). Flexural strength of prestressed concrete members, *PCI Journal*, 33(5):96-123.

Smith S. T. and J. G. Teng. (2001). Interfacial stresses in plated beams, *Engineering structures*, 23(7):857-871.

Steckel G. L., G. F. Hawkins and J. L. Bauer. (1999). Durability issues for composites in infrastructure, *Evolving and revolutionary technologies for the new millennium*, 2194-2208.

Stevens G. C. and M. J. Richardson. (1983). Factors influencing the glass transition of DGEBA-anhydride epoxy resins, *Polymer*, 24(7):851-858.

Stratford T. and L. A. Bisby. (2012). Effect of warm temperatures on externally bonded FRP strengthening, *Journal of Composites for Construction*, 16(3):235-244.

Stratford T. and J. Cadei. (2006). Elastic analysis of adhesion stresses for the design of a strengthening plate bonded to a beam, *Construction and Building Materials*, 20(1):34-45.

Tadeu A. J. B. and F. J. F. G. Branco. (2000). Shear tests of steel plates epoxy-bonded to concrete under temperature, *Journal of Materials in civil Engineering*, 12(1):74-80.

Täljsten B. (1997). Strengthening of beams by plate bonding, *Journal of materials in civil engineering*, 9(4):206-212.

Tammann G. A. (1933). *Der Glaszustand*.

Tavakkolizadeh M. and H. Saadatmanesh. (2003a). Repair of damaged steel-concrete composite girders using carbon fiber-reinforced polymer sheets, *Journal of Composites for Construction*, 7(4):311–322.

Tavakkolizadeh M. and H. Saadatmanesh. (2003b). Strengthening of steel-concrete composite girders using carbon fiber reinforced polymers sheets, *Journal of Structural Engineering*, 129(1):30-40.

Thomas S., C. Sinturel and R. Thomas. (2014). *Micro- and Nanostructured Epoxy/Rubber Blends*, Wiley-VCH Verlag GmbH & Co.

Tokyo Sokki Kenkyujo Co. TML standard strain gauges.

Tong M., L. G. Tham and F. T. K. Au. (2002). Extreme thermal loading on steel bridges in tropical region, *Journal of Bridge Engineering*, 7(6):357-366.

Trahair N. S. (1993). *Flexural-torsional buckling of structures*, CRC Press.

Trahair N. S., M. A. Bradford, D. Nethercot and L. Gardner. (2007). *The behaviour and design of steel structures to EC3*, Taylor & Francis Group.

Turi A. E. (1981). *Thermal Characterization of Polymeric Materials*, Academic press.

Tyfo-S. (2011). Tyfo® S Saturant Epoxy.

Vilnay O. (1988). The analysis of reinforced concrete beams strengthened by epoxy bonded steel plates, *International Journal of Cement Composites and Lightweight Concrete*, 10(2):73-78.

Volkersen O. (1938). Die nietkraftoerteilung in zubeanspruchten nietverbindungen mit konstanten loschonquerschnitten, *Luftfahrtforschung 15:41*,

Wagner M. (2009). *Thermal Analysis in Practice: Collected Applications Thermal Analysis*, METTLER TOLEDO.

Wakabayashi D., T. Miyashita, Y. Okuyama, N. Koide, A. Kobayashi, Y. Hidekuma, W. Horimoto and M. Nagai (2012). Study on repair method using CFRP for corroded steel girder ends, *in*: 28th US-Japan bridge Engineering workshop, Portland, Oregon, USA, 8-10 October.

Webb S. C., P. Shin and K. Peters. (2013). Fusion of global and local measurements of damage in bonded joints, *in*: Fracture and Fatigue, Volume 7: Proceedings of the 2013 Annual Conference on Experimental and Applied Mechanics, Conference Proceedings of the Society for Experimental Mechanics Series, Albuquerque, NM, USA, 2013.

Wilkinson T. and G. J. Hancock. (1999). Tests of Cold-Formed Rectangular Hollow Section Portal Frames, Department of Civil Engineering, The University of Sydney, July, 1999.

Wilkinson T., B. B. Ma, G. J. Hancock and B. Page. (1997). Tests for the compact web slenderness of cold-formed rectangular hollow sections,

Wu C.-S. (1992). Influence of post-curing and temperature effects on bulk density, glass transition and stress-strain behaviour of imidazole-cured epoxy network, *Journal of materials science*, 27(11):2952-2959.

Wu Z. S., K. Iwashita, S. Yagashiro, T. Ishikawa and Y. Hamaguchi. (2005). Temperature effect on bonding and debonding behavior between FRP sheets and concrete, *Journal of the Society of Materials Science*, 54(5):474-480.

Xia S. H. and J. G. Teng. (2005). Behaviour of FRP-to-steel bonded joints, *in*: Proceedings of the International Symposium on Bond Behaviour of FRP in Structures (BBFS 2005), Hong Kong, China, 7-9, December 2005.

Yang J., J. F. Chen and J. G. Teng. (2009). Interfacial stress analysis of plated beams under symmetric mechanical and thermal loading, *Construction and Building Materials*, 23(9):2973-2987.

Yang J., J. G. Teng and J. F. Chen. (2004). Interfacial stresses in soffit-plated reinforced concrete beams, *Proceedings of the ICE-Structures and Buildings*, 157(1):77-89.

Yang J. and Y. F. Wu. (2007). Interfacial stresses of FRP strengthened concrete beams: Effect of shear deformation, *Composite structures*, 80(3):343-351.

Yu Y., S. P. Chiew and C. K. Lee. (2011a). Bond failure of steel beams strengthened with FRP laminates–Part 1: Model development, *Composites Part B: Engineering*, 42(5):1114-1121.

Yu Y., S. P. Chiew and C. K. Lee. (2011b). Bond failure of steel beams strengthened with FRP laminates–Part 2: Verification, *Composites Part B: Engineering*, 42(5):1122-1134.

Zhang L. and J. G. Teng. (2010). Simple general solution for interfacial stresses in plated beams, *Journal of Composites for Construction*, 14(4):434-442.

Zhang Y., A. P. Vassilopoulos and T. Keller. (2010). Effects of low and high temperatures on tensile behavior of adhesively-bonded GFRP joints, *Composite Structures*, 92(7):1631-1639.

Zhao X.-L. and L. Zhang. (2007). State-of-the-art review on FRP strengthened steel structures, *Engineering Structures*, 29(8):1808-1823.

Ziemian R. D. (2010). *Guide to stability design criteria for metal structures*, John Wiley & Sons.

Zoghi M. (2013). *The International Handbook of FRP Composites in Civil Engineering*, CRC Press.

Appendix A

Filler Characterisation

This annex explains the determination of the fillers content in an adhesive. The amount of filler in adhesives has impact on thermo-physical and mechanical properties (ASTM D2584-02, 2002; British Standard ISO 14127, 2008). Burn off test was used in order to obtain the quantity of the filler in cured adhesives; the adhesives investigated in this research are Sikadur-330 and Tyfo-S (See Chapter 3).

A.1 Burn-off test

Burn off test is a common method designed to determine constituent content of composite materials (filler, resin, and fibre percentage) by weight or volume, and void content from constituent densities. The matrix resin is burned by ignition, which leaves the reinforcement and inorganic fabric unaffected. This method is, also, used glass or quartz reinforced composite materials.

A.1.1 Experimental preparation

Three specimens are cut from the remaining samples for the DMA and DSC experiments. Specimens prior to the test were lest at laboratory conditions (24±1°C and 45±5 % RH) for 24 hours. Although, fire laboratory facilities used for this test, moderate specimen size was selected to reduce the amount smoke produced, when they are heated until all organic material is fully dissolved, and possible error in case relatively small samples being used. Ceramic crucibles were selected for these experiments.

A.1.2 Experimental procedure

The ceramic crucibles were weighted using a laboratory balance Mettler Toledo (MS4002TSDR) with accuracy of 10 mg, and the weight was recorded as

($\boldsymbol{W_0}$). Specimens were placed in pre-weighted crucibles and then the weights were recorded as ($\boldsymbol{W_1}$). Bunsen burner used to ignite the organic material, till the resin was completely burned off, and then the residual (char and filler) and the crucible let to cool done to be weighted as ($\boldsymbol{W_2}$); this stages is only according to ASTM D2584-02 (2002). The resin burning process for adhesive Tyfo-s is shown in Figure A-1.

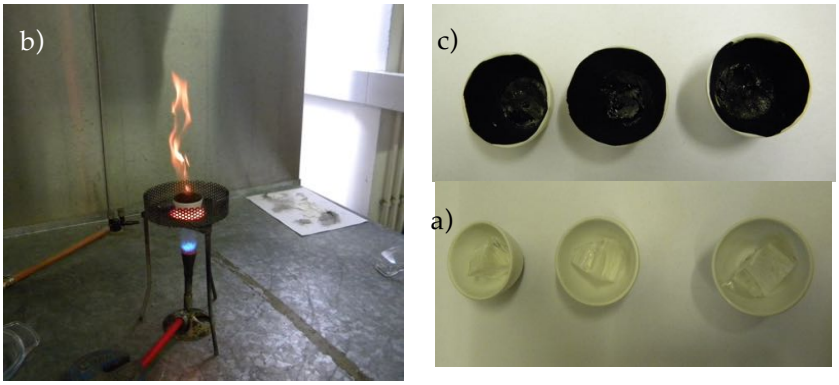

Figure A-1: a) Tyfo-S resin before burning b) During burning-off on Bunsen burner c) residue of the resin.

In order to ensure the epoxy resin was burned and only filler remained, the crucible and residual content then were placed in a high-temperature thermal muffle furnace as shown in Figure A-2. The specimens were left for at least six hours at a temperature between 600°C and 650°C. The crucible and remaining filler were reweighed and recorded as ($\boldsymbol{W_3}$).

Figure A-2:High-temperature thermal muffle furnace and crucible with the filler

A.2 Calculation of filler content

The recorded data for all three samples for the two investigated adhesives are listed in Table A-1. The filler content of the percentage ($\boldsymbol{W_{filler}}$) is calculated as follows:

$$\text{Filler Content (\%)} = \frac{\text{Weight of Remaining} \times 100}{\text{Original Weight of Specimen}}$$

$$\text{Filler and char Content (\%)} = \frac{(W_0 - W_2) \times 100}{(W_0 - W_1)}$$

$$\text{Filler Content (\%)} = \frac{(W_0 - W_3) \times 100}{(W_0 - W_1)}$$

Table A-1: Burn-off test results for Sikadur-330 and Tyfo-S adhesives

		Weight, (g)				***Weight, (%)***	
		W_0	W_1	W_2	W_3	$W_{char+filler}$	W_{filler}
Sikadur-330	**Sample 1**	22.86	29.25	24.82	24.04	30.70	18.50
	Sample 2	20.91	27.80	23.02	22.20	30.60	18.70
	Sample 3	20.67	28.55	23.31	22.13	33.50	18.50
				Avg ± SD		***31.6 ± 1.6***	***18.6 ± 0.13***
Tyfo-S	**Sample 1**	20.92	27.34	22.3	20.92	21.50	0
	Sample 2	22.99	30.07	24.13	22.99	16.10	0
	Sample 3	22.34	27.85	23.6	22.34	22.90	0
				Avg ± SD		***20.2 ± 3.50***	***0 ± 0***

Appendix B

DMA and DSC Test Results for Sikadur-330

B.1 Introduction

This appendix contains the test results from dynamic mechanical analysis DMA and differential scanning calorimetry DSC of Sikadur-330. Due to the small amount of variation in the test results, the average of three samples is presented.

The specimens are named in Section B.6 in the form of A-T-R, where the first letter 'A' refers to the adhesive type (S: Sikadur-330 and T: Tyfo-S). The number 'T' refers to the curing temperature (15, 24, 35, 50, 65 and 80°C), and the number 'R' refers to the relative humidity condition (0: 0% RH and 100: under distilled water); For example, S-15-0 represents Sikadur-330 cured at 15°C and 0% RH.

B.2 Sikadur-330 at dry condition using DMA

B.2.1 Curing age effect on T_g using DMA

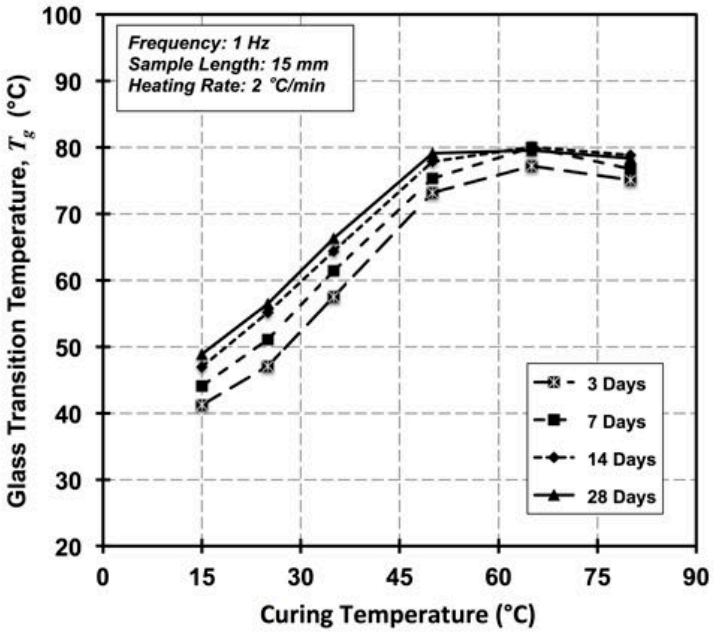

Figure B-1: Recorded T_g according to inflection point method at different age and curing temperature for Sikadur-330, dry condition

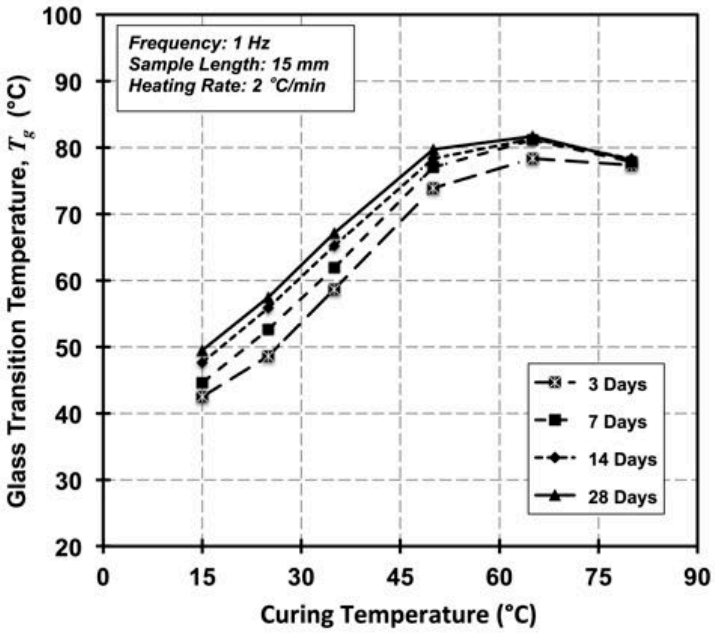

Figure B-2: Recorded T_g according to peak loss modulus method at different age and curing temperature for Sikadur-330, dry condition

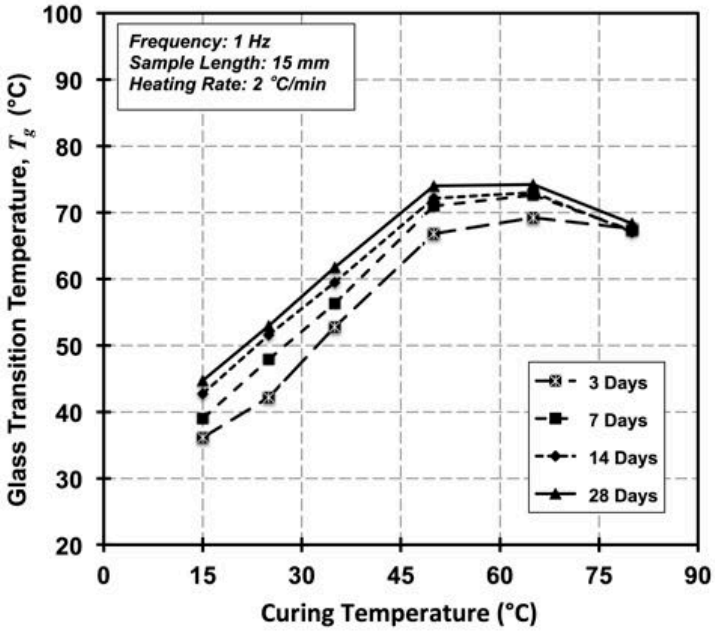

Figure B-3: Recorded T_g according to onset normal scale method at different age and curing temperature for Sikadur-330, dry condition

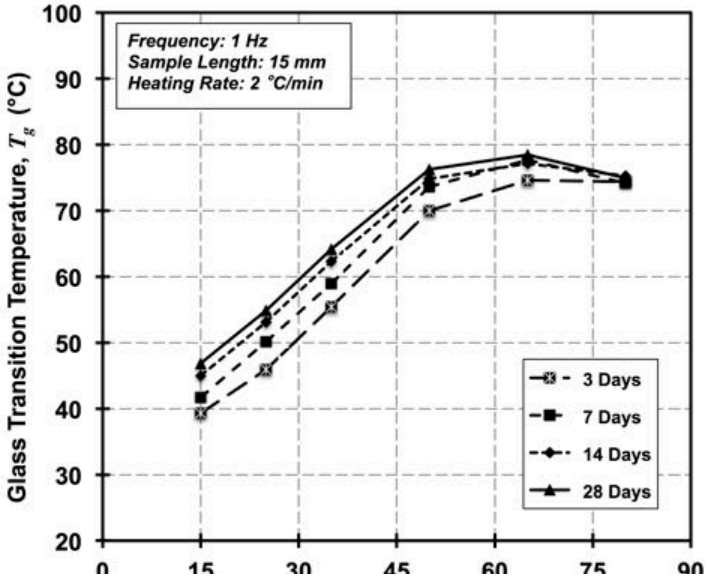

Figure B-4: Recorded T_g according to onset logarithmic scale method at different age and curing temperature for Sikadur-330, dry condition

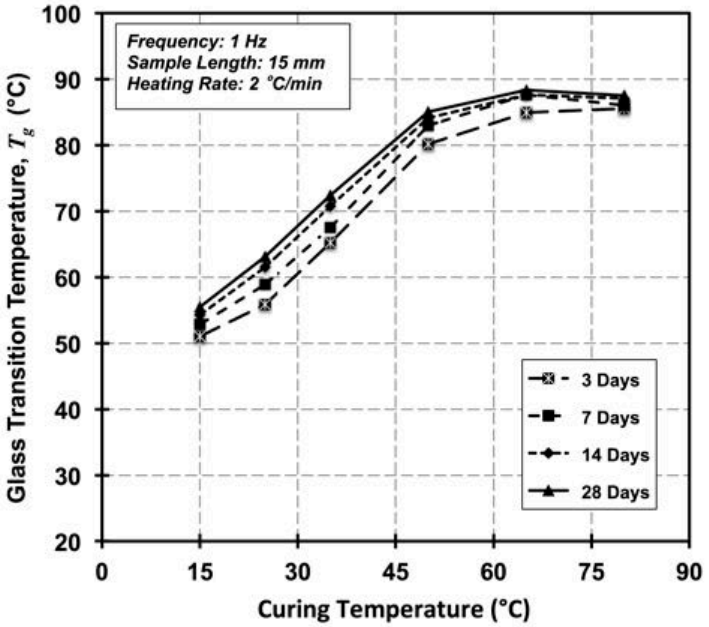

Figure B-5: Recorded T_g according to tan δ method at different age and curing temperature for Sikadur-330, dry condition

B.2.2 Curing temperature effect on T_g using DMA

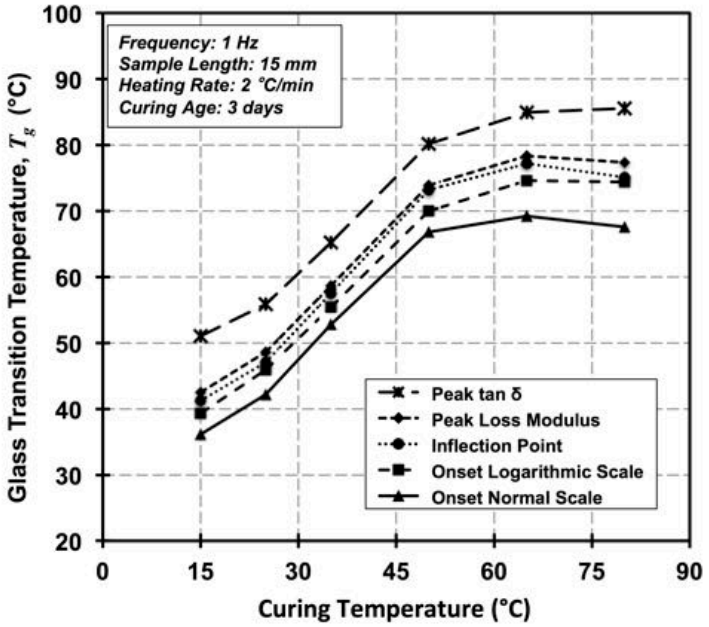

Figure B-6: Recorded T_g according to different methods at 3 days and different curing temperature for Sikadur-330, dry condition

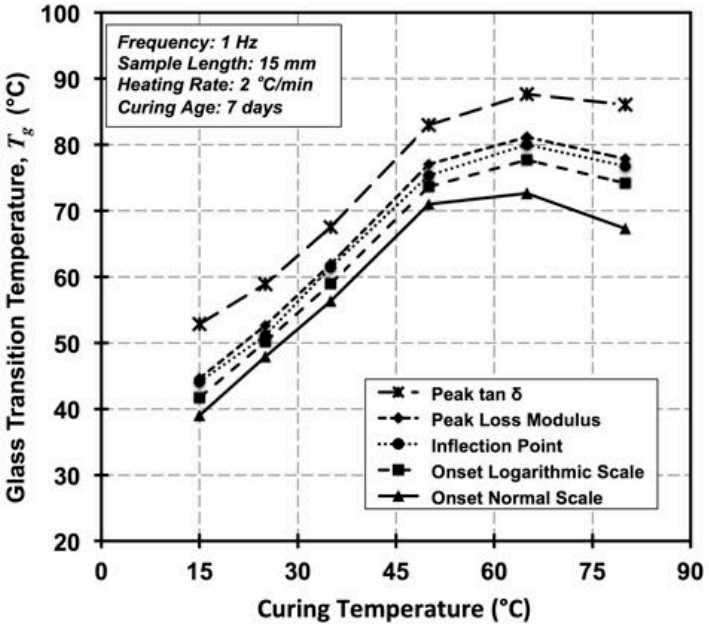

Figure B-7: Recorded T_g according to different methods at 7 days and different curing temperature for Sikadur-330, dry condition

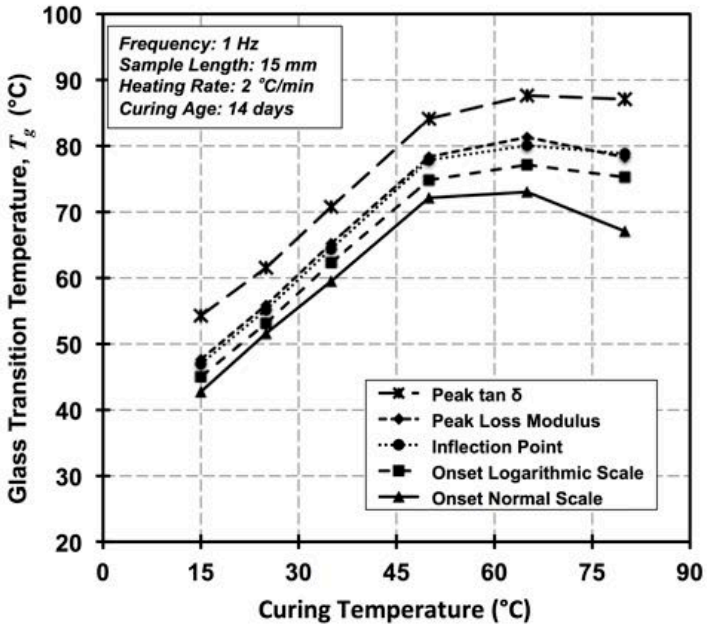

Figure B-8: Recorded T_g according to different methods at 14 days and different curing temperature for Sikadur-330, dry condition

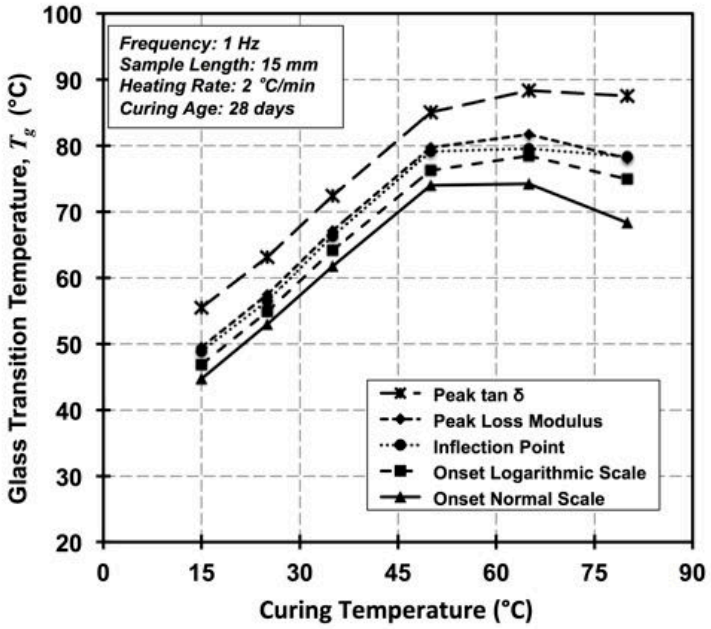

Figure B-9: Recorded T_g according to different methods at 28 days and different curing temperature for Sikadur-330, dry condition

B.2.3 Dry condition DMA test responses

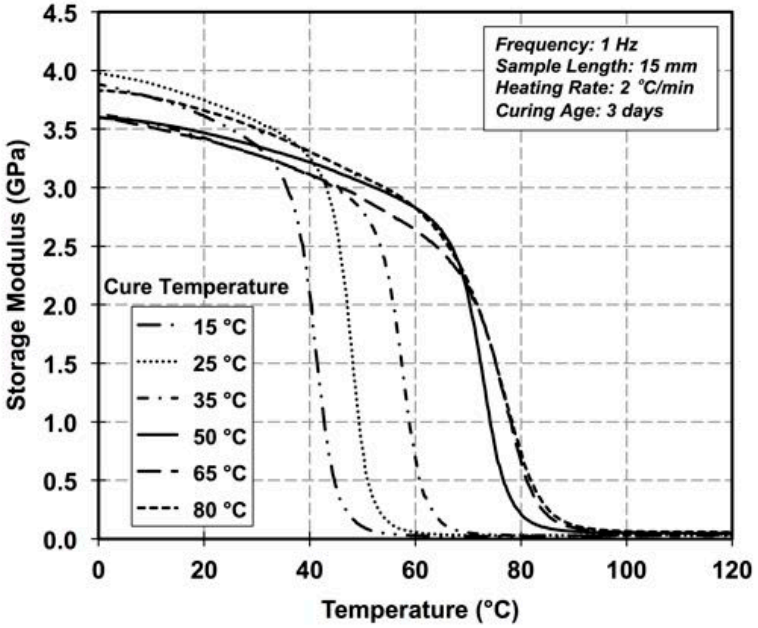

Storage modulus variation with temperature

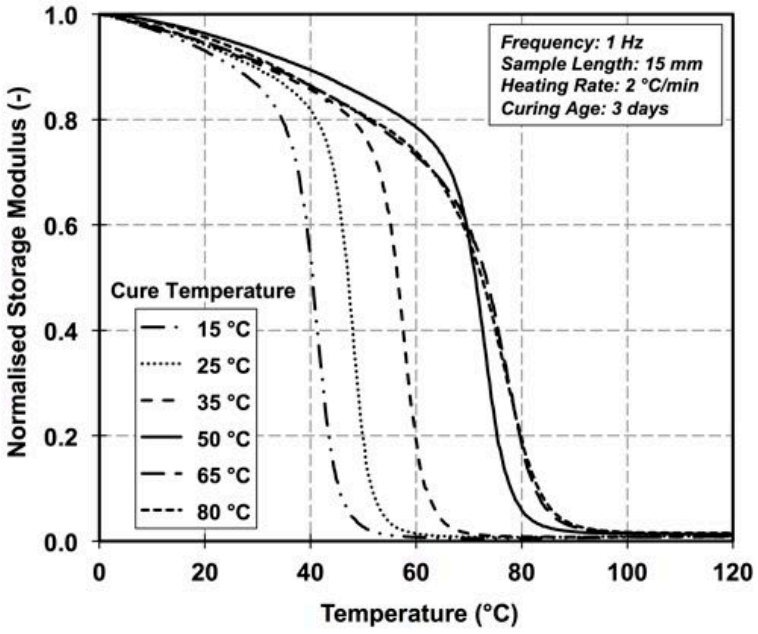

Normalised storage modulus variation with temperature

Figure B-10: Storage and normalised modulus variation with temperature for specimens cured at different temperature for 3 days, Sikadur-330 dry condition

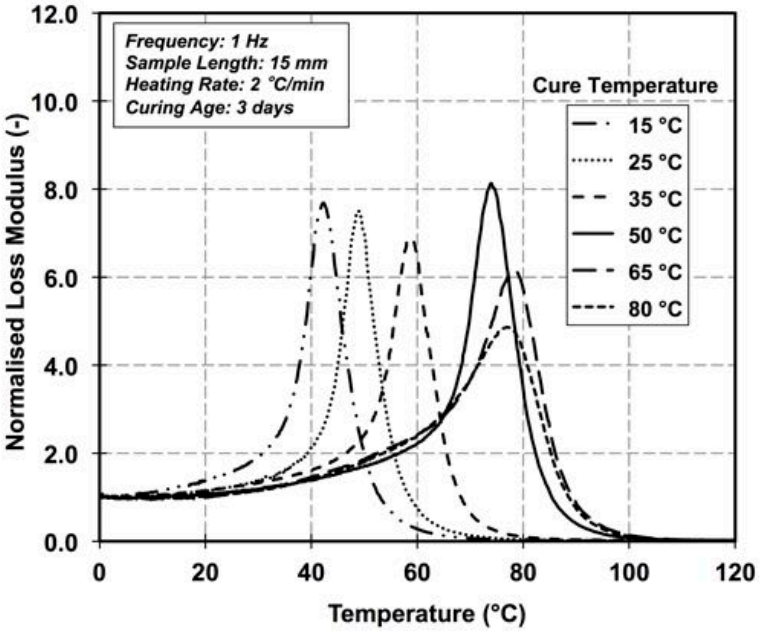

Normalised loss modulus variation with temperature

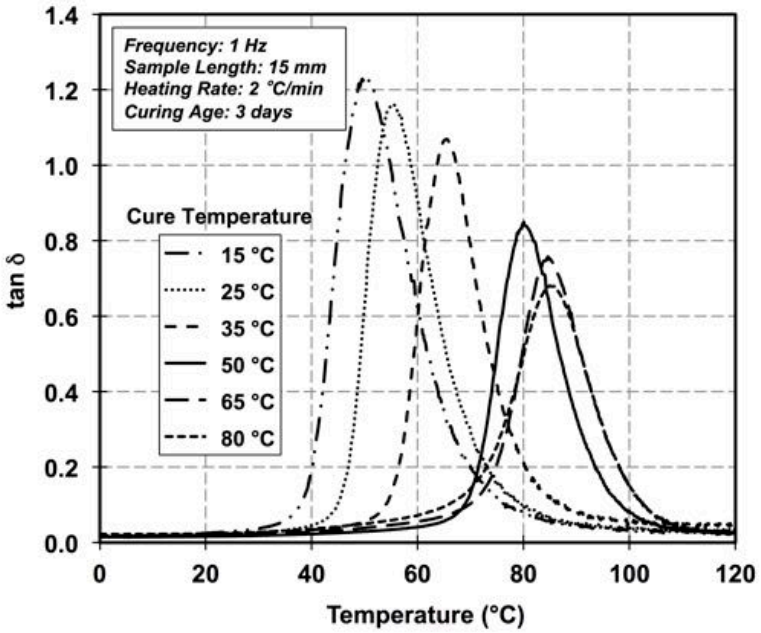

tan δ variation with temperature

Figure B-11: Normalised loss modulus and tan δ variation with temperature for specimens cured at different temperature for 3 days, Sikadur-330 dry condition

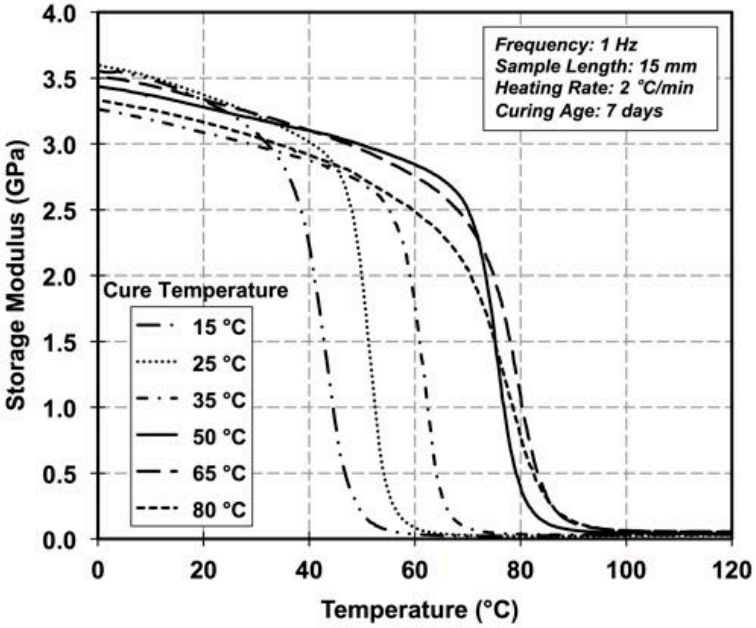

Storage modulus variation with temperature

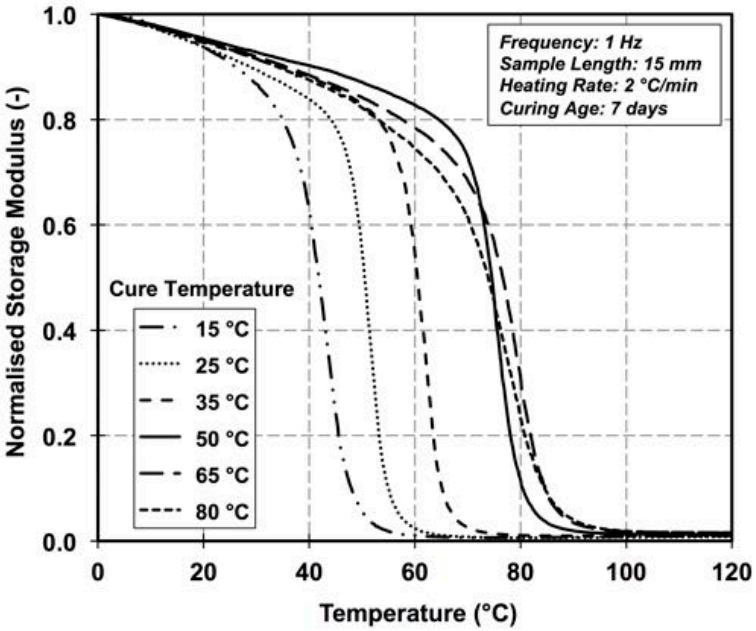

Normalised storage modulus variation with temperature

Figure B-12: Storage and normalised modulus variation with temperature for specimens cured at different temperature for 7 days, Sikadur-330 dry condition

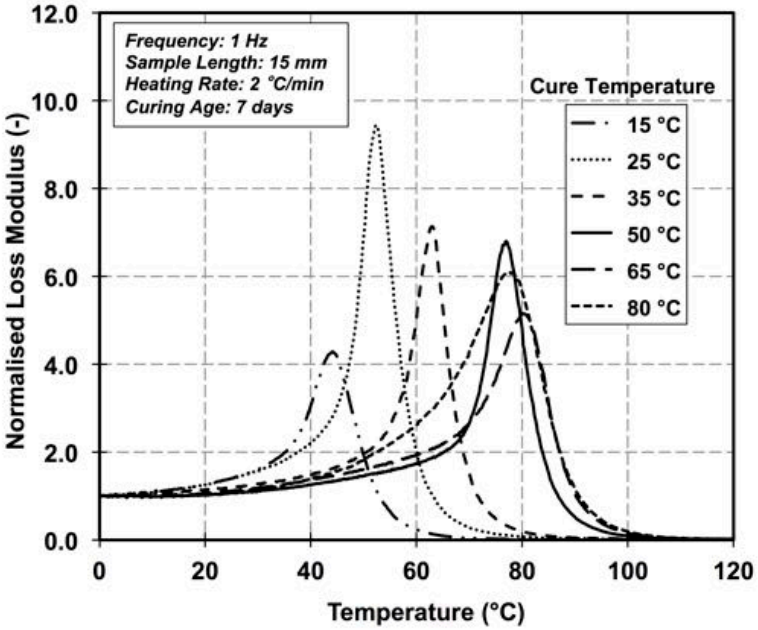

Normalised loss modulus variation with temperature

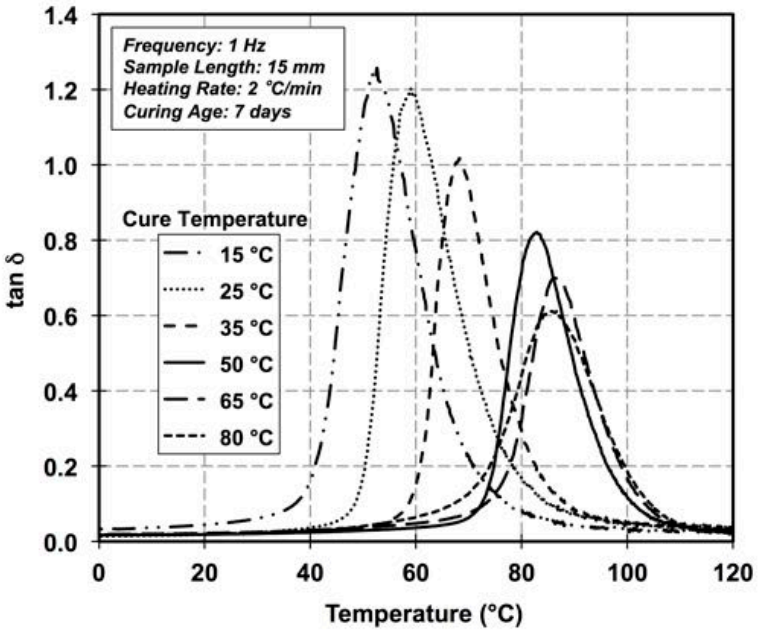

tan δ variation with temperature

Figure B-13: Normalised loss modulus and tan δ variation with temperature for specimens cured at different temperature for 7 days, Sikadur-330 dry condition

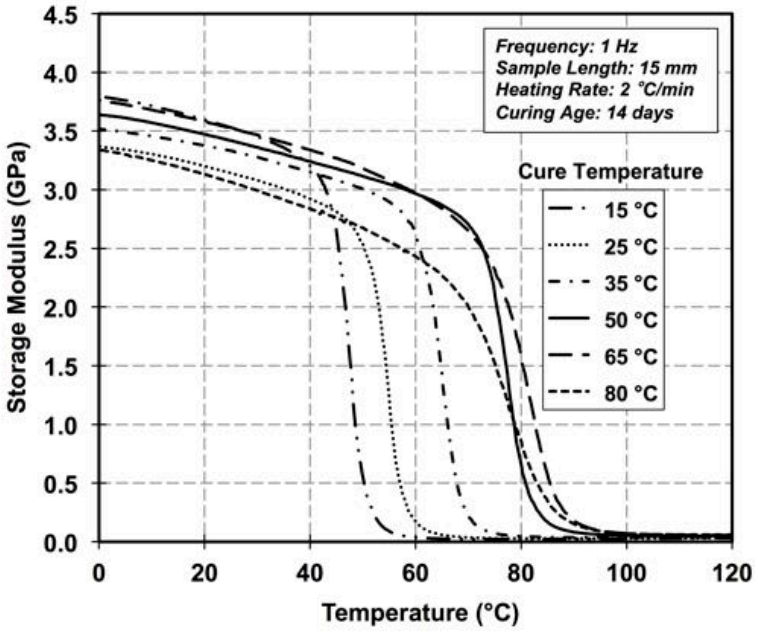

Storage modulus variation with temperature

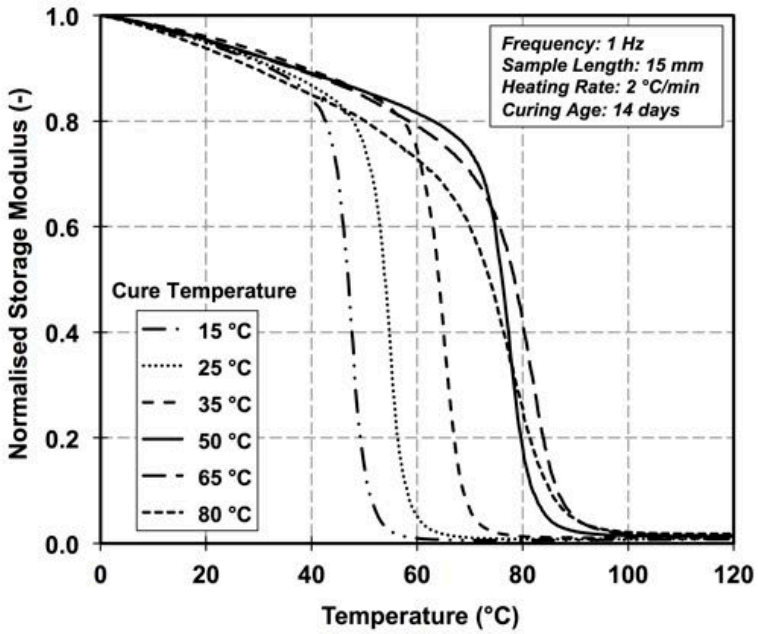

Normalised storage modulus variation with temperature

Figure B-14: Storage and normalised modulus variation with temperature for specimens cured at different temperature for 14 days, Sikadur-330 dry condition

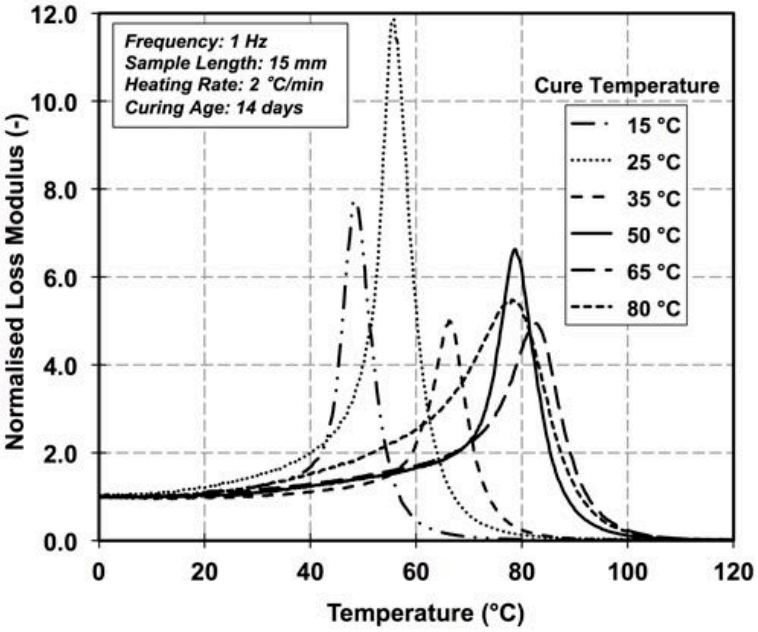

Normalised loss modulus variation with temperature

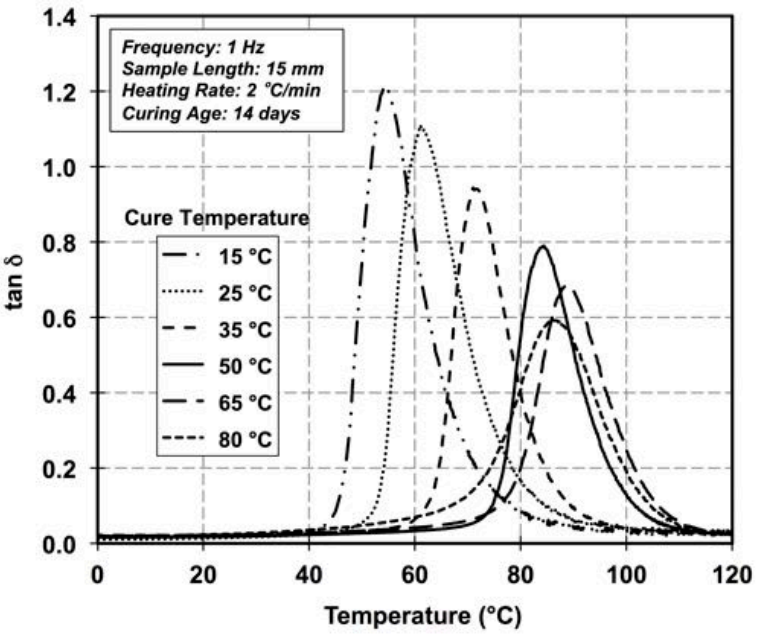

tan δ variation with temperature

Figure B-15: Normalised loss modulus and tan δ variation with temperature for specimens cured at different temperature for 14 days, Sikadur-330 dry condition

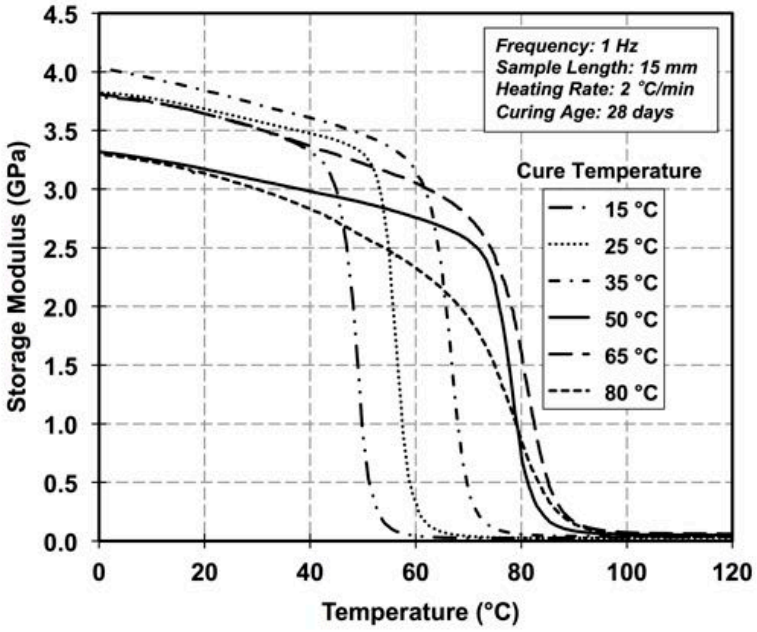

Storage modulus variation with temperature

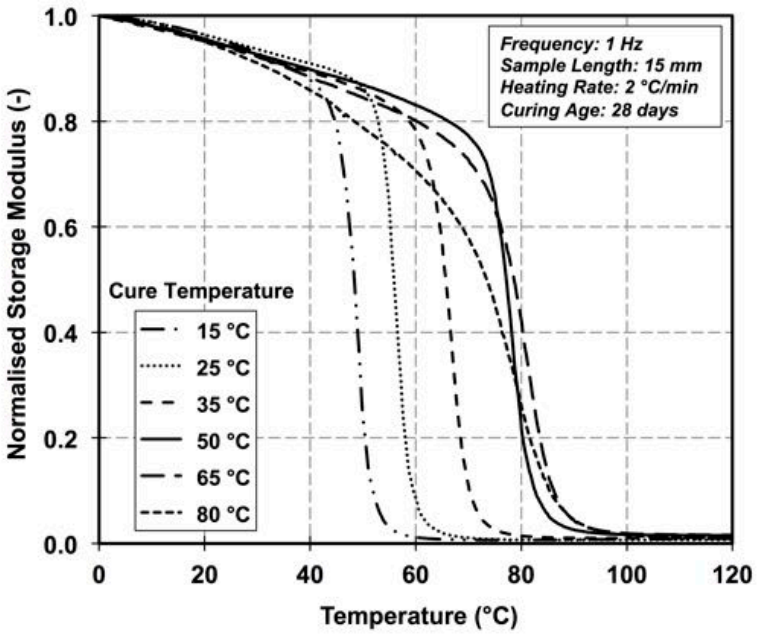

Normalised storage modulus variation with temperature

Figure B-16: Storage and normalised modulus variation with temperature for specimens cured at different temperature for 28 days, Sikadur-330 dry condition

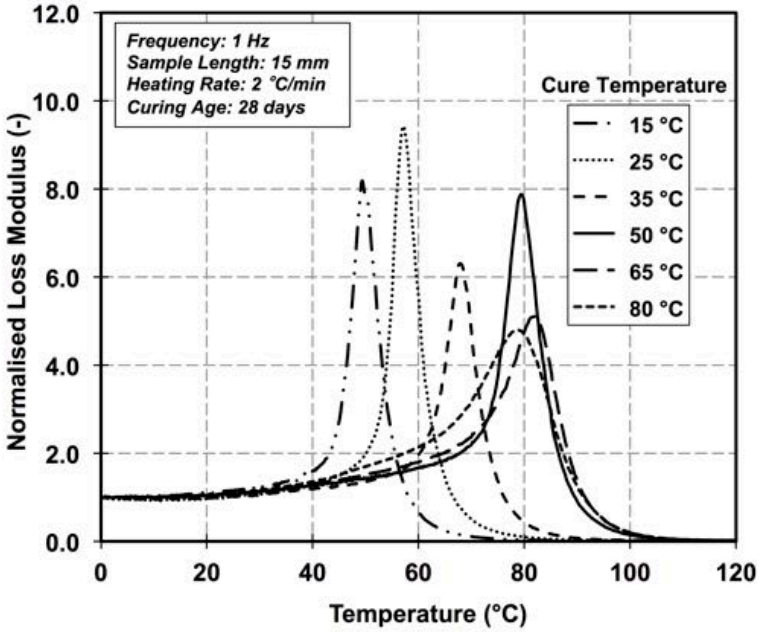

Normalised loss modulus variation with temperature

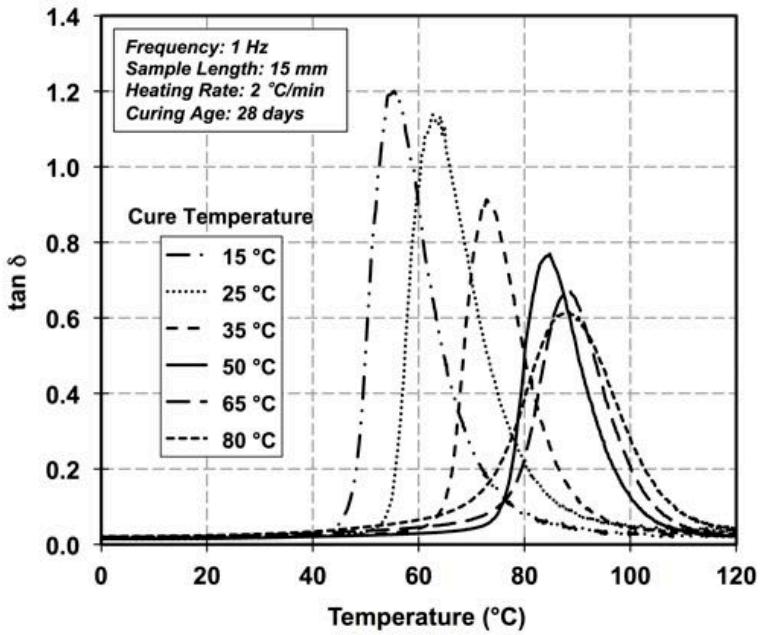

tan δ variation with temperature

Figure B-17: Normalised loss modulus and tan δ variation with temperature for specimens cured at different temperature for 28 days, Sikadur-330 dry condition

B.3 Sikadur-330 at saturated condition using DMA

B.3.1 Curing Age effect on T_g using DMA

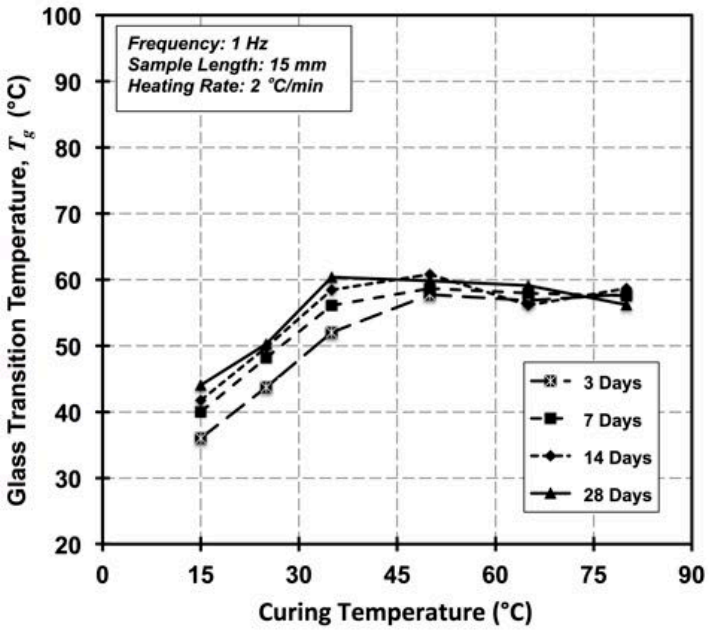

Figure B-18: Recorded T_g according to inflection point method at different age and curing temperature for Sikadur-330, saturated condition

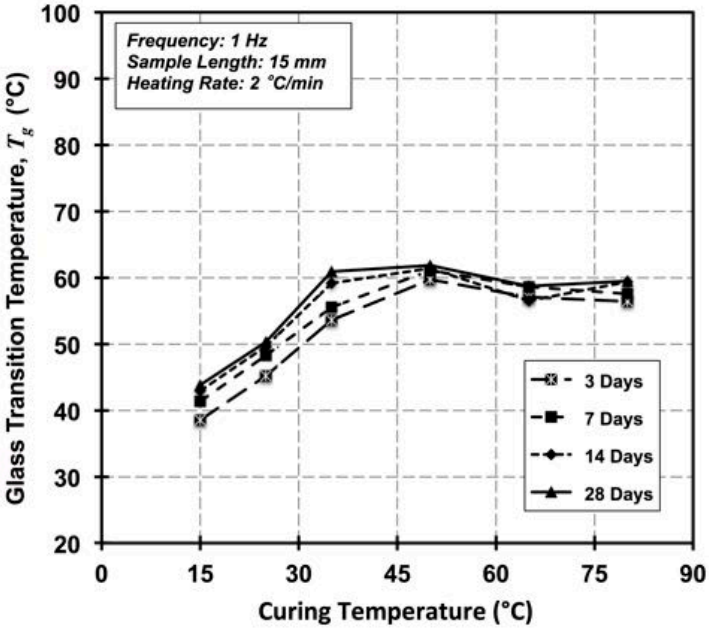

Figure B-19: Recorded T_g according to peak loss modulus method at different age and curing temperature for Sikadur-330, saturated condition

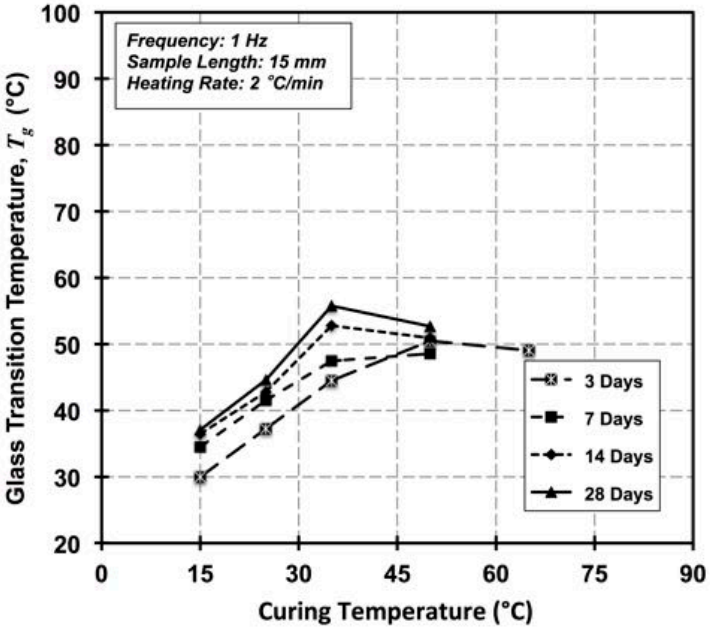

Figure B-20: Recorded T_g according to onset normal scale method at different age and curing temperature for Sikadur-330, saturated condition

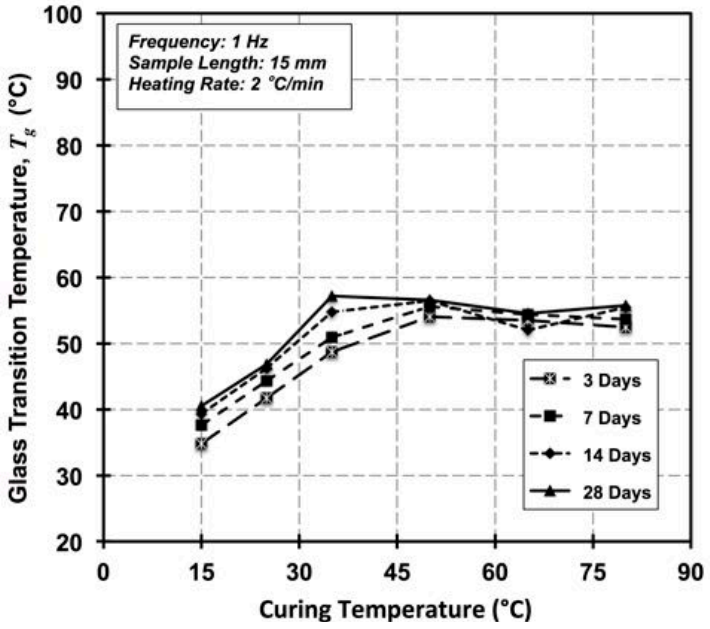

Figure B-21: Recorded T_g according to onset logarithmic scale method at different age and curing temperature for Sikadur-330, saturated condition

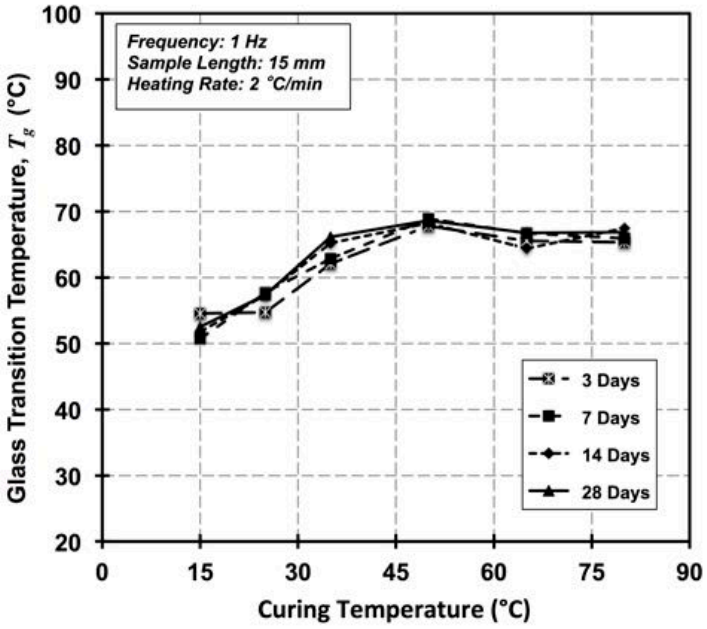

Figure B-22: Recorded T_g according to tan δ method at different age and curing temperature for Sikadur-330, saturated condition

B.3.2 Curing temperature effect on T_g using DMA

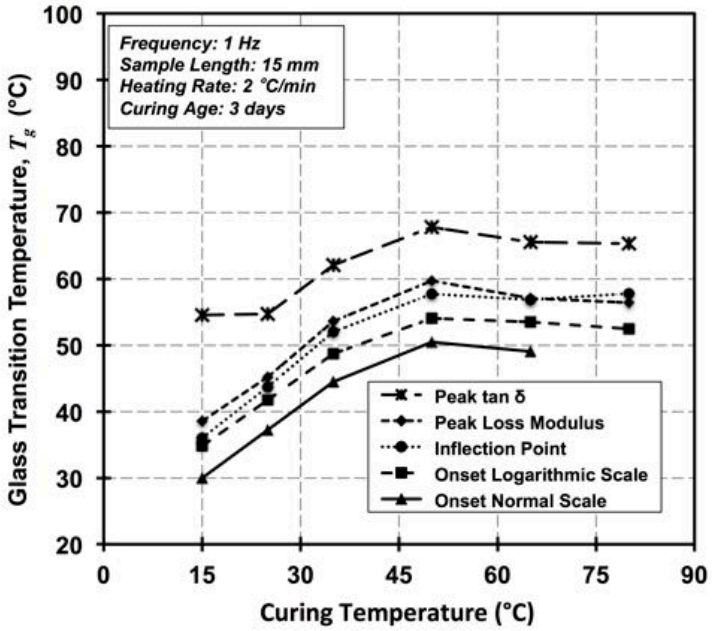

Figure B-23: Recorded T_g according to different methods at 3 days and different curing temperature for Sikadur-330, saturated condition

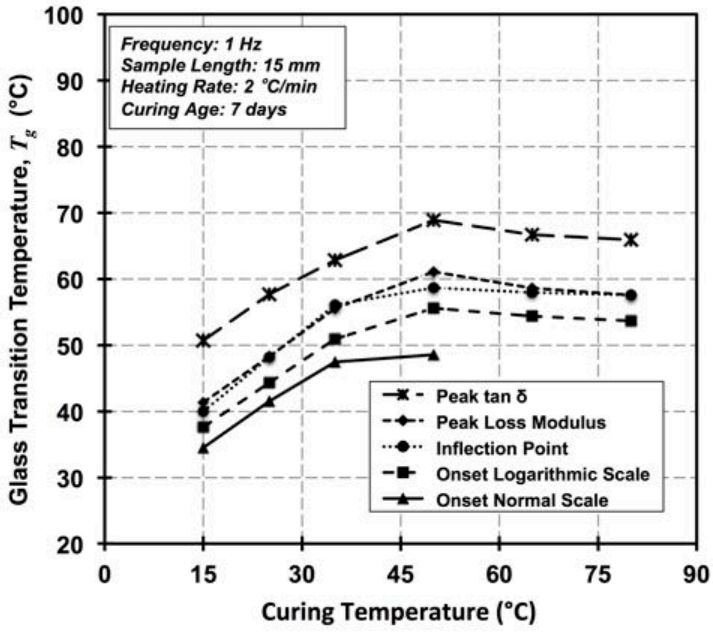

Figure B-24: Recorded T_g according to different methods at 7 days and different curing temperature for Sikadur-330, saturated condition

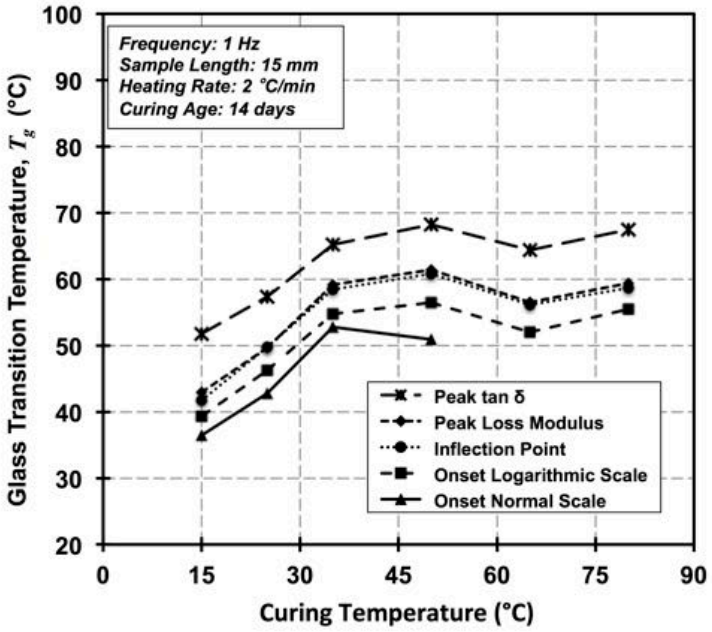

Figure B-25: Recorded T_g according to different methods at 14 days and different curing temperature for Sikadur-330, saturated condition

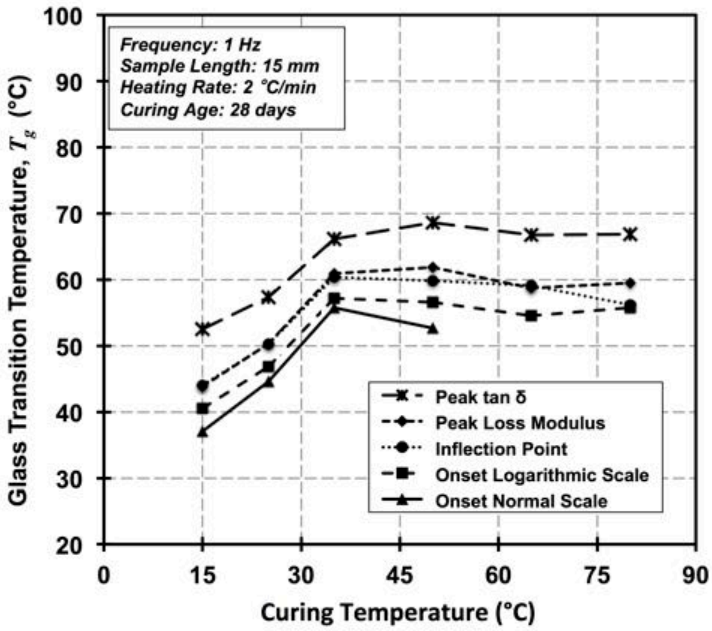

Figure B-26: Recorded T_g according to different methods at 28 days and different curing temperature for Sikadur-330, saturated condition

B.3.3 Saturated condition DMA test responses

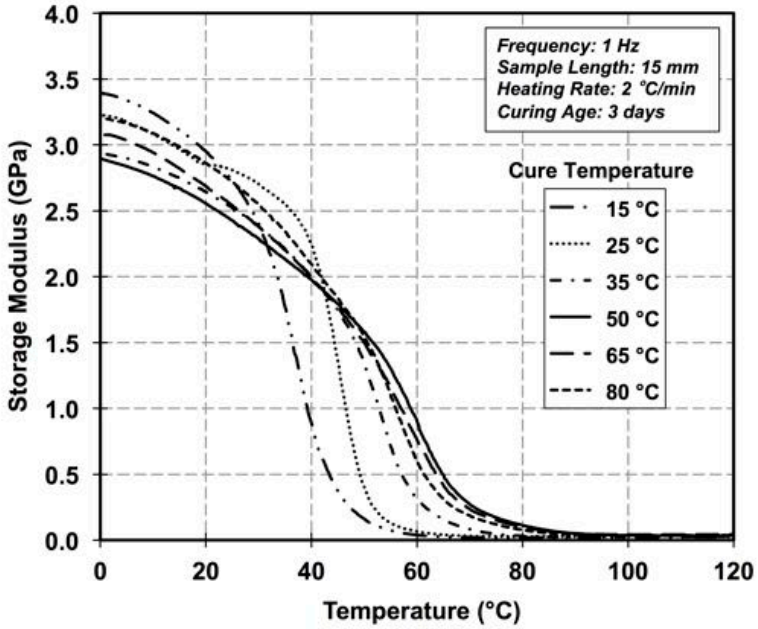

Storage modulus variation with temperature

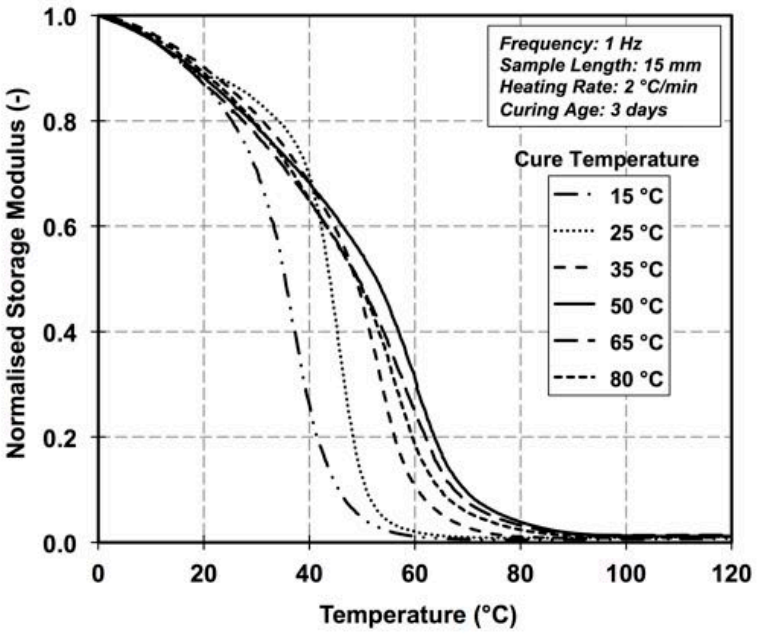

Normalised storage modulus variation with temperature

Figure B-27: Storage and normalised modulus variation with temperature for specimens cured at different temperature for 3 days, Sikadur-330 saturated condition

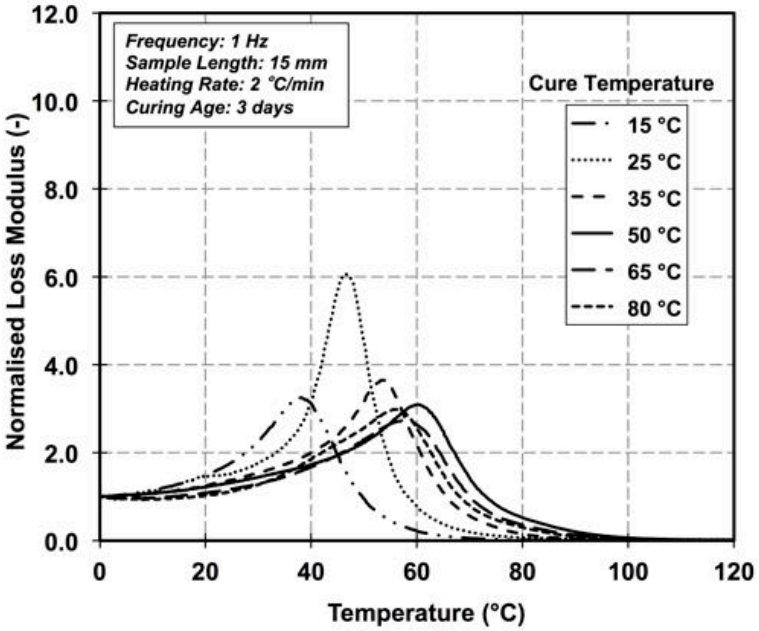

Normalised loss modulus variation with temperature

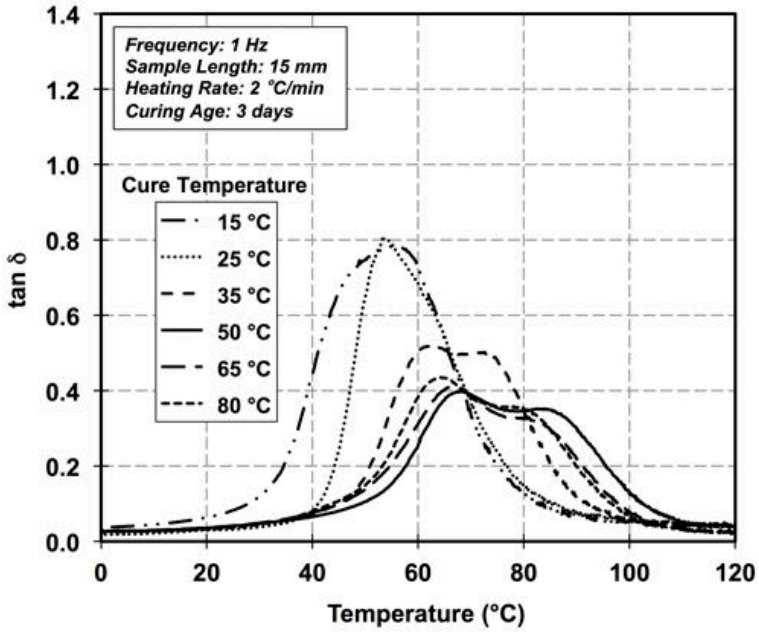

tan δ variation with temperature

Figure B-28: Normalised loss modulus and tan δ variation with temperature for specimens cured at different temperature for 3 days, Sikadur-330 saturated condition

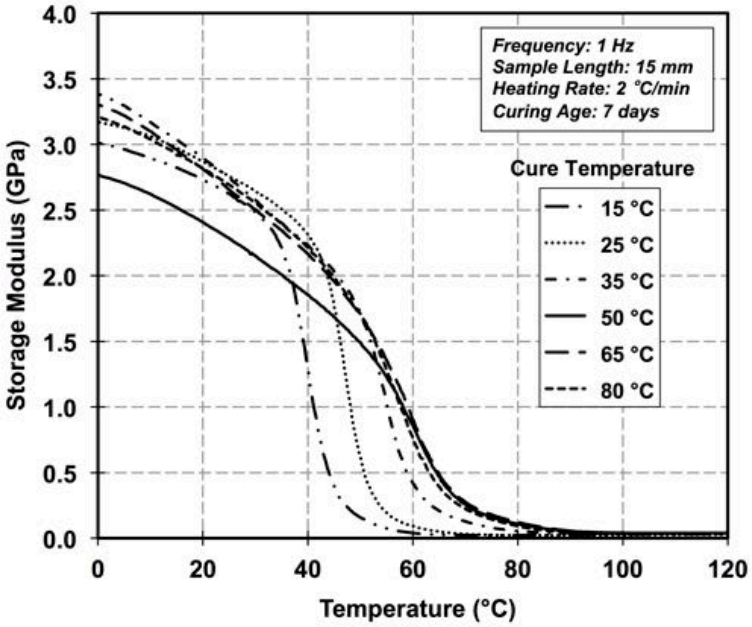

Storage modulus variation with temperature

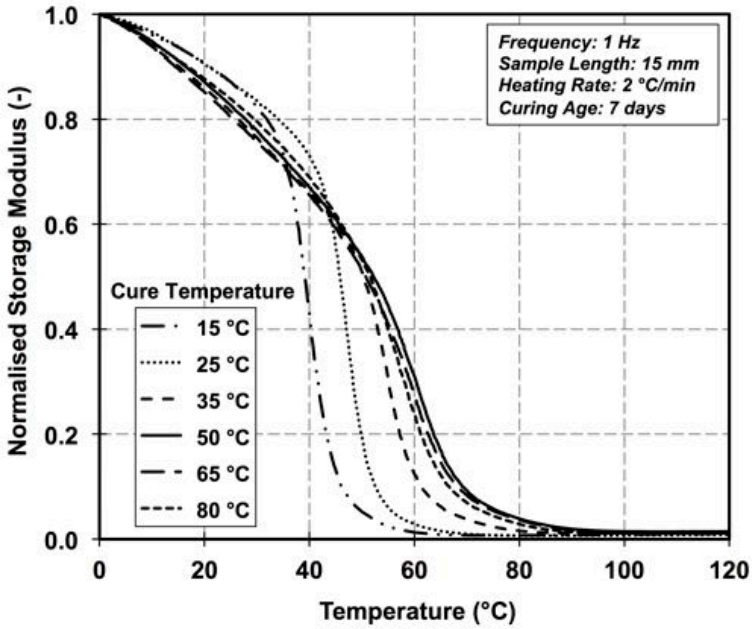

Normalised storage modulus variation with temperature

Figure B-29: Storage and normalised modulus variation with temperature for specimens cured at different temperature for 7 days, Sikadur-330 saturated condition

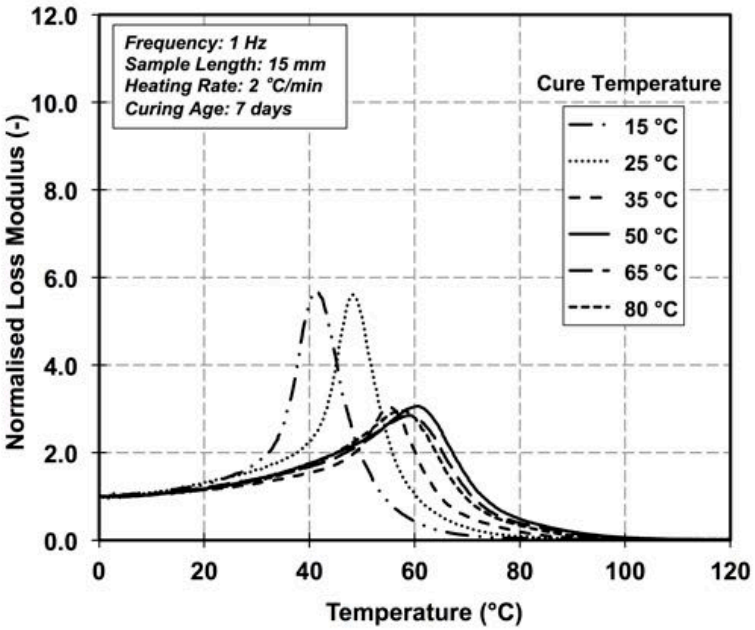

Normalised loss modulus variation with temperature

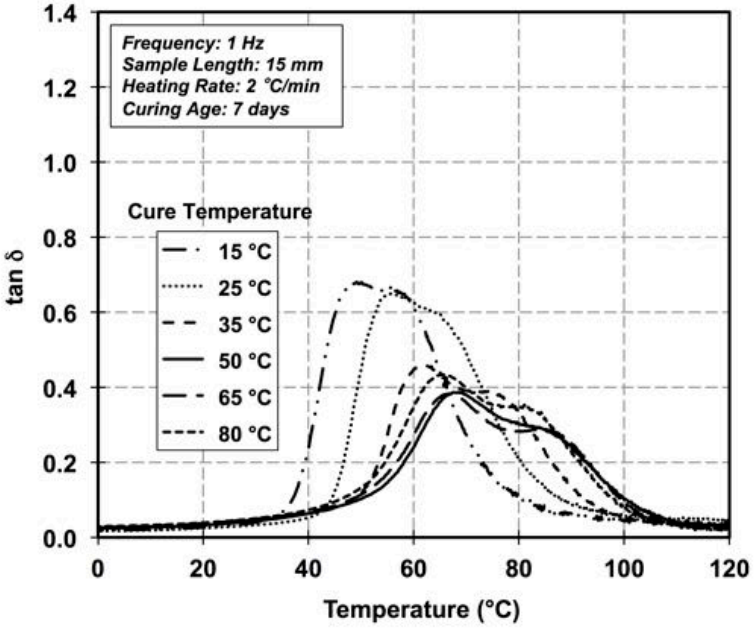

tan δ variation with temperature

Figure B-30: Normalised loss modulus and tan δ variation with temperature for specimens cured at different temperature for 7 days, Sikadur-330 saturated condition

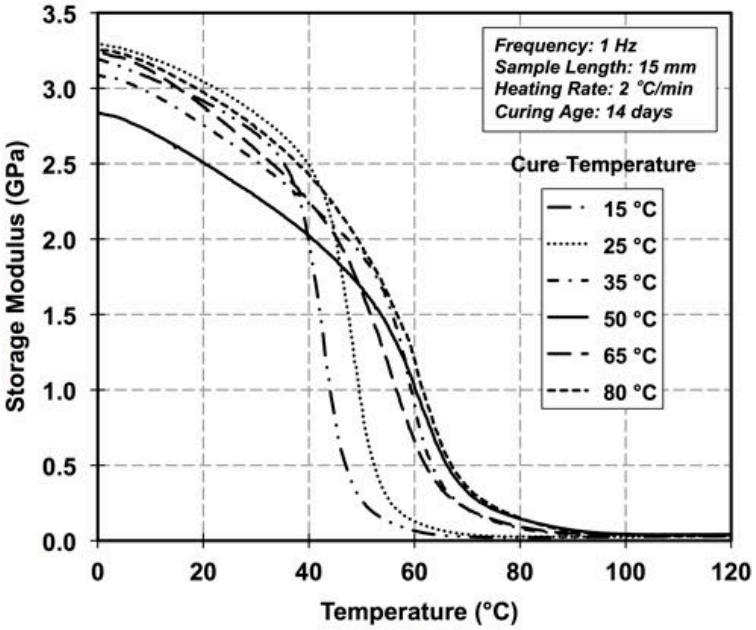

Storage modulus variation with temperature

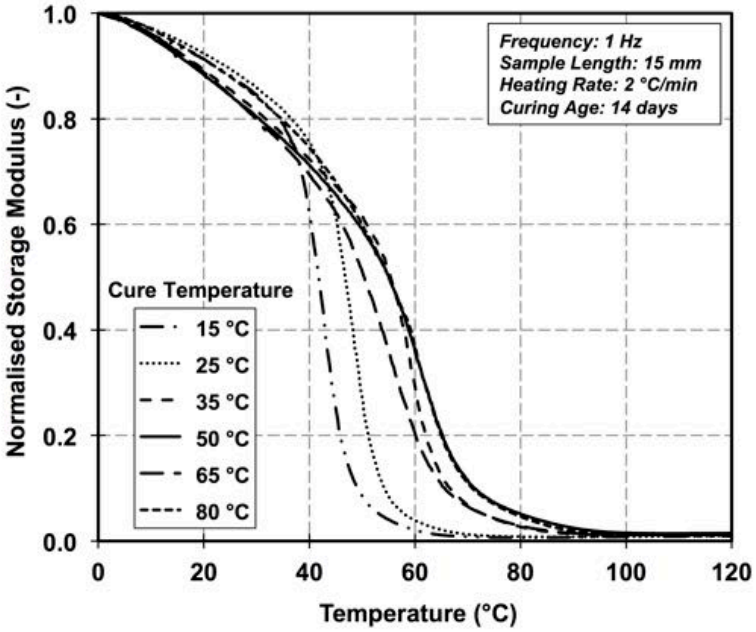

Normalised storage modulus variation with temperature

Figure B-31: Storage and normalised modulus variation with temperature for specimens cured at different temperature for 14 days, Sikadur-330 saturated condition

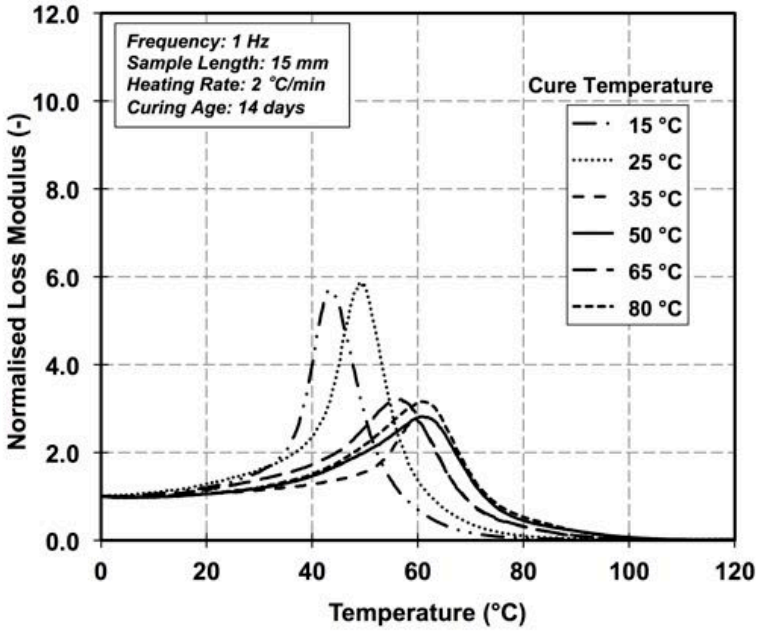

Normalised loss modulus variation with temperature

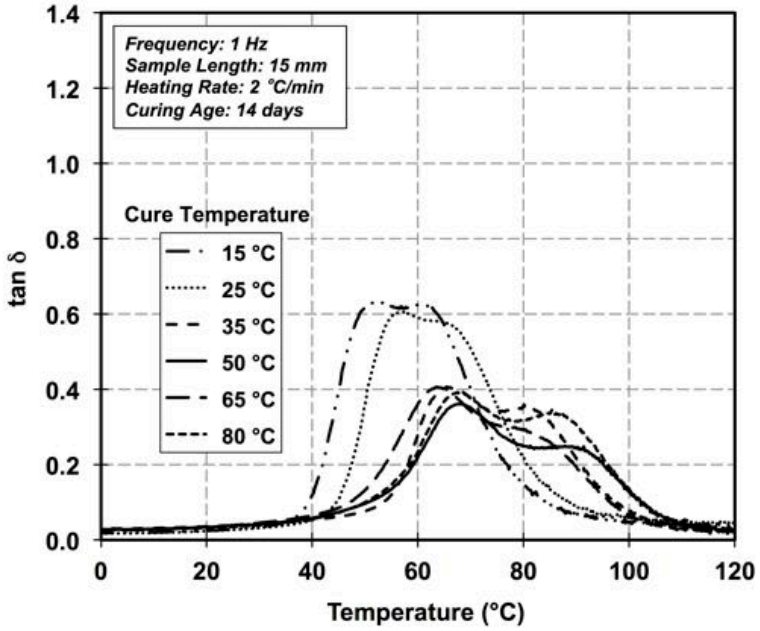

tan δ variation with temperature

Figure B-32: Normalised loss modulus and tan δ variation with temperature for specimens cured at different temperature for 14 days, Sikadur-330 saturated condition

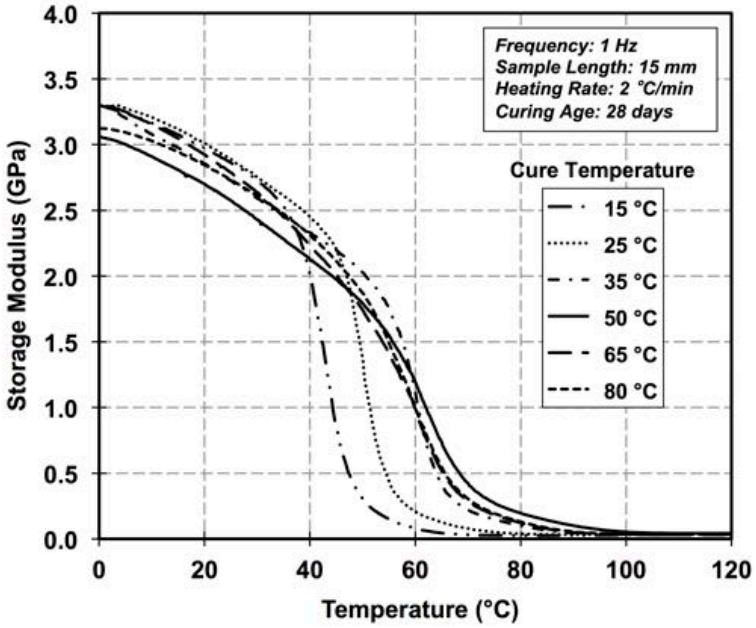

Storage modulus variation with temperature

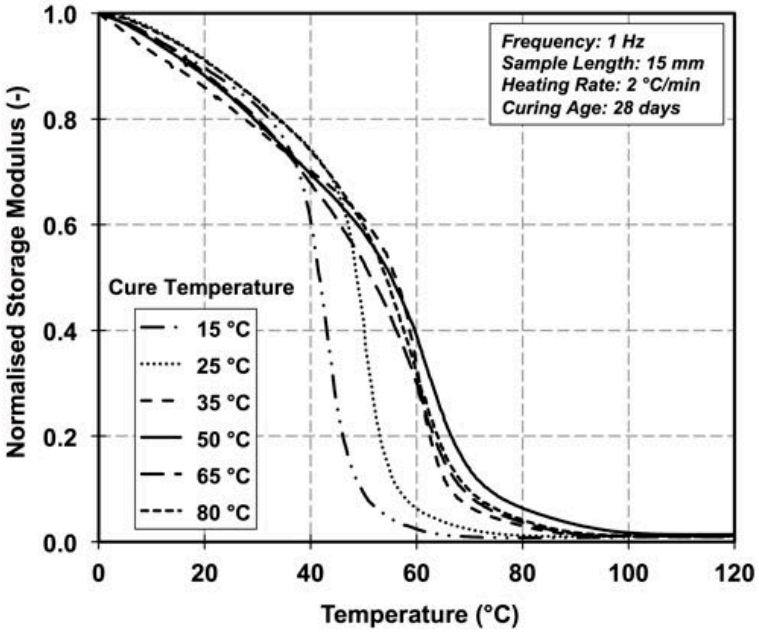

Normalised storage modulus variation with temperature

Figure B-33: Storage and normalised modulus variation with temperature for specimens cured at different temperature for 28 days, Sikadur-330 saturated condition

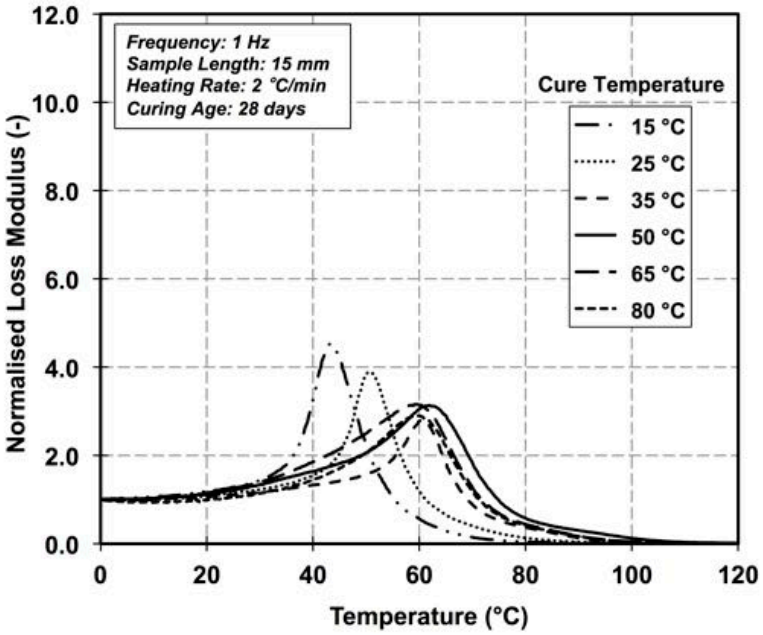

Normalised loss modulus variation with temperature

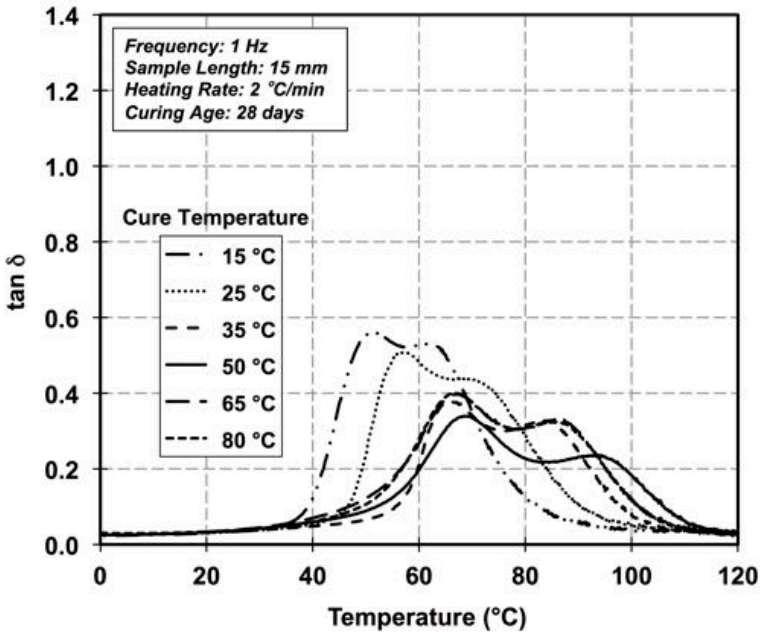

tan δ variation with temperature

Figure B-34: Normalised loss modulus and tan δ variation with temperature for specimens cured at different temperature for 28 days, Sikadur-330 saturated condition

B.4 Sikadur-330 at dry condition using DSC

B.4.1 Curing age effect on T_g using DSC

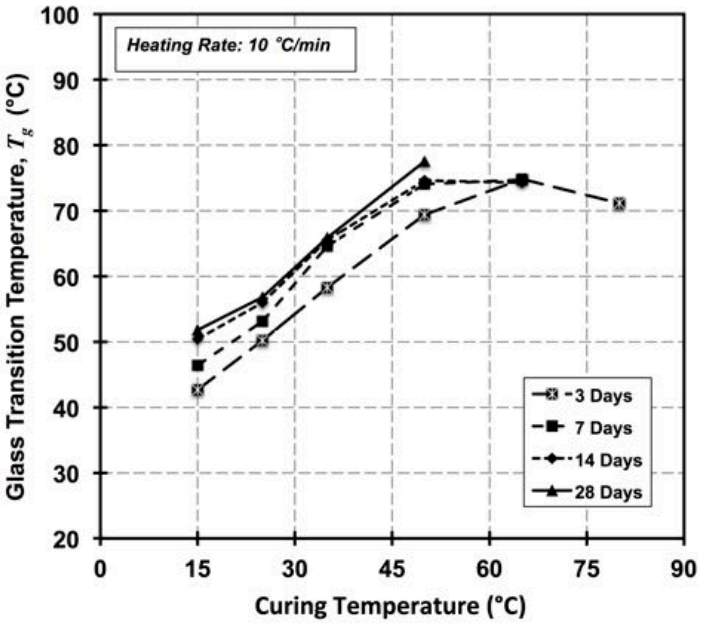

Figure B-35: Recorded T_g according to inflection point method at different age and curing temperature for Sikadur-330, dry condition

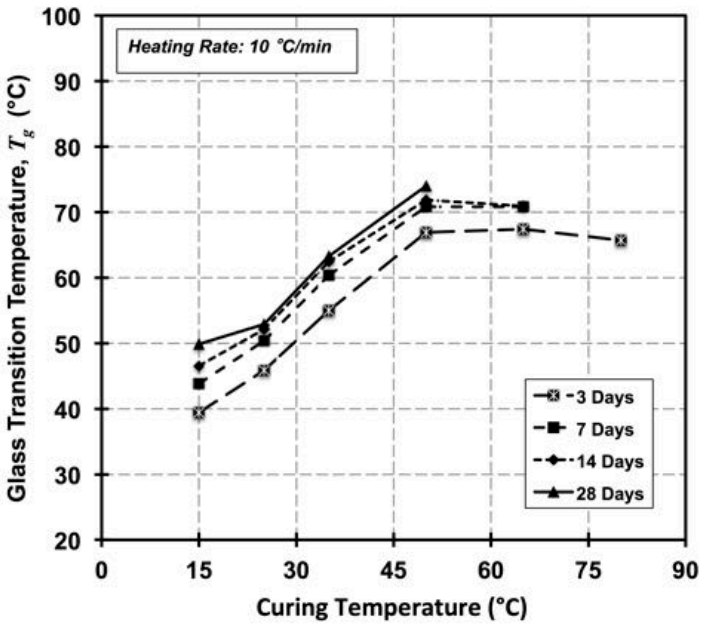

Figure B-36: Recorded T_g according to onset point method at different age and curing temperature for Sikadur-330, dry condition

B.4.2 Curing temperature effect on T_g using DSC

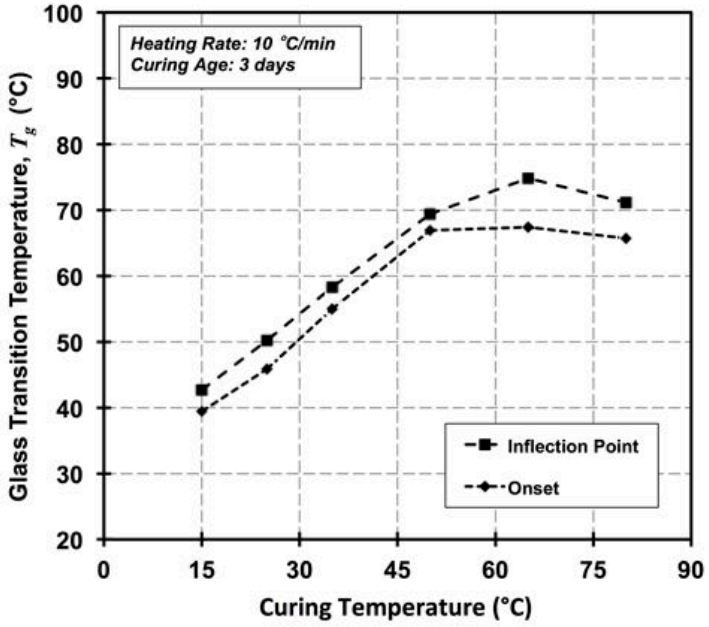

Figure B-37: Recorded T_g according to different methods at 3 days and different curing temperature for Sikadur-330, dry condition

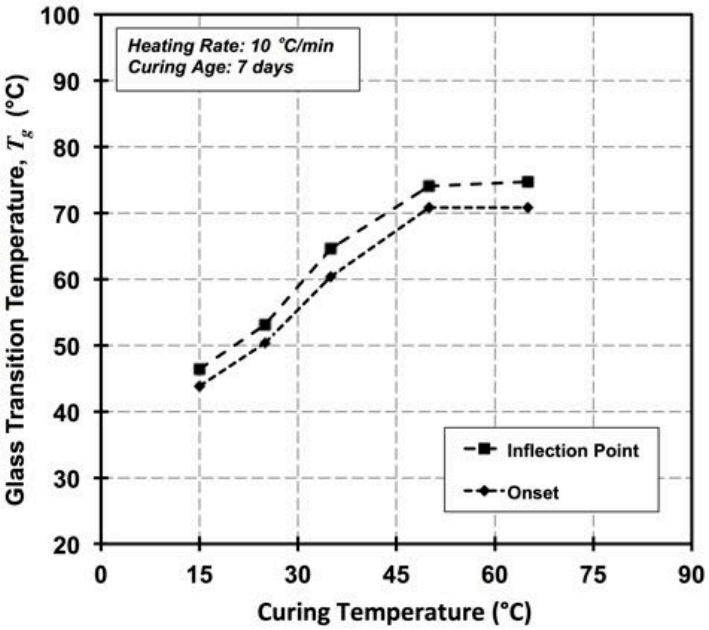

Figure B-38: Recorded T_g according to different methods at 7 days and different curing temperature for Sikadur-330, dry condition

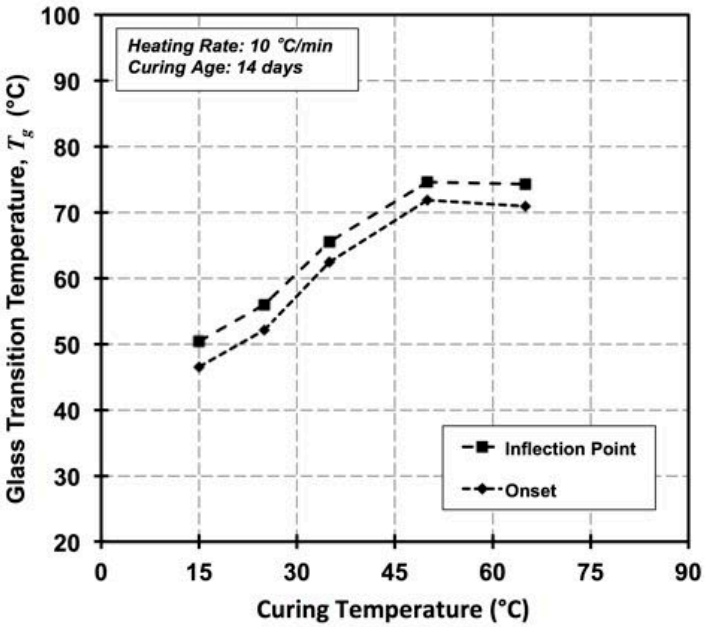

Figure B-39: Recorded T_g according to different methods at 14 days and different curing temperature for Sikadur-330, dry condition

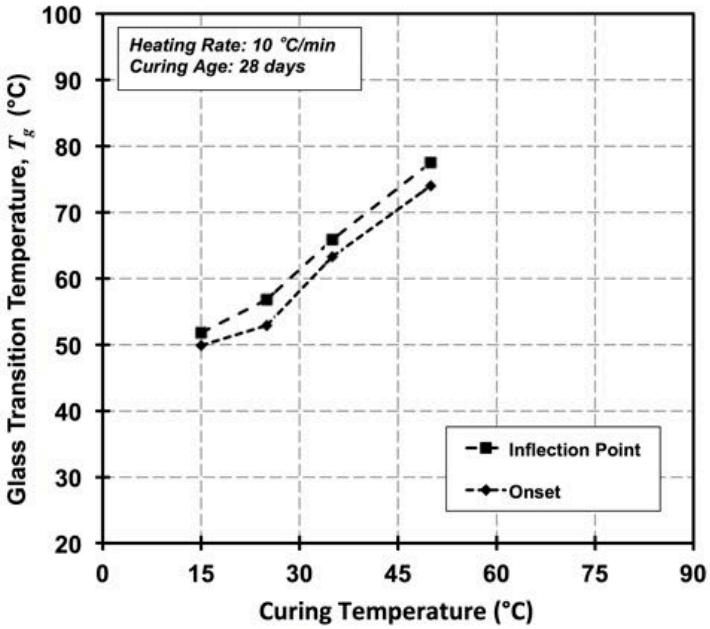

Figure B-40: Recorded T_g according to different methods at 28 days and different curing temperature for Sikadur-330, dry condition

B.4.3 Dry condition DSC test responses

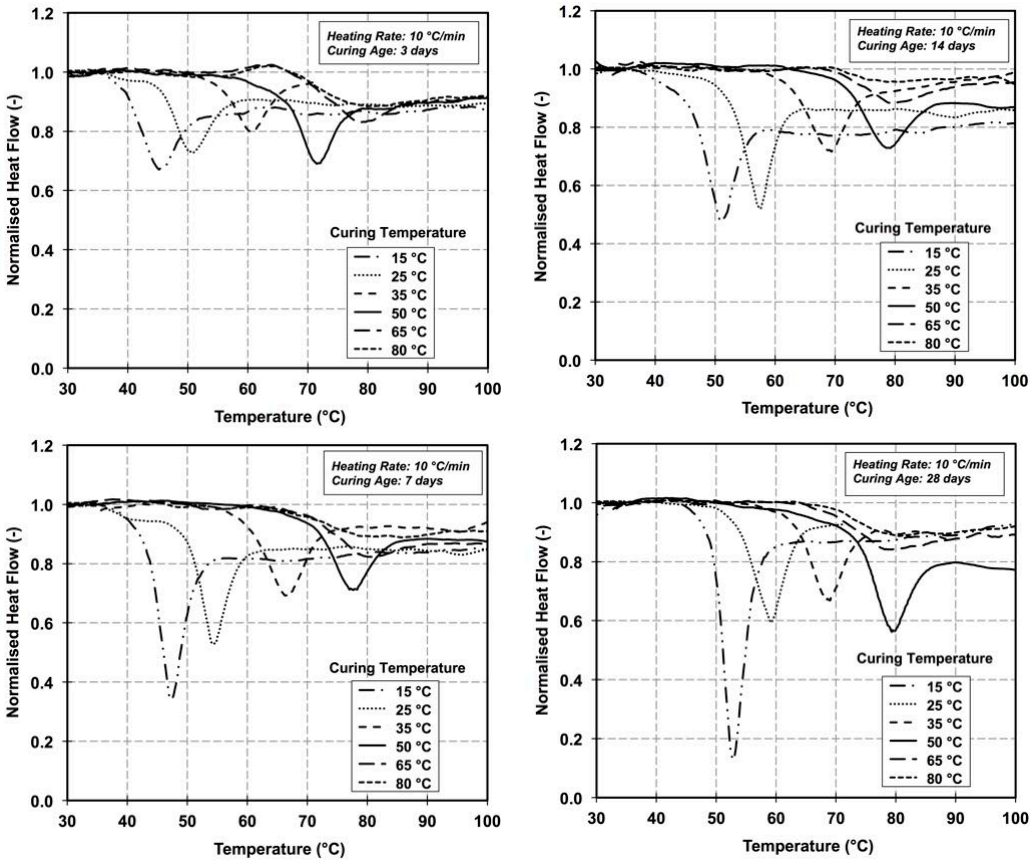

Figure B-41: Normalised heat flow variation with temperature for specimens cured at different temperatures for 3, 7, 14, and 28 days, Sikadur-330 dry condition

B.5 Sikadur-330 at saturate condition using DSC

B.5.1 Curing age effect on T_g using DSC

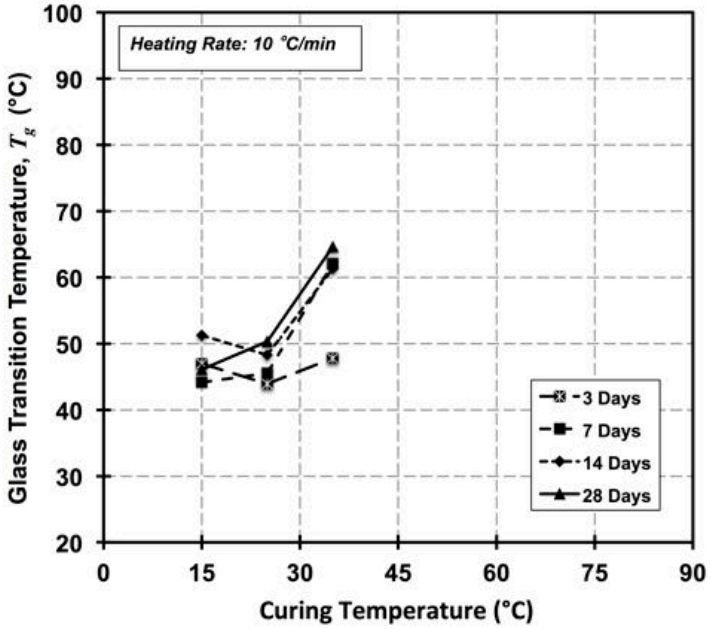

Figure B-42: Recorded T_g according to inflection point method at different age and curing temperature for Sikadur-330, saturated condition

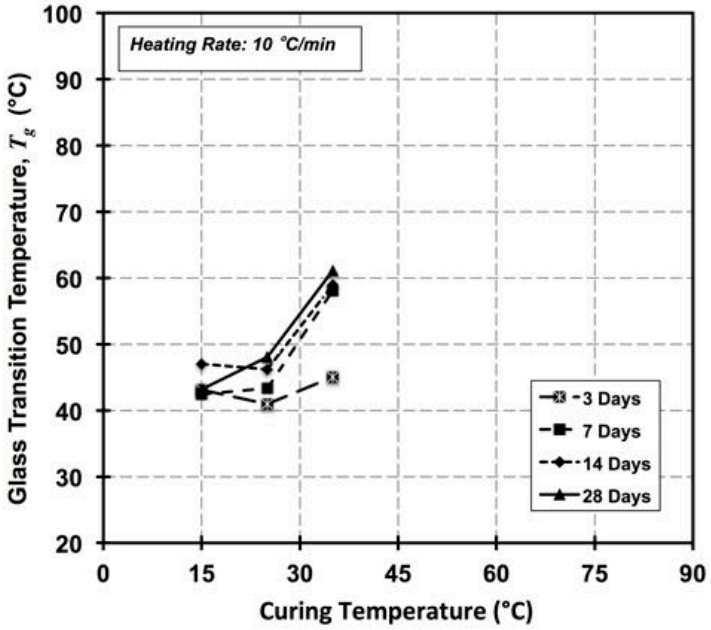

Figure B-43: Recorded T_g according to onset point method at different age and curing temperature for Sikadur-330, saturated condition

B.5.2 Curing temperature effect on T_g using DSC

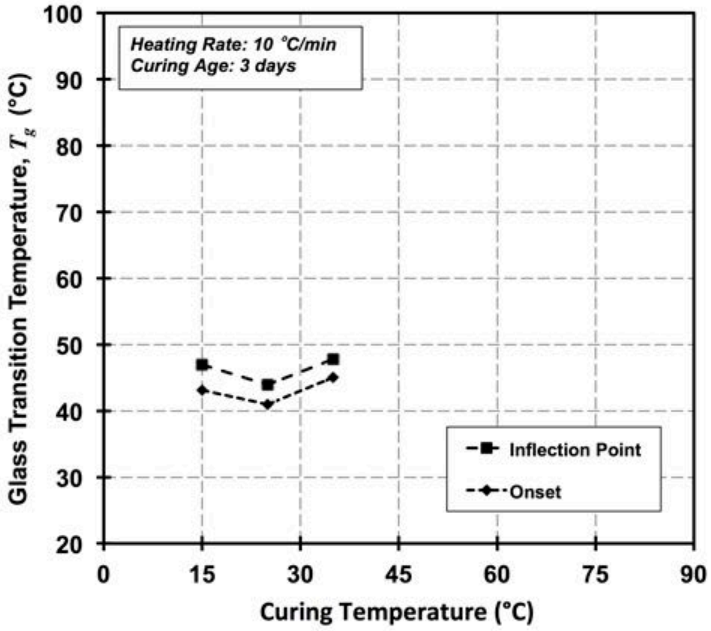

Figure B.B-44: Recorded T_g according to different methods at 3 days and different curing temperature for Sikadur-330, saturated condition

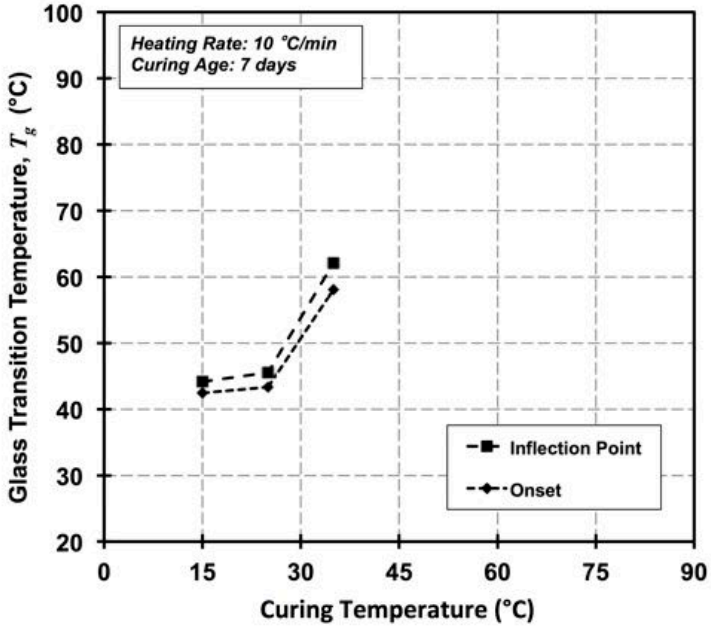

Figure B-45: Recorded T_g according to different methods at 7 days and different curing temperature for Sikadur-330, saturated condition

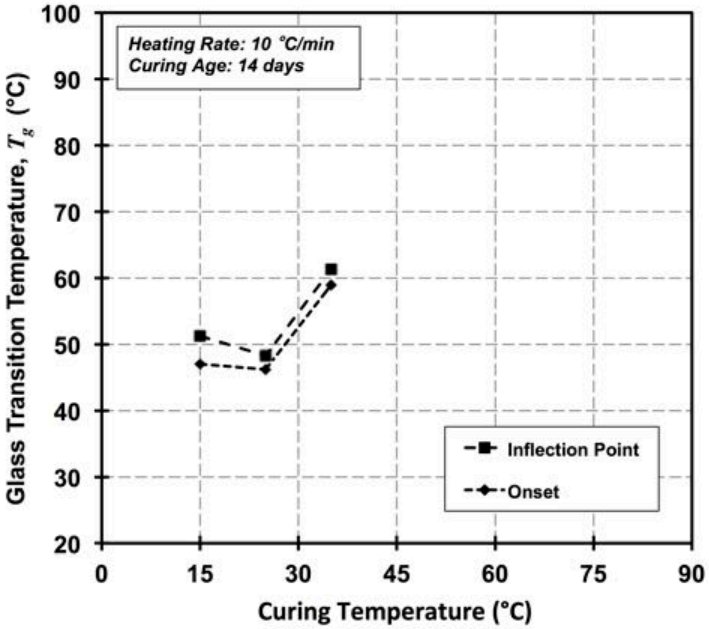

Figure B-46: Recorded T_g according to different methods at 14 days and different curing temperature for Sikadur-330, saturated condition

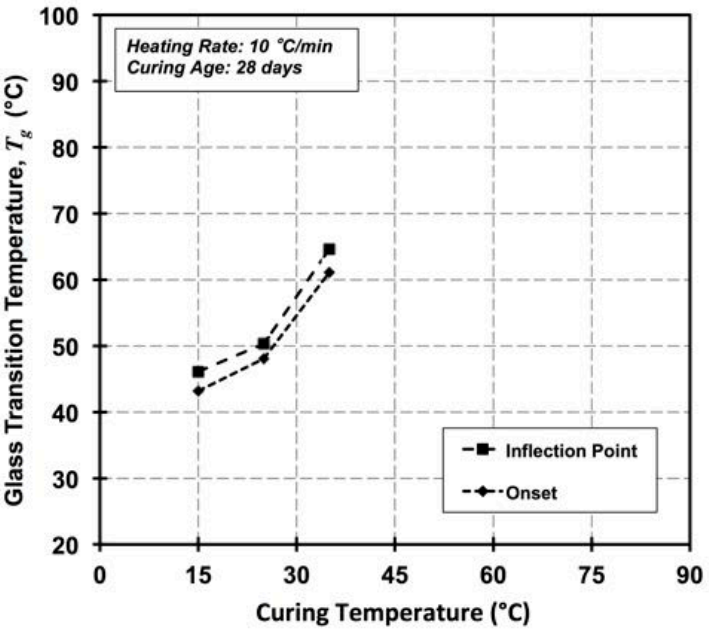

Figure B-47: Recorded T_g according to different methods at 28 days and different curing temperature for Sikadur-330, saturated condition

B.5.3 Saturated condition DSC test responses

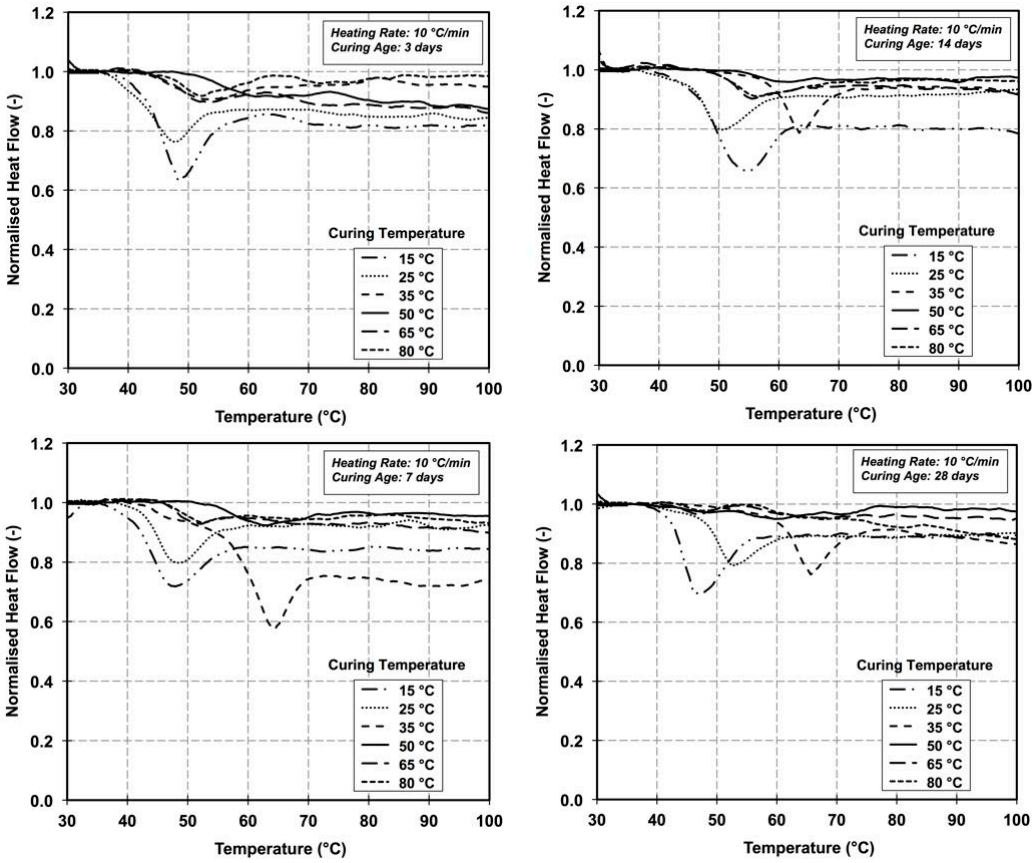

Figure B-48: Normalised heat flow variation with temperature for specimens cured at different temperatures for 3, 7, 14, and 28 days, Sikadur-330 saturated condition

B.6 Sikadur-330 tabulated results

Table B-1: tan δ, T_g at different ages and curing temperatures.

tan δ glass transition temperature, T_g °C at age						
Temperature	***RH %***	***Samples No.***	***3 days***	***7 days***	***14 days***	***28 days***
15°C	**0%**	**S-15-0**	51.3	52.9	54.6	56.2
			51.7	52.7	53.4	54.7
			50.0	52.9	54.8	55.5
		Avg ± SD	*51.0 ± 0.7*	*52.8 ± 0.1*	*54.3 ± 0.6*	*55.5 ± 0.6*
	100%	**S-15-100**	54.5	49.4	50.0	51.7
			55.5	50.5	52.2	52.5
			53.6	52.2	53.1	53.3
		Avg ± SD	*54.5 ± 0.8*	*50.7 ± 1.2*	*51.8 ± 1.3*	*52.5 ± 0.7*
24°C	**0%**	**S-24-0**	55.3	58.9	61.6	62.6
			55.8	59.0	61.5	63.5
			56.5	58.7	61.5	63.3
		Avg ± SD	*55.9 ± 0.5*	*58.9 ± 0.1*	*61.5 ± 0.0*	*63.1 ± 0.4*
	100%	**S-24-100**	54.0	58.5	56.8	57.5
			56.2	57.2	57.5	57.3
			54.0	57.4	57.7	57.2
		Avg ± SD	*54.7 ± 1.0*	*57.7 ± 0.6*	*57.3 ± 0.4*	*57.3 ± 0.1*
35°C	**0%**	**S-35-0**	65.4	68.2	70.5	73.0
			65.4	67.5	71.6	72.4
			64.9	66.8	70.1	71.9
		Avg ± SD	*65.2 ± 0.2*	*67.5 ± 0.6*	*70.7 ± 0.6*	*72.4 ± 0.4*
	100%	**S-35-100**	61.0	62.0	64.9	65.6
			62.7	63.4	65.8	66.5
			62.5	63.2	64.9	66.4
		Avg ± SD	*62.1 ± 0.8*	*62.9 ± 0.6*	*65.2 ± 0.4*	*66.2 ± 0.4*
50°C	**0%**	**S-50-0**	79.7	82.8	84.2	84.5
			80.6	83.0	84.7	84.7
			80.1	83.1	83.4	85.9
		Avg ± SD	*80.1 ± 0.4*	*83.0 ± 0.1*	*84.1 ± 0.5*	*85.0 ± 0.6*
	100%	**S-50-100**	67.9	68.8	68.0	68.8
			67.7	69.6	68.4	68.2
			67.8	68.2	68.3	68.9
		Avg ± SD	*67.8 ± 0.1*	*68.9 ± 0.6*	*68.2 ± 0.2*	*68.6 ± 0.3*
65°C	**0%**	**S-65-0**	85.3	86.8	89.1	88.3
			84.6	87.3	87.5	87.9
			85.0	88.8	86.3	88.9
		Avg ± SD	*85.0 ± 0.3*	*87.6 ± 0.8*	*87.6 ± 1.1*	*88.4 ± 0.4*
	100%	**S-65-100**	66.0	66.0	64.2	67.2
			66.8	67.1	65.0	67.0
			63.8	66.9	63.9	66.1
		Avg ± SD	*65.5 ± 1.3*	*66.7 ± 0.5*	*64.4 ± 0.5*	*66.8 ± 0.5*
80°C	**0%**	**S-80-0**	85.3	86.1	86.5	87.8
			85.2	85.5	87.1	87.2
			86.2	86.5	87.6	87.6
		Avg ± SD	*85.6 ± 0.4*	*86.0 ± 0.4*	*87.1 ± 0.4*	*87.5 ± 0.2*
	100%	**S-80-100**	66.3	65.4	67.4	66.5
			65.2	65.5	67.0	67.1
			64.4	66.8	67.9	66.9
		Avg ± SD	*65.3 ± 0.8*	*65.9 ± 0.6*	*67.4 ± 0.4*	*66.8 ± 0.2*

Table B-2: Peak loss modulus, T_g at different ages and curing temperatures

Peak loss modulus glass transition temperature, T_g °C at age						
Temperature	***RH %***	***Samples No.***	***3 days***	***7 days***	***14 days***	***28 days***
15°C	**0%**	**S-15-0**	43.1	45.1	48.5	50.3
			42.1	44.0	46.4	48.4
			42.3	44.7	48.0	49.7
		Avg ± SD	*42.5 ± 0.4*	*44.6 ± 0.5*	*47.6 ± 0.9*	*49.5 ± 0.8*
	100%	**S-15-100**	39.7	41.2	42.4	43.2
			37.9	41.1	43.4	43.9
			38.0	41.7	43.0	44.4
		Avg ± SD	*38.5 ± 0.8*	*41.3 ± 0.3*	*42.9 ± 0.4*	*43.8 ± 0.5*
24°C	**0%**	**S-24-0**	48.8	52.6	55.8	57.1
			49.3	52.4	56.1	57.8
			47.7	52.8	55.7	57.4
		Avg ± SD	*48.6 ± 0.7*	*52.6 ± 0.2*	*55.9 ± 0.2*	*57.4 ± 0.3*
	100%	**S-24-100**	46.5	48.6	50.4	50.4
			43.5	49.4	50.3	49.7
			45.6	46.9	48.3	50.8
		Avg ± SD	*45.2 ± 1.3*	*48.3 ± 1.0*	*49.7 ± 1.0*	*50.3 ± 0.5*
35°C	**0%**	**S-35-0**	59.1	62.8	64.9	68.1
			58.6	62.1	66.2	67.2
			58.3	60.9	64.5	66.1
		Avg ± SD	*58.7 ± 0.3*	*61.9 ± 0.8*	*65.2 ± 0.7*	*67.1 ± 0.8*
	100%	**S-35-100**	53.1	55.2	59.4	60.4
			53.5	55.9	59.4	61.3
			54.2	55.5	58.7	61.0
		Avg ± SD	*53.6 ± 0.5*	*55.5 ± 0.3*	*59.2 ± 0.3*	*60.9 ± 0.4*
50°C	**0%**	**S-50-0**	73.7	76.8	78.6	79.4
			73.9	77.1	78.7	79.4
			74.0	77.2	77.8	80.4
		Avg ± SD	*73.9 ± 0.1*	*77.0 ± 0.2*	*78.4 ± 0.4*	*79.7 ± 0.5*
	100%	**S-50-100**	60.2	60.7	60.7	61.5
			59.3	62.0	61.7	61.6
			59.7	60.5	61.9	62.5
		Avg ± SD	*59.7 ± 0.4*	*61.1 ± 0.7*	*61.4 ± 0.5*	*61.9 ± 0.4*
65°C	**0%**	**S-65-0**	78.0	80.1	82.6	81.2
			78.2	81.0	81.5	81.3
			78.9	82.4	79.9	82.6
		Avg ± SD	*78.4 ± 0.4*	*81.2 ± 0.9*	*81.3 ± 1.1*	*81.7 ± 0.6*
	100%	**S-65-100**	57.5	58.6	56.5	59.4
			57.6	59.0	57.0	58.9
			56.1	58.3	56.1	57.8
		Avg ± SD	*57.1 ± 0.7*	*58.6 ± 0.3*	*56.5 ± 0.4*	*58.7 ± 0.7*
80°C	**0%**	**S-80-0**	76.9	78.0	78.0	78.5
			76.9	77.6	78.7	77.9
			78.2	78.0	78.1	77.8
		Avg ± SD	*77.3 ± 0.6*	*77.9 ± 0.2*	*78.3 ± 0.3*	*78.1 ± 0.3*
	100%	**S-80-100**	57.0	57.3	59.2	59.3
			56.5	57.6	58.6	59.5
			55.8	57.8	60.4	59.6
		Avg ± SD	*56.4 ± 0.5*	*57.6 ± 0.2*	*59.4 ± 0.7*	*59.5 ± 0.1*

Table B-3: Inflection point of storage modulus, T_g at different ages and curing temperatures

Inflection point glass transition temperature, T_g °C at age						
Temperature	***RH %***	***Samples No.***	***3 days***	***7 days***	***14 days***	***28 days***
15°C	**0%**	**S-15-0**	42.8	44.3	48.2	49.5
			40.4	44.5	45.4	47.8
			40.5	43.4	47.3	49.3
		Avg ± SD	*41.2 ± 1.1*	*44.1 ± 0.5*	*47.0 ±1.2*	*48.9 ± 0.8*
	100%	**S-15-100**	37.3	40.0	40.5	44.3
			35.4	39.7	42.8	43.5
			35.3	40.2	41.8	44.3
		Avg ± SD	*36.0 ± 0.9*	*40.0 ± 0.2*	*41.7 ± 0.9*	*44.0 ± 0.4*
24°C	**0%**	**S-24-0**	47.3	50.3	55.0	56.7
			48.5	51.0	55.2	57.2
			45.4	52.0	55.3	55.5
	100%	**S-24-100**	45.4	46.8	50.3	50.3
			40.4	49.3	49.3	50.3
			45.3	48.4	49.7	50.1
		Avg ± SD	*43.7 ± 2.3*	*48.2 ± 1.0*	*49.8 ± 0.4*	*50.2 ± 0.1*
35°C	**0%**	**S-35-0**	58.0	62.2	65.0	67.0
			57.5	61.4	65.0	66.9
			57.1	60.7	63.3	65.0
		Avg ± SD	*57.5 ± 0.4*	*61.4 ± 0.6*	*64.4 ± 0.8*	*66.3 ± 0.9*
	100%	**S-35-100**	50.3	55.0	58.1	59.7
			52.0	58.5	58.4	60.7
			53.8	54.7	58.8	60.7
		Avg ± SD	*52.0 ± 1.4*	*56.1 ± 1.7*	*58.4 ± 0.3*	*60.4 ± 0.5*
50°C	**0%**	**S-50-0**	73.4	75.1	77.7	78.5
			72.9	75.8	78.4	78.6
			73.2	75.1	77.5	80.2
		Avg ± SD	*73.2 ± 0.2*	*75.3 ± 0.3*	*77.8 ± 0.4*	*79.1 ± 0.8*
	100%	**S-50-100**	60.4	57.9	60.1	60.4
			55.3	60.0	62.3	58.9
			57.5	58.1	60.1	60.3
		Avg ± SD	*57.7 ± 2.1*	*58.7 ± 0.1*	*60.8 ± 0.1*	*59.8 ± 0.7*
65°C	**0%**	**S-65-0**	76.9	80.0	79.9	79.9
			77.3	79.9	80.1	78.5
			77.4	80.1	80.1	80.1
		Avg ± SD	*77.2*	*80.0*	*80.0*	*79.5*
	100%	**S-65-100**	58.0	58.4	55.3	58.9
			57.7	57.6	55.9	58.0
			54.8	57.9	57.3	60.4
		Avg ± SD	*56.8 ± 1.4*	*58.0 ± 0.3*	*56.2 ± 0.8*	*59.1 ± 1.0*
80°C	**0%**	**S-80-0**	75.1	80.0	77.4	80.1
			75.2	75.2	78.7	77.5
			74.9	75.0	80.3	77.5
		Avg ± SD	*75.1 ± 0.1*	*76.8 ± 2.3*	*78.8 ± 1.2*	*78.4 ± 1.2*
	100%	**S-80-100**	59.9	60.4	58.0	53.0
			58.0	57.0	58.6	58.5
			55.5	55.3	59.4	57.0
		Avg ± SD	*57.8 ± 1.8*	*57.6 ± 2.1*	*58.7 ± 0.6*	*56.2 ± 2.3*

Table B-4: Logarithmic scale onset of storage modulus, T_g at different ages and curing temperatures

Logarithmic scale onset glass transition temperature, T_g°C at age						
Temperature	***RH %***	***Samples No.***	***3 days***	***7 days***	***14 days***	***28 days***
15°C	**0%**	**S-15-0**	40.0	42.7	45.7	47.6
			38.7	40.7	44.0	45.6
			39.2	41.7	45.3	47.4
		Avg ± SD	*39.3 ± 0.5*	*41.7 ± 0.8*	*45.0 ± 0.7*	*46.9 ± 0.9*
	100%	**S-15-100**	35.7	37.6	38.4	40.0
			34.3	37.0	40.0	40.6
			34.4	38.2	39.6	40.9
		Avg ± SD	*34.8 ± 0.6*	*37.6 ± 0.5*	*39.3 ± 0.7*	*40.5 ± 0.4*
24°C	**0%**	**S-24-0**	46.0	50.3	52.7	54.6
			46.6	49.8	53.4	55.2
			45.1	50.4	53.2	54.8
		Avg ± SD	*45.9 ± 0.6*	*50.2 ± 0.3*	*53.1 ± 0.3*	*54.9 ± 0.2*
	100%	**S-24-100**	43.3	44.7	46.5	46.9
			40.3	44.8	47.2	46.3
			41.6	43.5	45.1	47.3
		Avg ± SD	*41.7 ± 1.2*	*44.3 ± 0.6*	*46.3 ± 0.9*	*46.8 ± 0.4*
35°C	**0%**	**S-35-0**	55.9	60.1	61.7	65.0
			55.4	59.3	63.3	64.3
			54.9	57.5	61.8	63.2
		Avg ± SD	*55.4 ± 0.4*	*59.0 ± 1.1*	*62.3 ± 0.7*	*64.2 ± 0.7*
	100%	**S-35-100**	49.0	50.0	55.1	56.7
			47.8	51.3	54.6	57.4
			49.4	51.4	54.6	57.4
		Avg ± SD	*48.7 ± 0.7*	*50.9 ± 0.6*	*54.8 ± 0.2*	*57.2 ± 0.3*
50°C	**0%**	**S-50-0**	69.8	73.3	75.3	76.1
			70.2	73.6	75.0	75.9
			70.0	73.9	74.1	76.8
		Avg ± SD	*70.0 ± 0.2*	*73.6 ± 0.2*	*74.8 ± 0.5*	*76.3 ± 0.4*
	100%	**S-50-100**	54.4	54.7	56.3	57.0
			54.1	56.0	56.9	56.1
			53.7	56.1	56.2	56.6
		Avg ± SD	*54.1 ± 0.3*	*55.6 ± 0.6*	*56.5 ± 0.3*	*56.6 ± 0.4*
65°C	**0%**	**S-65-0**	75.2	76.7	77.9	78.5
			74.3	77.5	77.3	77.8
			74.3	78.8	76.2	79.1
		Avg ± SD	*74.6 ± 0.4*	*77.7 ± 0.9*	*77.1 ± 0.7*	*78.5 ± 0.5*
	100%	**S-65-100**	54.2	54.6	51.6	55.5
			54.3	54.1	53.5	54.5
			52.0	54.5	50.9	53.6
		Avg ± SD	*53.5 ± 1.1*	*54.4 ± 0.2*	*52.0 ± 0.5*	*54.5 ± 0.5*
80°C	**0%**	**S-80-0**	73.7	74.1	74.6	74.6
			73.9	73.9	75.7	75.6
			75.6	74.5	75.5	74.6
		Avg ± SD	*74.4 ± 0.9*	*74.2 ± 0.2*	*75.3 ± 0.5*	*74.9 ± 0.5*
	100%	**S-80-100**	53.4	55.0	56.0	55.6
			52.5	52.4	54.3	55.9
			51.5	53.6	56.1	55.8
		Avg ± SD	*52.5 ± 0.8*	*53.7 ± 1.1*	*55.5 ± 0.8*	*55.8 ± 0.1*

Table B-5: Normal scale onset of storage modulus, T_g at different ages and curing temperatures

Normal scale onset glass transition temperature, T_g°C at age						
Temperature	***RH %***	***Samples No.***	***3 days***	***7 days***	***14 days***	***28 days***
15°C	**0%**	**S-15-0**	37.1	40.7	43.9	45.7
			34.5	37.2	40.9	43.1
			36.8	39.1	43.4	45.3
		Avg ± SD	*36.1 ± 1.2*	*39.0 ± 1.4*	*42.7 ± 1.3*	*44.7 ± 1.1*
	100%	**S-15-100**	32.5	34.8	35.2	37.1
			28.5	34.0	37.5	37.2
			28.9	34.7	36.6	36.9
		Avg ± SD	*30.0 ± 1.8*	*34.5 ± 0.4*	*36.4 ± 0.9*	*37.1 ± 0.1*
24°C	**0%**	**S-24-0**	43.6	48.6	51.1	52.4
			44.3	47.5	52.0	53.2
			38.6	47.6	51.7	53.2
		Avg ± SD	*42.2 ± 2.5*	*47.9 ± 0.5*	*51.6 ± 0.4*	*52.9 ± 0.4*
	100%	**S-24-100**	39.9	41.5	45.1	45.0
			32.6	42.7	43.9	43.7
			39.2	40.3	39.4	45.0
		Avg ± SD	*37.2 ± 3.3*	*41.5 ± 1.0*	*42.8 ± 2.5*	*44.6 ± 0.6*
35°C	**0%**	**S-35-0**	53.3	57.0	58.9	62.5
			53.0	56.5	60.7	62.0
			52.0	55.4	58.8	60.8
		Avg ± SD	*52.8 ± 0.6*	*56.3 ± 0.7*	*59.5 ± 0.9*	*61.8 ± 0.7*
	100%	**S-35-100**	45.2	47.9	52.6	54.5
			42.7	48.6	53.3	56.5
			45.5	45.9	52.4	56.2
		Avg ± SD	*44.5 ± 1.3*	*47.5 ± 1.1*	*52.8 ± 0.4*	*55.7 ± 0.9*
50°C	**0%**	**S-50-0**	66.2	70.6	72.7	74.0
			67.0	71.2	72.3	73.6
			67.2	71.2	71.4	74.4
		Avg ± SD	*66.8 ± 0.4*	*71.0 ± 0.3*	*72.1 ± 0.5*	*74.0 ± 0.3*
	100%	**S-50-100**	49.9	47.5	50.1	51.6
			50.2	49.0	51.5	52.5
			51.4	49.2	51.1	53.9
		Avg ± SD	*50.5 ± 0.6*	*48.6 ± 0.8*	*50.9 ± 0.6*	*52.7 ± 0.9*
65°C	**0%**	**S-65-0**	70.5	72.1	73.9	74.7
			68.1	72.6	73.7	73.1
			69.0	73.2	71.5	74.9
		Avg ± SD	*69.2 ± 1.0*	*72.6 ± 0.4*	*73.0 ±1.1*	*74.2 ± 0.8*
	100%	**S-65-100**	51.3			
			48.1			
			47.7			
		Avg ± SD	*49.0 ± 1.6*			
80°C	**0%**	**S-80-0**	67.1	66.9	67.8	67.9
			67.4	67.6	64.0	70.3
			68.2	67.4	69.5	66.9
		Avg ± SD	*67.6 ± 0.5*	*67.3 ± 0.3*	*67.1 ± 2.3*	*68.4 ± 1.4*
	100%	**S-80-100**				
		Avg ± SD				

Table B-6: Onset, T_g at different ages and curing temperatures

Onset glass transition temperature, T_g °C at age						
Temperature	***RH %***	***Samples No.***	***3 days***	***7 days***	***14 days***	***28 days***
15°C	**0%**	**S-15-0**	39.2	44.0	46.2	49.8
			39.5	43.7	47.0	50.1
			39.6	43.8	46.4	49.6
		Avg ± SD	*39.4 ± 0.2*	*43.8 ± 0.1*	*46.5 ± 0.3*	*49.9 ± 0.2*
	100%	**S-15-100**	42.4	42.3	46.9	43.1
			43.1	42.4	47.1	42.7
			43.9	42.7	47.0	43.8
		Avg ± SD	*43.1 ± 0.6*	*42.4 ± 0.2*	*47.0 ± 0.1*	*43.2 ± 0.5*
24°C	**0%**	**S-24-0**	45.7	50.9	52.5	52.8
			45.6	50.5	52.4	53.3
			46.2	49.7	51.5	52.7
		Avg ± SD	*45.9 ± 0.3*	*50.4 ± 0.5*	*52.1 ± 0.4*	*52.9 ± 0.3*
	100%	**S-24-100**	40.2	43.6	46.4	48.0
			41.1	43.3	46.2	48.1
			41.5	43.2	46.0	48.1
		Avg ± SD	*40.9 ± 0.6*	*43.3 ± 0.2*	*46.2 ± 0.1*	*48.0 ± 0.1*
35°C	**0%**	**S-35-0**	54.9	60.0	62.3	63.5
			54.7	60.0	62.3	63.2
			55.4	61.1	62.8	63.3
		Avg ± SD	*55.0 ± 0.3*	*60.4 ± 0.5*	*62.5 ± 0.3*	*63.3 ± 0.1*
	100%	**S-35-100**	44.5	57.8	59.2	61.1
			45.0	58.3	58.9	61.5
			45.6	58.2	58.7	60.7
		Avg ± SD	*45.0 ± 0.5*	*58.1 ± 0.2*	*58.9 ± 0.2*	*61.1 ± 0.3*
50°C	**0%**	**S-50-0**	67.0	70.4	72.1	74.0
			67.1	72.0	72.0	74.0
			66.7	70.1	71.5	74.0
		Avg ± SD	*66.9 ± 0.2*	*70.8 ± 0.9*	*71.9 ± 0.3*	*74.0 ± 0.0*
	100%	**S-50-100**				
		Avg ± SD				
65°C	**0%**	**S-65-0**	67.4	69.3	71.0	
			66.1	71.2	70.9	
			68.7	71.9		
		Avg ± SD	*67.4 ± 1.1*	*70.8 ± 1.1*	*70.9 ± 0.1*	
	100%	**S-65-100**				
		Avg ± SD				
80°C	**0%**	**S-80-0**	65.7			
			-			
		Avg ± SD	*65.7 ± 0.0*			
	100%	**S-80-100**				
		Avg ± SD				

Table B-7: Inflection point, T_g at different ages and curing temperatures

Inflection point glass transition temperature, T_g °C at age						
Temperature	***RH %***	***Samples No.***	***3 days***	***7 days***	***14 days***	***28 days***
15°C	**0%**	**S-15-0**	42.4	47.0	50.5	52.0
			41.7	46.2	50.0	51.7
			44.0	46.0	50.7	51.6
		Avg ± SD	*42.7 ± 0.9*	*46.4 ± 0.4*	*50.4 ± 0.3*	*51.8 ± 0.1*
	100%	**S-15-100**	45.5	44.2	50.5	45.9
			47.4	44.1	51.6	46.1
			48.0	44.2	51.5	46.4
		Avg ± SD	*47.0 ± 1.0*	*44.2 ± 0.1*	*51.2 ± 0.5*	*46.1 ± 0.2*
24°C	**0%**	**S-24-0**	51.1	53.1	56.6	56.6
			49.2	53.5	55.9	57.3
			50.2	52.7	55.4	56.6
		Avg ± SD	*50.2 ± 0.8*	*53.1 ± 0.3*	*56.0 ± 0.5*	*56.8 ± 0.3*
	100%	**S-24-100**	43.8	45.5	47.9	49.9
			44.0	45.6	48.7	50.3
			43.9	45.6	48.1	50.7
		Avg ± SD	*43.9 ± 0.1*	*45.6 ± 0.0*	*48.3 ± 0.3*	*50.3 ± 0.3*
35°C	**0%**	**S-35-0**	57.7	64.6	64.9	66.2
			58.2	64.7	65.7	65.2
			58.9	64.5	66.0	66.2
		Avg ± SD	*58.3 ± 0.5*	*64.6 ± 0.1*	*65.5 ± 0.5*	*65.9 ± 0.5*
	100%	**S-35-100**	47.5	62.8	61.6	63.9
			47.4	61.8	61.2	65.2
			48.6	61.8	61.2	64.7
		Avg ± SD	*47.8 ± 0.5*	*62.1 ± 0.2*	*61.3 ± 0.5*	*64.6 ± 0.5*
50°C	**0%**	**S-50-0**	69.2	73.8	75.2	78.3
			69.9	75.9	74.8	76.4
			69.1	72.5	73.9	77.9
		Avg ± SD	*69.4 ± 0.3*	*74.1 ± 1.4*	*74.6 ± 0.5*	*77.5 ± 0.8*
	100%	**S-50-100**				
		Avg ± SD				
65°C	**0%**	**S-65-0**	75.5	72.3	75.0	
			74.8	76.4	73.6	
			74.1	75.4	-	
		Avg ± SD	*74.8 ± 0.6*	*74.7 ± 1.7*	*74.3 ± 0.7*	
	100%	**S-65-100**				
		Avg ± SD				
80°C	**0%**	**S-80-0**	75.1			
			-			
			67.2			
		Avg ± SD	*71.2 ±3.9*			
	100%	**S-80-100**				
		Avg ± SD				

Appendix C

DMA and DSC Test Results for Tyfo-S

C.1 Introduction

This appendix contains the test results from dynamic mechanical analysis DMA and differential scanning calorimetry DSC of Sikadur-330. Due to the small amount of variation in the test results, the average of three samples is presented.

The specimens are named in Section C.6 in the form of A-T-R, where the first letter 'A' refers to the adhesive type (S: Sikadur-330 and T: Tyfo-S). The number 'T' refers to the curing temperature (15, 24, 35, 50, 65 and 80°C), and the number 'R' refers to the relative humidity condition (0: 0% RH and 100: under distilled water); For example, T-15-0 represents Tyfo-S cured at 15°C and 0% RH.

C.2 Tyfo-S at dry condition using DMA

C.2.1 Curing age effect on T_g using DMA

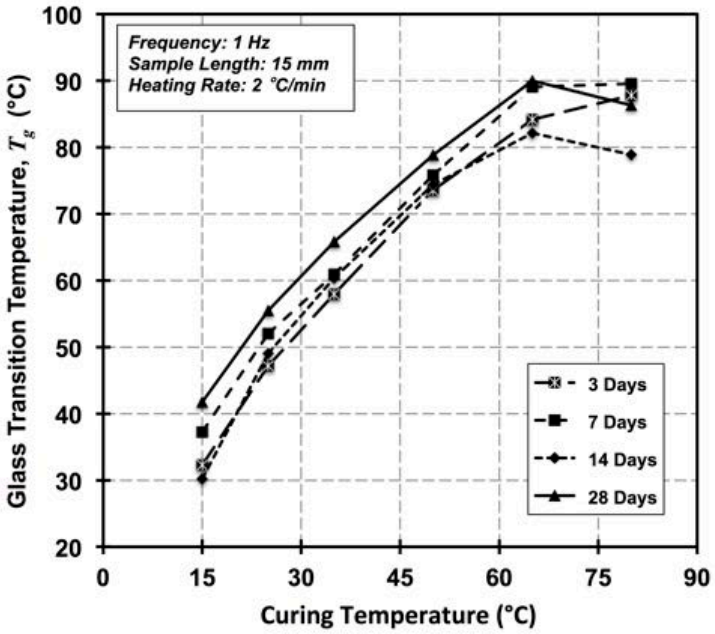

Figure C-1: Recorded T_g according to inflection point method at different age and curing temperature for Tyfo-S, dry condition

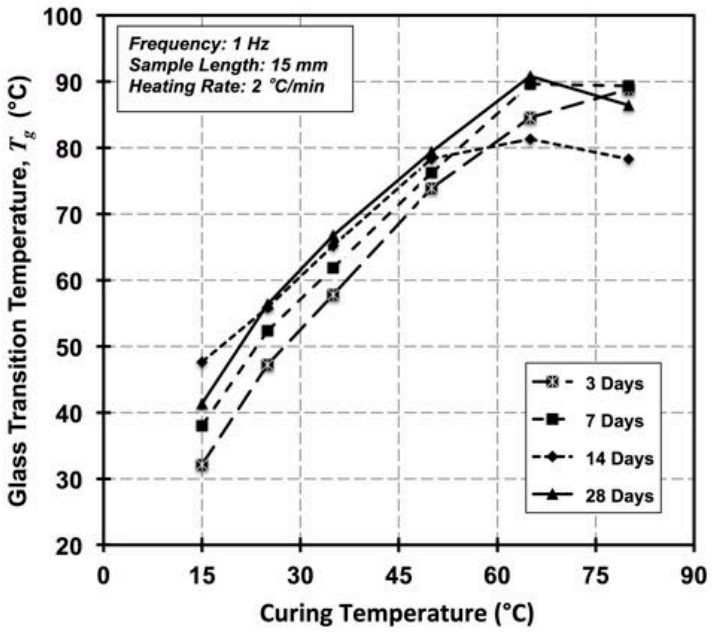

Figure C-2: Recorded T_g according to peak loss modulus method at different age and curing temperature for Tyfo-S, dry condition

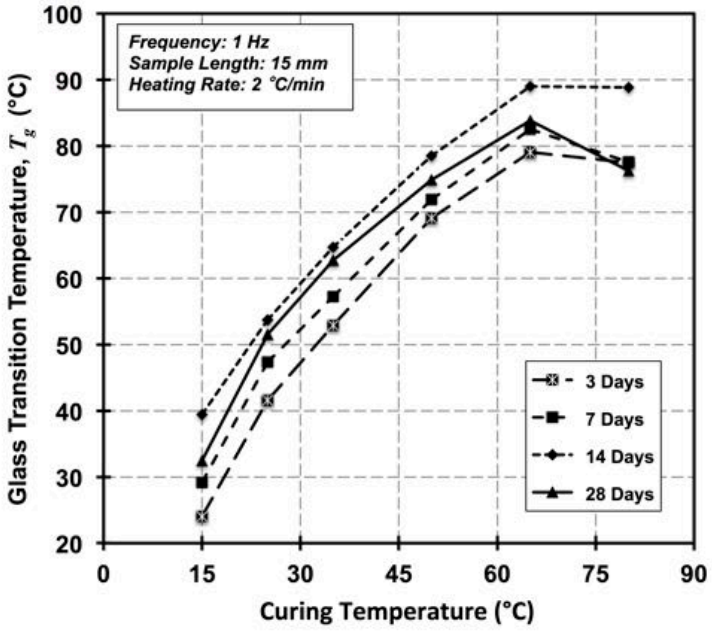

Figure C-3: Recorded T_g according to onset normal scale method at different age and curing temperature for Tyfo-S, dry condition

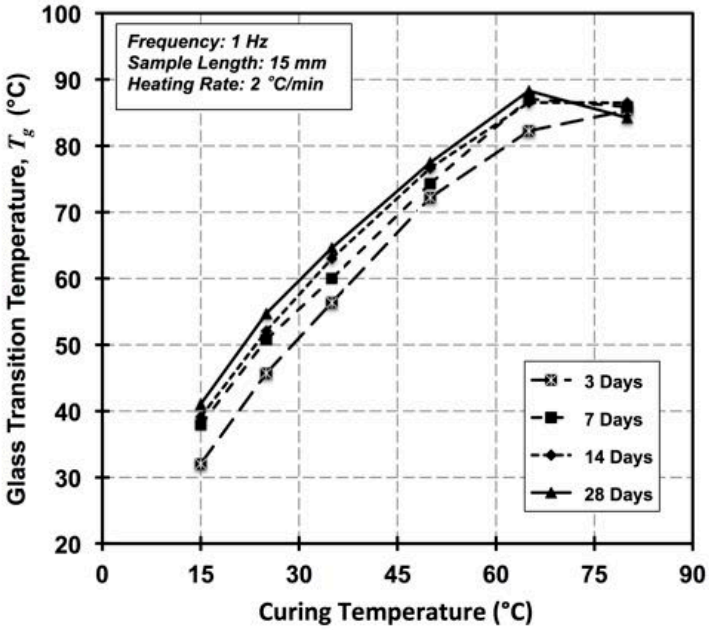

Figure C-4: Recorded T_g according to onset logarithmic scale method at different age and curing temperature for Tyfo-S, dry condition

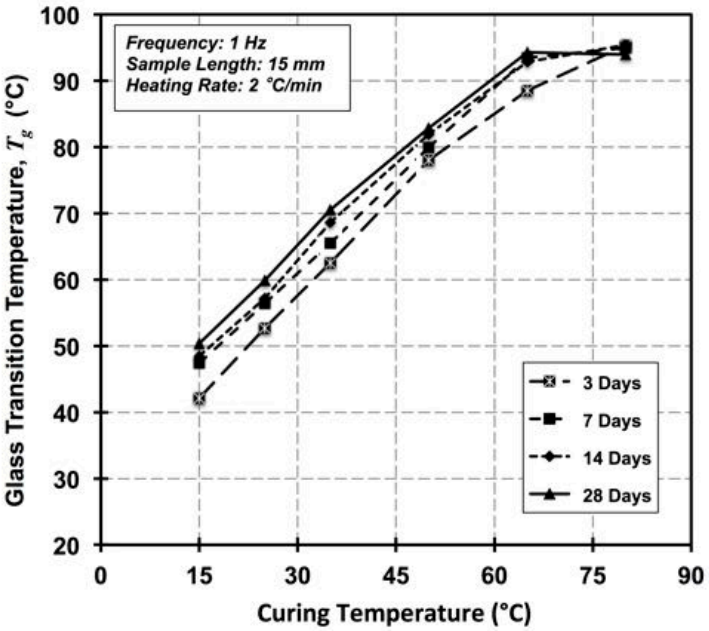

Figure C-5: Recorded T_g according to tan δ method at different age and curing temperature for Tyfo-S, dry condition

C.2.2 Curing temperature effect on T_g using DMA

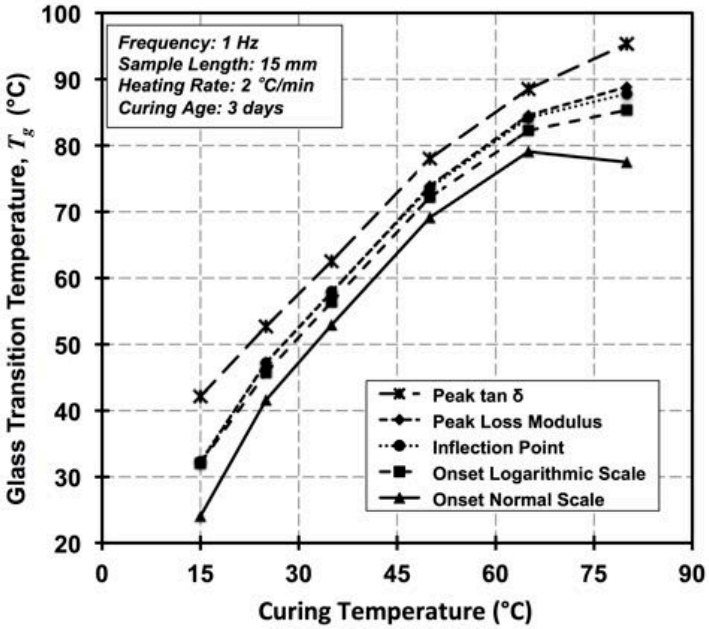

Figure C-6: Recorded T_g according to different methods at 3 days and different curing temperature for Tyfo-S, dry condition

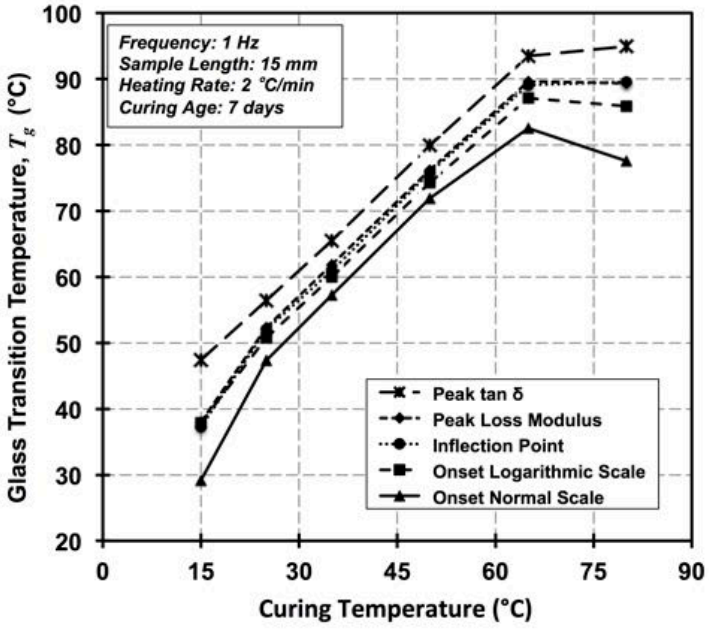

Figure C-7: Recorded T_g according to different methods at 7 days and different curing temperature for Tyfo-S, dry condition

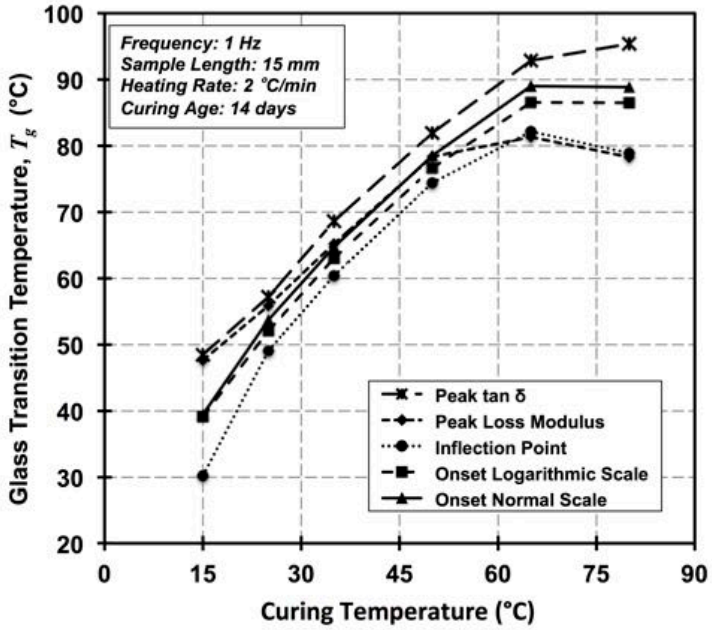

Figure C-8: Recorded T_g according to different methods at 14 days and different curing temperature for Tyfo-S, dry condition

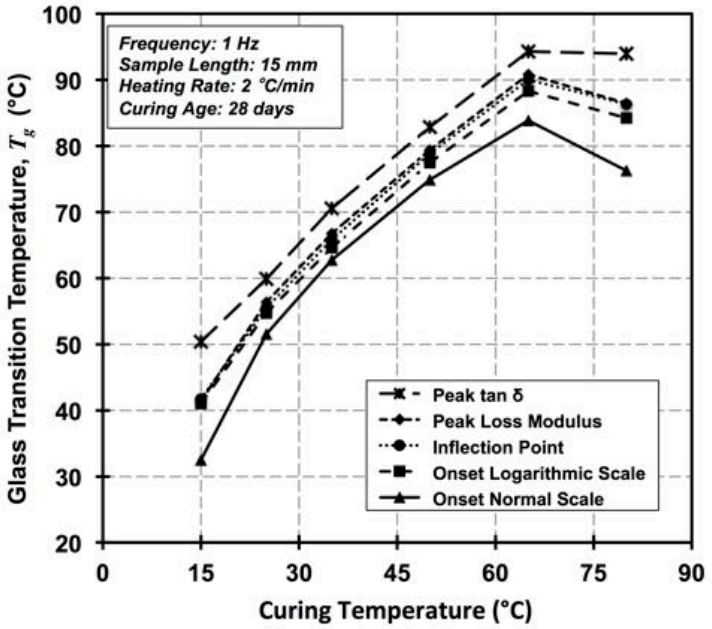

Figure C-9: Recorded T_g according to different methods at 28 days and different curing temperature for Tyfo-S, dry condition

C.2.3 Dry condition DMA test responses

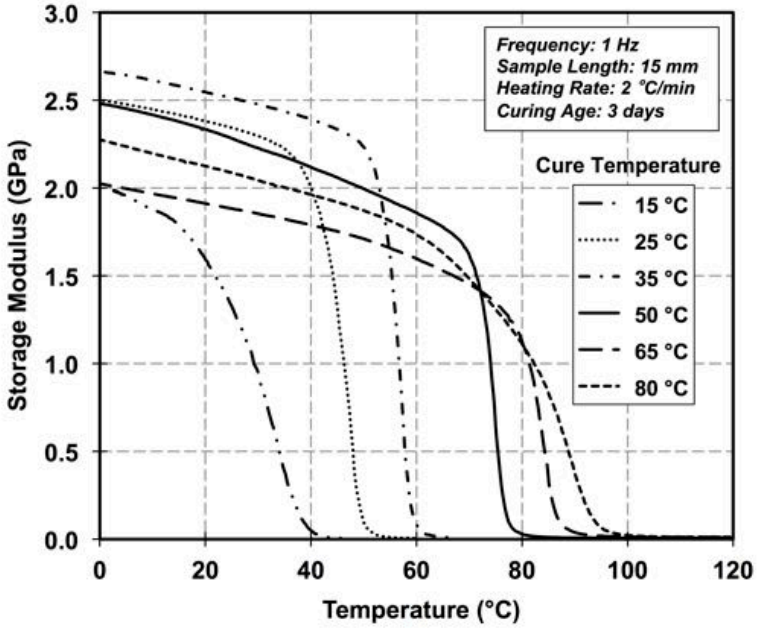

Storage modulus variation with temperature

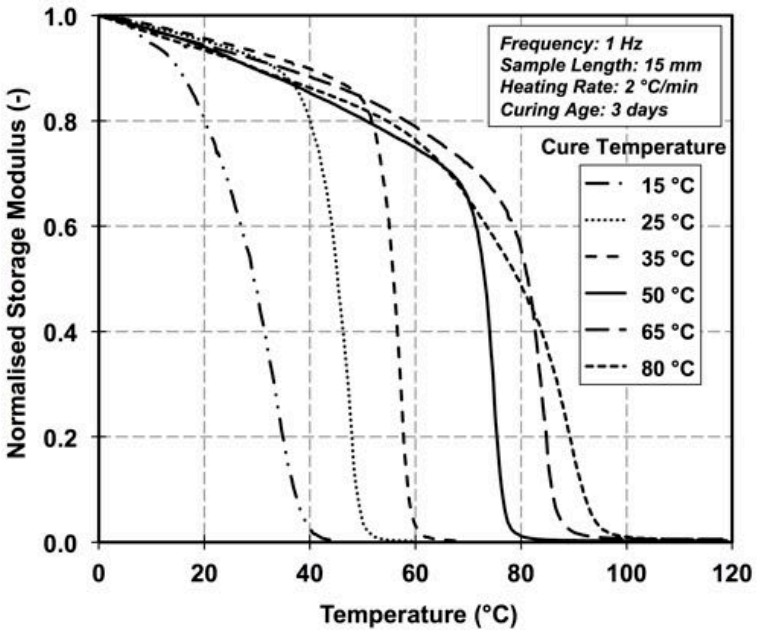

Normalised storage modulus variation with temperature

Figure C-10: Storage and normalised modulus variation with temperature for specimens cured at different temperature for 3 days, Tyfo-S dry condition

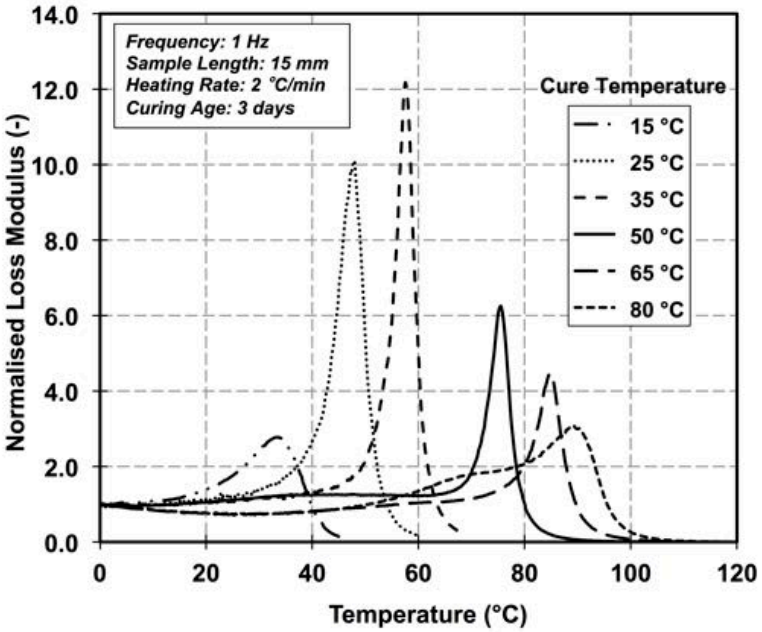

Normalised loss modulus variation with temperature

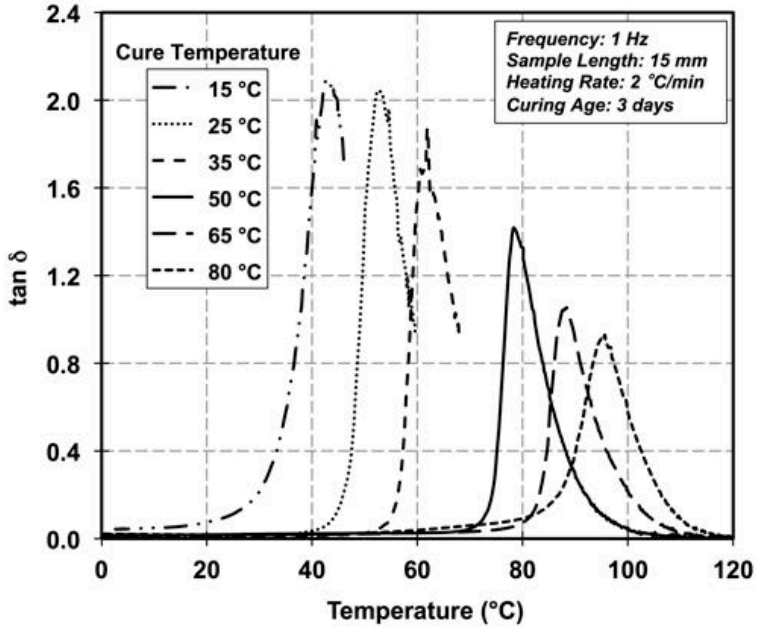

tan δ variation with temperature

Figure C-11: Normalised loss modulus and tan δ variation with temperature for specimens cured at different temperature for 3 days, Tyfo-S dry condition

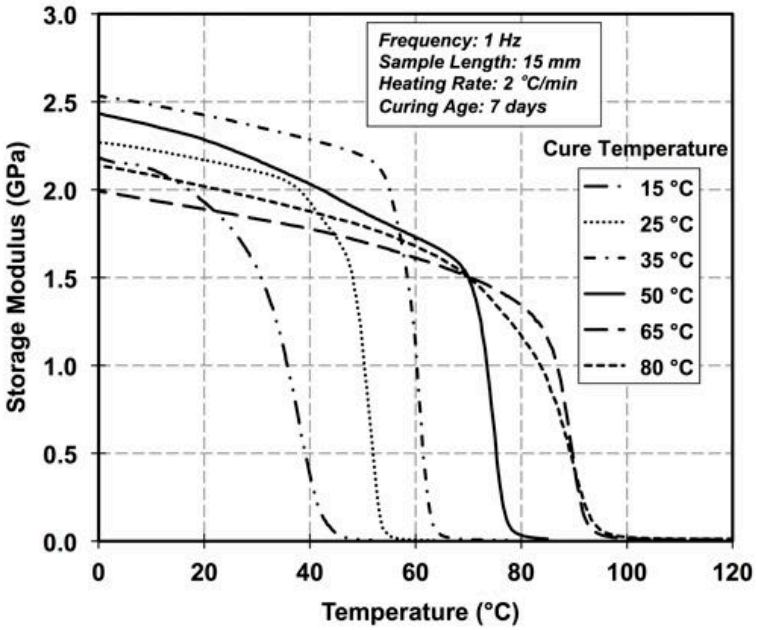

Storage modulus variation with temperature

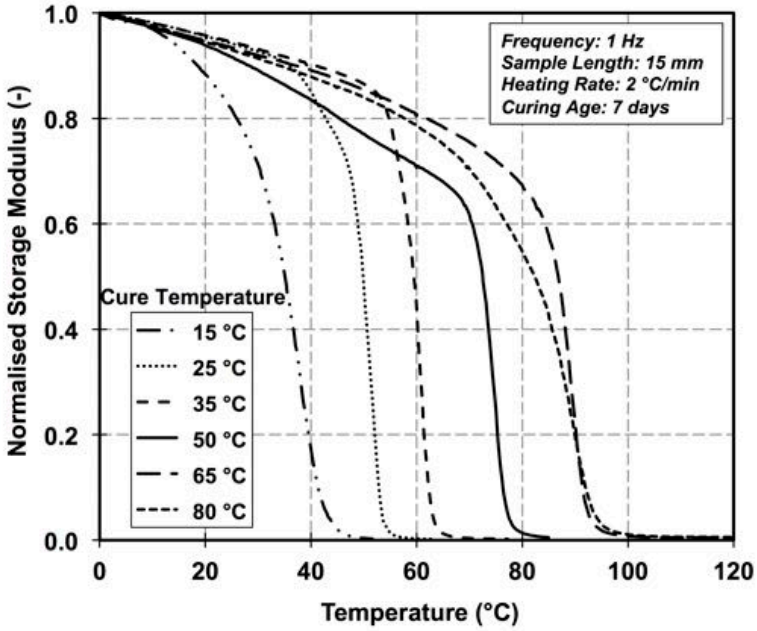

Normalised storage modulus variation with temperature

Figure C-12: Storage and normalised modulus variation with temperature for specimens cured at different temperature for 7 days, Tyfo-S dry condition

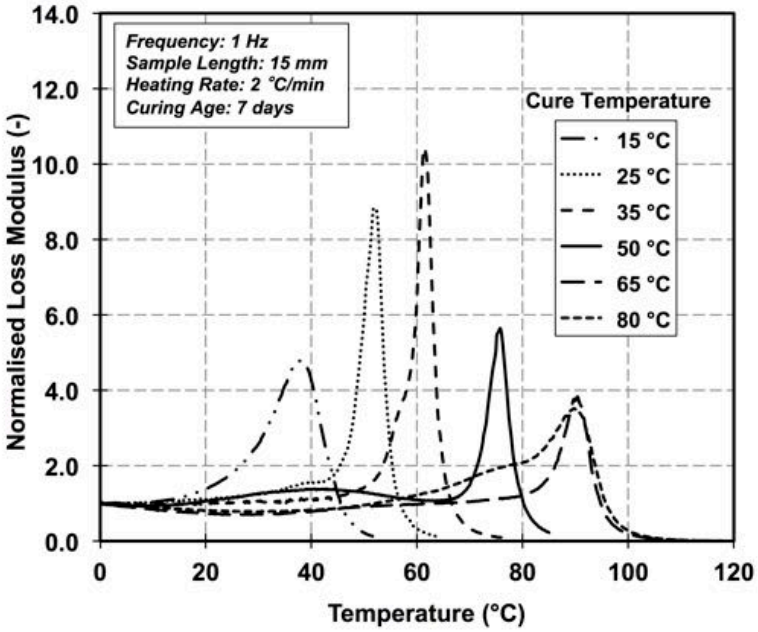

Normalised loss modulus variation with temperature

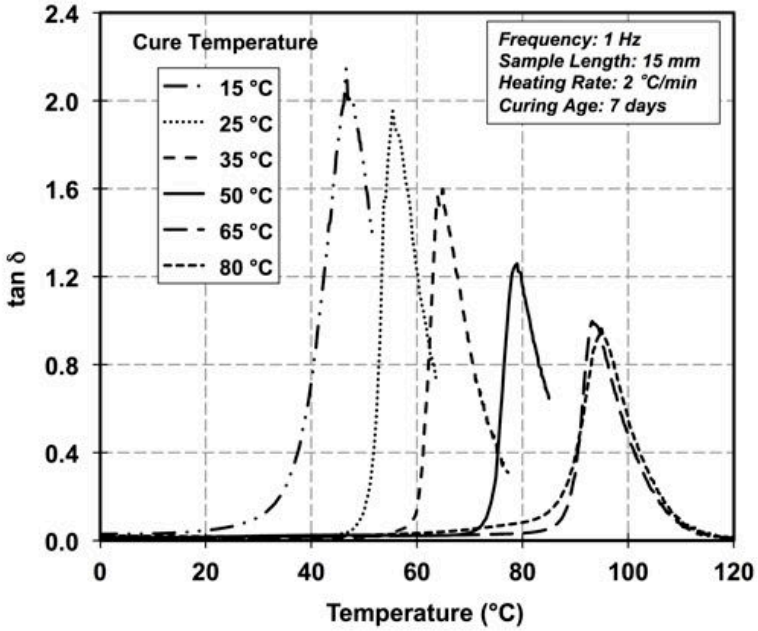

tan δ variation with temperature

Figure C-13: Normalised loss modulus and tan δ variation with temperature for specimens cured at different temperature for 7 days, Tyfo-S dry condition

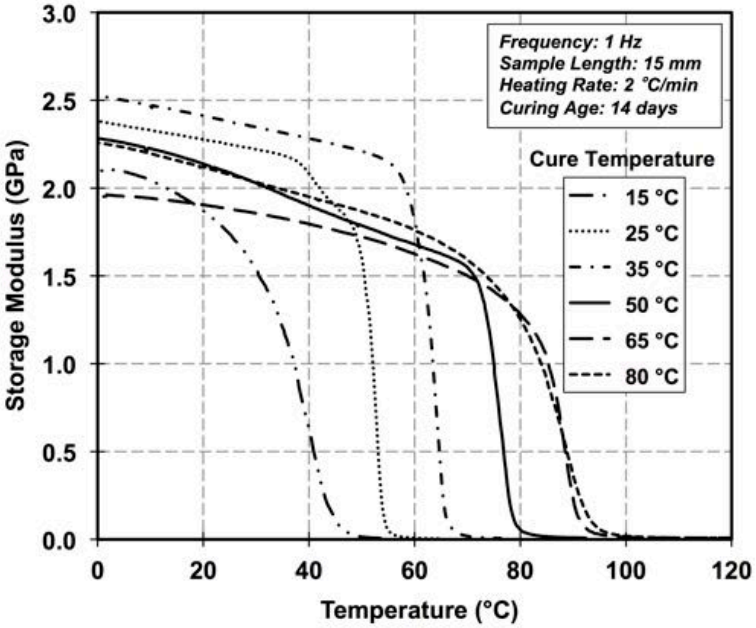

Storage modulus variation with temperature

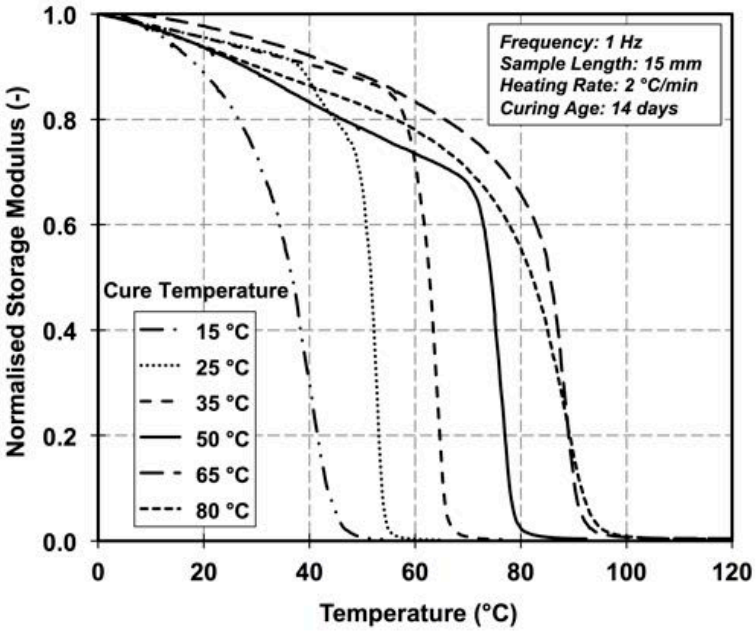

Normalised storage modulus variation with temperature

Figure C-14: Storage and normalised modulus variation with temperature for specimens cured at different temperature for 14 days, Tyfo-S dry condition

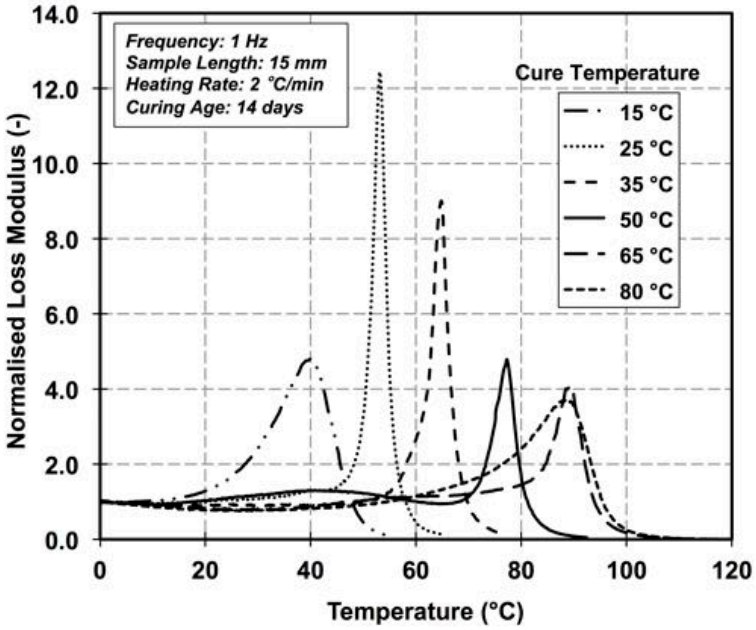

Normalised loss modulus variation with temperature

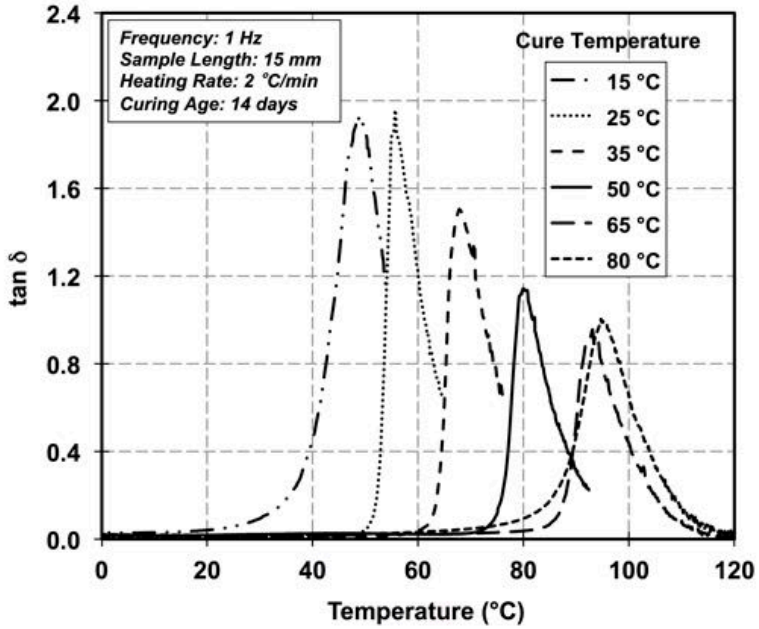

tan δ variation with temperature

Figure C-15: Normalised loss modulus and tan δ variation with temperature for specimens cured at different temperature for 14 days, Tyfo-S dry condition

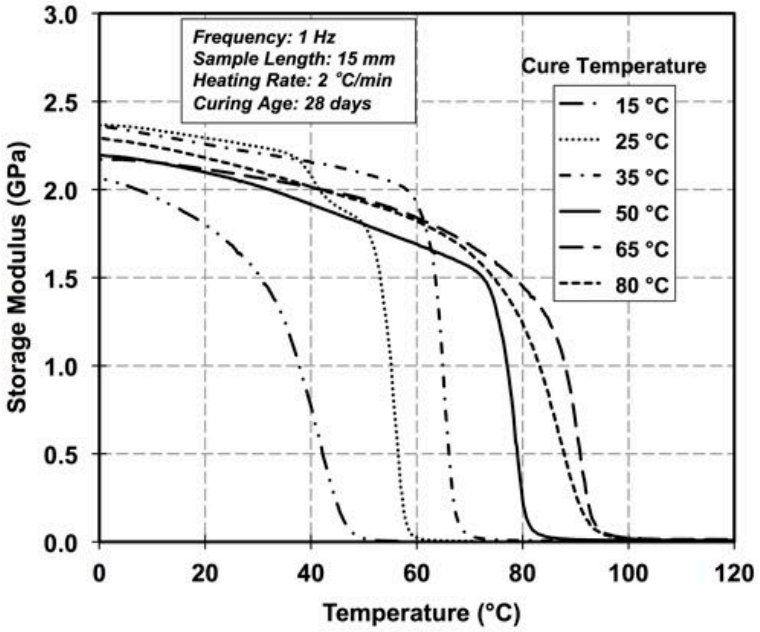

Storage modulus variation with temperature

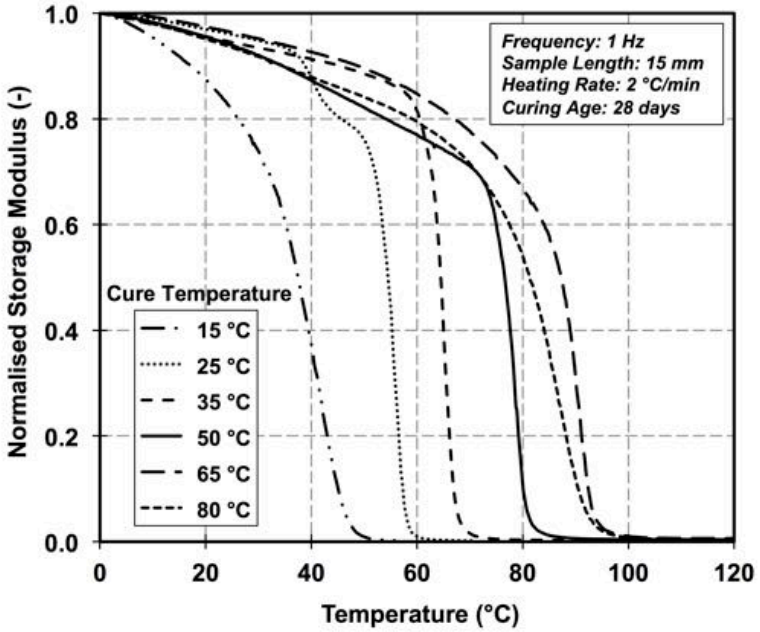

Normalised storage modulus variation with temperature

Figure C-16: Storage and normalised modulus variation with temperature for specimens cured at different temperature for 28 days, Tyfo-S dry condition

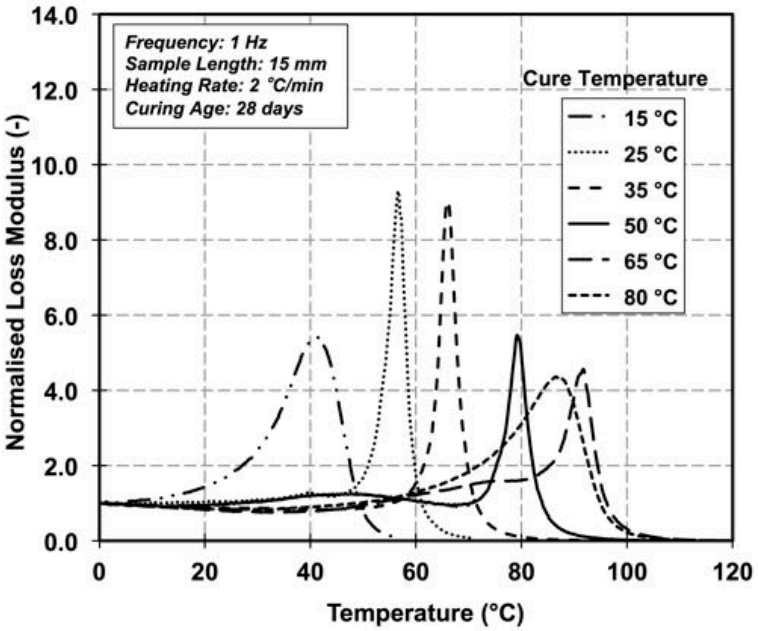

Normalised loss modulus variation with temperature

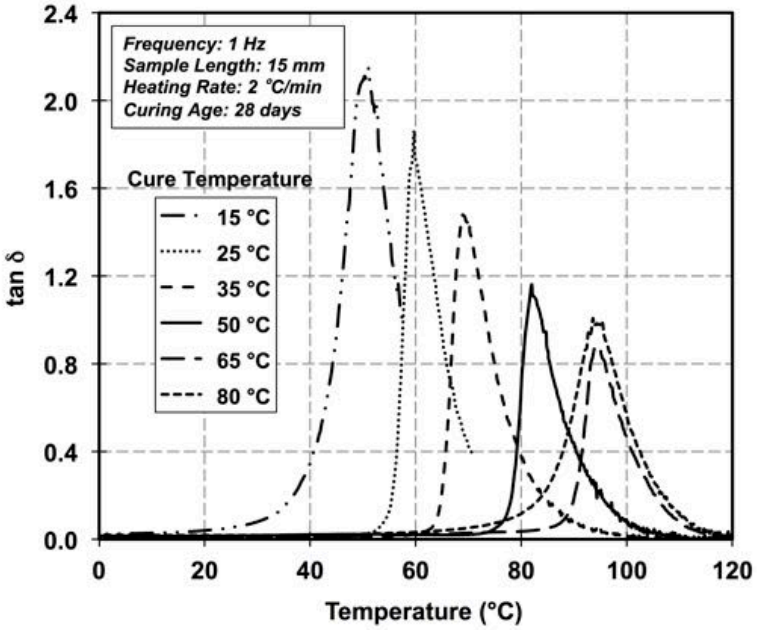

tan δ variation with temperature

Figure C-17: Normalised loss modulus and tan δ variation with temperature for specimens cured at different temperature for 28 days, Tyfo-S dry condition

C.3 Tyfo-S at saturated condition using DMA

C.3.1 Curing Age effect on T_g using DMA

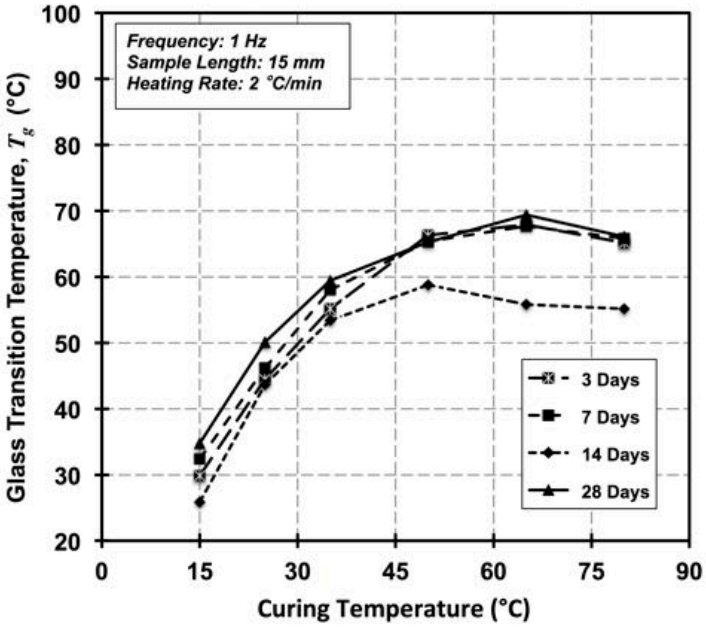

Figure C-18: Recorded T_g according to inflection point method at different age and curing temperature for Tyfo-S, saturated condition

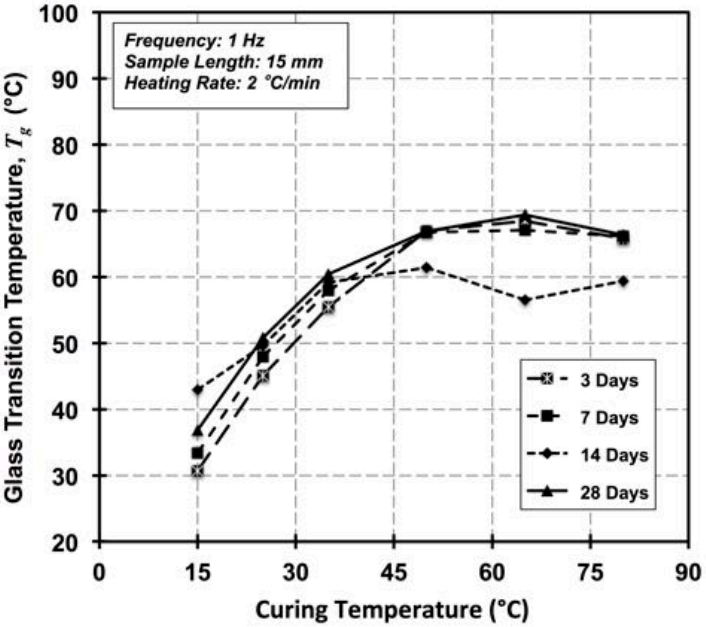

Figure C-19: Recorded T_g according to peak loss modulus method at different age and curing temperature for Tyfo-S, saturated condition

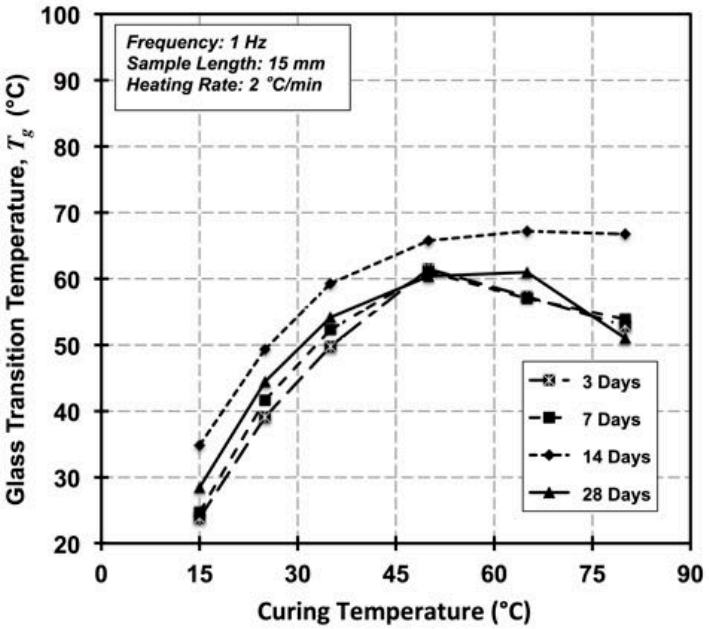

Figure C-20: Recorded T_g according to onset normal scale method at different age and curing temperature for Tyfo-S, saturated condition

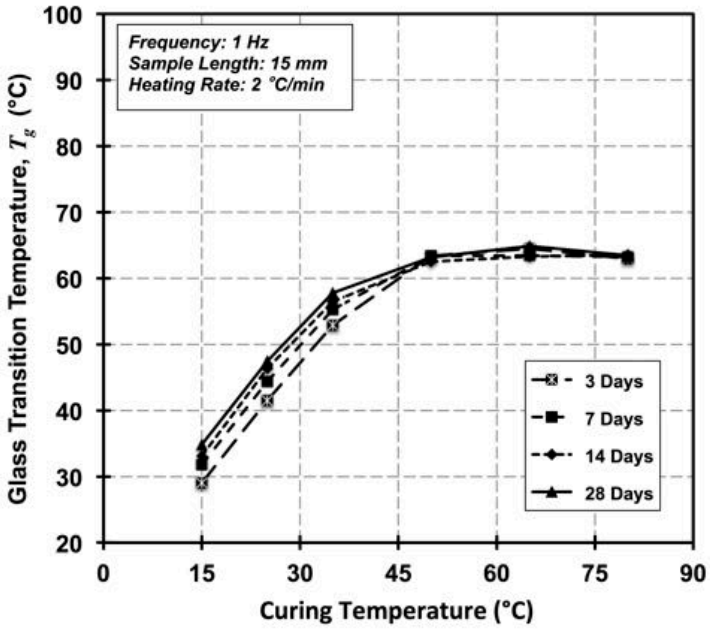

Figure C-21: Recorded T_g according to onset logarithmic scale method at different age and curing temperature for Tyfo-S, saturated condition

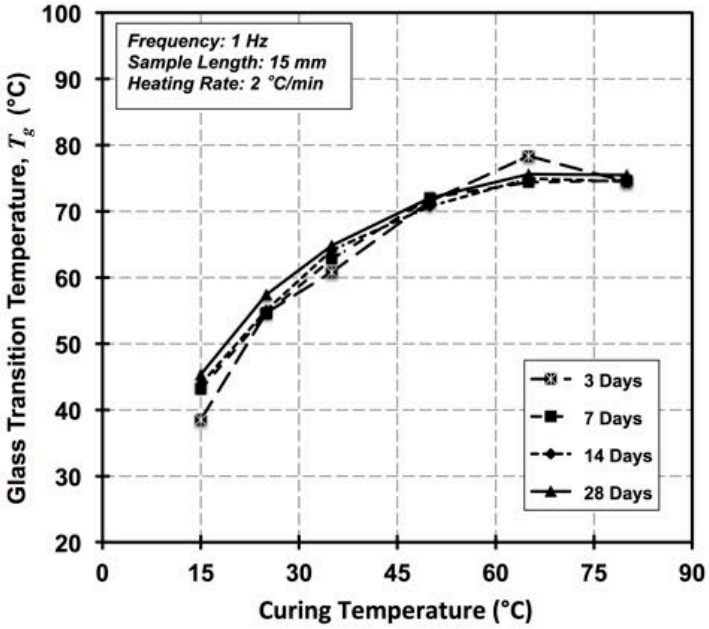

Figure C-22: Recorded T_g according to tan δ method at different age and curing temperature for Tyfo-S, saturated condition

C.3.2 Curing temperature effect on T_g using DMA

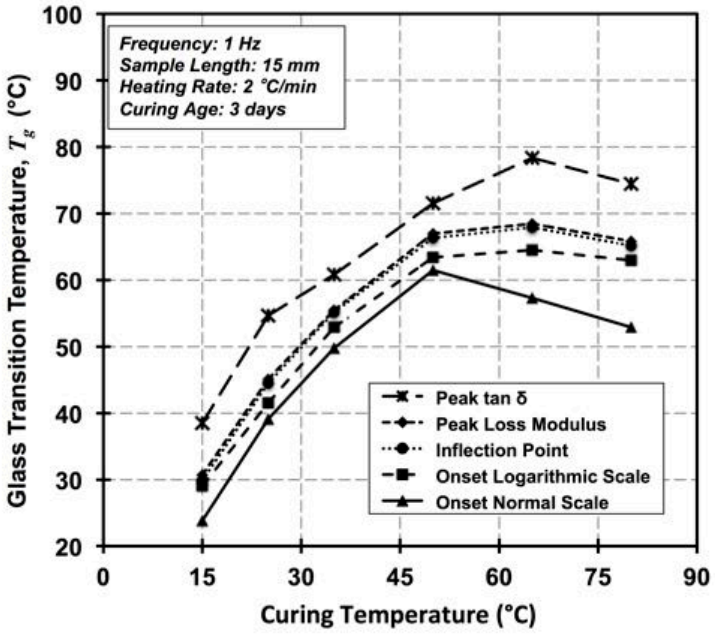

Figure C-23: Recorded T_g according to different methods at 3 days and different curing temperature for Tyfo-S, saturated condition

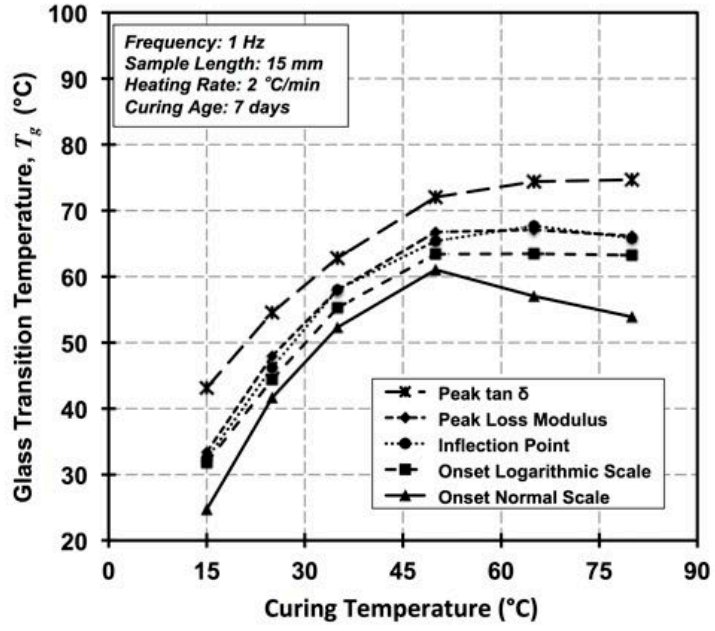

Figure C-24: Recorded T_g according to different methods at 7 days and different curing temperature for Tyfo-S, saturated condition

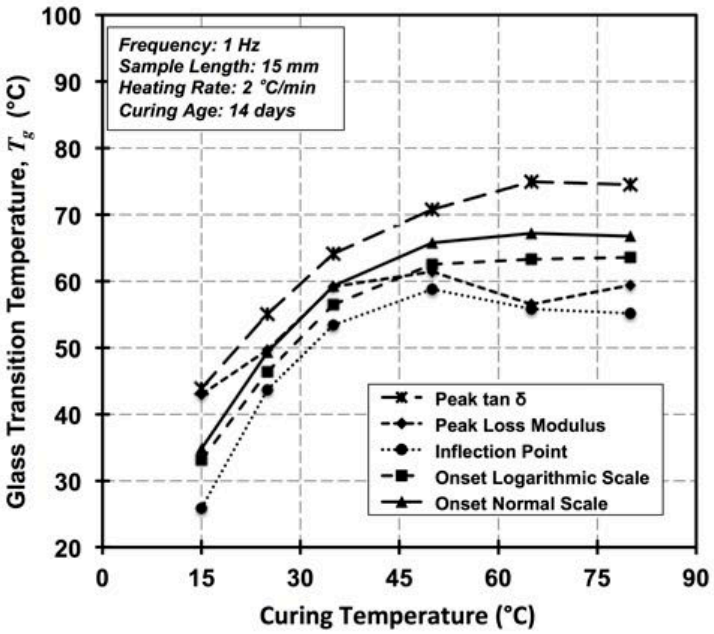

Figure C-25: Recorded T_g according to different methods at 14 days and different curing temperature for Tyfo-S, saturated condition

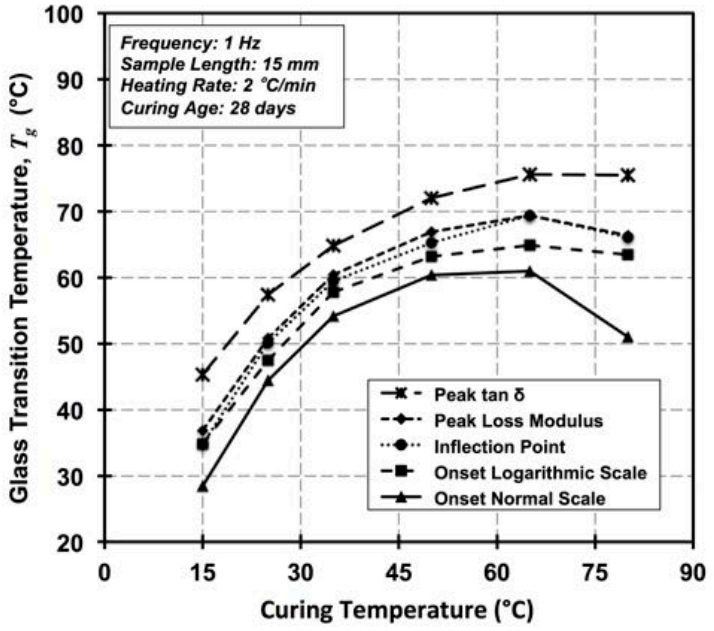

Figure C-26: Recorded T_g according to different methods at 28 days and different curing temperature for Tyfo-S, saturated condition

C.3.3 Saturated condition DMA test responses

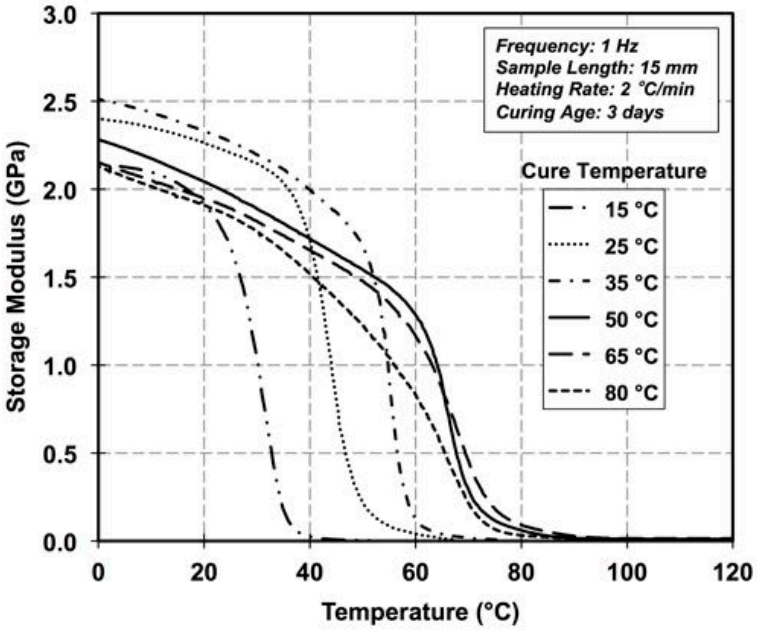

Storage modulus variation with temperature

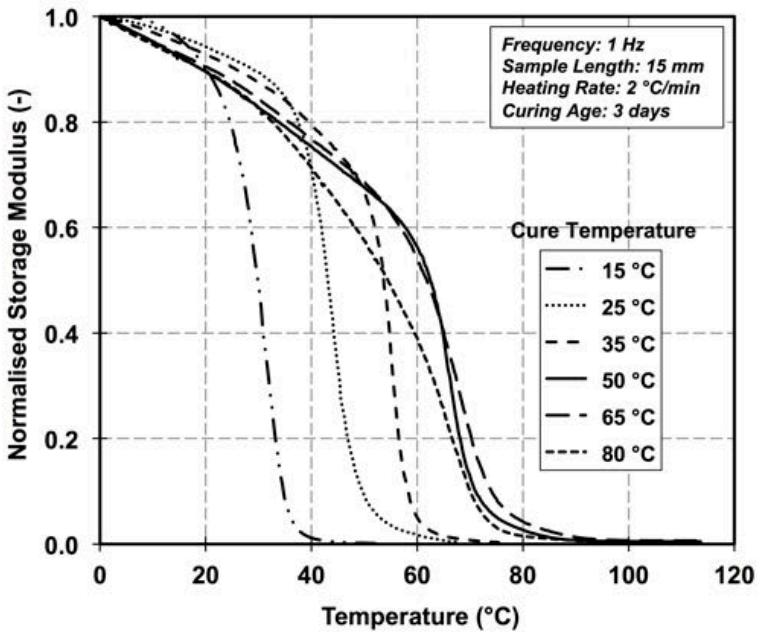

Normalised storage modulus variation with temperature

Figure C-27: Storage and normalised modulus variation with temperature for specimens cured at different temperature for 3 days, Tyfo-S saturated condition

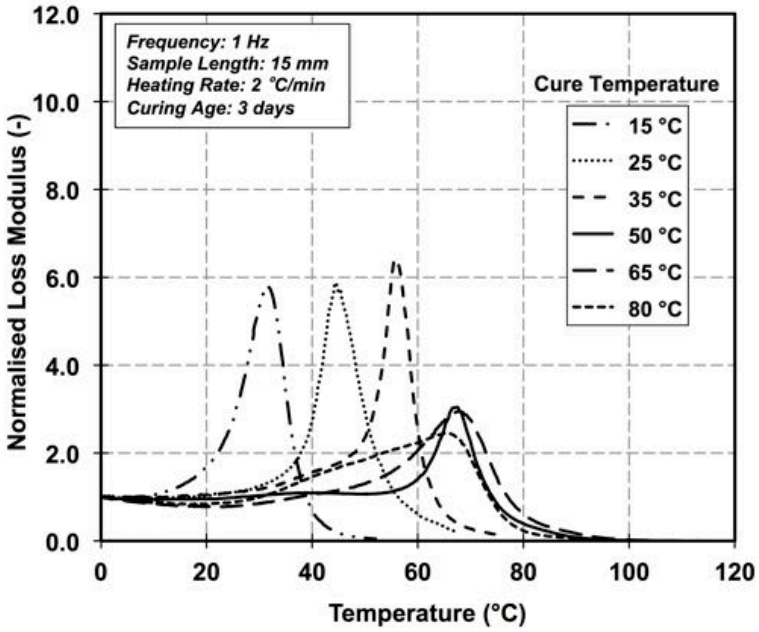

Normalised loss modulus variation with temperature

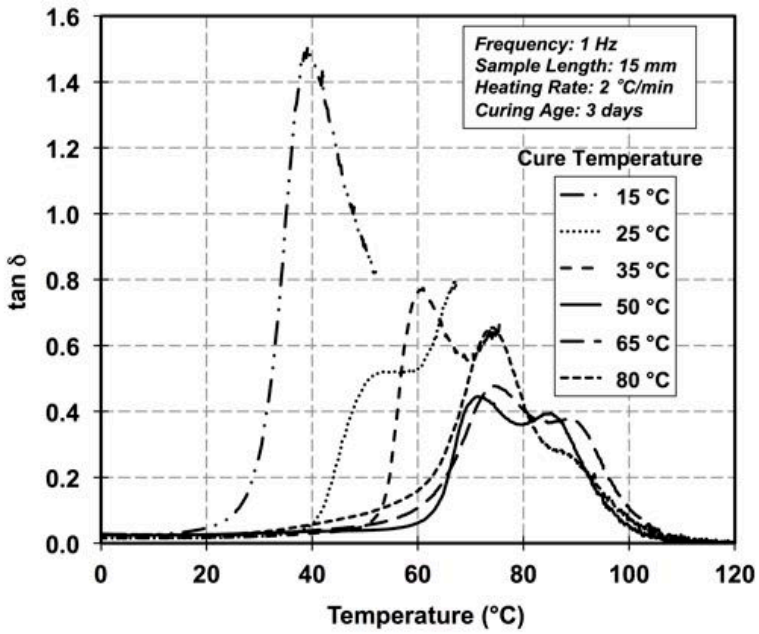

tan δ variation with temperature

Figure C-28: Normalised loss modulus and tan δ variation with temperature for specimens cured at different temperature for 3 days, Tyfo-S saturated condition

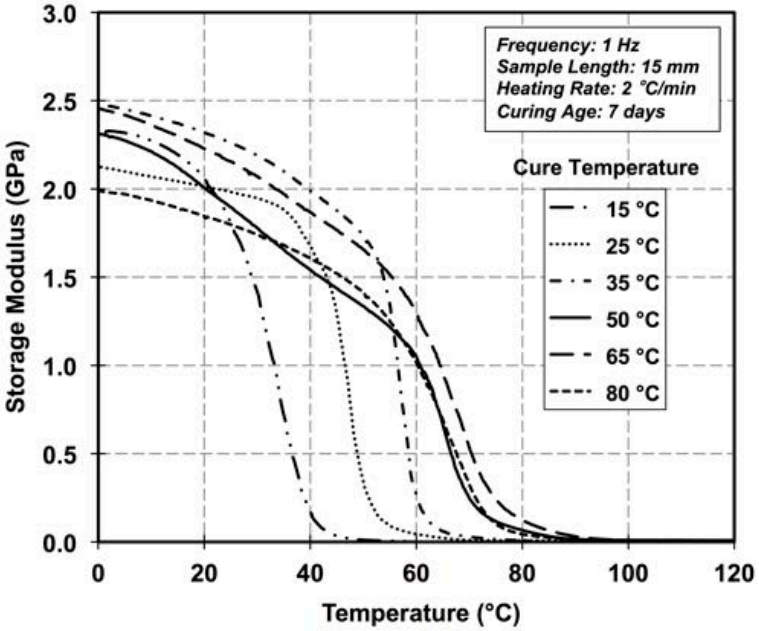

Storage modulus variation with temperature

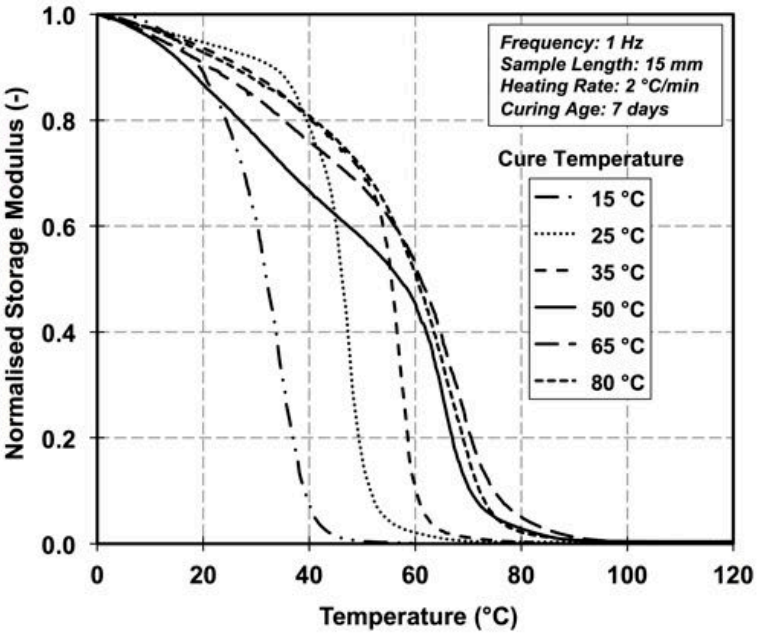

Normalised storage modulus variation with temperature

Figure C-29: Storage and normalised modulus variation with temperature for specimens cured at different temperature for 7 days, Tyfo-S saturated condition

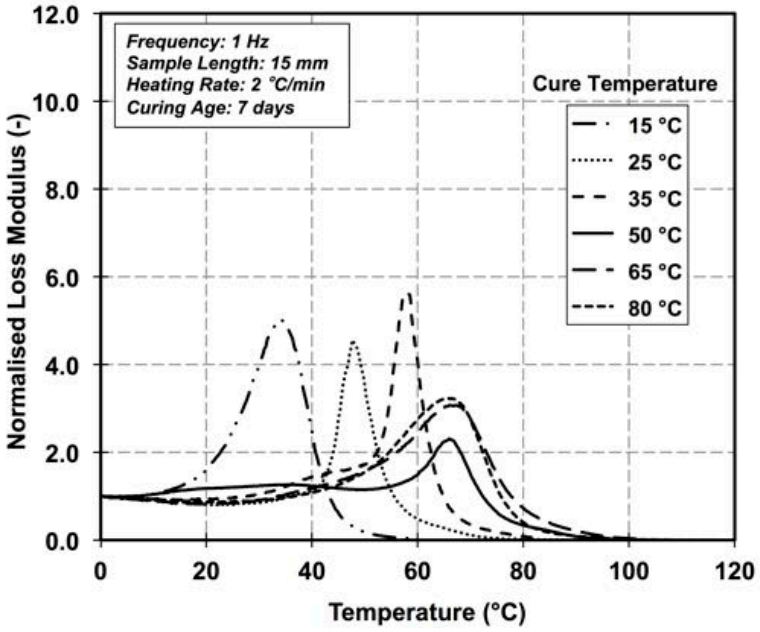

Normalised loss modulus variation with temperature

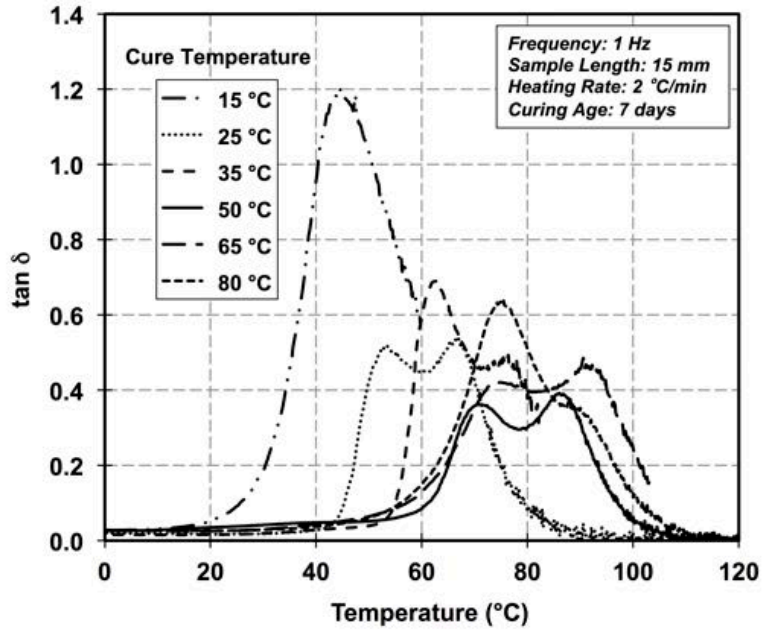

tan δ variation with temperature

Figure C-30: Normalised loss modulus and tan δ variation with temperature for specimens cured at different temperature for 7 days, Tyfo-S saturated condition

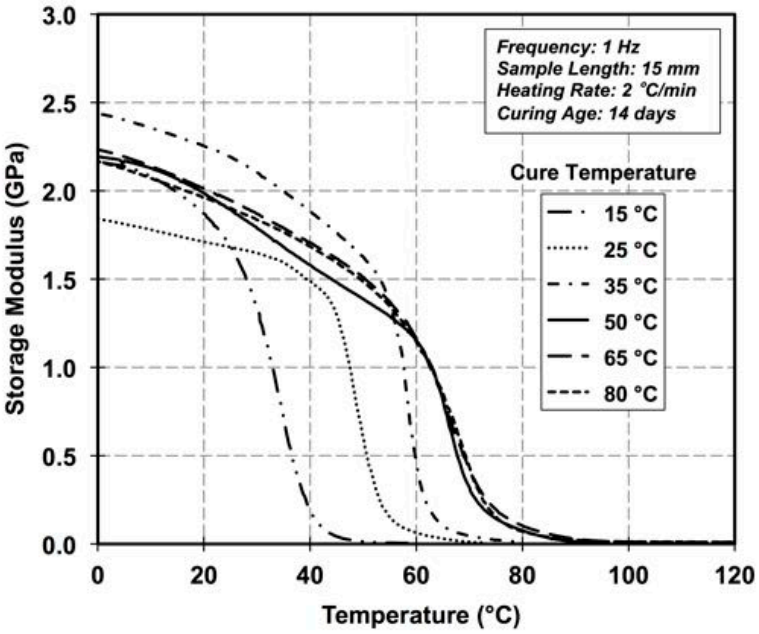

Storage modulus variation with temperature

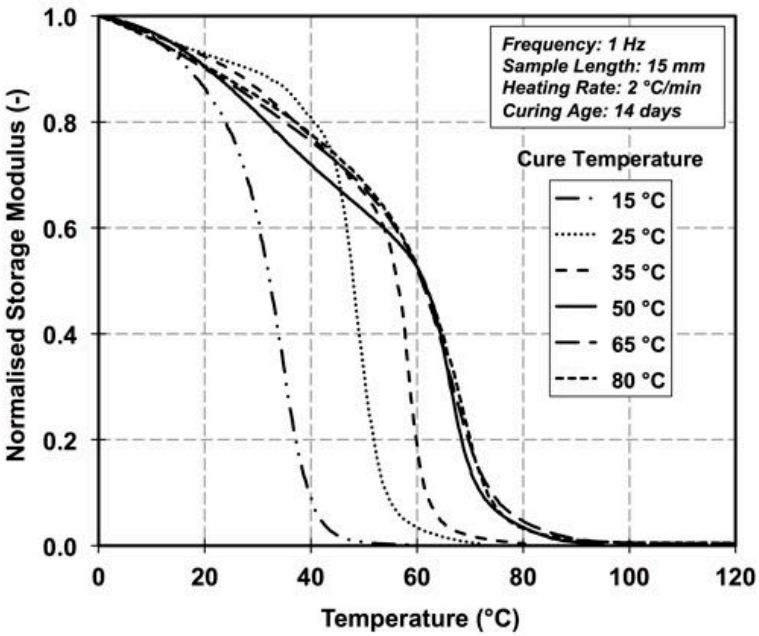

Normalised storage modulus variation with temperature

Figure C-31: Storage and normalised modulus variation with temperature for specimens cured at different temperature for 14 days, Tyfo-S saturated condition

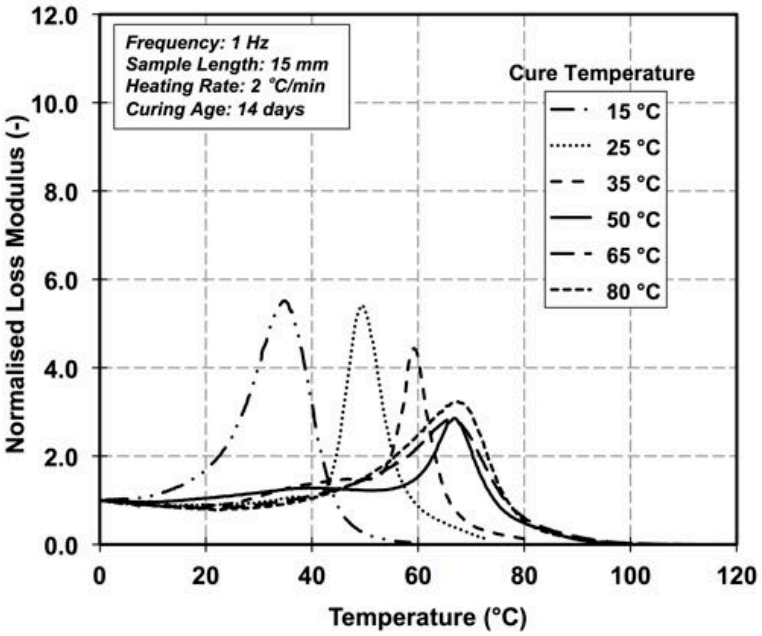

Normalised loss modulus variation with temperature

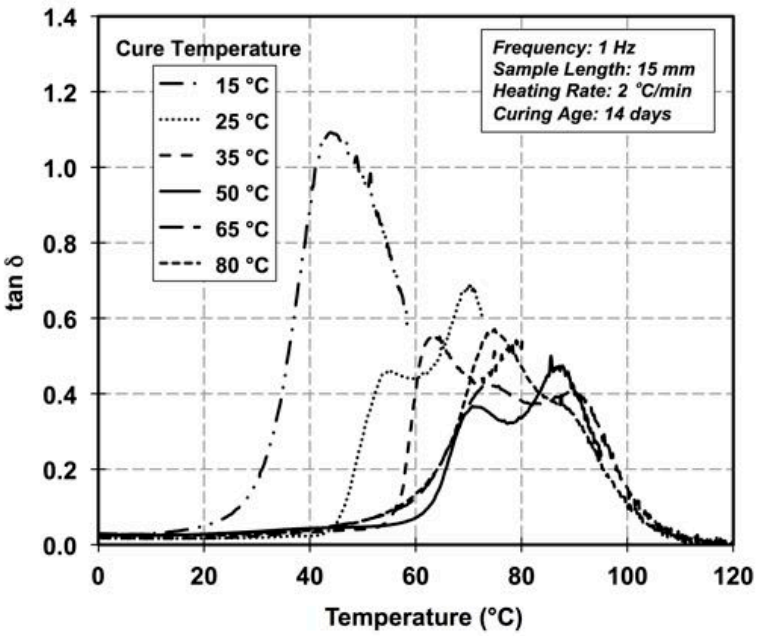

tan δ variation with temperature

Figure C-32: Normalised loss modulus and tan δ variation with temperature for specimens cured at different temperature for 14 days, Tyfo-S saturated condition

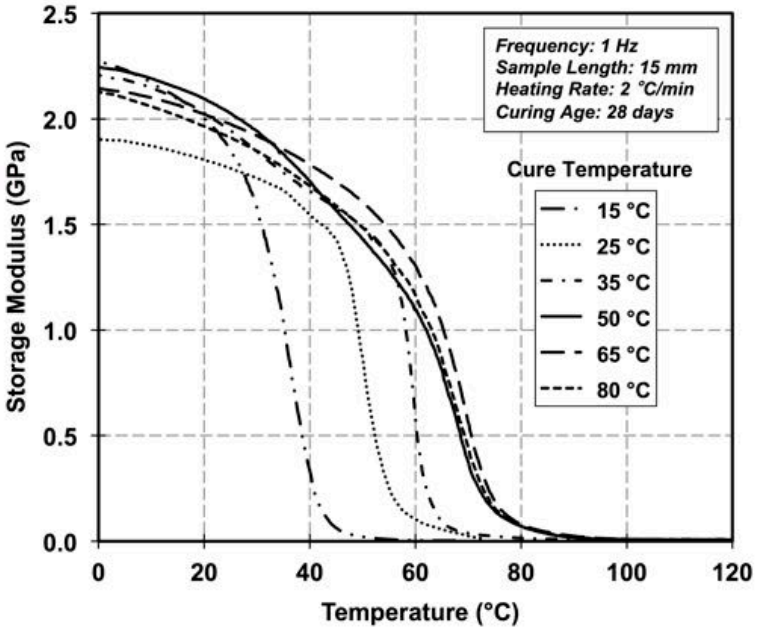

Storage modulus variation with temperature

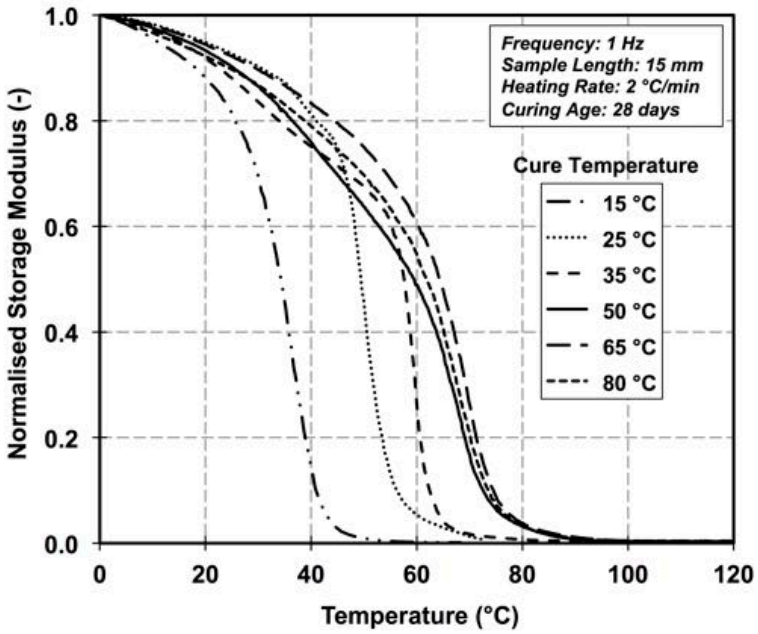

Normalised storage modulus variation with temperature

Figure C-33: Storage and normalised modulus variation with temperature for specimens cured at different temperature for 28 days, Tyfo-S saturated condition

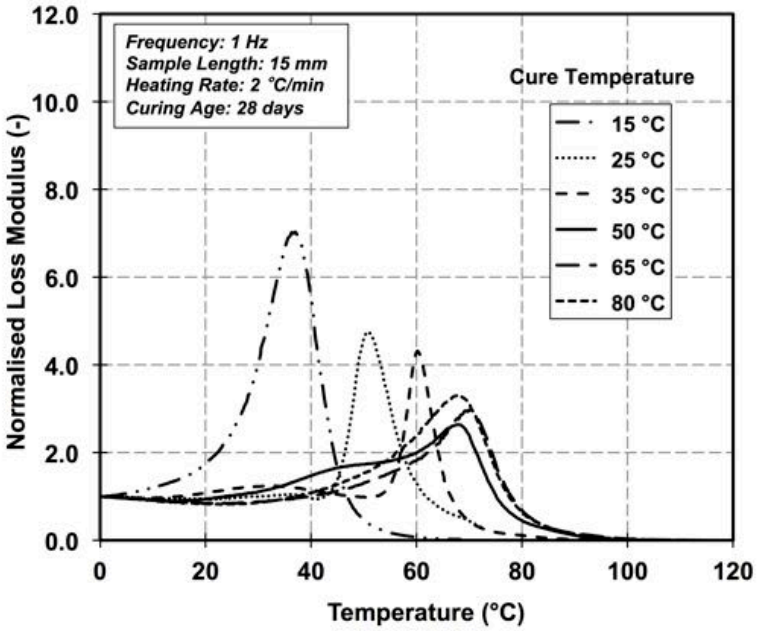

Normalised loss modulus variation with temperature

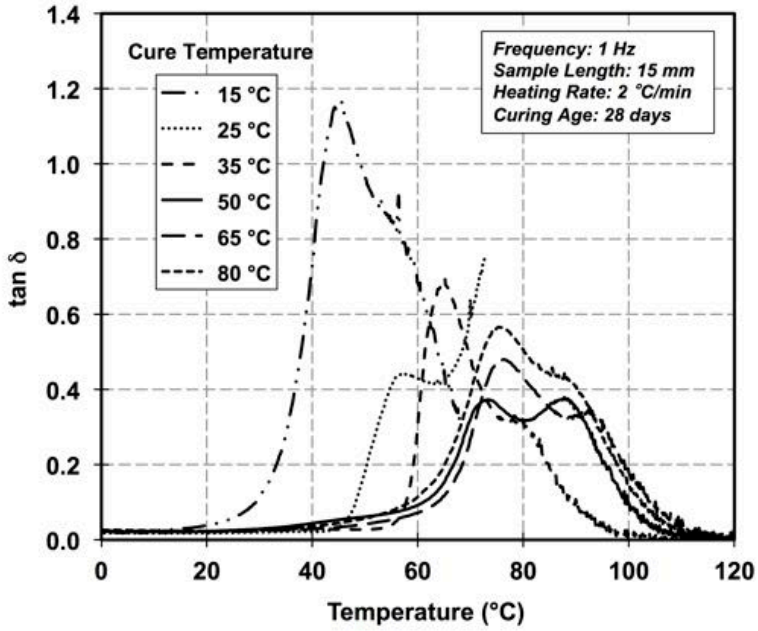

tan δ variation with temperature

Figure C-34: Normalised loss modulus and tan δ variation with temperature for specimens cured at different temperature for 28 days, Tyfo-S saturated condition

C.4 Tyfo-S at dry condition using DSC

C.4.1 Curing age effect on T_g using DSC

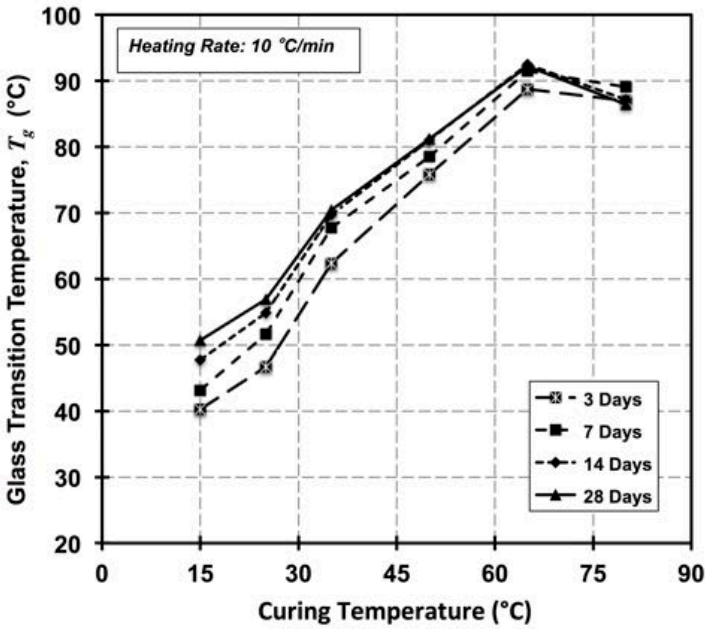

Figure C-35: Recorded T_g according to inflection point method at different age and curing temperature for Tyfo-S, dry condition

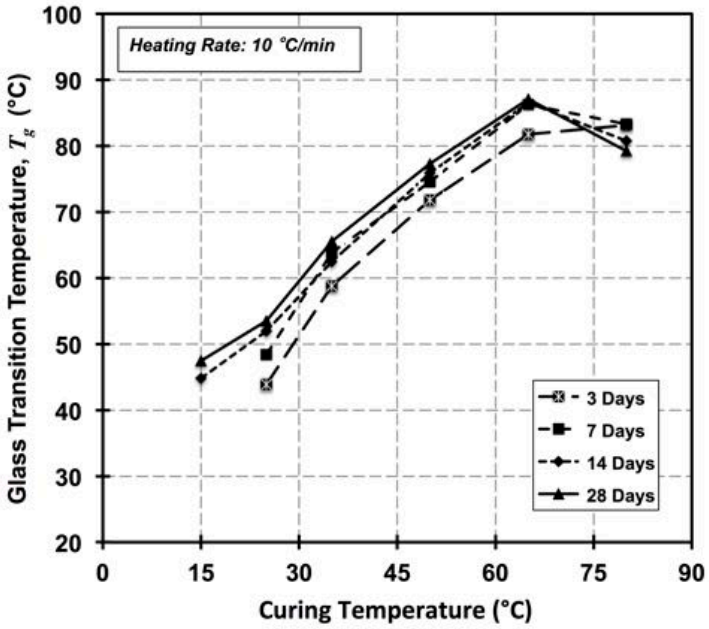

Figure C-36: Recorded T_g according to onset point method at different age and curing temperature for Tyfo-S, dry condition

C.4.2 Curing temperature effect on T_g using DSC

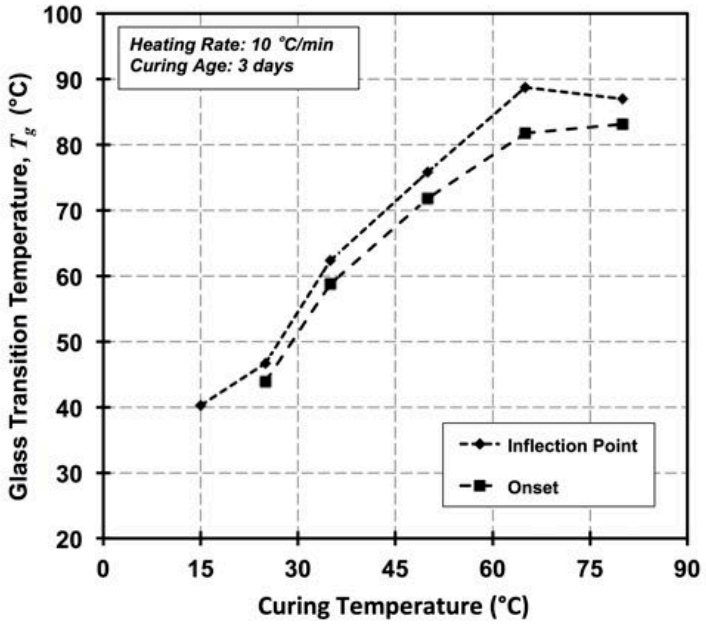

Figure C-37: Recorded T_g according to different methods at 3 days and different curing temperature for Tyfo-S, dry condition

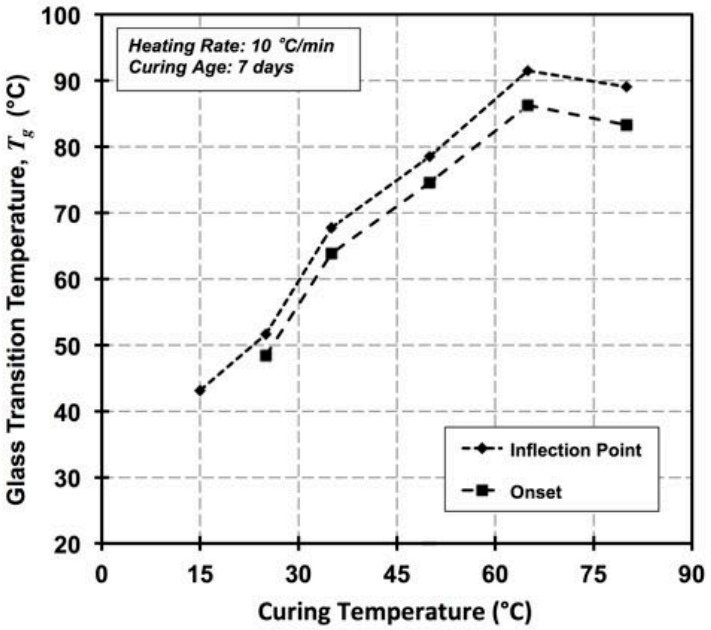

Figure C-38: Recorded T_g according to different methods at 7 days and different curing temperature for Tyfo-S, dry condition

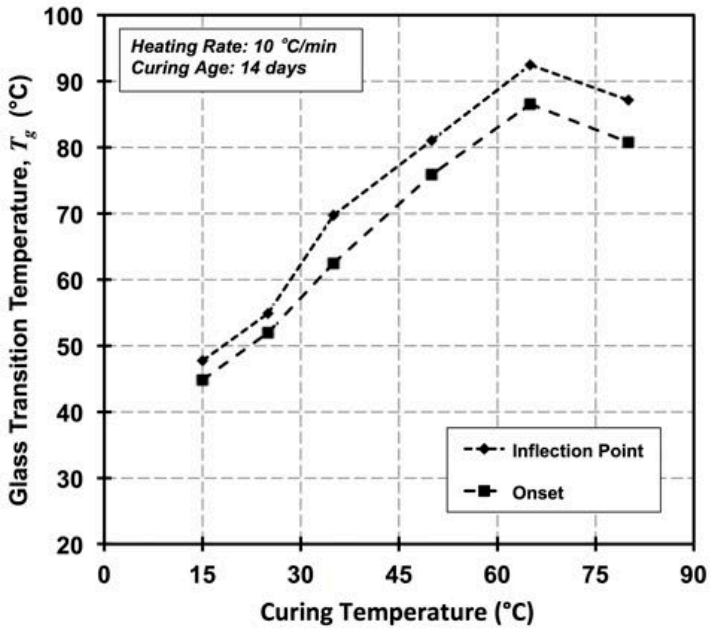

Figure C-39: Recorded T_g according to different methods at 14 days and different curing temperature for Tyfo-S, dry condition

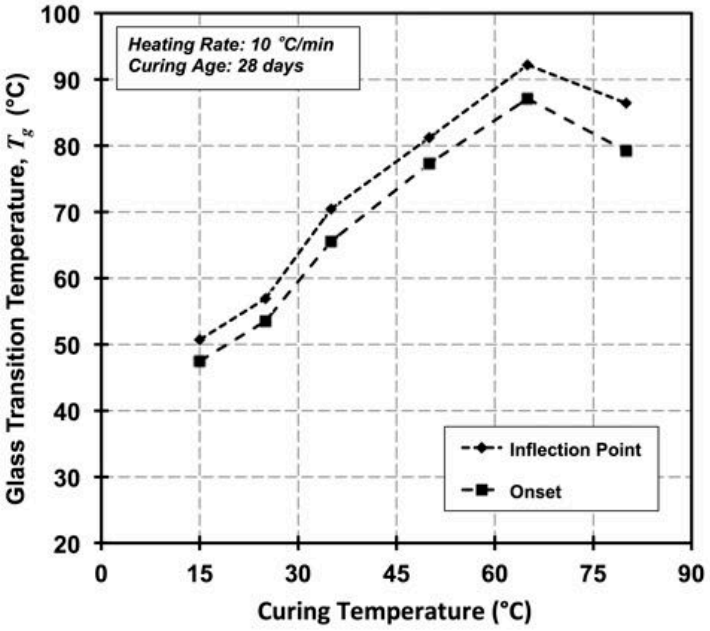

Figure C-40: Recorded T_g according to different methods at 28 days and different curing temperature for Tyfo-S, dry condition

C.4.3 Dry condition DSC test responses

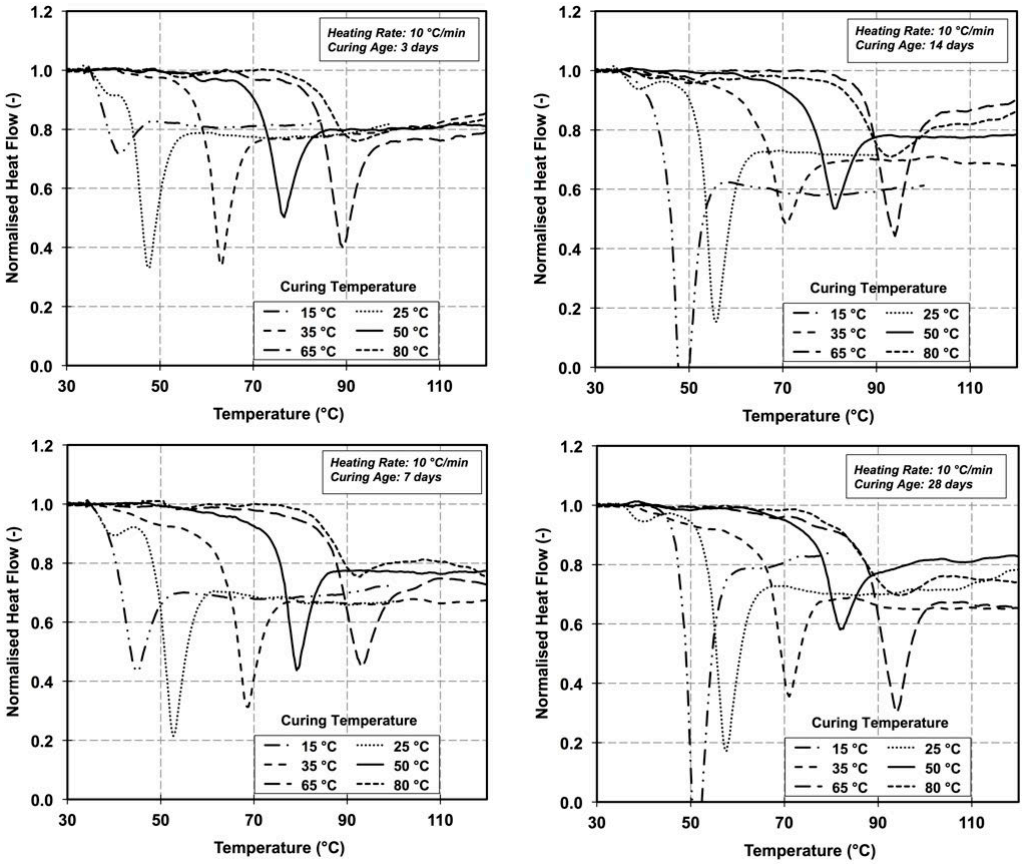

Figure C-41: Normalised heat flow variation with temperature for specimens cured at different temperatures for 3, 7, 14, and 28 days, Tyfo-S dry condition

C.5 Tyfo-S at saturate condition using DSC

C.5.1 Curing age effect on T_g using DSC

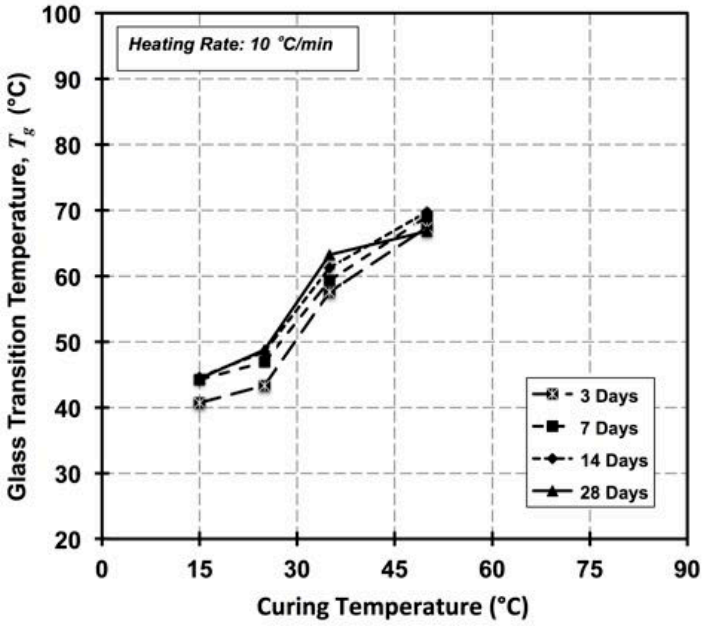

Figure C-42: Recorded T_g according to inflection point method at different age and curing temperature for Tyfo-S, saturated condition

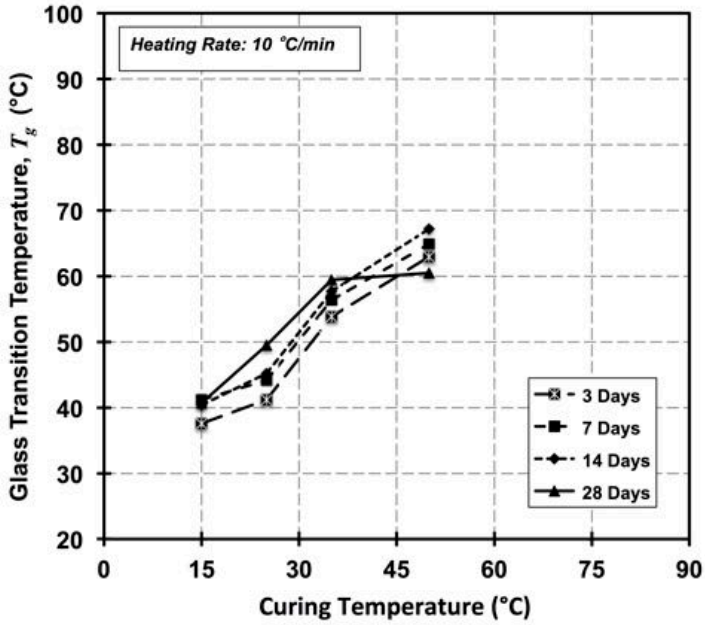

Figure C-43: Recorded T_g according to onset point method at different age and curing temperature for Tyfo-S, saturated condition

C.5.2 Curing temperature effect on T_g using DSC

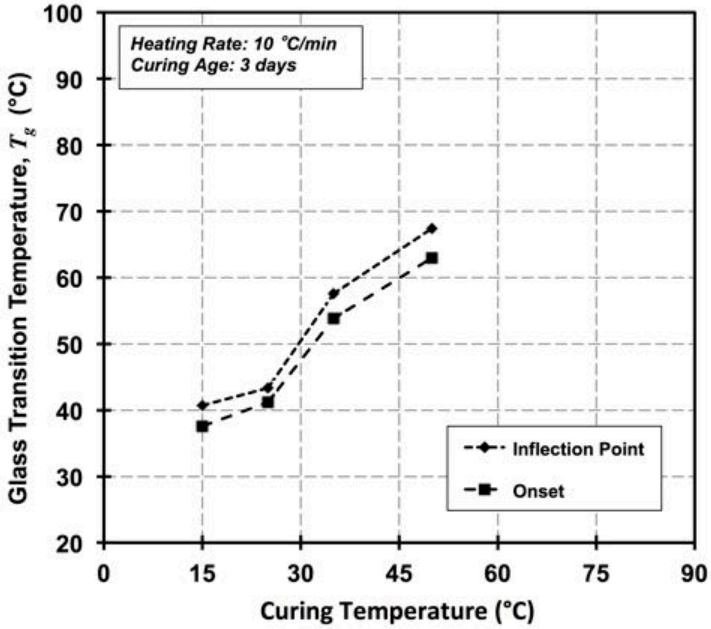

Figure B.C-44: Recorded T_g according to different methods at 3 days and different curing temperature for Tyfo-S, saturated condition

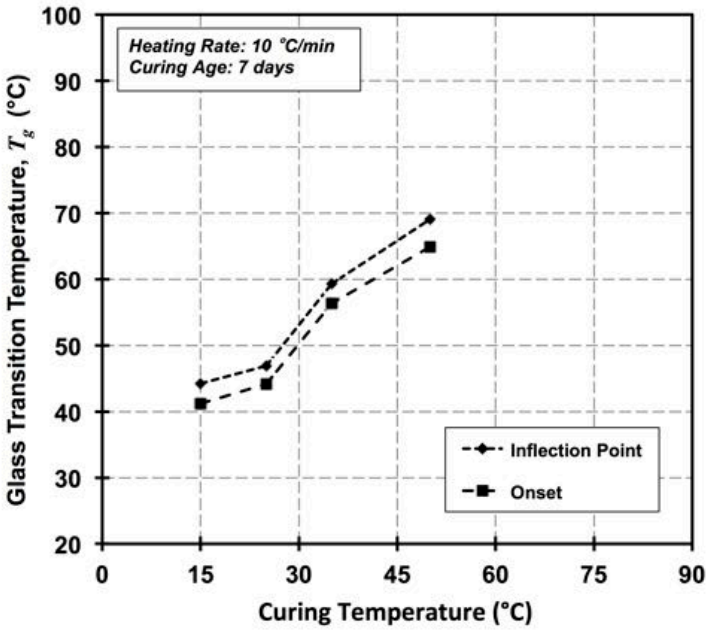

Figure C-45: Recorded T_g according to different methods at 7 days and different curing temperature for Tyfo-S, saturated condition

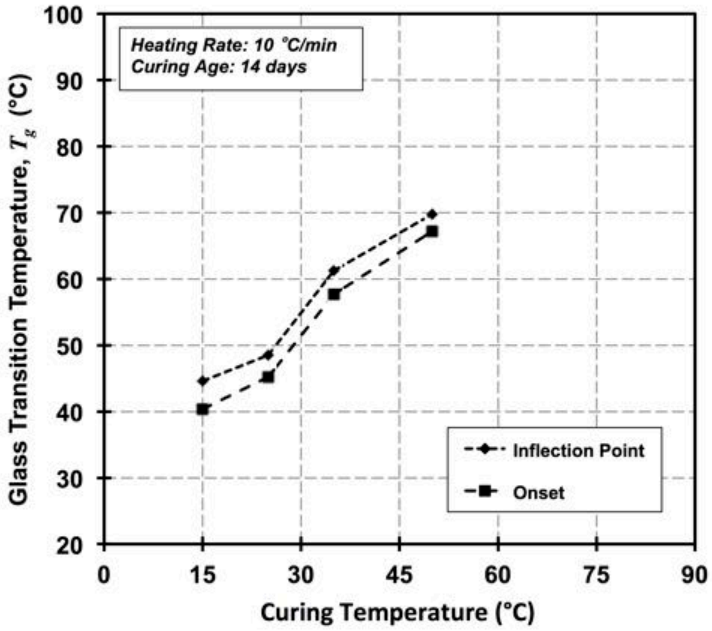

Figure C-46: Recorded T_g according to different methods at 14 days and different curing temperature for Tyfo-S, saturated condition

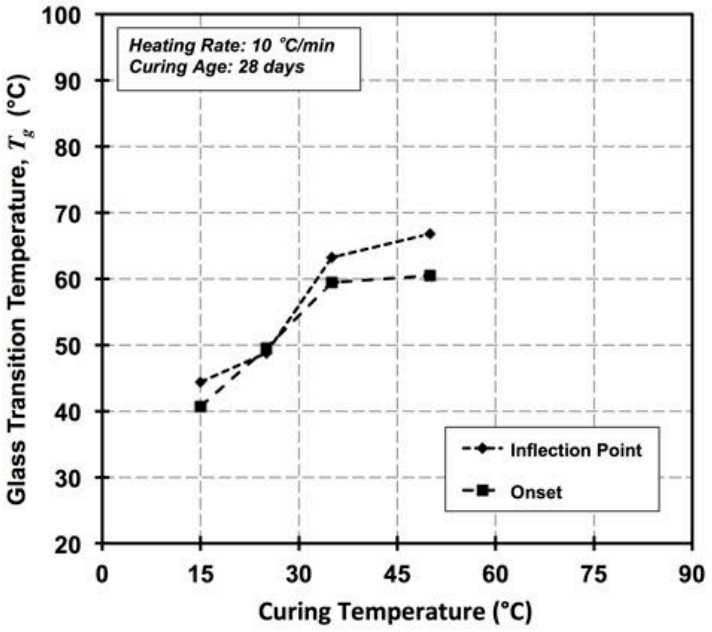

Figure C-47: Recorded T_g according to different methods at 28 days and different curing temperature for Tyfo-S, saturated condition

C.5.3 Saturated condition DSC test responses

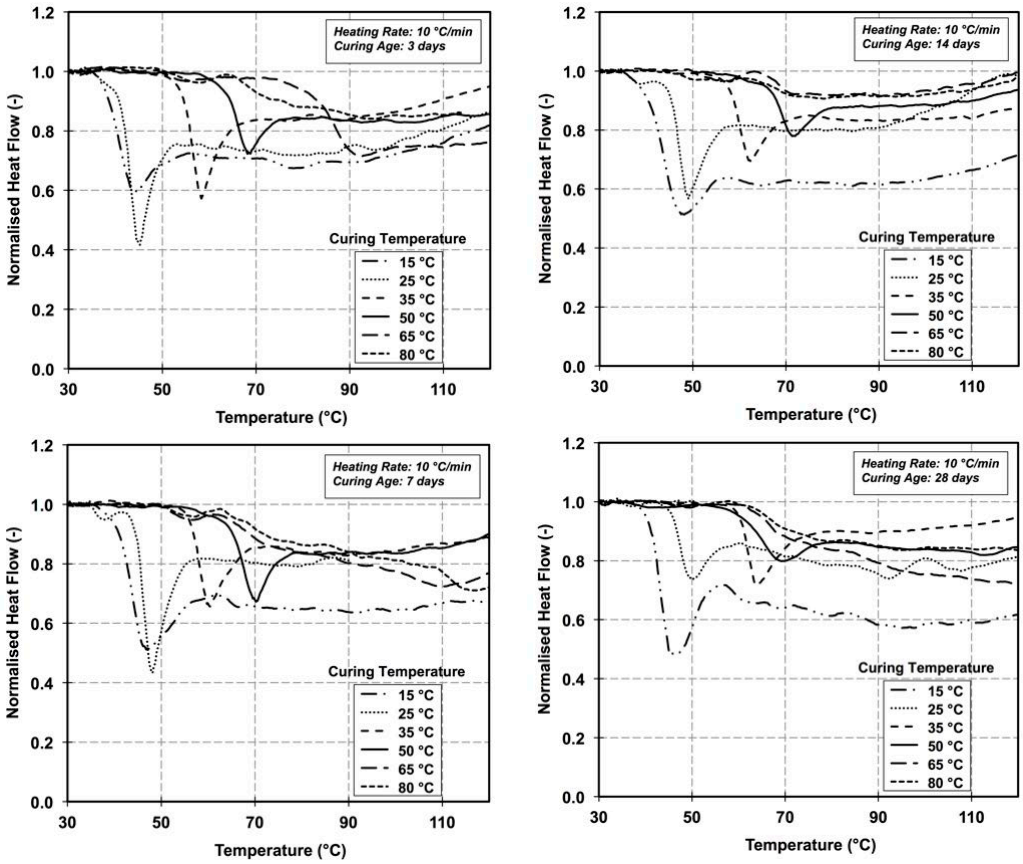

Figure C-48: Normalised heat flow variation with temperature for specimens cured at different temperatures for 3, 7, 14, and 28 days, Tyfo-S saturated condition

C.6 Tyfo-S tabulated results

Table C-1: tan δ, T_g at different ages and curing temperatures

tan δ glass transition temperature, T_g °C at age						
Temperature	***RH %***	***Samples No.***	***3 days***	***7 days***	***14 days***	***28 days***
15°C	**0%**	**T-15-0**	40.9	47.6	48.8	50.4
			43.0	47.1	48.7	50.0
			42.4	47.5	47.9	50.7
		Avg ± SD	*42.1 ± 0.9*	*47.4 ± 0.2*	*48.5 ± 0.4*	*50.4 ± 0.3*
	100%	**T-15-100**	37.2	41.9	43.2	45.1
			38.9	42.7	44.3	45.2
			39.4	44.8	44.1	45.7
		Avg ± SD	*38.5 ± 0.9*	*43.1 ± 1.2*	*43.9 ± 0.5*	*45.3 ± 0.3*
24°C	**0%**	**T-24-0**	53.3	56.1	56.1	59.5
			52.9	56.2	57.8	60.2
			51.9	56.9	57.6	59.9
		Avg ± SD	*52.7 ± 0.6*	*56.4 ± 0.4*	*57.2 ± 0.8*	*59.9 ± 0.3*
	100%	**T-24-100**	54.3	53.5	55.3	57.0
			55.5	54.9	54.6	57.7
			54.1	55.2	55.2	57.5
		Avg ± SD	*54.6 ± 0.6*	*54.5 ± 0.7*	*55.0 ± 0.3*	*57.4 ± 0.3*
35°C	**0%**	**T-35-0**	62.8	65.2	68.5	69.8
			61.5	66.3	68.1	71.1
			63.3	64.9	69.2	70.7
		Avg ± SD	*62.5 ± 0.8*	*65.5 ± 0.6*	*68.6 ± 0.5*	*70.5 ± 0.5*
	100%	**T-35-100**	61.1	62.5	63.6	64.6
			60.6	62.8	64.1	--
			60.7	63.0	64.6	65.0
		Avg ± SD	*60.8 ± 0.2*	*62.8 ± 0.2*	*64.1 ± 0.4*	*64.8 ± 0.2*
50°C	**0%**	**T-50-0**	79.4	79.3	80.4	83.7
			77.8	80.3	82.3	82.5
			76.8	80.2	83.0	82.4
		Avg ± SD	*78.0 ± 0.2*	*79.9 ± 0.2*	*81.9 ± 0.4*	*82.9 ± 0.2*
	100%	**T-50-100**	71.8	70.9	71.5	71.9
			72.4	72.6	69.8	71.0
			70.4	72.5	70.9	73.1
		Avg ± SD	*71.5 ± 1.1*	*72.0 ± 0.4*	*70.7 ± 1.1*	*72.0 ± 0.6*
65°C	**0%**	**T-65-0**	88.3	94.0	92.7	93.4
			88.6	93.5	92.8	94.9
			88.6	92.8	93.0	94.6
		Avg ± SD	*88.5 ± 0.1*	*93.4 ± 0.5*	*92.8 ± 0.1*	*94.3 ± 0.6*
	100%	**T-65-100**	74.9	74.8	74.0	75.0
			77.2	74.2	75.2	76.2
			83.0	74.2	75.6	75.6
		Avg ± SD	*78.4 ± 3.4*	*74.4 ± 0.3*	*74.9 ± 0.7*	*75.6 ± 0.5*
80°C	**0%**	**T-80-0**	95.6	95.0	95.0	93.8
			95.6	94.9	96.0	94.1
			94.8	95.0	95.2	94.0
		Avg ± SD	*95.3 ± 0.4*	*95.0 ± 0.0*	*95.4 ± 0.4*	*94.0 ± 0.1*
	100%	**T-80-100**	74.1	73.8	74.8	75.0
			74.6	75.0	73.3	75.7
			74.6	75.1	75.4	75.7
		Avg ± SD	*74.4 ± 0.2*	*74.6 ± 0.6*	*74.5 ± 0.9*	*75.5 ± 0.3*

Table C-2: Peak loss modulus, T_g at different ages and curing temperatures

Peak loss modulus glass transition temperature, T_g °C at age						
Temperature	***RH %***	***Samples No.***	***3 days***	***7 days***	***14 days***	***28 days***
15°C	**0%**	**T-15-0**	30.3	37.8	39.8	41.9
			33.4	37.5	39.8	41.0
			32.7	38.7	38.7	41.1
		Avg ± SD	*32.1 ± 1.3*	*38.0 ± 0.5*	*39.4 ± 0.5*	*41.3 ± 0.4*
	100%	**T-15-100**	29.8	33.3	34.6	36.6
			31.1	32.9	34.7	37.0
			31.1	33.9	35.1	36.9
		Avg ± SD	*30.7 ± 0.6*	*33.4 ± 0.4*	*34.8 ± 0.2*	*36.8 ± 0.2*
24°C	**0%**	**T-24-0**	47.6	52.8	53.0	56.3
			47.5	51.7	54.0	56.3
			46.6	52.6	54.1	56.5
		Avg ± SD	*47.2 ± 0.4*	*52.4 ± 0.5*	*53.7 ± 0.5*	*56.4 ± 0.1*
	100%	**T-24-100**	45.2	47.9	49.6	50.4
			44.6	47.9	48.6	51.4
			45.5	48.0	49.7	50.6
		Avg ± SD	*45.1 ± 0.4*	*47.9 ± 0.0*	*49.3 ± 0.5*	*50.8 ± 0.4*
35°C	**0%**	**T-35-0**	57.9	61.6	64.4	66.0
			57.4	62.7	64.5	67.1
			58.1	61.3	65.3	67.2
		Avg ± SD	*57.8 ± 0.3*	*61.9 ± 0.6*	*64.7 ± 0.4*	*66.8 ± 0.5*
	100%	**T-35-100**	55.1	57.6	59.3	61.2
			55.7	58.1	59.4	59.6
			55.6	58.1	59.1	60.4
		Avg ± SD	*55.5 ± 0.3*	*57.9 ± 0.2*	*59.3± 0.1*	*60.4 ± 0.7*
50°C	**0%**	**T-50-0**	75.0	75.4	77.0	80.0
			73.9	76.0	78.9	79.2
			72.8	77.8	79.7	79.0
		Avg ± SD	*73.9 ± 0.9*	*76.4 ± 1.0*	*78.5 ± 1.1*	*79.4 ± 0.4*
	100%	**T-50-100**	67.0	65.8	66.6	66.7
			68.0	66.8	64.8	66.3
			65.9	67.7	65.8	67.7
		Avg ± SD	*67.0 ± 0.9*	*66.8 ± 0.8*	*65.7 ± 0.7*	*66.9 ± 0.6*
65°C	**0%**	**T-65-0**	84.7	90.0	89.2	90.1
			84.5	89.7	89.0	91.2
			84.5	89.2	88.9	91.1
		Avg ± SD	*84.6 ± 0.1*	*89.6 ± 0.3*	*89.0 ± 0.1*	*90.8 ± 0.5*
	100%	**T-65-100**	67.3	66.7	65.9	69.5
			68.9	67.7	67.6	69.8
			69.1	66.8	68.0	68.8
		Avg ± SD	*68.4 ± 0.8*	*67.1 ± 0.4*	*67.2 ± 0.9*	*69.4 ± 0.4*
80°C	**0%**	**T-80-0**	88.8	89.3	88.3	86.0
			89.6	89.5	89.8	86.9
			88.2	89.2	88.5	86.3
		Avg ± SD	*88.9 ± 0.6*	*89.3 ± 0.7*	*88.9 ± 0.7*	*86.4 ± 0.4*
	100%	**T-80-100**	65.3	65.8	67.2	65.3
			65.4	65.9	67.1	65.9
			66.7	66.8	66.0	67.8
		Avg ± SD	*65.8 ± 0.6*	*66.2 ± 0.4*	*66.8 ± 0.5*	*66.3 ± 1.1*

Table C-3: Inflection point of storage modulus, T_g at different ages and curing temperatures

Inflection point glass transition temperature, T_g °C at age						
Temperature	***RH %***	***Samples No.***	***3 days***	***7 days***	***14 days***	***28 days***
15°C	**0%**	**T-15-0**	30.6	35.4	38.1	41.8
			33.7	38.1	40.4	42.0
			32.6	38.2	40.4	41.4
		Avg ± SD	*32.3 ± 1.3*	*37.2 ± 1.3*	*39.6 ± 1.1*	*41.7 ± 0.3*
	100%	**T-15-100**	30.4	30.5	35.4	33.4
			29.1	32.7	35.2	35.4
			30.1	33.9	35.9	35.5
		Avg ± SD	*29.8 ± 0.5*	*32.4 ± 1.4*	*35.5 ± 0.3*	*34.8 ± 1.0*
24°C	**0%**	**T-24-0**	47.9	51.9	52.9	55.5
			47.9	52.0	53.7	55.6
			45.8	52.1	53.3	55.4
		Avg ± SD	*47.2 ±1.0*	*52.0 ± 0.1*	*53.3 ± 0.4*	*55.5 ± 0.1*
	100%	**T-24-100**	45.3	47.4	48.1	50.3
			44.2	45.7	47.0	49.8
			43.9	45.5	48.0	50.2
		Avg ± SD	*44.5 ± 0.6*	*46.2 ± 0.9*	*47.7 ± 0.5*	*50.1 ± 0.2*
35°C	**0%**	**T-35-0**	57.8	60.4	63.7	64.9
			57.5	62.1	63.6	65.9
			58.6	60.3	64.5	66.6
		Avg ± SD	*58.0 ± 0.4*	*60.9 ± 0.8*	*63.9 ± 0.4*	*65.8 ± 0.7*
	100%	**T-35-100**	54.8	58.0	57.9	60.0
			55.6	58.7	57.9	58.5
			55.0	57.3	58.6	59.9
		Avg ± SD	*55.1 ± 0.4*	*58.0 ± 0.6*	*58.1 ± 0.3*	*59.5 ± 0.7*
50°C	**0%**	**T-50-0**	74.7	75.1	75.1	80.0
			73.7	75.1	77.5	78.3
			72.4	77.3	79.9	78.3
		Avg ± SD	*73.6 ± 0.9*	*75.8 ± 0.1*	*77.5 ± 2.0*	*78.9 ± 0.8*
	100%	**T-50-100**	65.3	63.3	65.2	65.2
			68.4	67.5	65.1	65.4
			65.2	65.2	63.1	65.2
		Avg ± SD	*66.3 ± 1.5*	*65.4 ± 1.7*	*64.5 ± 0.9*	*65.3 ± 0.1*
65°C	**0%**	**T-65-0**	85.1	90.0	88.6	89.8
			83.9	89.1	87.8	90.0
			83.5	88.1	87.4	90.3
		Avg ± SD	*84.2 ± 0.7*	*89.1 ± 0.8*	*87.9 ± 0.9*	*90.0 ± 0.2*
	100%	**T-65-100**	67.6	65.2	65.2	70.0
			70.8	68.8	70.5	69.7
			65.2	69.1	69.9	68.4
		Avg ± SD	*67.9 ± 2.3*	*67.7 ± 1.8*	*68.5 ± 2.4*	*69.4 ± 0.7*
80°C	**0%**	**T-80-0**	88.4	90.0	89.9	85.1
			90.0	88.8	90.2	86.6
			85.0	89.9	87.6	87.2
		Avg ± SD	*87.8 ± 2.1*	*89.6 ± 0.5*	*89.2 ± 1.2*	*86.3 ± 0.9*
	100%	**T-80-100**	65.2	64.8	70.4	65.2
			65.1	62.6	63.7	65.6
			65.2	70.0	70.1	67.4
		Avg ± SD	*65.2 ± 0.0*	*65.8 ± 3.1*	*68.1 ± 3.1*	*66.1 ± 1.0*

Table C-4: Logarithmic scale onset of storage modulus, T_g at different ages and curing temperatures

Logarithmic scale onset glass transition temperature, T_g°C at age						
Temperature	***RH %***	***Samples No.***	***3 days***	***7 days***	***14 days***	***28 days***
15°C	**0%**	**T-15-0**	29.9	37.5	39.1	41.0
			33.8	37.5	39.5	41.0
			32.4	38.7	38.7	41.1
		Avg ± SD	*32.0 ± 1.6*	*37.9 ± 0.6*	*39.1 ± 0.3*	*41.0 ± 0.0*
	100%	**T-15-100**	28.8	30.9	33.0	34.3
			28.3	31.5	33.4	35.0
			30.0	33.0	32.9	35.2
		Avg ± SD	*29.0 ± 0.7*	*31.8 ± 0.9*	*33.1 ± 0.2*	*34.8 ± 0.9*
24°C	**0%**	**T-24-0**	46.0	50.9	51.5	54.7
			45.9	50.3	52.3	54.6
			45.1	51.1	52.4	54.8
		Avg ± SD	*45.7 ± 0.4*	*50.8 ± 0.3*	*52.1 ± 0.4*	*54.7 ± 0.1*
	100%	**T-24-100**	41.5	44.4	46.7	46.6
			41.2	44.2	45.5	47.9
			41.9	44.5	46.8	47.9
		Avg ± SD	*41.5 ± 0.3*	*44.4 ± 0.1*	*46.3 ± 0.6*	*47.5 ± 0.6*
35°C	**0%**	**T-35-0**	56.5	59.6	62.7	63.8
			55.9	60.7	62.7	64.8
			56.6	59.6	63.6	65.2
		Avg ± SD	*56.3 ± 0.3*	*60.0 ± 0.5*	*63.0 ± 0.4*	*64.6 ± 0.6*
	100%	**T-35-100**	52.2	55.0	56.4	57.8
			53.2	55.3	56.7	57.7
			53.3	55.4	56.3	57.8
		Avg ± SD	*52.9 ± 0.5*	*55.2 ± 0.2*	*56.5 ± 0.2*	*57.8 ± 0.0*
50°C	**0%**	**T-50-0**	73.4	73.5	75.1	78.3
			72.1	74.2	77.0	77.2
			71.0	75.1	77.8	76.9
		Avg ± SD	*72.2 ± 1.0*	*74.3 ± 0.7*	*76.6 ± 1.2*	*77.5 ± 0.6*
	100%	**T-50-100**	63.4	62.6	63.6	64.2
			64.5	63.1	61.6	61.9
			62.3	64.5	62.4	63.5
		Avg ± SD	*63.4 ± 1.0*	*63.4 ± 0.2*	*62.5 ± 1.1*	*63.2 ± 0.6*
65°C	**0%**	**T-65-0**	82.1	87.6	86.7	87.7
			82.2	87.1	86.5	88.5
			82.4	86.5	86.4	88.7
		Avg ± SD	*82.2 ± 0.1*	*87.1 ± 0.4*	*86.5 ± 0.1*	*88.3 ± 0.4*
	100%	**T-65-100**	65.0	63.5	62.1	64.9
			63.7	64.4	63.6	65.7
			64.8	62.5	64.1	64.0
		Avg ± SD	*64.5 ± 0.6*	*63.5 ± 0.8*	*63.3 ± 0.8*	*64.9 ± 0.7*
80°C	**0%**	**T-80-0**	84.9	86.0	85.8	83.4
			85.8	86.6	87.5	84.3
			85.2	85.0	86.1	84.9
		Avg ± SD	*85.3 ± 0.4*	*85.9 ± 0.7*	*86.5 ± 0.7*	*84.2 ± 0.6*
	100%	**T-80-100**	62.3	62.8	64.5	63.2
			62.9	63.5	63.2	63.3
			63.7	63.4	62.9	63.9
		Avg ± SD	*63.0 ± 0.6*	*63.2 ± 0.3*	*63.5 ± 0.7*	*63.5 ± 0.3*

Table C-5: Normal scale onset of storage modulus, T_g at different ages and curing temperatures

Normal scale onset glass transition temperature, T_g°C at age						
Temperature	***RH %***	***Samples No.***	***3 days***	***7 days***	***14 days***	***28 days***
15°C	**0%**	**T-15-0**	23.7	28.3	30.5	33.2
			23.7	29.3	30.8	32.2
			24.7	29.9	29.2	32.0
		Avg ± SD	*24.0 ± 0.5*	*29.2 ± 0.7*	*30.2 ± 0.7*	*32.5 ± 0.5*
	100%	**T-15-100**	23.4	24.1	26.7	28.6
			23.4	24.8	25.6	28.5
			24.6	25.2	25.3	28.2
		Avg ± SD	*23.8 ± 0.6*	*24.7 ± 0.5*	*25.9 ± 0.6*	*28.4 ± 0.2*
24°C	**0%**	**T-24-0**	42.2	47.5	49.2	51.8
			41.8	46.9	48.6	51.2
			40.7	47.6	49.3	51.6
		Avg ± SD	*41.6 ± 0.6*	*47.3 ± 0.3*	*49.0 ± 0.3*	*51.5 ± 0.2*
	100%	**T-24-100**	39.3	42.3	43.7	43.4
			38.8	41.0	43.4	44.8
			39.2	41.5	43.9	45.1
		Avg ± SD	*39.1 ± 0.2*	*41.6 ± 0.5*	*43.7 ± 0.2*	*44.4 ± 0.7*
35°C	**0%**	**T-35-0**	53.7	57.3	60.1	62.1
			53.1	57.7	60.3	62.7
			51.9	56.7	60.7	63.4
		Avg ± SD	*52.9± 0.7*	*57.2 ± 0.4*	*60.4 ± 0.2*	*62.7 ± 0.5*
	100%	**T-35-100**	49.0	52.1	53.3	54.6
			50.3	52.2	53.8	54.3
			50.0	52.5	53.1	53.6
		Avg ± SD	*49.8 ± 0.6*	*52.3 ± 0.2*	*53.4 ± 0.3*	*54.2 ± 0.4*
50°C	**0%**	**T-50-0**	70.4	71.1	73.0	75.9
			69.4	71.8	74.6	74.5
			67.6	72.9	75.6	74.3
		Avg ± SD	*69.1 ± 1.2*	*71.9 ± 0.7*	*74.4 ± 1.1*	*74.9 ± 0.7*
	100%	**T-50-100**	61.6	60.4	61.4	59.8
			62.7	62.4	57.1	59.7
			60.1	60.3	57.9	61.6
		Avg ± SD	*61.5 ± 1.1*	*61.0 ± 1.0*	*58.8 ± 1.9*	*60.4 ± 0.9*
65°C	**0%**	**T-65-0**	78.8	84.2	82.7	83.0
			79.2	81.8	82.0	83.9
			79.2	81.5	81.7	84.6
		Avg ± SD	*79.1 ± 0.2*	*82.5 ± 1.2*	*82.1 ± 0.4*	*83.8 ± 0.7*
	100%	**T-65-100**	57.3	56.9	55.5	62.2
			57.0	58.0	54.5	60.3
			57.6	56.2	57.5	60.4
		Avg ± SD	*57.3 ± 0.2*	*57.0 ± 0.7*	*55.8 ± 1.2*	*61.0 ± 0.9*
80°C	**0%**	**T-80-0**	76.2	77.9	78.8	75.6
			79.1	79.2	79.2	76.4
			77.1	75.6	78.6	76.7
		Avg ± SD	*77.5 ± 1.2*	*77.6 ± 1.5*	*78.9 ± 0.2*	*76.2 ± 0.5*
	100%	**T-80-100**	48.8	55.6	57.2	47.6
			52.6	53.5	56.0	50.9
			57.3	52.5	52.3	54.6
		Avg ± SD	*52.9 ± 3.5*	*53.9 ± 1.3*	*55.2 ± 2.1*	*51.0 ± 2.9*

C.6.1 DSC results

Table C-6: Onset point, T_g at different ages and curing temperatures

Onset glass transition temperature, T_g°C at age						
Temperature	***RH %***	***Samples No.***	***3 days***	***7 days***	***14 days***	***28 days***
15°C	**0%**	**T-15-0**			45.7	47.3
					44.0	47.9
					46.0	47.1
		Avg ± SD			*45.2 ± 0.9*	*47.4 ± 0.3*
	100%	**T-15-100**	37.1	40.8	39.6	40.5
			37.7	41.3	40.5	40.5
			38.0	41.4	41.0	41.0
		Avg ± SD	*37.6 ± 0.4*	*41.2 ± 0.3*	*40.3 ± 0.6*	*40.7 ± 0.2*
24°C	**0%**	**T-24-0**	43.8	49.4	52.1	53.5
			43.6	48.7	52.1	53.8
			44.3	47.1	51.6	53.2
		Avg ± SD	*43.9 ± 0.3*	*48.4 ± 1.0*	*51.9 ± 0.3*	*53.5 ± 0.2*
	100%	**T-24-100**	40.8	44.0	45.0	46.1
			41.3	44.4	45.2	56.1
			41.5	44.1	45.4	46.3
		Avg ± SD	*41.2 ± 0.3*	*44.2 ± 0.2*	*45.2 ± 0.2*	*49.5± 4.7*
35°C	**0%**	**T-35-0**	59.0	63.8	66.2	65.6
			58.9	64.2	65.3	66.3
			58.5	63.5	55.9	64.8
		Avg ± SD	*58.8 ± 0.2*	*63.8 ± 0.3*	*62.5 ± 4.7*	*65.5 ± 0.6*
	100%	**T-35-100**	54.0	56.2	57.6	58.9
			53.4	55.6	57.6	59.9
			54.2	57.3	57.9	59.6
		Avg ± SD	*53.8 ± 0.3*	*56.4 ± 0.7*	*57.7 ± 0.1*	*59.4 ± 0.4*
50°C	**0%**	**T-50-0**	71.7	74.8	75.3	77.0
			71.8	74.6	75.6	77.0
			72.0	74.3	76.7	77.9
		Avg ± SD	*71.8 ± 0.1*	*74.6 ± 0.2*	*75.9 ± 0.6*	*77.3 ± 0.4*
	100%	**T-50-100**	62.4	64.8	67.1	59.9
			63.4	64.7	67.4	61.2
			63.1	65.1	67.1	60.4
		Avg ± SD	*63.0 ± 0.4*	*64.9 ± 0.2*	*67.2 ± 0.1*	*60.5 ± 0.5*
65°C	**0%**	**T-65-0**	82.3	86.8	85.6	87.1
			81.7	85.8	87.1	87.0
			81.2	86.1	86.9	87.1
		Avg ± SD	*81.7 ± 0.4*	*86.2 ± 0.4*	*86.5 ± 0.7*	*87.1 ± 0.1*
	100%	**T-65-100**				
		Avg ± SD				
80°C	**0%**	**T-80-0**	82.4	83.8	83.6	78.5
			83.4	83.0	79.7	80.0
			83.6	83.1	78.9	79.2
		Avg ± SD	*83.1 ± 0.5*	*83.3 ± 0.4*	*80.7 ± 2.0*	*79.2 ± 0.6*
	100%	**T-80-100**				
		Avg ± SD				

Table C-7: Inflection point, T_g at different ages and curing temperatures

Inflection point glass transition temperature, T_g °C at age						
Temperature	***RH %***	***Samples No.***	***3 days***	***7 days***	***14 days***	***28 days***
15°C	**0%**	**T-15-0**	39.9	43.6	47.9	50.4
			40.1	42.9	48.0	50.9
			40.7	42.9	47.3	50.8
		Avg ± SD	*40.3 ± 0.3*	*43.1 ± 0.4*	*47.7 ± 0.3*	*50.7 ± 0.2*
	100%	**T-15-100**	40.6	43.8	45.5	44.5
			40.7	44.9	44.1	44.5
			40.8	44.0	44.1	44.2
		Avg ± SD	*40.7 ± 0.1*	*44.2 ± 0.5*	*44.6 ± 0.7*	*44.4 ± 0.1*
24°C	**0%**	**T-24-0**	46.8	51.4	54.3	56.9
			46.4	51.4	55.5	56.7
			46.9	52.1	54.7	57.2
		Avg ± SD	*46.7 ± 0.2*	*51.6 ± 0.3*	*54.8 ± 0.5*	*56.9 ± 0.2*
	100%	**T-24-100**	43.0	47.2	48.6	47.9
			43.6	46.9	48.8	49.9
			43.4	46.7	48.0	48.6
		Avg ± SD	*43.3 ± 0.3*	*46.9 ± 0.2*	*48.5 ± 0.4*	*48.8 ± 0.8*
35°C	**0%**	**T-35-0**	62.6	67.4	70.5	70.8
			62.1	68.4	69.0	70.7
			62.4	67.5	69.7	69.7
		Avg ± SD	*62.4 ± 0.2*	*67.8 ± 0.5*	*69.7 ± 0.6*	*70.4 ± 0.5*
	100%	**T-35-100**	58.4	59.3	61.1	63.7
			57.3	58.2	61.8	63.8
			57.1	60.5	60.9	62.3
		Avg ± SD	*57.6 ± 0.6*	*59.3 ± 1.0*	*61.3 ± 0.4*	*63.2 ± 0.7*
50°C	**0%**	**T-50-0**	75.3	78.8	80.4	80.3
			75.7	78.1	79.7	81.7
			76.5	78.6	82.9	81.6
		Avg ± SD	*75.8 ± 0.5*	*78.5 ± 0.3*	*81.0 ± 1.4*	*81.2 ± 0.6*
	100%	**T-50-100**	67.2	68.3	69.6	66.7
			67.2	69.4	69.4	65.0
			67.8	69.4	70.3	68.8
		Avg ± SD	*67.4 ± 0.3*	*69.1 ± 0.5*	*69.8 ± 0.4*	*66.8 ± 1.6*
65°C	**0%**	**T-65-0**	87.5	90.8	92.3	92.6
			89.0	91.8	92.2	92.1
			89.8	91.9	92.8	91.9
		Avg ± SD	*88.8 ± 1.0*	*91.5 ± 0.5*	*92.5 ± 0.2*	*92.2 ± 0.3*
	100%	**T-65-100**				
		Avg ± SD				
80°C	**0%**	**T-80-0**	85.6	88.7	88.5	84.3
			87.2	91.0	84.5	87.7
			88.2	87.5	88.5	87.4
		Avg ± SD	*87.0 ± 1.1*	*89.1 ± 1.5*	*87.2 ± 1.9*	*86.5 ± 1.5*
	100%	**T-80-100**				
		Avg ± SD				

Appendix D

Coupon test

The material properties of the steel beam and plates were measured for later use in the analysis. Direct tensile tests were used to measure the steel's mechanical properties, such as tensile strength and Young's modulus. This section covers the details of the coupon specimens prepared and tested in this research, and it contains the test results obtained from the strain gauges and Digital Image Correlation DIC analysis.

D.1 Bulk material properties (coupon tests)

A total of 15 coupon specimens were tested. The coupons were cut from the hot rolled universal steel beams (UB 28×254×102); a set consists of three coupons. Table D-1 contains the number of coupons and labelling details. The sets were cut from the web, top flange, and bottom flange of the universal steel I-section. Additional set from the strengthening plate, which was welded to the top flange of the universal steel beams in fabrication of the test beams. All dog-bone specimens were taken from the low stressed area of the control specimens detailed in Chapter 5 after testing. A set of 2 mm thin plate, which was used in the fabrication of lap-shear specimens, was tested. The details of the lap-shear specimens are covered in detail in Chapter 5.

Table D-1: Coupon number and labelling details

	Specimen Location	***No. of specimen***	***Specimen Labels***
Universal beam UB 28×254×102	Top flange	3	TF_1, TF_2 and TF_3
	Web	3	W_1, W_2 and W_3
	Bottom flange	3	BF_1, BF_2 and BF_3
Strengthening plate	Plate section	3	SP_1, SP_2 and SP_3
2 mm thin plate	Plate section	3	TP_1, TP_2 and TP_3

D.1.1 Dogbone specimen preparation and test procedure

The steel material properties were found by cutting nine coupons (dog-bone steel specimens) from of the hot rolled universal steel beams (UB 28×254×102); according to ASTM A0370-77 (1977); ASTM A0370-03a (2003) and British Standard EN 10025 (2004) and British Standard ISO 4360 (1990) and extra three specimens from the compression flange strengthening plate. According to the ASTM standard the coupons shall be taken from the web of the section; on the other hand, as BS EN 10025 and BS 4360 recommends that the coupons be cut from the flanges. The coupons were taken according to the two standards to minimise statistical error. Figure D-1 shows the detailed dimensions of the coupons. Referee to Table D-1 for the labelling of the specimens.

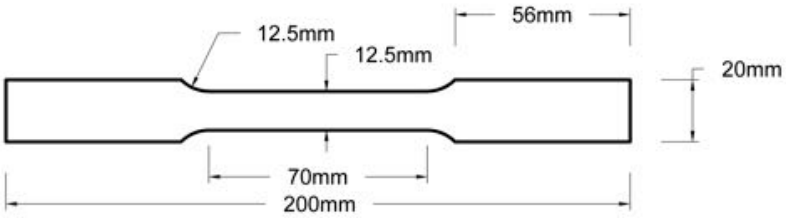

Figure D-1: Dimensions of steel dog-bone specimen

Linear strain gauges and DIC were used to obtain complete stress-strain relationships for the coupons. Prior to testing the coupons were grit blasted to remove the mill scale and prepare the surface for the strain gauges installation. The strain gauge manufacturer (Tokyo Sokki Kenkyujo Co.) recommends five mm length strain gauges. The gauges were installed on one side of the coupons and painting the opposite surface with black for the DIC analysis as shown in Figure D-2.

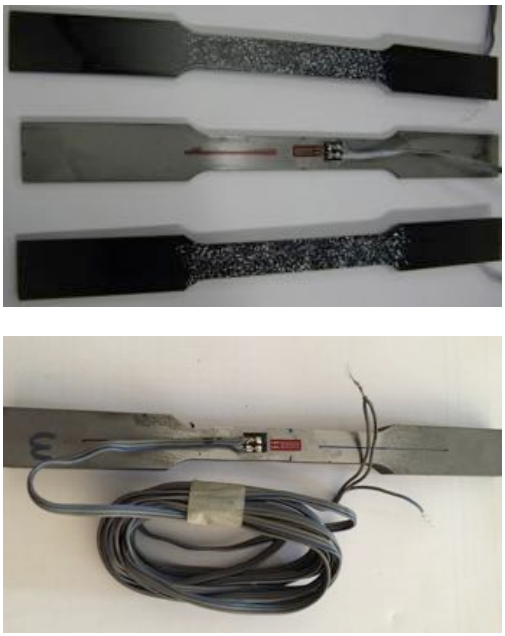

Figure D-2: Prepared and ready to test steel dog-bone specimens

Surface preparation is important to insure the strain gauges are in contact with the coupon surface; after the grit blasting aluminium oxide sand paper P120 and P400 were used respectively and then the strain gauges were mounted in the mid of the coupon gauge length. Also, it is important to have thin layer of paint for the DIC analysis, therefore, on thin layer paint applied.

The testing was carried out using displacement control method; the displacement rate was 1 mm/min except one sample from the web, which was tested at 2 mm/min. The strain values recorded using a Vishay 7000 data logging system. A universal hydraulic tension machine (Instron 600LX) used to load the samples and record the load values. The recorded data was used to establish the complete stress-strain curve for each coupon test; the strain from the strain was gauges used to plot elastic part of the response and determine the values of elastic modulus E, and yield strength 0.2% f_y. The majority of the strain gauges detached from the sample shortly after the material reached yielding in the adjacent locations to the strain gauges and the elongation exceeded the strain gauge capacity. The measured strain from the DIC analysis was used to complete the stress strain curve after yielding and the strain hardening stage. The DIC analysis was carried out using two different gauge lengths within the recommended gauge length by ASTM E8/E8M-09 (2009); the

results have showed good agreement. The presented DIC is the average of the two different gauge lengths.

Yield strength was based on a 0.2% offset, which is the minimum recommended by ASTM E8/E8M-09 (2009), 0.2% f_y strength, yield strain ε_y and young's modulus are reported from the strain values from the strain gauges. The ultimate strength f_u from the Instron reading and strain ε_u are reported from the DIC measures strain. The test set up is shown in Figure D-3. The approximate locations of the patches in the DIC analysis are shown in the Figure D-4.

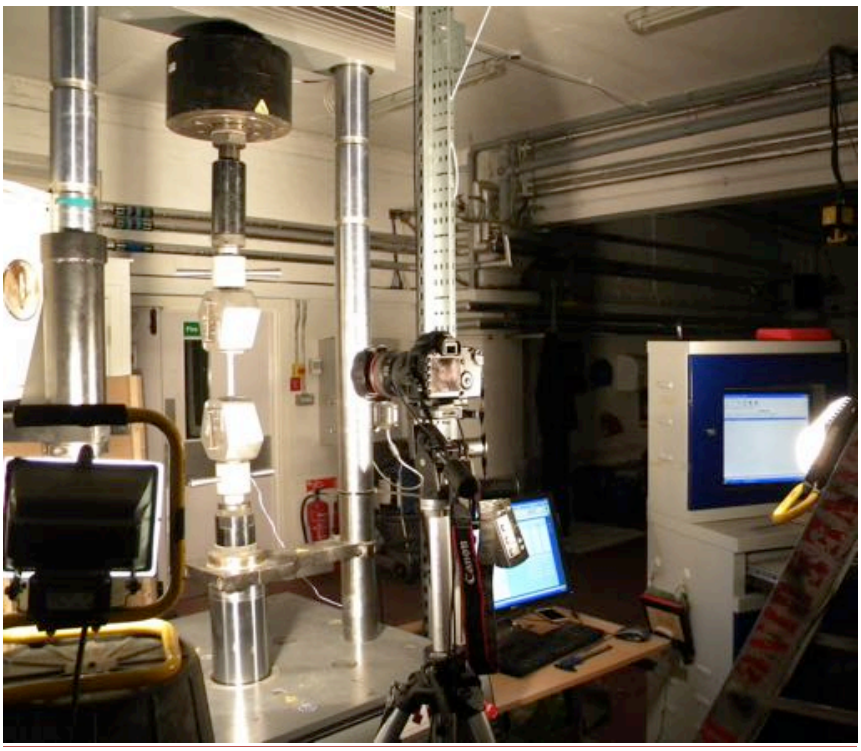

Figure D-3: Tensile test set up

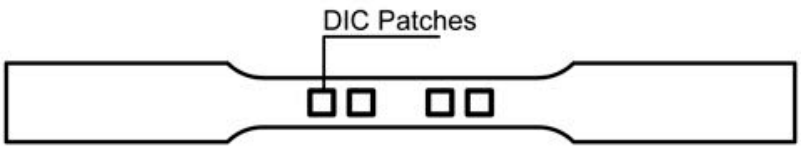

Figure D-4: Approximate location of the DIC patches in the analysis

D.1.2 Test results

The stress-strain curves obtained from the strain gauges and DIC are shown in Figure D-5 to Figure D-9. A yield plateau follows the linear stress-strain relationship in (the top plots) Figure D-5 to Figure D-9. The DIC analysis shows the strain hardening stage of coupons and all three samples of each set are in a good agreement, see (the bottom plots) Figure D-5 to Figure D-9.

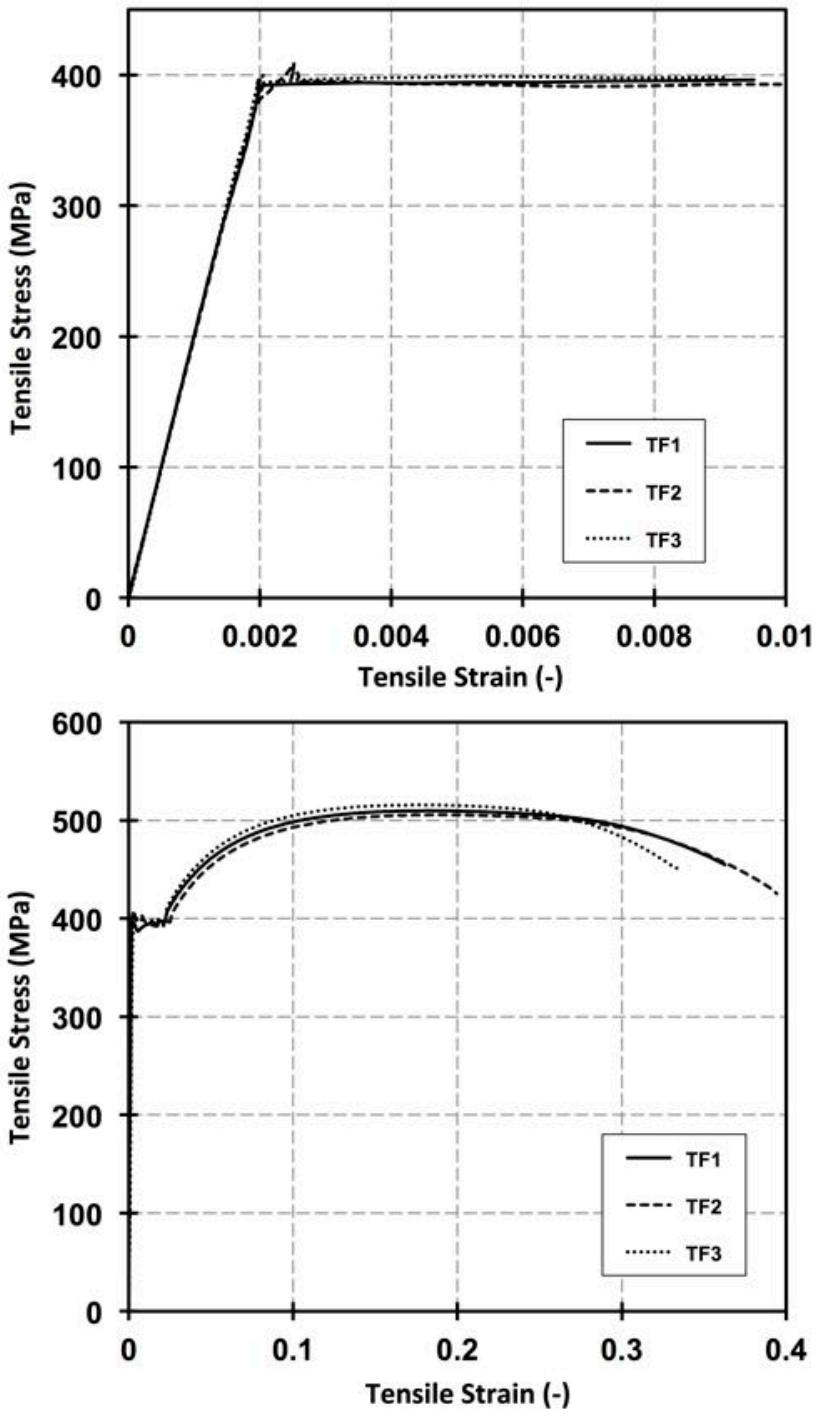

Figure D-5: Measured stress-strain curve of the top flange dog-bone tension specimens

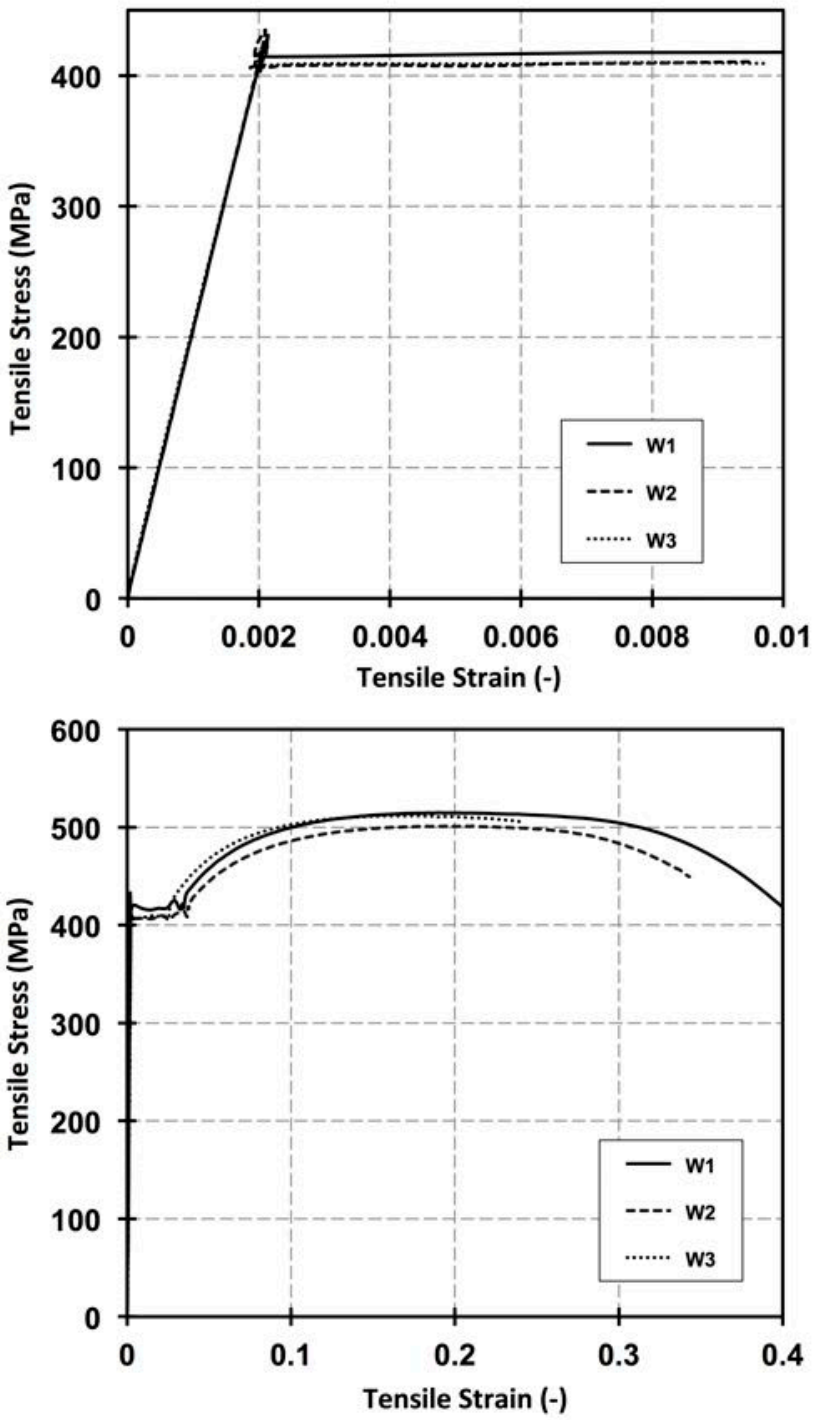

Figure D-6: Measured stress-strain curve of the web dog-bone tension specimens

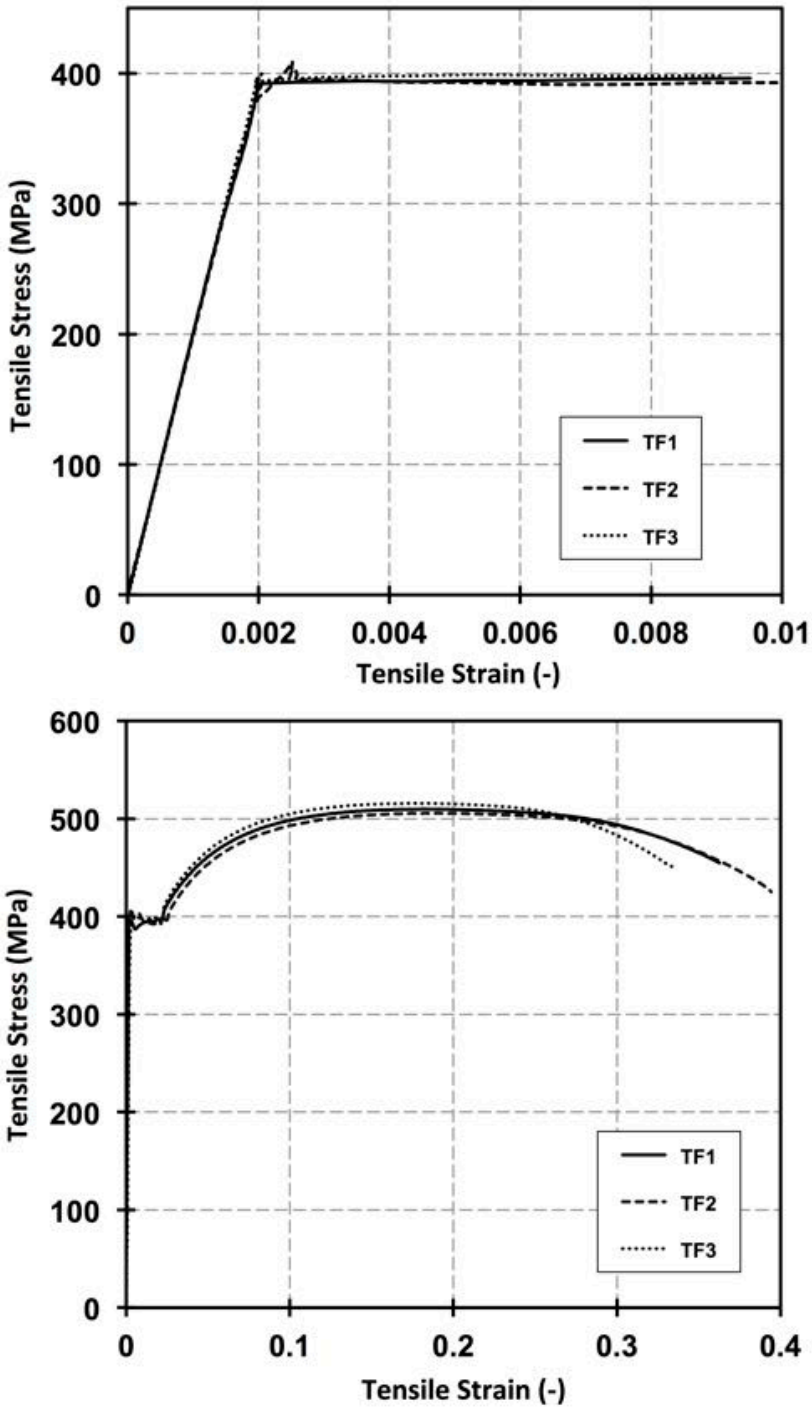

Figure D-7: Measured stress-strain curve of the top flange dog-bone tension specimens

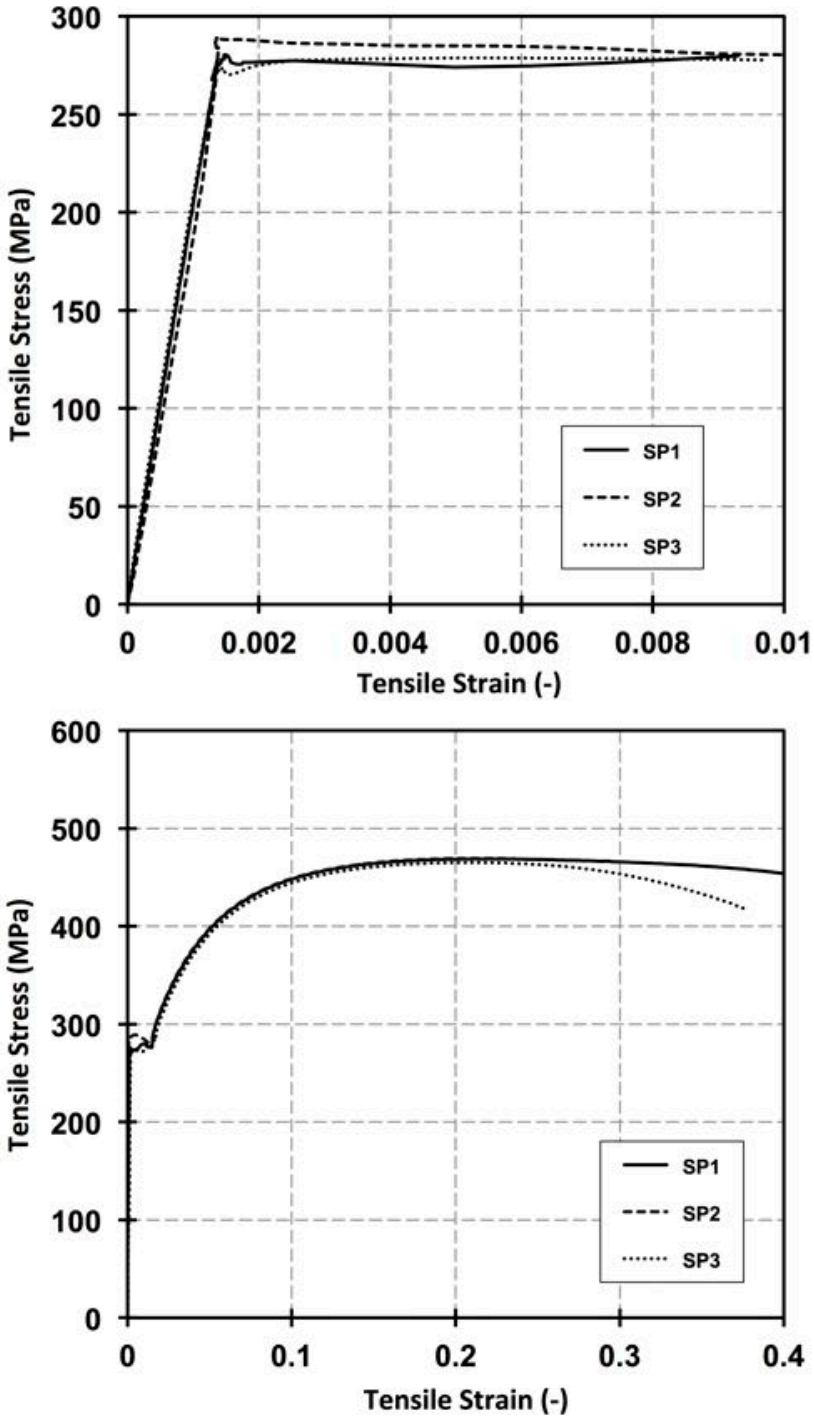

Figure D-8: Measured stress-strain curve of the top flange strengthening plate dog-bone tension specimens

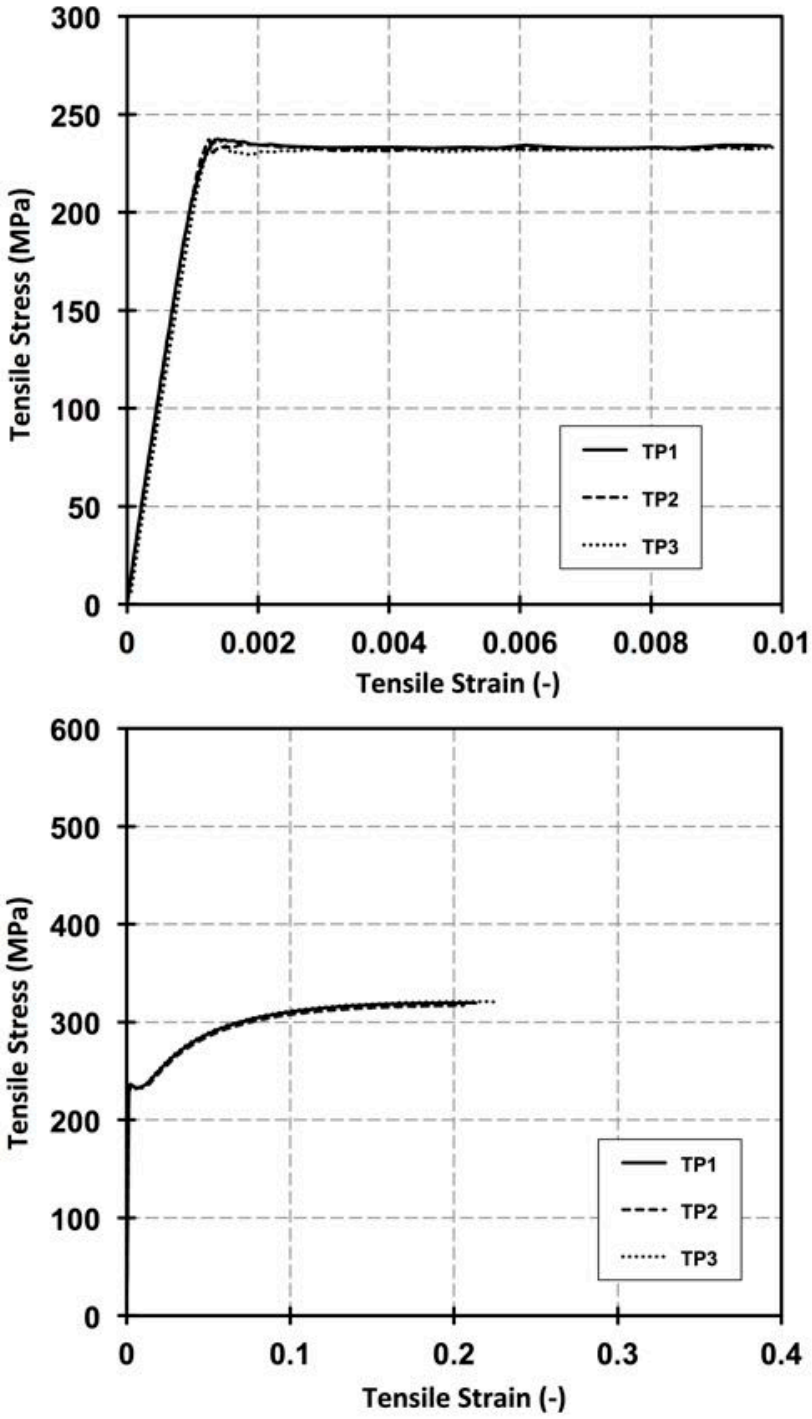

Figure D-9: Measured stress-strain curve of the 2 mm plate dog-bone tension specimens

Appendix E

Coupon test

This Appendix contains the models that were discussed in Section 6.3 and 6.4.

The flexural model was used to study strain hardening. It consists of two sections. First section is to find the moment-curvature relationship of a section. Second section is to find the load deflection relationship.

The bond model was used to estimate the FRP plate slip and compare the results from the model to the experiments. A first order analysis was used. The effect of couple shear and normal stresses are included. This due to the fact that the equal curvature of the beam and CFRP plates is not assumed.

It should be noted that there are equations and function that are not part of the modelling, but they have been kept for regular checks. The coding of sub functions is also included.

E.1 Flexural model

```
%%% Moment-curvature relationship %%%
clc
tic
format longEng

%Mesh Properties
n   = 20;       %Number of segments in each section of the beam
Inc = 1/n;      %Increment size to calculate strain distribution
Strainsteps = 10;
Curvaturesteps = 10;
% Given Limits
epsb0mMax   = 0.001;
epsb0mi     = epsb0mMax/Strainsteps;
curvatureMax    = (0.03/272.9);
curvaturei      = curvatureMax/Curvaturesteps;
%Strengthened Steel Dimentions
TSteel = 12.5;
BSteel = 100;
ASteel = BSteel*TSteel;
ISteel = (BSteel*TSteel^3)/12;

%Section Dimentions
Tw  = 6.3;
```

```
Ttf = 10;
Tbf = 10;
Btf = 102.2;
Bbf = 102.2;
d   = 240.4;
D   = d + Ttf + Tbf;
Atf = Ttf * Btf;
Abf = Tbf * Bbf;
Aw  = Tw  * d;
Abeam = Atf + Abf + Aw;

%Steel Properties
steelstress = 200;
steelstressr= 69;
Esteel      = 200000;
vsteel      = 0.3;
Gsteel      = 0.5*Esteel/(1+vsteel);
strainsteel = steelstress / Esteel;
strainsteelp= (steelstress-steelstressr) / Esteel;
Esteelr     = steelstressr / (2 * strainsteel - strainsteelp);

%Strengthened Steel Properties
strengthenedsteelstress = 200;
strengthenedsteelstressr= 69;
strengthenedEsteel      = 200000;
strengthenedstrainsteel = strengthenedsteelstress /
strengthenedEsteel;
strengthenedstrainsteelp= (strengthenedsteelstress-
strengthenedsteelstressr) / strengthenedEsteel;
strengthenedEsteelr     = strengthenedsteelstressr / (2 *
strengthenedstrainsteel - strengthenedstrainsteelp);

%Second Moment of Area
Dcom= D + TSteel;
Elasticyfromthebottom = ((ASteel * (Dcom - 0.5 * TSteel)) + (Atf *
(Dcom - (0.5 * Ttf) - TSteel)) + (Aw * (0.5 * d + Tbf)) + (Abf *
(0.5 * Tbf)))/(Abeam + ASteel);  % from the Bottom of the composite
section [mm];

Ixbeam = (((Tw*d^3)/12)+(Aw*(Elasticyfromthebottom-0.5*d-
Tbf)^2))+(((Btf*Ttf^3)/12)+(Ttf*Btf*(D-Elasticyfromthebottom-
0.5*Ttf)^2))+(((Bbf*Tbf^3)/12)+(Tbf*Bbf*(Elasticyfromthebottom-
0.5*Tbf)^2)) + (ISteel+(ASteel)*((Dcom-Elasticyfromthebottom-
0.5*TSteel))^2);
Iybeam =
((d*Tw^3)/12)+((Ttf*Btf^3)/12)+((Tbf*Bbf^3)/12)+((TSteel*BSteel^3)/1
2);

Ixcombeam = (((Tw*d^3)/12)+(Aw*(Elasticyfromthebottom-0.5*d-
Tbf)^2))+(((Btf*Ttf^3)/12)+(Ttf*Btf*(D-Elasticyfromthebottom-
0.5*Ttf)^2))+(((Bbf*Tbf^3)/12)+(Tbf*Bbf*(Elasticyfromthebottom-
0.5*Tbf)^2)) + (ISteel+(ASteel)*(Dcom-Elasticyfromthebottom-
0.5*TSteel)^2);
Iycombeam =
((d*Tw^3)/12)+((Ttf*Btf^3)/12)+((Tbf*Bbf^3)/12)+((TSteel*BSteel^3)/1
2);
```

```
ElasticMaxMbottom = steelstress * Ixcombeam / Elasticyfromthebottom;
ElasticMaxMtop    = steelstress * Ixcombeam / (Dcom -
Elasticyfromthebottom);

yp = (((Tbf + Tbf + d) * Tw * steelstress) + (Atf * steelstress) -
(Abf * steelstress) + (ASteel * strengthenedsteelstress)) / (2 * Tw
* steelstress);
Mp = (steelstress * Abf * (yp - Tbf / 2)) + (steelstress * (Tw * (yp
- Tbf)) * ((yp - Tbf) / 2)) + (steelstress * (Tw * (d-(yp-Tbf))) *
((d-(yp-Tbf))/2)) + (steelstress * Atf * (D - yp - (Ttf/2))) +
(strengthenedsteelstress * ASteel * (Dcom - yp - (TSteel/2)));

Assumedy = Elasticyfromthebottom;


in = round((Dcom*n)+1);
BB  = zeros (in,1);
H   = zeros (in,1);
F   = zeros (in,1);
Eb  = zeros (in,1);
f   = zeros (in,1);
QQti  = zeros (in,1);
QQci  = zeros (in,1);
MMti  = zeros (in,1);
MMci  = zeros (in,1);
EPS = zeros (in,1);
Moment    = zeros (1,1);
Load      = zeros (1,1);
Strain    = zeros (1,1);
Curvature = zeros (1,1);

i=0;
for i = i+1 : i+n*Tbf
    BB (i,1) = Bbf;
end
iTbf=i;
for i = i+1 : i+n*d+1
    BB (i,1) = Tw;
end
iw=i;
if Ttf == 0;
    iend=i;
end
if Ttf > 0;
for i = i+1 : i+n*Ttf
    BB (i,1) = Btf;
end
iTtf=i;
end
if TSteel == 0;
    iend=i;
end
if TSteel > 0;
for i = i+1 : i+n*TSteel
    BB (i,1) = BSteel;
end
    iend=i;
```

```
end


%Plastic Moment
[yppoint] =  round(yp * n);
Ap = (1/n) * steelstress * trapz (BB (1:yppoint));
A11 = ((iend-1) - (TSteel*n));
A1 = (1/n) * steelstress * trapz (BB (1:A11));
A2 = (1/n) * strengthenedsteelstress * trapz (BB (A11:iend));
A  = A1 + A2;
Plasticyfromthebottom = yp;
while round((A / Ap)*1e4) >= 2e4
Plasticyfromthebottom = Plasticyfromthebottom + (Inc);
[Plasticyfromthebottompoint] =  Plasticyfromthebottom * n;
Plasticyfromthebottompoint = round
(Plasticyfromthebottompoint*1e4)/1e4;
Ap1 = (1/n) * steelstress * trapz (BB
(1:round(Plasticyfromthebottompoint)));
A1  = (1/n) * steelstress * trapz (BB (1:A11));
A2  = (1/n) * strengthenedsteelstress * trapz (BB (A11:iend));
A   = A1 + A2;
Ap = Ap1;
end
[Plasticyfromthebottompoint] =  yp * n;
Plasticyfromthebottompoint = round
(Plasticyfromthebottompoint*1e4)/1e4;


h = yp;
Atp = 0;
for i = 1 : Plasticyfromthebottompoint
    Atp = Atp + ((BB(i,1)*(1/n)*(h-(1/(2*n)))) + ((BB(i+1,1)-
BB(i,1))*(0.5/n)*(h-(2/(3*n)))));
    h = h - (1/n);
end

h = 0;
Acp1 = 0;
for i = i-1 : A11
    Acp1 = Acp1 - ((BB(i,1)*(1/n)*(h+(1/(2*n)))) + ((BB(i+1,1)-
BB(i,1))*(0.5/n)*(h+(2/(3*n)))));
    h = h + (1/n);
end

Acp2 = 0;
for i = i+1 : iend-1
    Acp2 = Acp2 - ((BB(i,1)*(1/n)*(h+(1/(2*n)))) + ((BB(i+1,1)-
BB(i,1))*(0.5/n)*(h+(2/(3*n)))));
    h = h + (1/n);
end
PlasticMoment1 = steelstress * Atp;
PlasticMoment2 = steelstress * Acp1;
PlasticMoment3 = strengthenedsteelstress * Acp2;
PlasticMoment = PlasticMoment1 - PlasticMoment2 - PlasticMoment3;

I=1;
for epsb0m = [0, epsb0mi: epsb0mi : epsb0mMax];
```

```
II=1;
for curvature = [0, curvaturei: curvaturei : curvatureMax];
eps=(curvature*Assumedy);

h=0;
ind=0;
for i = 1 : iend
    h = round(h*1e10) / 1e10;
    EPS (i,1) =  eps * (Assumedy - h)/ Assumedy;
    H (i,1) = h;
    h=h+(1/n);
end

EPS (:,1) = (round(EPS (:,1)*1e8) / 1e8)-epsb0m;

i = 1;
y1 = 0;
while EPS (i,1) > 0
    i = i + 1;
    y1 = y1 + 1;
end

for i = 1 : y1
          f (i,1) = interp1q
(Realstrainbeamsection,Realstressbeamsection, EPS (i,1));
    ind=ind+1;
end
for i = ind+1 : (iend - (TSteel*n))
        f (i,1) = - interp1q
(Realstrainbeamsection,Realstressbeamsection,- EPS (i,1));
end
for i = (iend - (TSteel*n)) : iend
        f (i,1) = - interp1q
(Realstrainplatesection,Realstressplatesection,- EPS (i,1));
end


[centerpoint] =  Assumedy * n;
centerpoint = round (centerpoint);

F (:,1) = f (:,1) .* BB (:,1);
Q = trapz (F(1:iend))/n;
Qt= trapz (F(1:((iend+1)/2)))/n;
Qc= trapz (F((iend-1)/2:iend))/n;

if abs(Q)<1
    Q=0;
end

if curvature==0
y1 = centerpoint;
end
if round(y1)<=5
y1 = centerpoint;
end
```

```
%N.A and Cetroid at the same point
if y1 == centerpoint
h = Assumedy;
Mt=0;
for i = 1 : centerpoint
    Mt = Mt + ((F(i+1,1)*(1/n)*(h-(1/(2*n)))) + ((F(i,1)-
F(i+1,1))*(0.5/n)*(h-(2/(3*n)))));
    h=h-(1/n);
end
h=0;
Mc=0;
for i = centerpoint+1 : iend-1
    Mc = Mc - ((F(i,1)*(1/n)*(h+(1/(2*n)))) + ((F(i+1,1)-
F(i,1))*(0.5/n)*(h+(2/(3*n)))));
    h=h+(1/n);
end
moment = (Mc + Mt)/1e6;
end

%N.A bellow the Cetroid
if y1 < centerpoint
h = Assumedy;
Mt=0;
for i = 1 : y1
    Mt = Mt + ((F(i+1,1)*(1/n)*(h-(1/(2*n)))) + ((F(i,1)-
F(i+1,1))*(0.5/n)*(h-(1/(3*n)))));
    h=h-(1/n);
end
h=0;
Mc1=0;  %Above the centroid
for i = centerpoint+1 : iend-1
    Mc1 = Mc1 - ((F(i,1)*(1/n)*(h+(1/(2*n)))) + ((F(i+1,1)-
F(i,1))*(0.5/n)*(h+(2/(3*n)))));
    h=h+(1/n);
end

h=(centerpoint-y1+1)/n;
Mc2=0;  %Between the centroid and N.A
for i = y1 : centerpoint
    Mc2 = Mc2 + ((F(i,1)*(1/n)*(h-(1/(2*n)))) + ((F(i+1,1)-
F(i,1))*(0.5/n)*(h-(1/(3*n)))));
    h=h-(1/n);
end
Mc=Mc1+Mc2;
moment = (Mc + Mt)/1e6;
end

%N.A above the Cetroid
if y1 > centerpoint
h = Assumedy;
Mt1=0;  %below centroid
for i = 1 : centerpoint
    Mt1 = Mt1 + ((F(i+1,1)*(1/n)*(h-(1/(2*n)))) + ((F(i,1)-
F(i+1,1))*(0.5/n)*(h-(1/(3*n)))));
    h=h-(1/n);
end
h= 0;
```

```
Mt2=0;  %above cetroid
for i = centerpoint+1 : y1
    Mt2 = Mt2 + ((F(i+1,1)*(1/n)*(h-(1/(2*n)))) + ((F(i,1)-
F(i+1,1))*(0.5/n)*(h-(1/(3*n)))));
    h=h-(1/n);
end
Mt=Mt1+Mt2;
h= (y1-centerpoint)/n;
Mc=0;  %Above the centroid
for i = y1+1 : iend-1
    Mc = Mc - ((F(i,1)*(1/n)*(h+(1/(2*n)))) + ((F(i+1,1)-
F(i,1))*(0.5/n)*(h+(2/(3*n)))));
    h=h+(1/n);
end
moment = (Mc + Mt)/1e6;
end
if abs(moment)<1
    moment=0;
end

ElasticActualMbottom = f(1,1) * Ixcombeam / Elasticyfromthebottom;
ElasticActualMtop    = f(in,1) * Ixcombeam / (Dcom -
Elasticyfromthebottom);

Strain (I,1) = epsb0m;
Curvature (1,II) =  curvature;
Load (I,II) = -Q/1000;
Moment (I,II) = moment;

II=II+1;

figure (1)
subplot(1,2,1)
axis square
plot (EPS,H), grid on
hold on
title('[SECTION STRAIN]')
xlabel('Strain')
ylabel('Depth [mm] ')
zeroline_x = [0 , 0];
zeroline_y = [min(H) , max(H)];
plot (zeroline_x, zeroline_y, 'k')
drawnow

subplot(1,2,2)
axis square
plot (f,H), grid on
hold on
title('[SECTION STRESS]')
xlabel('Stress [MPa]')
ylabel('Depth [mm] ')
zeroline_x = [0 , 0];
zeroline_y = [min(H) , max(H)];
plot (zeroline_x, zeroline_y, 'k')
%hold off
drawnow
```

```
figure (2)
subplot(1,2,1)
axis square
%axis equal
plot (F/1000,H), grid on
hold on
title('[SECTION STRESS]')
xlabel('Stress [MPa]')
ylabel('Depth [mm] ')
zeroline_x = [0 , 0];
zeroline_y = [min(H) , max(H)];
plot (zeroline_x, zeroline_y, 'k')
%hold off
drawnow

subplot(1,2,2)
axis square
%axis equal
hold on
for i = 1:5*n:iend
xx = [-0.5*BB(i), 0.5*BB(i)];
yy = [H(i), H(i)];
plot (xx,yy), grid on
end
plot (0.5*BB,H), grid on
plot (-0.5*BB, H), grid on
title('[SECTION DIMENSIONS]')
xlabel('Width [mm]')
ylabel('Depth [mm] ')
%hold off
drawnow
end
I=I+1;
end

figure (3)
axis square
plot (Realstrainbeamsection,Realstressbeamsection), grid on
hold on
plot (Realstrainplatesection,Realstressplatesection,'r'), grid on
title('[STRESS PLOTS]')
xlabel('Strain [mm/mm]')
ylabel('Stress [MPa]')
drawnow

I = length (Strain);
II= length (Curvature);

[Curvatureplot,Strainplot] = meshgrid (Curvature,Strain);

figure (5)
surfc (Strainplot, Curvatureplot, Moment)
axis square
hold on
title('[MOMENT ENVELOPE PLOT]')
xlabel('Strain')
ylabel('Curvature')
```

```
zlabel('Moment [kN.m]')
%shading interp
colorbar

figure (6)
surfc (Strainplot, Curvatureplot, Load)
axis square
hold on
title('[LOAD ENVELOPE PLOT]')
xlabel('Strain')
ylabel('Curvature')
zlabel('Load [kN]')
%shading interp
colorbar
toc



%%% Stress-Strain relationship generator %%%
clc
tic
format longEng

beamyeildingstrength = 400;      %[MPa}
plateyeildingstrength = 280;      %[MPa}

nbeam = 0.1;        %[for low carbon steel the value is 0.26-0.34]
in general it can be between 0.2-0.5
nplate = 0.14;

Esteelbeam = 200000;
EsteelPlate= 200000;
epsMax = 0.032;

incrementn = 50;

    Realstrainbeamsection (incrementn+2,1) = zeros;
    Realstressbeamsection (incrementn+2,1) = zeros;
    Realstrainplatesection (incrementn+2,1) = zeros;
    Realstressplatesection (incrementn+2,1) = zeros;


strainbeam  = (beamyeildingstrength/Esteelbeam);
strainplate = (plateyeildingstrength/EsteelPlate);
    Realstrainbeamsection (2,1) = strainbeam;
    Realstressbeamsection (2,1) = beamyeildingstrength;
    Realstrainplatesection (2,1) = strainplate;
    Realstressplatesection (2,1) = plateyeildingstrength;
for i = 1 : incrementn
    strainbeam  =  strainbeam  + ((epsMax-
(beamyeildingstrength/Esteelbeam))/incrementn);
    strainplate =  strainplate + ((epsMax-
(plateyeildingstrength/EsteelPlate))/incrementn);

    stressbeam  = beamyeildingstrength  *
((Esteelbeam*strainbeam)/beamyeildingstrength)^nbeam;
```

```
    stressplate = plateyeildingstrength *
((EsteelPlate*strainplate)/plateyeildingstrength)^nplate;

    Realstrainbeamsection (i+2,1) = strainbeam;
    Realstressbeamsection (i+2,1) = stressbeam;
    Realstrainplatesection (i+2,1) = strainplate;
    Realstressplatesection (i+2,1) = stressplate;

end
figure (3)
axis square
plot (Realstrainbeamsection,Realstressbeamsection), grid on
hold on
plot (Realstrainplatesection,Realstressplatesection,'r'), grid on
title('[STRESS PLOTS]')
xlabel('Strain [mm/mm]')
ylabel('Stress [MPa]')
drawnow
toc


%%% Load-deflection relationship generator %%%

% Load Increment Method
clc
tic
format long
%load-Diflection

MomentMax     = 221.42;  %[kN.m] Total Applied Moment
startingratio = 0.4;
Momenti       = 1;       %[kN]
Length        = 1350;    %[mm] Half of the length
Lengthpoint   = 1000;    %[mm] Position of the wanted diflection
from the suport
Loadlocation  = 1000;    %[mm] From the supports

No.ofSegments = 1350;

Limit = round ((1-startingratio)*MomentMax/Momenti);

moment    = zeros (No.ofSegments,1);
curvature = zeros (No.ofSegments,1);
Load      = zeros (Limit,1);
Loadipoint= zeros (Limit,1);
Deflection= zeros (Limit,1);
Rotation  = zeros (Limit,1);
Deflectionipoint= zeros (Limit,1);
DeflectionipointT= zeros (Limit,1);
Rotationipoint  = zeros (Limit,1);
defi = zeros (No.ofSegments,1);
roti = zeros (No.ofSegments,1);
rotipoint = zeros ((Lengthpoint/Length) * No.ofSegments,1);
defipoint = zeros ((Lengthpoint/Length) * No.ofSegments,1);
x = zeros (No.ofSegments,1);
xx = zeros (No.ofSegments,1);
xxipoint = zeros (Limit,1);
```

```
inci = 0;
for M =[0 , (startingratio * MomentMax): Momenti : MomentMax]
inci = inci +1;
x=0;
for i = 1 : No.ofSegments
    if x <= Loadlocation
        moment (i,1) = (M * x /Loadlocation) * 1e6;
    elseif x > Loadlocation;
        moment (i,1) = M * 1e6;

    end
curvature (i,1) = interp1 (Moment,Curvature,moment (i,1));
    xx (i,1) = x;
    x = x + (Length/No.ofSegments);
end


rot=0;
x=(Length/No.ofSegments);
for i = 1 : No.ofSegments-1
    rot  = rot + ((curvature(i,1)* Length/No.ofSegments) +
((curvature(i+1,1)-curvature(i,1))*(0.5*(Length/No.ofSegments))));
    x = x + (Length/No.ofSegments);
    roti (i+1,1) = rot;
end
for i = 1:No.ofSegments-1
   ZZZ (i,1) = trapz (curvature(1:i))* Length/No.ofSegments;
end
    roti (1,1) = 0;
roti (:,1) = roti (:,1) - max(roti);

def=0;
for i = 1 : No.ofSegments-1
    def  = def + (((roti(i,1)* Length/No.ofSegments)) +
((roti(i+1,1)-roti(i,1))*(0.5*Length/No.ofSegments)));
    defi (i+1,1) = def;
end
    defi (1,1) = 0;


rotipoint=0;
for i = 1 : (Lengthpoint/Length) * No.ofSegments
    rotipoint (i,1) = roti (i,1);
    defipoint (i,1) = defi (i,1);
    xxipoint  (i,1) = xx (i,1);
end


figure (4)
subplot(2,2,1)
axis square
plot (xx,moment/1e6), grid on
hold on
title('[MOMENT-POSITION PLOT]')
xlabel('Position')
```

```
ylabel('Moment [kN.m]')

subplot(2,2,2)
axis square
plot (xx,curvature), grid on
hold on
title('[CURVATURE-POSITION PLOT]')
xlabel('Position [mm]')
ylabel('Curvature')


subplot(2,2,3)
axis square
plot (xx,defi), grid on
hold on
title('[DIFLECTIO-POSITION PLOT]')
xlabel('Position [mm]')
ylabel('Diflection [mm]')

subplot(2,2,4)
axis square
plot (xx,roti), grid on
hold on
title('[ROTATION-POSITION PLOT]')
xlabel('Position [mm]')
ylabel('Rotation')

%reduction factor from Timoshenko beam
omega = 2.327e-3;
C = interp1q (Moment,Curvature,M);
extradiflection = omega * C * (2*Length)^2;

Load (inci,1) = 2*M;
Deflection (inci,1) = -defi (No.ofSegments);
Rotation (inci,1) = -roti (No.ofSegments);
Deflectionipoint (inci,1) = -defipoint ((Lengthpoint/Length) *
No.ofSegments);
DeflectionipointT (inci,1) = -defipoint ((Lengthpoint/Length) *
No.ofSegments)+extradiflection;
Rotationipoint   (inci,1) = -rotipoint ((Lengthpoint/Length) *
No.ofSegments);
end

figure (5)
axis square
plot (Deflection, Load,'c'), grid on
hold on
plot (Deflectionipoint, Load,'r'), grid on
title('[LOAD-DEFLECTION PLOT]')
xlabel('Deflection [mm]')
ylabel('Total Load [kN]')
```

E.2 Bond analysis model

```
clear
```

```
clc
format long
nn1=1;
tic
HeatedSL = 0;
HeatedEL = 675;
n = 4000;

curingtemperature = 5;
%5 referes to Beam no.5_25
%6 referes to Beam no.6_30
%7 referes to Beam no.7_50
%8 referes to Beam no.8_50

plasticlength = zeros (1,1);
temperature = zeros (1,1);
slippage  = zeros (1,1);
load  = zeros (1,1);

Roomtemperature = 23;

it=1;
for PP = 350
for Platetemperature    = 23:0.1:100;
    Adhesivetemperature = Platetemperature;
%Loading conditions

%Mechanical Loading
P = PP;                     %Total Load in [kN]

%Thermal Loading
DT = Platetemperature - Roomtemperature;       %Change in
Temperature [C]


%Beam properties
b  = 102.2;                  %Beam Width in [mm]
tb = 272.9;                  %Beam Depth in [mm]
Ab = 3.55852e+03;            %Beam Area in [mm^2]
Eb = 200000;                 %Beam Modulus of Elasticity in [MPa]
Ib = 5.659028852983059e+07;  %Beam Secound Moment of Area in [mm^4]
yb = 165.67;                 %Beam nutral axis [mm]
Thb = 11e-6;                 %Beam Coefficient of Thermal Expansion
in [/C]

%Plate properties
tp = 1.4;                   %Plate Thikness in [mm]
wp = 100;                   %Plate Wedth in [mm]
Ap = tp*wp;                 %Plate Area in [mm^2]
Ep = 170000;                %Plate Modulus of Elasticity in [MPa]
Ip = (wp*tp^3)/12;          %Plate Secound Moment of Area in [mm^4]
Thp = 0.6e-6;               %Plate Coefficient of Thermal Expansion
in [/degC]

Lb = 2700;                  %The Length of  Plate Beam in [mm]
Lp = 1350;                  %The Length of  CFRP Plate in [mm]
```

```
Bb = 1000;                  %The Distance of the Point Load from the
support [mm]
L0 = 0.5*(Lb-Lp);           %The Space between the supports and the
plate ends in [mm]
per = 0.5;
h = (per*Lp)/(n-1);

%Adhesive properties changes with temperature
 [Reductionfactor] =
DMA_Curves_Temperature_Thesis( curingtemperature,
Adhesivetemperature, Roomtemperature );

if Adhesivetemperature <= Roomtemperature;
   Adhesivetemperature  = Roomtemperature;
   Reductionfactor = 1;
end
   reducedmodulus = Reductionfactor
   reducedshearmodulus = Reductionfactor;
   reducedshearstrength = Reductionfactor;

%Adhesive properties
ta = 1.3 ;                  %Adhesive Thikness in [mm]
Ea = 4500;                  %Adhesive Modulus of Elasticity in [MPa]
shearmax = 1000;              %Adhesive maximun Shear Stress [MPa]
normalmax= 1000;              %Adhesive maximun Shear Stress [MPa]
Ga  = 1692;                 %Adhesive Shear Modulus [MPa]
gammamax =shearmax/Ga;      %Adhesive maximun shear strain

HeatedEa = Ea*reducedmodulus;                    %Adhesive Modulus of
Elasticity in [MPa]
Heatedshearmax = shearmax*reducedshearstrength; %Adhesive maximun
Shear Stress [MPa]
Heatednormalmax= normalmax*reducedshearstrength;%Adhesive maximun
Normal Stress [MPa]
HeatedGa  = Ga*reducedshearmodulus;              %Adhesive Shear
Modulus [MPa]
Heatedgammamax =Heatedshearmax/HeatedGa;         %Adhesive maximun
shear strain

%Heated Area
HeatedSn=floor(0.5*HeatedSL/h);
HeatedEn=floor(0.5*HeatedEL/h);
if HeatedSn==0;
   HeatedSn=1;
end
% Vector creation
c3    = zeros (n,1);
c1    = zeros (n,1);
c2    = zeros (n,1);
o1    = zeros (n,1);
o2    = zeros (n,1);
k     = zeros (n,1);
c6    = zeros (n,1);
c5    = zeros (n,1);
c4    = zeros (n,1);
u1    = zeros (n,1);
u2    = zeros (n,1);
```

```
v     = zeros (n,1);
A     = zeros (n,n);
B     = zeros (n,1);
A2    = zeros (n,n);
B2    = zeros (n,1);
shear = zeros (n/2,1);
gamma = zeros (n/2,1);
slip  = zeros (n/2,1);
normal= zeros (n/2,1);
curpbx =zeros (n/2,1);
curpbx1=zeros (n/2,1);
epspbth=zeros (n/2,1);
epspbx =zeros (n/2,1);
Gaa    =zeros (n,1);
Eaa    =zeros (n,1);
mp    = zeros (n/2,1);
np    = zeros (n/2,1);
lnp   = zeros (n/2,1);
m     = zeros (n/2,1);

for i=1:n
    Gaa (i,1)= Ga;
for ii=HeatedSn:HeatedEn+1
    Gaa (ii,1)= HeatedGa;
end
end
for i=1:n
    Eaa (i,1)= Ea;
for ii=HeatedSn:HeatedEn+1
    Eaa (ii,1)= HeatedEa;
end
end
%Reaction &  Calculation
R1 = 1000*P/2;
%Strain Eq.
for g=HeatedSn:HeatedEn
   epspbth (g,1)= DT*(Thp-Thb);
   epspbth (g+1,1)= DT*(Thp-Thb);
end
hh=0;
for i=1:n/2
    if hh-(Bb-L0)<0
       xb=0;
    else xb=hh-(Bb-L0);
    end
    m (i,1)=  R1*((hh+L0)-xb);
    hh=hh+2*h;
end

for i=1:n/2
    epspbx (i,1) = epspbth (i,1) - (((yb-05*ta)/(Eb*Ib)) * m (i,1));
end
ii=1;
for i=n/2+1:n
    curpbx (i,1) = ((1/(Eb*Ib)) * m (ii,1));
    ii=ii+1;
end
```

```
for i=1:n/2
    curpbx1 (i,1)= curpbx (n/2+i);
end

%Shear Stress
z = yb+ta+0.5*tp;
yp = 0.5*tp;
for i=1:n/2
    c3 (i,1)= ta/(Gaa(i,1)*b);
    c1 (i,1)= (1/(Ep*Ap))+(1/(Eb*Ab))+(((yp+yb)*(2*yb-
ta))/(2*(Eb*Ib)));
    c2 (i,1)= (yb/(Eb*Ib))-(yp/(Ep*Ip))+((0.5*ta)*(((1/(Ep*Ip))-
(1/(Eb*Ib)))));
    o1 (i,1)= c1 (i,1)/c3(i,1);
    o2 (i,1)= c2 (i,1)/c3(i,1);
    k  (i,1)= 1/c3 (i,1);
end
for i=n/2:n
    c6 (i,1) = ta/(Eaa (i,1)*b);
    c4 (i,1)= (yb+yp)/(Eb*Ib);
    c5 (i,1)= (1/(Ep*Ip))+(1/(Eb*Ib));
    u1 (i,1)= c4 (i,1)/c6 (i,1);
    u2 (i,1)= c5 (i,1)/c6 (i,1);
    v  (i,1)= 1/c6 (i,1);
end
for i=1:n
    for j=1:n/2
        if i==j
        A(i,j)=-(2+(o1 (i,1)*h^2)-(o2 (i,1)*yp*h^2));
        end
    end
    for j=1+n/2:n
        if i==j
        A(i,j)= 6 + (u2 (i,1)*h^4);
        end
    end
end
for i=1:n
    for j=1:n/2
        if i==j-1
        A(i,j)=1;
        elseif i==j+1
        A(i,j)=1;
        end
    end
    for j=1+n/2:n
        if i==j-1
        A(i,j)=-4;
        elseif i==j+1
        A(i,j)=-4;
        elseif i==j-2
        A(i,j)=1;
        elseif i==j+2
        A(i,j)=1;
        end
    end
end
```

```
for i=1:n
    for j=1:n
        if i==j-n/2
            A (i,j) = -o2 (i,1)*h^2;
        end
    end
end
for i=1+n/2:n
    for j=1:n
        if i==j+n/2
            A (i,j) = 6*yp + (u1 (i,1)*h^4);
        end
    end
    for j=1:n
        if i==(j+n/2)-1
        A(i,j)=-4*yp;
        elseif i==(j+n/2)+1
        A(i,j)=-4*yp;
        elseif i==(j+n/2)-2
        A(i,j)=1*yp;
        elseif i==(j+n/2)+2
        A(i,j)=1*yp;
        end
    end
end
%zero point at the overlap cells
A(n/2,n/2+1)=0;
A(n/2,n/2+2)=0;
A(n/2-1,n/2+1)=0;
A(n/2+1,n/2)=0;
A(n/2+1,n/2-1)=0;
A(n/2+2,n/2)=0;
A(n,n/2+1)=0;
A(n,n/2+2)=0;
A(n-1,n/2+1)=0;


%Plate force from shear equations
A(n/2,n/2-1)=1;
A(n/2,n/2)=-0.5*(2+(o1 (n/2,1)*h^2)-(o2 (n/2,1)*yp*h^2));

%Plate moment from shear equations
A(1,n/2+1)=0;

%Plate moment from normal equations
A(n/2+1,n/2+2)=0;
A(n/2+1,n/2+3)=1;
A(n,n)= 3 + (u2 (i,1)*h^4);
A(n-1,n-1)= 3 + (u2 (i,1)*h^4);
A(n,n-1)=-4;
A(n,n-2)=1;
A(n-1,n-2)=-4;
A(n-1,n-3)=1;
A(n-1,n)=0;

%Plate force from normal equations
A(n/2+1,2)=0;
```

```
A(n/2+1,3)=yp;
A(n,n/2)=  3*yp + (u1 (i,1)*h^4);
A(n-1,n/2-1)=  3*yp + (u1 (i,1)*h^4);
A(n,n/2-1)=-4*yp;
A(n,n/2-2)=1*yp;
A(n-1,n/2-2)=-4*yp;
A(n-1,n/2-3)=1*yp;
A(n-1,n/2)=0;

for i=1:n/2
    B(i,1)= epspbx (i,1) * k (i,1) * h^2;
end
    B(i,1)=0.5*epspbx (i,1) * k (i,1) * h^2;
for i=n/2+1:n
    B(i,1)= curpbx (i,1) * v (i,1) * h^4;
end
x=A\B;
X (2:n+1,1)= x;

%Plate Force
for i=1:n/2
    np (i,1)=X(i);
end
%Plate Moment
for i=1:n/2
    mp (i,1)=X(n/2+i);
    mp (1,1)=0;
end
hh=0;
for g=1:n/2
    lnp (g,1)=hh;
    hh=hh+2*h;
end
%Shear Stress
for g=2:n/2-1
    hh=hh+2*h;
    shear (1,1)   = ((-np(3,1)+4*np(2,1)-3*np(1,1))/(2*h*b));
    gamma (1,1)   = shear (1,1)/Gaa (1,1);
    slip  (1,1)   = ta * gamma (1,1);
    shear (g,1)   = (np(g+1,1)-np(g-1,1))/(2*h*b);
    gamma (g,1)   = shear (g,1)/Gaa (g,1);
    slip  (g,1)   = ta * gamma (g,1);
    shear (n/2,1) = ((np(n/2-2,1)-4*np(n/2-
1,1)+3*np(n/2,1))/(2*h*b));
    gamma (n/2,1) = shear (n/2,1)/Gaa (n/2,1);
    slip  (n/2,1) = ta * gamma (n/2,1);
end

%Normal Stress
for g2=2:n/2-1
    normal (1,1)  = ((2*mp(1,1)-5*mp(2,1)+4*mp(3,1)-
mp(4,1))/(h*h*b))+ yp*((2*np(1,1)-5*np(2,1)+4*np(3,1)-
np(4,1))/(b*h^2));
    normal (g2,1) = ((mp(g2-1,1)-
2*mp(g2,1)+mp(g2+1,1))/(b*h^2))+yp*(np(g2-1,1)-
2*np(g2,1)+np(g2+1,1))/(b*h^2);
```

```
    normal (n/2,1)= ((2*mp(n/2,1)-5*mp(n/2-1,1)+4*mp(n/2-2,1)-
mp(n/2-3,1))/(h*h*b))+ yp*((2*np(n/2,1)-5*np(n/2-1,1)+4*np(n/2-2,1)-
np(n/2-3,1))/(b*h^2));
end

ips=0;
for i=0:n/2-1
    if shear (i+1,1) > shearmax
        ips = ips + 1;
    end
end

%Modified Streses
while shear (1,1)/Heatedshearmax>=1+1E-20
for i=1:n
    for j=1:n/2
        if i==j
        A(i,j)=-(2+(o1 (i,1)*h^2)-(o2 (i,1)*yp*h^2));
        if j<=ips
            A (i,j) = -2;
        end
        end
    end
    for j=1+n/2:n
        if i==j
        A(i,j)= 6 + (u2 (i,1)*h^4);
        if j<=ips+n/2
            A (i,j) = 6;
        end
        end
    end
end


for i=1:n
    for j=1:n/2
        if i==j-1
        A(i,j)=1;
        elseif i==j+1
        A(i,j)=1;
        end
    end
    for j=1+n/2:n
        if i==j-1
        A(i,j)=-4;
        elseif i==j+1
        A(i,j)=-4;
        elseif i==j-2
        A(i,j)=1;
        elseif i==j+2
        A(i,j)=1;
        end
    end
end

for i=1:n
    for j=1:n
```

```
        if i==j-n/2
            A (i,j) = -o2 (i,1)*h^2;
        if j-n/2<=ips
           A (i,j) = 0;
        end
        end
    end
end
for i=1+n/2:n
    for j=1:n
        if i==j+n/2
            A (i,j) = 6*yp + (u1 (i,1)*h^4) ;
        if j+n/2<=ips+n/2
           A (i,j) = 6*yp;
        end
        end
    end
    for j=1:n
        if i==(j+n/2)-1
        A(i,j)=-4*yp;
        elseif i==(j+n/2)+1
        A(i,j)=-4*yp;
        elseif i==(j+n/2)-2
        A(i,j)=1*yp;
        elseif i==(j+n/2)+2
        A(i,j)=1*yp;
        end
    end
end
%zero point at the overlap cells
A(n/2,n/2+1)=0;
A(n/2,n/2+2)=0;
A(n/2-1,n/2+1)=0;
A(n/2+1,n/2)=0;
A(n/2+1,n/2-1)=0;
A(n/2+2,n/2)=0;
A(n,n/2+1)=0;
A(n,n/2+2)=0;
A(n-1,n/2+1)=0;

%Plate force from shear equations
A(n/2,n/2-1)=1;
A(n/2,n/2)=-0.5*(2+(o1 (n/2,1)*h^2)-(o2 (n/2,1)*yp*h^2));

%Plate moment from shear equations
A(1,n/2+1)=0;

%Plate moment from normal equations
A(n/2+1,n/2+2)=0;
A(n/2+1,n/2+3)=1;
A(n,n)= 3 + (u2 (i,1)*h^4);
A(n-1,n-1)= 3 + (u2 (i,1)*h^4);
A(n,n-1)=-4;
A(n,n-2)=1;
A(n-1,n-2)=-4;
A(n-1,n-3)=1;
A(n-1,n)=0;
```

```
%Plate force from normal equations
A(n/2+1,2)=0;
A(n/2+1,3)=yp;
A(n,n/2)=  3*yp + (u1 (i,1)*h^4);
A(n-1,n/2-1)=  3*yp + (u1 (i,1)*h^4);
A(n,n/2-1)=-4*yp;
A(n,n/2-2)=1*yp;
A(n-1,n/2-2)=-4*yp;
A(n-1,n/2-3)=1*yp;
A(n-1,n/2)=0;

for i=1:n/2
    B(i,1)= epspbx (i,1) * k (i,1) * h^2;
    if i<=ips;
       B (i,1)=0;
    end
end
B(i,1)=0.5*epspbx (i,1) * k (i,1) * h^2;

for i=n/2+1:n
    B(i,1)= curpbx (i,1) * v (i,1) * h^4;
    if i<=ips+n/2
       B (i,1) = 0;
    end
end
x=A\B;
X (2:n+1,1)= x;

for i=1:n/2
    np (i,1)=X(i);
end
for i=1:n/2
    mp (i,1)=X(n/2+i);
    mp (1,1)=0;
end

hh=0;
for g=1:n/2
    lnp (g,1)=hh;
    hh=hh+2*h;
end

%Shear Stress
for g=2:n/2-1
    hh=hh+2*h;
    shear (1,1)   = ((-np(3,1)+4*np(2,1)-3*np(1,1))/(2*h*b));
    gamma (1,1)   = shear (1,1)/Gaa (1,1);
    slip  (1,1)   = ta * gamma (1,1);
    shear (g,1)   = (np(g+1,1)-np(g-1,1))/(2*h*b);
    gamma (g,1)   = shear (g,1)/Gaa (g,1);
    slip  (g,1)   = ta * gamma (g,1);
    shear (n/2,1) = ((np(n/2-2,1)-4*np(n/2-
1,1)+3*np(n/2,1))/(2*h*b));
    gamma (n/2,1) = shear (n/2,1)/Gaa (n/2,1);
    slip  (n/2,1) = ta * gamma (n/2,1);
end
```

```
%Normal Stress
for g2=2:n/2-1
    normal (1,1)  = ((2*mp(1,1)-5*mp(2,1)+4*mp(3,1)-
mp(4,1))/(h*h*b))+ yp*((2*np(1,1)-5*np(2,1)+4*np(3,1)-
np(4,1))/(b*h^2));
    normal (g2,1) = ((mp(g2-1,1)-
2*mp(g2,1)+mp(g2+1,1))/(b*h^2))+yp*(np(g2-1,1)-
2*np(g2,1)+np(g2+1,1))/(b*h^2);
    normal (n/2,1)= ((2*mp(n/2,1)-5*mp(n/2-1,1)+4*mp(n/2-2,1)-
mp(n/2-3,1))/(h*h*b))+ yp*((2*np(n/2,1)-5*np(n/2-1,1)+4*np(n/2-2,1)-
np(n/2-3,1))/(b*h^2));
end

ips=ips+1;
end

figure (1)
%clf
plot (lnp,shear,'red'), grid on
hold on
plot (lnp,normal,'red'), grid on
title('[SHEAR AND NORMAL STRESS]')
xlabel('Position [mm]')
ylabel('Shear and Normal Stress [MPa]')
xlim([0 HeatedEL])
%hold off
drawnow

figure (2)
%clf
axis equal
subplot(2,2,1)
plot (lnp,epspbx,'black'), grid on
xlabel('Position [mm]')
ylabel('Strain Distribution')
xlim([0 HeatedEL])
hold on
subplot(2,2,2)
hold on
plot (lnp,curpbx1,'cyan'), grid on
xlabel('Position [mm]')
ylabel('Curvecure Distribution')
xlim([0 HeatedEL])

subplot(2,2,3)
%clf
plot (lnp,np,'black'), grid on
hold on
title('[SPLATE FORCE]')
xlabel('Position')
ylabel('Plate force [kN]')
xlim([0 HeatedEL])
%hold off
drawnow

subplot(2,2,4)
```

```
%clf
plot (lnp,mp,'cyan'), grid on
hold on
title('[SPLATE MOMENT]')
xlabel('Position')
ylabel('Plate moment [kN.m')
xlim([0 HeatedEL])
%hold off
drawnow


figure (3)
subplot(2,2,1)
%clf
plot (lnp,shear,'black'), grid on
hold on
title('[SHEAR STRESS]')
xlabel('Position')
ylabel('Shear stress')
xlim([0 HeatedEL])
%hold off
drawnow

subplot(2,2,2)
%clf
plot (lnp,normal,'black'), grid on
hold on
title('[NORMAL STRESS]')
xlabel('Position')
ylabel('Normal stress')
xlim([0 HeatedEL])
%hold off
drawnow

subplot(2,2,3)
%clf
plot (lnp,slip,'black'), grid on
hold on
title('[PLATE SLIP]')
xlabel('Position [mm]')
ylabel('SLIP AT THE END OF THE PLATE [mm]')
xlim([0 HeatedEL])
%hold off
drawnow

subplot(2,2,4)
%clf
plot (lnp,gamma,'black'), grid on
hold on
title('[SHEAR STRAIN]')
xlabel('Position')
ylabel('Shear strain')
xlim([0 HeatedEL])
%hold off
drawnow
```

```
plasticlength (it,1)= ips*h;
temperature (it,1)= Platetemperature;
slippage (it,1)= slip(1,1);
load (it,1)= P;

it=it+1;
end
end
figure (4)
plot (temperature, slippage,'black'), grid on
title('[SLIPPAGE WITH TEMPERATURE VARIATION]')
xlabel('Temperature [degC]')
ylabel('Slippage [mm]')
xlim([0 max(Platetemperature)])
drawnow

figure (13)
plot (lnp,np,'red'), grid on
hold on
title('[SPLATE FORCE]')
xlabel('Position')
ylabel('Plate force [kN]')
drawnow

figure (14)
plot (lnp,mp,'red'), grid on
hold on
title('[SPLATE MOMENT]')
xlabel('Position')
ylabel('Plate moment [kN.m')
drawnow



nn (nn1,1) = n
shear1 (nn1,1)= max (shear)
normal1 (nn1,1)= max (normal)
nn1 =nn1+1
toc



%%% DMA Modulus variation with Temperature %%%

function [Reductionfactor] =
DMA_Curves_Temperature_Thesis( curingtemperature,
Adhesivetemperature, Roomtemperature )
clc
%UNTITLED Summary of this function goes here
%   Detailed explanation goes here

if curingtemperature == 5;
DMA = xlsread ('C:\Users\Daryan\Documents\MATLAB\All Bond
Modeling\FDM\Thesis analysis\Thesis_DMA_Combination.xls', 'Beam5');
end
if curingtemperature == 6;
```

```
DMA = xlsread ('C:\Users\Daryan\Documents\MATLAB\All Bond
Modeling\FDM\Thesis analysis\Thesis_DMA_Combination.xls', 'Beam6');
end
if curingtemperature == 7;
DMA = xlsread ('C:\Users\Daryan\Documents\MATLAB\All Bond
Modeling\FDM\Thesis analysis\Thesis_DMA_Combination.xls',
'Beam7&8');
end
if curingtemperature == 8;
DMA = xlsread ('C:\Users\Daryan\Documents\MATLAB\All Bond
Modeling\FDM\Thesis analysis\Thesis_DMA_Combination.xls',
'Beam7&8');
end

time           = DMA (3:end,1);
temperature    = DMA (3:end,2);
complexmodulus = DMA (3:end,3);

i0=4;
while DMA (i0,2) <= 0 || DMA (i0,2) == 0
    i0=i0+1;
end

if DMA (i0,2) > abs (DMA (i0-1,2))
   i0= i0-1;
end
  Time0 = DMA (i0,1);
  Temp0 = DMA (i0,2);
  complexmodulus0 = DMA (i0,3);

iRoomtemperature=i0;
while DMA (iRoomtemperature,2) <= Roomtemperature || DMA
(iRoomtemperature,2) == Roomtemperature
 iRoomtemperature = iRoomtemperature + 1;
end

if DMA (iRoomtemperature,2) - Roomtemperature > DMA
(iRoomtemperature - 1,2) - Roomtemperature
   iRoomtemperature= iRoomtemperature - 1;
end
TimeRoomtemperature = DMA (iRoomtemperature,1);
TempRoomtemperature = DMA (iRoomtemperature,2)
complexmodulusRoomtemperature = DMA (iRoomtemperature,3);
iAdhesivetemperature = iRoomtemperature;
while DMA (iAdhesivetemperature,2)  <= Adhesivetemperature || DMA
(iAdhesivetemperature,2) == Adhesivetemperature
 iAdhesivetemperature = iAdhesivetemperature + 1;
end

if DMA (iAdhesivetemperature,2) - Adhesivetemperature > DMA
(iAdhesivetemperature - 1,2) - Adhesivetemperature
   iAdhesivetemperature = iAdhesivetemperature - 1;
end
Adhesivetime = DMA (iAdhesivetemperature,1);
Adhesivetemperature = DMA (iAdhesivetemperature,2);
Adhesivemodulustemperature = DMA (iAdhesivetemperature,3);
```

```
Reductionfactor = DMA (iAdhesivetemperature,3)/DMA
(iRoomtemperature,3);

figure (8)
plot (temperature,complexmodulus/DMA (iRoomtemperature,3)), grid on
hold on
scatter(DMA(iAdhesivetemperature,2),(DMA
(iAdhesivetemperature,3)/DMA (iRoomtemperature,3)),80,'r','filled')
title('[Temperature Vs. Complexmodulus]')
xlabel('Temperature [C deg]')
ylabel('Normalised Complexmodulus [Mpa]')
xlim([0 120])
ylim([0 1.2])
drawnow

figure (9)
plot (time,complexmodulus/DMA (iRoomtemperature,3)), grid on
hold on
scatter(DMA(iAdhesivetemperature,1),(DMA
(iAdhesivetemperature,3)/DMA (iRoomtemperature,3)),80,'r','filled')
title('[Time Vs. Complexmodulus]')
xlabel('Time [Min]')
ylabel('Normalised Complexmodulus [Mpa]')
xlim([0 60])
ylim([0 1.2])
drawnow
end
```